CORA Cork Open Research Archive
Cartlann Taighde Oscailte Chorcaí

Title	Heterogeneous catalysts for the degradation and upcycling of plastic waste
Authors	Breen, Rachel
Publication date	2025
Original Citation	Breen, R. 2025. Heterogeneous catalysts for the degradation and upcycling of plastic waste. PhD Thesis, University College Cork.
Type of publication	Doctoral thesis
Rights	© 2025, Rachel Breen. - https://creativecommons.org/licenses/by-nc-nd/4.0/
Download date	2026-11-02 23:36:45
Item downloaded from	https://hdl.handle.net/10468/18440



UCC
University College Cork, Ireland
Coláiste na hOllscoile Corcaigh

Heterogeneous Catalysts for the Degradation and Upcycling of Plastic Waste



A thesis presented for the degree of Doctor of Philosophy to the National University of Ireland, Cork

September 2025

Thesis Presented By:

Rachel Breen, BSc

School of Chemistry

University College Cork, Ireland

Head of School: Prof. Anita Maguire

Supervisor: **Dr Gillian Collins**

Co-supervisor: **Prof. Justin Holmes**

Declaration

This is to certify that the work I am submitting is my own and has not been submitted for another degree, either at University College Cork or elsewhere. All external references and sources are clearly acknowledged and identified within the contents. I have read and understood the regulations of University College Cork concerning plagiarism and intellectual property.

Signed

Rachel Breen

Rachel Breen

Abstract

This thesis investigates the development and optimisation of heterogeneous catalytic processes to convert waste polymers into high-value product streams, providing a sustainable alternative to current global plastic management strategies. An emphasis is placed on catalyst design and characterisation, optimisation of reaction parameters such as catalyst and reagent loadings, reaction time and temperature and product analysis. The aim for Chapter 3 was to design and synthesise various heterogeneous catalysts for the glycolysis of polyethylene terephthalate (PET) to its monomer bis(2-hydroxyethyl)terephthalate (BHET). A porous SiO_2 support was implemented and functionalised with different amine ligands which were suitable for iron ion immobilisation. The nature of the organic ligand influenced the steric and electronic effects which influenced the catalytic behaviour. Nanoparticles were synthesised via calcination and chemical reduction from the ion immobilised catalysts which were found to possess superior catalytic activity. The nanoparticle catalyst synthesised by chemical reduction gave the highest mass loss PET and isolated yield BHET. X-ray photoelectron spectroscopy (XPS) analysis revealed the preservation of the organic ligand for the chemically reduced nanoparticle catalyst which was responsible for the enhanced activity relative to other catalysts owing to dual catalytic activity occurring from the iron nanoparticle and the amine ligand.

Some activity from the ligand-only catalysts in Chapter 3 influenced the work presented in Chapter 4 which focuses on the development of metal-free heterogeneous catalysts for the depolymerisation of PET and PLA. Three guanidine catalysts were immobilised on porous SiO_2 with a range of nitrogen environments and were evaluated under conventional thermal and microwave assisted heating methods to find the best method for converting these plastics to their monomers with high yields. The use of microwave-assisted heating dramatically shortened reaction times. The guanidine ligand with the most nitrogen environments was the best performing, indicative that the availability of nitrogen environments was crucial for both PET and PLA depolymerisation.

The motivation for Chapter 5 arose from a review of the literature, which highlighted that polyolefins, such as polyethylene, have significantly higher global production rates than polyesters like PET. Additionally, literature article outputs on the chemical recycling of polyolefins significantly lacked when compared with output of polyesters, likely owing to the challenges associated with chemical inertness and stability of polyolefins, making them resistant to chemical degradation. Chapter 5 describes the method development for the Fenton oxidation of low-density polyethylene (LDPE). The product mixture was screened using high performance liquid chromatography (HPLC) and the main products identified were short chain mono and di carboxylic acids. Two catalyst families were developed: metal oxide composite catalysts and carbon-based catalysts, which were used to optimise the Fenton oxidation process. The superior activity of a Fe_2O_3-CeO_2 composite in Chapter 5 motivated the development of Chapter 6, while the use of carbon-based catalysts formulated the motivation behind Chapter 7.

Chapter 6 describes the synthesis of a Fe-CeO_2 solid solution catalyst synthesised in 3 Fe:Ce ratios. Each of the solid solution catalysts outperformed bare Fe_2O_3 and CeO_2 which was attributed to a synergistic and stabilisation effect of the Fe-CeO_2 composite. The presence of solid solution formation was confirmed using Raman spectroscopy, X-ray diffraction (XRD) and transmission electron microscopy (TEM), with CeO_2 lattice saturation and formation of Fe_2O_3 aggregates evident for the catalyst with the highest Fe loading. The catalyst with a 1:1 molar ratio resulted in the highest mass loss LDPE and carboxylic acid yield highlighting the importance of tuning metal molar ratio in the catalyst. The catalysts were also effective at pH7 and exhibited excellent recyclability owing to the stability of the solid solution structure. An appendix to chapter 6 outlines the results of a collaborative project carried out with the School of Physics in Trinity College Dublin on the synthesis and characterisation of quasi-2D Fe-CeO_2 nanoflakes obtained from cryogenic exfoliation.

Chapter 7 examines the application of unmodified biochar as a sustainable, carbon-based catalyst for the Fenton-type oxidation of low-density polyethylene (LDPE) into low-molecular-weight carboxylic

acids. The influence of biochar source and pyrolysis temperature on material properties was characterised using multiple analytical techniques, and catalytic performance was evaluated in relation to these physicochemical properties. As part of collaborative work with the School of Engineering in University College Cork, anaerobic digestion was employed to convert the product mixtures of carboxylic acids to methane as a potential strategy to mitigate complex downstream processing for short-chain carboxylic acids. An appendix to Chapter 7 outlines the development of a sustainable materials workshop developed for undergraduate students on the characterisation of biochar. The workshop is centred around the complexity of biochar's structure and promotes collaborative efforts between undergraduate and postgraduate students. This thesis will be presented in the format of Thesis by Publication.

Acknowledgements

I would like to wholeheartedly thank my supervisor Dr Gillian Collins and co-supervisor Prof. Justin Holmes. Thank you both for granting me the opportunity to pursue a PhD and for supporting me all the way. Gillian, thank you for your endless encouragement, pep talks and patience with correcting. Thank you both for being great fun and for making my experience a brilliant one.

Thank you to technical staff, especially Dr Ian O Connor and Dr Trevor Carey for supporting me when I needed it. Thank you to technical officers Dr Sally O Hanlon, Dr Tom O Mahony, Dr Donal Keane and Dr Dennis Lynch for your help with instrumentation and running analysis. A special thank you to Dr Anna Hogan for her generous support and assistance with HPLC, which was invaluable for my research. Thank you also to all support and administration staff especially to Tina, Imelda and Mark for all your help over the years.

Thank you to MCAG and lunch crew members past and present for the laughs and the nights out over the years. Special thanks to Éadaoin for taking me under her wing when I first started and for the bench breaks when we needed them! Thank you to Eleanor for our sunny walks to the ERI and iced coffees; to Anjali for her excellent company in 115, and to Rupa for her generosity and help with analysis in Tyndall. I am also grateful to the girls in Gillian's group—Doireann, Rebecca, Clodagh, and Forest – you are all amazing and the coffee breaks and laughs have made writing that bit easier.

To my friends – Clodagh, Hollie, Aislinn, Lauren, Mary, Aoife, Jessie, Ciara and Tim for your support and understanding over the past 4 years – you are all the best friends I could ask for. To Niall – Thank you for always being there - your support and encouragement have meant so much to me.

To my fantastic family – Mom, Dad, Clare and Lucy – your love, understanding, patience and support has gotten me through the last 4 years. I am very lucky to have you all.

Abbreviations

AC	Activated Carbon
ACA	ϵ-aminocaproic acid
AD	Anaerobic Digestion
BDHETA	N^1,N^1,N^4N^4-tetrakis-(2-hydroxy-ethyl)-terephthalamide
BE	Binding Energy
BET	Brauner-Emmet-Teller
BHBT	Bis(4-hydroxybutyl terephthalate)
BHEOET	Bis-[2-(2-hydroxy-ethoxy)-ethylterephthalate
BHET	Bis(hydroxyethyl) terephthalate
BHETA	Bis(2-hydroxyethyl) terephthalamide
BI	Biodegradability Index
BPA	Bis phenol A
BTX	Benzene, Toluene, Xylene
CI	Carbonyl Index
CNT	Carbon Nanotube
COD	Chemical Oxygen Demand
CPMAS	Cross-Polarisation Magic-Angle Spinning
DAT	Diamine Toluene
DEA	Diethylamine
DEG	Diethylene Glycol
DFT	Density Functional Theory
DMT	Dimethyl Terephthalate
DOC	Dissolved Organic Carbon
EA	Ethylamine
EDX	Energy Dispersive X-ray
EG	Ethylene Glycol
EtLA	Ethyl Lactate
ETOH	Ethanol
FTIR	Fourier Transform Infrared Spectroscopy
HDMA	Hexamethylenediamine
HDPE	High-density Polyethylene
HPLC	High Performance Liquid Chromatography
HTMAB	Hexadecyltrimethylammonium Bromide

LCA	Life Cycle Assessment
LDPE	Low-density Polyethylene
LHV	Lower Heating Value
MA	Methylamine
MAH	Monocyclic Aromatic Hydrocarbon
MCF	Mesoporous Cellular Foam
MeLA	Methyl Lactate
MEOH	Methanol
MOF	Metal Organic Framework
MW	Microwave
MWAHE	Microwave-Absorbing Heating Element
MWCNT	Multi-walled Carbon Nanotube
NMR	Nuclear Magnetic Resonance
NP	Nanoparticle
ON	Octane Number
PA	Polyamide
PBT	Polybutylene terephthalate
PC	Polycarbonate
PES	Polyester
PET	Polyethylene Terephthalate
PLA	Polylactic acid
POP	Persistent Organic Pollutants
PP	Polypropylene
PPE	Personal Protective Equipment
PPTA	Poly(*p*-phenylene Terephthalamide)
PS	Polystyrene
PTC	Phase Transfer Catalyst
PUR	Polyurethane
PVC	Polyvinylchloride
SEM	Scanning Electron Microscopy
TEM	Transmission Electron Microscopy
THF	Tetrahydrofuran
TPA	Terephthalic Acid
TXRF	Total-reflection X-ray Fluorescence
URE	Undergraduate Research Experience

VFA	Volatile Fatty Acid
XPS	X-ray Photoelectron Spectroscopy
XRD	X-ray Diffraction

Thesis Outline

The purpose of this section is to present a high-level synthesis of the results chapters of this thesis and outline the interrelationship between its individual chapters components. It defines the central research question, outlines the primary objectives and themes, and explains how each chapter contributes to the resolution of the central research question.

The central research question for this thesis investigates if catalytic processes can be developed and optimised to convert waste polymers into high-value product streams, providing a sustainable alternative to current global plastic management strategies. This thesis aims to evaluate heterogeneous catalytic systems for plastic depolymerisation reactions to optimise reaction efficiency and yield of value-added products. An emphasis is placed on catalyst design and characterisation, optimisation of reaction parameters such as catalyst and reagent loadings, reaction time and temperature and product analysis.

At the outset of this doctoral research, collaborative work was carried out with Dr Éadaoin Casey, a senior PhD candidate, on the development and optimisation of heterogeneous catalytic systems for the glycolytic depolymerisation of polyethylene terephthalate (PET). The research focused on identifying key catalyst design parameters to improve the efficiency using Fe-immobilised on porous SiO_2 functionalised with different amine ligands. The outcomes of this study have been published in *ACS Sustainable Chemistry & Engineering* (full reference provided in the bibliography) and are presented in Chapter 3 of this thesis.

During the course of the research on ligand-aided Fe_2O_3 heterogeneous catalysts, glycolysis activity was unexpectedly observed in certain metal-free SiO_2 catalysts functionalised with amine ligands. This observation promoted the development of Chapter 4, which focuses on the synthesis and characterisation of metal-free heterogeneous catalysts based on guanidine-functionalised porous SiO_2, and investigates their application in the glycolysis of PET and the methanolysis of polylactic acid (PLA). This chapter demonstrates the advantages of microwave-assisted heating, which induced rapid

heating effects and significantly reduced reaction times. These findings provided a strong rationale for the continued application of microwave-assisted heating throughout the subsequent experimental work of this thesis and is published work in *RSC Sustainability*.

The thesis research initially focused on polyester depolymerisation, specifically targeting PET and PLA, where heterogeneous catalyst systems were developed and optimised. However, as the work progressed, attention pivoted towards polyolefins, specifically polyethylene, which has received comparatively less attention in the field of chemical recycling, despite being produced in significantly higher volumes than polyesters and exhibiting markedly low recycling rates. This identified gap in the literature motivated the development of the subsequent chapters of this thesis, which address the challenges associated with polyolefin recycling. Chapter 5 outlines the initial methodological development of heterogeneous catalysts for the microwave-assisted depolymerisation of low-density polyethylene (LDPE) into organic acid products, forming the foundation for the investigations presented in the later chapters.

Chapter 6 subsequently outlines a more detailed study on the design and synthesis of metal-based Fe-CeO_2 solid solution catalysts for microwave-assisted degradation of LDPE, and the work is published in *RSC Catalysis Science and Technology*. While working on Fe-CeO_2 catalysts, a collaborative interaction with the School of Physics in Trinity College Dublin led to the evaluation of cryogenic exfoliation for the synthesis of 2D Fe-CeO_2 nanoplatelets. The outcomes of this work are presented in an appendix to Chapter 6.

The development of metal-free catalysts for PET glycolysis in Chapter 4 and carbon-based catalysts for LDPE oxidation in Chapter 5 led to the motivation for Chapter 7. Chapter 7 investigates the use of biochar as a sustainable metal-free heterogeneous Fenton catalyst for LDPE oxidation. As part of a collaboration with the School of Engineering in UCC, this work also examines the potential of anaerobic digestion as a way of transforming the organic acid products obtained into methane. This manuscript is currently in review in *ACS Sustainable Chemistry and Engineering*.

An Appendix to Chapter 7 describes a publication that emerged from work related to Chapter 7, focusing on the characterisation of biochar. This project was carried out with a student participating in an Undergraduate Research Experience during a summer research placement. The resulting chemical education publication (*ACS Journal of Chemical Education*) outlined the integration of research into undergraduate teaching, which was further developed into a sustainable materials workshop for undergraduate students. Figure 1 provides an illustrative flow chart of the chapters presented in this thesis.

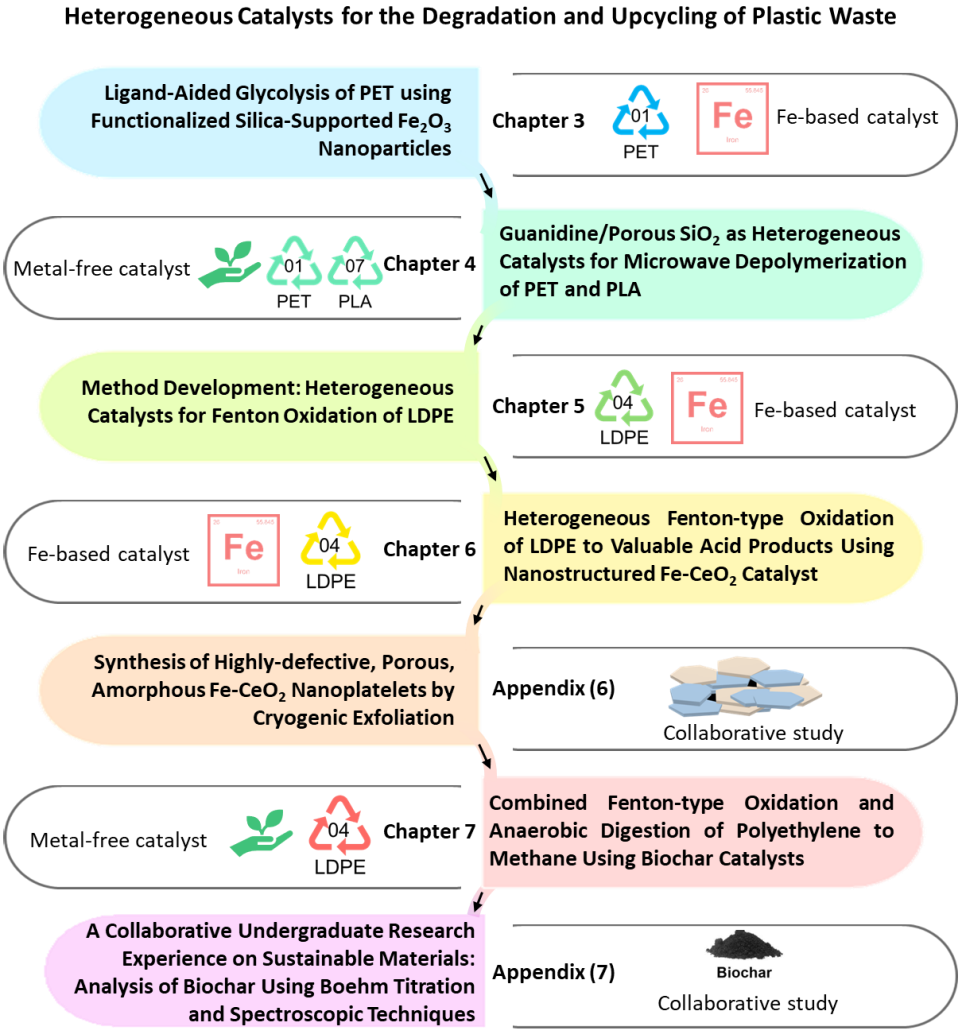


Figure 1: Schematic flow representation of chapters and appendices presented in this thesis.

Publications arising from this thesis:

The thesis is presented as a thesis by publication, collating the publications that have emerged from this work.

1. **Breen, R**; Holmes, J. D.; Collins, G. Recent Advances in Chemical Upcycling of Plastic Waste: Microwave-assisted Heating and Heterogeneous Catalysis. *RSC EES Catalysis* (in review). (Chapter 1)

2. Casey, É.; **Breen, R**.; Gómez, J. S.; Kentgens, A. P. M.; Pareras, G.; Rimola, A.; Holmes, J. D.; Collins, G. Ligand-Aided Glycolysis of PET Using Functionalized Silica-Supported Fe_2O_3 Nanoparticles. *ACS Sustainable Chemistry & Engineering* **2023**, *11* (43), 15544-15555. DOI: 10.1021/acssuschemeng.3c03585. (Chapter 3)

3. Casey, É.; **Breen, R**.; Pareras, G.; Rimola, A.; Holmes, J. D.; Collins, G. Guanidine functionalized porous SiO_2 as heterogeneous catalysts for microwave depolymerization of PET and PLA. *RSC Sustainability* **2024**, *2* (4), 1040-1051, 10.1039/D3SU00425B. DOI: 10.1039/D3SU00425B. (Chapter 4)

4. **Breen, R**.; Holmes, J. D.; Collins, G. Heterogeneous Fenton-type oxidative degradation of low-density polyethylene to valuable acid products using a nanostructured Fe–CeO_2 solid solution catalyst. *Catalysis Science & Technology* **2025**, 10.1039/D4CY01384K. DOI: 10.1039/D4CY01384K. (Chapter 6)

5. **Breen, R**.; Hackula, A.; Holmes, J. D.; Wall, D. M.; Collins, G. Combined Fenton-type Oxidation and Anaerobic Digestion of Polyethylene to Methane Using Biochar Catalysts**.** *ACS Sustainable Chemistry and Engineering* (in review). (Chapter 7)

6. **Breen, R**.; Goggin, C.; J.; Holmes, J. D.; Collins, G. A Collaborative Cocurricular Undergraduate Research Experience on Sustainable Materials: Analysis of Biochar Using the Boehm Titration and Spectroscopic Techniques. ACS *J. Chem. Educ.* 2025, 102, 3, 1323–1332 DOI: 10.1021/acs.jchemed.4c01110 (Appendix 7)

Table of Contents

Chapter 1: Introduction **1**

1.1 Introduction 2
1.2 Fundamentals of Microwave-assisted Catalysis 6
1.3 Microwave-assisted Heterogeneous Catalytic Upcycling of Polymers 12
1.3.1 Polyesters 12
1.3.2 Polyolefins 19
1.3.3 Other Plastics 29
1.4 Summary & Outlook 34
1.4 References 36

Chapter 2: Experimental **44**

2.1 Introduction 44
2.2 Electron Microscopy 44
2.3 Energy Dispersive X-ray Analysis (EDX) 46
2.4 Fourier Transform Infrared Spectroscopy (FTIR) 46
2.5 Raman Spectroscopy 47
2.6 Total-reflection X-ray Fluorescence Spectroscopy (TXRF) 48
2.7 X-ray Diffraction (XRD) 49
2.8 X-ray Photoelectron Spectroscopy 50
2.9 High-Performance Liquid Chromatography (HPLC) 52
2.10 Nuclear Magnetic Resonance Spectroscopy (NMR) 53
2.11 Milestone Flexiwave Microwave Reactor 54
2.12 References 56

Chapter 3: Ligand-Aided Glycolysis of PET Using Functionalised Silica-Supported Fe_2O_3 Nanoparticles **57**

3.1 Introduction 59
3.2 Results and Discussion 61
3.2.1 Catalyst design and synthesis 61
3.2.2 Catalytic evaluation of in PET glycolysis 68
3.3 Conclusions 78
3.4 References 80
3.5 Appendix: Supporting Information 84

Chapter 4: Guanidine Functionalised Porous SiO_2 as Heterogeneous Catalysts for Microwave Depolymerisation of PET and PLA **100**

4.1 Introduction 102
4.2 Results and Discussion 104
4.2.1 Synthesis and characterisation of guanidine functionalised SiO_2 104
4.2.2 Catalytic evaluation of heterogeneous guanidine catalysts 109
4.2.3 Mechanistic insights into cyanoguanidine functionalised SiO2 using density functional theory 116

4.2.4 PLA degradation mechanism..... 120
4.3 Conclusions..... 122
4.4 References..... 124
4.5 Appendix: Supporting Information..... 128

Chapter 5: Method Development: Heterogeneous Catalysts for Fenton Oxidation of LDPE 144

5.1 Introduction – A focus on polyolefin plastics..... 144
5.2 Experimental..... 149
5.2.1 Synthesis of metal oxide catalysts..... 150
5.2.2 Synthesis of ionic liquid-doped carbon catalysts..... 151
5.2.3 Fenton oxidation reactions..... 151
5.2.4 Product analysis..... 152
5.3 Results and discussion..... 153
5.3.1 Synthesis and characterisation of metal oxide composites as heterogeneous Fenton catalysts..... 153
5.3.2 Synthesis and characterisation of carbon-based heterogeneous Fenton catalysts..... 159
5.4 Conclusion & outlook..... 167
5.5 References..... 169

Chapter 6: Heterogeneous Fenton-type Oxidative Degradation of Low-density Polyethylene to Valuable Acid Products Using a Nanostructured Fe-CeO_2 Solid Solution Catalyst 173

6.1 Introduction..... 174
6.2 Results and Discussion..... 178
6.2.1 Synthesis and characterisation of Fe-CeO_2 solid solution..... 178
6.2.2 Catalytic evaluation of Fe-CeO_2 solid solution catalyst for oxidative degradation of polyethylene..... 185
.
6.2.3 Catalytic optimisation of polyethylene degradation under neutral pH..... 188
6.2.4 Reaction time series..... 190
6.2.5 Catalyst recyclability..... 192
6.3 Conclusions..... 196
6.4 References..... 198
6.5 Appendix I: Supporting Information..... 205
6.6 Appendix II: Characterisation of Fe-CeO_2 Nanoflakes Synthesised by Cryogenic Exfoliation..... 219

Chapter 7: Combined Fenton-type Oxidation and Anaerobic Digestion of Polyethylene to Methane Using Biochar Catalysts 237

7.1 Introduction 238
7.2 Results..... 242
7.2.1 Biochar characterisation..... 242
7.2.2 Catalytic evaluation of biochar for Fenton-type oxidative degradation of LDPE..... 249
7.2.3 Conversion of carboxylic acid products to methane via anaerobic digestion..... 252

7.2.4 Mass and energy balance: system mass and energy balances of integrated LDPE oxidation and anaerobic digestion..... 256
7.3 Conclusion & future work..... 258
7.4 References..... 261
7.5 Appendix I: Supporting Information..... 266
7.6 Appendix II: A Collaborative Co-Curricular Undergraduate Research Experience on Sustainable Materials: Analysis of Biochar using the Boehm Titration and Spectroscopic Techniques..... 279
7.6.1 Introduction..... 280
7.6.2 Motivation and objectives of activity..... 281
7.6.3 Experimental focus and design..... 282
7.6.4 Student feedback..... 298
7.6.5 Pedagogical reflection..... 299
7.6.6 Conclusion..... 300
7.6.7 References..... 302
7.6.8 Supporting Information..... 305

Chapter 8: Conclusions **319**

8.1 Conclusions & Outlook..... 319

Chapter 1

Recent Advances in Chemical Upcycling of Plastic Waste: Microwave-assisted Heating and Heterogeneous Catalysis

Rachel Breen[1,2], Justin D. Holmes[1,2], Gillian Collins[1,2]

[1] School of Chemistry, University College Cork, Cork, T12 YN60, Ireland.

[2] AMBER Centre, Sustainability Institute, University College Cork, Cork, T23 XE10, Ireland.

Publication: ***Breen, R****; Holmes, J. D.; Collins, G. Recent Advances in Chemical Upcycling of Plastic Waste: Microwave-assisted Heating and Heterogeneous Catalysis. RSC EES Catalysis (in review).*

Abstract

The chemical upcycling of plastic waste offers a sustainable pathway to transform discarded polymers into valuable chemical feedstocks and fuels. Among emerging approaches, microwave (MW)-assisted heating has gained significant attention for its ability to deliver rapid, uniform energy input, dramatically reducing reaction times compared with conventional thermal methods. When coupled with heterogeneous catalysis, MW irradiation can lower activation barriers for depolymerisation, enhance product selectivity and reduce overall energy demand. Heterogeneous catalysts also provide advantages in recovery, reuse and process scalability, making them attractive for industrial adoption. Recent research has focused on tailoring catalyst composition, structure, and surface properties to optimise MW–catalyst interactions across a wide range of polymer types, including polyesters, polyolefins, polystyrene, polyamides and polyvinyl chlorides. This review summarises the fundamental principles of MW-assisted catalysis and critically examines recent advances in catalyst design, reaction optimisation and mechanistic understanding.

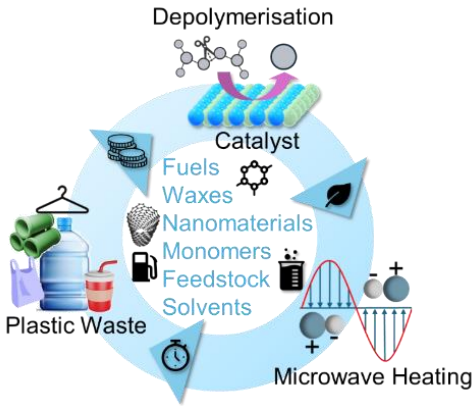


Table Of Contents Graphic

1.1 Introduction:

A material once described as the 'greatest finding in the millennium', now poses an undeniable threat to the future of our planet. Owing to its tensile strength, lightweight and versatility, plastic production has increase 200-fold since the 1940's[1]. Plastic pollution has become widespread across the environment, accumulating in both terrestrial and marine ecosystems and even within human bodies. It poses significant risks due to the release of chemical additives through leaching and degradation, as well as the formation of microplastics. These issues stem largely from the global mismanagement of plastic waste and the limitations of current recycling methods.

About 400 million tons of plastic is produced globally each year. Worldwide, it is estimated that only 9 % of plastic waste is recycled by mechanical recycling.[2, 3] This involves sorting, washing, grinding, melting and reprocessing of plastic waste into pellets for new products which often results in a downcycled, lower quality product. Polyolefins such as low-density polyethylene (LDPE) and polypropylene (PP) are generally unsuitable for mechanical recycling due to degradation of mechanical properties during processing as well as the presence of additives and multi-layered plastic structures.[4] While advancements in sorting technologies, decontamination protocols and pre-treatments have enhanced the viability of mechanical recycling as a valorisation pathway for certain plastic types, significant challenges remain including the limited capacity to process mixed and contaminated plastic wastes.[5] Incineration allows for energy recovery and it is estimated that about 10 % of household

energy requirements in Europe are currently fulfilled using this method.[6] However, incineration contributes to greenhouse gas emissions through the release of CO_2 and may also emit persistent organic pollutants (POP) which pose significant environmental and health risks.[7] According to reports by the Organisation for Economic Co-operation and Development (OECD)[3], 50 % of global waste plastic is disposed of in regulated landfill sites.[2] While landfilling is a low energy method that does not require sorting of plastic waste, it poses long term environmental risks such as the leaching of microplastics, additives and plasticisers into soil and water streams. The drawbacks associated with the current plastic waste management techniques have resulted in increasing attention towards chemical recycling of plastic waste. Chemical recycling enables upcycling of plastic waste by breaking them into original monomers (closed-loop recycling), which can be repolymerised into high-quality polymers. Alternatively, plastics can be converted into high quality fuels, feedstock chemicals or materials (open-loop recycling).[8-10] While energy requirements for chemical recycling methods are generally high to overcome polymer stability, approaches such as MW-assisted heating and catalyst development are being investigated to reduce energy usage and maximise efficiency.[11, 12] The European Commission's Joint Research Centre found that based on Life Cycle Assessments (LCA), mechanical and chemical recycling are far more beneficial from a climate perspective than landfill and incineration for energy recovery.[13] To address the limitations inherent to mechanical recycling, chemical recycling has emerged as a complementary approach capable of processing plastic waste streams for the recovery of monomers or valuable chemical feedstock. A summary of current plastic waste management methods compared with chemical recycling is presented in Figure 1 a).

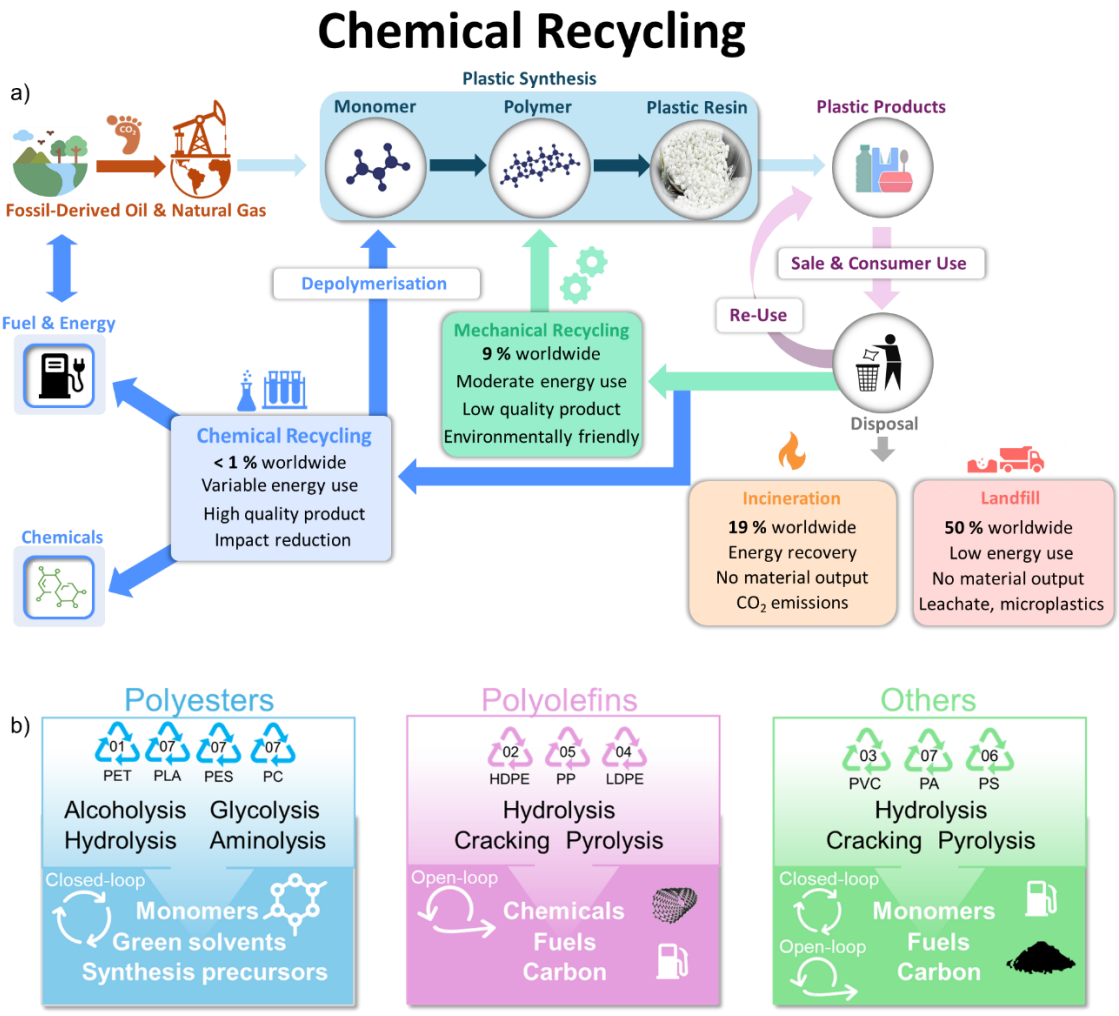


Figure 1: a) Outline of current plastic waste management strategies compared with chemical recycling.[3] b) Summary of key chemical recycling pathways for polyesters, polyolefins and other plastics.

A summary of chemical recycling pathways for polyesters, polyolefins and other plastics is illustrated in Figure 1 b. Polyesters such as PET, PLA, PES and polycarbonates (PC) are well-suited to selective depolymerisation methods such as alcoholysis, glycolysis, hydrolysis and aminolysis. These processes yield defined monomers, green solvents and chemical feedstocks that can be directly repolymerised, enabling closed-loop recycling. In contrast, polyolefins such as LDPE, PP, and high-density polyethylene (HDPE), due to their non-polar, saturated hydrocarbon backbones, primarily degrade via energy-intensive processes such as pyrolysis, catalytic cracking or oxidative degradation. These methods yield

a broader spectrum of products such as gases, liquid fuels, olefins, aromatics, waxes, organic acids and carbon nanomaterials, making them better suited for open-loop recycling. Other polymers include polystyrene (PS), polyvinyl chloride (PVC), and polyamide (PA) and high temperature pyrolysis and cracking are typically reported for PS and PVC, while PA can be depolymerised in a closed-loop system, similar to polyesters.

The importance of chemical recycling is emphasised by various review articles that have emerged in recent years. Several comprehensive reviews on the chemical recycling of polyethylene terephthalate (PET) have been reported.[17-21] Broader reviews on the catalytic depolymerisation of polyesters have also been conducted which include reports on polycarbonates towards closed-loop recycling and upcycling.[22-24] Li *et al.*[25] carried out a comprehensive review on closed and open-loop recycling methods for biodegradable polylactic acid (PLA) plastics. A number of focused reviews have also explored chemical recycling routes for polyolefins.[15, 26-28] Qin and co-workers reviewed advanced catalytic systems for the chemical recycling of different plastic types,[29] while Chu *et al.* emphasised the significance of rational catalyst design in chemical recycling processes.[30] Luo and co-workers provided a comparative review of mechanical recycling and recent advances in chemical recycling technologies.[31] Additionally, there is a growing recognition of the importance of undertaking assessments of economic and environmental sustainability of proposed methodologies.[32-34]

Among the various chemical recycling technologies, MW-assisted heterogeneous catalysis has emerged as an energy-efficient approach by reducing reaction times and allowing for catalyst recyclability.[14] Heterogeneous catalysts are particularly advantageous for industrial scale-up due to their ease of recovery and regeneration.[15] Additionally, MW-assisted heating has been shown to significantly reduce reaction times when compared with conventional thermal heating for plastic degradation. When coupled with MW-assisted heating, heterogeneous catalysts have demonstrated excellent stability and catalytic performance. Interactions between MW and solid catalysts can produce special thermal effects or ‘hot spots’ as well as MW plasmas, accelerating reactions at the

catalyst surface.[16] MW-assisted heating has been shown to enhance activity, selectivity and stability of heterogeneous catalysts.

This review provides an overview of recent developments in chemical recycling technologies, with a particular emphasis on heterogeneous catalysts coupled with MW-assisted heating. The focus is placed on the role of MW in enhancing energy efficiency of catalytic depolymerisation reactions and recent advances in the design and application of advanced heterogeneous catalysts to promote MW absorption and improve process yield and selectivity. We will discuss the fundamentals of MW-assisted heating for catalytic applications and explore MW-assisted chemical recycling strategies for a range of polymer types including polyesters (PET, PLA, PES and PC), polyolefins (LDPE, HDPE, PP) and other plastics such as PA, PS and PVC.

1.2 Fundamentals of MW-assisted Catalysis:

MWs are a type of electromagnetic radiation, and range in wavelengths from 1 mm to 1 m and frequencies from 300 MHz to 300 GHz, with most lab-based MW reactors operating at a frequency of 2.45 GHz. When materials are subject to MW irradiation, the polarisation of dipoles or charges within the material cannot instantly follow the rapidly oscillating electric field, leading to a lag known as dielectric relaxation. This results in heat generation due to energy loss from the friction between molecules. The quantity of energy loss from the system due to electromagnetic relaxation depends on the dielectric and magnetic properties of a material.

Selective heating of materials under MW irradiation can be related to the complex permeability and permittivity of the specific material, which affects magnetic and dielectric heating, respectively.[35] The complex permittivity of a material determines a material's dielectric heating by a MW-electric field, and is defined as:

$$\varepsilon^* = \varepsilon' - j\varepsilon'' \quad \textbf{Eqn.1}$$

Where ε^* is the complex permittivity, ε' relates to a materials ability to hold electrical energy and is the real component of the dielectric permittivity, and ε'' is known as the dielectric loss factor which relates to the material's ability to convert the electric energy into heat and is the imaginary component of the dielectric permittivity.[36]

As dielectric heating is commonly reported for catalytic processes carried out under MW irradiation, most literature reported use of the loss tangent ($\tan\delta$) to assess a materials susceptibility to penetration by electric field and subsequently dissipate the energy as heat. The loss tangent of a material can be calculated using:

$$tan\delta = \frac{\varepsilon''}{\varepsilon'}$$ **Eqn. 2**

A material with a high loss tangent can therefore be easily heated in a MW-electric field, while materials with low loss tangents are less susceptible to heating in a MW-electric field.

The complex permeability of a material determines the material's magnetic heating in a MW-magnetic field, and is defined as:

$$\mu^* = \mu' - j\mu''$$ **Eqn. 3**

Where μ^* is the complex permeability, μ' is defined as the real component of the complex permeability and relates to the ability of the material to hold magnetic energy in the MW-magnetic field, and μ'' is defined as the imaginary component and represents the magnetic loss, which accounts for energy dissipation due to magnetic relaxation effects. In equations 1 and 3, j accounts for phase shifts in alternating fields and ensures proper mathematical representation of energy losses.[37]

The quantity of energy absorbed by the material which is dissipated as heat can be expressed as:

$$P_{abs} = \frac{1}{2}\sigma|E|^2 + \pi f\varepsilon^0\varepsilon'|E|^2 + \pi f\mu_0\mu''|H|^2$$ **Eqn. 4**

Where P_{abs} relates to the volumetric power absorbed (Wm^{-3}), σ is the conductivity which is given as $\pi f\varepsilon^0\varepsilon'$, where f is the frequency (Hz), ε^0 and μ_0 are the dielectric constant and magnetic permeability

in the vacuum, respectively, ε' and μ'' are the relative dielectric and magnetic losses, respectively, and $|E|$ and $|H|$ are the electric and magnetic field intensity, respectively.[38]

Solid materials have been classified as absorbers (dielectric), perfect conductors or insulators based on how they interact with MW-electric fields, illustrated in Figure 2. Absorbers such as dielectric materials allow MWs to penetrate below their surface, perfect conductors such as metals reflect MWs with no penetration and insulators allow MWs to pass through them with little or no losses, for example, glass.

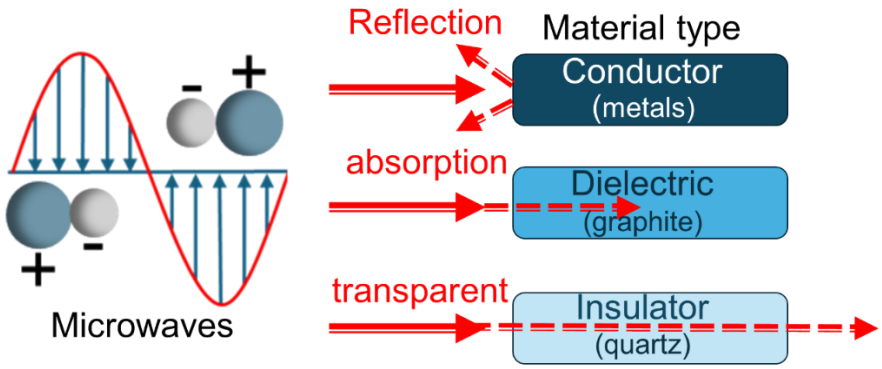


Figure 2: Classification of solid materials and their interactions with MW conductors, dielectric and insulators. Figure adapted from Ref. [38]

In heterogeneous catalysis, MW heating has been reported to increase reaction efficiency and product selectivity due to rapid heating and hotspot formation at the catalyst surface, as well as the generation of micro-plasmas leading to accelerated activation of reactants.[35] Figure 3 a) illustrates the distinct mechanisms of MW-induced hotspots compared with micro-plasmas highlighting their respective thermal and non-thermal catalytic activation pathways. Hot spots are localised regions of elevated temperature within the catalyst or at its surface, arising from non-uniform MW absorption in areas with high dielectric losses.[39] In contrast, micro-plasmas are localised electrical discharges consisting of ionised gas, typically composed of high energy electrons, ions and radicals. Micro-plasma formation occurs in regions of enhanced electromagnetic field often associated with sharp points or defects on a catalyst surface.[40] Hotspots and micro-plasmas can coexist on a catalyst particle when a region

contains both electric field enhancement points and strong dielectric zones. Thermal imaging has been used to capture hotspot formations at the contact point of silicon carbide (SiC) spheres with diameters ranging from 2.38 to 3.97 mm, as shown in Figure 3 b).[41] The purpose of this study was to directly observe local high temperature regions using *in situ* emission spectroscopy. The images and the corresponding temperature distribution profile along the contact region reveals localised high temperature zones resulting from increased electromagnetic fields at particle contact points under MW-irradiation. The temperature at the contact point was approximately 150 °C higher than surrounding regions. In the same study the temperature distributions were also modelled for the vicinal contact points of magnetite (Fe_3O_4) catalyst spheres under MW-irradiation shown in Figure 3 c). The surface temperature at the contact point was reported to be 190 °C higher than surrounding regions due to the localised concentration of electromagnetic fields at the particle interfaces. The morphology of a solid catalyst material has also been shown to influence their dielectric properties, thereby affecting the spatial distribution of the electromagnetic field. A comparison between Cu_2O cubes and spiked morphologies (Figure 3 d) showed that the complex permittivity of the spiked particles was 20 % higher than cube-shaped particles. This enhancement was attributed to the increased electric field intensity at the sharp tips of the spiked nanostructures, which alters the polarisability and subsequently enhances dielectric properties beneficial for catalytic applications, as shown in Figure 3 e).[42]

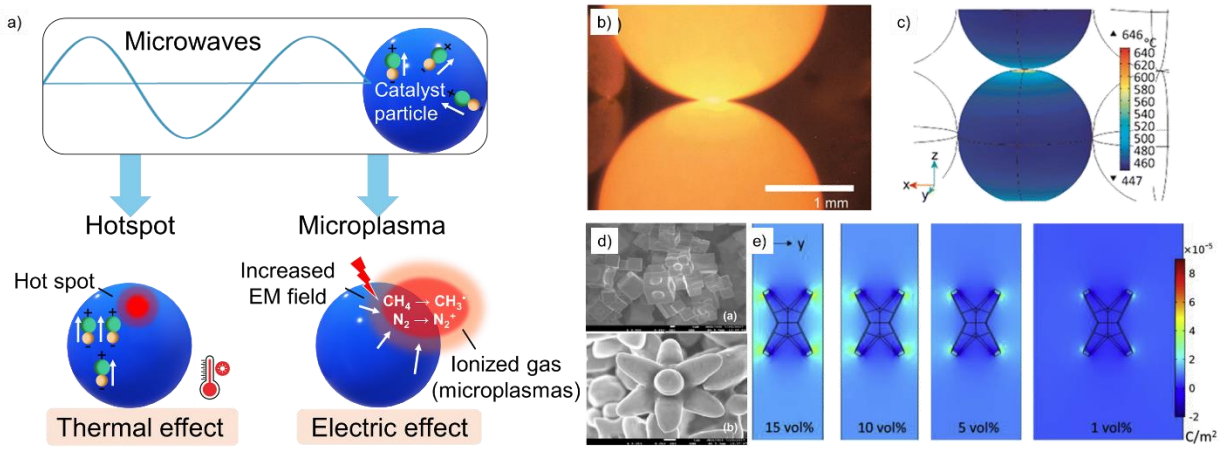


Figure 3: a) Schematic representation of hot spot and plasma formation on catalyst surface under MW irradiation, b) thermal imaging to reveal hotspot formation on SiC spheres under MW-irradiation and temperature distribution profile, c) temperature simulation data for hotspot formation on magnetite spheres under MW-irradiation. Reproduced with permission from Ref. [41] d) SEM images of Cu_2O cubes and spikes and e) illustration of calculated dipole density for spiked Cu_2O at different volume fractions. Reproduced with permission from Ref.[42]

MW-assisted heating has gained significant attention for plastic depolymerisation reactions due to its rapid and volumetric heating capabilities, which can help to overcome the inherent thermal stability of polymers. MW-assisted heating has been widely reported to outperform conventional thermal heating for PET, PLA, LDPE and PP degradation reactions by reducing reaction time and lowering the overall energy consumption.[43, 44] Most plastics are generally poor MW absorbers because of long polymer chains which limit dipole rotation under an electromagnetic field resulting in low dielectric losses.[45] However, the MW absorbing properties of polymers is highly dependent on their chemical composition. Polymers containing polar functionalities such as PET and PC exhibit an increased dielectric loss with increasing temperature, particularly above their glass transition temperature (T_g), under MW-irradiation.[45] Polar solvents such as water or ethylene glycol are beneficial as they exhibit high dielectric losses under MW-irradiation leading to enhanced heating of the reaction solution. Additionally, MW-absorbing catalysts such as carbon nanomaterials[46] or metal oxides can be used to further improve heating efficiency.[47] In solvent-free plastic degradation reactions such as pyrolysis,

solid MW absorbers are often added to facilitate efficient heating of the polymer. Solid MW absorbers convert MW irradiation to thermal energy by two mechanisms: dipole polarisation and dipole rotation, which are illustrated schematically in Figure 4. In dipole polarisation, permanent or induced dipoles attempt to align with the rapidly oscillating electric field which generates internal friction and heat. In dipole rotation, the fluctuating electric field causes polar molecules to rotate back and forth as they attempt to align with the changing electric field.[48]

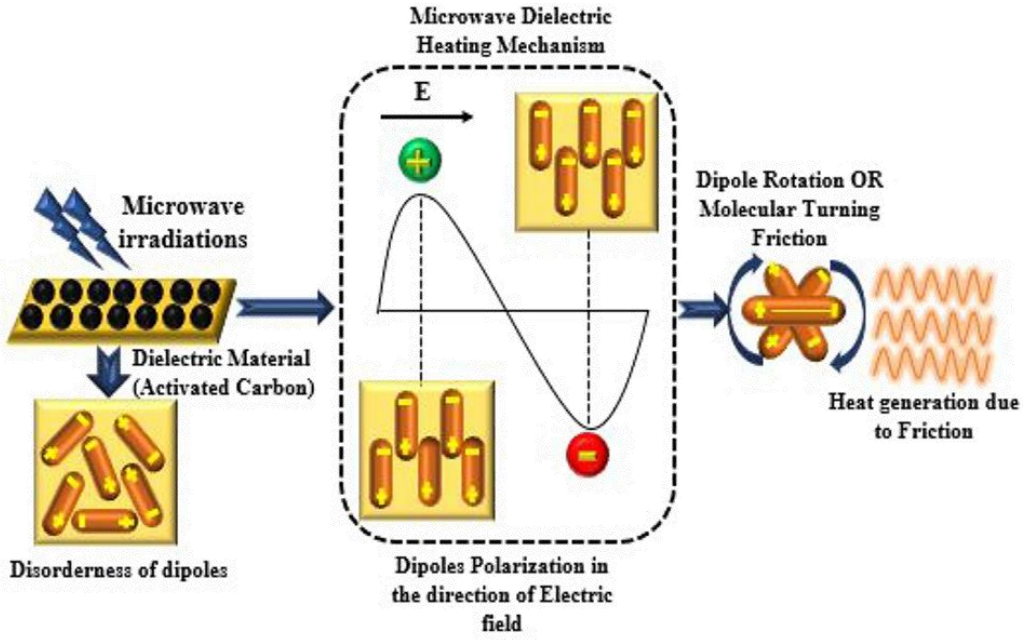


Figure 4: Dipole polarisation and dipole rotation mechanisms of MW heating on AC as a MW-absorber for polyolefin pyrolysis. Figure reproduced with permission from Ref.[48]

Effective MW heating in polymer degradation reactions typically requires the use of MW-absorbing catalysts, the addition of non-catalytic susceptors such as activated carbon, or the use of polar solvents. These strategies compensate for the inherently poor MW absorption of most polymers and enable efficient conversion of electromagnetic energy to heat. Catalytic MW-assisted degradation therefore represents a promising and potentially sustainable approach for converting waste polymers into valuable chemicals, offering rapid, energy-efficient processing with reduced environmental impact.

1.3 MW-assisted Heterogeneous Catalytic Upcycling of Polymers:

In recent years, many studies have been conducted on MW-assisted catalytic degradation of different types of plastic. Here, we summarise some of the findings based on plastic types including polyesters, polyolefins and other plastics.

1.3.1 MW-assisted Heterogeneous Catalytic Upcycling of Polyesters:

Polyesters are a class of synthetic polymers characterised by the presence of ester functional groups in their main chain. Polyesters are formed through a condensation reaction between diols and dicarboxylic acids or their derivatives, resulting in long chains linked by ester bonds.[49] They can be broadly categorised into thermoplastic and thermosetting types, each with distinct physical properties and applications.[50] Polyesters are widely used in textiles, packaging, bottles, containers and engineering materials due to their durability, chemical resistance, and versatility.

The chemical recycling of polyesters is well reported due to the presence of reactive ester bonds, allowing them to be efficiently broken down into their monomers and repolymerised, making them particularly suitable for closed loop recycling systems. Polyester linkages can be cleaved through trans-esterification reactions with a range of nucleophiles, enabling a variety of different depolymerisation routes such as hydrolysis[21], alcoholysis[51], glycolysis[52] and amminolysis[53].

The most common polyester is PET, known for its use in beverage bottles and synthetic fibres. PET is commonly synthesised via the condensation reaction of dimethyl terephthalate (DMT) or terephthalic acid (TPA) with EG.[50] Glycolysis and aminolysis are among the most reported chemical recycling routes for PET. In glycolysis, PET undergoes a transesterification reaction with diols, typically EG, to yield the monomer bis(hydroxyethyl) terephthalate (BHET).[52] In aminolysis, amines such as ethanolamine (EA) or methylamine (MA) act as nucleophiles which form amide linkages to yield terephthalamide derivates such as bis(2-hydroxyethyl) terephthalamide (BHETA) which are valuable chemicals for the synthesis of polymers, resin and surfactants.[54]

ZnO and ZnO-composites are well reported heterogeneous catalysts for PET glycolysis owing to their Lewis acidic nature, high thermal stability, selectivity, low toxicity and exhibit high performance after multiple cycles.[55-57] The influence of catalyst morphology on MW-assisted PET glycolysis using EG was demonstrated in a study using ZnO platelets, revealing a strong correlation between ZnO morphology and catalytic activity.[58] The favourable orientation of the Zn(001) surface facet on the nanoplatelets showed enhanced catalytic activity over other morphologies of ZnO. A size effect was also observed with yield increasing by more than 20 % with smaller particle size. The enhanced catalytic activity was attributed to smaller particle size for ZnO platelets over other morphologies such as plates, hexagonal disks and prisms resulting in a higher surface area. Additionally, the favouring exposure of the (001) facet for the platelets was attributed to the non-centrosymmetric crystal structure of ZnO resulting in a more polar hexagonal (001) facet increasing its ability to form hydrogen bonds. This work also demonstrated the effect of rapid MW heating, achieving a BHET yield of > 95 % in 45 min, compared with 60 % yield under the same conditions using conventional thermal heating. Lastly, LCA found that BHET production via ZnO-catalysed glycolysis resulted in a significant decrease in greenhouse gas emissions when compared with current DMT-based synthesis methods and two $Zn(OAc)_2$ homogeneous catalysts reported in the literature.[59, 60]

Dispersing metal catalysts on a support material can enhance their stability, increase surface area and improve catalytic efficiency by maximising active site exposure. In this case, Kaolin supported-Nb_2O_5 is an effective catalyst for PET aminolysis using EA as a reagent reported by Ravathi *et al.*[61], achieving high yields (95 %) of bis(2-hydroxyethyl)terephthalamide (BHETA) in 30 min. For this work, PET was obtained from beverage bottles as well as coloured polyester fibres, and the catalyst also acted as an efficient absorbent of the colourant impurities. A Kaolin clay support was used to enhance the surface parameters of Nb_2O_5 and improve catalytic activity. The BET surface area increased from 13.54 m^2g^{-1} for Nb_2O_5 to 30.62 m^2g^{-1} for the Kaoiln-Nb_2O_5 and the BHETA yield obtained from both catalysts were 82 % and 95 %, respectively, which was attributed to the enhanced specific surface area.

The use of a multifunctional heterogeneous catalysts that can drive multiple reaction pathways is highly advantageous and significantly increases the practical value of the catalyst. A study by Anbarasu *et al.*[62] reported the design and synthesis of In-ZnO/g-C_3N_4 and Sb-ZnO nanocomposites for both glycolysis and aminolysis of PET fibres. The addition of In and Sb were reported to improve the Lewis-acidity of the catalyst and lower the band gap energy, while immobilisation on a graphitic carbon nitride support was to enhance MW-absorbing properties of the catalyst. A 95 % yield of BHETA was obtained after 15 min for the aminolysis reaction using EA while 92 % BHET was obtained after 60 min for the glycolysis reaction. While these catalysts showed excellent activity and recyclability, shifting away from heavy and toxic metallic catalysts is essential for advancing green and sustainable chemistry in the chemical depolymerisation of plastics.

Similarly, Vinitha and coworkers[63] reported the use of Ag/ZnO nanoparticles for the chemical recycling of coloured PET textiles. The catalysts showed bifunctionality as they were effective in both MW-assisted aminolysis and glycolysis of PET. Glycolysis was carried out using EG to yield BHET and diethylene glycol (DEG) to yield bis-2-(2-hydroxy-ethoxy)-ethylterephthalate (BHEOET). Aminolysis was carried out using EA to yield BHETA and diethanolamine (DEA) to produce N^1,N^1,N^4N^4-tetrakis-(2-hydroxy-ethyl)-terephthalamide (BDHETA). The Ag/ZnO catalyst outperformed the ZnO catalyst for both glycolysis and aminolysis reactions which was attributed to a decrease in bandgap energy and decrease in crystallite size on incorporation of the Ag, enhancing the MW heating properties and Lewis acidity of the catalyst. The Ag/ZnO catalyst achieved a 90 % yield of BHET using EG and 86 % maximum yield of BHEOET using DEG after 30 min. The use of EA as an aminolysis reagent was more effective than DEA and achieved a maximum BHETA yield of 96 % while the maximum yield of BDHETA achieved was 90 % in 15 min of reaction time.

The development of metal-free catalysts is important in the transition towards more sustainable and cost-effective catalysis. Casey and coworkers[43] reported mesoporous SiO_2 functionalised with guanidine ligands as metal free organocatalysts. Guanidine compounds are strong bases that are

effective homogeneous organocatalysts for PET glycolysis due to their strong Lewis base properties, enabling them to act as nucleophiles that increase the reactivity of EG towards the carbonyl group of PET.[64] The guanidine-functionalised SiO_2 catalysts were effective for the glycolysis of PET using EG achieving an isolated BHET yield of 80 % after 30 min, while 3 h was required to achieve similar yields under conventional thermal heating. Additionally, the catalysts displayed superior recyclability over successive MW cycles when compared with conventional thermal heating which resulted in faster catalyst deactivation. Another advantage of basic guanidine catalysts is their ability to promote the glycolysis of PET to bis(4-hydroxybutyl terephthalate) (BHBT), a useful monomer for synthesising polybutylene terephthalate (PBT). This reaction is achieved using 1,4-butanediol (BD) instead of EG as the glycolysis reagent. When PET glycolysis with 1,4-BD is carried out in the presence of a Lewis acid catalyst, such as a metal salt, the 1,4-BD tends to undergo an undesirable cyclisation reaction to form tetrahydrofuran (THF). This highlights the benefit of using a Lewis base catalyst like guanidine, which avoids this side reaction.

PLA is a bio-based aliphatic polyester synthesised primarily through the polymerisation of lactic acid derived from renewable resources.[65] Production and use of PLA has increased as its bio-based and technically biodegradable nature, may make it a more sustainable option than traditional fossil derived polymers. While PLA can undergo industrial composting under controlled conditions its biodegradability is generally limited under ambient or marine environments, and concerns about its environmental persistence if improperly managed have been growing.[66] Therefore, it is also critical to develop chemical recycling pathways for bio-based polymers such as PLA. Hydrolysis of PLA, typically carried out under acidic or basic conditions at elevated temperatures offers a pathway for lactic acid recovery, which can be repolymerised to produce PLA.[67] Alcoholysis using ethanol or methanol in the presence of a catalyst such as Zn(OAc) can produce methyl lactate (MeLa) or ethyl lactate (EtLa), which are high value green solvents.[68]

The use of a phase-transfer catalyst such as hexadecyltrimethylammonium bromide (HTMAB) has been reported to enhance MW-assisted hydrolysis of PLA in aqueous NaOH to yield lactic acid.[69] The catalyst facilitates the reaction by transporting hydroxide ions from the aqueous phase to the solid organic phase, enabling easier attack on the PLA chains. Optimal conditions for achieving over 90 % PLA degradation involved heating at 100 °C for 10 min, with a maximum MW power of 10 W to reach this temperature. This represents a relatively mild and efficient depolymerisation pathway for PLA.

Lewis acid salts such as Zn(OAc) and Zn(II) triflate are excellent homogeneous catalysts for the methanolysis of PLA to yield MeLa.[70] Under MW-assisted heating, the conversion of PLA to MeLa over these Zn salts was successful with > 99 % yield monomer yield achieved in 10 min at 160 °C. Under conventional heating, the methanolysis of PLA over a Zn(II) imino monophenolate complex catalyst was reported to yield 63 % monomer in 30 min at 130 °C.[71] While homogeneous catalysts such as the above mentioned metal salts are effective and result in short reaction times, heterogeneous catalysts provide the key advantage of easy separation and recovery after reaction. Guanidine functionalised porous SiO_2 are effective heterogeneous catalysts for PLA methanolysis.[43] A MeLa yield of 42 % was achieved after 72 h of thermal heating at 130 °C, while a 30 % MeLa yield was achieved after 30 min of MW-assisted heating at 130 °C, substantially reducing the reaction time. Density functional theory (DFT) modelled the interaction between the guanidine ligand (dicyanamide) with PLA and found that the N-rich environments in the ligand promoted the nucleophilic attack of the C=O group on PLA.

Polyethylene furan-2,5-dicarboxylate (PEF) is also a bio-based polyester used in packaging, textiles and electronics. PEF can undergo glycolysis in the presence of EG to yield bis(2-hydroxyethyl) furan-2,5-dicarboxylate (BHEF) which can be repolymerised to PEF in a single condensation step. The MW-assisted glycolysis of PEF to BHEF over a ZnO catalyst was reported by Najmi and co-workers.[72] Yields of BHEF of ~90 % were achieved in 40 min at 175 °C with 100 W of MW irradiation. In absence of the catalyst, large quantities of oligomers were present, however the addition of ZnO facilitated the rapid depolymerisation of oligomeric species to monomeric BEF owing to its Lewis acid properties.

Polycarbonates (PC) are polyesters typically made through a chemical reaction called condensation polymerisation, usually involving bisphenol A (BPA) and either carbonyl chloride or diphenyl carbonate Owing to a combination of high impact resistance, optical clarity and thermal stability they are widely used in applications such as automotive components, optical lenses, electronic housings and construction materials.[73] Recycling of PC presents significant challenges due to its susceptibility to hydrolytic and thermal degradation during mechanical processing recycling, leading to molecular weight reduction and deterioration of physical properties.[74] Chemical recycling methods, such as hydrolysis[75], alcoholysis[76], and glycolysis[77], have been developed to depolymerise PC into monomers such as BPA, or oligomers. BPA is a valuable product due to its role as a precursor in the production of polymers and epoxy resins. The methanolysis of PC was reported by Chen *et al.*[78] over ultrasmall (~ 4 nm) ZnO nanoparticle catalysts, yielding 98 % (BPA) after 1 h at 120 °C of conventional thermal heating. The proposed mechanism involves the interaction of the carbonyl group of PC with the Zn^{2+} of the catalyst, resulting in an electropositive carbon atom which is subsequently attacked by the electronegative O atom in MeOH. This leads to the cleavage of the C-O bond, depolymerising the PC into BPA and dimethyl carbonate (DMC). The alkaline hydrolysis of PC has also been reported using a cationic surfactant, 1-hexadecyl trimethylammonium bromide (HTMAB) as a phase transfer catalyst.[79] The cationic functionality of the catalyst transports the OH anion to the surface of the PC via interfacial mechanism, resulting in attack of the C-O groups and depolymerisation of PC. The PTC returns to the aqueous phase and forms BPA. Full PC depolymerisation was achieved in 10 min at 160 °C MW heating, which was significantly shorter than 1 h reported previously using thermal heating. A similar report found the uncatalysed methanolysis of PC under MW irradiation to achieve yields of 94 % BPA at 190 °C in 3 h of reaction time.[80]

Table 1 – Summary of catalysts, conditions and main products for MW-assisted depolymerisation of polyesters.

Polymer	Catalyst	Conditions	Products	Ref
PET	ZnO	210 °C, 30 min, 850 W	BHET	[58]
PET, PES	Kaolin-Nb_2O_5	140 °C, 30 min, 180 W	BHETA	[61]
PES	In-ZnO-g-C_3N_4	180-200 °C, 60 min, 300 W	BHET	[62]
PES	In-ZnO-g-C_3N_4	125-150 °C, 15 min, 180 W	BHETA	[62]
PET, PES	Ag-ZnO	150-180 °C, 15 min, 180 W	BHETA	[63]
PET, PES	Ag-ZnO	180-200 °C, 30 min, 300 W	BHET	[63]
PET	SiO_2-Guanidine	210 °C, 30 min, 800 W (upper limit)	BHET	[43]
PLA	HTMAB	100 °C, 10min, 2-10 W	Lactic acid	[69]
PLA	Zn(OAc), Zn(II) triflate	160 °C, 10 min, n/a	MeLa	[70]
PLA	SiO_2-Guanidine	130 °C, 30 min, 800 W (upper limit)	MeLa	[43]
PEF	ZnO	175 °C, 40 min 100 W	BHEF	[72]
PC	HTMAB	160 °C, 10 min, 17 W	BPA	[79]

Abbreviations: PET = polyethylene terephthalate; BHET = bis(2-hydroxyethyl) terephthalate; PES = polyester; BHETA = bis(2-hydroxyethyl) terephthalamide; PLA = polylactic acid; HTMAB = hexadecyl(trimethyl)ammonium bromide; MeLa = methyl lactate; PEF = polyethylene furonate; BPA = bisphenol A; PC = polycarbonate.

MW-assisted catalysis has emerged as a highly effective and sustainable approach for the chemical recycling of polyesters as described above. This chemical recycling method enables the rapid depolymerisation of these polymers into valuable monomers under relatively mild conditions which enables a closed-loop system. The use of MW heating significantly shortens reaction times compared

to conventional methods, improving energy efficiency and process scalability. MW-assisted heterogeneous catalysis offers as a promising strategy for addressing plastic waste and supporting circular material use.

1.3.2 MW-assisted Heterogeneous Catalytic Upcycling of Polyolefins:

Polyolefins are a major class of commodity polymers and include common plastics such as LDPE, HDPE and PP. Polyethylene accounts for roughly one third of overall plastic pollution workdwide.[81] Polyolefins are synthesised through the chain growth polymerisation of simple olefins like ethylene and propylene using catalyst systems under controlled conditions. Known for their chemical resistance, durability and low-cost, polyolefins are used extensively in packaging, textiles and automotive parts. However, their saturated hydrocarbon backbone structures make them particularly resistant to chemical degradation, posing significant challenges for waste management and sustainability. As a result, developing efficient catalytic chemical recycling pathways for polyolefins is a growing area of interest.

Catalytic pyrolysis is the most extensively reported chemical recycling technique for polyolefin recycling and involves heating the polymers to high temperatures (typically >300 °C) in the presence of a catalyst under inert atmosphere. The product distribution depends strongly on the catalyst used and the specific pyrolysis conditions. Catalytic pyrolysis over zeolite catalysts will typically yield a range of short chain hydrocarbon gases such as methane, ethylene and propylene, longer chain gasoline range hydrocarbons and aromatics such as benzene, toluene and xylene (BTX) derivatives which are useful fuels and waxes.[82, 83] In contrast, Fe or other metal-containing catalysts typically favour the formation of solid carbon materials, such as carbon nanotubes (CNT), along with hydrogen gas (H_2), rather than short chain hydrocarbons.[84] This is because Fe (or other metals) can promote the dehydrogenation of the hydrocarbon chain in the polyolefin to form H_2 and carbon, while the strong Lewis acid sites on zeolite catalysts can protonate the long hydrocarbon chains in polyolefins leading

to carbocation formation and subsequently β-scission reactions that break the long chains into smaller hydrocarbon fractions.[83]

MW-assisted catalytic pyrolysis methods have been reported to achieve lower energy consumption, enhanced yield and improved quality of the liquid oil products obtained from polyolefin pyrolysis when compared with conventional pyrolysis due to rapid heating effects and hotspot formation associated with MW.[85] Zeolites are widely used in catalytic pyrolysis due to the ease with which their structures can be tuned to optimise porosity and stability.[86] Luong *et al.*[87] reported catalytic pyrolysis of LDPE over zeolite H-ZSM-5 in a MW reactor. Optimal conditions were 300-400 °C, 30 min, to yield C_1-C_3 paraffinic hydrocarbons (37 %), smaller amounts of BTX (12 %) and coke (< 10 %). While MW heating achieved 100 % conversion, under comparable conditions with conventional heating only 90 % conversion was achieved, as well as lower BTX yields, highlighting the energy efficiency of MW-assisted pyrolysis. Infrared imaging revealed hotspot formation on the catalyst surface during the reaction.

Vatankhah and coworkers[88] reported the MW-assisted pyrolysis of LDPE over a metal-promoted zeolite catalyst, illustrated in Figure 6 a). Zn was incorporated into the zeolite structure on a SiC support which was employed as an efficient MW absorber. The MW was reported to selectively heat the SiC, creating a temperature gradient between the catalyst and the plastic surfaces meaning only the LDPE that is in direct contact with the catalyst surface underwent cracking which increases process selectivity by minimising random scissions within the polymer. The simultaneous cracking and catalytic aromatisation of LDPE was achieved at 360°C in 8 min. In the absence of Zn, the HZSM-5 catalyst achieved 75 % selectivity towards C_2-C_4 alkenes. Incorporation of the Zn to HZSM-5 resulted in a liquid product consisting of 94 % aromatics with 64 % selectivity towards BTX. The enhanced aromatisation performance of the Zn-incorporated catalyst was attributed to the synergistic effect of Brønsted acid sites from the zeolite and Lewis acid sites from Zn^{2+} and $[ZnOH]^+$ species.

Similarly, Ding and coworkers[89] reported a two-step MW-assisted catalytic pyrolysis of LDPE utilising the synergistic effect between a zeolite and NiO. The first step involved the conversion of LDPE to

aliphatic compounds over the NiO catalyst under MW-assisted heating at 500 °C, followed by the conversion of these products to high octane number (ON) oil compounds over a HY zeolite at 450 °C. While it did not significantly increase the yield, the addition of NiO to the system increased the selectivity towards valuable high ON compounds via a H abstraction mechanism which proceeded due to accelerated reaction rates that arose from hot spot generation by the NiO under MW heating.

The MW-assisted catalytic pyrolysis of LDPE over a ruthenium-modified zeolite (Ru/ZSM-5) was reported by Tuli *et al.*[90] The pyrolysis reactions were carried out at 300 °C with a 30 min hold time. A relatively high loading of 50 wt. % catalyst was used. The Ru-ZSM-5 catalyst was easily regenerated at 550 °C after completing a reaction and showed excellent recyclability. A comparative study of thermal and MW reactions demonstrated that MW heating resulted in higher selectivity towards aromatic products while conventional heating favoured aliphatic compounds. Hot spot formation was observed on the catalyst particles under MW-irradiation using an IR camera (see Figure 6 b) and increased with successive cycles owing to Ru aggregation within the catalyst. Irfan *et al.*[48] reported the catalytic MW pyrolysis of HDPE and PP over a Na-modified ZSM-5 catalyst. The reactions were carried out at 400-450 °C, 1000 W for 24 min and yielded mainly liquid oil consisting of aromatic hydrocarbons with some carbon nanotube (CNT) formation and H_2 gas. The Na-modified zeolite acted as a nucleation site for CNT growth, which was driven by H_2 formation. The proposed mechanism for CNT formation is shown in Figure 6 c). SEM analysis showed the formation of crystalline CNTs with a maximum outer diameter measurement of 93 nm.

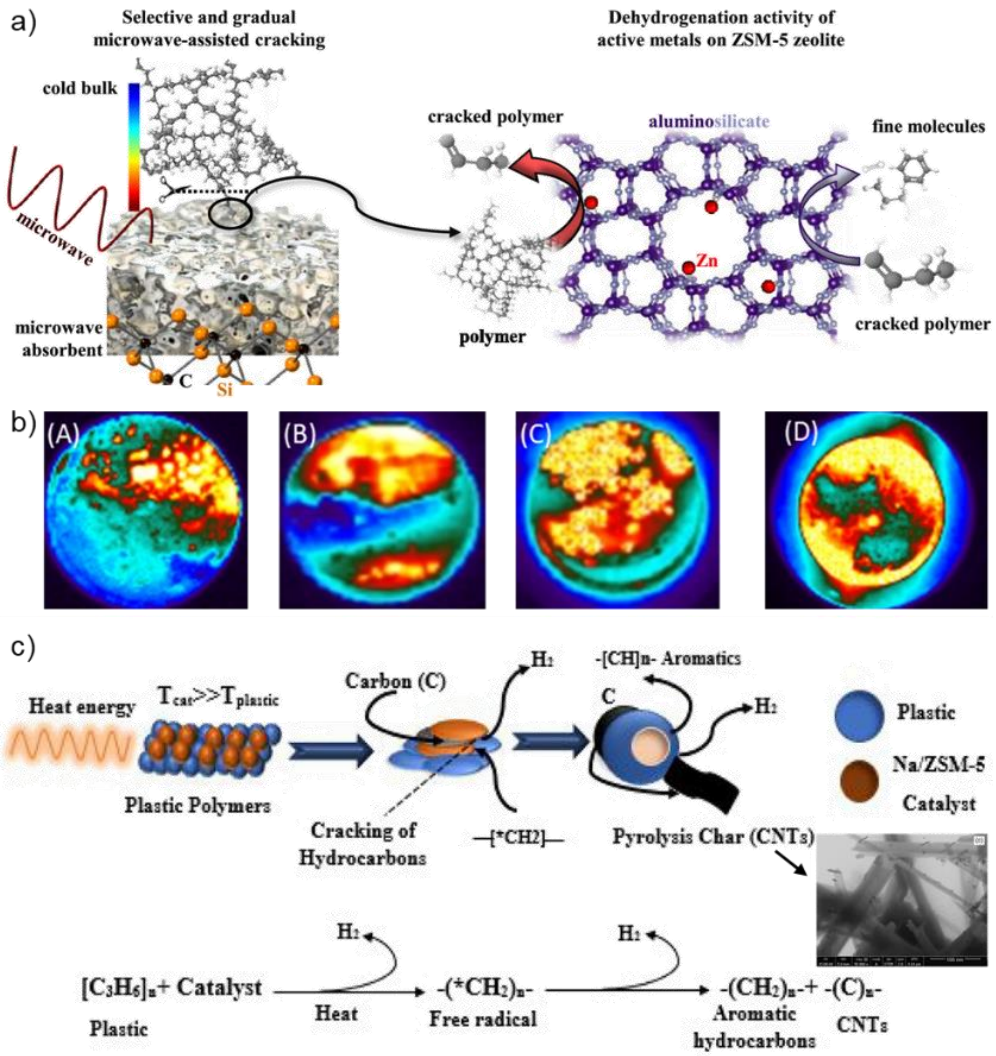


Figure 6: a) Proposed mechanism for the MW-assisted cracking of LDPE over Zn-HZSM-5 catalyst. Reproduced with permission from Ref.[88] b) IR camera images showing hotspot formation on Ru/ZSM-5 catalyst surface during catalytic pyrolysis of LDPE. Reproduced with permission from Ref. [90] c) Proposed mechanism for MW-assisted pyrolysis of HDPE and PP using a Na/ZSM-5 catalyst. Reproduced with permission from Ref. [48]

The use of transition metal catalysts such as Fe, Ni, and Co during the catalytic pyrolysis of polyolefins has been commonly reported to yield predominantly CNTs and H_2 via a catalytic chemical vapor deposition type mechanism. During pyrolysis, the catalyst breaks down the hydrocarbon molecules into H_2 gas and reactive carbon species which dissolve into the metal catalyst. Once saturated, excess carbon precipitates out as the catalyst acts as a nucleation site for the growth of CNTs. Bimetallic

catalysts are commonly reported for polyolefin degradation reactions due to synergistic and stabilisation effects. Effective solid state MW dehydrogenation of PE over Ni-Fe, Ni-Co and Co-Fe catalysts (average diameter 8.3 nm) has been demonstrated.[91] The reaction produced H_2, a solid fraction consisting of CNTs and an oil fraction consisting of C_{20+} linear hydrocarbons. The optimal conditions for the MW reactor were 500 °C, 800 W with 5 min reaction time under an argon flow of 100 mL min^{-1}. Notably, MW-assisted catalytic dehydrogenation promoted the formation of carbon nanomaterials, while conventional thermal heating favoured a larger oil yield. A comparison of the solid carbon products obtained from MW versus thermal heating is shown in Figure 7 a). During MW-assisted dehydrogenation, multiwalled CNTs are formed via selective growth on metal catalyst particle surfaces driven by rapid heating effects, while thermal heating results in poor CNT production efficiency as very few tubular structures were observed. A related study by Shoukat and co-workers[92] reported the use of magnetic ferrite catalysts, namely $NiZnFe_2O_4$, $NiMgFe_2O_4$ and $MgZnFe_2O_4$ for the catalytic conversion of HDPE waste into H_2 and CNT at 450 °C. The ferrite catalysts played a dual role, facilitating both catalytic growth of CNTs and MW absorption to enable rapid heating. The $NiZnFe_2O_4$ and $MgZnFe_2O_4$ catalysts gave higher yields of H_2 and CNT than the $NiMgFe_2O_4$ catalyst. Jie *et al.*[93] reported the conversion of HDPE and PP to H_2 and multiwalled CNTs over a $FeAlO_x$ catalyst. The reactions were performed at a power of 1000 W for 3-5 min with temperatures reaching ~350 °C. Hydrogen was rapidly extracted via an interfacial polarisation and a dehydrogenation mechanism with 97 % of the H_2 released from the plastic in just 20 s. The solid carbon residue was composed of 92 wt. % multi-walled CNTs. Shen *et al.*[39] investigated the catalytic performance of Fe immobilised on various supports - SiC, AC, and SiO_2, for the MW-assisted pyrolysis of HDPE to produce H_2 and CNTs. The study revealed a strong correlation between the catalyst's dielectric loss (ϵ'') and the rate of the pyrolysis reaction, with higher dielectric loss leading to faster reaction rates and increased yields of H_2 and solid CNTs, as opposed to liquid products. SEM images of the resulting CNTs are presented in Figure 7 b). CNTs synthesised using the Fe@AC catalyst had an average diameter of 141 ± 20 nm, whereas a much smaller diameter was observed for those produced with the Fe@SiC, averaging 26 ± 6 nm. This size

difference was attributed to the variation in dielectric loss values as Fe@AC exhibited a high ϵ'' of 156.79, while Fe@SiC had a significantly lower value of 3.95. The Fe@SiO_2 exhibited a dielectric loss value of ϵ'' = 0.11, which did not support CNT formation. The high dielectric loss of Fe@AC facilitated rapid heating of the catalyst particles under MW heating, accelerating CNT growth. The mechanism is illustrated in Figure 7 c) and can be described in three steps. The first step involves the rapid heating of the Fe catalyst particle under MW-irradiation which induces cracking on neighbouring HDPE particles producing volatile hydrocarbons (C_9-C_{40}). Secondly, the volatile hydrocarbons are further broken down into shorter chain hydrocarbons such as methane and ethane. In the last step, short chain hydrocarbons (C_1-C_5) decompose on the Fe-based catalyst surface, breaking C–H bonds to produce H_2 and solid carbon. Unlike thermal pyrolysis, MW-induced local heating on the catalyst surface promotes the crystallisation of amorphous carbon into cylindrical networks, leading to CNT formation.

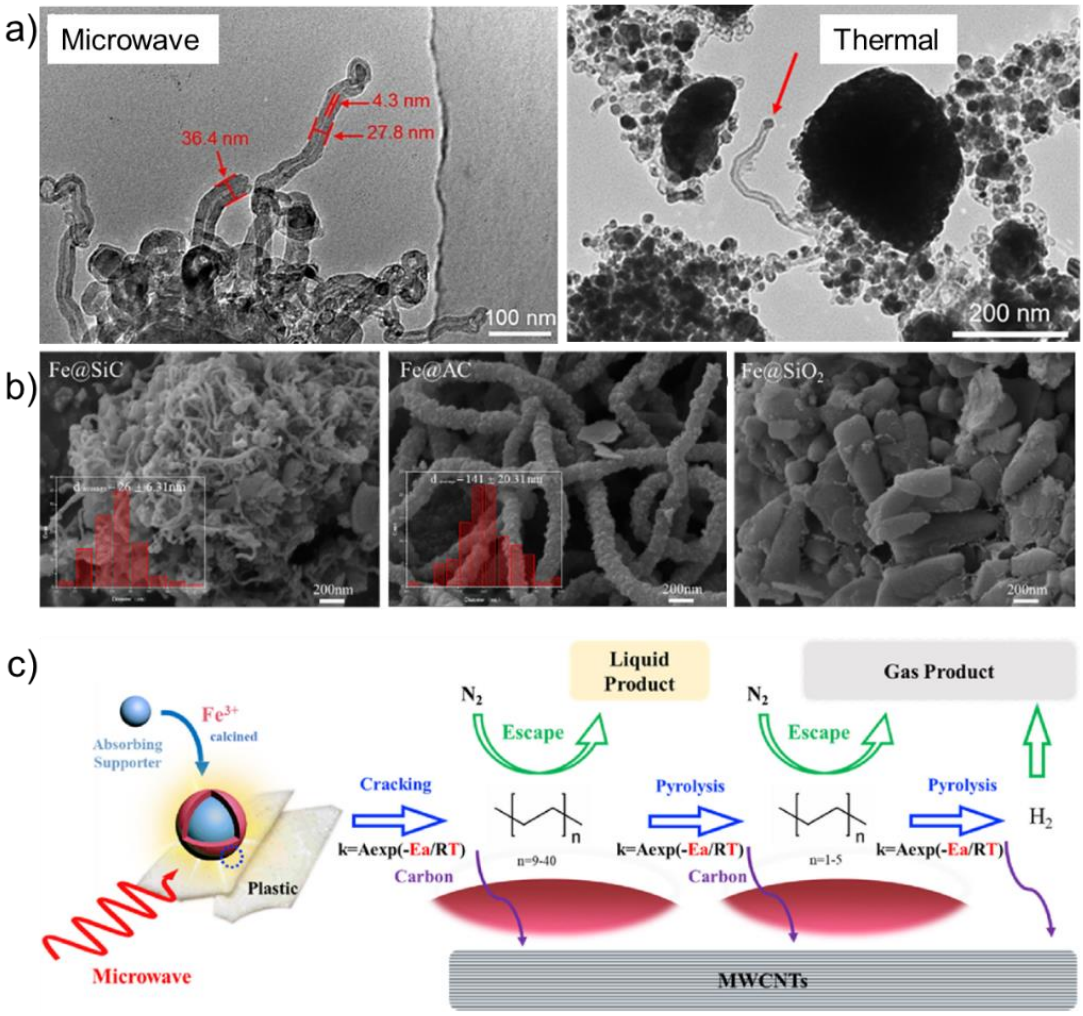


Figure 7: a) TEM images of solid carbon product obtained from MW and thermal heating. Reproduced with permission from Ref.[91] b) SEM images of solid carbon products obtained on Fe@SiC, Fe@AC and Fe@SiO_2 catalysts, respectively. c) Schematic diagram for the 3-step mechanism of the MW-assisted pyrolysis of HDPE over Fe-based catalysts. Reproduced with permission from Ref.[39]

Zhao *et al.*[44] used ZnO nanorods for conversion of LDPE and PP to hydrocarbons at 280 °C, yielding 46-60 wt. % C_{20}^{+} products, within 30 min. Interestingly, TEM analysis revealed progressive etching of the ZnO rods with each pyrolysis cycle. This was attributed to reduction of ZnO to Zn clusters by H_2 released during dehydrogenation. The Zn clusters were identified as effective active sites for C-C cleavage.

Innovative approaches for MW depolymerisation of polyolefins include the use of MW-absorbing heating elements (MWAHE) and liquid metal catalysts to maximise utilisation of the MW heating effect.

Activated carbon and silicon carbide (SiC) were evaluated as MWAHE[94], where their role is not to directly catalyse the reaction, but to effectively heat the HDPE in MW-assisted pyrolysis. The process consisted of two steps: an initial crude cracking at 620 °C, followed by secondary cracking at 950 °C, resulting in gasification yields of 95 % using a low power input of 80 W. The main products obtained were carbon monoxide, methane, carbon dioxide, acetylene, ethylene, ethane, propane, propylene, n-butane and i-butane. The AC MWAHE resulted in higher gas yields (84 %) than the SiC MWAHE (66 %), however, SiC resulted in higher selectivity towards ethylene (64 vol %) compared to AC (33 vol %). The superior performance of the AC was attributed to the emission of discharge plasmas from the AC when irradiated with MWs due to its high dielectric loss properties, which has been reported to increase microscopic surface temperatures to > 750 °C, as shown in Figure 8 a), while this effect was not observed for SiC.

Figure 8 b) illustrates a unique approach reported by Gao and coworkers[95] utilising a liquid metal eutectic gallium indium alloy (EGaIn) as an effective catalyst for LDPE, HDPE and PP conversion to olefin monomers. The use of a liquid metal catalyst is reported to eliminate the deactivation that is commonly reported for solid heterogeneous catalysts. Additionally, their properties such as fluidity, high electrical and thermal conductivities make them excellent MW catalysts. The liquid metal catalyst was first coated onto the plastic particles, the thickness of which was carefully tailored to match the MW penetration depth to facilitate efficient MW absorption, a consideration that is rarely reported in MW studies. Due to the conductivity of the liquid metal, the coated plastic particles generated a high temperature arc discharge plasma when subject to 600 W of MW power, resulting in full depolymerisation of the polyolefins in 25 min, with high selectivity towards $C_{2\text{-}4}$ olefins (50 % for PE and 65 % for PP). The liquid-metal catalyst was also self-separating and demonstrated excellent recyclability over 30 cycles.

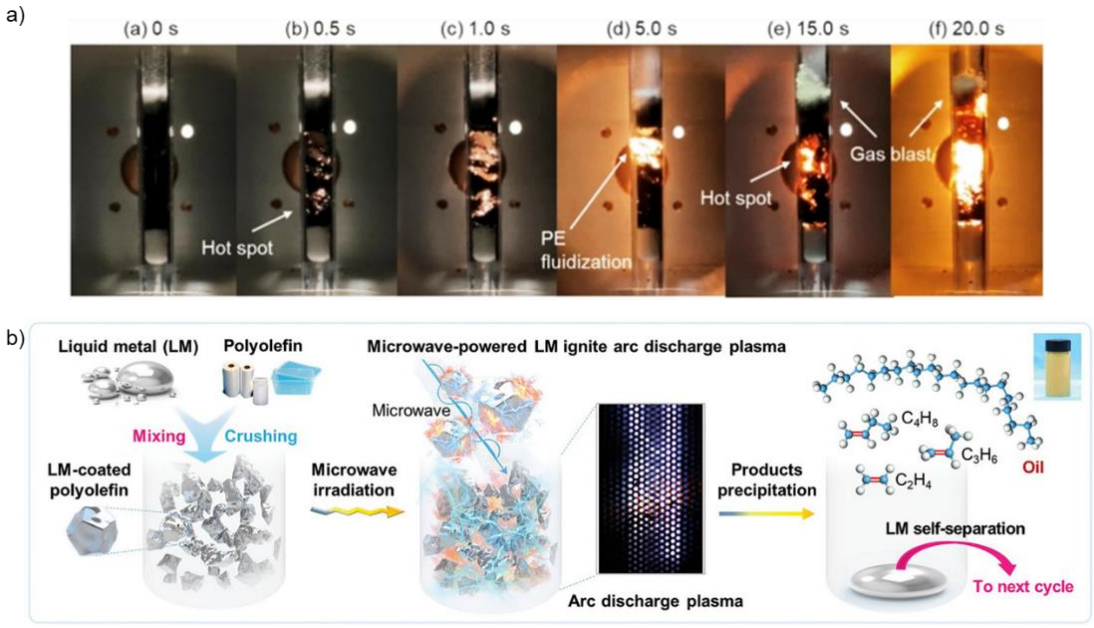


Figure 8: a) Hot spot and discharge plasma observation for pyrolysis of PE with AC MWAHE. Figure reproduced from Ref.[94] b) reaction scheme of polyolefin pyrolysis using liquid metal catalyst. Reproduced with permission from Ref.[95]

Outside of catalytic pyrolysis, another chemical recycling route reported for polyolefins is oxidative degradation. This method involves the use of oxidising agents such as oxygen gas (O_2), ozone (O_3), acids, like nitric acid (HNO_3) and peroxides, in the presence of catalysts. The oxidative degradation mechanism typically proceeds via radical oxidation followed by C-C chain scission, and yields small, oxygenated molecules such as carboxylic acids, ketones and alcohols which serve as valuable chemical intermediates.[27, 96] Oxidative degradation is emerging as a milder depolymerisation method of polyolefins. The MW-assisted oxidative degradation of LDPE in nitric acid has been reported to proceed at 180 °C in 1 h at 1200 W to yield dicarboxylic acids via a chain scission and radical oxidation mechanism.[97] Fenton and Fenton-like processes, which use aqueous H_2O_2 and a redox catalyst to generate reactive oxygen species have also been reported for the conversion of polyolefins into oxygenated products such as carboxylic acids and esters[98, 99] and also for the destruction of microplastics to gaseous products[100, 101]. Fenton oxidation pathways facilitate the oxidative degradation of polymers while eliminating the use of hazardous or toxic reagents. Breen *et al.*[102] reported the use

of Fenton oxidation to convert LDPE to carboxylic acid products over a Fe-CeO_2 solid solution catalyst. A synergistic effect was reported between Ce and Fe in the catalyst achieving acid yields of 71 % under neutral pH. The main products obtained were formic acid, acetic acid, propionic acid and succinic acid. 90 % LDPE degradation was achieved at 180 °C in 3 h with an average power usage of 300 W. The Fenton oxidation of LDPE was carried out under conventional thermal heating and was reported to not proceed to any extent.

Table 2 – Summary of catalysts, conditions and main products for MW-assisted depolymerisation of polyolefins.

Polymer	Catalyst	Conditions	Main Product	Ref
LDPE	HZSM-5	300 – 400 °C, N_2, 30 min, 1000 W (max W)	Paraffinic (C_1-C_4), BTX, olefins	[87]
LDPE	Zn-HSM-5	360 °C, N_2, 8 min, 1000 W (max W)	Gas (H_2, C_2-C_4), Oil (MAH, BTX)	[88]
LDPE	1. Pyrolysis NiO 2. Catalysis HY (2 stage)	1. 450 – 600 °C 2. 350 – 500 °C	Gasoline (C_5-C_{12}), aromatics, aliphatics	[89]
LDPE	Ru/ZSM-5	300 °C, N_2, 30 min, 900 W (max W)	BTX, olefins	[90]
HDPE, PP	Na/ZSM-5	400-450 °C, N_2, 24 min, 1000 W	H_2, carbon nanotubes, liquid oil	[48]
LDPE	$Ni_3Co_2O_x$	500 °C, Ar, 5 min, 800 W	H_2, carbon nanotubes	[91]
HDPE	$NiZnFe_2O_4$, $NiMgFe_2O_4$ $MgZnFe_2O_4$	450 °C, N_2, 8 min, 1000 W	H_2, carbon nanotubes	[92]
HDPE	$FeAlO_x$	350 °C, Ar, 5 min, 1000 W	H_2, carbon nanotubes	[93]
LDPE, PP	Zn/b-ZnO	30 min, 280 °C, 240 – 400 W	Lubricant-base oil	[44]
HDPE	Fe@SiC, Fe@AC, Fe@SiO_2	500 °C, N_2, 1 hr, 800 W	H_2, carbon nanotubes	[39]
HDPE	SiC/AC MWAHE	620 °C (1), 950 °C (2), N_2, 3 min, 500 W	C_2H_4, CH_4	[94]

PP, LDPE, HDPE	EGaIn	300°C, Ar, 25 min, 600 W	C_2-C_4	[95]
LDPE	Fe-CeO_2	180 °C, 3 h, 300 W	RCOOH, $R(COOH)_2$ (C_1-C_7)	[102]

Abbreviations: LDPE = low-density polyethylene; HZSM = hydrogen zeolite Socony Mobil-5; BTX = benzene, toluene, xylene; MAH = monocyclic aromatic hydrocarbons; HDPE = high-density polyethylene; PP = polypropylene; MWAHE = microwave-absorbing heating element

The use of MW heating is an effective method for upcycling of polyolefins to value-added fuels and carbon materials through open-loop pathways. Product selectivity can be influenced by tuning the reaction conditions including the choice of catalyst used. MW-assisted heterogeneous catalysis has potential for effectively converting waste polyolefin streams to valuable chemicals via open-loop pathways.

1.3.3 MW-assisted Heterogeneous Catalytic Upcycling of Other Plastics:

In addition to polyesters and polyolefins, the chemical recycling of other plastics such as PS, PAs PUR and PVC, is gaining increasing attention. These polymers pose unique challenges due to their diverse chemical structures and additives. MW-assisted processes offer a promising route by enabling rapid, energy-efficient depolymerisation tailored to these complex polymer types.

Polystyrene (PS) is a widely used thermoplastic polymer composed of a saturated hydrocarbon backbone with conjugated benzene rings as side groups. Its chemical structure imparts rigidity, clarity, and good insulation properties, making it suitable for a broad range of applications, including packaging materials, disposable food containers and insulation.[103] While PS can be mechanically recycled, its low density and contamination issues often make this route inefficient.[104] As a result, chemical recycling methods such as thermal depolymerisation, pyrolysis, and MW-assisted depolymerisation have been explored to recover monomeric styrene and valuable aromatic compounds such as BTX[105], offering a more sustainable solution for PS waste.

PS can undergo catalytic pyrolysis reactions like polyolefins but typically yield higher amounts of aromatic products such as BTX. An investigation into the effect of Fe-based MW absorbers – Fe, Fe_3O_4 and FeS_2 for the MW-assisted conversion of PS to aromatic hydrocarbons was explored by Fan *et al*.[106] High oil yields of > 92 % were achieved for all 3 Fe-based materials. The dominant product obtained for Fe and Fe_3O_4 was aromatic hydrocarbons arising from the aromatic group of the PS chain. FeS_2 showed a high selectivity towards aliphatic hydrocarbons compared to the other Fe-based catalysts. Luong *et al.*[87] reported the catalytic pyrolysis of PS over zeolite H-ZSM-5 in a MW reactor. Due to the aromaticity of PS, the main product obtained was BTX (65 %) with small amounts of coke (11 %) and paraffin (5 %), with selectivity towards BTX increasing with temperature from 300 ˚C to 400 ˚C. Optimal conditions were achieved at 400 °C in 30 min. The use of biochar, a sustainable carbon material obtained from the pyrolysis of biomass, was implemented as a MW-absorbing material to enhance the MW-assisted catalytic pyrolysis of PS to yield aromatic products.[107] The product obtained was mainly pyrolysis oil which was composed of styrene, cyclopropyl methylbenzene, and alkylbenzene derivates. The oil was rich in carbon content (~ 92 wt. %) with C_8 - C_{24} aromatic hydrocarbons. At 300 and 450 W of MW power, the oil yield was higher than that of the gas yield, however, at 600 W of MW power, the gas yield exceeded the oil yield. The pyrolysis experiments were carried out at 600 ˚C in a time range of 14 – 38 min.

Polyamides (PA) are characterised by the presence of recurring amide linkages (-CONH-) in their backbone. They can be synthesised via condensation polymerisation of diamines with dicarboxylic acids or via ring-opening polymerisation of lactams. They exhibit excellent mechanical strength, abrasion resistance, thermal stability, and chemical resistance, making them widely used in automotive components, textiles, films, electrical connectors.[108] PA can be chemically recycled by methods such as ammonolysis, alcoholysis and can be readily hydrolysed in the present of an acid or a base to yield the monomeric lactams.[109]

Klun *et al.*[110] reported the phosphoric acid catalysed hydrolysis of polyamide-6 (PA-6) to yield ϵ-aminocaproic acid (ACA), the aliphatic form of the PA-6 monomer. PA-6 underwent full depolymerisation in 20 min with a MW input of 200 W and a temperature of 260 °C. Some cyclic species were also detected at lower phosphoric acid concentrations (10 wt. %), however higher acid concentrations (>70 wt. %) resulted in their conversion to linear species. The MW-assisted, HCl catalysed hydrolysis of a range of aliphatic PAs including PA-66, PA-1010, PA-11 and PA-12, to dicarboxylic acids and diamines has been reported.[111] These PAs are comprised of different chain lengths obtained from polymerisation of diamines and carboxylic acids with different number of carbon atoms. PA-66 is composed of a hexamethylene diamine (C6) group and one adipic acid (C6) group, and PA-1010 is composed of one decamethylene diamine (C10) group and one sebacic group (C10). On the other hand, PA-11 and PA-12 refer to repeating units of 11- aminoundecanoic acid and 12-aminododecanoic acid, respectively. In the HCl-catalysed hydrolysis, PA-66 and PA-1010 can be depolymerised into their corresponding dicarboxylic acid and diamine chloride counterparts, while PA 11 and PA 12 can be depolymerised into their amino acid chloride counterparts. Owing to the presence of shorter chains between reactive functional groups, PA-66 was depolymerised 10 min at 200 °C (~150 W), while PA 1010, PA 11 and PA 12 are composed of less polar long chains and required 15-20 min to achieve full depolymerisation. It was found that the rate of reaction was dependent on the molar ratio of HCl to amide bonds in the polymer. For PA66 as at equimolar ratios of HCl to amide groups, a 96 % degree of PA degradation was observed from NMR. When a 0.5 molar equivalent of HCl to amide was used, this decreased to 50 % degree of degradation.

Frisa-Rubio *et al.*[112] developed a mathematical model for the scaled-up multi-frequency MW depolymerisation of PA-6 and PA-66 via HCl catalysed hydrolysis to yield 6 aminocaproic acid (6-ACA), and hexamethylenediamine (HDMA) and adipic acid (AA), respectively. The simulation demonstrated complete PA degradation and high monomer yields in under 10 min. The study also modelled the glycolysis of polyurethane (PU) to polyol diamine toluene (DAT), which the optimal conditions were simulated to be 230 °C for 40 min. A different approach was reported by Alberti and co-workers[113],

who reported a ring closing transformation of PA-6 over a 4-dimethylaminopyridine organo-catalyst to form the monomer *N*-acetylated caprolactam. Additionally, the acetyl group can react with 2-aminoethanol to form *N*-acetyle2-aminoethanol which is a starting material for poly(vinyl) amides. The depolymerisation of PA-6 to N-acetylcaprolactam proceeded after 15 min at 250 °C, while the acyl transfer step proceeded after 2h at 180 °C. The successful use of a homogeneous organo-catalyst suggests potential for developing heterogeneous organo-catalysts for easier catalyst separation and recycling for this reaction pathway. Furthermore, implementation of MW heating could enhance reaction efficiency. Poly(*p*-phenylene Terephthalamide) (PPTA), or commercially known as Kevlar or Twaron, is a highly crystalline aromatic polyamide that can be spun into fibres. Despite its lightweight characteristics, it exhibits significantly higher specific strength than steel, making it favourable for applications such as ropes, cables and advanced composites.[114] Recycling of waste fibres poses significant challenges due to a large decrease in material quality after the mechanical recycling process and are usually not recycled after being used.[115] Benninga *et al.*[116] reported the use of MW-assisted heating for the alkaline hydrolysis of PPTA to monomers TPA and p-phenyldiamine (PPD) achieving full conversion in 15 min at 260 °C.

PVC is a widely used polymer consisting of repeating chloroalkane units produced via the free-radical polymerisation of vinyl chloride monomers. Its chemical resistance, flame retardancy and durability, combined with the ability to tailor its mechanical characteristics through plasticisation, have led to extensive use in applications such as construction (e.g. pipes, window frames, flooring), medical devices, packaging, and cables.[117, 118] Mechanical recycling of PVC is limited by the thermal instability of the polymer as PVC tends to undergo dehydrochlorination, releasing HCl gas.[119] Chemical recycling of PVC often requires a dechlorination step and can be carried out using techniques such as hydrogenation, pyrolysis, gasification and catalytic degradation.[120] Pyrolysis and gasification of PVC is complicated by the release of HCl and the potential formation of hazardous byproducts including dioxins and furans.[121]

Ye *et al.*[122] reported the pyrolysis of PVC over Fe_3O_4, where the catalyst reacts with Cl_2 gas at high temperatures (400 °C) forming $FeCl_2$, thereby mitigating harmful HCl emissions typically formed during PVC pyrolysis. The process proceeds in two stages described in Scheme 1.

1. $\mathrm{PVC} + \mathrm{Fe_3O_4} \rightarrow \mathrm{FeCl_2} + \left(\diagup\!\diagdown\right)_n + \mathrm{H_2O} + \mathrm{HCl} + \mathrm{H_2} + \mathrm{volatiles}$

2. $\mathrm{FeCl_2} + \mathrm{Fe_3O_4} + \left(\diagup\!\diagdown\right)_n \rightarrow \mathrm{Fe} + \mathrm{Fe_3C} + \mathrm{C} + \mathrm{H_2O} + (\mathrm{CO})_x + \mathrm{H_2} + \mathrm{volatiles}$

Scheme 1: Reaction equations for stage 1 and 2 of co-pyrolysis of PVC with Fe_3O_4 to mitigate Cl_2 emissions.

The first stage occurs below 673 K involving dechlorination of PVC to form $FeCl_2$ and HCl, leaving a solid residue of polyenes. The second stage occurs above 673 K where further reaction between $FeCl_2$, Fe_3O_4 and polyenes yield solid carbon char, iron carbides and volatiles. Complete PVC decomposition was achieved within 5 min using 1800 W/h and an estimated temperature of 300 °C. PVC-coated power cables were also recycled via MW-assisted pyrolysis at 250 °C and 100–300 W for 120 s, to recover HCl, carbon black and the interior copper.[123]

Table 3 – Summary of catalysts, conditions and main products for MW-assisted depolymerisation of other plastics.

Polymer	Catalyst	Conditions	Products	Ref
PS	Fe / Fe_3O_4 / FeS_2	460 °C, 60 min, 650 W	Aromatic hydrocarbons (C8 – C16)	**106**
PS	H-ZSM-5	400 °C, 30 min	BTX	**87**
PS	Biochar susceptor	600 °C, 14 – 38 min, 300 – 600 W	styrene, cyclopropyl methylbenzene, and alkylbenzene	107
PA-6	H_3PO_4	260 °C, 20 min, 200 W	ACA	**110**
PA-66, PA-1010,	HCl	200 °C, 10/17 min, ~150 W	Adipic acid, hexamethylene diamine, Sebacic acid, 1, 10 decanediamine	**111**

PA-11, PA-12	HCl	200 °C 15/20 min, ~150 W	11-aminoundecanoic acidxHCl 12-aminododecanoic acidxHCl	[111]
PA-6	4-dimethyl-aminopyridine	250 °C, 15 min (thermal)	Caprolactam, *N*-acetyled 2-aminoethanol	[113]
PPTA	NaOH	240-260 °C, 15 min, 500 W	TPA, PPD	[116]
PVC	Fe_3O_4	400 °C (thermal)	Fe_3C, solid carbon char, $FeCl_2$	[122]
PVC/ Cu cable	-	250 °C, 2 min, 100 – 300 W,	HCl, carbon black	[123]

Abbreviations: PS = polystyrene; HZSM = hydrogen zeolite Socony Mobil-5; BTX = benzene, toluene, xylene, PA = polyamide; ACA = aminocaproic acid; PPTA = poly(p-phenylene terephthalamide); TPA = terephthalic acid; PPD = p-phenyldiamine PVC = polyvinyl chloride.

These findings highlight the applicability of MW-assisted heating for a wide range of polymers including PS, PA, and PVC. PAs can be depolymerised to monomers in a closed-loop chemical recycling system, while PS and PVC can be converted to fuel and solid carbon in open-loop systems. Further research is essential to explore more pathways for MW-assisted heterogeneous catalysis for the chemical recycling of these plastics.

1.4 Summary and Outlook

This review has highlighted recent advances in MW-assisted heterogeneous catalysis as a transformative approach for the chemical upcycling of plastics. MW heating offers rapid, energy-efficient and selective activation of catalysts and reaction media, overcoming some of the limitations of conventional thermal processes. A wide range of catalyst types, including metal oxides, organocatalysts, modified zeolite and carbon-based materials have demonstrated effectiveness in catalytic pyrolysis and closed loop depolymerisation reactions. MW-assisted catalytic depolymerisation has been successfully applied to a broad spectrum of polymers, including polyolefins, polyesters, polystyrene, polyamides, polycarbonates, and PVC. In many studies, the catalysts show excellent recyclability over multiple cycles, a key advantage of heterogeneous catalysts

and a valuable characteristic when considering scale-up. Mechanistic insights such as hotspot formation, microplasmas and the strategic use of MW-absorbing materials have enabled rapid depolymerisation, of plastics with poor intrinsic MW absorption such as polyolefins.

Despite these advances, chemical recycling faces several challenges that must be addressed for widespread adoption. Many current processes require high energy input, expensive catalysts, difficulty scaling or exhibit limited selectivity when dealing with mixed or contaminated plastic streams. To overcome these challenges, future research should prioritise the development of robust, selective and low-cost catalysts, reactor designs that can efficiently handle real-world waste plastics, and incorporate life cycle and technoeconomic assessment to evaluate the environmental and economic benefits of MW technologies. With continued advancements in catalyst design, reactor engineering and integrated sustainability assessments, MW-assisted catalytic upcycling has potential to be an important valorisation technology for transition toward a circular and more sustainable plastic economy.

1.5 References:

(1) Rafey, A.; Siddiqui, F. Z. A review of plastic waste management in India – challenges and opportunities. *International Journal of Environmental Analytical Chemistry* **2023**, *103* (16), 3971-3987. DOI: 10.1080/03067319.2021.1917560.

(2) Naderi Kalali, E.; Lotfian, S.; Entezar Shabestari, M.; Khayatzadeh, S.; Zhao, C.; Yazdani Nezhad, H. A critical review of the current progress of plastic waste recycling technology in structural materials. *Current Opinion in Green and Sustainable Chemistry* **2023**, *40*, 100763. DOI: https://doi.org/10.1016/j.cogsc.2023.100763.

(3) Development, O. f. E. C.-o. a. *Global Plastics Outlook: Economic Drivers, Environmental Impacts and Policy Options*; Paris, 2022. https://www.oecd.org/en/publications/global-plastics-outlook_de747aef-en/full-report.html (accessed 27/07/2025).

(4) Bertin, S.; Robin, J.-J. Study and characterization of virgin and recycled LDPE/PP blends. *European Polymer Journal* **2002**, *38* (11), 2255-2264. DOI: https://doi.org/10.1016/S0014-3057(02)00111-8.

(5) Ragaert, K.; Delva, L.; Van Geem, K. Mechanical and chemical recycling of solid plastic waste. *Waste Management* **2017**, *69*, 24-58. DOI: https://doi.org/10.1016/j.wasman.2017.07.044.

(6) Nayanathara Thathsarani Pilapitiya, P. G. C.; Ratnayake, A. S. The world of plastic waste: A review. *Cleaner Materials* **2024**, *11*, 100220. DOI: https://doi.org/10.1016/j.clema.2024.100220.

(7) Li, N.; Liu, H.; Cheng, Z.; Yan, B.; Chen, G.; Wang, S. Conversion of plastic waste into fuels: A critical review. *Journal of Hazardous Materials* **2022**, *424*, 127460. DOI: https://doi.org/10.1016/j.jhazmat.2021.127460.

(8) Jiang, J.; Shi, K.; Zhang, X.; Yu, K.; Zhang, H.; He, J.; Ju, Y.; Liu, J. From plastic waste to wealth using chemical recycling: A review. *Journal of Environmental Chemical Engineering* **2022**, *10* (1), 106867. DOI: https://doi.org/10.1016/j.jece.2021.106867.

(9) Martínez-Narro, G.; Hassan, S.; Phan, A. N. Chemical recycling of plastic waste for sustainable polymer manufacturing – A critical review. *Journal of Environmental Chemical Engineering* **2024**, *12* (2), 112323. DOI: https://doi.org/10.1016/j.jece.2024.112323.

(10) Rahimi, A.; García, J. M. Chemical recycling of waste plastics for new materials production. *Nature Reviews Chemistry* **2017**, *1* (6), 0046. DOI: 10.1038/s41570-017-0046.

(11) Jiang, Z.; Liang, Y.; Guo, F.; Wang, Y.; Li, R.; Tang, A.; Tu, Y.; Zhang, X.; Wang, J.; Li, S.; et al. Microwave-Assisted Pyrolysis-A New Way for the Sustainable Recycling and Upgrading of Plastic and Biomass: A Review. *ChemSusChem* **2024**, *17* (21), e202400129. DOI: https://doi.org/10.1002/cssc.202400129 (accessed 2025/03/20).

(12) Schade, A.; Melzer, M.; Zimmermann, S.; Schwarz, T.; Stoewe, K.; Kuhn, H. Plastic Waste Recycling–A Chemical Recycling Perspective. *ACS Sustainable Chemistry & Engineering* **2024**, *12* (33), 12270-12288. DOI: 10.1021/acssuschemeng.4c02551.

(13) European Commission: Joint Research, C.; Garcia-Gutierrez, P.; Amadei, A.; Klenert, D.; Nessi, S.; Tonini, D.; Tosches, D.; Ardente, F.; Saveyn, H. *Environmental and economic assessment of plastic waste recycling – A comparison of mechanical, physical, chemical recycling and energy recovery of plastic waste*; Publications Office of the European Union, 2023. DOI: doi/10.2760/0472.

(14) Rashid, M. A. M.; Kim, K. H.; Jeong, K. Microwave-Assisted Depolymerization of Natural and Synthetic Polymers. In *Depolymerization: Concepts, Progress, and Challenges Volume 3: Emerging Trends*, ACS Symposium Series, Vol. 1501; American Chemical Society, 2025; pp 15-31.

(15) Chu, M.; Tu, W.; Yang, S.; Zhang, C.; Li, Q.; Zhang, Q.; Chen, J. Sustainable chemical upcycling of waste polyolefins by heterogeneous catalysis. *SusMat* **2022**, *2* (2), 161-185. DOI: https://doi.org/10.1002/sus2.55 (accessed 2025/02/11).

(16) Li, H.; Zhang, C.; Pang, C.; Li, X.; Gao, X. The Advances in the Special Microwave Effects of the Heterogeneous Catalytic Reactions. *Frontiers in Chemistry* **2020**, *8*, Review.

(17) Bohre, A.; Jadhao, P. R.; Tripathi, K.; Pant, K. K.; Likozar, B.; Saha, B. Chemical Recycling Processes of Waste Polyethylene Terephthalate Using Solid Catalysts. *ChemSusChem* **2023**, *16* (14). DOI: 10.1002/cssc.202300142.

(18) Babaei, M.; Jalilian, M.; Shahbaz, K. Chemical recycling of Polyethylene terephthalate: A mini-review. *Journal of Environmental Chemical Engineering* **2024**, *12* (3), 112507. DOI: https://doi.org/10.1016/j.jece.2024.112507.
(19) Muringayil Joseph, T.; Azat, S.; Ahmadi, Z.; Moini Jazani, O.; Esmaeili, A.; Kianfar, E.; Haponiuk, J.; Thomas, S. Polyethylene terephthalate (PET) recycling: A review. *Case Studies in Chemical and Environmental Engineering* **2024**, *9*, 100673. DOI: https://doi.org/10.1016/j.cscee.2024.100673.
(20) Guo, Z.; Wu, J.; Wang, J. Chemical degradation and recycling of polyethylene terephthalate (PET): a review. *RSC Sustainability* **2025**, *3* (5), 2111-2133, 10.1039/D4SU00658E. DOI: 10.1039/D4SU00658E.
(21) Abedsoltan, H. A focused review on recycling and hydrolysis techniques of polyethylene terephthalate. *Polymer Engineering & Science* **2023**, *63* (9), 2651-2674. DOI: https://doi.org/10.1002/pen.26406 (accessed 2025/05/09).
(22) Weng, Y.; Hong, C.-B.; Zhang, Y.; Liu, H. Catalytic depolymerization of polyester plastics toward closed-loop recycling and upcycling. *Green Chemistry* **2024**, *26* (2), 571-592, 10.1039/D3GC04174C. DOI: 10.1039/D3GC04174C.
(23) Wang, S.; Li, J.; Li, X.; Tu, Y. Recent advances in the chemical recycling of polyesters. *Fundamental Research* **2024**. DOI: https://doi.org/10.1016/j.fmre.2024.05.014.
(24) Payne, J.; Jones, M. D. The Chemical Recycling of Polyesters for a Circular Plastics Economy: Challenges and Emerging Opportunities. *ChemSusChem* **2021**, *14* (19), 4041-4070. DOI: https://doi.org/10.1002/cssc.202100400 (accessed 2025/05/09).
(25) Li, Y.; Wang, S.; Qian, S.; Liu, Z.; Weng, Y.; Zhang, Y. Depolymerization and Re/Upcycling of Biodegradable PLA Plastics. *ACS Omega* **2024**, *9* (12), 13509-13521. DOI: 10.1021/acsomega.3c08674.
(26) Faust, K.; Denifl, P.; Hapke, M. Recent Advances in Catalytic Chemical Recycling of Polyolefins. *ChemCatChem* **2023**, *15* (13), e202300310. DOI: https://doi.org/10.1002/cctc.202300310 (accessed 2024/07/04).
(27) Sun, J.; Dong, J.; Gao, L.; Zhao, Y.-Q.; Moon, H.; Scott, S. L. Catalytic Upcycling of Polyolefins. *Chemical Reviews* **2024**, *124* (16), 9457-9579. DOI: 10.1021/acs.chemrev.3c00943.
(28) Zou, L.; Xu, R.; Wang, H.; Wang, Z.; Sun, Y.; Li, M. Chemical recycling of polyolefins: a closed-loop cycle of waste to olefins. *National Science Review* **2023**, *10* (9), nwad207. DOI: 10.1093/nsr/nwad207 (accessed 5/9/2025).
(29) Qin, J.; Wu, F.; Dou, Y.; Zhao, D.; Hélix-Nielsen, C.; Zhang, W. Advanced Catalysts for the Chemical Recycling of Plastic Waste. *Advanced Materials* **2025**, *n/a* (n/a), 2418138. DOI: https://doi.org/10.1002/adma.202418138 (accessed 2025/05/09).
(30) Chu, M.; Liu, Y.; Lou, X.; Zhang, Q.; Chen, J. Rational Design of Chemical Catalysis for Plastic Recycling. *ACS Catalysis* **2022**, *12* (8), 4659-4679. DOI: 10.1021/acscatal.2c01286.
(31) Luo, H.; Tyrrell, H.; Bai, J.; Ibrahim Muazu, R.; Long, X. Fundamental, technical and environmental overviews of plastic chemical recycling. *Green Chemistry* **2024**, *26* (23), 11444-11467, 10.1039/D4GC03127J. DOI: 10.1039/D4GC03127J.
(32) Nixon, K. D.; Schyns, Z. O. G.; Luo, Y.; Ierapetritou, M. G.; Vlachos, D. G.; Korley, L. T. J.; Epps, I. I. I. T. H. Analyses of circular solutions for advanced plastics waste recycling. *Nature Chemical Engineering* **2024**, *1* (10), 615-626. DOI: 10.1038/s44286-024-00121-6.
(33) Yadav, G.; Singh, A.; Dutta, A.; Uekert, T.; DesVeaux, J. S.; Nicholson, S. R.; Tan, E. C. D.; Mukarakate, C.; Schaidle, J. A.; Wrasman, C. J.; et al. Techno-economic analysis and life cycle assessment for catalytic fast pyrolysis of mixed plastic waste. *Energy & Environmental Science* **2023**, *16* (9), 3638-3653, 10.1039/D3EE00749A. DOI: 10.1039/D3EE00749A.
(34) Huang, P.; Ahamed, A.; Sun, R.; De Hoe, G. X.; Pitcher, J.; Mushing, A.; Lourenço, F.; Shaver, M. P. Circularizing PET-G Multimaterials: Life Cycle Assessment and Techno-Economic Analysis. *ACS Sustainable Chemistry & Engineering* **2023**, *11* (42), 15328-15337. DOI: 10.1021/acssuschemeng.3c04047.
(35) Muley, P. D.; Wang, Y.; Hu, J.; Shekhawat, D. Microwave-assisted heterogeneous catalysis. In *Catalysis: Volume 33*, Spivey, J., Han, Y.-F., Shekhawat, D. Eds.; Vol. 33; The Royal Society of Chemistry, 2021; p 0.

(36) Meloni, E.; Iervolino, G.; Palma, V. Basics of Microwave Heating and Recent Advances. In *Advances in Microwave-assisted Heterogeneous Catalysis*, Hu, J., Reddy, B. M. Eds.; Vol. 45; Royal Society of Chemistry, 2023; p 0.
(37) Sun, J.; Hayward, J. S.; Barter, M.; Slocombe, D. R.; Bartley, J. K. Designing Heterogeneous Catalysts for Microwave Assisted Selective Oxygenation. *ChemCatChem* **2024**, *16* (19), e202301586. DOI: https://doi.org/10.1002/cctc.202301586 (accessed 2025/02/19).
(38) Palma, V.; Barba, D.; Cortese, M.; Martino, M.; Renda, S.; Meloni, E. Microwaves and Heterogeneous Catalysis: A Review on Selected Catalytic Processes. In *Catalysts*, 2020; Vol. 10.
(39) Shen, X.; Zhao, Z.; Li, H.; Gao, X.; Fan, X. Microwave-assisted pyrolysis of plastics with iron-based catalysts for hydrogen and carbon nanotubes production. *Materials Today Chemistry* **2022**, *26*, 101166. DOI: https://doi.org/10.1016/j.mtchem.2022.101166.
(40) Zhang, F.; Zhang, X.; Song, Z.; Li, X.; Zhao, X.; Sun, J.; Mao, Y.; Wang, X.; Wang, W. Promotion of microwave discharge over carbon catalysts for CO2 reforming of CH4 to syngas. *Fuel* **2023**, *331*, 125914. DOI: https://doi.org/10.1016/j.fuel.2022.125914.
(41) Haneishi, N.; Tsubaki, S.; Abe, E.; Maitani, M. M.; Suzuki, E.-i.; Fujii, S.; Fukushima, J.; Takizawa, H.; Wada, Y. Enhancement of Fixed-bed Flow Reactions under Microwave Irradiation by Local Heating at the Vicinal Contact Points of Catalyst Particles. *Scientific Reports* **2019**, *9* (1), 222. DOI: 10.1038/s41598-018-35988-y.
(42) Musho, T. D.; Wildfire, C.; Houlihan, N. M.; Sabolsky, E. M.; Shekhawat, D. Study of Cu2O particle morphology on microwave field enhancement. *Materials Chemistry and Physics* **2018**, *216*, 278-284. DOI: https://doi.org/10.1016/j.matchemphys.2018.05.059.
(43) Casey, É.; Breen, R.; Pareras, G.; Rimola, A.; Holmes, J. D.; Collins, G. Guanidine functionalized porous SiO2 as heterogeneous catalysts for microwave depolymerization of PET and PLA. *RSC Sustainability* **2024**, *2* (4), 1040-1051, 10.1039/D3SU00425B. DOI: 10.1039/D3SU00425B.
(44) Zhao, J.; Liu, B.; Xiong, L.; Liu, W.; Wang, D.; Ma, W.; Jiang, L.; Yang, J.; Wang, P.; Xiao, T.; et al. Highly selective upcycling of plastic mixture waste by microwave-assisted catalysis over Zn/b-ZnO. *Nature Communications* **2025**, *16* (1), 1726. DOI: 10.1038/s41467-024-55584-1.
(45) Adam, M.; Hjalmarsson, N.; Lee, C. S.; Irvine, D. J.; Robinson, J.; Binner, E. Understanding microwave interactions with polymers to enable advanced plastic chemical recycling. *Polymer Testing* **2024**, *137*, 108483. DOI: https://doi.org/10.1016/j.polymertesting.2024.108483.
(46) Zhang, F.; Li, N.; Shi, J.-F.; Xu, L.; Jia, L.-C.; Wang, Y.-Y.; Yan, D.-X. Recent progress on carbon-based microwave absorption materials for multifunctional applications: A review. *Composites Part B: Engineering* **2024**, *283*, 111646. DOI: https://doi.org/10.1016/j.compositesb.2024.111646.
(47) Hou, T.; Wang, B.; Jia, Z.; Wu, H.; Lan, D.; Huang, Z.; Feng, A.; Ma, M.; Wu, G. A review of metal oxide-related microwave absorbing materials from the dimension and morphology perspective. *Journal of Materials Science: Materials in Electronics* **2019**, *30* (12), 10961-10984. DOI: 10.1007/s10854-019-01537-0.
(48) Irfan, M.; Saleem, R.; Shoukat, B.; Hussain, H.; Shukrullah, S.; Naz, M. Y.; Rahman, S.; Ghanim, A. A. J.; Nawalany, G.; Jakubowski, T. Production of combustible fuels and carbon nanotubes from plastic wastes using an in-situ catalytic microwave pyrolysis process. *Scientific Reports* **2023**, *13* (1), 9057. DOI: 10.1038/s41598-023-36254-6.
(49) Katoh, T.; Ogawa, Y.; Ohta, Y.; Yokozawa, T. Synthesis of polyester by means of polycondensation of diol ester and dicarboxylic acid ester through ester–ester exchange reaction. *Journal of Polymer Science* **2021**, *59* (9), 787-797. DOI: https://doi.org/10.1002/pol.20210032 (accessed 2025/07/01).
(50) Deopura, B. L.; Padaki, N. V. Chapter 5 - Synthetic Textile Fibres: Polyamide, Polyester and Aramid Fibres. In *Textiles and Fashion*, Sinclair, R. Ed.; Woodhead Publishing, 2015; pp 97-114.
(51) Cao, J.; Liang, H.; Yang, J.; Zhu, Z.; Deng, J.; Li, X.; Elimelech, M.; Lu, X. Depolymerization mechanisms and closed-loop assessment in polyester waste recycling. *Nature Communications* **2024**, *15* (1), 6266. DOI: 10.1038/s41467-024-50702-5.
(52) Enache, A.-C.; Grecu, I.; Samoila, P. Polyethylene Terephthalate (PET) Recycled by Catalytic Glycolysis: A Bridge toward Circular Economy Principles. In *Materials*, 2024; Vol. 17.

(53) Shukla, S. R.; Harad, A. M. Aminolysis of polyethylene terephthalate waste. *Polymer Degradation and Stability* **2006**, *91* (8), 1850-1854. DOI: https://doi.org/10.1016/j.polymdegradstab.2005.11.005.
(54) Achilias, D. S.; Tsintzou, G. P.; Nikolaidis, A. K.; Bikiaris, D. N.; Karayannidis, G. P. Aminolytic depolymerization of poly(ethylene terephthalate) waste in a microwave reactor. *Polymer International* **2011**, *60* (3), 500-506. DOI: https://doi.org/10.1002/pi.2976 (accessed 2025/07/01).
(55) Yao, H.; Liu, L.; Yan, D.; Zhou, Q.; Xin, J.; Lu, X.; Zhang, S. Colorless BHET obtained from PET by modified mesoporous catalyst ZnO/SBA-15. *Chemical Engineering Science* **2022**, *248*, 117109. DOI: https://doi.org/10.1016/j.ces.2021.117109.
(56) Cao, J.; Lin, Y.; Jiang, W.; Wang, W.; Li, X.; Zhou, T.; Sun, P.; Pan, B.; Li, A.; Zhang, Q. Mechanism of the Significant Acceleration of Polyethylene Terephthalate Glycolysis by Defective Ultrathin ZnO Nanosheets with Heteroatom Doping. *ACS Sustainable Chemistry & Engineering* **2022**, *10* (17), 5476-5488. DOI: 10.1021/acssuschemeng.1c08656.
(57) Du, J.-T.; Sun, Q.; Zeng, X.-F.; Wang, D.; Wang, J.-X.; Chen, J.-F. ZnO nanodispersion as pseudohomogeneous catalyst for alcoholysis of polyethylene terephthalate. *Chemical Engineering Science* **2020**, *220*, 115642. DOI: https://doi.org/10.1016/j.ces.2020.115642.
(58) Selvam, E.; Luo, Y.; Ierapetritou, M.; Lobo, R. F.; Vlachos, D. G. Microwave-assisted depolymerization of PET over heterogeneous catalysts. *Catalysis Today* **2023**, *418*, 114124. DOI: https://doi.org/10.1016/j.cattod.2023.114124.
(59) Xi, G.; Lu, M.; Sun, C. Study on depolymerization of waste polyethylene terephthalate into monomer of bis(2-hydroxyethyl terephthalate). *Polymer Degradation and Stability* **2005**, *87* (1), 117-120. DOI: https://doi.org/10.1016/j.polymdegradstab.2004.07.017.
(60) Chen, F.; Wang, G.; Shi, C.; Zhang, Y.; Zhang, L.; Li, W.; Yang, F. Kinetics of glycolysis of poly(ethylene terephthalate) under microwave irradiation. *Journal of Applied Polymer Science* **2013**, *127* (4), 2809-2815. DOI: https://doi.org/10.1002/app.37608 (accessed 2025/06/17).
(61) Revathi, M.; Sivamurugan, V.; Dhanalakshmi, R.; Biju Bennie, R.; Joel, C. Kaolin supported niobia for microwave-assisted aminolytic depolymerization in the chemical recycling of polyester waste. *Ceramics International* **2024**, *50* (17, Part B), 30483-30492. DOI: https://doi.org/10.1016/j.ceramint.2024.05.346.
(62) Anbarasu, M.; Vinitha, V.; Preeyanghaa, M.; Neppolian, B.; Sivamurugan, V. Valorization of PES Textile Waste Through Glycolysis and Aminolysis Using Bimetallic ZnO and Carbon Nitride Nanocomposites. *Journal of Cluster Science* **2024**, *35* (4), 1105-1125. DOI: 10.1007/s10876-023-02534-4.
(63) Vinitha, V.; Preeyanghaa, M.; Anbarasu, M.; Neppolian, B.; Sivamurugan, V. Chemical recycling of polyester textile wastes using silver-doped zinc oxide nanoparticles: an economical solution for circular economy. *Environmental Science and Pollution Research* **2023**, *30* (30), 75401-75416. DOI: 10.1007/s11356-023-27567-0.
(64) Fukushima, K.; Coulembier, O.; Lecuyer, J. M.; Almegren, H. A.; Alabdulrahman, A. M.; Alsewailem, F. D.; McNeil, M. A.; Dubois, P.; Waymouth, R. M.; Horn, H. W.; et al. Organocatalytic depolymerization of poly(ethylene terephthalate). *Journal of Polymer Science Part A: Polymer Chemistry* **2011**, *49* (5), 1273-1281. DOI: https://doi.org/10.1002/pola.24551 (accessed 2025/07/28).
(65) Ramezani Dana, H.; Ebrahimi, F. Synthesis, properties, and applications of polylactic acid-based polymers. *Polymer Engineering & Science* **2023**, *63* (1), 22-43. DOI: https://doi.org/10.1002/pen.26193 (accessed 2025/07/02).
(66) Hussain, M.; Khan, S. M.; Shafiq, M.; Abbas, N. A review on PLA-based biodegradable materials for biomedical applications. *Giant* **2024**, *18*, 100261. DOI: https://doi.org/10.1016/j.giant.2024.100261.
(67) Limsukon, W.; Rubino, M.; Rabnawaz, M.; Lim, L.-T.; Auras, R. Hydrolytic degradation of poly(lactic acid): Unraveling correlations between temperature and the three phase structures. *Polymer Degradation and Stability* **2023**, *217*, 110537. DOI: https://doi.org/10.1016/j.polymdegradstab.2023.110537.

(68) McKeown, P.; Jones, M. D. The Chemical Recycling of PLA: A Review. In *Sustainable Chemistry*, 2020; Vol. 1, pp 1-22.
(69) Siddiqui, M. N.; Kolokotsiou, L.; Vouvoudi, E.; Redhwi, H. H.; Al-Arfaj, A. A.; Achilias, D. S. Depolymerization of PLA by Phase Transfer Catalysed Alkaline Hydrolysis in a Microwave Reactor. *Journal of Polymers and the Environment* **2020**, *28* (6), 1664-1672. DOI: 10.1007/s10924-020-01716-9.
(70) Cheung, E.; Alberti, C.; Enthaler, S. Chemical Recycling of End-of-Life Poly(lactide) via Zinc-Catalyzed Depolymerization and Polymerization. *ChemistryOpen* **2020**, *9* (12), 1224-1228. DOI: https://doi.org/10.1002/open.202000243 (accessed 2025/07/02).
(71) Román-Ramírez, L. A.; McKeown, P.; Jones, M. D.; Wood, J. Poly(lactic acid) Degradation into Methyl Lactate Catalyzed by a Well-Defined Zn(II) Complex. *ACS Catalysis* **2019**, *9* (1), 409-416. DOI: 10.1021/acscatal.8b04863.
(72) Najmi, S.; Huang, D.; Duncan, A.; Slanac, D.; Hutchenson, K.; Hughes, J.; Poladi, R.; Vlachos, D. G. Closed-loop chemical recycling of polyethylene furan-2,5-dicarboxylate (PEF) under microwave-assisted heating. *Green Chemistry* **2025**, 10.1039/D5GC01583A. DOI: 10.1039/D5GC01583A.
(73) Takeuchi, K. 5.16 - Polycarbonates. In *Polymer Science: A Comprehensive Reference*, Matyjaszewski, K., Möller, M. Eds.; Elsevier, 2012; pp 363-376.
(74) Sambyal, P.; Najmi, P.; Sharma, D.; Khoshbakhti, E.; Hosseini, H.; Milani, A. S.; Arjmand, M. Plastic recycling: Challenges and opportunities. *The Canadian Journal of Chemical Engineering* **2025**, *103* (6), 2462-2498. DOI: https://doi.org/10.1002/cjce.25531 (accessed 2025/07/02).
(75) Grause, G.; Tsukada, N.; Hall, W. J.; Kameda, T.; Williams, P. T.; Yoshioka, T. High-value products from the catalytic hydrolysis of polycarbonate waste. *Polymer Journal* **2010**, *42* (6), 438-442. DOI: 10.1038/pj.2010.21.
(76) Guo, J.; Liu, M.; Gu, Y.; Wang, Y.; Gao, J.; Liu, F. Efficient Alcoholysis of Polycarbonate Catalyzed by Recyclable Lewis Acidic Ionic Liquids. *Industrial & Engineering Chemistry Research* **2018**, *57* (32), 10915-10921. DOI: 10.1021/acs.iecr.8b02201.
(77) Kim, D.; Kim, B.-k.; Cho, Y.; Han, M.; Kim, B.-S. Kinetics of Polycarbonate Glycolysis in Ethylene Glycol. *Industrial & Engineering Chemistry Research* **2009**, *48* (2), 685-691. DOI: 10.1021/ie8010947.
(78) Chen, T.-B.; Yun, L.-X.; Zhang, B.; Gu, Y.-H.; Zhang, H.-T.; Zeng, X.-F.; Wang, J.-X. Highly Efficient Depolymerization of Polycarbonate Enabled by Dispersions of Ultrasmall ZnO Nanoparticles. *Industrial & Engineering Chemistry Research* **2024**, *63* (42), 17868-17877. DOI: 10.1021/acs.iecr.4c03059.
(79) Tsintzou, G. P.; Antonakou, E. V.; Achilias, D. S. Environmentally friendly chemical recycling of poly(bisphenol-A carbonate) through phase transfer-catalysed alkaline hydrolysis under microwave irradiation. *Journal of Hazardous Materials* **2012**, *241-242*, 137-145. DOI: https://doi.org/10.1016/j.jhazmat.2012.09.027.
(80) Ikenaga, K.; Higuchi, K.; Kohri, S.; Kusakabe, K. Depolymerization of polycarbonate by methanol under pressurized microwave irradiation. *IOP Conference Series: Materials Science and Engineering* **2018**, *458* (1), 012037. DOI: 10.1088/1757-899X/458/1/012037.
(81) Schwab, S. T.; Baur, M.; Nelson, T. F.; Mecking, S. Synthesis and Deconstruction of Polyethylene-type Materials. *Chemical Reviews* **2024**, *124* (5), 2327-2351. DOI: 10.1021/acs.chemrev.3c00587.
(82) Yang, G.; Peng, P.; Guo, H.; Song, H.; Li, Z. The catalytic pyrolysis of waste polyolefins by zeolite-based catalysts: A critical review on the structure-acidity synergies of catalysts. *Polymer Degradation and Stability* **2024**, *222*, 110712. DOI: https://doi.org/10.1016/j.polymdegradstab.2024.110712.
(83) Thangaraj, B.; Lee, Y.-K. Review on recent development in catalytic cracking of waste polyolefins: Effect of zeolite-based catalysts and reaction parameters. *Fuel* **2025**, *380*, 133220. DOI: https://doi.org/10.1016/j.fuel.2024.133220.
(84) Tasleem, S.; Soliman, A.; Alsharaeh, E. H. Recent developments in catalytic materials and reactors for the catalytic pyrolysis of plastic waste into hydrogen: a critical review with a focus on the circular economy. *RSC Advances* **2025**, *15* (26), 20881-20907, 10.1039/D5RA03170B. DOI: 10.1039/D5RA03170B.

(85) Oh, S.; Stache, E. E. Recent advances in oxidative degradation of plastics. *Chemical Society Reviews* **2024**, *53* (14), 7309-7327, 10.1039/D4CS00407H. DOI: 10.1039/D4CS00407H.
(86) Putra, P. H. M.; Rozali, S.; Patah, M. F. A.; Idris, A. A review of microwave pyrolysis as a sustainable plastic waste management technique. *Journal of Environmental Management* **2022**, *303*, 114240. DOI: https://doi.org/10.1016/j.jenvman.2021.114240.
(87) Qie, Z.; Xiang, H.; Xiang, H.; Zou, R.; Alhelali, A.; Alhassawi, H.; Ding, S.; Jiao, Y.; Holmes, S. M.; Garforth, A. A.; et al. Catalytic pyrolysis of high-density polyethylene (HDPE) over hierarchical ZSM-5 zeolites produced by microwave-assisted chelation-alkaline treatment. *Fuel* **2024**, *368*, 131532. DOI: https://doi.org/10.1016/j.fuel.2024.131532.
(88) Luong, T.; Luo, C.; Robinson, B.; Hu, J.; Wang, Y. Microwave Catalytic Co-Upcycling of Polyethylene and Polystyrene. *ACS Sustainable Resource Management* **2024**, *1* (8), 1750-1758. DOI: 10.1021/acssusresmgt.4c00110.
(89) Vatankhah, F.; Carrillo García, A.; Chaouki, J. Role of Bifunctional Metal-Promoted Zeolitic Catalyst in Microwave-Assisted Pyrolysis of Polyethylene to Monocyclic Aromatics. *Energy & Fuels* **2024**, *38* (21), 20562-20576. DOI: 10.1021/acs.energyfuels.4c03692.
(90) Ding, K.; Liu, S.; Huang, Y.; Liu, S.; Zhou, N.; Peng, P.; Wang, Y.; Chen, P.; Ruan, R. Catalytic microwave-assisted pyrolysis of plastic waste over NiO and HY for gasoline-range hydrocarbons production. *Energy Conversion and Management* **2019**, *196*, 1316-1325. DOI: https://doi.org/10.1016/j.enconman.2019.07.001.
(91) Tuli, V.; Luo, C.; Robinson, B.; Hu, J.; Wang, Y. Microwave-assisted catalytic technology for sustainable production of valuable chemicals from plastic waste with enhanced catalyst reusability. *Chemical Engineering Journal* **2024**, *489*, 151551. DOI: https://doi.org/10.1016/j.cej.2024.151551.
(92) Zhao, J.; Gao, J.; Wang, D.; Chen, Y.; Zhang, L.; Ma, W.; Zhao, S. Microwave-intensified catalytic upcycling of plastic waste into hydrogen and carbon nanotubes over self-dispersing bimetallic catalysts. *Chemical Engineering Journal* **2024**, *483*, 149270. DOI: https://doi.org/10.1016/j.cej.2024.149270.
(93) Shoukat, B.; Hussain, H.; Naz, M. Y.; Ibrahim, A. A.; Shukrullah, S.; Khan, Y.; Zhang, Y. Microwave-Assisted Catalytic Deconstruction of Plastics Waste into Nanostructured Carbon and Hydrogen Fuel Using Composite Magnetic Ferrite Catalysts. *Scientifica* **2024**, *2024* (1), 3318047. DOI: https://doi.org/10.1155/2024/3318047 (accessed 2025/03/25).
(94) Jie, X.; Li, W.; Slocombe, D.; Gao, Y.; Banerjee, I.; Gonzalez-Cortes, S.; Yao, B.; AlMegren, H.; Alshihri, S.; Dilworth, J.; et al. Microwave-initiated catalytic deconstruction of plastic waste into hydrogen and high-value carbons. *Nature Catalysis* **2020**, *3* (11), 902-912. DOI: 10.1038/s41929-020-00518-5.
(95) Kondo, H.; Sawai, A.; Hirabayashi, K.; Nakanishi, A.; Fukumoto, K.; Tanaka, Y.; Horikoshi, S. Continuous process design of the microwave chemical recycling of waste plastics using microwave-absorbing heating elements. *Sci Rep* **2024**, *14* (1), 21952. DOI: 10.1038/s41598-024-71958-3 From NLM.
(96) Gao, J.; Zhao, J.; Xing, Z.; Guo, M.; Xie, H.; Ma, W.; Liu, J. Microwave-Powered Liquid Metal Degradation of Polyolefins. *Advanced Materials* **2025**, *37* (6), 2412539. DOI: https://doi.org/10.1002/adma.202412539 (accessed 2025/03/19).
(97) Bäckström, E.; Odelius, K.; Hakkarainen, M. Trash to Treasure: Microwave-Assisted Conversion of Polyethylene to Functional Chemicals. *Industrial & Engineering Chemistry Research* **2017**, *56* (50), 14814-14821. DOI: 10.1021/acs.iecr.7b04091.
(98) Chow, C.-F.; Wong, W.-L.; Ho, K. Y.-F.; Chan, C.-S.; Gong, C.-B. Combined Chemical Activation and Fenton Degradation to Convert Waste Polyethylene into High-Value Fine Chemicals. *Chemistry – A European Journal* **2016**, *22* (28), 9513-9518. DOI: https://doi.org/10.1002/chem.201600856 (accessed 2024/01/23).
(99) Ghatge, S.; Yang, Y.; Ko, Y.; Yoon, Y.; Ahn, J.-H.; Kim, J. J.; Hur, H.-G. Degradation of sulfonated polyethylene by a bio-photo-fenton approach using glucose oxidase immobilized on titanium dioxide. *Journal of Hazardous Materials* **2022**, *423*, 127067. DOI: https://doi.org/10.1016/j.jhazmat.2021.127067.

(100) Dos Santos, N. d. O.; Busquets, R.; Campos, L. C. Insights into the removal of microplastics and microfibres by Advanced Oxidation Processes. *Science of The Total Environment* **2023**, *861*, 160665. DOI: https://doi.org/10.1016/j.scitotenv.2022.160665.
(101) Hu, K.; Zhou, P.; Yang, Y.; Hall, T.; Nie, G.; Yao, Y.; Duan, X.; Wang, S. Degradation of Microplastics by a Thermal Fenton Reaction. *ACS ES&T Engineering* **2022**, *2* (1), 110-120. DOI: 10.1021/acsestengg.1c00323.
(102) Breen, R.; Holmes, J. D.; Collins, G. Heterogeneous Fenton-type oxidative degradation of low-density polyethylene to valuable acid products using a nanostructured Fe–CeO2 solid solution catalyst. *Catalysis Science & Technology* **2025**, 10.1039/D4CY01384K. DOI: 10.1039/D4CY01384K.
(103) Xu, Z.; Sun, D.; Xu, J.; Yang, R.; Russell, J. D.; Liu, G. Progress and Challenges in Polystyrene Recycling and Upcycling. *ChemSusChem* **2024**, *17* (17), e202400474. DOI: https://doi.org/10.1002/cssc.202400474 (accessed 2025/07/07).
(104) Commission, E. Proposal for a regulation of the European Parliament and of the Council on packaging and packaging waste, amending Regulation (EU) 2019/1020 and Directive (EU) 2019/904, and repealing Directive 94/62/EC. 2022.
(105) Gonzalez-Aguilar, A. M.; Pérez-García, V.; Riesco-Ávila, J. M. A Thermo-Catalytic Pyrolysis of Polystyrene Waste Review: A Systematic, Statistical, and Bibliometric Approach. In *Polymers*, 2023; Vol. 15.
(106) Fan, S.; Zhang, Y.; Cui, L.; Xiong, Q.; Maqsood, T. Conversion of Polystyrene Plastic into Aviation Fuel through Microwave-Assisted Pyrolysis as Affected by Iron-Based Microwave Absorbents. *ACS Sustainable Chemistry & Engineering* **2023**, *11* (3), 1054-1066. DOI: 10.1021/acssuschemeng.2c05880.
(107) Kachhadiya, K.; Patel, D.; Vijaybhai, G. J.; Raghuvanshi, P.; Surya, D. V.; Dharaskar, S.; Kumar, G. P.; Reddy, B. R.; Remya, N.; Kumar, T. H.; et al. Conversion of waste polystyrene into valuable aromatic hydrocarbons via microwave-assisted pyrolysis. *Environmental Science and Pollution Research* **2024**, *31* (46), 57509-57522. DOI: 10.1007/s11356-023-28294-2.
(108) Kohutiar, M.; Kakošová, L.; Krbata, M.; Janík, R.; Fekiač, J. J.; Breznická, A.; Eckert, M.; Mikuš, P.; Timárová, Ľ. Comprehensive Review: Technological Approaches, Properties, and Applications of Pure and Reinforced Polyamide 6 (PA6) and Polyamide 12 (PA12) Composite Materials. In *Polymers*, 2025; Vol. 17.
(109) Hirschberg, V.; Rodrigue, D. Recycling of polyamides: Processes and conditions. *Journal of Polymer Science* **2023**, *61* (17), 1937-1958. DOI: https://doi.org/10.1002/pol.20230154 (accessed 2025/07/07).
(110) Klun, U.; Kržan, A. Rapid microwave induced depolymerization of polyamide-6. *Polymer* **2000**, *41* (11), 4361-4365. DOI: https://doi.org/10.1016/S0032-3861(99)00658-8.
(111) Češarek, U.; Pahovnik, D.; Žagar, E. Chemical Recycling of Aliphatic Polyamides by Microwave-Assisted Hydrolysis for Efficient Monomer Recovery. *ACS Sustainable Chemistry & Engineering* **2020**, *8* (43), 16274-16282. DOI: 10.1021/acssuschemeng.0c05706.
(112) Frisa-Rubio, A.; González-Niño, C.; Royo, P.; García-Polanco, N.; Martínez-Hernández, D.; Royo-Pascual, L.; Fiesser, S.; Žagar, E.; García-Armingol, T. Chemical recycling of plastics assisted by microwave multi-frequency heating. *Cleaner Engineering and Technology* **2021**, *5*, 100297. DOI: https://doi.org/10.1016/j.clet.2021.100297.
(113) Alberti, C.; Figueira, R.; Hofmann, M.; Koschke, S.; Enthaler, S. Chemical Recycling of End-of-Life Polyamide 6 via Ring Closing Depolymerization. *ChemistrySelect* **2019**, *4* (43), 12638-12642. DOI: https://doi.org/10.1002/slct.201903970 (accessed 2025/05/15).
(114) Tanner, D.; Fitzgerald, J. A.; Phillips, B. R. The Kevlar Story—an Advanced Materials Case Study. *Angewandte Chemie International Edition in English* **1989**, *28* (5), 649-654. DOI: https://doi.org/10.1002/anie.198906491 (accessed 2025/03/21).
(115) Gore, P. M.; Kandasubramanian, B. Functionalized Aramid Fibers and Composites for Protective Applications: A Review. *Industrial & Engineering Chemistry Research* **2018**, *57* (49), 16537-16563. DOI: 10.1021/acs.iecr.8b04903.

(116) Benninga, J.; Gebben, B.; Folkersma, R.; Voet, V. S. D.; Loos, K. Rapid Microwave-Assisted Chemical Recycling of Poly(p-Phenylene Terephthalamide). *Journal of the American Chemical Society* **2025**, *147* (9), 7191-7195. DOI: 10.1021/jacs.4c17791.
(117) Campisi, L.; La Motta, C.; Napierska, D. Polyvinyl chloride (PVC), its additives, microplastic and human health: Unresolved and emerging issues. *Science of The Total Environment* **2025**, *960*, 178276. DOI: https://doi.org/10.1016/j.scitotenv.2024.178276.
(118) Zhang, X.; Feng, X.; Guo, W.; Zhang, C.; Zhang, X. Chemically recyclable polyvinyl chloride-like plastics. *Nature Communications* **2024**, *15* (1), 8536. DOI: 10.1038/s41467-024-52852-y.
(119) Havaei, M.; Akin, O.; Locaspi, A.; John Varghese, R.; Minette, F.; Romers, E.; De Meester, S.; Van Geem, K. M. Beyond the Landfill: A critical review of techniques for End-of-Life Polyvinyl chloride (PVC) valorization. *Waste Management* **2025**, *193*, 105-134. DOI: https://doi.org/10.1016/j.wasman.2024.11.023.
(120) Lu, L.; Li, W.; Cheng, Y.; Liu, M. Chemical recycling technologies for PVC waste and PVC-containing plastic waste: A review. *Waste Management* **2023**, *166*, 245-258. DOI: https://doi.org/10.1016/j.wasman.2023.05.012.
(121) Jerzak, W.; Magdziarz, A. Dehydrochlorination of polyvinyl chloride and co-pyrolysis with maize cob: Insight into product composition and thermal behaviour. *Thermochimica Acta* **2025**, *749*, 180023. DOI: https://doi.org/10.1016/j.tca.2025.180023.
(122) Ye, L.; Li, T.; Hong, L. Co-pyrolysis of Fe3O4-poly(vinyl chloride) (PVC) mixtures: Mitigation of chlorine emissions during PVC recycling. *Waste Management* **2021**, *126*, 832-842. DOI: https://doi.org/10.1016/j.wasman.2021.04.021.
(123) Horikoshi, S.; Hachisuga, N.; Serpone, N. Recycling of e-waste power cables using microwave-induced pyrolysis – process characteristics and facile recovery of copper metal. *RSC Advances* **2024**, *14* (41), 29955-29964, 10.1039/D4RA05602G. DOI: 10.1039/D4RA05602G.

Chapter 2

Experimental

2.1 Introduction

The purpose of this chapter is to provide a brief overview of the instrumentation used for characterisation throughout this thesis. Materials characterisation was carried out using techniques such as energy dispersive x-ray analysis (EDX), Fourier transform infrared spectroscopy (FTIR), Raman spectroscopy, scanning electron microscopy (SEM), transmission electron spectroscopy (TEM), total-reflection x-ray fluorescence spectroscopy (TXRF), x-ray diffraction (XRD), and x-ray photoelectron spectroscopy (XPS). The molecular structure of products formed from the reactions were identified using nuclear magnetic resonance (NMR) and high-performance liquid chromatography (HPLC). Catalytic depolymerisation reactions were carried out in a Milestone Flexiwave microwave system using an SK-15 rotor and high-pressure vessels.

2.2 Electron Microscopy

Electron microscopy is a technique that allows observation of materials at the nanoscale and can provide in-depth information on its structural and chemical properties. Specifically, the particle size, morphology and crystal structure of a catalyst. Electron microscopy allows for the investigation of nanomaterials using high resolution imaging technology. It is a widely used technique that has applications across fields such as biomedical, electronic devices, materials and industry. The two types of electron microscopy mentioned in this thesis are scanning electron microscopy (SEM) and transmission electron microscopy (TEM).

The scanning electron microscope works by projecting a focused stream of electrons on to the surface of a specimen which is fixed to a stub in the chamber of the microscope under vacuum to prevent the sample from interacting with the electron beam. Specialised detectors on the microscope, for this work specifically secondary electron (SE) detectors and InLens detectors, can detect signals produced from

secondary or backscattered electrons (BE) in the sample. Specialised software can convert the signals into high resolution images which can allow for detailed analysis of the morphology and topography of a nanomaterial. In this work, scanning electron microscopy (SEM) was performed on a Zeiss Supra 40 high resolution SEM at an accelerating voltage of 5 kV.

The transmission electron microscope works by accelerating a high energy electron beam though a very thin amount (<100 nm) of sample on a TEM grid, and an image is then produced from an electron detector allowing observation of the sample at the nanometer scale. TEM facilitates an in-depth analysis of nanomaterials, specifically the morphology and crystallinity of the sample at the nano scale. TEM can be used to determine the d-spacings of lattice fringes in a sample. Fast Fourier Transform images are inverse images of high-resolution TEM and can provide information about the crystal phase of a sample by use of diffraction. For this work, TEM was performed using a JEOL 2100 electron microscope at an operating voltage of 200 kV and FEI Titan TEM at an operating voltage of 300 kV. Image J software was used to determine particle diameters with excel used to calculate the mean particle diameters and to determine the *d*-spacing for crystal structures.

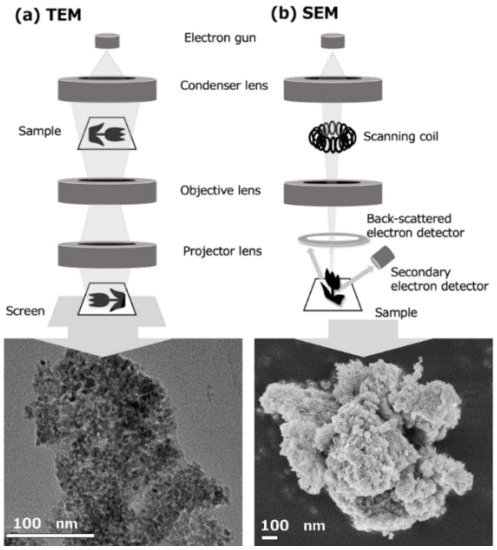


Figure 1: a) Schematic for typical TEM setup[1] with TEM image of Fe-CeO_2 catalyst, b) Schematic for typical SEM setup[1] with SEM image of Fe-CeO_2 catalyst. Reproduced with permissions from Ref[1].

2.3 Energy Dispersive X-ray Analysis (EDX)

Energy dispersive x-ray analysis (EDX) is a tool often used coupled with SEM or TEM that uses x-rays to map and quantify elements in a material. In this work, EDX was predominantly used to identify and quantify elements in catalytic materials. EDX works on a principle known as Moseley's Law which relates atomic number to the frequency of energy released by the atom when subject to x-rays. Specifically, an x-ray beam will interact with core electrons causing them to be ejected from the shell. Higher energy electrons then undergo relaxation to fill in the hole left by the ejected electron, which results in the emission of X-rays from the atom characteristic to that element. A detector can capture the emitted x-rays and convert them to voltage signals which are processed to create a spectrum or a map. Aztec software was used in this work to generate data including spectra, atomic % of elements and elemental colour mapping.

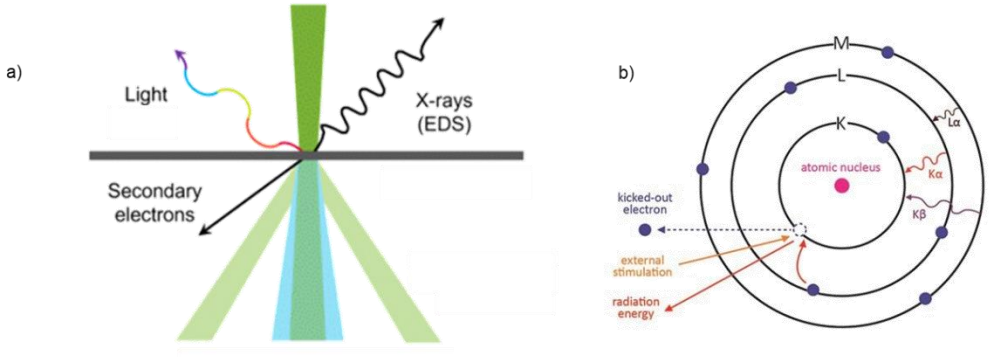


Figure 2: a) Schematic diagram of EDX instrument set up. Reproduced from Ref[2], b) schematic diagram of EDX characterisation. Reproduced from Ref[3]

2.4 Fourier Transform Infrared Spectroscopy (FTIR)

Fourier-transform infrared spectroscopy (FTIR) is a technique that allows for structural information to be deducted for a sample based on its interaction between with light. Infrared energy is passed through a sample, with some energy being absorbed and some passed through. The absorbed infrared energy is then converted to rotational and vibrational energy by the molecules in the sample and the

transmitted light results in the generation of a spectrum typically from 4000 cm^{-1} to 450 cm^{-1} with certain functional groups appearing at characteristic wavelengths. In a spectrum, elemental and structural information can be deducted about a sample based on the wavenumber, intensity and broadness of a peak. In this work, FTIR is used to identify functional groups on samples the carbonyl index (CI), given by equation 1:

The carbonyl index is a widely used parameter to quantify the degree of oxidation or degradation in polymers, especially polyolefins like polyethylene or polypropylene, by measuring the relative amount of carbonyl groups (C=O) formed during oxidation. The calculation of the CI is based on the relative intensity or integrated peak area of the carbonyl absorption band in the infrared spectrum, normalised to a reference band that is considered stable and unaffected by the degradation process. In this work, the integrated peak area of the carbonyl peak (~1748 cm^{-1}) was used, normalised to the reference band appearing at approximately 1465 cm^{-1} corresponding to CH bending vibrations.[4]

$$Carbonyl\ Index\ (CI) = \frac{Area\ under\ band \sim 1748\ cm^{-1}}{Area\ under\ band \sim 1465\ cm^{-1}} \quad \textbf{Eqn. 1}$$

2.5 Raman Spectroscopy

Raman spectroscopy is a vibrational spectroscopic technique based on the inelastic scattering of monochromatic light by a material. Insights can be provided into the chemical and electronic structure of a sample as the photons from a light source interact with atoms in the sample causing a shift in energy. High-intensity monochromatic lasers (532 nm or 785 nm) are typically used as the light source. When the laser interacts with a material, most photons are elastically scattered (Rayleigh scattering) without any change in energy. However, a small fraction of the incident photons undergo inelastic scattering (Raman scattering), where they gain or lose energy through interactions with molecular vibrational modes. Raman scattering can be Stokes scattering or Anti-Stokes scattering. Stokes scattering is more common and occurs when the scattered photon has a lower energy than the incident photon due to energy transfer to the molecular vibration. Anti-Stokes occurs when the scattered

photon has higher energy than the incident photon as it gains energy from a pre-excited molecular vibration. The Raman shift (cm^{-1}) is then measured as a spectrum and corresponds to specific molecular vibrations. Raman spectroscopy can be a useful tool for material identification and structural characterisation. In this work, Raman spectroscopy was performed using an Oceanview InVia Raman Spectrometer using a 25 mW Ar-ion laser under 532 nm excitation. The beam was focused onto the samples using a 40x objective lens and spectra were collected using a RenCam CCD camera. The analysis is used to characterise nanomaterials and biomass-derived catalyst materials.

2.6 Total-reflection x-ray fluorescence spectroscopy (TXRF)

Total-reflection x-ray fluorescence spectroscopy (TXRF) is a surface elemental analysis method typically used for ultra-trace analysis of materials. It is an energy dispersive technique in which an incident beam is aimed at a thin film of sample (10 µm sample dispersion drop cast on a sample disc) at an angle which is less than the critical angle of external total reflection for x-rays, which results in the reflection of the excitation beam photons at this surface. Total reflection X-ray fluorescence spectroscopy was (TXRF) was carried out using an S2 Picofox TXRF Spectrometer with a scan time of 250 s. Where an internal standard was used for quantification, the solid sample was dispersed in deionised H_2O and sonicated for 10 minutes. 50 µL of sample dispersion was then combined with 50 µL of nickel (Ni) internal standard (1000 mg/L) and this mixture was further sonicated for 10 minutes. 10 µL of the resulting mixture was drop cast onto the sample disc for analysis. Quantification using an internal standard and correlating concentration of analyte with relative sensitivities to the net intensities of the analyte and the Ni internal standard was calculated by the following equation[5]:

$$C_A = \frac{\frac{N_A}{S_A}}{\frac{N_{IS}}{S_{IS}}} \times C_{IS} \quad \textbf{Eqn. 2}$$

Where C_A and C_{IS} are the concentrations of the analyte and the IS, respectively. N_A and N_{IS} refer to the net intensities of the analyte and the internal standard, and S_A and S_{IS} are the relative sensitivities of the analyte and internal standard, respectively.

Where absolute quantification was used to approximately quantify sample impurities, the sample was sonicated in deionised H_2O for 10 minutes 10 µL of this mixture was drop cast on to a sample disc for analysis. Absolute quantification is based on the measured absolute sensitivity for Ni for the instrument and is approximated by the software according to the following equation:

$$m_i = \frac{N_i \cdot S_{Ni}}{S_i \cdot s_{Ni} \cdot T \cdot I} \quad \textbf{Eqn. 3}$$

Where m_i is the absolute amount of an analysed element within the sample, N_i is the net pulse number within the measurement spectrum of the analyte, S_{Ni} is the relative sensitivity of Ni, S_i is the relative sensitivity of the analyte, s_{Ni} is the absolute sensitivity of Ni in counts ($s^{-1}ng^{-1}mA^{-1}$), T is the measurement time and I is the tube current in mA. (adapted from the Bruker S2 Picofox TXRF manual).

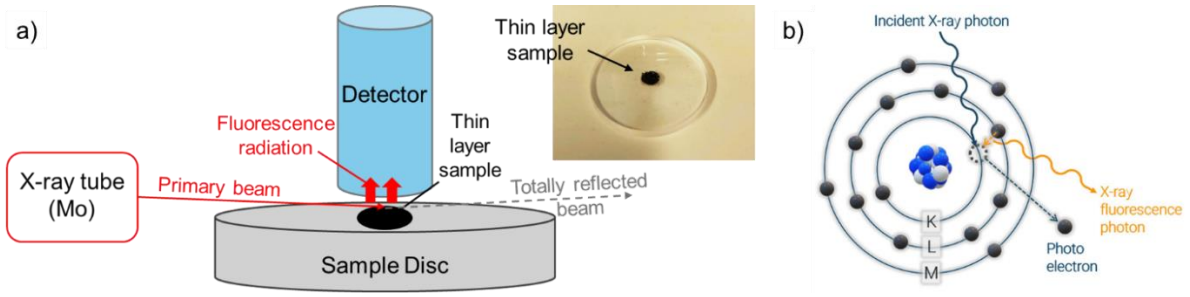


Figure 3: a) TXRF instrument set up, b) TXRF principal schematic. Reproduced from Ref[6].

2.7 X-ray Diffraction (XRD)

X-ray diffraction is a useful tool to determine the crystallographic structure of a material. An XRD instrument is composed of a source, target and detector. The x-ray source, which is typically Cu-α radiation, sends a high energy x-ray beam directly at the sample on the target. As the x-rays hit the crystal structure within the sample, they are scattered by the atoms in the material. Due to the well-ordered nature of atoms in a crystalline sample, the x-rays are scattered in a predictable pattern. Bragg's Law describes the diffraction of x-rays off a crystal structure:

$$n\lambda = 2d \sin\theta \quad \textbf{Eqn. 4}$$

Where n is an integer referred to as the order of diffraction, λ is the incident x-ray wavelength, d is the spacing between crystal planes and θ is the diffraction angle. At specific angles, the diffracted x-rays interfere with one another which is referred to as constructive interference and result in the detection of a diffraction peak. In this work, X-ray Diffraction (XRD) was carried out on a PANalytical X'Pert PRO with Cu Kα radiation and a constant step of 0.0098° 2θ and a counting time of 149.97 seconds per step. Crystallite size was calculated by the Scherrer equation shown below.

$$D_{hkl} = \frac{k_\lambda}{B_{hkl} cos\theta_{hkl}} \quad \textbf{Eqn. 5}$$

Where D_{hkl} is the crystallite size perpendicular to the hkl plane, k is a constant (0.9) for spherical samples with cubic symmetry, λ is the wavelength of x-ray radiation, B_{hkl} is the full width at half maximum (FWHM) of the hkl diffraction peak and θ_{hkl} is the Bragg angle of the (hkl) peak.

2.8 X-ray Photoelectron Spectroscopy (XPS)

XPS is a sensitive surface analysis technique that can provide both qualitative and quantitative information about the composition of a material. It can also provide useful information about the chemical and electronic state of elements in a material. During XPS analysis, a sample is bombarded with x-ray irradiation, typically Al Kα or Mg Kα which are absorbed by core-level electrons. If the incident energy is larger than the binding energy of the electron to the nucleus, the electron is ejected. This is called the photoelectric effect. The kinetic energy (KE) of the ejected electrons can then be measured by the detector and the binding energy (BE) can be found from the kinetic energy data from the following equation:

$$BE = h\nu - (KE - \phi) \quad \textbf{Eqn. 6}$$

Where BE is the binding energy of the ejected electron, $h\nu$ is the x-ray photon energy, KE is the kinetic energy of the detected electron and ϕ is the work function of the spectrometer. XPS measurements are typically reported in BE as KE depends on the photon energy used in the experiment, whereas BE remains constant for an element regardless of the source used in the experiment and directly relates

to the strength of attachment of an electron to an atomic nucleus. XPS spectra are typically calibrated using a C 1s reference peak at 284.8 eV. Initially, a survey spectrum is collected from 0-1400 eV which detects all elements that are present in the sample. Next, the core levels of the elements present in the sample are scanned which allows for the determination of the oxidation state and identification of different environments based on chemical shifts of characteristic binding energies for a sample. The spectrum obtained is a plot of count of electrons detected vs. binding energy. The area under the peak is proportional to the number of atoms of that element. Doublets can arise for electrons in p, d and f orbitals due to spin-orbit coupling. This splitting occurs due to the interaction between the electron's intrinsic spin and its orbital angular momentum, resulting in two closely spaced energy levels that appear as a doublet in the spectrum. In this work XPS was carried out using a KRATOS ACIS 165 monochromatised X-ray photoelectron spectrometer equipped with an Al Kα (hv = 1486.6 eV) X-ray source. Spectra were collected at a take-off angle of 90 ° and all spectra were referenced to the C 1s peak at 284.8 eV.

2.9 High Performance Liquid Chromatography (HPLC)

HPLC is a useful analytical technique that is used to separate, identify and quantify compounds in a mixture. A liquid mobile phase carries the sample through a column (stationary phase) which can achieve separation based on varying interactions with the stationary phase. In this work, the column used is an Agilent Hi-Plex H size exclusion column which operates under ion-exchange and size-exclusion principles with specific applications for organic acid, sugars and carbohydrate analysis. The Hi-Plex H column is packed with sulfonated polystyrene-divinylbenzene resin, which has controlled pore sizes, allowing small molecule to enter and elute more slowly, while larger molecules elute more quickly. The typical mobile phase for this column is dilute (0.005 M) H_2SO_4, which protonates the column, facilitating ion exchange effects. In this work, HPLC was used to separate the acid products formed from the Fenton oxidation of LDPE. The product mixture was analysed using an Agilent 1200 HPLC coupled to a UV detector (210 nm). 500 uL of product mixture was added to 500 uL of mobile phase to give a dilution factor of 2. The column used was an Agilent Hi-Plex H (300 x 7.7 mm) size exclusion column. The mobile phase was 2.5 mM sulfuric acid at a flow rate of 0.5 $mLmin^{-1}$ and the temperature was set to 50 °C, following Bäckström et al.'s method and the column specifications.[7] The concentration of each product present in the sample was then calculated against calibration curves that were made by standards of carboxylic acids: succinic, formic, glutaric, acetic, adipic, propionic, butyric and pimelic acid. The yield was calculated relative to the initial weight of LDPE as shown below.

$$Mass\ of\ end\ product\ (g) = Conc\ of\ end\ product\ (gL^{-1})\ x\ reaction\ volume\ (L)$$ **Eqn. 7**

$$Yield\ of\ Organic\ Products\ (\%) = \frac{Mass\ of\ end\ products\ (g)}{Mass\ of\ starting\ material\ (g)}\ x\ 100\ \%$$ **Eqn. 8**

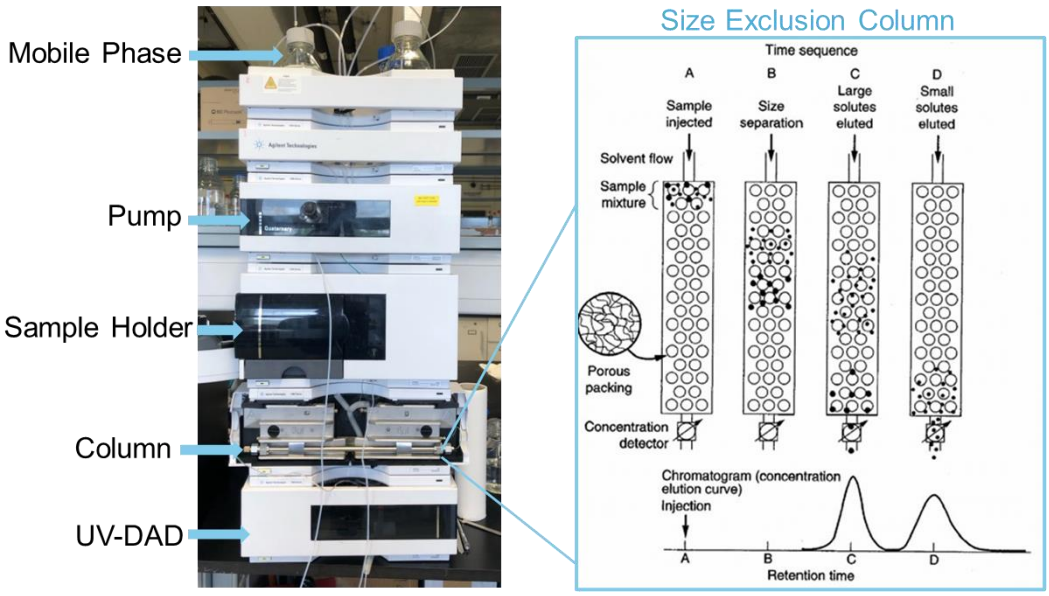


Figure 4: HPLC set up used for this work and schematic for mechanism of size exclusion column reproduced from Ref[8].

2.10 Nuclear Magnetic Resonance Spectroscopy (NMR)

NMR is a characterisation technique used to determine the molecular structure of a sample at atomic level. The principle is based on how atomic nuclei interact when subject to a magnetic field. When an external magnetic field is applied to nuclei that have a non-zero nuclear spin (odd mass number or odd number of protons/neutrons), an energy transfer occurs from the initial energy to higher energy levels. The wavelength of the characteristic energy transfer corresponds to radio frequencies and when the spin returns to its initial level, energy is emitted at the same frequency. This gives rise to a signal which is processed as an NMR spectrum. The most common magnetic nuclei are ^{1}H, ^{13}C and ^{29}Si. In this work, NMR was used to identify and assess the purity of products obtained from plastic degradation reactions. Specifically, the monomer bis(2-hydroxyethyl) terephthalate (BHET) and bis(4-hydroxyethyl) terephthalate from polyethylene terephthalate (PET), and methyl lactate from polylactic acid (PLA).

2.11 Milestone Flexiwave Microwave Reactor

All microwave-assisted reactions were carried out in a Milestone-Flexiwave equipped with High-Pressure SK-15S attachment shown in Figure 5. Typically, plastic, catalyst and solvent were placed in the white Teflon (PTFE) vessels. The PTFE vessels have a very dense structure and are chemically inert to most organic solvents. They also have low permeability to gases and vapours, are thermal insulators and microwave transparent. The PTFE vessels are placed inside highly resistant polyether ether ketone (PEEK) safety shields during the reaction to prevent deformation of the vessels at high temperatures and pressures. The vessels are sealed by placing the vessel cover and safety spring and by securing into the rotor segment using a torque wrench. The safety spring will facilitate the instantaneous release of overpressure when pressure reaches > 100 bar. PET glycolysis reactions were typically carried out at 210 °C for 30 min, while LDPE oxidative degradation reactions were typically carried out at 180 °C for 3 h. Microwave-assisted heating enhances plastic depolymerisation reactions by providing rapid, volumetric heating by interactions with good microwave absorbers such as polar solvents or metal catalysts. Unlike conventional thermal heating which relies on thermal conduction, microwave-assisted heating can form internal ‘hot spots’ when interacting with an absorbing material, causing rapid heating at the molecular level resulting in faster reaction kinetics and improved reaction efficiency.



Figure 5: Milestone Flexiwave reactor with High-Pressure SK15S vessels. (adapted from Milestone Flexiwave manual)

2.12 References:

(1) Son, R.; Yamazawa, K.; Oguchi, A.; Suga, M.; Tamura, M.; Murakawa, Y.; Kume, S. Morphomics via Next-generation Electron Microscopy. **2021**, arXiv:2111.14373.
(2) Gatan, I. *What is EDS?* 2025. https://www.gatan.com/techniques/eds (accessed 28/03/2025).
(3) Boratto, M. Semiconducting and Insulating oxides applied to electronic devices. 2018.
(4) Almond, J.; Sugumaar, P.; Wenzel, M. N.; Hill, G.; Wallis, C. Determination of the carbonyl index of polyethylene and polypropylene using specified area under band methodology with ATR-FTIR spectroscopy. **2020**, *20* (1), 369-381. DOI: doi:10.1515/epoly-2020-0041 (accessed 2024-02-05).
(5) Schmeling, M. Total reflection X-ray fluorescence. **2019**, *4* (7). DOI: doi:10.1515/psr-2017-0161 (accessed 2024-02-29).
(6) Bruker. *Principles of XRF Spectroscopy*. 2025. https://www.bruker.com/en/products-and-solutions/elemental-analyzers/xrf-spectrometers/how-does-xrf-work.html (accessed 28/03/2025).
(7) Bäckström, E.; Odelius, K.; Hakkarainen, M. Trash to Treasure: Microwave-Assisted Conversion of Polyethylene to Functional Chemicals. *Industrial & Engineering Chemistry Research* **2017**, *56* (50), 14814-14821. DOI: 10.1021/acs.iecr.7b04091.
(8) Haidar Ahmad, I. Studying Chemical and Sequence Length Heterogeneities In copolymers. **2011**.

Chapter 3

Ligand-Aided Glycolysis of PET using Functionalised Silica Supported Fe_2O_3 Nanoparticles

Éadaoin Casey[1,2], **Rachel Breen**[1,2], Jennifer S. Gómez[3], Arno P. M. Kentgens[3], Gerard Pareras[4], Albert Rimola[4], Justin. D. Holmes[1,2], Gillian Collins[1,2]*

[1] School of Chemistry, University College Cork, Cork, T12 YN60, Ireland.

[2] AMBER Centre, Environmental Research Institute, University College Cork, Cork, T23 XE10, Ireland.

[3] Institute for Molecules and Materials, Radboud University, Nijmegen, 6525 AJ, The Netherlands.

[4]Departament de Química, Universitat Autònoma de Barcelona, 08193 Bellaterra, Catalonia, Spain.

Publication: *Casey, É.; **Breen, R**.; Gómez, J. S.; Kentgens, A. P. M.; Pareras, G.; Rimola, A.; Holmes, J. D.; Collins, G. Ligand-Aided Glycolysis of PET Using Functionalized Silica-Supported Fe_2O_3 Nanoparticles. ACS Sustainable Chemistry & Engineering* ***2023****, 11 (43), 15544-15555. DOI: 10.1021/acssuschemeng.3c03585.*

Author Contributions:

My contribution to the research included catalyst synthesis, SEM and XRD analysis of catalysts and PET glycolysis reactions and optimisation. In addition, I contributed to the preparation of the manuscript through data analysis, writing, and figure development. The research was carried out in collaboration with Dr Éadaoin Casey within our research group and formed part of a wider project that also included joint work with postdoctoral researcher Dr. Gerard Pareras, under the supervision of Prof. Albert Rimola at the Universitat Autònoma de Barcelona (UAB). Dr Pareras performed the computational work using density functional theory (DFT).

Abstract

The development of efficient catalysts for the chemical recycling of polyethylene terephthalate (PET) is essential to tackling the global issue of plastic waste. There has been intense interest into heterogeneous catalysts as a sustainable catalyst system for PET depolymerisation, having the advantage of easy separation and reuse after the reaction. In this work, we explore heterogeneous catalyst design by comparing metal-ion (Fe^{3+}) and metal oxide nanoparticle (Fe_2O_3 NP) catalysts immobilised on mesoporous silica (SiO_2) functionalised with different N-containing amine ligands. Quantitative solid-state Nuclear Magnetic Resonance (NMR) spectroscopy confirms successful grafting and elucidates the bonding mode of the organic ligands on the SiO_2 surface. The surface amines ligands act as organocatalysts enhancing the catalytic activity of the active metal species. The Fe_2O_3 NP catalysts in the presence of organic ligands outperform bare Fe_2O_3 NPs, Fe^{3+} ion immobilised catalysts and homogeneous $FeCl_3$ salts, with equivalent Fe loading. X-ray photoelectron spectroscopy (XPS) analysis indicates charge transfer between the amine ligands and Fe_2O_3 NPs and the electron donating ability of the N groups and hydrogen bonding may also play a role in the higher performance of the amine ligand-assisted Fe_2O_3 NP catalysts. Density functional theory (DFT) calculations also reveal the reactivity of the ion immobilised catalysts is strongly correlated to the ligand-metal binding energy and that the products in the glycolysis reaction catalysed by the NP catalysts are stabilised showing a significant exergonic character compared to single ion immobilised Fe^{3+} ions.

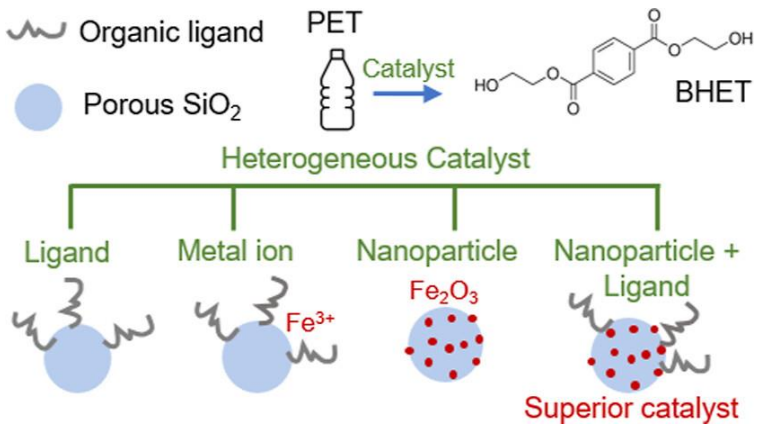


Table of Contents Graphic

3.1 Introduction

In recent years, research into developing pathways to convert waste polymers into its constituent monomers or value-added products has grown exponentially with the key goal of achieving a circular economy in the polymer life cycle.[1] Polyethylene terephthalate (PET) is a very useful polymer in our everyday life from textiles, packaging, beverages among many others.[2, 3] However, it is also one of the largest components of post-consumer plastic waste in landfills highlighting the need for effective recycling strategies for this polymer. This has gained huge interest for researchers to find low cost, and environmentally friendly ways of degrading PET to useful monomers with the aim of achieving a circular economy in the polymer life cycle.[2, 4] There are a variety of chemical recycling pathways for PET including, hydrolysis,[5] alcoholysis[6] and glycolysis.[3, 7] Glycolysis is particularly attractive due to its low cost an mild reaction conditions compared to other depolymerisation pathways.[8] The process involves the transesterification reaction of PET with excess glycol, usually ethylene glycol, to obtain bis-(hydroxyethyl) terephthalate (BHET).[9] BHET can be repolymerised to PET and it is also used in the synthesis of unsaturated polyesters, rigid or flexible polyurethanes, and other fine chemicals.[10] The glycolysis of PET is typically performed in the presence of a catalyst as the reaction is slow and requires evaluated temperatures in the absence of a catalyst.[11] Homogeneous catalysts such as metal salts,[12] metal oxides[13] and ionic liquids[2, 14] are most commonly used, however, this leads to issues regarding catalyst recovery and contamination of the BHET product. Numerous heterogeneous catalysts have been developed for PET glycolysis, which are advantageous compared to homogeneous catalyst as they can be easily recovered and reused. Biomass derived heterogeneous catalysts have been prepared from waste orange peel ash,[15] waste bamboo leaf ash and calcium oxide based catalysts made from eggshells and seafood shells.[16] Cobalt nanoparticles (3 nm) stabilised by tannic acid ligands showed high activity for PET glycolysis with 96% conversion and 77% BHET yield.[17] Various metal oxides nanostructures have been reported such as ZnO[18] and Fe_3O_4 [19] nano dispersions. Son *et al.*[20] reported the use of exfoliated manganese oxide nanosheets for PET glycolysis, leading to full conversion of PET at 0.01 wt % catalyst, at 200 °C after 30 min. Molybdenum doped ultrathin ZnO nanosheets displays far superior yields of BHET (94.5 %) than standard undoped ZnO catalysts (54.7 %) which have been previously reported in literature.[21] The Mo atoms replace Zn atoms at defect sites forming Mo-Zn bonds, influencing the electronic structure of the catalyst, and promoted electron

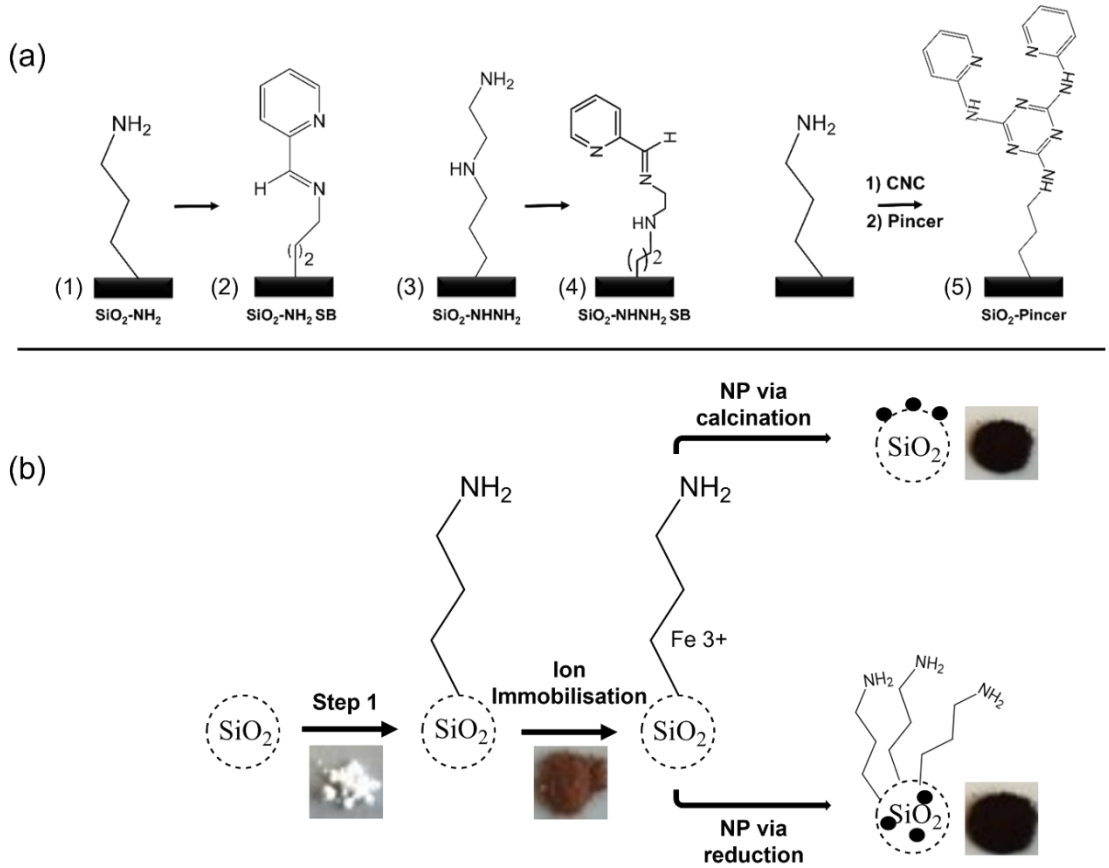
transfer of the glycolysis reaction. Mesoporous SBA-15 catalysts doped with ZnO gave a 91 % BHET yield, and the catalyst displayed good stability and high catalytic activity when recycled. Ion based heterogeneous catalysts such as metal organic frameworks (MOFs)[22, 23] and zeolites[24] have also been reported as good catalysts for the depolymerisation of PET due to their highly ordered structures, high surface areas and porosity.[23] Yang *et al*.[25] reported the use of metal azolate framework-6 catalyst (a sub class of MOFs) with a high density of zinc ion species immobilised on the surface achieving 92.4 % conversion of PET and 81.7 % yield of BHET. Wang *et al.*[26] investigated the use of metal ions immobilised on a polymer ionic liquid, [BVim]NTf_2-Zn^{2+}, which gave 95.4 % PET conversion and 77.8 % BHET yield.

It is evident from the literature that a wide variety of heterogeneous catalysts are effective for PET glycolysis ranging for ion immobilised catalysts to nanoparticles and Table S1 summaries reports of heterogeneous catalysts and conditions in the literature. The aim of this work is to gain insight into the optimum heterogeneous catalyst design for PET glycolysis with a particular focus on the immobilisation of metal-ion and nanoparticle-based catalysts. Surface modification of a catalyst support such as SiO_2, with organic linkers is a convenient strategy to immobilise a high density of transition metal ions dispersed on a support material. The nature of the organic linker used to tether the ion can influence the steric and the electronic environment with the metal centre, which in turn can influence catalytic activity.[27] In this work Fe ions were immobilised onto porous silica functionalised with different organic linkers, which are illustrated in scheme 1. Solid state NMR is used for quantitative analysis of the modified surfaces. The ion-based catalysts were then converted to NP catalysts either by calcination, which removes the organic ligands or by chemical reduction which preserves the ligand. The heterogeneous catalysts were evaluated for PET glycolysis to gain insight into how the immobilisation of the metal species and the organic ligands influenced catalytic performance. Finally, DFT calculations were carried out to unveil the reaction mechanism, this way correlating experimental observations with an atomistic interpretation.

3.2 Results and Discussion

3.2.1 Catalyst design and synthesis

Silica is an excellent catalytic support material that allows the surface chemistry to be easily altered through surface functionalisation using silylation chemistry.[28] Mesoporous cellular foam (MCF) SiO_2 is a three-dimensional (3D) connected pore structure that was chosen in this study because of its relatively large pore diameter (100 nm) in comparison to other porous silicas. Scheme 1 (a) shows the synthesis pathways to prepare mesoporous SiO_2 with five different capping ligands SiO_2-NH_2 (1), SiO_2-NH_2-SB (2), SiO_2-NH-NH_2 (3), SiO_2-NH-NH_2-SB (4) and SiO_2-pincer (5) (see Supporting Information for Experimental section and reaction details).



Scheme 1: (a) Synthesis pathways to prepare mesoporous SiO_2 with five different organic capping ligands SiO_2-NH_2 (1); SiO_2-NH_2-SB (2); SiO_2-NH-NH_2 (3), SiO_2-NH-NH_2-SB (4) and SiO_2-pincer (5) and (b) the catalysts preparation scheme.

XPS was employed to verify successful functionalisation of the SiO_2 support with each of the five ligands. After functionalisation, a N signal appeared in all the N 1s core levels as shown in Figure 1 (a). All catalysts displayed a dominant peak at a binding energy (BE) of 399 eV, attributed to the amine functional group and a shoulder peak at ~400-402 eV, attributed to protonated amines typically observed on modified SiO_2.[29] No N signal was detected in the bare SiO_2. The O 1s core level, in Figure 1 (b) also confirms functionalisation with the BE of the bare silica centred at 533.75 eV downshifted to 532.5 eV, associated with the loss of Si-OH groups after surface modification.[30] The Si 2p core level, of bare SiO_2, shown in the Supporting Information Figure S2, shows a single peak at 104.25 eV and after functionalisation, the Si 2p peak can be deconvoluted in several peaks associated with different Si environments.

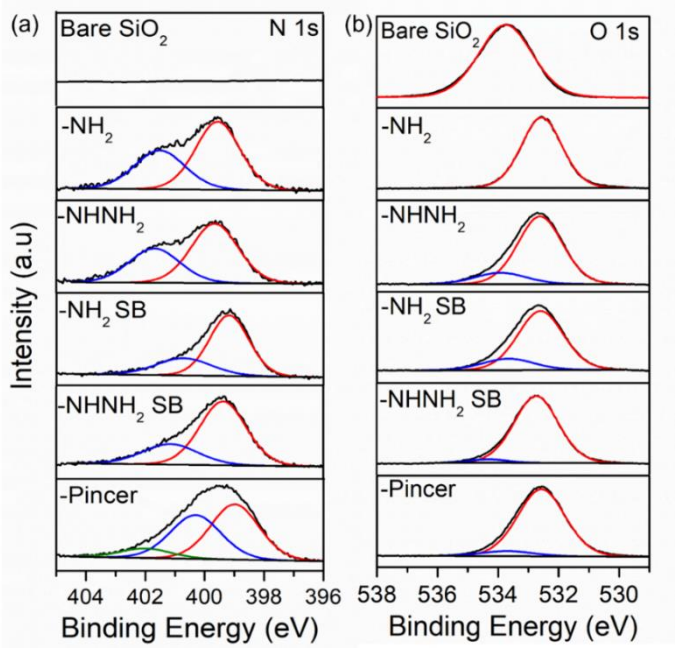


Figure 1: XPS analysis of the (a) N 1s spectra and (b) O 1s core level for bare silica and the functionalised SiO_2 with -NH_2 (1), -NH_2 SB (2), -$NHNH_2$ (3), -$NHNH_2$ SB (4) and pincer (5), respectively**.**

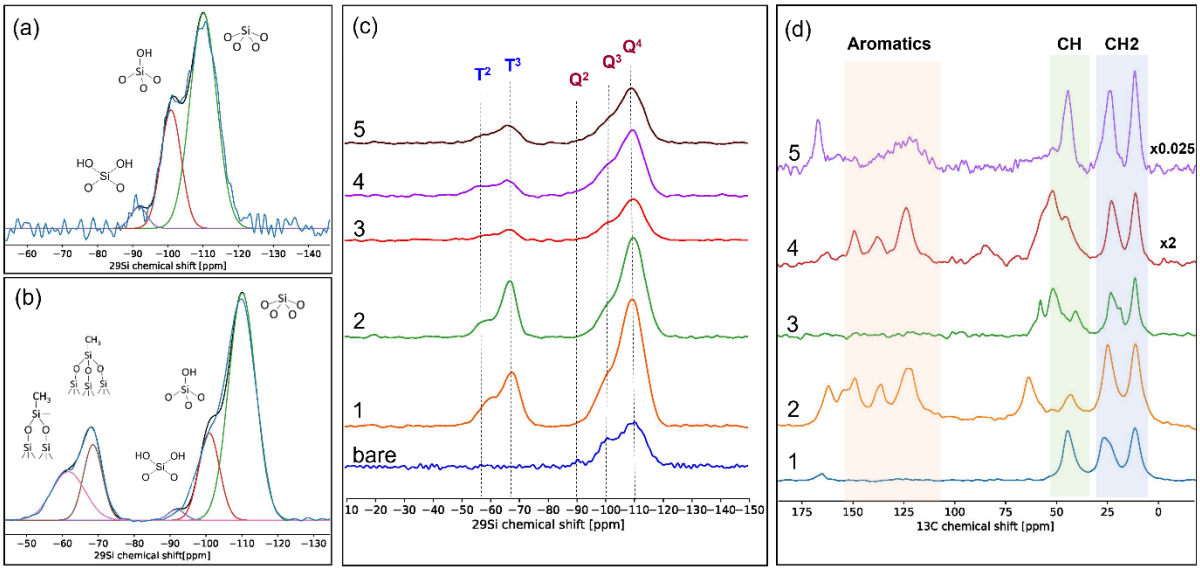


Figure 2: 1D (a) ^{29}Si MAS NMR spectra together with their deconvolution of bare silica and (b) functionalised SiO_2-NH_2 (1). (c) Stacked plot of the ^{29}Si MAS NMR spectra of all samples; bare silica, SiO_2-NH_2 (1), SiO_2-NH_2-SB (2), SiO_2-NH-NH_2 (3), SiO_2-NH-NH_2-SB (4) and SiO_2-pincer (5); (d) $^{1}H^{13}C$ CPMAS NMR spectra of the functionalised silica with ligands (1) to (5).

It is well recognised that silylation chemistry can result in significantly more complicated surface attachment chemistry than is often illustrated across the literature.[29] Solid state NMR is a powerful tool to provide insight into the grafting chemistry.[31, 32] The 1D ^{29}Si and ^{13}C NMR spectra of the bare and five different functionalised SiO_2 are presented in Figure 2. For the ^{29}Si NMR spectra, spectral deconvolution was carried out using ssNake[33] (using Gaussian/Lorentzian line-shapes for fitting) to identify the individual species present. The ^{29}Si NMR spectrum of bare SiO_2 (Figure 2 a) exhibit resonances at ca. at −91.8, −100.9, and −110.1 ppm, corresponding to Q^2, Q^3 and Q^4 sites, respectively. Detailed fitting of these spectra is shown in Figure 2 (a and b).The spectra of all six samples in Figure 2(c), show the presence of $Si(SiO)_n(OH)_{4-n}$ sites (denoted Q^n with n = 2, 3 and 4), characteristic of silica-type materials.[34]

Figure (c) compares the NMR spectra of the unfunctionalised and functionalised SiO_2. The spectra of the functionalised SiO_2 show the appearance of two peaks centred at −67.3 and −60 ppm, which arise

from T^2 ($(\equiv SiO-)_2SiR(-OH)$), with R being the alkyl chain)) and T^3 ($(\equiv SiO-)_3SiR$) sites, respectively,[32, 35] confirming the successful grafting of the amine groups onto SiO_2.

Quantitative ^{29}Si NMR spectra allowed the determination of the relative surface coverage of each species present (Q^n and T^n sites) (see Table 1). The relative areas of Q^4 sites remains almost constant in all the samples, and the degree of condensation of the Si atoms as calculated in Table 1 remain almost constant for all the ligands, confirming that the SiO_2 structure remains intact after functionalisation. In addition, the low content of Q^2 sites indicates the preference of the ligands to occupy Q^2 sites. The relative areas of Q^n sites can be used to determine the degree of surface functionalisation, giving surface coverages between 40-73 %, as shown in Table 1. However, no clear correlation between the surface coverage and structure of the ligand was found but the analysis demonstrates that the attachment of the ligand, and therefore coverage is strongly influenced by the primary linker molecule. When the Schiff base (SB) ligand is reacted with SiO_2-NH_2 to convert ligand 1 to ligand 2 there is a decrease in Q^2+Q^3 sites (with increasing T^3+T^2), indicating that the SB precursor (2-pyridinecarboxaldehyde) is attaching to surface -OH groups of the SiO_2 particles in addition to the terminal -NH_2 groups. Consequently, the SB ligand has a significantly higher surface coverage (73 %) compared to the other ligands. This statement is supported by the appearance of an additional peak in the ^{13}C CPMAS spectra of the SiO_2-NH_2 SB and SiO_2-NH-NH_2 SB catalysts (in the region of 50-100 ppm) (Figure S3). This signal could be attributed to the presence of an aldehyde group[36] with the surface silanol groups, which would explain the differences observed in ^{29}Si NMR. In contrast, using the SiO_2-NH-NH_2 ligand (Ligand 3 & 4) to attach the SB resulted in an increase in the relative areas for the Q^2+Q^3. This observation may indicate that the NH_2 groups on the diamino ligands interact with SiO_2 surface likely due to the longer ligand length and, therefore, silanol groups can be introduced by re-hydroxlation.[37] Consequently, the surface coverage of the SiO_2-NH-NH_2-SB catalyst was the lowest of the ligands.

Figure 2 (d) shows the stacked ^{13}C CPMAS spectra of the functionalised Si-NH_2 catalysts with their principal functional groups. The presence of the alkyl groups appearing in SiO_2-NH_2 (1) and SiO_2-NH-NH_2 (3) catalysts (from 60 to 10 ppm) further confirms successful grafting of both amine ligands onto SiO_2.[38, 39] The SiO_2-NH_2 SB and SiO_2-NH-NH_2 SB catalysts, show the presence of aromatic peaks between 175-100 ppm confirming successful functionalisation with the Schiff base ligands.[39] The alkyl groups and aromatic peaks were also observed in SiO_2-pincer when the spectrum was recorded at ~40°C confirming successful functionalisation of the pincer ligand.

Table 1: ^{29}Si NMR quantitative data for each of five different capping ligands SiO_2-NH_2 (ligand 1); SiO_2-NH_2-SB (ligand 2); SiO_2-NH-NH_2 (ligand 3), SiO_2-NH-NH_2-SB (ligand 4) and SiO_2-pincer (ligand 5).

	Sample	% Si sites					$Q^3 + Q^2$	$T^3 + T^2$	Relative surface coverage*	Degree condens. Si atoms†
		Q^4	Q^3	Q^2	T^3	T^2				
-	SiO_2	68.2	27.8	4.1	-	-	31.8	-	-	-
Ligand 1	SiO_2 + NH_2	58.5	15.1	1.5	15.7	9.1	16.6	24.8	47.7	92.4
Ligand 2	SiO_2 + NH_2SB	61.1	8	0.4	12.1	18.4	8.4	30.5	73.6	91.7
Ligand 3	SiO_2 + $NHNH_2$	68.5	15.2	1.4	8.2	6.8	16.6	15.0	48.0	93.3
Ligand 4	SiO_2 + $NHNH_2$SB	65.8	18.5	1.7	4.9	9.1	20.2	13.9	36.5	91.5
Ligand 5	SiO_2 + Pincer	61.7	18.4	0.6	9.9	9.4	19.0	19.2	40.3	92.0

*The relative surface coverage was determined using the equation $100 - \left[\frac{(Q^2+Q^3)\text{ligand}}{(Q^2+Q^3)\text{SiO}_2} \cdot 100\right]$

†The degree of condensation of Si atoms was determined using $\frac{\sum_{n=2}^{4} nI(Q^n)}{4} + \frac{\sum_{n=1}^{3} nI(T^n)}{3} \cdot 100$. (see Supporting Information for details).

After organic functionalisation, Fe ions were immobilised onto the SiO_2 (see Experimental section for details). We chose iron as the metal catalyst as iron salts are effective for glycolysis of PET and have lower environmental impact compared to other effective metal ion catalysts such as Zn^{2+}. Inductively coupled plasma-mass spectroscopy (ICP-MS) was used to determine the Fe loading in each of the catalysts. Table S2 (see Supporting information), displays the quantitative results with the Fe loadings for each ligand, with the highest loading for the simple amine ligand SiO_2-NH_2 (4172.8 ppm) and lowest for the SiO_2-pincer ligand (3904 ppm) which can be expected given the bulky nature of the ligand. The Fe ion immobilised catalysts were then converted to iron oxide nanoparticle (NP) catalysts by calcination at 450 °C, which removed the organic ligands on the SiO_2 surface, or by treatment with aqueous $NaBH_4$ as a rapid reducing agent, which preserved the organic ligands, as represented in Scheme 1(b).

Figure 3(a-c) shows the TEM analysis of the SiO_2 before and after NP formation by calcination and chemical reduction, respectively and associated SEM images are shown in the Supporting Information figure S4. Catalysts prepared by calcination produced larger NPs compared to catalysts produced by chemical reduction, which is to be expected as rapid reduction by $NaBH_4$ is known to produce small diameter NPs.[40] XRD analysis of the calcined catalysts, shown in Figure 3(d), shows the characteristic peaks for α-Fe_2O_3 in excellent agreement with JCPDS card no. 33-0664. Diffraction peaks were not observed from the catalyst produced by chemical reduction. Although challenging to visual due to their small size and low atomic mass contrast in TEM, the presence of nanoparticles embedded in the SiO_2 can be seen in TEM figure 3 c). EDX mapping of the catalyst prepared by chemical reduction is shown in figure 3 (e-h) and confirm the uniform presence of Fe across the SiO_2 support.

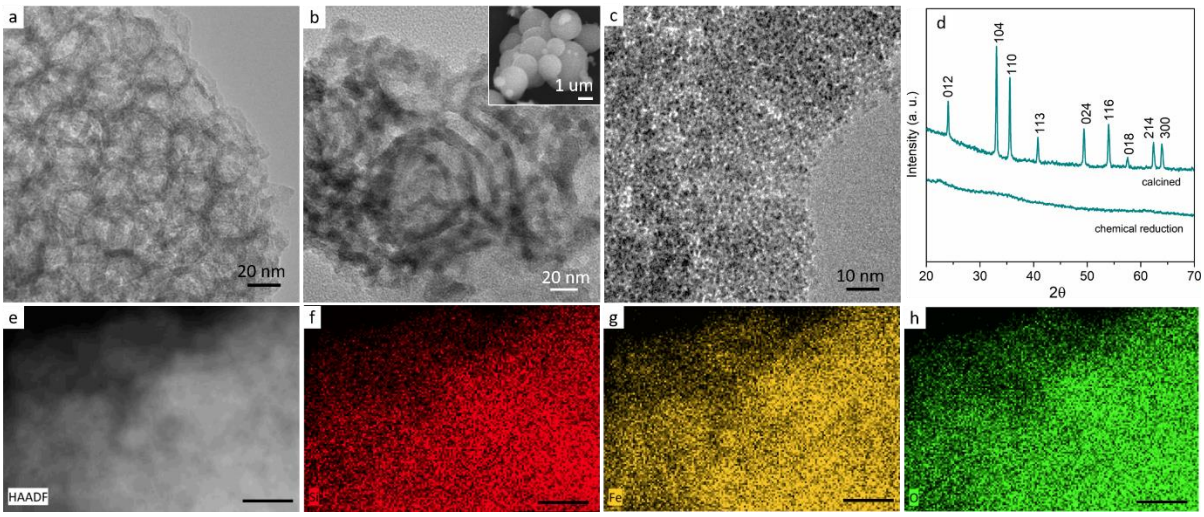


Figure 3: TEM images of SiO_2 support (a) before Fe-ion immobilised (b) after calcination and (c) after chemical reduction. (d) XRD of SiO_2 catalysts prepared by calcination and chemical reduction (e) high angle angular dark field image of SiO_2 catalyst after chemical reduction and associated (f) Si, (g) Fe and (h) O EDX maps. Scale bars in e-f are 100 nm.

XPS analysis of the NP catalysts was carried out to determine the chemical states of the iron oxide NP and assess the interaction of the ligand and the NPs. Figure 4(a) shows the Fe 2p spectrum for the SiO_2-NH_2-SB NP prepared by calcination (C) and reducing agent (R), which are very similar. The Fe $2p_{3/2}$ is located at a BE of 711 eV and in good agreement with that reported for Fe_2O_3.[41] The Fe $2p_{3/2}$ also has a clear shake up satellite peak at 718 eV, characteristic of Fe^{3+}, further indicating Fe_2O_3 . The formation of Fe_2O_3 nanoparticles during chemical reduction can be attributed to the process being conducted in aqueous solution under air, which causes the initially reduced Fe^{2+} to undergo oxidation back to Fe^{3+}. Figure 4 (b) shows the O 1s core level before Fe adsorption with a dominant peak at 532.6 eV associated with the SiO_2. After NP formation an additional peak at a BE of 530.2 eV appears in the O 1s for catalysts prepared by calcination and chemical reduction, which is in excellent agreement with the BE for Fe-O-Fe, consistent with the formation of NPs.[42] The O 1s core level of the other NP catalysts, shown in the Supporting Information figure S5, display the same trend with the appearance

of the Fe-O-Fe peak in catalyst prepared by annealing and chemical reduction, which is attributed to NP formation. The Fe 3p shown in the Supporting Information Figure S6 is fit to a single peak a BE of 55 eV, again indicating the presence of Fe_2O_3. Figure 4(c) shows the N 1s core level of the SiO_2-NH_2-SB catalyst, with a dominant peak at a BE of 399 eV, due to the amine functional group and a shoulder peak at 401 eV, attributed to protonated amines, as aminosilane protonation occurs from the support Si-OH.[29] The peak intensity of the N 1s in the calcined catalyst decreases substantially, as excepted due to loss of the ligand but there are residual ligands present. The Si:N ratio estimates that ~85% of the ligands are removed. The N 1s peak of both the calcined and $NaBH_4$-treated catalysts is upshifted to a BE of 339.8 eV, indicating charge transfer from the organic ligand to the Fe_2O_3 NPs. XPS analysis of the other catalysts also show the same trend with the N 1s core level shifting upward (see Supporting Information Figure S7).

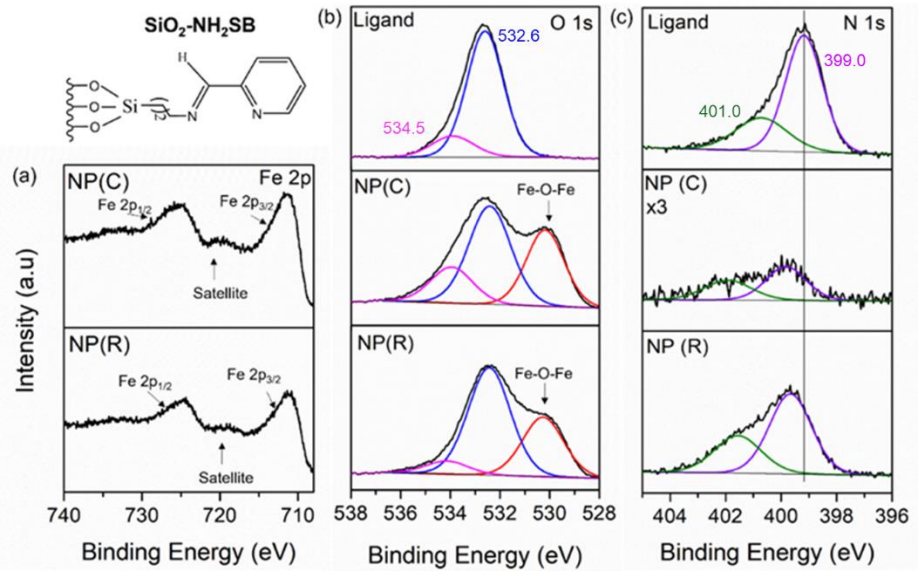


Figure 4: XPS core level spectra of (a) Fe 2p (b) O 1s and (c) N 1s for the SiO_2-NH-SB and the corresponding Fe_2O_3 NP catalysts prepared via calcination (C) and chemical reduction (R).

3.2.2 Catalytic Evaluation in PET Glycolysis

The catalytic performance of all twenty catalysts for the glycolysis of PET was investigated under the

same reaction conditions. Figure 5 (a-d) compares the PET conversion and isolated yields of BHET for (a) SiO_2 modified with the organic ligands *i.e.* before metal loading, (b) the Fe ion-based catalysts (c), the Fe_2O_3 NPs prepared by calcination (d), and the ligand-Fe_2O_3 NP catalysts prepared by chemical reduction. It worth noting that analysis of the supernatant showed residual BHET remaining in the solution left after recrystallisation, but no BHET dimer was detected by NMR. The activity of the functionalised SiO_2 was tested as reference before the immobilising the iron ion precursor. Interestingly, the SiO_2 consisting only of the organic ligand attached to the surface displayed moderately good PET conversion as shown in Figure 4(a). Good catalyst activity corresponded to organic ligands with terminal primary amines *i.e.* the NH_2 and NH-NH_2 ligands, having a conversion of 61 % and 75 %, respectively. This activity is associated with the ligands being organic bases and depolymerisation occurred by based-catalysed glycolysis of PET. Strong organic bases such as guanidines are popular for homogeneous catalysed PET glycolysis and are attractive as they offer a metal-free depolymerisation route but organocatalysts can lead to contamination in the monomer product. While we did not further investigate the catalytic activity of the organically functionalised i.e. metal-free SiO_2 in this study, the results in Figure 4(a) nevertheless illustrate the potential of using heterogeneous organocatalysts for PET glycolysis. The bare SiO_2 support did not catalyse the reaction to any extent.

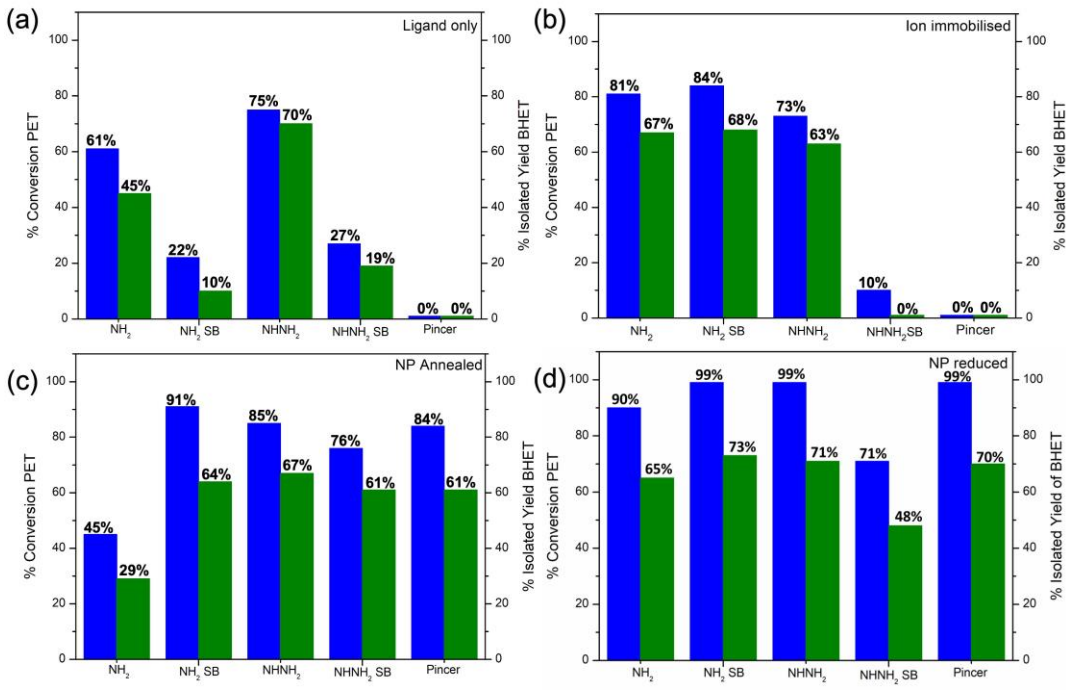


Figure 5: Percentage conversion of PET (blue) and isolated yield of BHET (green) obtained from glycolysis reaction catalysed by (a) organic ligand modified SiO_2 (before metal loading), (b) iron-ion immobilised SiO_2, (c) Fe_2O_3-NP SiO_2 via calcination, (d) Fe_2O_3-NP SiO_2 prepared by chemical reduction.

Figure 5 (b) compares the catalytic results after Fe ion immobilisation. The PET conversion increased for Fe immobilised on the SiO_2-NH_2, and SiO_2-NH_2-SB, with conversions of 81 % and 84 %, respectively, which is expected due to the presence of Fe^{3+} ions. A notable conclusion from Figure 5(b) is the considerable difference in activity observed between the Fe ions immobilised onto SiO_2 using the two Schiff base ligands. High conversion was observed for Fe ion immobilised using the SiO_2-NH_2–SB ligand (84 %), however only a 10 % conversion was observed when using a SiO_2-NH-NH_2-SB ligand. While the Fe loading used in the reaction was equivalent, the organic ligand coverage on the SiO_2-NH_2–SB catalyst (74 % surface coverage) is much greater than of the SiO_2-NH-NH_2-SB (37 % surface coverage) as previously described by the solid-state NMR analysis, indicating that the organic ligand and coordination chemistry of the iron on the surface modified SiO_2 plays a crucial role in the observed

catalytic behaviour. The Fe^{3+} ions immobilised using the pincer ligand did not catalyse the reaction to any extent, which was attributed to the tight binding the Fe ions to the ligand.

Figure 5(c) and (d) show the PET conversion and isolated yields obtained using the NP catalysts obtained by calcination or chemical reduction, respectively. Generally, the NP catalysts displayed similar or higher PET conversions and BHET yields compared to their ion-immobilised version, regardless of whether they were prepared by calcination or reduction, with exception of one catalyst: SiO_2-NH_2. The conversion of PET decreased from 81% in the ion SiO_2-Fe^{3+}-NH_2 catalyst to 45% when the catalyst was converted to NPs by calcination. However, when the catalyst was prepared by chemical reduction a conversion of 90% was obtained. This trend is attributed to dual catalytic depolymerisation, as reported by Dove and co-workers,[43] due to the preservation of the amine ligands, which are catalytically active in the reaction, as also seen in Figure 5(a). All the NP catalysts prepared by chemical reduction were superior to catalysts prepared by calcination, attributed the formation of smaller NPs and also the presence of the amine ligands that remain on the surface. In addition of the based catalysis glycolysis, synergistic effects have been shown to occur between metal salts and organic additives for PET glycolysis under homogeneous conditions. A recent report showed the addition of anisole to homogeneous PET glycolysis using alkali metal salts facilitated a lower reaction temperature.[44] DFT calculations suggested that the electron donating methoxy group in anisole transfers electron density to carbonyl O atom making it more nucleophilic and thereby susceptible to attack by metal ion species. The electron donating ability of N containing groups in the ligands, as evidenced by XPS analysis, may have a similar effect in aiding glycolysis. Additionally, the role of H-bonding using N-containing organocatalysts for PET glycolysis has been shown to be important in activating the carbonyl group of PET and the –OH of EG.[45]

The catalytic evaluation highlights some important features of catalyst design for PET glycolysis: (i) the organic ligand used to bind the metal ion can significantly impact the catalytic performance as illustrated by the different reactivity behaviour, (ii) the metal oxide NP catalysts are in general superior

to metal ion immobilised catalysts, and (iii) the presence of both the organic ligand and metal oxide NP (*i.e.* catalysts prepared by chemical reducing agent) gave the best performance. We used DFT calculations to rationalise the observed catalytic trends and gain further insights into the reaction.

Firstly, we analyse the strength of the interaction between the Fe^{3+} metal cation and the functionalised surface, by calculating the interaction energies (see Experimental Section in the Supporting Information for details). We performed optimisations of the functionalised SiO_2/Fe^{3+} surfaces considering three possible electronic spin states, translated to three different electronic spin multiplicities (M = 2, 4, 6), showing that the high-spin M=6 is the ground state (see Supporting Information Table S3). The nature of the surface under study allows the SiO_2 surface to be functionalised with up to three organic linkers in the same unit cell. The calculated ΔE_{int} values represented in Table 2 are for the different organic linkers containing one, two, or three ligands (1L, 2L and 3L, respectively).

The organic ligands present a similar trend, with ΔE_{int} dramatically decreasing as fewer ligands are involved, meaning that the iron ion is trapped within a net of coordinating bonds between the organic ligands (see Figure 6, where the SiO_2-ligand structures interacting with Fe^{3+} are shown). The two poorest performing catalysts, Fe^{3+} immobilised on SiO_2-NH-NH_2-SB and SiO_2-pincer, have the most favourable ΔE_{int} values as shown in Table 2, which effectively traps the ion in between the three sterically bulky organic ligands. For the SiO_2-pincer catalyst, the Fe^{3+} is coordinated with six N groups of the three pyridine rings. For SiO_2-NH-NH_2-SB catalyst, the Fe^{3+} is coordinated to the three imine and the three pyridinic N groups. For these ligands, Fe^{3+} presents the most favourable interaction energies, the metal being coordinated in an octahedral geometry, and so sterically blocked from reacting, giving poor performance as observed. In the SiO_2-NH_2-SB catalyst Fe^{3+} is coordinated between three pyridinic Ns and two imine groups but, unlike the SiO_2-NH-NH_2-SB catalyst, the metal ion is not octahedrally coordinated, resulting in a slightly lower ΔE_{int} value. This less ΔE_{int} and lower coordination geometry results in a less sterically hindered Fe^{3+} centre, which would contribute to a better catalytic

performance of the SiO_2-NH_2-SB catalyst (84% conversion) compared to the SiO_2-NH-NH_2-SB catalyst (10 % conversion). A high favourable metal ion ΔE_{int} is also attributed to why the performance for the SiO_2-NH-NH_2 catalyst did not improve after Fe ion immobilisation. In this system, the ligand only catalyst demonstrated relatively good reactivity with 75% PET conversion. After Fe ion immobilisation (loading 4043.3 ppm), there was no change in the PET conversion (73 %). In this catalyst the Fe^{3+} ion is coordinated to six amine groups, combining three primary amines and three secondary amines, in an octahedral geometry. The high interaction energy limits the participation of the Fe^{3+} in the reaction and furthermore, the presence of Fe^{3+} also prevents the terminal amine groups from catalysing the reaction. This contrasts with the SiO_2-NH_2 catalyst where Fe^{3+} is coordinated only by three amine groups giving it a lower BE and so the PET conversion increased after Fe^{3+} immobilisation.

Table 2: Calculated interaction energies (ΔE_{int}, in kcal·mol^{-1}) for the Fe^{+3} ion coordination with the organic ligands supported on the SiO_2 surfaces in the solvent phase (water).

Structure	1L	2L	3L
SiO_2-NH_2	-1.66	-80.73	-143.30
SiO_2-NH_2-SB	-40.90	-172.47	-200.58
SiO_2-NH-NH_2	-123.83	-173.80	-258.27
SiO_2-NH-NH_2-SB	-84.48	-227.11	-303.82
SiO_2-Pincer	-132.54	-273.49	-290.01

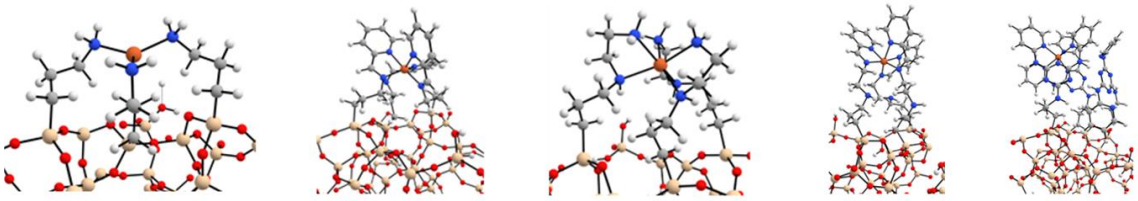


Figure 6: Optimised geometries for the different SiO_2/ligands coordinating the Fe^{3+} ion. Colour scheme: grey (C), white (H), blue (N), orange (Fe), red (O) and beige (Si).

The glycolysis reaction using the Fe^{3+} ion and the NP catalysts were also modelled. The glycolysis of PET is the molecular degradation of the polymer by ethylene glycol (EG) through a trans-esterification reaction, where the ester linkage breaks and is transformed into hydroxyl groups (see Supporting Information Figure S7). The reaction process starts with the coordination of PET to the metal centre by the oxygen of the carbonyl group of the ester. Since both ester groups are only separated by two -CH_2 it is possible to face the coordination of both adjacent ester groups. The following step is the transesterification of the ester by the EG, where the carbonyl carbon is attacked by the free electron pair present on the hydroxyl group of EG. This is followed by the binding between the hydroxyl ethyl group of EG with the carbonyl carbon of PET, resulting in breaking the long polymer chain into two short oligomers. The subsequent glycolysis will break this oligomer forming the BHET product.

This mechanism for PET depolymerisation was modelled here in the absence and in the presence of either a single Fe^{3+} ion immobilised catalyst or the NP catalyst (see Figure 7). In these simulations, two repetitive units of the PET polymer (A) were accounted for. In modelling the Fe^{3+} ion immobilised catalyst, it is important to consider the availability of the metal centre as active site. Therefore, systems where the Fe^{+3} ion is fully coordinated or trapped between the most voluminous ligands will not perform well due to steric hindrance (e.g., SiO_2-$NHNH_2$-SB and SiO_2-Pincer), as experimentally demonstrated. Therefore, the system selected to represent the single Fe^{3+} ion catalysts was the SiO_2-NH_2 catalyst (see Figure 7 (a)). Although this is the system presenting the less favourable ΔE_{int}, it is the structure presenting the least steric impediments. The NP catalyst, to keep the simulations computationally affordable, has been modelled here as an iron oxide nanocluster using the Bulk Cut Nanoparticle Model (BCN-M), a computational tool that automatically generates Wulff-like nanoparticle and nanocluster models for binary materials with controlled stoichiometry.[46] This program, by introducing all the data relative to the Fe_2O_3 surfaces, generated as a minimal cluster a species of stoichiometry Fe_6O_8, in which 4 iron centres have a formal oxidation state of Fe^{3+} and the other two Fe^{2+}. This composition makes that our NC model has 28 total of unpaired electrons (5 unpaired electrons for the four Fe^{3+} cations and 4 unpaired electrons for the two Fe^{2+} cations)

rendering our NC to have a total electronic spin multiplicity of 29. Although the nanocluster (NC) does not perfectly match an Fe_2O_3 system (due to technical limitations of the software), since the structural modelling of nanostructures of binary ionic systems is a highly delicate task, we assume that the BCN-M-generated Fe_6O_8 NC is reasonable enough to reproduce the chemistry of a Fe_2O_3 supported on a SiO_2 surface. Thus, we simulated the PET decomposition catalysed by Fe_2O_3 NPs, using the adsorbed Fe_6O_8 NC on a silica surface as a catalyst model (see Figure 7 (b)).

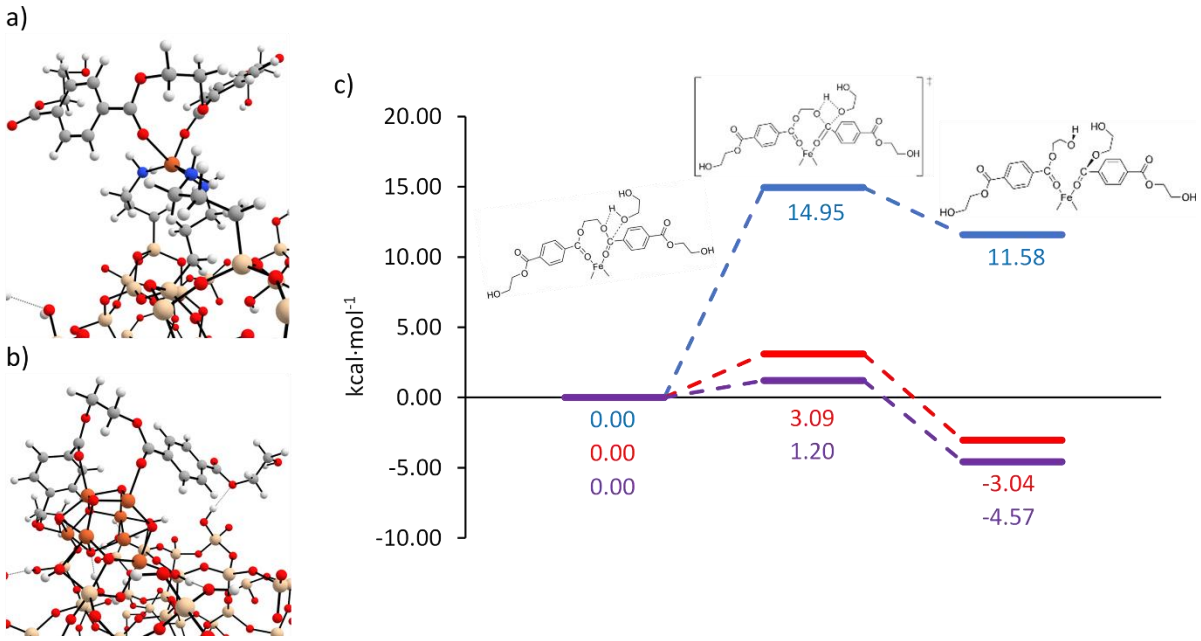


Figure 7: (a) Optimised geometry of the adsorbed PET molecular cluster over the Fe^{+3} ion. (b) Optimised geometry of the adsorbed PET over the iron oxide NC. Colour scheme: grey (C), white (H), blue (N), orange (Fe), red (O) and beige (Si). (c) Relative Gibbs energy profiles at 190 °C (in kcal·mol^{-1}) for PET glycolysis considering EG as a solvent, via uncatalysed (blue colour), catalysed by a single atom Fe^{+3} (red colour) and catalysed by the iron oxide nanocluster (purple colour).

Figure 7 (c) depicts the potential energy surfaces (PESs) for the uncatalysed reaction and those catalysed by single Fe^{3+} immobilised on SiO_2-NH_2 and by the NC catalyst. For the catalysed reaction, the insets figure shows the PET fragment coordinates with the metal centre through the carbonyl

group [Fe-O=C]. The transesterification reaction mechanism proposed here goes through a fourth-membered ring transition state ($TS_{A\text{-}B}$) where the carbonyl carbon of the PET molecular cluster is attacked by the hydroxyl group of the EG subsequently forming the hydroxyl-carbonyl bond. Energetic values show that the uncatalysed reaction not only goes through a high energy barrier, but it also presents an endergonic character. The activation energy is significantly reduced when performing the reaction with the Fe^{3+} and NC catalysts, which are similar but lower in the latter case (3.09 kcal mol^{-1} vs 1.20 kcal mol^{-1}, respectively). The reactions with Fe^{3+} and the NC also revert the thermodynamics, becoming exoergic processes. Interestingly, reaction free energies are slightly more favourable than those catalysed by Fe^{3+}, -4.57 and -3.04 kcal mol^{-1}, respectively), due to that the NC presents more anchoring points that confer stability to the products. Finally, for the sake of comparison, we also performed the same study using a larger NC with stoichiometry $(Fe_2O_3)(FeO)_{11}$, that is, with predominance of formally Fe^{2+} species (see Table S4). Interestingly, the energy barriers are similar for the two NC types (1.35 kcal mol^{-1} on the larger NC) but differ on their reaction energies, *i.e.*, that associated with the larger NC is dramatically more favourable (-16.20 kcal mol^{-1}), which also due to the presence of more interacting points that stabilise the newly formed products. Therefore, when performing the glycolysis reaction catalysed by the NP based catalysts, it is enhanced not only kinetically as the activation energy is lower but also, thermodynamically, favouring the products formation. The increased exergonic character is the main difference between the single Fe^{3+} ion catalyst and the NP system, due to stabilisation of the products and so therefore the metal oxide NP catalyst show superior reaction performance.

Finally, we used the best performing catalyst as identified by the evaluation study *i.e.,* the Fe_2O_3 NP catalysts prepared by reduction using the SiO_2-NH_2-SB and SiO_2-pincer ligands, to further study the impact of reaction parameters such as temperature, time, catalyst loading and PET:EG ratio. Figure 8 (a) compares the effect of reaction temperature and catalyst concentration. The PET conversions decreased at lower catalyst loading reaching full conversion at 100 mg SiO_2 catalyst (0.4 wt % Fe). The

optimal temperature of the reaction was found to be 190 °C, with PET conversions decreasing at lower temperatures. Figure 8(b) shows the ratio of PET: EG was critical for the reaction with a ratio of 1:5 being optimal for full PET conversion. On decreasing the ratio to 1:3, there was insufficient EG to cover the PET for the reaction to proceed smoothly. Figure 8 (c) shows a reaction time series, carried out under the same conditions and iron loading, ranging from one to three hours for the heterogeneous SiO_2 catalysts compared with a homogeneous $FeCl_3$ catalyst. Interestingly, while all catalysts could achieve full PET conversion, both the heterogeneous catalysts display higher PET conversions compared to the homogeneous catalyst. It is clear that under these conditions the Fe_2O_3 NP catalyst outperformed the ion-immobilised catalyst but also a homogeneous catalyst of equivalent Fe loading. This is attributed to the small diameter and high dispersion of the NPs on the SiO_2 support, as evidenced by TEM and the presence of the organic ligands which have a promotional effect on the PET glycolysis due to being organic amines. Figure S9 shows the recyclability of the SiO_2-NP pincer catalyst tested over five cycles. The catalyst achieved full PET conversion on two reaction recycles. The conversion does drop after the third cycle (82 %) but still displays favourable recyclability given the low loading metal (0.4 wt%) of the catalyst. An additional benefit of using a heterogeneous catalyst was the very low metal contamination in the BHET product, which was analysed by ICP-MS (see Supporting Information table S2). Metal contamination in the BHET monomer from the catalyst in PET glycolysis often necessitates additional purification steps. BHET obtained using $FeCl_3$ as the catalyst contained 4.9 ppm of Fe and visually had a pale yellow-orange colour, while the BHET obtained using the heterogeneous catalyst was colourless, with an Fe concentration measured to be 1.3 ppm. Finally, the use of additives and colourants are commonly found in post-consumer plastic and their impact on catalyst performance is not always explored. The Fe_2O_3 NP catalyst was used to depolymerise black and green coloured PET as shown in Figure 8 (d), giving high PET conversions of 94 % for both black and green plastic showing that this catalyst can effectively be used for coloured post-consumer PET.

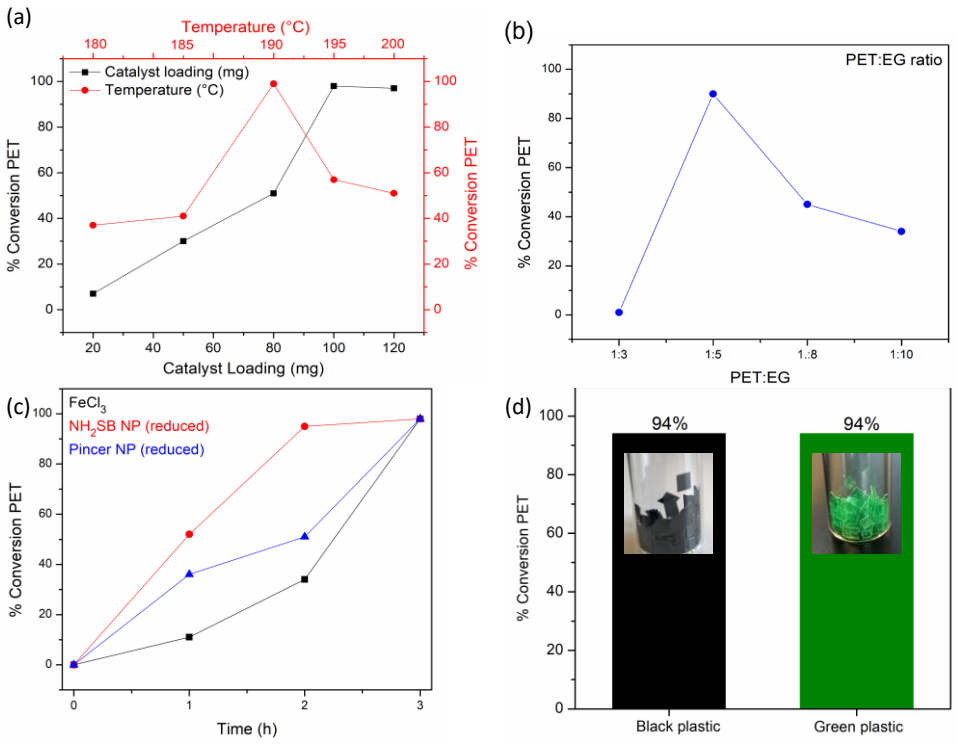


Figure 8: (a) Optimisation of catalyst loading (w.r.t the SiO_2 mass) and reaction temperature, (b) PET:EG ratio optimisation, (c) time series of $FeCl_3$, SiO_2-Fe_2O_3 pincer NP and SiO_2- Fe_2O_3-NH_2SB NP both prepared via a reducing agent. (d) Application of heterogeneous catalysts to coloured post-consumer PET.

3.3 Conclusions

In conclusion, we investigated the catalyst design for the glycolysis of PET using heterogeneous mesoporous SiO_2 catalysts. The SiO_2 support was modified with a range of N containing organic ligands used for the immobilisation of Fe ions. Solid-state NMR allowed for the investigation of the structures of the modified SiO_2 supports confirming the successful grafting of the ligands and reveal the distinct types of silicon environments. Surface coverages were found to be between 40-73 % based on quantitative ^{29}Si NMR experiments. The Fe-ion immobilised catalysts were converted into Fe_2O_3 NP supported catalysts by calcination or treatment with aqueous $NaBH_4$ as confirmed by TEM and XPS. In general, the NP based catalysts performed better than their ion immobilised catalysts and the presence of both the Fe_2O_3 NP and organic ligand displayed the best performance giving full PET

conversion and highest BHET yields. The ligand assisted Fe_2O_3 NP catalyst also outperformed a homogeneous $FeCl_3$ catalyst. The superior performance the ligand stabilised Fe_2O_3 NP catalyst was attributed to cooperative effects between the organic ligand and the NPs. The N containing amine ligands facilitate base catalysed glycolysis of PET, similar to homogeneous organocatalysts and also behave as Lewis bases to facilitate electron transfer to the carbonyl group making it more susceptible to nucleophilic attack by the metal catalyst. This work shows the significant potential of nanoparticle based heterogeneous catalysts for PET glycolysis and the use of organically functionalised support material to further enhance catalytic activity.

3.4 References

(1) Johansen, M. R.; Christensen, T. B.; Ramos, T. M.; Syberg, K. A review of the plastic value chain from a circular economy perspective. *Journal of Environmental Management* **2022**, *302*, 113975.
(2) Liu, Y.; Yao, X.; Yao, H.; Zhou, Q.; Xin, J.; Lu, X.; Zhang, S. Degradation of poly(ethylene terephthalate) catalyzed by metal-free choline-based ionic liquids. *Green Chemistry* **2020**, *22* (10), 3122-3131, 10.1039/D0GC00327A.
(3) Siddiqui, M. N.; Redhwi, H. H.; Al-Arfaj, A. A.; Achilias, D. S. Chemical Recycling of PET in the Presence of the Bio-Based Polymers, PLA, PHB and PEF: A Review. *Sustainability* **2021**, *13* (19), 10528.
(4) Hou, Q.; Zhen, M.; Qian, H.; Nie, Y.; Bai, X.; Xia, T.; Rehman, M. L. U.; Li, Q.; Ju, M. Cell Reports Phys. *Sci* **2021**, *2*, 100514.
(5) Stanica-Ezeanu, D.; Matei, D. Natural depolymerization of waste poly(ethylene terephthalate) by neutral hydrolysis in marine water. *Scientific Reports* **2021**, *11* (1), 4431. Yang, W.; Liu, R.; Li, C.; Song, Y.; Hu, C. Hydrolysis of waste polyethylene terephthalate catalyzed by easily recyclable terephthalic acid. *Waste Management* **2021**, *135*, 267-274.
(6) Chen, J.; Lv, J.; Ji, Y.; Ding, J.; Yang, X.; Zou, M.; Xing, L. Alcoholysis of PET to produce dioctyl terephthalate by isooctyl alcohol with ionic liquid as cosolvent. *Polymer Degradation and Stability* **2014**, *107*, 178-183. Scremin, D. M.; Miyazaki, D. Y.; Lunelli, C. E.; Silva, S. A.; Zawadzki, S. F. PET Recycling by Alcoholysis Using a New Heterogeneous Catalyst: Study and its Use in Polyurethane Adhesives Preparation. *Macromolecular Symposia* **2019**, *383* (1), 1800027, (acccessed 2022/08/23).
(7) Wang, L.; Nelson, G. A.; Toland, J.; Holbrey, J. D. Glycolysis of PET Using 1,3-Dimethylimidazolium-2-Carboxylate as an Organocatalyst. *ACS Sustainable Chemistry & Engineering* **2020**, *8* (35), 13362-13368.
(8) Uekert, T.; Singh, A.; Desveaux, J. S.; Ghosh, T.; Bhatt, A.; Yadav, G.; Afzal, S.; Walzberg, J.; Knauer, K. M.; Nicholson, S. R.; et al. Technical, Economic, and Environmental Comparison of Closed-Loop Recycling Technologies for Common Plastics. *ACS Sustainable Chemistry & Engineering* **2023**, *11* (3), 965-978.
(9) Chen, F.; Wang, G.; Shi, C.; Zhang, Y.; Zhang, L.; Li, W.; Yang, F. Kinetics of glycolysis of poly(ethylene terephthalate) under microwave irradiation. *Journal of Applied Polymer Science* **2013**, *127* (4), 2809-2815, (acccessed 2022/08/23).
(10) Vollmer, I.; Jenks, M. J. F.; Roelands, M. C. P.; White, R. J.; van Harmelen, T.; de Wild, P.; van der Laan, G. P.; Meirer, F.; Keurentjes, J. T. F.; Weckhuysen, B. M. Beyond Mechanical Recycling: Giving New Life to Plastic Waste. *Angewandte Chemie International Edition* **2020**, *59* (36), 15402-15423, (acccessed 2022/12/15).
(11) Duque-Ingunza, I.; López-Fonseca, R.; de Rivas, B.; Gutiérrez-Ortiz, J. I. Process optimization for catalytic glycolysis of post-consumer PET wastes. *Journal of Chemical Technology & Biotechnology* **2014**, *89* (1), 97-103, (acccessed 2022/08/22).
(12) Shukla, S. R.; Kulkarni, K. S. Depolymerization of poly(ethylene terephthalate) waste. *Journal of Applied Polymer Science* **2002**, *85* (8), 1765-1770, (acccessed 2022/08/22). López-Fonseca, R.; Duque-Ingunza, I.; de Rivas, B.; Flores-Giraldo, L.; Gutiérrez-Ortiz, J. I. Kinetics of catalytic glycolysis of PET wastes with sodium carbonate. *Chemical Engineering Journal* **2011**, *168* (1), 312-320. Fang, P.; Liu, B.; Xu, J.; Zhou, Q.; Zhang, S.; Ma, J.; lu, X. High-efficiency glycolysis of poly(ethylene terephthalate) by sandwich-structure polyoxometalate catalyst with two active sites. *Polymer Degradation and Stability* **2018**, *156*, 22-31.
(13) Chen, F.; Wang, G.; Li, W.; Yang, F. Glycolysis of Poly(ethylene terephthalate) over Mg–Al Mixed Oxides Catalysts Derived from Hydrotalcites. *Industrial & Engineering Chemistry Research* **2013**, *52* (2), 565-571. Fuentes, C. A.; Gallegos, M. V.; García, J. R.; Sambeth, J.; Peluso, M. A. Catalytic Glycolysis of Poly(ethylene terephthalate) Using Zinc and Cobalt Oxides Recycled from Spent Batteries. *Waste and Biomass Valorization* **2020**, *11* (9), 4991-5001.
(14) Wang, Q.; Geng, Y.; Lu, X.; Zhang, S. First-Row Transition Metal-Containing Ionic Liquids as Highly Active Catalysts for the Glycolysis of Poly(ethylene terephthalate) (PET). *ACS Sustainable Chemistry &*

Engineering **2015**, *3* (2), 340-348. Yue, Q. F.; Xiao, L. F.; Zhang, M. L.; Bai, X. F. The Glycolysis of Poly(ethylene terephthalate) Waste: Lewis Acidic Ionic Liquids as High Efficient Catalysts. *Polymers* **2013**, *5* (4), 1258-1271.
(15) Lalhmangaihzuala, S.; Laldinpuii, Z.; Lalmuanpuia, C.; Vanlaldinpuia, K. Glycolysis of Poly(Ethylene Terephthalate) Using Biomass-Waste Derived Recyclable Heterogeneous Catalyst. *Polymers* **2021**, *13* (1), 37.
(16) Yunita, I.; Putisompon, S.; Chumkaeo, P.; Poonsawat, T.; Somsook, E. Effective catalysts derived from waste ostrich eggshells for glycolysis of post-consumer PET bottles. *Chemical Papers* **2019**, *73* (6), 1547-1560. Laldinpuii, Z.; Lalhmangaihzuala, S.; Pachuau, Z.; Vanlaldinpuia, K. Depolymerization of poly(ethylene terephthalate) waste with biomass-waste derived recyclable heterogeneous catalyst. *Waste Management* **2021**, *126*, 1-10.
(17) Veregue, F. R.; Pereira da Silva, C. T.; Moisés, M. P.; Meneguin, J. G.; Guilherme, M. R.; Arroyo, P. A.; Favaro, S. L.; Radovanovic, E.; Girotto, E. M.; Rinaldi, A. W. Ultrasmall Cobalt Nanoparticles as a Catalyst for PET Glycolysis: A Green Protocol for Pure Hydroxyethyl Terephthalate Precipitation without Water. *ACS Sustainable Chemistry & Engineering* **2018**, *6* (9), 12017-12024.
(18) Du, J.-T.; Sun, Q.; Zeng, X.-F.; Wang, D.; Wang, J.-X.; Chen, J.-F. ZnO nanodispersion as pseudohomogeneous catalyst for alcoholysis of polyethylene terephthalate. *Chemical Engineering Science* **2020**, *220*, 115642.
(19) Sun, Q.; Zheng, Y.-Y.; Yun, L.-X.; Wu, H.; Liu, R.-K.; Du, J.-T.; Gu, Y.-H.; Shen, Z.-G.; Wang, J.-X. Fe3O4 Nanodispersions as Efficient and Recoverable Magnetic Nanocatalysts for Sustainable PET Glycolysis. *ACS Sustainable Chemistry & Engineering* **2023**, *11* (19), 7586-7595.
(20) Son, S. G.; Jin, S. B.; Kim, S. J.; Park, H. J.; Shin, J.; Ryu, T.; Jeong, J.-M.; Choi, B. G. Exfoliated manganese oxide nanosheets as highly active catalysts for glycolysis of polyethylene terephthalate. *FlatChem* **2022**, *36*, 100430.
(21) Cao, J.; Lin, Y.; Jiang, W.; Wang, W.; Li, X.; Zhou, T.; Sun, P.; Pan, B.; Li, A.; Zhang, Q. Mechanism of the Significant Acceleration of Polyethylene Terephthalate Glycolysis by Defective Ultrathin ZnO Nanosheets with Heteroatom Doping. *ACS Sustainable Chemistry & Engineering* **2022**, *10* (17), 5476-5488.
(22) Suo, Q.; Zi, J.; Bai, Z.; Qi, S. The Glycolysis of Poly(ethylene terephthalate) Promoted by Metal Organic Framework (MOF) Catalysts. *Catalysis Letters* **2017**, *147* (1), 240-252.
(23) Wu, Y.; Wang, X.; Kirlikovali, K. O.; Gong, X.; Atilgan, A.; Ma, K.; Schweitzer, N. M.; Gianneschi, N. C.; Li, Z.; Zhang, X.; et al. Catalytic Degradation of Polyethylene Terephthalate Using a Phase-Transitional Zirconium-Based Metal–Organic Framework. *Angewandte Chemie International Edition* **2022**, *61* (24), e202117528, (acccessed 2022/11/14).
(24) Shukla, S. R.; Palekar, V.; Pingale, N. Zeolite catalyzed glycolysis of poly(ethylene terephthalate) bottle waste. *Journal of Applied Polymer Science* **2008**, *110* (1), 501-506, (acccessed 2022/11/14).
(25) Yang, R.-X.; Bieh, Y.-T.; Chen, C. H.; Hsu, C.-Y.; Kato, Y.; Yamamoto, H.; Tsung, C.-K.; Wu, K. C. W. Heterogeneous Metal Azolate Framework-6 (MAF-6) Catalysts with High Zinc Density for Enhanced Polyethylene Terephthalate (PET) Conversion. *ACS Sustainable Chemistry & Engineering* **2021**, *9* (19), 6541-6550.
(26) Wang, T.; Shen, C.; Yu, G.; Chen, X. Metal ions immobilized on polymer ionic liquid as novel efficient and facile recycled catalyst for glycolysis of PET. *Polymer Degradation and Stability* **2021**, *194*, 109751.
(27) Kim, J.; Song, B.; Chung, I.; Park, J.; Yun, Y. High-performance Pt catalysts supported on amine-functionalized silica for enantioselective hydrogenation of α-keto ester. *Journal of Catalysis* **2021**, *396*, 81-91.
(28) Li, H.; Chen, X.; Shen, D.; Wu, F.; Pleixats, R.; Pan, J. Functionalized silica nanoparticles: classification, synthetic approaches and recent advances in adsorption applications. *Nanoscale* **2021**, *13* (38), 15998-16016, 10.1039/D1NR04048K.

(29) Graf, N.; Yegen, E.; Gross, T.; Lippitz, A.; Weigel, W.; Krakert, S.; Terfort, A.; Unger, W. E. S. XPS and NEXAFS studies of aliphatic and aromatic amine species on functionalized surfaces. *Surface Science* **2009**, *603* (18), 2849-2860.
(30) Paengjun, N.; Vibulyaseak, K.; Ogawa, M. Heterostructural transformation of mesoporous silica–titania hybrids. *Scientific Reports* **2021**, *11* (1), 3210.
(31) Millot, Y.; Hervier, A.; Ayari, J.; Hmili, N.; Blanchard, J.; Boujday, S. Revisiting Alkoxysilane Assembly on Silica Surfaces: Grafting versus Homo-Condensation in Solution. *Journal of the American Chemical Society* **2023**, *145* (12), 6671-6681.
(32) Cui, J.; Chatterjee, P.; Slowing, I. I.; Kobayashi, T. In Situ 29Si solid-state NMR study of grafting of organoalkoxysilanes to mesoporous silica nanoparticles. *Microporous and Mesoporous Materials* **2022**, *339*, 112019.
(33) van Meerten, S. G. J.; Franssen, W. M. J.; Kentgens, A. P. M. ssNake: A cross-platform open-source NMR data processing and fitting application. *Journal of Magnetic Resonance* **2019**, *301*, 56-66.
(34) Liu, C. C.; Maciel, G. E. The Fumed Silica Surface: A Study by NMR. *Journal of the American Chemical Society* **1996**, *118* (21), 5103-5119. Lippmaa, E.; Maegi, M.; Samoson, A.; Engelhardt, G.; Grimmer, A. R. Structural studies of silicates by solid-state high-resolution silicon-29 NMR. *Journal of the American Chemical Society* **1980**, *102* (15), 4889-4893. Lechert, H. G. Engelhardt und D. Michel: High Resolution Solid State NMR of Silicates and Zeolites. John Wiley & Sons, Chichester, New York, Brisbane, Toronto, Singapore, 1987. 485 Seiten, Preis: $ 55.–. *Berichte der Bunsengesellschaft für physikalische Chemie* **1988**, *92* (9), 1059-1059, (acccessed 2023/05/17).
(35) Cheng, R.; Liu, X.; Fang, Y.; Terano, M.; Liu, B. High-resolution 29Si CP/MAS solid state NMR spectroscopy and DFT investigation on the role of geminal and single silanols in grafting chromium species over Phillips Cr/silica catalyst. *Applied Catalysis A: General* **2017**, *543*, 26-33. Bruch, M. D.; Fatunmbi, H. O. Nuclear magnetic resonance analysis of silica gel surfaces modified with mixed, amine-containing ligands. *Journal of Chromatography A* **2003**, *1021* (1), 61-70.
(36) Srikanth, C. S.; Chuang, S. S. C. Spectroscopic Investigation into Oxidative Degradation of Silica-Supported Amine Sorbents for CO2 Capture. *ChemSusChem* **2012**, *5* (8), 1435-1442, (acccessed 2023/05/17).
(37) Vallet-Regí, M.; Schüth, F.; Lozano, D.; Colilla, M.; Manzano, M. Engineering mesoporous silica nanoparticles for drug delivery: where are we after two decades? *Chemical Society Reviews* **2022**, *51* (13), 5365-5451, 10.1039/D1CS00659B.
(38) Mafra, L.; Čendak, T.; Schneider, S.; Wiper, P. V.; Pires, J.; Gomes, J. R. B.; Pinto, M. L. Structure of Chemisorbed CO2 Species in Amine-Functionalized Mesoporous Silicas Studied by Solid-State NMR and Computer Modeling. *Journal of the American Chemical Society* **2017**, *139* (1), Vieira, R.; Marin-Montesinos, I.; Pereira, J.; Fonseca, R.; Ilkaeva, M.; Sardo, M.; Mafra, L. “Hidden” CO2 in Amine-Modified Porous Silicas Enables Full Quantitative NMR Identification of Physi- and Chemisorbed CO2 Species. *The Journal of Physical Chemistry C* **2021**, *125* (27), 14797-14806.
(39) dos Santos, T. C.; Bourrelly, S.; Llewellyn, P. L.; de M. Carneiro, J. W.; Machado Ronconi, C. Adsorption of CO2 on amine-functionalised MCM-41: experimental and theoretical studies. *Physical Chemistry Chemical Physics* **2015**, *17* (16), 11095-11102, 10.1039/C5CP00581G.
(40) Desforges, A.; Backov, R.; Deleuze, H.; Mondain-Monval, O. Generation of Palladium Nanoparticles within Macrocellular Polymeric Supports: Application to Heterogeneous Catalysis of the Suzuki–Miyaura Coupling Reaction. *Advanced Functional Materials* **2005**, *15* (10), 1689-1695.
(41) Yamashita, T.; Hayes, P. Analysis of XPS spectra of Fe2+ and Fe3+ ions in oxide materials. *Applied Surface Science* **2008**, *254* (8), 2441-2449.
(42) Poulin, S.; França, R.; Moreau-Bélanger, L.; Sacher, E. Confirmation of X-ray Photoelectron Spectroscopy Peak Attributions of Nanoparticulate Iron Oxides, Using Symmetric Peak Component Line Shapes. *The Journal of Physical Chemistry C* **2010**, *114* (24), 10711-10718.
(43) Delle Chiaie, K. R.; McMahon, F. R.; Williams, E. J.; Price, M. J.; Dove, A. P. Dual-catalytic depolymerization of polyethylene terephthalate (PET). *Polymer Chemistry* **2020**, *11* (8), 1450-1453, 10.1039/C9PY01920K.

(44) Le, N. H.; Ngoc Van, T. T.; Shong, B.; Cho, J. Low-Temperature Glycolysis of Polyethylene Terephthalate. *ACS Sustainable Chemistry & Engineering* **2022**, *10* (51), 17261-17273.
(45) Wang, Z.; Jin, Y.; Wang, Y.; Tang, Z.; Wang, S.; Xiao, G.; Su, H. Cyanamide as a Highly Efficient Organocatalyst for the Glycolysis Recycling of PET. *ACS Sustainable Chemistry & Engineering* **2022**, *10* (24), 7965-7973.
(46) González, D.; Camino, B.; Heras-Domingo, J.; Rimola, A.; Rodríguez-Santiago, L.; Solans-Monfort, X.; Sodupe, M. BCN-M: A Free Computational Tool for Generating Wulff-like Nanoparticle Models with Controlled Stoichiometry. *The Journal of Physical Chemistry C* **2020**, *124* (1), 1227-1237.

3.5 Appendix: Supporting Information

Ligand-Aided Glycolysis of PET using Functionalised Silica Supported Fe_2O_3 Nanoparticles

*Casey, É.; **Breen, R**.; Gómez, J. S.; Kentgens, A. P. M.; Pareras, G.; Rimola, A.; Holmes, J. D.; Collins, G. Ligand-Aided Glycolysis of PET Using Functionalized Silica-Supported Fe_2O_3 Nanoparticles. ACS Sustainable Chemistry & Engineering **2023**, 11 (43), 15544-15555. DOI: 10.1021/acssuschemeng.3c03585.*

Item	Title
Table S1	Heterogeneous catalyst reported in the literature
Figure S1	^1H liquid NMR spectrum of the BHET product formed from the glycolysis of PET.
Figure S2	XPS analysis of the Si 2p core level for bare SiO_2 and the functionalized SiO_2
Figure S3	$^1H \rightarrow {}^{13}C$ CPMAS solid state NMR spectra of Schiff base ligand attached to (a) SiO_2-NH_2 (Ligand 2) and (b) SiO_2 – $NHNH_2$ ((Ligand 4) catalyst.
Table S2	ICP-MS for Fe loading for each ion and NP catalyst
Figure S4	SEM images of (a) mesoporous cellular foam (b) ion-immobilized SiO2 (c) NP immobilized SiO_2.
Figure S5	Fe 3p XPS spectrum of SiO_2-pincer catalyst indicating the presence of Fe_2O_3.
Figure S6	O 1s core level XPS spectra of ligand only catalyst sand NP catalyst prepared by calcination (C) and using $NaBH_4$ (R) for SiO_2-NH_2, SiO_2- $NHNH_2$, SiO_2-$NHNH_2$ SB and SiO_2-pincer ligands.
Figure S7	N 1s XPS core level spectra of ligand only and both calcined and chemically reduced NP catalysts for SiO_2-NH_2, SiO_2-$NHNH_2$, SiO_2-$NHNH_2$ SB and SiO_2-pincer ligands.
Table S3	Calculated relative energies (in kcal·mol^{-1}) for the three different spin multiplicities, doublet (D), quadruplet (Q) and sextet (S), for the Fe^{+3} ion using the SiO_2-NH_2 system as a test case.
Figure S8	Mechanism for the PET glycolysis reaction.

Table S4	Calculated relative Gibbs energies for the modelled reaction systems, considering 463.15 K and ethylene glycol (EG) as a solvent ($\Delta G_{EG(463.15\ K)}$), including the uncatalyzed process, and the reaction catalyzed by the Fe^{+3} ion, the Fe_2O_3 nanoparticle ($(Fe_2O_3)_2(FeO)_2$) and the FeO nanoparticle ($(Fe_2O_3)(FeO)_{11}$).

Table S1: Summary of literature reports using heterogeneous catalysts for PET glycolysis

Entry	Catalyst	Catalyst Loading (wt %)	Temp (°C)	Time (min)	BHET Yield	Ref
1	Review					1
2	n-ZnO	5 %	190	60	90	2
3	ZnO	1 %	260	60	67	3
4	Co_3O_4	2 %	260	60	63	3
5	Mn_3O_4	2 %	260	60	74	3
6	Co NPs	1.5 %	180	180	77	4
7	ZnO	1 %	196	120	50	5
8	CoO	1 %	196	120	10	5
9	CoZnO	1 %	196	120	80	5
10	ɤ-Fe_2O_3	1 %	300	60	90	6
11	CeO_2	1 %	300	60	25	6
12	Fe^{III} nanosheet	1 %	200	30	100*	7
13	Fe_2O_3-MWCNT	5 %	190	120	100*	8
14	MWCNT	5 %	190	120	78*	8
15	Magnetite	5 %	190	120	62	8
16	Titanate nanotubes	0.3 %	196	120	84	9
17	Na- Titanate nanotubes	0.3 %	196	180	80	10
18	Zn- Titanate nanotubes	0.3 %	196	180	87	10
19	GO-Mn_3O_4	-	300	80	97*	11
20	MnO_2/HGO	0.01 %	200	10	100*	7
21	ɤFe_2O.NGO	9 %	195	180	100*	12
22	Pd/h-BN	0.01 %	100	30	92*	13
23	Fe_2O_3NPs@h-BNNs	0.01 %	200	300	100*	13
24	Fe_3O_4@SiO_2@(mim)[$FeCl_4$]	15 %	180	1440	100*	14
25	rGO\[TESPMI]$_2CoCl_4$	15 %	190	180	95	15
26	hydrocalcites;Mg:Al molar ratio 2	1 %	196	50	61	16
27	hydrocalcites; Mg:Al molar ratio 3	1 %	196	50	66	16
28	hydrocalcites;Mg:Al molar ratio -4	1 %	196	50	31	16
29	Calcined hydrocalcites; Mg:Al molar ratio 2	1 %	196	50	76	16
30	Calcined hydrocalcites; Mg:Al molar ratio 3	1 %	196	50	81	16
31	Calcined hydrocalcites; Mg:Al molar ratio 4	1 %	196	50	66	16
32	Mg-Al-O@Fe_3O_4	0. 1 %	240	90	80	17
33	ZnAl-1	1 %	196	85	66	18

34	ZnAl-2	1 %	196	85	75	18
35	ZnAl-3	1 %	196	85	76	18
36	ZnAl-4	1 %	196	85	76	18
37	(Mg-Zn)-Al LDH	1 %	190	180	75	19
38	S/Zn-Ti-300°C	0.3 %	180	180	72	20
39	SCZ	0.3 %	180	180	72	21
39	$ZnMn_2O_4$	1 %	260	60	92	3
40	$CoMn_2O_4$	1 %	260	60	89	3
41	$ZnCo_2O_4$	1 %	260	60	81	3
42	$CoFe_2O_4$/C10-OAC	0.02 %	195	150	95	22

* Indicates the reported BHET was not an isolated yield.

Experimental

Chemicals and Materials

3-aminopropylytrimethoxysilane (APTMS), 3-(2-aminoethyl-aminopropyl)trimethoxysilane (AEAPTMS), 2-pyridine carboxaldehyde, cyanuric chloride (CNC), N,N diisopropylethylamine (DIEA), sodium borohydride ($NaBH_4$), iron (III) chloride ($FeCl_3.4H_2O$), ammonium hydroxide solution (30-33%), methanol, ethanol, toluene, acetonitrile, tetrahydrofuran and ethylene glycol were all purchased from Sigma Aldrich. Mesoporous cellular foam (MCF) SiO_2 was purchased from Glantreo Ltd. PET was obtained from wastewater bottles after labels and lids being removed were cut into 1 mm x 1 mm pieces for glycolysis experiments. Repeating unit of 192.68 g mol^{-1} was used as the molecular weight of PET.

Synthesis of surface modified mesoporous cellular foam SiO_2

Synthesis of SiO_2-NH_2 (Ligand 1): 2 g of MCF SiO_2 was placed in a round bottom flask along with 4 mL of 3-ATPMS and 75 mL toluene. The mixture was refluxed at 120 °C for 12 h under argon. Once reaction had completed, the solid product (SiO_2-NH_2) was suction filtered and washed with ethanol before dried at 60 °C.

Synthesis of SiO_2-NH_2-SB (Ligand 2): 1 g of the SiO_2-NH_2 prepared in the previous step, was placed in a round bottom flask along with 1.2 mL 2-pyridinecarboxaldehyde and 50 mL ethanol. The reaction mixture was refluxed at 60 °C for 24 h. Once completed, the solid product (SiO_2-NH-SB) was filtered

and washed with ethanol before being dried at 60 °C.

Synthesis of SiO_2-$NHNH_2$ (Ligand 3): 2 g of MCF SiO_2 was placed in a round bottom flask along with 4 mL of AEAPTMS and 75 mL toluene. Mixture was refluxed at 120 °C for 12 h under argon. Once reaction had completed, the solid product (SiO2-$NHNH_2$) was vacuum filtered and washed with ethanol before dried at 60 °C.

Synthesis of SiO_2-$NHNH_2$ SB (Ligand 4): 1 g SiO_2-$NHNH_2$ prepared in the previous step, was placed in a round bottom flask along with 1.2 mL 2-pyridinecarboxaldehyde and 50 mL ethanol. The reaction mixture was refluxed at 60 °C for 24 h. Once completed, solid product (SiO_2-$NHNH_2$ SB) was filtered and washed with ethanol before being dried at 60 °C.

Synthesis of SiO_2-Pincer (Ligand 5): 1.4 g SiO_2-NH_2, 1.8 g cyanuric chloride (CNC), 1.8 mL DIEA and 40 mL THF were added to a round bottom flask. The reaction mixture was left to stir in an ice bath under argon for 8 h. The product SiO_2-CNC was filtered off and washed with THF (5 x 20 mL) and dried overnight. In a three-neck round bottom flask, 1.5 g of the SiO_2-CNC was dispersed in 30 mL dry acetonitrile, 2 g 2-aminopyridine and 2 mL DIEA were added and refluxed for 48 h. After completion, the solid product (SiO_2-Pincer) was filtered off and washed with methanol (5 x 30 mL) and dried at 50 °C overnight.

Fe ion immobilization onto ligand modified SiO_2

Fe species were immobilized onto each of the functionalized SiO_2 supports by stirring 2 g $FeCl_3.4H_2O$ and 1 g of the ligand modified SiO_2 with 50 mL H_2O for 1 h. Once completed, 1 mL ammonium hydroxide solution was added, and pH of the solution adjusted from 2 to 12. The product was filtered off and washed with copious amounts of H_2O.

Synthesis of Fe_2O_3 NPs on SiO_2

The Fe ion-based catalysts were converted into iron oxide nanoparticle catalysts by calcination or chemical reduction. Catalysts were annealed in a tube furnace at 450 °C for 3 h in air. For chemical

reduction method, 0.5 g of the Fe-ion immobilized SiO_2 were placed in a 50 mL beaker. A freshly prepared solution of $NaBH_4$ (0.095 g, 2.5 mmol) and 2 mL H_2O was rapidly added under vigorous stirring, turning the catalyst from orange to brown-black. The solution was stirred for 1 h before filtering and washing with copious amounts of H_2O.

Glycolysis reaction of PET to form BHET

In a typical procedure, 1 g of PET, 0.1 g catalyst and 5 mL of ethylene glycol were refluxed at 190 °C for 3 h. Once reaction was complete, 5 mL of ice-cold H_2O was added to the reaction filtered off and dried. The catalyst was separated by filtration. The filtrate was placed in the fridge overnight after which the BHET crystallized out the solution. The BHET crystals were collected be filtration, washed with water and dried overnight before being weighed. The percentage PET conversion and isolated BHET yield calculated be the equation 1 and equation 2, respectively.

$$\% \text{ Conversion of PET: } \frac{W_0 - W_1}{W_0} \cdot 100 \quad \textbf{Eqn. 1}$$

Where W_0 is the initial weight of the PET used and W_1 is the weight of the unreacted PET after the reaction.

$$\% \text{ Yield of BHET: } \frac{W_{BHET}/M_{BHET}}{W_0/M_{PET}} \cdot 100 \quad \textbf{Eqn. 2}$$

Where, W_{BHET} is the weight of the BHET product after recrystallization, M_{BHET} is the molecular weight of BHET, W_0 is the initial weight of PET used and M_{PET} is the molecular weight of the repeat unit of PET.

NMR analysis confirmed that no formation of dimers or oligomers occurred and that BHET was the only product formed in the reaction. The ^1H liquid-state NMR spectrum of BHET can be seen in the supplementary information Figure S1, where the four main peaks were a singlet at 8.12 ppm corresponding to the aromatic ring protons, an OH triplet at 5.01 ppm, a CH_2 triplet at 4.32 ppm and a quartet at 3.77 ppm for the CH_2 next to the OH group. Residual solvent d_6-DMSO was located at 2.51

ppm. The results are in good agreement with literature values of BHET.[23]

Materials Characterization

X-ray Photoelectron Spectroscopy (XPS) was acquired using a KRATOS AXIS 165 monochromatized X-ray photoelectron spectrometer equipped with an Al Kα (hv = 1486.6 eV) X-ray source. Spectra were collected at a take-off angle of 90° and all spectra were referenced to the C 1s peak at 284.8 eV. Transmission electron microscopy (TEM) analysis was performed using a FEI Titan TEM, at an operating voltage of 300 kV. The iron loading in the catalyst was determined by inductively coupled plasma mass spectroscopy (ICP-MS) using an Agilent 7700 ICP-MS equipped with nickel-tip with copper base sampler cones. Autosamples (Agilent Technology, Japan) were used for all measurements. All measurements were performed in three replicates from each vial. In brief, the ICP-MS was operated in full quantitative mode with a Ni sampler and skimmer cones, MicroMist glass concentric nebulizer and quartz Scott-type spray chamber. Samples were quantified based on external calibrations constructed using standard solutions prepared on the day of analysis. Standard solutions were prepared from TraceCERT®, 1 mg/L Fe in nitric acid (Sigma-Aldrich, UK). Method blanks and certified references materials (Environmental Spike Mix, Agilent) were used to monitor the system performance and instrumental drift. Full data were recorded and analysed with Agilent Mass Hunter Data Software (version 4.6 C.01.08).

^{1}H liquid-state NMR spectra were acquired on a Bruker Avance III NMR spectrometer operating at B_0 = 7.05 T (ν_0 = 300.13 MHz for ^{1}H), in proton-coupled mode. Samples were dissolved in deuterated chloroform ($CDCl_3$) or deuterated d_6-DMSO and tetramethysilane (TMS) was used as the internal standard.

Solid-state NMR experiments were carried out on numerous instruments. ^{29}Si NMR experiments were recorded at B_0 = 7.05 T (ν_0 = 300.13 MHz for ^{1}H) using a Varian VNMRS spectrometer, equipped with a 9.5 mm HX probes employing a MAS rate ν_R = 4 kHz. ^{29}Si one pulse excitation (SPE) experiments were acquired averaging 128 transients with a recycle delay of 1800 s, employing an rf-field strength of $\nu_1 \approx$

42 kHz. The integrals for the Q^4 sites were corrected for the extremely T_1 extracted from saturation-recovery curves. $^1H\rightarrow$ ^{29}Si CPMAS CPMG experiments were recorded with a CP contact time of 2 ms, a recycle delay of 5 s, and 512 transients. For the CPMG train, each full echo was 6 ms in duration and a total of 12 echoes were collected. ^{29}Si chemical shifts were referenced using a solid sample of zeolite 4A (δ_{iso} = −89.70 ppm).

$^1H\rightarrow^{13}C$ CPMAS NMR measurements for **SiO_2-NH_2 (Ligand 1)** and **SiO_2-NH_2-SB (Ligand 2)** were carried out on a Bruker Avance NEO 600 MHz spectrometer (B_0= 14.1 T) employing a Varian 3.2 mm HXY probe at ν_R= 14 kHz. The initial π/2 pulse was 2.17 μs corresponding to an rf-field of ~ 115 KHz and was followed by a CP contact time of 1 ms. The $^1H\rightarrow$ ^{13}C CPMAS spectra were recorded using recycle intervals of 8 s (Ligand 1) and 10 s (Ligand 2) and were the result of averaging 1024 transients. SPINAL ^1H decoupling[24] (~50 kHz) was applied during acquisition. The Hartmann-Hahn condition[25-26] was calibrated using a powdered sample of adamantane. ^{13}C chemical shifts were referenced using a solid sample of adamantane (δ_{iso} = 29.47 and 38.52 ppm).

$^1H\rightarrow^{13}C$ CPMAS NMR measurements for SiO_2-$NHNH_2$ (Ligand 3), SiO_2-$NHNH_2$ SB (Ligand 4) and SiO_2-Pincer (Ligand 5) were recorded on a Bruker Avance NEO 850 MHz spectrometer (B_0= 19.97 T) using a Varian 3.2 mm HXY probe. The samples were spun at a MAS rate, ν_R = 15 kHz. The experiments were acquired under the following experimental conditions: ^1H 90° pulse was set to 2.55 μs corresponding to an rf-field of ~ 98 kHz. The VACP contact time was 1 ms (for ligands 3 and 4) and 10 ms (for ligand 5) using an 80-100 % ramp shape at the ^1H channel, while the RF nutation frequency on the ^{13}C channel was 65 kHz. The spectra were recorded using recycle intervals of 3.5 s (Ligand 3), 2.5 s (Ligand 4) and 7 s (Ligand 5) and were the result of averaging 2048 (Ligands 3 and 4) and 10240 (Ligand 5) transients. SPINAL ^1H decoupling[24] (~80 kHz) was applied during acquisition. The Hartmann-Hahn condition[25-26] was calibrated using a powdered sample of glycine. For Ligand 5; the $^1H\rightarrow^{13}C$ CPMAS spectrum was acquired at −40°C to decrease the dynamics in the sample which reduced the CP efficiency. For all solid-state NMR experiments, rotors were packed in air. Data processing was carried out using Bruker TopSpin (version 4.1.3) and ssNake (version 1.3).[27]

The relative surface coverage obtained from the quantitative ^{29}Si MAS NMR spectra was estimated using equation 3 and expressed with respect to the bare SiO_2 support. The degree of condensation of the Si atoms was estimated using equation:[28]

$$100 - \frac{(Q^2+Q^3)ligand}{(Q^2+Q^3)SiO_2} \cdot 100 \quad \textbf{Eqn. 3}$$

$$\frac{\sum_{n=2}^{4} nI(Q^n)}{4} + \frac{\sum_{n=2}^{3} nI(T^n)}{3} \cdot 100 \quad \textbf{Eqn. 4}$$

Density functional theory (DFT) calculations

Density functional theory (DFT) simulations were carried out using the CP2K package.[29] The mesoporous SiO_2 structure studied here has been computationally represented as a periodic amorphous silica (SiO_2) surface. The surface selected has a silanol density of 7.2 OH/nm^2 assuring the maximum number of Si atoms available to be functionalized in the unit cell.[30] For the initial SiO_2 surface, both internal atomic positions and cell parameters were optimized (resulting with dimensions of 13.34 x 13.73 x 49.21 Å^3. The following optimizations were performed only relaxing the geometry parameters. Optimizations were carried out using the semi-local Perdew–Burke–Ernzerhof (PBEsol) functional,[31] combined with a double-ζ basis set (DZVP-MOLOPT-SR-GTH Gaussian basis set) for all the atom types, together with the Grimme D3BJ correction term to the electronic energy,[32] and a cutoff set at 500 Ry for the plane wave auxiliary basis set. Core electrons were described with the Goedecker–Teter–Hutter pseudopotentials[33] and valence ones with a mixed Gaussian and plane-wave (GPW) approach.[34] Solvation effects were considered by performing a single point energy calculations on the optimized systems adopting the self-consistent continuum solvation (SCCS) model as implemented in CP2K, aiming to reproduce the experimental conditions of water and ethylene glycol as solvents.[35] Binding energies (BE) have been calculated by applying the counterpoise correction in order to avoid basis-set superimposition errors (BSSE). In CP2K, the interaction energy $\Delta\mathbf{E_{int}}$ of the metal on the SiO_2 structure can be calculated defining 2 fragments **A** and **B**, as shown in equation 5.

$$\boldsymbol{E_{int} = E_{AB} - (E_A + E_B)} \quad \textbf{Eqn. 5}$$

where $\mathbf{E_{AB}}$ is the absolute potential energy of the SiO_2/metal system, $\mathbf{E_A}$ corresponds to the absolute potential energy of the bare silica and $\mathbf{E_B}$ is the absolute potential energy of the naked metal**.**

Finally, to determine the nature of the stationary points of the potential energy surfaces (i.e., local minima and saddle points) the corresponding vibrational harmonic frequencies were calculated at the PBE-D3BJ/DZVP level using the finite differences method. A partial Hessian approach was used to reduce the computational cost of the calculations and the vibrational frequencies were calculated on the optimized geometries only for a fragment of the entire system, which included the metal centre and the organic ligands for the single atom Fe^{3+} structures and, the metal-nanocluster and the adsorbates for the FeO nanoparticle structures.

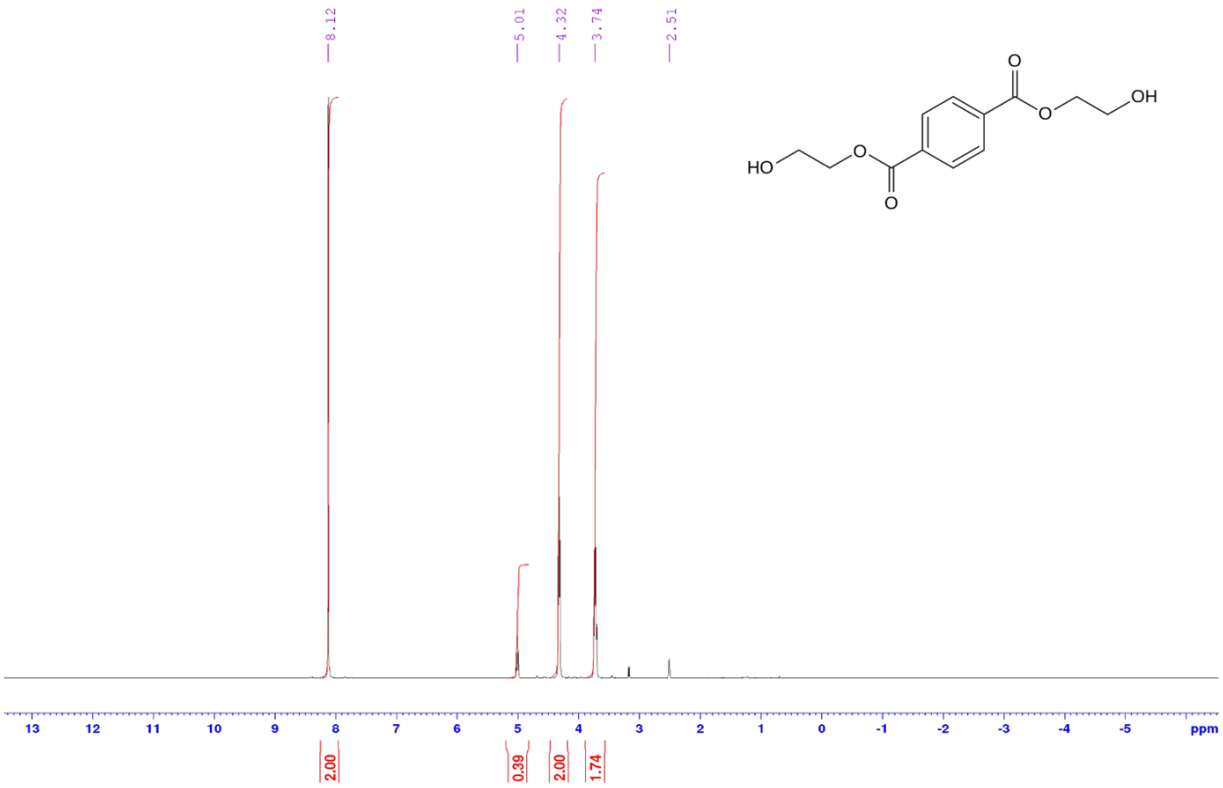


Figure S1: ^{1}H liquid NMR spectrum of the BHET product formed from the glycolysis of PET.

NMR analysis confirmed that no formation of dimers or oligomers occurred and that BHET was the only product formed in the reaction. The ^{1}H liquid NMR spectrum of BHET shows the four main peaks were a singlet at 8.12 ppm corresponding to an aromatic ring, an OH triplet at 5.01 ppm, CH_2 triplet

at 4.32 ppm and CH_2 quartet at 3.77 ppm. Residual solvent d_6-DMSO was located at 2.51 ppm. The results are in good agreement with literature values of BHET.[1]

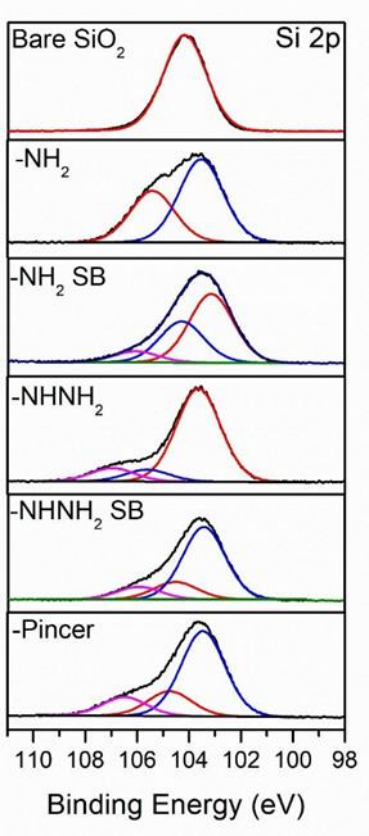


Figure S2: XPS analysis of the Si 2p core level for bare SiO_2 and the functionalized SiO_2 with $-NH_2$ (Ligand 1), $-NH_2$ SB (Ligand 2), $-NHNH_2$ (Ligand 3), $-NHNH_2$ SB (Ligand 4) and pincer (Ligand 5) ligands, respectively.

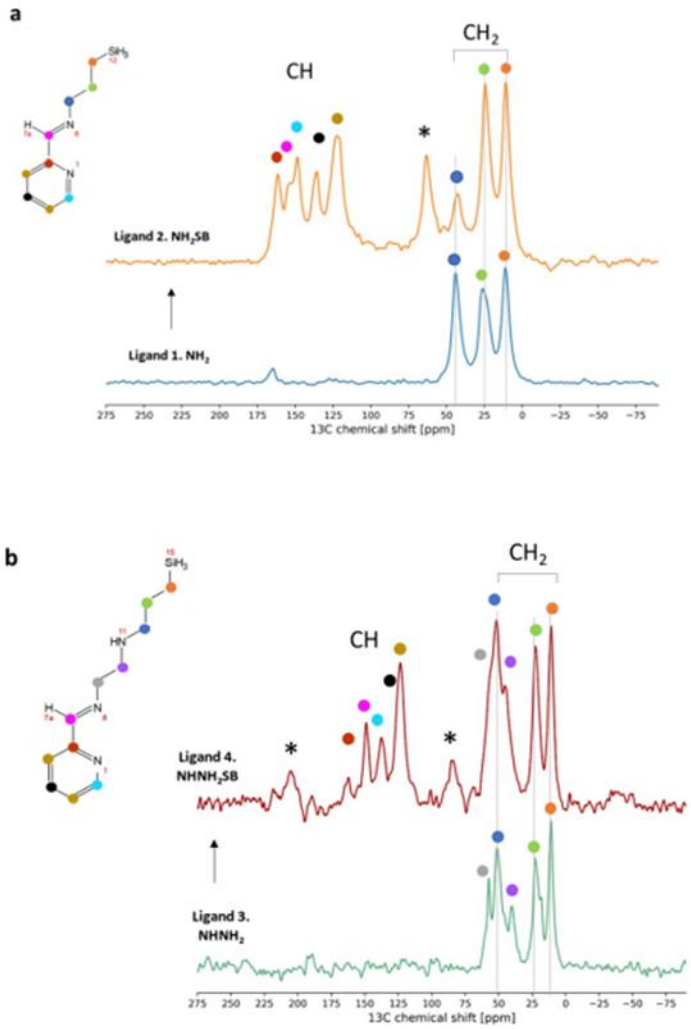


Figure S3: $^{1}H \rightarrow ^{13}C$ CPMAS solid state NMR spectra of Schiff base ligand attached to (a) SiO_2-NH_2 (Ligand 2) and (b) SiO_2 – $NHNH_2$ ((Ligand 4) catalyst. * Indicates the presence of additional peaks.

Table S2: ICP-MS for Fe loading for each ion and NP catalyst

Fe loading on SiO_2 supported catalysts	
Catalyst	**Fe Loading**
SiO_2-Fe-NH_2	4173 ppm
SiO_2-Fe NH_2SB	4981 ppm
SiO_2-Fe $NHNH_2$	4043 ppm
SiO_2-Fe $NHNH_2$ SB	3964 ppm
SiO_2-Fe pincer	3904 ppm
Fe metal contamination in BHET product obtained from different catalysts	
BHET obtained using $FeCl_3$ (homogeneous)	4.6 ppm
BHET obtained using SiO_2-Fe_2O_3 NP (heterogeneous)	1.3 ppm

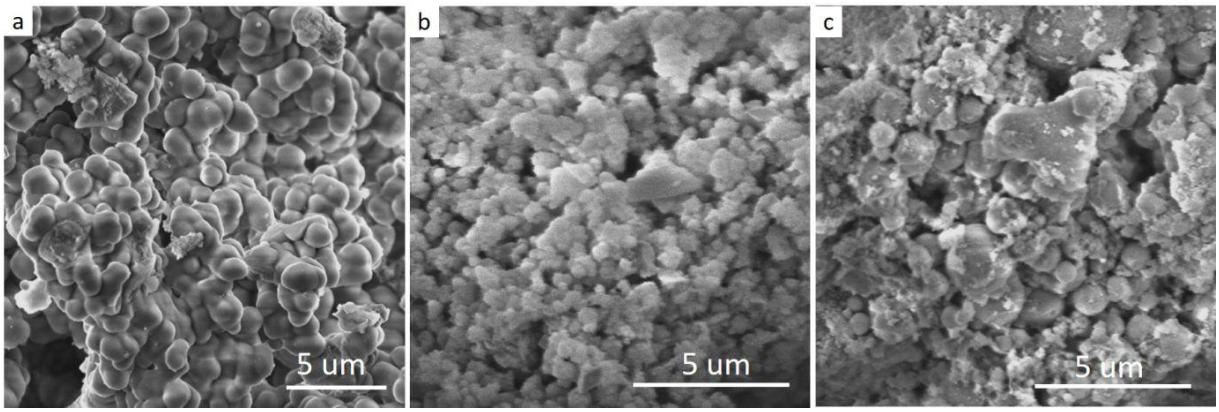


Figure S4: SEM images of (a) mesoporous cellular foam (a) Fe-ion-immobilized SiO_2 (c) Fe_2O_3 NP immobilized SiO_2.

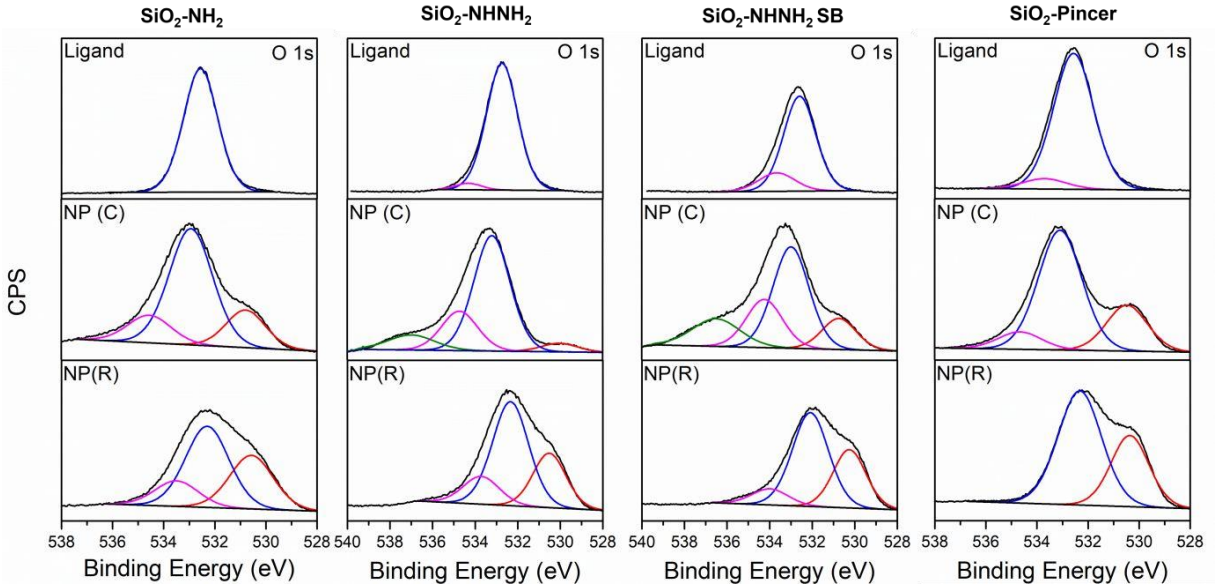


Figure S6: O 1s core level XPS spectra of ligand only catalyst sand NP catalyst prepared by calcination (C) and using $NaBH_4$ (R) for SiO_2-NH_2, SiO_2-$NHNH_2$, SiO_2-$NHNH_2$ SB and SiO_2-pincer ligands.

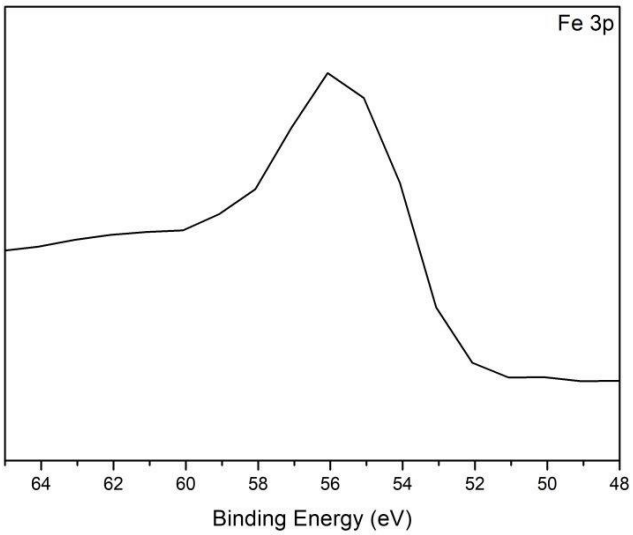


Figure S5: Fe 3p XPS spectrum of SiO_2-pincer catalyst indicating the presence of Fe_2O_3.

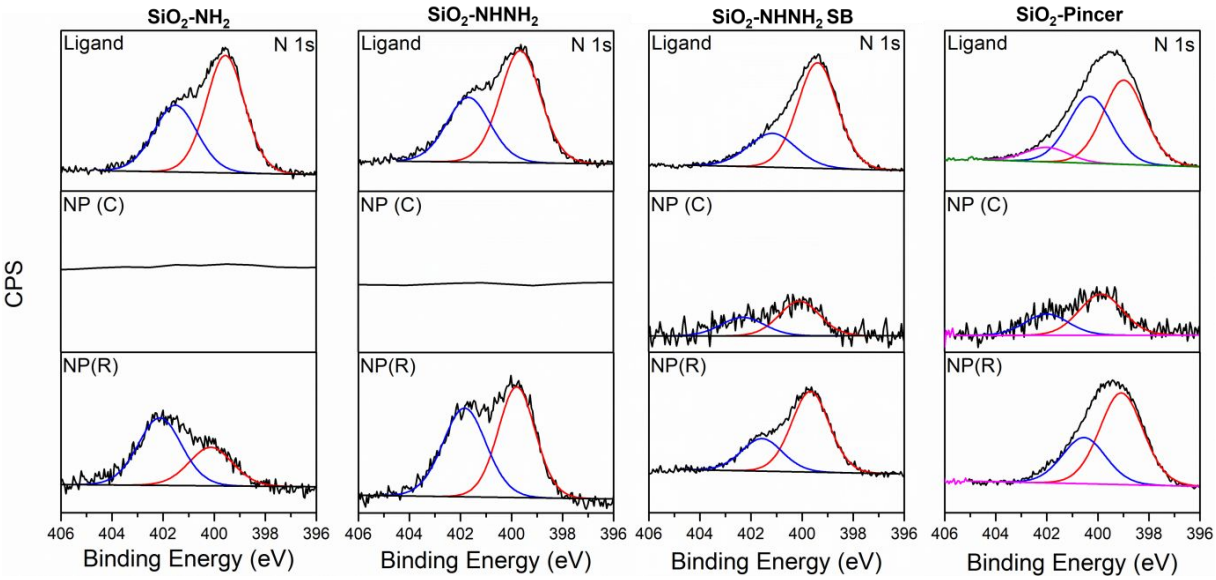


Figure S7: N 1s XPS core level spectra of ligand only and both calcined and chemically reduced NP catalysts for SiO_2-NH_2, SiO_2-$NHNH_2$, SiO_2-$NHNH_2$ SB and SiO_2-pincer ligands.

Table S3. Calculated relative energies (in kcal·mol^{-1}) for the three different spin multiplicities, doublet (D), quadruplet (Q) and sextet (S), for the Fe^{+3} ion using the SiO_2-NH_2 system as a test case.

System	Rel. E. (kcal·mol^{-1})
SiO_2-NH_2-(D)	10.72
SiO_2-NH_2-(Q)	1.76
SiO_2-NH_2-(S)	0.00

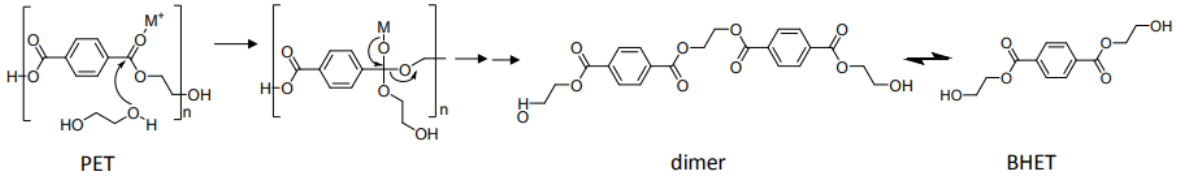


Figure S8: Mechanism for the PET glycolysis reaction.

Table S4: Calculated relative Gibbs energies for the modelled reaction systems, considering 463.15 K and ethylene glycol (EG) as a solvent ($\Delta G_{EG(463.15\ K)}$), including the uncatalyzed process, and the reaction catalyzed by the Fe^{+3} ion, the Fe_2O_3 nanoparticle ($(Fe_2O_3)_2(FeO)_2$) and the FeO nanoparticle ($(Fe_2O_3)(FeO)_{11}$).

System	Uncatalysed	Fe^{3+}	$(Fe_2O_3)_2(FeO)_2$	$(Fe_2O_3)_2(FeO)_{11}$
	$\Delta G_{EG(463.15\ K)}$	$\Delta G_{EG(463.15\ K)}$	$\Delta G_{EG(463.15\ K)}$	$\Delta G_{EG(463.15\ K)}$
A	0.00	0.00	0.00	0.00
TS_{A-B}	14.95	3.09	1.20	1.35
C	11.58	-3.04	-4.57	-16.20

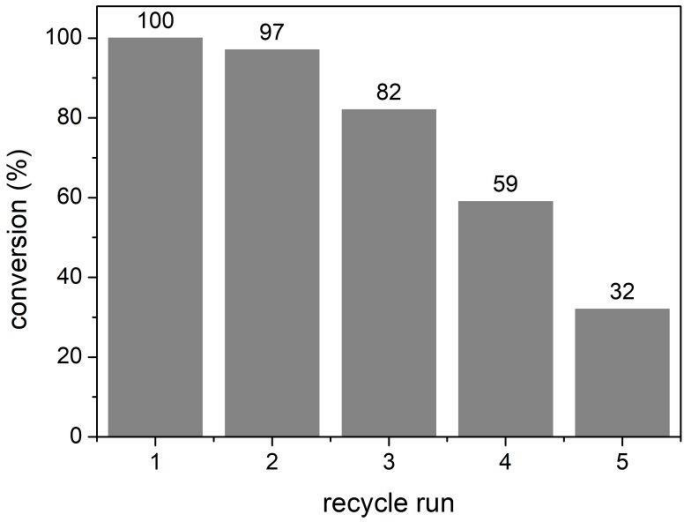


Figure S9: Catalyst recyclability of the SiO_2-NP pincer catalyst over five reaction cycles.

References

(1) Bohre, A.; Jadhao, P. R.; Tripathi, K.; Pant, K. K.; Likozar, B.; Saha, B., Chemical Recycling Processes of Waste Polyethylene Terephthalate Using Solid Catalysts. *ChemSusChem* **2023,** *16* (14).
(2) Alzuhairi, M. A. H.; Khalil, B. I.; Hadi, R. S., Nano ZnO Catalyst for Chemical Recycling of Polyethylene terephthalate (PET). *Engineering and Technology Journal* **2017,** *35* (8), 831-837.
(3) Imran, M.; Kim, D. H.; Al-Masry, W. A.; Mahmood, A.; Hassan, A.; Haider, S.; Ramay, S. M., Manganese-, cobalt-, and zinc-based mixed-oxide spinels as novel catalysts for the chemical recycling of poly(ethylene terephthalate) via glycolysis. *Polymer Degradation and Stability* **2013,** *98* (4), 904-915.
(4) Veregue, F. R.; Pereira da Silva, C. T.; Moisés, M. P.; Meneguin, J. G.; Guilherme, M. R.; Arroyo, P. A.; Favaro, S. L.; Radovanovic, E.; Girotto, E. M.; Rinaldi, A. W., Ultrasmall Cobalt Nanoparticles as a Catalyst for PET Glycolysis: A Green Protocol for Pure Hydroxyethyl Terephthalate Precipitation without Water. ACS Sustainable Chemistry & Engineering 2018, 6 (9), 12017-12024.
(5) Fuentes, C. A.; Gallegos, M. V.; García, J. R.; Sambeth, J.; Peluso, M. A., Catalytic Glycolysis of Poly(ethylene terephthalate) Using Zinc and Cobalt Oxides Recycled from Spent Batteries. Waste and Biomass Valorization 2020, 11 (9), 4991-5001.
(6) Bartolome, L.; Imran, M.; Lee, K. G.; Sangalang, A.; Ahn, J. K.; Kim, D. H., Superparamagnetic γ-Fe ₂ O ₃ nanoparticles as an easily recoverable catalyst for the chemical recycling of PET. Green Chem. 2014, 16 (1), 279-286.
(7) Jeong, J.-M.; Jin, S. B.; Son, S. G.; Suh, H.; Moon, J.-M.; Choi, B. G., Fast and facile synthesis of two-dimensional Fe ^{III} nanosheets based on fluid-shear exfoliation for highly catalytic glycolysis of poly(ethylene terephthalate). Reaction Chemistry & Engineering 2021, 6 (2), 297-303.
(8) Al-Sabagh, A. M.; Yehia, F. Z.; Harding, D. R. K.; Eshaq, G.; ElMetwally, A. E., Fe ₃ O ₄ -boosted MWCNT as an efficient sustainable catalyst for PET glycolysis. Green Chemistry 2016, 18 (14), 3997-4003.
(9) Lima, G. R.; Monteiro, W. F.; Ligabue, R.; Santana, R. M. C., Titanate Nanotubes as New Nanostrutured Catalyst for Depolymerization of PET by Glycolysis Reaction. Materials Research 2017, 20 (suppl 2), 588-595.
(10) Lima, G. R.; Monteiro, W. F.; Toledo, B. O.; Ligabue, R. A.; Santana, R. M. C., Titanate Nanotubes Modified With Zinc and Its Application in Post-Consumer PET Depolymerization. Macromolecular Symposia 2019, 383 (1), 1800008-1800008.
(11) Park, G.; Bartolome, L.; Lee, K. G.; Lee, S. J.; Kim, D. H.; Park, T. J., One-step sonochemical synthesis of a graphene oxide–manganese oxide nanocomposite for catalytic glycolysis of poly(ethylene terephthalate). Nanoscale 2012, 4 (13), 3879-3879.
(12) Nabid, M. R.; Bide, Y.; Fereidouni, N.; Etemadi, B., Maghemite/nitrogen-doped graphene hybrid material as a reusable bifunctional catalyst for glycolysis of polyethylene terephthalate. Polymer Degradation and Stability 2017, 144, 434-441.
(13) Jeong, J. M.; Jin, S. B.; Park, H. J.; Park, S. H.; Jeon, H.; Suh, H.; Park, Y. J.; Seo, D.; Hwang, S. Y.; Kim, D. H.; Choi, B. G., Large-Scale Fast Fluid Dynamic Processes for the Syntheses of 2D Nanohybrids of Metal Nanoparticle-Deposited Boron Nitride Nanosheet and Their Glycolysis of Poly(ethylene terephthalate). Advanced Materials Interfaces 2020, 7 (16), 2000599-2000599.
(14) Cano, I.; Martin, C.; Fernandes, J. A.; Lodge, R. W.; Dupont, J.; Casado-Carmona, F. A.; Lucena, R.; Cardenas, S.; Sans, V.; de Pedro, I., Paramagnetic ionic liquid-coated SiO2@Fe3O4 nanoparticles—The next generation of magnetically recoverable nanocatalysts applied in the glycolysis of PET. Applied Catalysis B: Environmental 2020, 260, 118110-118110.
(15) Najafi-Shoa, S.; Barikani, M.; Ehsani, M.; Ghaffari, M., Cobalt-based ionic liquid grafted on graphene as a heterogeneous catalyst for poly (ethylene terephthalate) glycolysis. Polymer Degradation and Stability 2021, 192, 109691-109691.
(16) Chen, F.; Wang, G.; Li, W.; Yang, F., Glycolysis of Poly(ethylene terephthalate) over Mg–Al Mixed Oxides Catalysts Derived from Hydrotalcites. Industrial & Engineering Chemistry Research 2013, 52 (2), 565-571.

(17) Guo, Z.; Adolfsson, E.; Tam, P. L., Nanostructured micro particles as a low-cost and sustainable catalyst in the recycling of PET fiber waste by the glycolysis method. Waste Management 2021, 126, 559-566.
(18) Chen, F.; Yang, F.; Wang, G.; Li, W., Calcined Zn/Al hydrotalcites as solid base catalysts for glycolysis of poly(ethylene terephthalate). Journal of Applied Polymer Science 2014, 131 (22), n/a- n/a.
(19) Eshaq, G.; ElMetwally, A. E., (Mg–Zn)–Al layered double hydroxide as a regenerable catalyst for the catalytic glycolysis of polyethylene terephthalate. Journal of Molecular Liquids 2016, 214, 1-6.
(20) Zhu, M.; Li, S.; Li, Z.; Lu, X.; Zhang, S., Investigation of solid catalysts for glycolysis of polyethylene terephthalate. Chemical Engineering Journal 2012, 185-186, 168-177.
(21) Zhu, M.; Li, Z.; Wang, Q.; Zhou, X.; Lu, X., Characterization of Solid Acid Catalysts and Their Reactivity in the Glycolysis of Poly(ethylene terephthalate). Industrial & Engineering Chemistry Research 2012, 51 (36), 11659-11666.
(22) Wang, T.; Zheng, Y.; Yu, G.; Chen, X., Glycolysis of polyethylene terephthalate: Magnetic nanoparticle CoFe2O4 catalyst modified using ionic liquid as surfactant. European Polymer Journal 2021, 155, 110590-110590.
(23) Li, M.; Huang, Y.; Yu, T.; Chen, S.; Ju, A.; Ge, M., Chemical recycling of waste poly(ethylene terephthalate) fibers into azo disperse dyestuffs. RSC Advances 2014, 4 (87), 46476-46480.
(24) Fung, B. M.; Khitrin, A. K.; Ermolaev, K., An Improved Broadband Decoupling Sequence for Liquid Crystals and Solids. Journal of Magnetic Resonance 2000, 142 (1), 97-101.
(25) Stejskal, E. O.; Schaefer, J.; Waugh, J. S., Magic-angle spinning and polarization transfer in proton-enhanced NMR. Journal of Magnetic Resonance (1969) 1977, 28 (1), 105-112.
(26) Meier, B. H., Cross polarization under fast magic angle spinning: thermodynamical considerations. Chemical Physics Letters 1992, 188 (3), 201-207.
(27) van Meerten, S. G. J.; Franssen, W. M. J.; Kentgens, A. P. M., ssNake: A cross-platform open-source NMR data processing and fitting application. Journal of Magnetic Resonance 2019, 301, 56- 66.
(28) Shin, J. H.; Schoenfisch, M. H., Inorganic/Organic Hybrid Silica Nanoparticles as a Nitric Oxide Delivery Scaffold. Chemistry of materials : a publication of the American Chemical Society 2008, 20 (1), 239-249.
(29) Hutter, J.; Iannuzzi, M.; Schiffmann, F.; VandeVondele, J., cp2k: atomistic simulations of condensed matter systems. WIREs Computational Molecular Science 2014, 4 (1), 15-25.
(30) Ugliengo, P.; Sodupe, M.; Musso, F.; Bush, I. J.; Orlando, R.; Dovesi, R., Realistic Models of Hydroxylated Amorphous Silica Surfaces and MCM-41 Mesoporous Material Simulated by Large- scale Periodic B3LYP Calculations. Advanced Materials 2008, 20 (23), 4579-4583.
(31) Perdew, J. P.; Ruzsinszky, A.; Csonka, G. I.; Vydrov, O. A.; Scuseria, G. E.; Constantin, L. A.; Zhou, X.; Burke, K., Restoring the Density-Gradient Expansion for Exchange in Solids and Surfaces. Physical Review Letters 2008, 100 (13), 136406.
(32) Grimme, S.; Antony, J.; Ehrlich, S.; Krieg, H., A consistent and accurate ab initio parametrization of density functional dispersion correction (DFT-D) for the 94 elements H-Pu. The Journal of Chemical Physics 2010, 132 (15), 154104.
(33) Goedecker, S.; Teter, M.; Hutter, J., Separable dual-space Gaussian pseudopotentials.
(34) Physical Review B 1996, 54 (3), 1703-1710.
(35) Lippert, B. G.; Parrinello, J. H.; Michele, A hybrid Gaussian and plane wave density functional scheme. Molecular Physics 1997, 92 (3), 477-488.
(36) Andreussi, O.; Dabo, I.; Marzari, N., Revised self-consistent continuum solvation in electronic-structure calculations. J Chem Phys 2012, 136 (6), 064102.

Chapter 4

Guanidine Functionalised Porous SiO_2 as Heterogeneous Catalysts for Microwave Depolymerisation of PET and PLA

Éadaoin Casey[1,2], **Rachel Breen**[1,2], Gerard Pareras[3], Albert Rimola[3], Justin. D Holmes[1,2] and Gillian Collins[1,2]*

[1] School of Chemistry, University College Cork, Cork, T12 YN60, Ireland.

[2] AMBER Centre, Environmental Research Institute, University College Cork, Cork, T23 XE10, Ireland.

[3]Departament de Química, Universitat Autònoma de Barcelona, 08193 Bellaterra, Catalonia, Spain.

Publication: *Casey, É.; **Breen, R**.; Pareras, G.; Rimola, A.; Holmes, J. D.; Collins, G. Guanidine functionalized porous SiO_2 as heterogeneous catalysts for microwave depolymerization of PET and PLA. RSC Sustainability **2024**, 2 (4), 1040-1051, 10.1039/D3SU00425B. DOI: 10.1039/D3SU00425B.*

Author Contributions:

My contribution to the research includes thermal PET glycolysis to BHET and PLA methanolysis reactions. I carried out all the microwave reactions reported in the manuscript. I was responsible for developing the experimental method for the depolymerisation of PET to the BHBT monomer and preformed all associated analysis for these reactions and product analysis. Additionally, I contributed to manuscript preparation including data analysis, writing and figure preparation. The research was conducted in collaboration with Dr Éadaoin Casey within our research group and as part of a broader effort that also involved a collaboration with postdoctoral researcher Dr Gerard Pareras under the supervision of Prof. Albert Rimola at Universitat Autònoma de Barcelona (UAB). Dr Pareras carried out the computational work using density functional theory.

Abstract

Chemical recycling is an important strategy to tackle the growing global problem of plastic waste pollution. The development of metal-free catalysts for depolymerisation of plastics is attractive as it avoids the use of metal salts, which are potentially damaging to the environment. Here we report a metal-free heterogeneous catalyst for the glycolysis of polyethylene terephthalate (PET) and methanolysis of polylactic acid (PLA). The catalysts are synthesised by covalent surface modification of mesoporous silica (SiO_2) with guanidine ligands and evaluated under conventional thermal and microwave-assisted heating. A surface bound cyanoguanidine ligand was found to be the best catalyst giving 100 % PET conversion with 80 % BHET yield. The nature of the catalyst support material influenced the catalytic performance of the guanidine ligands with porous SiO_2 supports outperforming activated carbon under conventional thermal glycolysis, while the opposite trend was observed with microwave assisted glycolysis. Dedicated density functional theory (DFT) computations were performed to simulate the depolymerisation processes, characterise the free energy profiles of the reaction mechanisms, and identify the important role of hydrogen bonding in the reaction mechanism.

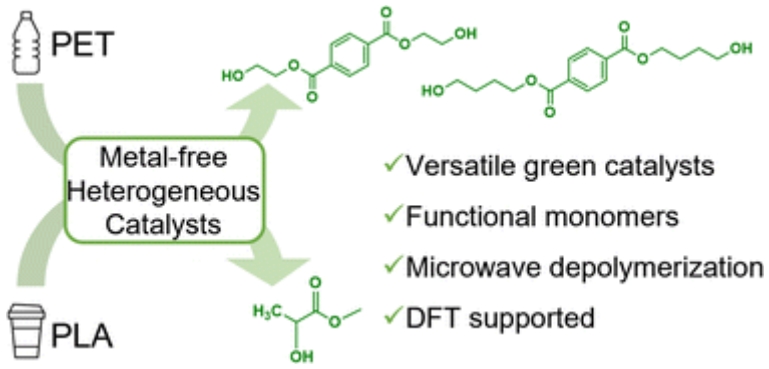


Table of Contents Graphic

4.1 Introduction

Plastics are ubiquitous to our everyday lives owing to their low cost, versatility, and ease of production. Their uses range from lifelong plastic materials for household appliances, building materials and electronics to the single use plastics such as shopping bags, straws, food packaging and water bottles. The high demand of single use plastics, which has increased dramatically in the last 50 years from 15 to 311 million tons and is expected to double by 2035, has led to a drastic increase in plastic waste. In recent years, researchers have developed numerous pathways to convert plastic waste into monomers or value-added products forming a circular economy in the polymer life cycle.[1,2] Polyethylene terephthalate (PET) is a thermoplastic polyester and used in a wider range of applications such as textiles, food and beverage packaging and in single use plastics, which are a key contributor to the problem of post-consumer plastic waste. There has been intensive investigation into this polymer with the aim sustainably converting it into a valuable monomer moving away from environmentally detrimental practices such as incineration.[3, 4] Glycolysis is one of the most effective methods for depolymerisation of PET as it can be achieved under mild conditions with a relatively low cost. The method involves reacting PET, excess diol, usually ethylene glycol (EG) and a catalyst, with the product bis(2-hydroxyethyl) terephthalate (BHET) being obtained. Many catalysts are effective for this transformation such as metal oxides[5, 6], nanoparticles[7-9], metal salts and metal-containing ionic liquids[5, 10, 11], and organocatalysts.[12-18]

Metal-free catalysts are especially appealing due to their environmentally friendly and sustainable nature, serving as an advantageous option compared to metal-based catalysts. Many metal-free catalysts are homogeneous organocatalysts and Table S1 in the Supplementary Information displays literature reports using different metal-free catalysts. Fukushima and co-workers[19] reported the use of commercially available guanidine catalyst 1,5,7-triazabicyclo[4.4.0]dec-5-ene (TBD) as a highly effective catalyst for the glycolysis of PET in the presence of EG. PET was fully converted and an isolated yield of 78 % was obtained at 190 °C, 10 mol % catalyst, 1:5 ratio PET:EG after 325 min. For comparison, when the reaction was completed in the absence of TBD, PET was fully converted after

40 h at 190 °C. Le *et al*.[20] reported the catalytic activity of TBD in a co-solvent assisted glycolysis reaction were 100 % conversion of PET and 82 % yield of BHET was achieved at 153 °C after 2 h. While organocatalysts show excellent efficiency for PET depolymerisation, a key drawback is the lack of easy recovery, which can result in contamination of the monomer product. A combined metal-free and heterogeneous catalyst design is attractive as it provides an easy separation route after the depolymerisation reaction. Chipurici *et al.*[21] demonstrated a synthesis of heterogeneous catalysts with guanidine superbases chemically grafted on silica-coated Fe_3O_4 magnetic nanoparticles for transesterification of waste oil. Fehér *et al*.[13] reported an eco-friendly organocatalyst using TBD supported on silica gel for PET glycolysis depolymerisation, achieving 100 % conversion of PET and 88 % yield of BHET. The optimal reaction conditions were 190 °C, 15.5 mol % catalyst, EG: PET molar ratio of 12.6, and 1.7 h reaction time.

The use of microwave assisted depolymerisation of plastics has also seen a huge interest due to the significant reduction in reaction time and energy consumption, improving the energy efficiency for various plastics such as the glycolysis of PET[22, 23] and polyurethane[24], hydrolysis of polyamides[25] and polyolefins.[26] Microwave assisted reactions enable rapid volumetric heating and uniform heat transfer resulting in increased reaction rates, product selectivity and increased yields over conventional thermal methods.[27] The most common catalysts reported for microwave assisted reaction glycolysis for the PET depolymerisation reaction are metal salts and metal oxides. The possibility of combining microwave assisted heating with a heterogeneous metal-free catalyst is highly attractive depolymerisation route for PET.

Recently, there has been great interest in biodegradable plastics such as polylactic acid (PLA) as an alternative to fossil-fuel derived plastics. The PLA market has increased exponentially in recent years as the physical properties are similar to non-biodegradable plastics such PET. While often branded as an eco-friendly biodegradable plastic, PLA only degrades at an appreciable rate under specific conditions such as those generated in industrial composing facilities. In the natural environment, PLA

persists for hundreds of years.[28] Therefore, instead of disposing of PLA to composting sites, upcycling strategies are needed to enable a more sustainable use of the PLA. Methanolysis can be used to transform PLA to methyl lactate (MeLa), which is attractive as a green solvent. Several literature reports have shown inorganic metal salts such as $FeCl_3$ and ZnAc to be active catalysts. Román-Ramírez *et al*.[28] produced MeLa from the chemical degradation of PLA using an ethylenediamine Zn(II) complex. Petrus and co workers[29], synthesised multiple alkyl lactates using metal containing catalysts with temperatures ranging from 80 to 260 °C and reported that a combination of high temperatures and pressure with excess alcohol leads to an increase in the lactate production and yield.

This article describes the process of creating guanidine-based heterogeneous catalysts, achieved through surface functionalisation of porous SiO_2 supports and highlights the adaptability of these catalysts in various applications, including PET glycolysis for the production of the BHET, butanolysis of PET to form bishydroxybutyl terephthalate (BHBT), and PLA methanolysis to yield MeLA. The catalysts can be used under both conventional thermal and microwave assisted depolymerisation. Density functional theory (DFT) calculations were used to model the surface bound guanidine ligands in the PET and PLA depolymerisation reactions to obtain unique atomic scale information of the processes and rationalise the experimental findings.

4.2 Results and discussion

4.2.1 Synthesis and characterisation of guanidine functionalised SiO_2

The use of porous SiO_2 as a support enables surface modification via functionalisation with organic ligands. Mesoporous cellular foam SiO_2 was functionalised with three different guanidine precursors using a one pot method (see Supplementary Information for experimental details) to produce SiO_2-DCG (**1**), SiO_2-EDG (**2**) and SiO_2-DCD (**3**) catalysts, as illustrated in Figure 1.

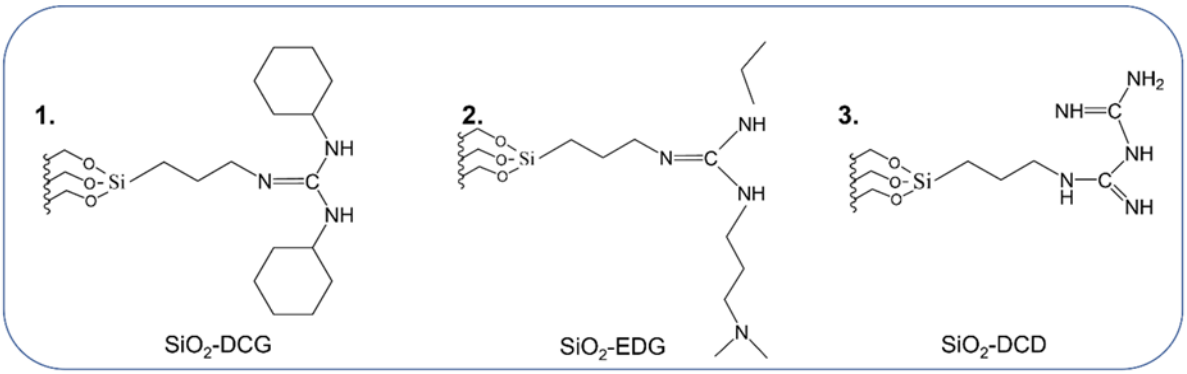


Figure 1: Schematic illustrating the three guanidine-type ligands used to functionalise mesoporous cellular foam SiO_2 via alkoxysilane attachment.

Surface area and porosity measurements were obtained using N_2-physisorption at −196 °C (see Supplementary Information for details). Figure 2 shows the N_2-physisorption isotherms of the bare and modified SiO_2. The catalysts showed a typical type-IV isotherm with a H1 hysteresis loop which is a typical feature for this type of large pore mesoporous material. The surface area of the catalyst decreased after functionalisation from 412 $m^2\ g^{-1}$ for bare SiO_2 to 182 $m^2\ g^{-1}$, 101 $m^2\ g^{-1}$ and 38 $m^2\ g^{-1}$, for the DGC, ECG and DCD modified SiO_2, respectively (See Table S2). Similar reductions in surface area have been reported in literature for amino functionalised SBA-15 and MCM-41, indicating a degree of pore blockage occurred with functionalisation.[30] The SiO_2-DCD catalyst have a substantially reduced surface area, when compared to the -EDG and -DCG ligands, which may be attributed to smaller size of the DCD ligands. Multilayer silylation reactions resulting in polysilane structures multi-layered silylated surfaces are also possible.[31] Figure 2 (b) also shows the decrease in pore diameter after modification, which is associated with functionalisation of the internal pores. [30]The pore size of the bare SiO_2 is 102 Å, which decreases for the SiO_2-EDG (82 Å) and SiO_2-DCD (79 Å) catalysts but remains similar after DCG modification (100 Å), may be attributed to the bulky cyclohexyl side groups of the guanidine ligand. Figure 3 (a) shows a scanning electron microscopy (SEM) image of the bare SiO_2, and Figure 3(b) show a transmission electron microscopy (TEM) of the mesoporous cellular foam SiO_2.

Higher resolution SEM images of the MCF, -DCG, -EDG and -DCD modified SiO_2 are illustrated in Figure 3 (c-f), respectively and the Supplementary Information Figure S1.

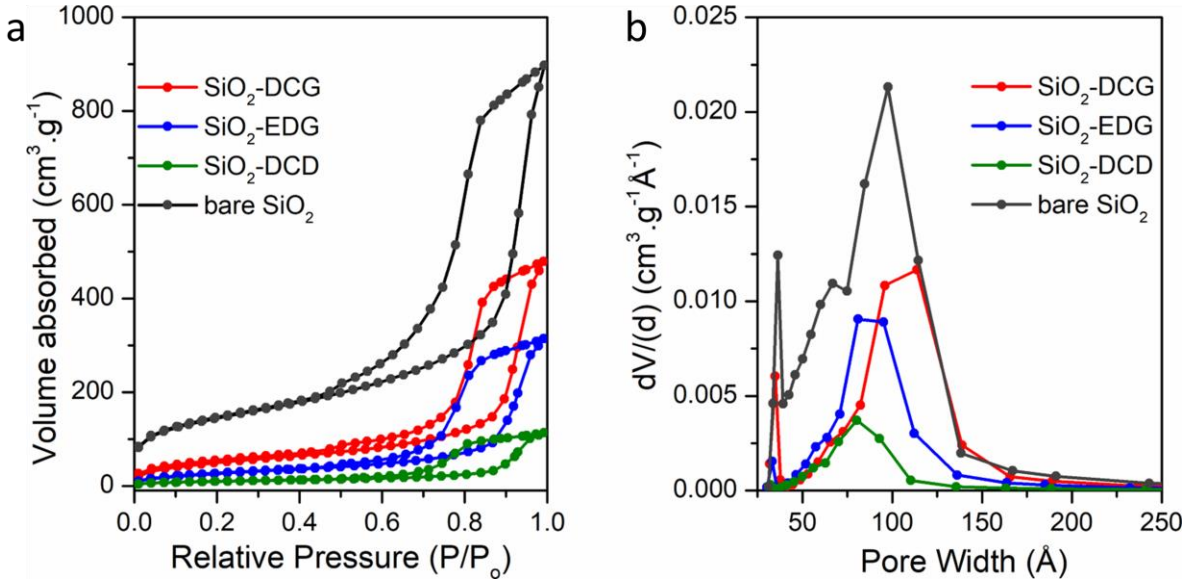


Figure 2: N_2-physisorption isotherms of the bare and modified SiO_2 showing (a) pore volume and (b) the pore size distribution.

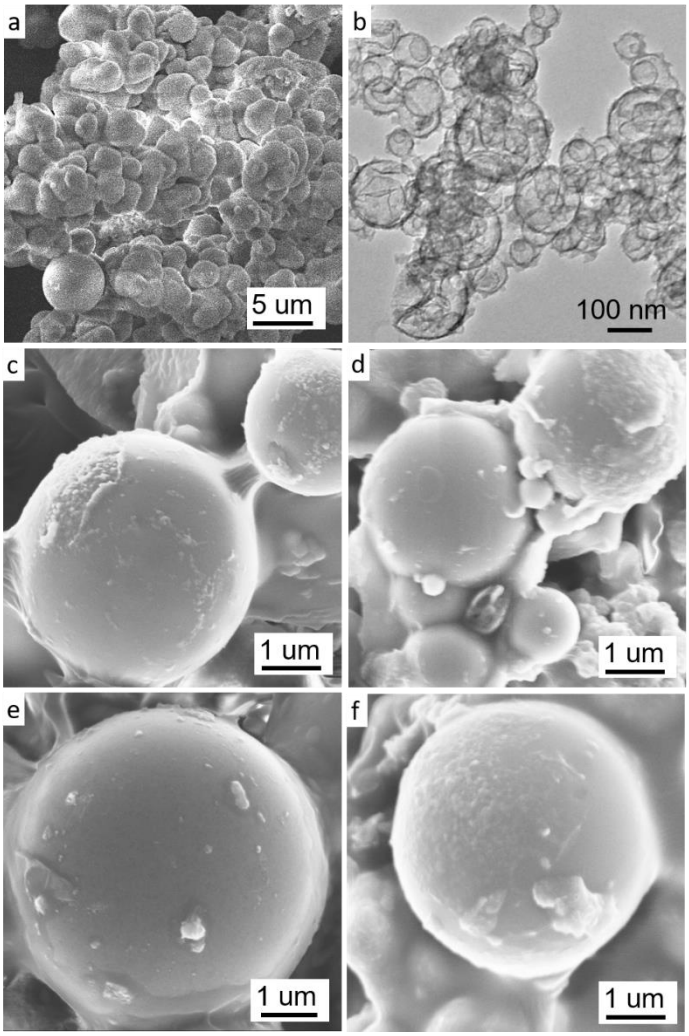


Figure 3: (a)-(c) SEM and TEM images of the bare mesoporous cellular foam SiO_2 and after functionalisation with the (d) DCG, (e) EDG and (f) DCD ligands.

XPS was employed to verify successful functionalisation of the guanidine ligands to the SiO_2 support. The survey spectra show the appearance of a N 1s and C 1s peak after functionalisation (Supplementary Information Figure S2). The N 1s core level shown in Figure 4 (a), of the three catalysts revealed the presence of a dominant peak at a binding energy (BE) of 400.2, 400.2 and 399.8 eV, for SiO_2-DCG, EDG and DCD catalysts, respectively, which is characteristic of amine species.[32] A small shoulder peak was observed at a higher BE assigned to protonated N species. Covalent attachment of the alkoxysilane ligands is further evidenced by the O 1s and Si 2p core level, shown in Figure 4(b) and (c). The O 1s of the bare SiO_2 is centred at 533.8 eV and is downshifted to 532 eV after

functionalisation, associated with the loss of Si-OH groups due to covalent modification of the surface.[33] This downshift in the BE is also observed in the Si 2p core level scans of the functionalised SiO_2.

FTIR was employed to investigate the surface of the modified SiO_2 catalysts as seen in Figure 4(d). The Si-O-X region of interest is located between 950 cm^{-1} and 1250 cm^{-1} and typically appears as broad features.[34] Peak assignment in this region is also difficult because of contributions from several species such as Si-O-Si and Si-O-C, but changes in the spectral region on functionalisation are clearly identified. Bare SiO_2 particles exhibit peaks at 1060 cm^{-1} and 950 cm^{-1} which can be indexed to Si–O–Si stretching, and the Si-OH bond stretch, respectively.[35] For the EDG and DCD catalyst there is a significant decrease in the Si-OH peak and a strong peak emerges at 1038 cm^{-1}, which is in excellent agreement with the Si-O-C stretching vibration. For the DCG catalyst, this peak is less defined and the small decrease in the Si-OH peak is observed, which may indicate a weaker covalent attachment, likely to originate from the bulky side groups. The modified SiO_2 catalyst shows appearance of a peak at 1636 cm^{-1} associated to N-H bending[34], correlating well with the N 1s XPS, although peaks in this region have also been attributed to adsorbed water, formed from the condensation reaction of surface Si-OH and the alkoxysilane precursor. The SiO_2-DCD ligand has an additional peak at 1560 cm^{-1} assigned to primary amine N–H stretching vibrations. Both FTIR and XPS both indicate covalent attachment of the guanidine ligands onto the support.

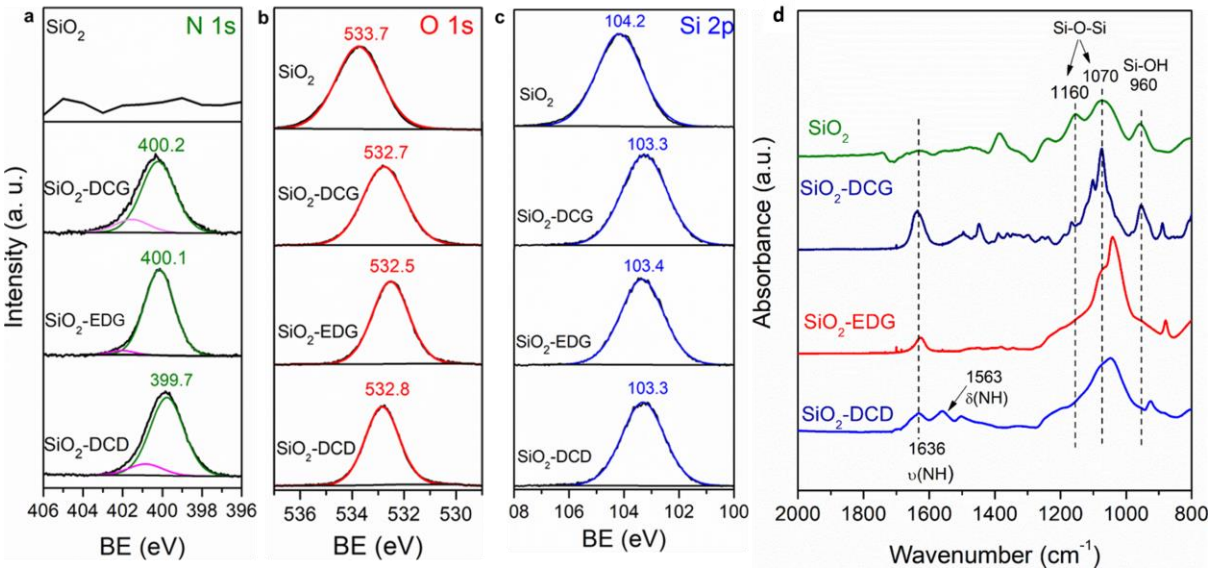


Figure 4: XPS analysis of core level scans (a) N 1s, (b) O 1s and (c) Si 2p for SiO_2, SiO_2-DCG, SiO_2-EDG and SiO_2-DCD catalysts. (b) ATR-FTIR of bare and guanidine functionalised SiO_2 catalysts.

TGA was used to assess the thermal stability of each of the SiO_2 guanidine catalysts and to estimate the amount of organic species present after functionalisation, is shown in the Supplementary Information Figure S3. The initial weight loss observed in all the guanidine grafted SiO_2 is attributed to water and residual solvent molecules on the surface. The second weight-loss step can be assigned to the release of the organosilanes and the guanidine derivatives from the silica surface. Based on mass loss observed between 120 °C to 350 °C, the organic content was found to be 23%, 20% and 25% for the DCG, EGC and DCD functionalised SiO_2, respectively. The EDG and DCD catalysts have a slightly higher thermal stability, with mass loss not occurring until ~250 °C, compared to the DCG ligand where mass loss starts to occur ~220°C.

4.2.2 Catalytic evaluation of heterogeneous guanidine catalysts

The catalytic performance of the three SiO_2 supported guanidine catalysts was investigated for the depolymerisation of PET to BHET under conventional thermal and microwave assisted glycolysis. Figure 5 (a)-(c) compares the reaction time series (0-4 h) for each catalyst evaluating PET conversion

and isolated BHET yields obtained under conventional thermal conditions at 190 °C for 3 h and 100 mg catalyst. The bare SiO_2 did not catalyse the reaction to any extent. The SiO_2-DCD catalyst displayed the best catalytic activity which under thermal depolymerisation gave full PET conversion and isolated yield of BHET was 70%. ^{1}H NMR of the isolated BHET can be found in the Supplementary Information Figure S4. Analysis of the filtrate after recrystallisation revealed residual BHET in the solution but no dimers were detected by NMR. The superior performance of the SiO_2-DCD catalyst may be due to the structure having more nitrogen environments, which have been reported to be beneficial in increasing the catalytic activity.[7, 36]. The DCD ligands also have less steric constraints compared to the EDG and DCG catalysts, associated with the bulky side groups and steric effects have been shown to lower the performance of metal containing ionic liquids.[22] At longer reaction times the BHET yield decreased, which is indicative of dimerisation as mechanistically the glycolysis reaction undergoes an equilibrium reaction between the monomer and dimers which in turn lowers the yield of BHET.[37] Increasing the PET:EG ratio decreased conversions under thermal conditions and in the optimal ratio was found to be 1:5.

The catalysts were then evaluated using microwave assisted heating instead of conventional heating. Reactions ran under the same conditions, 190 °C, gave full conversion PET but resulted in inferior yield of 58 %. An optimisation study of the reaction parameters for microwave assisted glycolysis was initially performed, as shown in the Supplementary Information in Table S3 and Figure S5. Different optimal parameters are observed for reactions under thermal and MW assisted heating. It was found that increasing the temperature greatly increased PET conversion while lowering reaction times (30 min). Each of the catalysts performed best at 210 °C, a higher PET: EG ratio (1:10) and sufficient agitation of the reaction mixture by using a high stirring speed (960 rpm) was also important. Figure 5(b-d) shows reaction time series (0-40 min) for each catalyst evaluating PET conversion and isolated BHET yields obtained under microwave-assisted heating. Optimum reaction conditions were 210 °C, 30 min, 960 rpm, 100 mg catalyst and 1:10 PET:EG ratio, giving an 80 % BHET yield. The significant

reduction in reaction time associated with efficient microwave heating[38] and is a clear advantage of using a microwave assisted route.

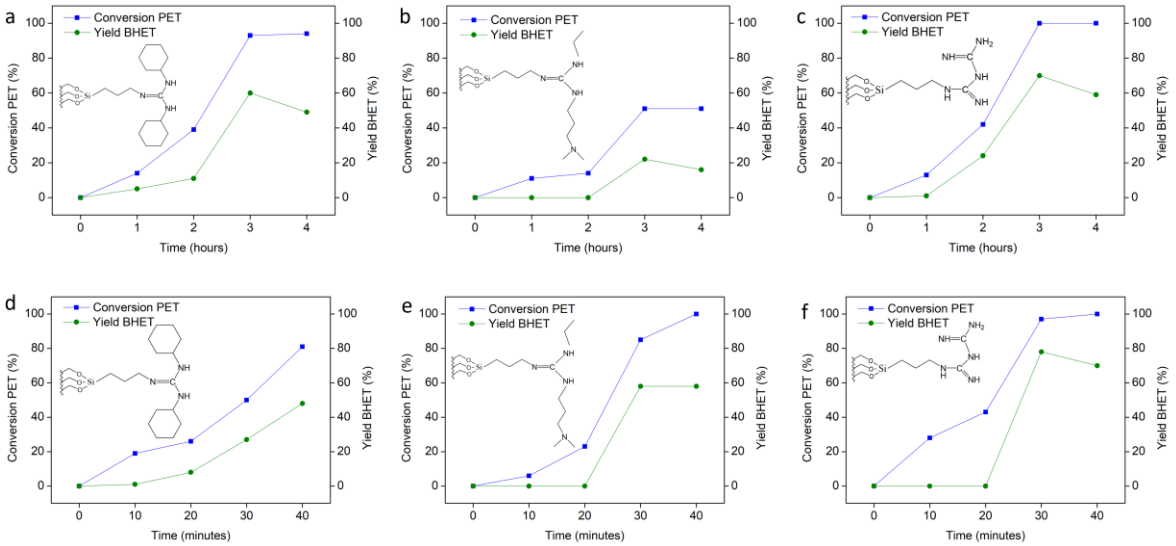


Figure 5: Reaction time series for the depolymerisation of PET to BHET under conventional thermal heating reaction using optimised conditions (190 °C, PET:EG 1:5) for the (a) DCG, (b) EDG and (c) DCD modified SiO_2 catalysts. Reaction time series for with microwave assisted heating using optimised conditions (210 °C, PET:EG 1:10) (d) DCG, (e) EDG and (f) DCD modified SiO_2 catalysts.

The cyanoguanidine ligand *i.e.* SiO_2-DCD, emerged as the most effective catalyst under both conventional heating and microwave assisted routes but the catalyst reactivity trend observed under microwave assisted glycolysis was different to conventional thermal glycolysis. The SiO_2-EDG catalyst was sluggish under conventional heating but demonstrated a favourable performance under microwave heating. The SiO_2-DCG catalyst performed well under thermal conditions (93 % PET conversions) but was the least effective catalyst under microwave conditions, despite the higher temperature resulting in only 50 % PET conversion. TGA showed that the SiO_2-DCG ligand had the lowest thermal stability, and this may have contributed to the poor performance of this ligand under microwave assisted heating compared to conventional thermal heating. Microwave heating is

fundamentally different from conventional heating because microwaves and can penetrate deep into the sample heating it volumetrically as opposed to conventional thermal heating, which heat materials from the outside *via* standard heat-transfer mechanisms, *i.e.*, through convection, conduction and radiation. The acceleration effect of microwave on reaction kinetics associated with the volumetric heated is a well-known and reported phenomenon, the specific mechanisms occurring within particular reactions often remains unclear.[39]

The best microwave-responsive catalysts are those that can absorb microwave irradiation and while SiO_2 is a microwave absorber, carbon-based catalysts have also been widely used in microwave assisted reactions such as biomass conversion, phenol oxidation and NO_x reduction.[40] To evaluate the role of the support material, the poorest performing guanidine ligand under microwave glycolysis, DCG was grafted onto on acid-treated activated carbon and evaluated under the same reaction conditions. The PET conversion obtained using the DCG ligand increased from 50 % using a SiO_2 support to 100 % using activated carbon. Interestingly, the same trend was not observed when the reactions were conducted under conventional heating, with PET conversion using carbon supported catalysts decreasing to 63 % compared to the SiO_2 support (93 %) (see Supplementary Information Figure S6). This result demonstrates the important role of the support material on the catalytic behaviour of heterogeneous catalysts for microwave assisted glycolysis compared to conventional heating. While the exact origin of these support effects requires further investigation, they are likely related to differences in the heating characteristics and thermal stability of the two materials under microwave and conventional thermal heating. The recyclability performance of the catalyst was also tested over five reaction cycles, for the DCD catalyst both thermally and MW assisted heating (see Supplementary Information Figure S7). The MW assisted recyclability test displayed slightly better conversion (100, 100, 94, 90, 84 %) than the thermally heating reactions (100, 100, 90, 85, 81 %). Interestingly, the recyclability performance of the DCG was inferior falling over successive cycles. This difference in recyclable performance may be due to the lower thermal stability of the DCG catalyst as indicated by TGA.

Glycolysis of PET using EG to form the valuable BHET monomer, has been intensively studied as a key reaction for chemical recycling of PET, but glycolysis of PET can also be carried out using other diols such as propyl glycol, 1,4-butanediol (BD) and triethylene glycol.[41] These reactions, while much less explored in comparison to glycolysis with EG, have numerous applications such as the formation of oligomeric precursors that can be used as building blocks to synthesise other polymers with higher economic value such as polyurethane foams and unsaturated polyesters applied as polymer concrete and mortar materials.[42, 43] One example is the production of the polyester polybutylene terephthalate (PBT) from recycled PET by using BD in place of EG. The use of traditional metal-based catalysts such metal salts and oxides is problematic, as these efficiently catalyse the cyclodehydration reaction of BD to form THF.[44] Therefore, the use of a metal free catalyst offers a distinct advantage to limit this undesired side reaction for the depolymerisation pathway, as illustrated in Figure 6(a). Glycolysis of PET using BD was carried out using the SiO_2-DCD catalyst at 210 °C under microwave heating. Optimum mass loss of PET and formation of the desired bis(4-hydroxybutyl) terephthalate (BHBT) product was obtained after 6 h, as shown in the reaction time series in the Supplementary Information Figure S8. The NMR analysis of the crude product shown in Figure 6 (b) confirms formation of BHBT product with a singlet at δ = 8.09 ppm corresponding to the aromatic protons. The distinguishable feature of the BHBT NMR is the presence of 2 quintets at δ = 1.76 and δ = 1.55 ppm arising from CH_2 groups, labelled c and d, respectively. The peak arising from the OH protons appears at δ = 4.45 ppm, in good agreement with literature reports for mono(4-hydroxybutyl) terephthalate by 1H NMR.[45] The ^{1}H NMR of THF, 1,4-BD and EG are also shown in Figure 6(b) and indicate that the undesired cyclodehydration reaction of BD to THF did not occur using the metal-free catalysts.

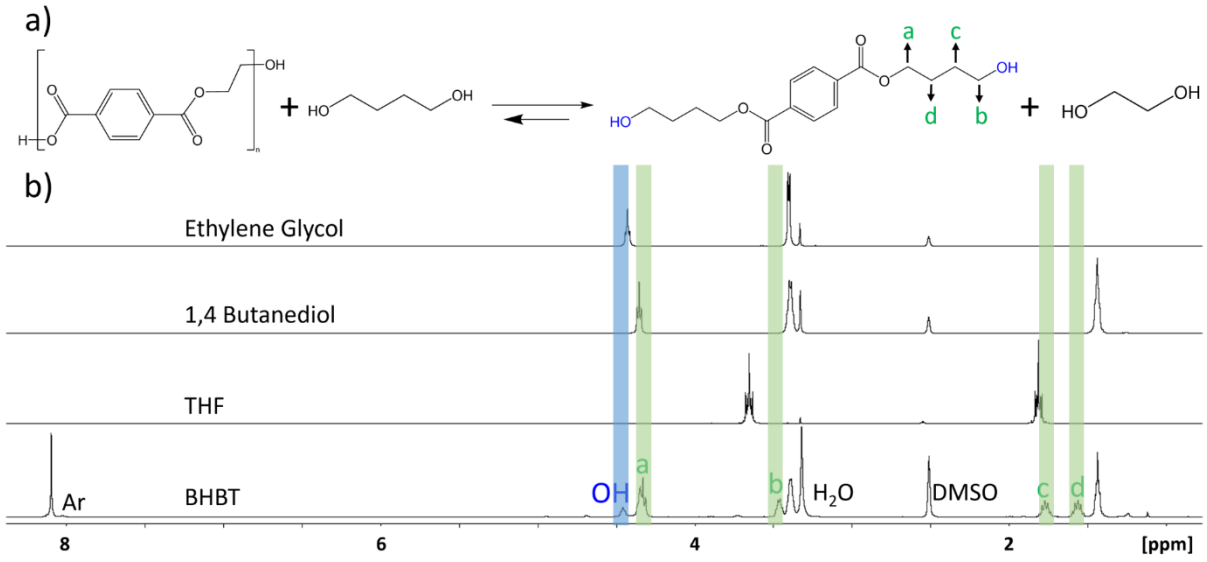


Figure 6: (a) Reaction scheme showing glycolysis of PET using 1,4 butanediol. **(b)** NMR analysis of reaction product showing formation of bis(4-hydroxybutyl) terephthalate (BHBT) and no undesired THF product.

We further investigated the versatility of the metal-free SiO_2-guanidine catalysts by evaluating their applicability in the methanolysis of PLA to methyl lactate (MeLa) under both thermal and microwave assisted heating. Methanolysis of PLA is typically carried out using a metal catalyst in a pressurised vessel at 120°C with reaction times reported up to 3 days.[28,46,47]. The reaction scheme for depolymerisation of PLA to MeLa can be seen in Figure 7, where methanol (MeOH) and THF are used as the protic source and solvent, respectively. Initially, an optimisation study was performed thermally to find the best reaction conditions. The role of the THF is to increase the solubility of the PLA and reaction did not proceed in the absence of THF. The depolymerisation was carried out under standard reflux conditions but resulted in low PLA conversions due to the low boiling points of MeOH and THF. Therefore, sealed glass vessels were used to achieve higher temperatures for the reaction. Lamberti *et al*.[48] reported the mechanism is a two-step reversible reaction that the PLA chains quickly converted to chain end oligomers which then slowly forms the product MeLa. As the reaction proceeds, the amount of internal oligomers decreased as the polymer chains were degraded, producing more chain end oligomers and subsequently the MeLa monomer. Reactions with a higher yield of MeLa had a

lower percentage of internal oligomers and a higher percentage of chain end oligomers as the depolymerisation process proceeds, which can be observed with the NMR analysis to evaluate the product distribution, as shown in Figure 7. The ^{1}H NMR of the products matched previously reported values which are internal (Int) methine (5.09–5.21 ppm), chain end methine (CE) (4.30–4.39 ppm/5.09–5.21 ppm), and MeLa (4.23–4.29 ppm).[28] Using the sealed glass vessels, with reaction conditions of 130 °C, 3 h, 250 rpm and 2:3 ratio of MeOH:THF, full conversion of PLA was achieved with yield of MeLa and both chain end and internal methine oligomers being 17, 54, 29 %, respectively. Román-Ramírez and co-workers,[28] achieved similar MeLa yield using a Zn catalyst under thermal conditions. Due to the presence of the equilibrium reaction between the oligomers and MeLa, removing the MeLa as it is formed can shift the reaction equilibrium and increase the yield. There have also been reports of using an autoclave to perform the degradation of PLA to MeLa, where the higher pressure can also increase MeLa yield.[48] Carrying out the reaction in an autoclave it was possible to get full conversion of PLA and further increasing the yield of MeLa to 42 % after 72 h (Figure7 (c)). The higher MeLa yields and minimal internal methine oligomers demonstrate the beneficial impact of the high pressure in the autoclave reactor, however the use of long reaction times is not desirable. Therefore, the use of microwave assisted methanolysis was next explored and Table S4 in the Supporting Information, summarises the optimisation of the reaction conditions. While microwave heating did not lead to further enhancements in MeLa yield, it did significantly reduce the reaction time. After 30 min PLA was fully converted yielding 30, 62, 8 %, MeLa, chain end and, internal methine oligomers, respectively, which substantially reduces the reaction time.

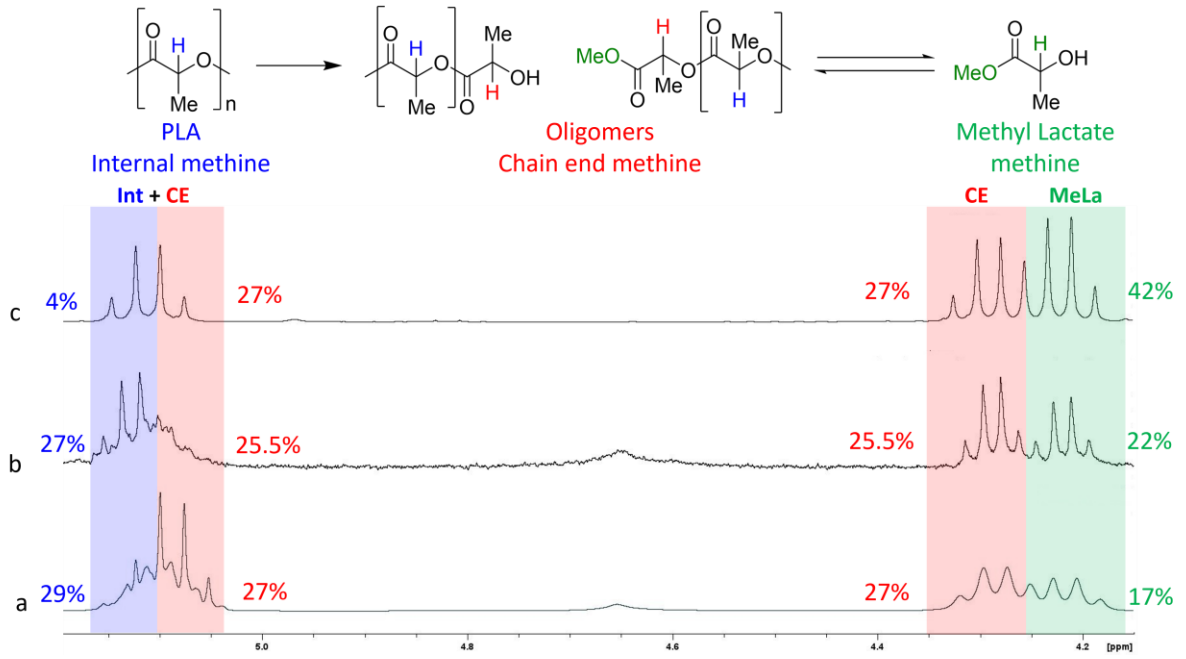


Figure 7: [1]H NMR stacked spectra of the products obtained from the methanolysis of PLA to MeLa for (a) sealed vessel reaction at 4 h, (b) 20 h reaction in an autoclave and (c) 72 h autoclave reaction. Each reaction was performed at 130 °C with 0.05 g catalyst loading.

4.2.3 Mechanistic insights into cyanoguanidine functionalised SiO_2 using density functional theory

Surface bound guanidines supported on mesoporous SiO_2 and in particular the dicyandiamide ligands are effective catalyst for PET glycolysis, butanolysis and PLA methanolysis. DFT calculations were carried out to gain further insight into the catalytic role of the most reactive guanidine-derivative. Geometry optimisations were carried out using the semi-local Perdew–Burke–Ernzerhof (PBEsol) function[49], combined with a double-ζ basis set (DZVP-MOLOPT-SR-GTH gaussian basis set) for all the atom types, together with the Grimme's D3(BJ) dispersion correction to the potential energy[50], and a cutoff set at 500 Ry for the plane wave auxiliary basis set. Core electrons were described with the Goedecker–Teter–Hutter pseudopotentials[51] and valence ones with a mixed Gaussian and plane-wave (GPW) approach.[52]

To prove the accuracy of the DFT PBE-D3(BJ) method used in this work, a preliminary benchmarking study with a reaction model (see Experimental section for details Figure S9) was performed. In this benchmark, we optimised the (non-catalysed) reaction model under at PBE-D3(BJ)/DZVP level, and then we performed single point energy calculations at the DLPNO-CCSD(T)[53] level of theory calculations done with the ORCA 5.0.3 programme suite.[54] Results illustrated in Table S5) show that the relative error for the energy barrier is only of 4.6 % (energy barriers of 36.05 and 37.79 kcal/mol at PBE-D3(BJ) and DLPNO-CCSD(T), respectively), indicating that the method used is accurate and reliable for predicting the energy barriers of the reactions investigated in this work.

The SiO_2-DCD catalyst surface model was constructed by attaching the DCD ligand on an outermost silicon atom of the SiO_2 surface. However, the guanidine when supported on the SiO_2 can present two tautomeric forms: one composed of a primary amine, two secondary amines and two imines and the other comprising of two primary amines, one secondary amine and two imines, as illustrated in the Supplementary Information Figure S10. Therefore, initial calculations were carried out to identify the more stable configuration and results indicate that the system with two primary imines (Figure S8(b)) is 5 kcal mol^{-1} more stable. Therefore, when we refer to the SiO_2–DCD catalyst, we are only considering this structure.

The glycolysis of PET is the molecular degradation of the polymer by EG through a trans-esterification reaction, where the C-O ester bond breaks and is transformed into hydroxyl groups forming BHET. In order to simulate the reaction processes, we modelled the polymer considering the oligomer with only two repetitive units of PET (see Figure 8 (a)) and using EG as solvent adopting a continuum model (see Experimental Section in the Supplementary Information). Briefly, the reaction proceeds through a transesterification of the ester by the EG, where the ester carbon atom is attacked by the lone pair electrons of the hydroxyl group of EG forming a C-O bond, followed by a proton transfer from the hydroxyl group of EG to the ester O atom of PET. This results with the breaking of the oligomer **1**, forming the BHET product **2**, through the transition state $\mathbf{TS_{1\text{-}2}}$, as illustrated in Figure 8(a). The same

mechanism is proposed for the SiO_2 -DCD system, in which the catalyst can activate the C=O bond of the PET by stabilising [C=O···H-N] hydrogen bonds, making the bonds more prone to the nucleophilic attack of EG (Figure 8 (b)). The formation of H-bonds has been shown to be beneficial for PET degradation using ionic liquid catalysts.[55]

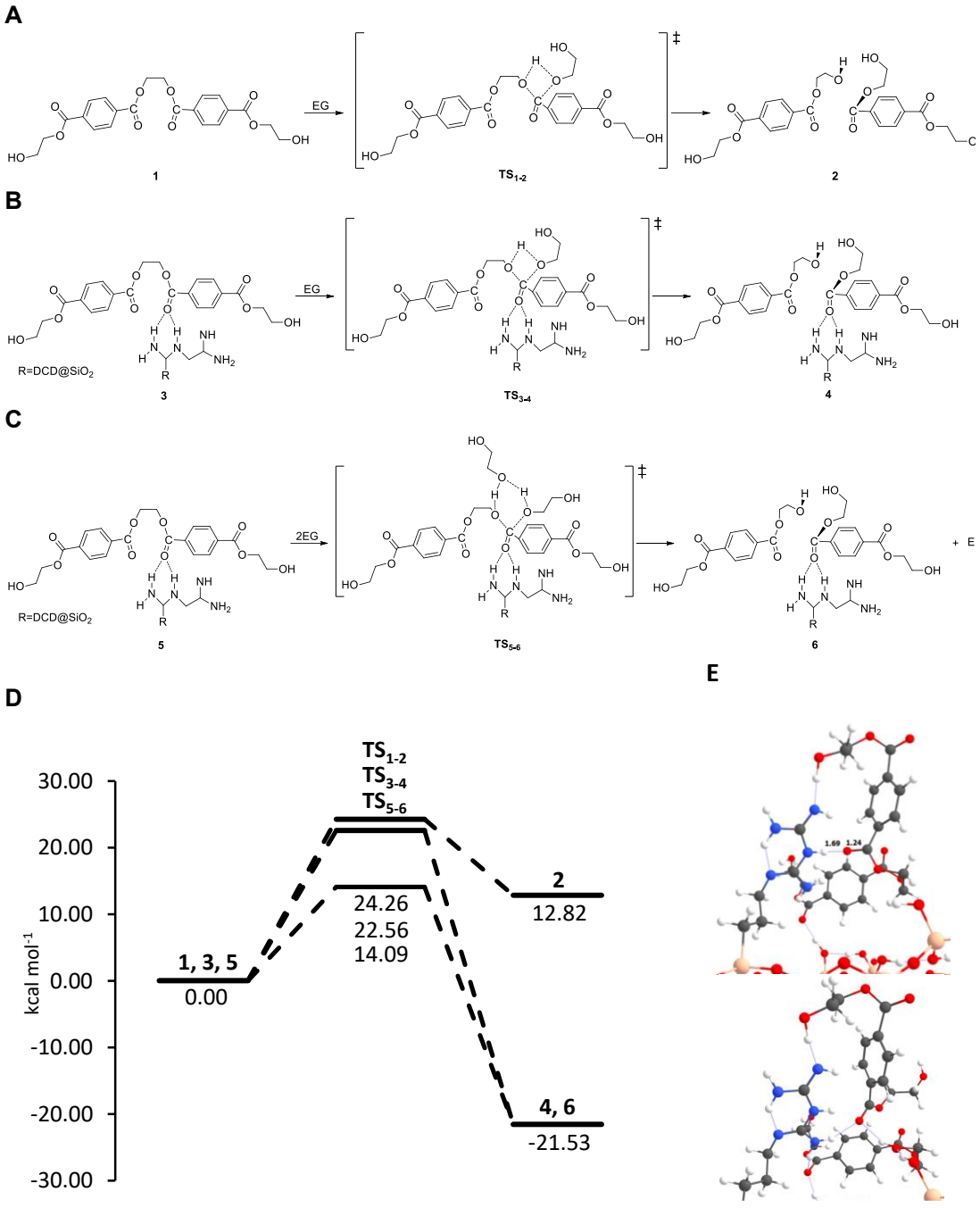


Figure 8: (A)-(C) Reaction mechanisms proposed for the PET depolymerisation uncatalysed and catalysed by SiO_2-DCD, considering one and two units of EG, respectively. (D) Energy profiles

representing the relative Gibbs free energies at 190 °C (in kcal mol^{-1}) considering EG as the solvent for the proposed uncatalysed and catalysed reaction mechanisms. (e) Optimised structures for the reactant **3** and product **4**, relevant distances are in Angstroms (Å) and the hydrogen bonds are represented with blue dotted lines. Colour scheme: grey for C, red for O, white for H, blue for N and beige for Si.

Energetic data collected in the energy profiles displayed in figure 8(d) show a subtle reduction of the free energy barrier of around 2 kcal mol^{-1} for the SiO_2-DCD system compared to the uncatalysed process. As mentioned above, the catalytic activity of the DCD ligand is associated with activation of the C=O bond of the oligomer via hydrogen bonds with the amino groups. This activation is relatively low, as the H-bonds do not significantly perturb the C=O bond length (1.24 and 1.22 Å in SiO_2-DCD and isolated DCD, respectively, see Figure 8(e). More significant effect relates to the change in the thermodynamics. While the uncatalysed reaction shows an endergonic character, the catalysed reaction is exergonic, with a favourable reaction free energy of -21.53 kcal mol^{-1} at 190 °C. This change in the thermodynamics is due to the different anchoring positions offered by the amino groups on the SiO_2 surface that generate a net gain in hydrogen bonds with the newly formed BHET product, thereby inducing an extra stabilisation effect, which is not possible in the uncatalysed reaction.

Results show that SiO_2-DCD alone, although favouring the thermodynamics with respect to the uncatalysed systems, does not exert strong catalytic effects since they do not induce a significant energy barrier decrease, with relatively high free energy barriers (22.56 kcal mol^{-1}). This does align with the experimental observations, which demonstrate fast PET degradation in the presence of the catalyst. To rationalise this, the role of the EG in the reaction was next considered. The EG behaves are the reactant and solvent and can directly participate in the proton transfer elementary step. Without accounting the participation of the solvent, the transition state presents a 4-membered ring, which is geometrically highly strained, as illustrated in figure 10 (b), and accordingly infers a high energy barrier. In contrast, if EG can assist the proton transfer by receiving one proton and donating

another one (establishing a proton relay mechanism) the TS structure presents a 6th-membered ring, which is geometrically less strained thereby presenting a lower energy barrier (Figure 10 (c)). To evaluate the role of the EG, a benchmarking with n = 2, 3 and 4 EG molecules has been carried out with the uncatalysed system. Results indicate that already with two units of EG there is a reduction of the barrier by 5 kcal mol^{-1}. Interestingly, an increase of the number of EG molecules does not further decrease the free energy barrier, which remains at ca. 17 kcal mol^{-1}, as the barriers show a reduction of 7.20 and 7.83 kcal mol^{-1} (three and four EG units, respectively) compared with the uncatalysed reaction (see Table S6 in Supporting Information). After assessing the crucial role of the EG, we next computed the reaction on the SiO_2–DCD catalysts considering two EG molecules, results indicate a decrease of the free energy barrier to 14.09 kcal mol^{-1}, correlating with the experimental findings.

4.2.4 PLA degradation mechanism

Similar to PET degradation, PLA depolymerisation by the addition of protic low molecular weight alcohols, in this case MeOH, proceeds by the transesterification of PLA. On a first step, PLA breaks forming the oligomer chain end methine, followed by a second transesterification of the oligomer, finally obtaining the MeLa product. The reaction process modelled here to assess the catalytic role of the SiO_2-DCD is focused only on the last step of the depolymerisation, *i.e.* the oligomer cleavage in two units of MeLa, using THF as the solvent and adopting a continuum model (see Experimental Section for computational details). The reaction proceeds through nucleophilic attack of the carbonyl group by the lone pair electrons on the hydroxyl group of MeOH, which is followed by a proton transfer from the MeOH to the ester O, resulting in breaking of the oligomer **1** forming the MeLa product **2** (see Figure 9 (a)).

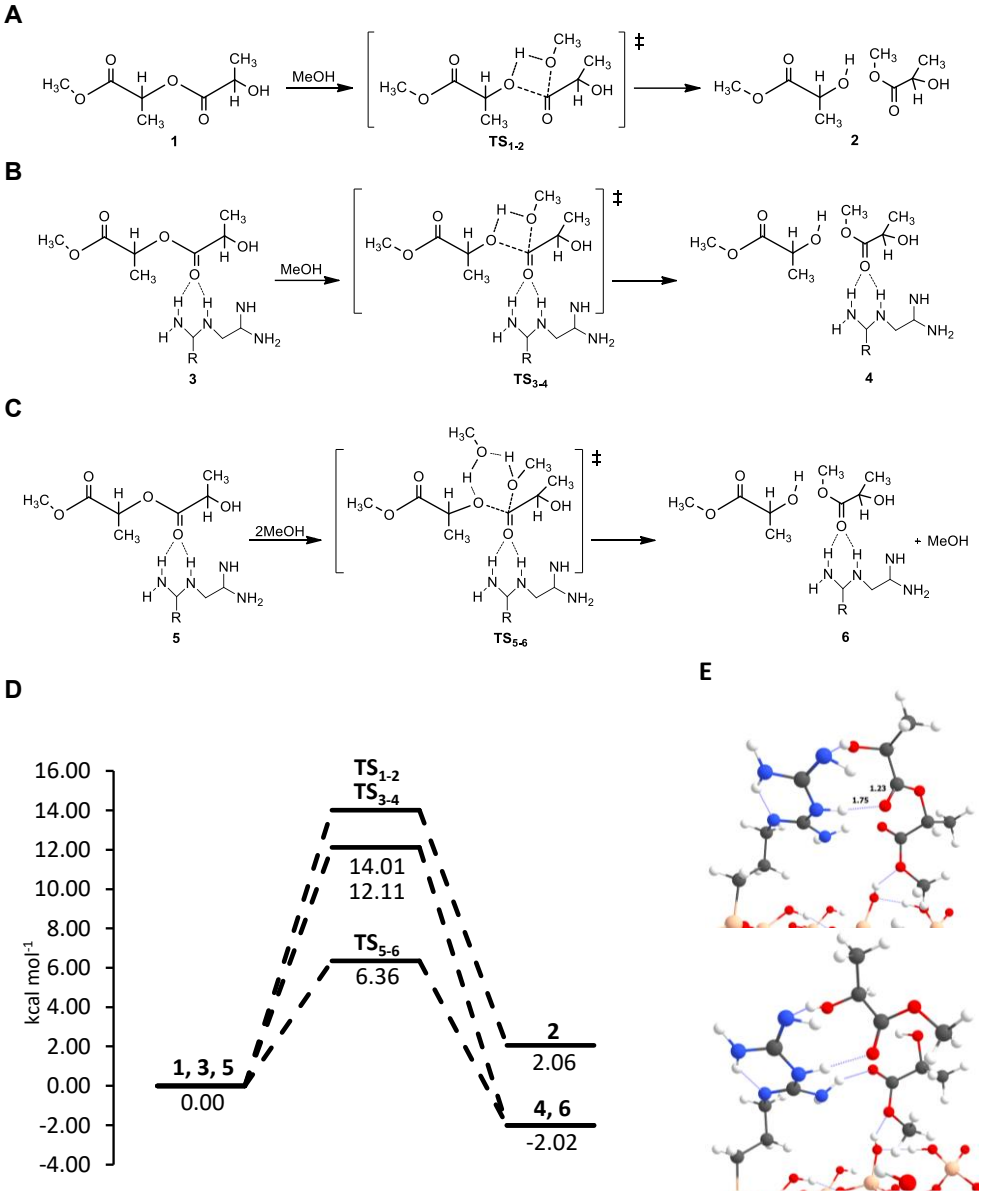


Figure 9: (A)-(C) Reaction mechanisms proposed for the PLA depolymerisation uncatalysed and catalysed by SiO_2–DCD considering one and two units of EG, respectively. (D) Energy profiles representing the relative Gibbs free energies at 130 °C (in kcal·mol^{-1}) considering THF as the solvent, for the proposed uncatalysed and catalysed reaction mechanisms. (E) Optimised structures for the reactant **3** and product **4**, relevant distances are in Angstroms (Å) and the hydrogen bonds are represented with blue dotted lines. Colour scheme: grey for C, red for O, white for H, blue for N and beige for Si.

The energy profile showed in Figure 9 (d) reveals the free energy barrier for the transesterification process is reduced by ~2 kcal mol^{-1} when using the SiO_2-DCD system with respect to the uncatalysed

process. Similar to the PET mechanism, the capability of the SiO_2-DCD catalyst to activate the C=O bond in PLA is rather limited, in this case the C=O bond being enlarged from 1.23 Å in the isolated PLA to 1.24 Å in the SiO_2-DCD, which is translated to a slight energy barrier decrease (see Figure 9 (e)). Although the small reaction enhancement, the presence of the catalyst has also an effect on the thermodynamics of the process. As mentioned above, the breaking of the oligomer to finally form the MeLa product is in equilibrium, which is confirmed by the computed energetic values for the uncatalysed process (i.e., slightly endergonic, with a reaction free energy at 190 °C of +2.06 kcal mol^{-1}). However, in the presence of the SiO_2-DCD catalyst, the MeLa product is stabilised, now presenting an exergonic character with a reaction free energy of -2.02 kcal mol^{-1}. Similar to PET degradation, the SiO_2-DCD surface provides different amino binding positions, creating additional hydrogen bonds with MeLa (Figure 9 (e)), therefore supplying an extra stabilisation of the product. However, for PLA, the product stabilisation is less significant compared to PET degradation and the equilibrium between the oligomer chains and the MeLa product is still present. Despite the slight decrease in the reaction energy barrier, this reaction can also be catalysed by the MeOH solvent which can participate in a proton relay mechanism due to being a protic solvent with the capability to exchange protons. We simulated this process considering the participation of two units of MeOH (one being the reactant and the other the solvent proton transfer assistant) and found that the new barrier is allocated at 6.36 kcal mol^{-1} (see Figure 9(d)). Similar to that observed for PET degradation, the participation of the reactant in the proton transfer step plays an important role in the mechanism.

4.3 Conclusions

This work demonstrates that SiO_2 and carbon supports covalently functionalised with different guanidine ligands are effective heterogeneous metal free catalysts for the depolymerisation of PET and PLA. The three catalysts displayed good catalytic activity with high PET conversions under both thermal and microwave assisted methods. Different optimal conditions were found for the catalysts

under conventional heating and microwave assisted heating. The SiO_2-DCD catalyst, which is a cyanoguanidine ligand, performed best, and this is likely due to its nitrogen rich environment. The nature of the support material influenced the catalytic performance, and the use of activated carbon as a support material was beneficial for microwave-assisted glycolysis. To assess the versatility of the surface immobilised guanidine catalysts, the methanolysis of PLA to MeLa, was demonstrated with microwave assisting heating greatly improving the reaction time. DFT simulations provide a deep understanding of the reaction mechanisms for both PET and PLA degradation processes, concretely unveiling the role of the SiO_2-DCD catalyst, which throughout its ability to create a net of hydrogen bonds is not only able to enhance the reaction processes kinetically but also thermodynamically by stabilising both BHET and MeLA products. The catalytic role of the corresponding additional reactive molecules (EG and MeOH) is also highlighted when they participate in the reaction by assisting proton transfer processes, which infers an additional reduction of the free energy barriers. This work demonstrates that guanidine functionalised SiO_2 based are versatile heterogeneous catalysts for both recyclability of PET and PLA to high quality monomers.

Conflicts of interest

There are no conflicts to declare.

Acknowledgements

This research was funded by Science Foundation Ireland (AMBER Grant No: 12/RC2278_P2). G.P. and A.R. gratefully acknowledge the computer resources and technical support provided by the Barcelona Supercomputing Centre (CNS-BSC) and the Consorci de Serveis Universitaris de Catalunya (CSUC).

4.4 References

(1) J, R. B.; V, G. S. A systematic review on plastic waste conversion for a circular economy: recent trends and emerging technologies. *Catalysis Science & Technology* 2023, *13* (8), 2291-2302, 10.1039/D2CY02066A. DOI: 10.1039/D2CY02066A.

(2) Kosloski-Oh, S. C.; Wood, Z. A.; Manjarrez, Y.; de los Rios, J. P.; Fieser, M. E. Catalytic methods for chemical recycling or upcycling of commercial polymers. *Materials Horizons* 2021, *8* (4), 1084-1129, 10.1039/D0MH01286F. DOI: 10.1039/D0MH01286F.

(3) Luo, Y.; Selvam, E.; Vlachos, D. G.; Ierapetritou, M. Economic and Environmental Benefits of Modular Microwave-Assisted Polyethylene Terephthalate Depolymerization. *ACS Sustainable Chemistry & Engineering* 2023, *11* (10), 4209-4218. DOI: 10.1021/acssuschemeng.2c07203.

(4) Cao, F.; Wang, L.; Zheng, R.; Guo, L.; Chen, Y.; Qian, X. Research and progress of chemical depolymerization of waste PET and high-value application of its depolymerization products. *RSC Advances* 2022, *12* (49), 31564-31576, 10.1039/D2RA06499E. DOI: 10.1039/D2RA06499E.

(5) Bohre, A.; Jadhao, P. R.; Tripathi, K.; Pant, K. K.; Likozar, B.; Saha, B. Chemical Recycling Processes of Waste Polyethylene Terephthalate Using Solid Catalysts. *ChemSusChem* 2023, *16* (14), e202300142. DOI: https://doi.org/10.1002/cssc.202300142.

(6) Shirazimoghaddam, S.; Amin, I.; Faria Albanese, J. A.; Shiju, N. R. Chemical Recycling of Used PET by Glycolysis Using Niobia-Based Catalysts. *ACS Engineering Au* 2023, *3* (1), 37-44. DOI: 10.1021/acsengineeringau.2c00029.

(7) Casey, É.; Breen, R.; Gómez, J. S.; Kentgens, A. P. M.; Pareras, G.; Rimola, A.; Holmes, J. D.; Collins, G. Ligand-Aided Glycolysis of PET Using Functionalized Silica-Supported Fe2O3 Nanoparticles. *ACS Sustainable Chemistry & Engineering* 2023, *11* (43), 15544-15555. DOI: 10.1021/acssuschemeng.3c03585.

(8) Jo, Y.; Kim, E. J.; Kim, J.; An, K. Efficient Fe3O4 nanoparticle catalysts for depolymerization of polyethylene terephthalate. *Green Chemistry* 2023, *25* (20), 8160-8171, 10.1039/D3GC01707A. DOI: 10.1039/D3GC01707A.

(9) Veregue, F. R.; Pereira da Silva, C. T.; Moisés, M. P.; Meneguin, J. G.; Guilherme, M. R.; Arroyo, P. A.; Favaro, S. L.; Radovanovic, E.; Girotto, E. M.; Rinaldi, A. W. Ultrasmall Cobalt Nanoparticles as a Catalyst for PET Glycolysis: A Green Protocol for Pure Hydroxyethyl Terephthalate Precipitation without Water. *ACS Sustainable Chemistry & Engineering* 2018, *6* (9), 12017-12024. DOI: 10.1021/acssuschemeng.8b02294.

(10) Khoonkari, M.; Haghighi, A. H.; Sefidbakht, Y.; Shekoohi, K.; Ghaderian, A. Chemical Recycling of PET Wastes with Different Catalysts. *International Journal of Polymer Science* 2015, *2015*, 124524. DOI: 10.1155/2015/124524.

(11) Bush, N. G.; Dinh, C. H.; Catterton, C. L.; Fieser, M. E. Understanding the important variables to optimize glycolysis of polyethylene terephthalate with lanthanide-containing ionic liquids. *RSC Sustainability* 2023, *1* (4), 938-947, 10.1039/D3SU00090G. DOI: 10.1039/D3SU00090G.

(12) Wang, L.; Nelson, G. A.; Toland, J.; Holbrey, J. D. Glycolysis of PET Using 1,3-Dimethylimidazolium-2-Carboxylate as an Organocatalyst. *ACS Sustainable Chemistry & Engineering* 2020, *8* (35), 13362-13368. DOI: 10.1021/acssuschemeng.0c04108.

(13) Fehér, Z.; Kiss, J.; Kisszékelyi, P.; Molnár, J.; Huszthy, P.; Kárpáti, L.; Kupai, J. Optimisation of PET glycolysis by applying recyclable heterogeneous organocatalysts. *Green Chemistry* 2022, *24* (21), 8447-8459, 10.1039/D2GC02860C. DOI: 10.1039/D2GC02860C.

(14) Jehanno, C.; Flores, I.; Dove, A. P.; Müller, A. J.; Ruipérez, F.; Sardon, H. Organocatalysed depolymerisation of PET in a fully sustainable cycle using thermally stable protic ionic salt. *Green Chemistry* 2018, *20* (6), 1205-1212, 10.1039/C7GC03396F. DOI: 10.1039/C7GC03396F.

(15) Kamber, N. E.; Tsujii, Y.; Keets, K.; Waymouth, R. M.; Pratt, R. C.; Nyce, G. W.; Hedrick, J. L. The Depolymerization of Poly(ethylene terephthalate) (PET) Using N-Heterocyclic Carbenes from Ionic Liquids. *Journal of Chemical Education* 2010, *87* (5), 519-521. DOI: 10.1021/ed800152c.

(16) Liu, Y.; Yao, X.; Yao, H.; Zhou, Q.; Xin, J.; Lu, X.; Zhang, S. Degradation of poly(ethylene terephthalate) catalyzed by metal-free choline-based ionic liquids. *Green Chemistry* 2020, *22* (10), 3122-3131, 10.1039/D0GC00327A. DOI: 10.1039/D0GC00327A.
(17) Kaiho, S.; Hmayed, A. A. R.; Delle Chiaie, K. R.; Worch, J. C.; Dove, A. P. Designing Thermally Stable Organocatalysts for Poly(ethylene terephthalate) Synthesis: Toward a One-Pot, Closed-Loop Chemical Recycling System for PET. *Macromolecules* 2022, *55* (23), 10628-10639. DOI: 10.1021/acs.macromol.2c01410.
(18) Jehanno, C.; Pérez-Madrigal, M. M.; Demarteau, J.; Sardon, H.; Dove, A. P. Organocatalysis for depolymerisation. *Polymer Chemistry* 2019, *10* (2), 172-186, 10.1039/C8PY01284A. DOI: 10.1039/C8PY01284A.
(19) Fukushima, K.; Coulembier, O.; Lecuyer, J. M.; Almegren, H. A.; Alabdulrahman, A. M.; Alsewailem, F. D.; McNeil, M. A.; Dubois, P.; Waymouth, R. M.; Horn, H. W.; et al. Organocatalytic depolymerization of poly(ethylene terephthalate). *Journal of Polymer Science Part A: Polymer Chemistry* 2011, *49* (5), 1273-1281, https://doi.org/10.1002/pola.24551. DOI: https://doi.org/10.1002/pola.24551 (accessed 2022/11/28).
(20) Le, N. H.; Ngoc Van, T. T.; Shong, B.; Cho, J. Low-Temperature Glycolysis of Polyethylene Terephthalate. *ACS Sustainable Chemistry & Engineering* 2022. DOI: 10.1021/acssuschemeng.2c05570.
(21) Chipurici, P.; Vlaicu, A.; Călinescu, I.; Vînătoru, M.; Busuioc, C.; Dinescu, A.; Ghebaur, A.; Rusen, E.; Voicu, G.; Ignat, M.; et al. Magnetic silica particles functionalized with guanidine derivatives for microwave-assisted transesterification of waste oil. *Scientific Reports* 2021, *11* (1), 17518. DOI: 10.1038/s41598-021-97097-7.
(22) Scé, F.; Cano, I.; Martin, C.; Beobide, G.; Castillo, Ó.; de Pedro, I. Comparing conventional and microwave-assisted heating in PET degradation mediated by imidazolium-based halometallate complexes. *New Journal of Chemistry* 2019, *43* (8), 3476-3485, 10.1039/C8NJ06090H. DOI: 10.1039/C8NJ06090H.
(23) Selvam, E.; Luo, Y.; Ierapetritou, M.; Lobo, R. F.; Vlachos, D. G. Microwave-assisted depolymerization of PET over heterogeneous catalysts. *Catalysis Today* 2023, *418*, 114124. DOI: https://doi.org/10.1016/j.cattod.2023.114124.
(24) Donadini, R.; Boaretti, C.; Lorenzetti, A.; Roso, M.; Penzo, D.; Dal Lago, E.; Modesti, M. Chemical Recycling of Polyurethane Waste via a Microwave-Assisted Glycolysis Process. *ACS Omega* 2023, *8* (5), 4655-4666. DOI: 10.1021/acsomega.2c06297.
(25) Češarek, U.; Pahovnik, D.; Žagar, E. Chemical Recycling of Aliphatic Polyamides by Microwave-Assisted Hydrolysis for Efficient Monomer Recovery. *ACS Sustainable Chemistry & Engineering* 2020, *8* (43), 16274-16282. DOI: 10.1021/acssuschemeng.0c05706.
(26) Selvam, E.; Kots, P. A.; Hernandez, B.; Malhotra, A.; Chen, W.; Catala-Civera, J. M.; Santamaria, J.; Ierapetritou, M.; Vlachos, D. G. Plastic waste upgrade to olefins via mild slurry microwave pyrolysis over solid acids. *Chemical Engineering Journal* 2023, *454*, 140332. DOI: https://doi.org/10.1016/j.cej.2022.140332.
(27) Muley, P. D.; Wang, Y.; Hu, J.; Shekhawat, D. Microwave-assisted heterogeneous catalysis. In *Catalysis: Volume 33*, Vol. 33; The Royal Society of Chemistry, 2021; pp 1-37.
(28) Román-Ramírez, L. A.; McKeown, P.; Jones, M. D.; Wood, J. Poly(lactic acid) Degradation into Methyl Lactate Catalyzed by a Well-Defined Zn(II) Complex. *ACS Catalysis* 2019, *9* (1), 409-416. DOI: 10.1021/acscatal.8b04863.
(29) Petrus, R.; Bykowski, D.; Sobota, P. Solvothermal Alcoholysis Routes for Recycling Polylactide Waste as Lactic Acid Esters. *ACS Catalysis* 2016, *6* (8), 5222-5235. DOI: 10.1021/acscatal.6b01009.
(30) Meka, A. K.; Gopalakrishna, A.; Iriarte-Mesa, C.; Rewatkar, P.; Qu, Z.; Wu, X.; Cao, Y.; Prasadam, I.; Janjua, T. I.; Kleitz, F.; et al. Influence of Pore Size and Surface Functionalization of Mesoporous Silica Nanoparticles on the Solubility and Antioxidant Activity of Confined Coenzyme Q10. *Molecular Pharmaceutics* 2023, *20* (6), 2966-2977. DOI: 10.1021/acs.molpharmaceut.3c00017.

(31) Yoshida, W.; Castro, R. P.; Jou, J.-D.; Cohen, Y. Multilayer Alkoxysilane Silylation of Oxide Surfaces. *Langmuir* 2001, *17* (19), 5882-5888. DOI: 10.1021/la001780s.
(32) Truica-Marasescu, F.; Wertheimer, M. R. Nitrogen-Rich Plasma-Polymer Films for Biomedical Applications. *Plasma Processes and Polymers* 2008, *5* (1), 44-57, https://doi.org/10.1002/ppap.200700077. DOI: https://doi.org/10.1002/ppap.200700077 (accessed 2022/12/10).
(33) Paengjun, N.; Vibulyaseak, K.; Ogawa, M. Heterostructural transformation of mesoporous silica–titania hybrids. *Scientific Reports* 2021, *11* (1), 3210. DOI: 10.1038/s41598-020-80584-8.
(34) Tian, R.; Seitz, O.; Li, M.; Hu, W.; Chabal, Y. J.; Gao, J. Infrared Characterization of Interfacial Si−O Bond Formation on Silanized Flat SiO2/Si Surfaces. *Langmuir* 2010, *26* (7), 4563-4566. DOI: 10.1021/la904597c.
(35) Pasternack, R. M.; Rivillon Amy, S.; Chabal, Y. J. Attachment of 3-(Aminopropyl)triethoxysilane on Silicon Oxide Surfaces: Dependence on Solution Temperature. *Langmuir* 2008, *24* (22), 12963-12971. DOI: 10.1021/la8024827.
(36) Zhang, J.; Huang, Z.; Xie, Y.; Jiang, X. Modulating the catalytic activity of gold nanoparticles using amine-terminated ligands. *Chemical Science* 2022, *13* (4), 1080-1087. DOI: 10.1039/d1sc05933e From NLM.
(37) Lalhmangaihzuala, S.; Laldinpuii, Z.; Lalmuanpuia, C.; Vanlaldinpuia, K. Glycolysis of Poly(Ethylene Terephthalate) Using Biomass-Waste Derived Recyclable Heterogeneous Catalyst. *Polymers* 2021, *13* (1). DOI: 10.3390/polym13010037.
(38) de la Hoz, A.; Díaz-Ortiz, Á.; Moreno, A. Microwaves in organic synthesis. Thermal and non-thermal microwave effects. *Chemical Society Reviews* 2005, *34* (2), 164-178, 10.1039/B411438H. DOI: 10.1039/B411438H.
(39) Palma, V.; Barba, D.; Cortese, M.; Martino, M.; Renda, S.; Meloni, E. Microwaves and Heterogeneous Catalysis: A Review on Selected Catalytic Processes. *Catalysts* 2020, *10* (2), 246.
(40) Ji, T.; Zhu, J. Microwave-Responsive Nanomaterials for Catalysis. In *Responsive Nanomaterials for Sustainable Applications*, Sun, Z., Liao, T. Eds.; Springer International Publishing, 2020; pp 65-91.
(41) Mansour, S. H.; Ikladious, N. E. Depolymerization of poly(ethylene terephthalate) wastes using 1,4-butanediol and triethylene glycol. *Polymer Testing* 2002, *21* (5), 497-505. DOI: https://doi.org/10.1016/S0142-9418(01)00115-5.
(42) Abdelaal, M. Y.; Sobahi, T. R.; Makki, M. S. I. Chemical transformation of pet waste through glycolysis. *Construction and Building Materials* 2011, *25* (8), 3267-3271. DOI: https://doi.org/10.1016/j.conbuildmat.2011.03.013.
(43) Öztürk, Y.; Güçlü, G. Unsaturated Polyester Resins Obtained from Glycolysis Products of Waste PET. *Polymer-Plastics Technology and Engineering* 2005, *43* (5), 1539-1552. DOI: 10.1081/PPT-200030272.
(44) Cho, M.; Yang, J.; Noh, S.; Joe, H.; Han, M. Production of polybutylene terephthalate (PBT) oligomer from Recycled polyethylene terephthalate (PET). *Korean Chemical Engineering Research* 2016, *54* (4), 437–442.
(45) Perz, V.; Bleymaier, K.; Sinkel, C.; Kueper, U.; Bonnekessel, M.; Ribitsch, D.; Guebitz, G. M. Data on synthesis of oligomeric and polymeric poly(butylene adipate-co-butylene terephthalate) model substrates for the investigation of enzymatic hydrolysis. *Data in Brief* 2016, *7*, 291-298. DOI: https://doi.org/10.1016/j.dib.2016.02.029.
(46) Song, X.; Zhang, X.; Wang, H.; Liu, F.; Yu, S.; Liu, S. Methanolysis of poly(lactic acid) (PLA) catalyzed by ionic liquids. *Polymer Degradation and Stability* 2013, *98* (12), 2760-2764. DOI: https://doi.org/10.1016/j.polymdegradstab.2013.10.012.
(47) Alberti, C.; Enthaler, S. Depolymerization of End-of-Life Poly(lactide) to Lactide via Zinc-Catalysis. *ChemistrySelect* 2020, *5* (46), 14759-14763. DOI: https://doi.org/10.1002/slct.202003979.
(48) Lamberti, F. M.; Ingram, A.; Wood, J. Synergistic Dual Catalytic System and Kinetics for the Alcoholysis of Poly(Lactic Acid). In *Processes*, 2021; Vol. 9.

(49) Perdew, J. P.; Ruzsinszky, A.; Csonka, G. I.; Vydrov, O. A.; Scuseria, G. E.; Constantin, L. A.; Zhou, X.; Burke, K. Restoring the Density-Gradient Expansion for Exchange in Solids and Surfaces. *Physical Review Letters* 2008, *100* (13), 136406. DOI: 10.1103/PhysRevLett.100.136406.
(50) Grimme, S.; Antony, J.; Ehrlich, S.; Krieg, H. A consistent and accurate ab initio parametrization of density functional dispersion correction (DFT-D) for the 94 elements H-Pu. *The Journal of Chemical Physics* 2010, *132* (15). DOI: 10.1063/1.3382344 (accessed 10/18/2023).
(51) Goedecker, S.; Teter, M.; Hutter, J. Separable dual-space Gaussian pseudopotentials. *Physical Review B* 1996, *54* (3), 1703-1710. DOI: 10.1103/PhysRevB.54.1703.
(52) Lippert, G.; Hutter, J.; Parrinello, M. A hybrid Gaussian and plane wave density functional scheme. *Molecular Physics* 1997, *92*, 477-488. DOI: 10.1080/002689797170220.
(53) Riplinger, C.; Pinski, P.; Becker, U.; Valeev, E. F.; Neese, F. Sparse maps—A systematic infrastructure for reduced-scaling electronic structure methods. II. Linear scaling domain based pair natural orbital coupled cluster theory. *The Journal of Chemical Physics* 2016, *144* (2), 024109. DOI: 10.1063/1.4939030 (accessed 1/15/2024).
(54) Neese, F. Software update: The ORCA program system—Version 5.0. *WIREs Computational Molecular Science* 2022, *12* (5), e1606. DOI: https://doi.org/10.1002/wcms.1606 (accessed 2024/01/15).
(55) Yao, H.; Lu, X.; Ji, L.; Tan, X.; Zhang, S. Multiple Hydrogen Bonds Promote the Nonmetallic Degradation Process of Polyethylene Terephthalate with an Amino Acid Ionic Liquid Catalyst. *Industrial & Engineering Chemistry Research* 2021, *60* (10), 4180-4188. DOI: 10.1021/acs.iecr.0c06073.

4.5 Appendix: Supporting Information

Guanidine Functionalised Porous SiO_2 as Heterogeneous Catalysts for Microwave Depolymerisation of PET and PLA

*Casey, É.; **Breen, R**.; Pareras, G.; Rimola, A.; Holmes, J. D.; Collins, G. Guanidine functionalized porous SiO_2 as heterogeneous catalysts for microwave depolymerization of PET and PLA. RSC Sustainability **2024**, 2 (4), 1040-1051, 10.1039/D3SU00425B. DOI: 10.1039/D3SU00425B.*

Table S1: Literature reports of homogeneous organocatalysts for PET glycolysis.

Catalyst	**PET:Cat**	**Conditions**	**BHET Yield %**	***Reference***
[Ch][OAc]	5 wt %	180 °C, 240 min	85.2	[1]
[bmim]Cl	80 wt %	180 °C, 480 min	41.6	[2]
Urea	10 wt %	180 °C, 180 min	78	[3]
[Bmim]OH	5 wt %	190 °C, 120 min	71.2	[4]
TBD: MSA salt	0.5 eq	180 °C, 120 min	91	[5]
t-BuP_2	2.4 wt %	190 °C, 90 min	92.7	[6]
$[Ch]_3[PO_4]$	90 wt %	120 °C, 180 min	60.6	[7]
[Ch][Gly]	5 wt %	150 °C, 6 h	51	[8]
TBD based protic ionic salts	20 wt %	190 °C, 120 min	83.5	[9]
cyanamide	5 wt %	190 °C, 150 min	95.2	[10]

Experimental

Chemicals

Mesoporous cellular foam (MCF) SiO_2 was obtained from Glantreo. (APTES), N,N dicyclohexylcarbodimine (DCC), 1-ethyl-3-(3-dimethylaminopropyl) carbodiimide (EDC), dicyandiamide (DCD) , methanol, ethanol, toluene, tetrahydrofuran and ethylene glycol were all purchased from Sigma Aldrich. PET was obtained from post-consumer water bottles after lids and labels were removed. Commercial PLA was obtained from Vegware lids. The plastics were cut into 1 mm x 1 mm pieces for glycolysis and methanolysis experiments. Repeating unit of 192.68 g/mol was used as the molecular weight of PET.

Synthesis of SiO_2-DCG

In a 100 ml round bottom flask, 10 mmol of the guanidine precursor, N,N dicylcohexylcarbodimine (DCC), 1-ethyl-3-(3-dimethylaminopropyl) carbodiimide (EDC)) or dicyandiamide (DCD) was dissolved in 20 ml of dry toluene under argon. 2.1 ml of 3-aminopropyltriethoxylsilane (APTES) was added, and the reaction was refluxed at 100 °C for 24 h under Ar. Next 1 g of SiO_2 was added and the reaction was left to refluxed for a further 24 h. When the reaction had completed, the resulting mixture was filtered and washed with copious amounts of ethanol and the product and dried at 60°C in an oven.

Thermal glycolysis of PET

In a typical procedure, 1 g of PET, 0.1 g catalyst and 5 ml of ethylene glycol were refluxed at 190 °C for 3 h. Once reaction was complete, 5 ml of ice-cold H_2O was added to the reaction, filtered off and dried. The catalyst was separated by filtration. The filtrate was placed in the fridge overnight after which the BHET crystallised out the solution. The BHET crystals were collected be filtration, washed with water and dried overnight before being weighed to calculate the % yield. PET conversion and yield were calculated by the equations below.

$$\% \text{ Conversion of PET: } \frac{W_0 - W_1}{W_0} \; x \; 100 \quad \textbf{Eqn. 1}$$

Where W_0 is the initial weight of the PET used and W_1 is the weight of the unreacted PET after the reaction.

$$\% \text{ Yield of BHET: } \frac{W_{BHET}/M_{BHET}}{W_0/M_{PET}} \; x \; 100 \quad \textbf{Eqn. 2}$$

Where, W_{BHET} is weight of the BHET product after recrystallisation, M_{BHET} is the molecular weight of BHET, W_0 is the initial weight of PET used and M_{PET} is the repeating unit of PET (192.68 g/mol).

Microwave assisted glycolysis of PET

Initial MW assisted reactions were carried out under the same conditions as the thermally heated reactions, followed by an optimisation study as detailed in Table S4. Optimal conditions were found to be 1 g of PET, 0.1 g catalyst and 10 ml ethylene glycol were added to the Milestone Flexiwave SK-15 high pressure digestion rotors and the reactions were carried out at between 10-60 min ranging from 190-220 °C with a stir speed of 960 rpm, ramp time of 5 min and at 800 W. The recrystallisation step post-reaction was the same as for thermal glycolysis.

Methanolysis of PLA

0.5 g PLA, 50 mg catalyst, 5 ml MeOH and 7.5 ml of tetrahydrofuran (THF) was placed in an autoclave and sealed tight, which was then placed into oven at 130 °C for 20 h. Once reaction was complete, the resulting mixture was filtered and washed with excess MeOH, and the solvent was removed via rotary evaporation leaving the product MeLa. The unreacted plastic was collected from the filter paper, dried and weighed to calculate the PLA mass loss.

Microwave assisted methanolysis of PLA

0.5 g PLA, 50 mg catalyst, and a ratio of 2:3 methanol : THF were added to Teflon tubes and reacted in a Flexiwave microwave at 130 °C with a ramp time of 5 min for times ranging from 10-60 min and at 800 W.

$$\% \text{ Conversion of PLA: } \frac{W_0 - W_1}{W_0} \; x \; 100 \quad \textbf{Eqn. 3}$$

Where W_0 is the initial weight of the PLA used and W_1 is the weight of the unreacted PLA after the reaction.

Materials Characterisation

Scanning electron microscopy (SEM) was performed using a FEI Quanta 650 SEM at an accelerating voltage of 5 kV. The samples were gold coated using a Quorum 150T S magnetron sputtering system as they were non-conductive. X-ray Photoelectron Spectroscopy (XPS) was acquired using a KRATOS AXIS 165 monochromatised X-ray photoelectron spectrometer equipped with an Al Kα (hv = 1486.6 eV) X-ray source. Spectra were collected at a take-off angle of 90 ˚C and all spectra were referenced to the C 1s peak at 284.8 eV. Transmission electron microscopy (TEM) analysis was performed using a JEOL 2100 electron microscope at an operating voltage of 200 kV. Fourier transform infrared (FTIR) spectra were recorded on a Perkin Elmer Spectrum Two FT-IR Spectrometer operating in the range of 4000-450 cm^{-1} with a resolution of 4 cm^{-1} and spectra were averaged from 20 scans. BET sorption analysis was performed on a Micromeritics Tristar II surface area and porosity analyser. Prior to analysis, each sample was degassed for 3 h at 400 °C and measurements were performed at -169.15 °C (77 K). The surface area was determined using the BET (Brunauer-Emmett-Teller) method. The pore volume, pore diameter and pore size distribution were determined using the BJH (Barrett-Joyner-Halenda) method.[11] Termogravimetric analysis (TGA) was carried out on a TA Instruments Thermogravimetric Analyzer TGA Q500 V20.13 Build 39. Nuclear magnetic resonance (NMR) samples were run in deuterated chloroform ($CDCl_3$). 1H NMR spectra were recorded on Bruker Avance III 300 NMR spectrometers, in proton-coupled mode using tetramethylsilane (TMS) as the internal standard. Microwave reactions were performed in Teflon vessels in a milestone Flexiwave microwave synthesis platform with a SK-15 high pressure rotor equipped with an IR temperature sensor.

Computational details

Density functional theory (DFT) simulations were carried out using the CP2K package.[12] The mesoporous SiO_2 structure used in the experiments was computationally represented as a periodic

amorphous silica (SiO_2) surface. The chosen SiO_2 surface presents a silanol density of 7.2 OH/nm^2 assuring the maximum number of Si atoms available to be functionalised in the unit cell.[13] For the initial bare SiO_2 surface, both internal atomic positions and cell parameters were optimised (resulting with dimensions of a=13.34 Å, b=13.73 Å and c=49.21 Å, in which the last one represents an empty space between surface replicas). The rest of the optimisations (namely, with the ligands and to simulate reactivity) were performed only relaxing the atomic positions keeping the cell parameters fixed. Geometry optimisations were carried out using the semi-local Perdew–Burke–Ernzerhof (PBEsol) functional[14], combined with a double-ζ basis set (DZVP-MOLOPT-SR-GTH gaussian basis set) for all the atom types, together with the Grimme's D3(BJ) dispersion correction to the potential energy,[15] and a cutoff set at 500 Ry for the plane wave auxiliary basis set. Core electrons were described with the Goedecker–Teter–Hutter pseudopotentials[16] and valence ones with a mixed Gaussian and plane-wave (GPW) approach.[17] Solvation effects were considered by performing single point energy calculations on the optimised systems adopting the self-consistent continuum solvation (SCCS) model as implemented in CP2K, aiming to reproduce the experimental conditions of ethylene glycol (EG) and tetrahydrofuran (THF) as solvents.[18]

Finally, to determine the nature of the stationary points of the potential energy surfaces (i.e., local minima and saddle points) the corresponding vibrational harmonic frequencies were calculated at the PBE-D3BJ/DZVP level using the finite differences method. For frequency calculations, a partial Hessian approach was used to reduce the computational cost of the calculations, and the vibrational frequencies were calculated on only on a fragment of the system that represents the most chemically relevant part, *i.e.*, the reactive atoms and the surface site.

Table S2: BET analysis of bare SiO_2, SiO_2-DCG, SiO_2-EDG and SiO_2-DCD catalysts.

	Surface Area m^2g^{-1}	**Pore diameter (Å)**	**Pore volume cm^3g^{-1}**
SiO_2	412.4	108	0.5342

SiO_2-DCG	182.2	100	0.4247
SiO_2-EDG	101.8	90	0.4778
SiO_2-DCD	38.4	84	0.1711

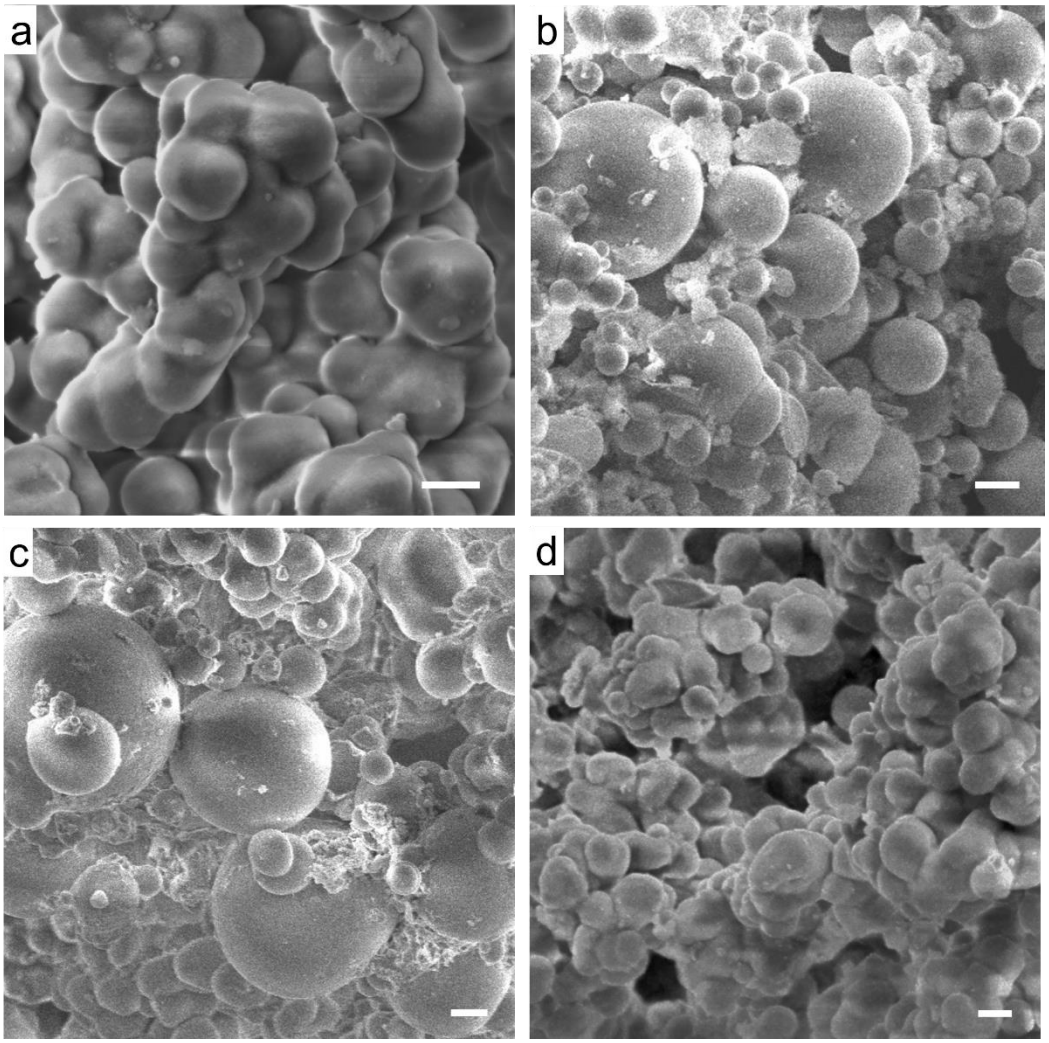


Figure S1: SEM images of (a) bare SiO_2 and after functionalisation with the (b) DCG (c) EDG and (d) DCD ligands.

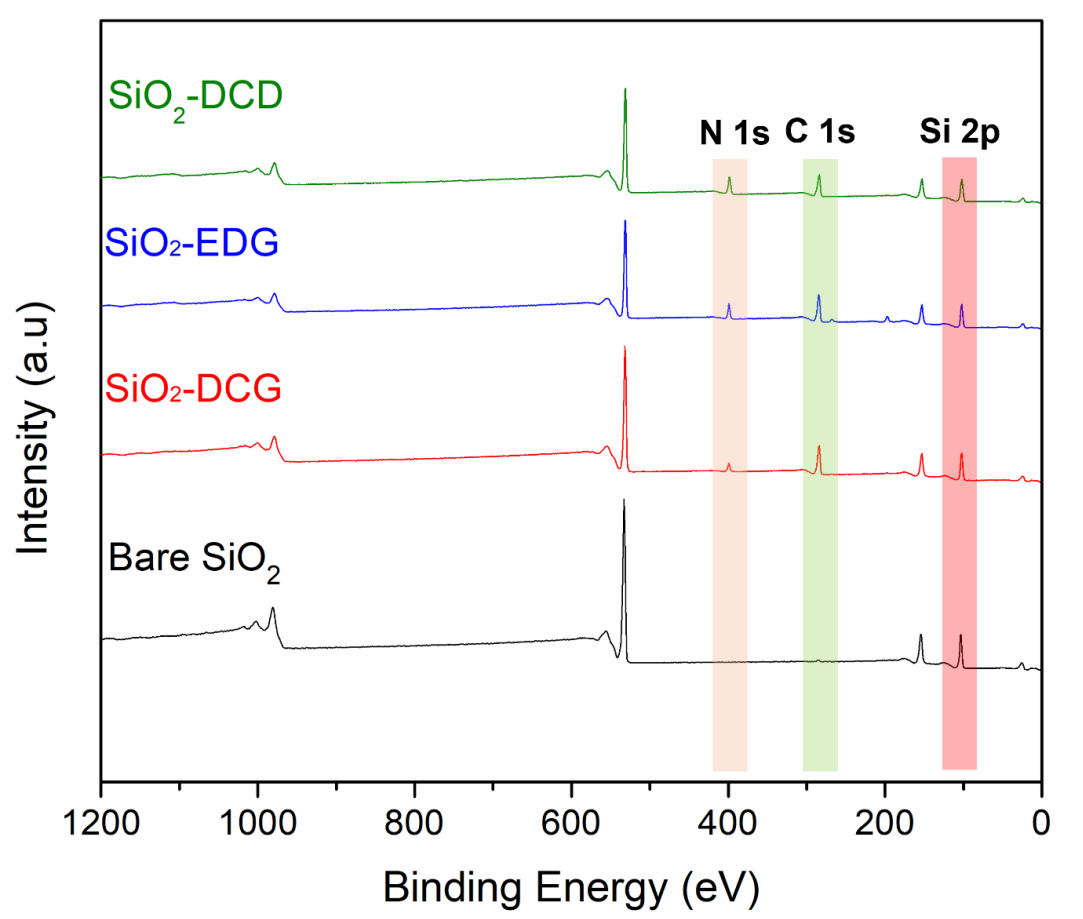


Figure S2: XPS Survey scan for bare SiO_2, SiO_2-DCG, SiO_2-EDG and SiO_2-DCD catalysts.

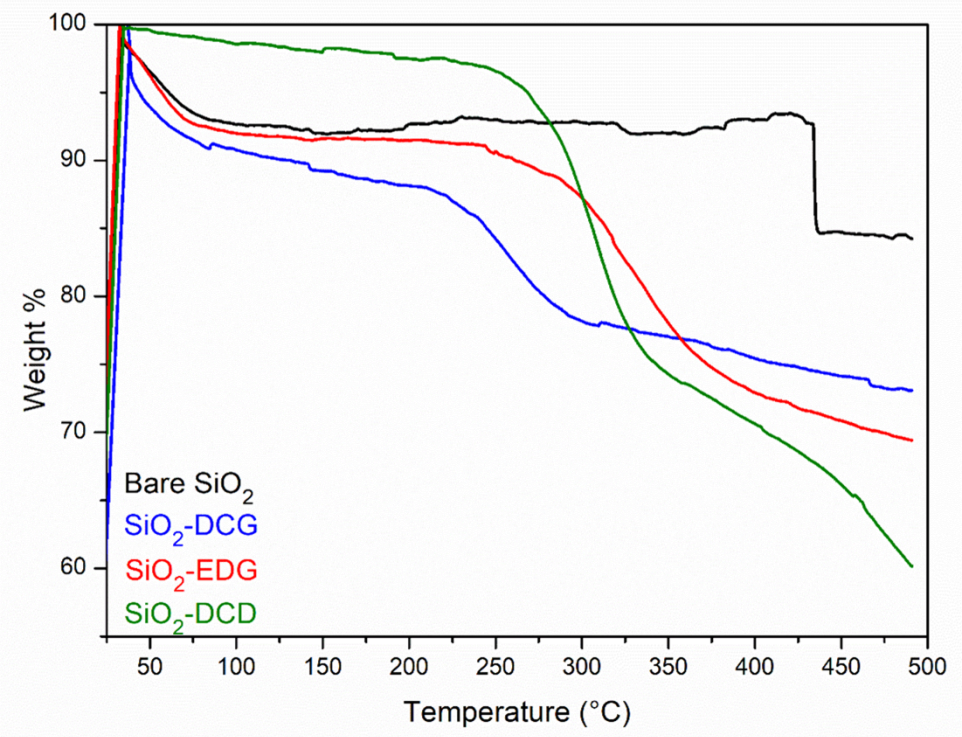


Figure S3: Thermogravimetric analysis of bare SiO_2, SiO_2-DCG, SiO_2-EDG and SiO_2-DCD. The absence of initial mass loss at 100 °C for SiO_2-DCD was attributed to more thorough drying, resulting in lower residual water content.

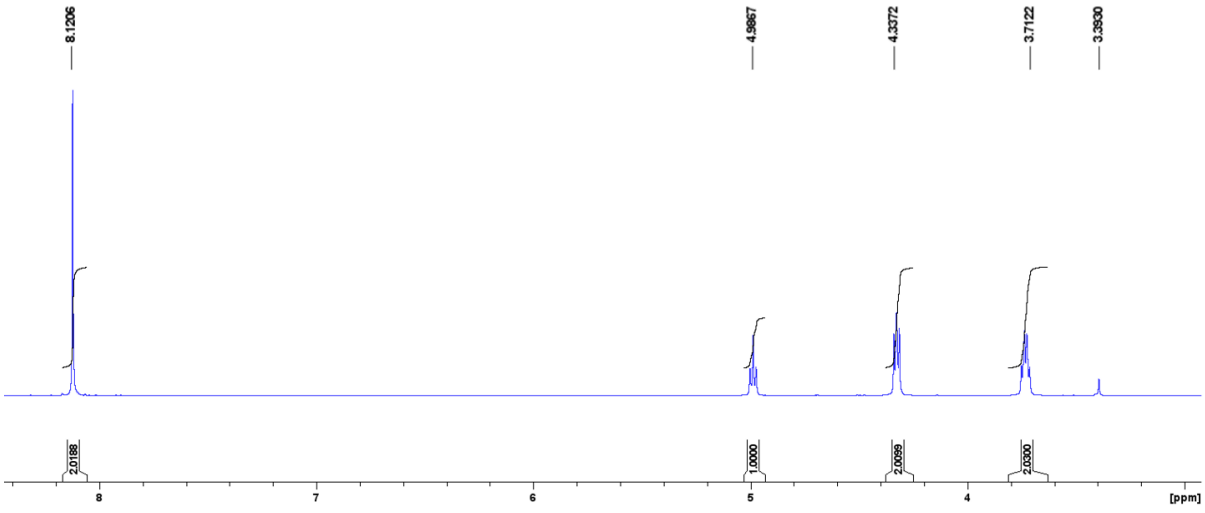


Figure S4: 1H NMR of the product BHET

NMR analysis confirmed that no formation of dimers or oligomers occurred and that BHET was the only product formed in the reaction. The 1H NMR spectrum of BHET can be seen in figure S5, where the four main peaks were a singlet at 8.12 ppm corresponding to an aromatic ring, an OH triplet at 4.96 ppm, CH_2 triplet at 4.33 ppm and CH_2 quartet at 3.71 ppm. Residual solvent d_6-DMSO was located at 2.51 ppm. The results are in good agreement with literature values of BHET.

Table S3: Optimisation of microwave PET depolymerisation parameters.

Catalyst	Time	Stir Speed	Temperature	Conversion PET
No catalyst	40 min	960 rpm	190 °C	0 %
No catalyst	40 min	960 rpm	210 °C	10 %
SiO2 (bare)	40 min	960 rpm	190 °C	10 %
SiO2 (bare)	40 min	960 rpm	210 °C	30 %
SiO_2-DCG	30 min	960 rpm	190 °C	6 %
SiO_2-DCG	30 min	960 rpm	200 °C	20 %
SiO_2-DCG	30 min	960 rpm	210 °C	50 %
SiO_2-DCG	40 min	960 rpm	210 °C	81 %
SiO_2-DCD	30 min	960 rpm	190 °C	23 %
SiO_2-DCD	30 min	960 rpm	200 °C	39 %
SiO_2-DCD	30 min	960 rpm	210 °C	93 %
SiO_2-DCD	40 min	960 rpm	210 °C	100 %
SiO_2-DCD	40 min	256 rpm	210 °C	85 %
SiO_2-EDG	30 min	960 rpm	190 °C	4 %
SiO_2-EDG	30 min	960 rpm	200 °C	16 %
SiO_2-EDG	30 min	960 rpm	210 °C	85 %
SiO_2-EDG	40 min	960 rpm	210 °C	100 %

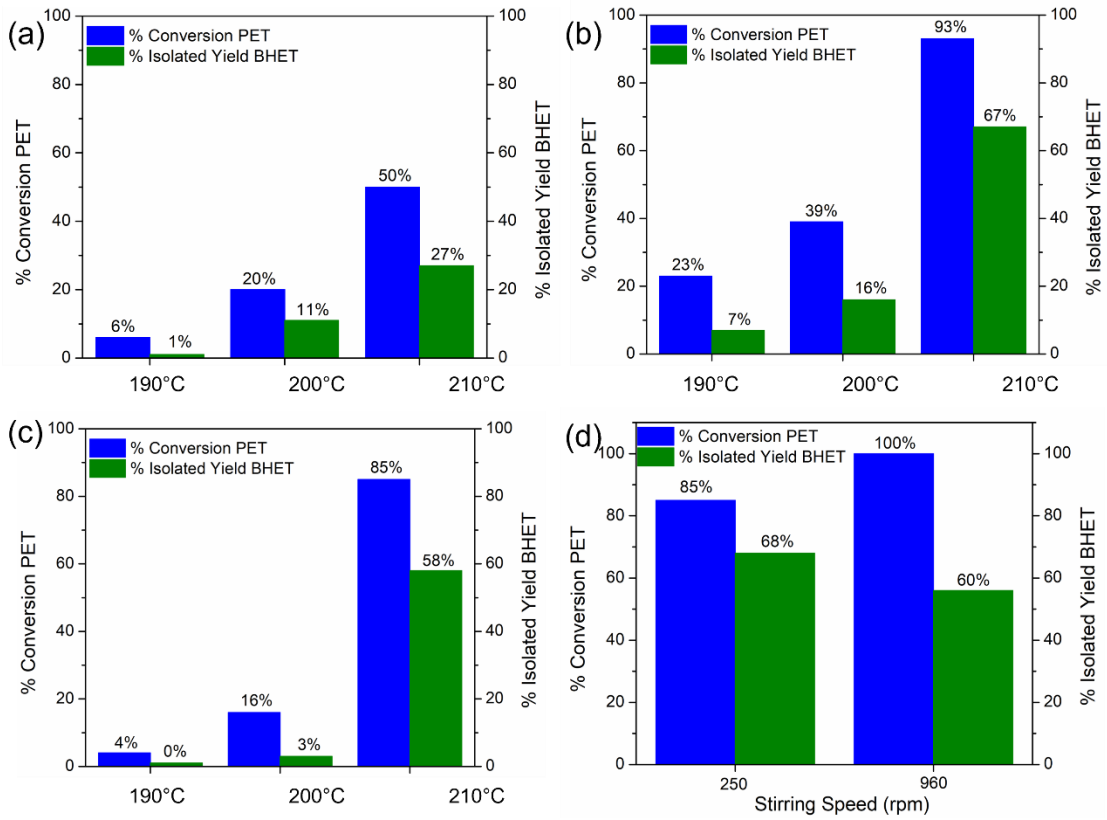


Figure S5: Microwave assisted glycolysis of PET under different reaction temperatures for (a) SiO_2-DCG, (b) SiO_2-EDG and (c) SiO_2-DCD and catalysts (d) Stir speed optimisation.

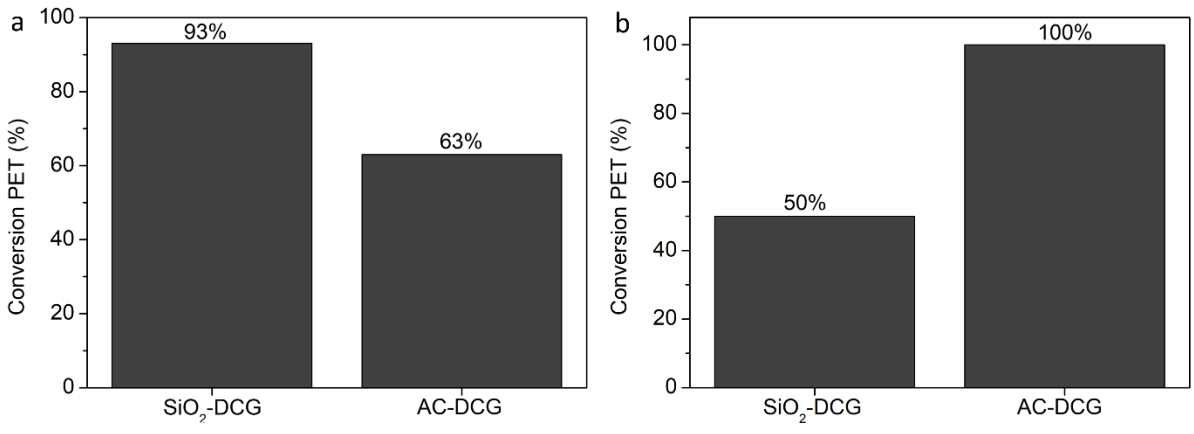


Figure S6: Comparison of PET glycolysis using DCG ligands supported on activated carbon and SiO_2 using a) conventional heating at a temperature of 190 °C and b) microwave-assisted heating at a temperature of 210 °C.

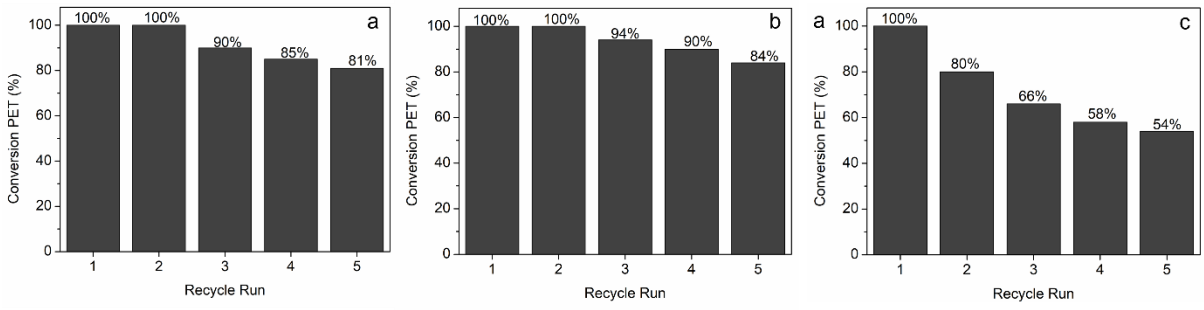


Figure S7: Recyclability performance of the SiO_2-DCD catalyst under optimised thermal conditions and (b) optimised MW conditions (c) SiO_2-DCG catalyst under thermal conditions.

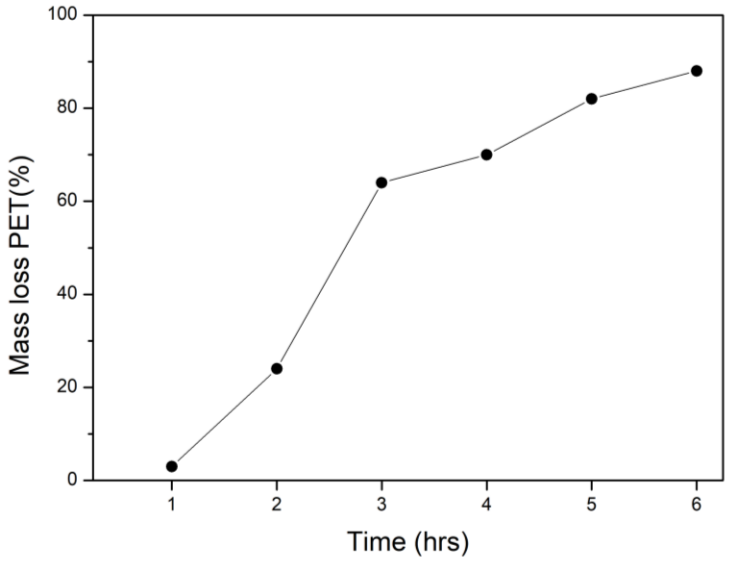


Figure S8: Time series of mass loss PET using 1,4 butanediol as a solvent.

Table S4: Reaction optimisation of methanolysis of PLA under microwave irradiation.

Catalyst	MeOH	THF	Temp	Time	Stirring	Mass Loss PLA	Oligomers	MeLa
EDG	2 ml	3 ml	80 °C	30 min	256 rpm	0 %	-	-
DCD	2 ml	3 ml	80 °C	30 min	256 rpm	35 %	-	-
DCG	2 ml	3 ml	80 °C	30 min	960 rpm	14 %	-	-

EDG	2 ml	3 ml	80 °C	30 min	960 rpm	5 %	-	-
DCD	2 ml	3 ml	80 °C	30 min	960 rpm	7 %	-	-
DCG	5 ml	-	130 °C	30 min	960 rpm	96 %	100 %	trace
DCG	2 ml	3 ml	130 °C	30 min	960 rpm	96 %	100 %	trace
DCG	1 ml	4 ml	130 °C	30 min	960 rpm	91 %	100 %	trace
EDG	2 ml	3 ml	130 °C	30 min	960 rpm	84 %	100 %	-
DCG	2 ml	3 ml	130 °C	30 min	960 rpm	100 %	70 %	30%
DCD	2 ml	3 ml	130 °C	30 min	960 rpm	97 %	70 %	12 %
DCG	2 ml	3 ml	130 °C	90 min	960 rpm	100 %	68 %	30%

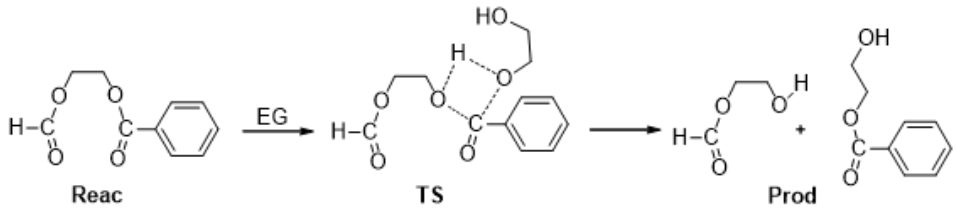
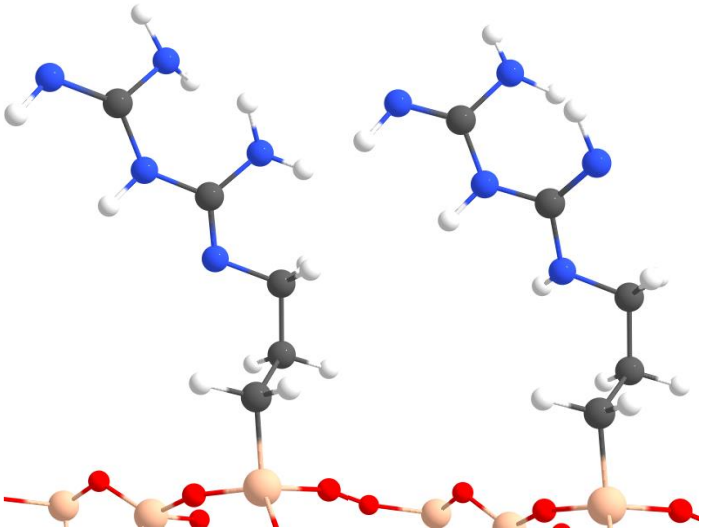


Figure S9. Reaction model used for the benchmarking study.

Table S5. Computed relative energies (in kcal mol^{-1}) for the reaction model used in the benchmarking study. Optimised geometries were carried out at PBE-D3(BJ)/DZVP theory level and single point energy calculations at DLPNO-CCSD(T). In parenthesis, the relative error (in %) for the potential energy barrier is also shown.

System	PBE/DZVP	DLPNO-CCSD(T)
Reac	0.00	0.00
TS	36.05	37.79 (4.6%)
Prod	-7.22	-5.36



(a) **(b)**

Figure S10 (a): Optimised structure for the SiO_2-DCD tautomer with one primary amine, two secondary amine and two imines. **(b)** Optimised structure for the DCD@SiO_2 tautomer with two primary amines, one secondary amine and two imines. Colour scheme: grey for C, red for O, white for H, blue for N and beige for Si.

Table S6. Collected the relative Gibbs energies at 190 °C in kcal mol^{-1} for the uncatalysed PET depolymerisation reaction considering 1, 2, 3 and 4 units of ethylene glycol (EG) involved in the transition state.

System	**1 EG** *kcal mol^{-1}*	**2 EG** *kcal mol^{-1}*	**3 EG** *kcal mol^{-1}*	**4EG** *kcal mol^{-1}*
1	0.00	0.00	0.00	0.00
TS_{1-2}	24.26	19.29	17.06	16.43
2	12.82	12.82	12.82	12.82

References

(1) Liu, Y.; Yao, X.; Yao, H.; Zhou, Q.; Xin, J.; Lu, X.; Zhang, S. Degradation of poly(ethylene terephthalate) catalyzed by metal-free choline-based ionic liquids. *Green Chemistry* 2020, *22* (10), 3122-3131, 10.1039/D0GC00327A. DOI: 10.1039/D0GC00327A.

(2) Wang, H.; Liu, Y.; Li, Z.; Zhang, X.; Zhang, S.; Zhang, Y. Glycolysis of poly(ethylene terephthalate) catalyzed by ionic liquids. *European Polymer Journal* 2009, *45* (5), 1535-1544. DOI: https://doi.org/10.1016/j.eurpolymj.2009.01.025.

(3) Wang, Q.; Yao, X.; Tang, S.; Lu, X.; Zhang, X.; Zhang, S. Urea as an efficient and reusable catalyst for the glycolysis of poly(ethylene terephthalate) wastes and the role of hydrogen bond in this process. *Green Chemistry* 2012, *14* (9), 2559-2566, 10.1039/C2GC35696A. DOI: 10.1039/C2GC35696A.

(4) Yue, Q. F.; Wang, C. X.; Zhang, L. N.; Ni, Y.; Jin, Y. X. Glycolysis of poly(ethylene terephthalate) (PET) using basic ionic liquids as catalysts. *Polymer Degradation and Stability* 2011, *96* (4), 399-403. DOI: https://doi.org/10.1016/j.polymdegradstab.2010.12.020.

(5) Jehanno, C.; Flores, I.; Dove, A. P.; Müller, A. J.; Ruipérez, F.; Sardon, H. Organocatalysed depolymerisation of PET in a fully sustainable cycle using thermally stable protic ionic salt. *Green Chemistry* 2018, *20* (6), 1205-1212, 10.1039/C7GC03396F. DOI: 10.1039/C7GC03396F.

(6) Fan, C.; Zhang, L.; Zhu, C.; Cao, J.; Xu, Y.; Sun, P.; Zeng, G.; Jiang, W.; Zhang, Q. Efficient glycolysis of PET catalyzed by a metal-free phosphazene base: the important role of EG−. *Green Chemistry* 2022, *24* (3), 1294-1301, 10.1039/D1GC03885K. DOI: 10.1039/D1GC03885K.

(7) Sun, J.; Liu, D.; Young, R. P.; Cruz, A. G.; Isern, N. G.; Schuerg, T.; Cort, J. R.; Simmons, B. A.; Singh, S. Solubilization and Upgrading of High Polyethylene Terephthalate Loadings in a Low-Costing Bifunctional Ionic Liquid. *ChemSusChem* 2018, *11* (4), 781-792. DOI: https://doi.org/10.1002/cssc.201701798 (accessed 2024/01/15).

(8) Marullo, S.; Rizzo, C.; Dintcheva, N. T.; D'Anna, F. Amino Acid-Based Cholinium Ionic Liquids as Sustainable Catalysts for PET Depolymerization. *ACS Sustainable Chemistry & Engineering* 2021, *9* (45), 15157-15165. DOI: 10.1021/acssuschemeng.1c04060.

(9) Zhu, C.; Yang, L.; Chen, C.; Zeng, G.; Jiang, W. Metal-free recycling of waste polyethylene terephthalate mediated by TBD protic ionic salts: the crucial role of anionic ligands. *Physical Chemistry Chemical Physics* 2023, *25* (41), 27936-27941, 10.1039/D3CP03590E. DOI: 10.1039/D3CP03590E.

(10) Wang, Z.; Jin, Y.; Wang, Y.; Tang, Z.; Wang, S.; Xiao, G.; Su, H. Cyanamide as a Highly Efficient Organocatalyst for the Glycolysis Recycling of PET. *ACS Sustainable Chemistry & Engineering* 2022, *10* (24), 7965-7973. DOI: 10.1021/acssuschemeng.2c01235.

(11) Brunauer, S.; Emmett, P. H.; Teller, E. Adsorption of Gases in Multimolecular Layers. *Journal of the American Chemical Society* 1938, *60* (2), 309-319. DOI: 10.1021/ja01269a023.

(12) Hutter, J.; Iannuzzi, M.; Schiffmann, F.; VandeVondele, J. cp2k: atomistic simulations of condensed matter systems. *WIREs Computational Molecular Science* 2014, *4* (1), 15-25. DOI: https://doi.org/10.1002/wcms.1159 (accessed 2023/10/18).

(13) Ugliengo, P.; Sodupe, M.; Musso, F.; Bush, I. J.; Orlando, R.; Dovesi, R. Realistic Models of Hydroxylated Amorphous Silica Surfaces and MCM-41 Mesoporous Material Simulated by Large-scale Periodic B3LYP Calculations. *Advanced Materials* 2008, *20* (23), 4579-4583. DOI: https://doi.org/10.1002/adma.200801489 (accessed 2023/10/18).

(14) Perdew, J. P.; Ruzsinszky, A.; Csonka, G. I.; Vydrov, O. A.; Scuseria, G. E.; Constantin, L. A.; Zhou, X.; Burke, K. Restoring the Density-Gradient Expansion for Exchange in Solids and Surfaces. *Physical Review Letters* 2008, *100* (13), 136406. DOI: 10.1103/PhysRevLett.100.136406.

(15) Grimme, S.; Antony, J.; Ehrlich, S.; Krieg, H. A consistent and accurate ab initio parametrization of density functional dispersion correction (DFT-D) for the 94 elements H-Pu. *The Journal of Chemical Physics* 2010, *132* (15). DOI: 10.1063/1.3382344 (accessed 10/18/2023).

(16) Goedecker, S.; Teter, M.; Hutter, J. Separable dual-space Gaussian pseudopotentials. *Physical Review B* 1996, *54* (3), 1703-1710. DOI: 10.1103/PhysRevB.54.1703.

(17) Lippert, G.; Hutter, J.; Parrinello, M. A hybrid Gaussian and plane wave density functional scheme. *Molecular Physics* 1997, *92*, 477-488. DOI: 10.1080/002689797170220.
(18) Andreussi, O.; Dabo, I.; Marzari, N. Revised self-consistent continuum solvation in electronic-structure calculations. *The Journal of Chemical Physics* 2012, *136* (6). DOI: 10.1063/1.3676407 (accessed 10/18/2023).

Chapter 5:

Method Development: Heterogeneous Catalysts for Fenton Oxidation of LDPE

Preface

This chapter presents the method development for designing heterogeneous Fenton-type catalysts for the oxidative degradation of low-density polyethylene (LDPE) to carboxylic acid products, minimising over oxidation to gaseous products. Two distinct catalyst groups were developed in parallel: metal oxide composites and carbon-based catalysts. Among the investigated catalyst, the best performing catalyst was a Fe_2O_3-CeO_2 metal oxide composite which was further developed into a published manuscript outlined in Chapter 6. The efficacy of the doped carbon Fenton catalysts influenced the use of biochar Fenton catalysts in Chapter 7. This chapter outlines the synthesis and design of these catalyst systems, catalyst characterisation, method development and reaction optimisation.

5.1 Introduction – A focus on Polyolefin Plastics

Chemical recycling of plastic waste has gained significant traction in the last decade. As current methods such as mechanical recycling and incineration with energy recovery fail to address the escalating accumulation of global plastic waste, research is focusing more on innovative technologies to recover valuable chemicals from these waste materials. In the past 10 years, the number of literature reports on the chemical recycling of polyesters such as PET have increased drastically as they readily undergo depolymerisation reactions such as hydrolysis, alcoholysis, methanolysis and aminolysis at relatively mild conditions owing to the presence of reactive oxygen and aromatic groups in their structures.[1] In contrast, comparatively fewer studies have focused on the chemical recycling of polyolefins such as polyethylene (PE) and polypropylene (PP). These polymers are characterised by highly stable, inert hydrocarbon chains, making them considerably more resistant to depolymerisation than condensation polymers such as polyesters. A comparison of the number of literature reports on

the chemical recycling of PET compared with chemical recycling of LDPE from 2015 - 2024 is illustrated in Figure 1 a). In 2015 literature including 'chemical recycling PET' had reached 34 publications (Web of Science) while literature including 'chemical recycling LDPE' only reached 10 publications. Literature on the chemical recycling of PET increased dramatically from 2015 to 2024, with the most recent data recording 316 publications on the chemical recycling of PET in 2024. There is a significant difference between publications on PET and LDPE, as the most recent data reported only 52 publications on the chemical recycling of LDPE in 2024. When these research trends are compared with global production volumes, the imbalance becomes more evident (Figure 1). PET demand increased from 20 Mt in 2015 to 29 Mt in 2024. In contrast, LDPE demand was significantly higher, rising from 93 Mt in 2015 to 116 Mt in 2024. The disparity in global production can be attributed to the lower production cost and wider application range of LDPE, which is commonly used in single-use products with short life cycle. Additionally, PET is more rigid making it better suited for mechanical recycling, whereas the high ductility and flexibility of LDPE make it difficult to process, making it less suitable for mechanical recycling.

The high production rate and low recycling rate of LDPE when compared with PET highlights the urgent need to improve chemical recycling pathways for LDPE. Addressing this gap in research is essential to align recycling technologies with current market demands. Consequently, this chapter and the subsequent sections of this thesis focus on the development of chemical recycling strategies for LDPE.

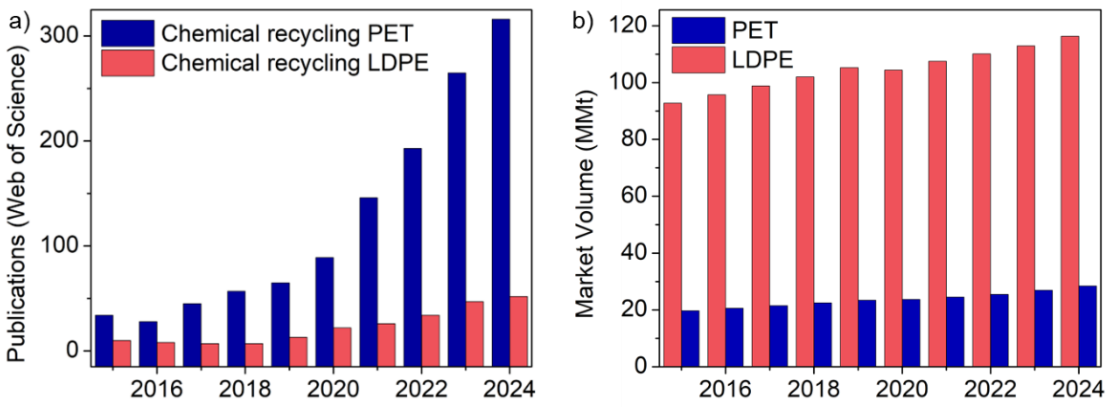
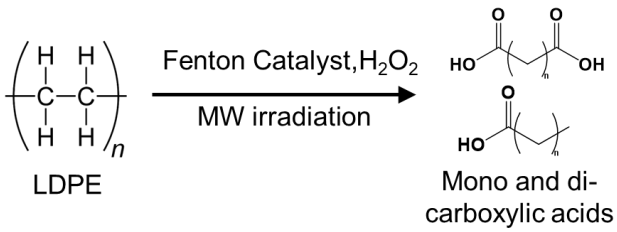


Figure 1: Number of publications containing "Chemical recycling PET" compared with "Chemical recycling LDPE" searched on Web of Science.[2, 3] Plastic market volume in million metric tonnes of LDPE and PET, figures obtained from Statistica.[4, 5]

Catalytic pyrolysis is a valuable chemical recycling pathway for polyolefins, and the addition of microwave-assisted heating can drastically shorten reaction times due to localised plasma and hot spot formations.[7] The value-added product obtained from pyrolysis can be tuned based on the catalyst system. For example, iron-based catalysts are reported to yield H_2 and valuable carbon nanomaterials such as carbon nanotubes by providing nucleation sites for their growth[8] while zeolite-based catalysts will yield valuable aliphatic or aromatic molecules which are useful fuels.[9] Efforts to achieve milder reaction conditions include the microwave-assisted oxidative degradation of LDPE in nitric acid reported by Bäckstrom and coworkers[10] which could proceed at much lower temperatures (180 °C) than pyrolysis reactions (> 300 °C). This process yielded a mixture of dicarboxylic acids, mainly succinic acid owing to a favourable transition state via a "zip" fragmentation mechanism. However, the use of highly corrosive strong oxidisers such as HNO_3 is unfavourable both for industry scale-up and from a green chemistry perspective. Another attractive chemical recycling pathway for polyethylene is Fenton oxidation, which is favourable due to the use of aqueous media. Hu *et al.*[11] reported the thermal Fenton degradation of a mixture of microplastics (high-density polyethylene (HDPE), polyvinyl chloride (PVC), polystyrene (PS), LDPE and PP) to yield CO_2 and H_2O at 140 °C for 12 h using a homogeneous

Fe^{2+} catalyst. Ortiz *et al*.[12] employed Fenton oxidation for microplastics containing a mixture of PET, PVC, PE, and PS using a homogeneous Fe^{3+} catalyst in a milling system at 80 ℃ over 3 – 5 2 min milling cycles. Surface oxidation and degradation of the MPs was observed to a further degree for PET and PS due to reactive aromatic groups. PP, PE and PVC were more resistant to degradation, and the presence of Cl in PVC made it the most resistant to oxidation. To overcome the chemical inertness and stability of the PE chain, Chow *et al.*[13] reported a pretreatment with chlorosulfuric acid and grafting of Fe^{3+} to the polymer chain which facilitated the Fenton oxidation of LDPE and HDPE to proceed in 20 min at room temperature and in the dark. One drawback of this method is the use of chlorosulfuric acid, which is toxic and highly corrosive. One method to avoid use of toxic chemicals was reported by Nguyen *et al.*[14] and involved the simultaneous mechano-cracking and Fenton oxidation of polyethylene. The process proceeded at room temperature with milling times from 1 – 2 hours and yielded oligomeric products with alcohol and carboxylic acid groups which can be useful intermediates for fuel production. In the literature, Fenton oxidation of plastics is often reported to result in complete mineralisation to gaseous products. However, little attention has been given to the potential formation of valuable oxygenated intermediates. Consequently, the characterisation and quantification of oxygenated species generated from the Fenton oxidative degradation of LDPE remain largely underexplored.

Initially, microwave-assisted HNO_3 oxidative degradation of LDPE as reported by Bäckstrom and co workers[10] was evaluated in our group, however, the addition of a catalyst to the system did not significantly enhance the reaction. To address both performance and sustainability, the focus then shifted towards greener reagents, with particular emphasis on Fenton oxidation which takes place in aqueous H_2O_2 and is more environmentally preferable than HNO_3 as it will decompose to H_2O and O_2 and has low environmental persistence while HNO_3 will generate toxic NO_x by-products. The microwave-assisted Fenton oxidation of LDPE yields mixtures of mono and dicarboxylic acids, illustrated in **scheme 1**.



Scheme 1: Microwave-assisted Fenton oxidation of LDPE.

Traditionally, a Fenton catalyst involves homogeneous Fe ions in the presence of H_2O_2 to yield $HO^{\bullet}$ and $HOO^{\bullet}$. Recently, heterogeneous Fe catalysts such as Fe_2O_3 and Fe_3O_4 are reported to have several benefits over homogeneous Fe salts including higher stability at a wider pH range and significantly reduced Fe leaching and sludge formation.[15] In the presence of H_2O_2, the oxidation of Fe^{2+} to produce $^{\bullet}OH$ radicals has much faster reaction kinetics (k = 55 $M^{-1}s^{-1}$) than the reduction of Fe^{3+} to produce $HOO^{\bullet}$ radicals (k = $2x10^{-3}$ $M^{-1}s^{-1}$). One drawback of heterogeneous Fenton catalysts is the strongly bonded Fe oxides in heterogeneous catalysts exhibit much lower $Fe^{2+} \leftrightarrow Fe^{3+}$ reactivity than homogeneous Fe salts. To improve this reactivity and stability, a second metal oxide such as Mn, Cu, Ce or Co are often employed to modify the electronic environments and coordination of redox active metal ions which can and with stabilisation and regeneration of Fe^{2+}/Fe^{3+} in a Fenton system.[16] These considerations motivated the development of metal oxide composite catalysts in this chapter. The metal composites investigated were Fe_2O_3-CuO, Fe_2O_3-CeO_2 and Fe_2O_3-BiOCl, as well as pristine Fe_2O_3.

The second catalyst group developed in this work were carbon-based Fenton catalysts. Specifically, activated carbon (AC) was doped using ionic liquid (IL) precursors and used as a support to immobilise Fe^{3+}. Grafting Fe species onto support materials such as (AC) can improve dispersion of Fe, prevent aggregation and enhance catalyst surface area.[17] Iron supported on N-doped carbon displays excellent catalytic activity and stability for the Fenton-type degradation of *p*-nitrophenol from wastewater, with negligible Fe leaching.[20] The incorporation of O and N functionalities to AC can also improve Fe immobilisation and microwave (MW) adsorption properties of the catalyst. ILs have been widely researched for catalytic applications due to their interesting properties such as low melting point, non-

volatility, electrical conductivity, tuneability and high thermal stability.[18] Sahraie *et al.*[19] demonstrated that IL precursors carbonise at high temperatures in the presence of AC to form doped carbon materials with excellent thermal stabilities and electrical conductivity. These catalysts demonstrated excellent activity as oxidation-reduction electrocatalysts due to the electronic properties of the heteroatom doped graphitic materials. The IL/Fe-doped carbon catalysts used in this study were adapted from the method reported by Sahraie and co-workers[19] as they share structural and chemical similarities with reported carbon/Fe-based high-performing Fenton catalysts.

In addition to synthetic carbons, biomass-derived doped carbons represent an attractive sustainable alternative, enabling waste valorisation while providing high-performance supports for Fenton catalysis. Biomass can be thermally treated in the presence of Fe salts to form Fe-doped carbon nanomaterials with enhanced surface area that exhibit excellent Fenton catalytic activity for dye degradation.[21-23] The use of biochar as a Fenton-type catalyst is discussed in greater detail in Chapter 7 of this thesis.

5.2 Experimental

Iron (III) chloride, activated carbon, succinic acid, glutaric acid, formic acid, acetic acid, adipic acid, propionic acid, butyric acid, nitric acid, sulfuric acid, CeO_2 nanopowder, $Fe(SO_4)_3$ and $CuSO_4$ were purchased from Sigma Aldrich. 1-ethyl, 3 methyl imidazolium dicyanamide, 1-ethyl, 3-methyl imidazolium acetate and BiOCl were purchased from abcr Ireland. LDPE was selected from Corning centrifuge tube bags, washed with deionised water, cut into 1x1 mm squares and dried before use. LDPE powder (500 µm), with a density of 0.91 - 0.96 gml^{-1} was purchased from Fisher Ireland.

See Experimental Chapter 2 for details on materials characterisation techniques.

5.2.1 Synthesis of metal oxide catalysts

i) Fe_2O_3

2.43g of $FeCl_3$ and 2.01 g $FeSO_4$ were added to a 100 mL RBF along with 50 mL deionised water. The solution was sonicated for 30 minutes before the pH was adjusted to 12 using saturated NaOH solution with stirring. The resulting solution was then refluxed at 85 °C for 16 h. The solid Fe_2O_3 particles were collected by suction filtration, washed with water and dried overnight in air at 75 °C.

ii) Fe_2O_3-BiOCl

1 g Fe_2O_3 and 0.5 g BiOCl were placed in a 100 mL RBF along with 20 mL deionised water and the mixture was sonicated for 5 h. The resulting particles were collected by centrifuging at 1000 rpm for 2 minutes. These were washed with water and then ethanol and dried overnight in air at 75 °C.[27]

iii) Fe_2O_3-CuO

1.46 g Fe_2O_3 was added to a 100 mL RBF along with 1 g $CuSO_4$ and 50 mL deionised H_2O and allowed to stir at 250 rpm for 10 minutes. The solution was then heated to 90 °C and a pH of 12 was achieved by adding saturated NaOH dropwise. The solution was left to reflux for 1 h before being left to cool. The precipitate was collected by suction filtration, washed with excess water and dried overnight in air at 75 °C.

iv) Fe_2O_3-CeO_2

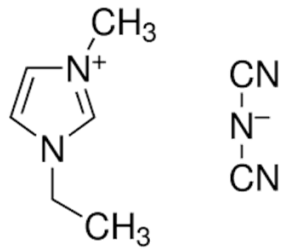
0.5 g Fe_2O_3 and 0.5 g CeO_2 nanopowder were dispersed in 50 mL solution of 0.2 M NaOH (0.399 g in 50 mL DI H_2O) The mixture was stirred at 80 °C under N_2 for 1 h before being filtered and washed with ethanol and deionised H_2O. The resulting solid was dried overnight in air at 75 °C.

5.2.2 Synthesis of ionic liquid-doped carbon catalysts

IL-CN and IL-OAc

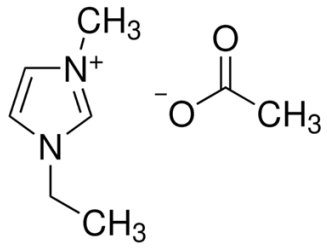
400 mg of activated carbon was added to a beaker along with 550 mg of IL salt (1-ethyl, 3 methyl imidazolium dicyanamide or 1-ethyl, 3-methyl imidazolium acetate shown in Figure 2 i) and ii), respectively) and 311 mg of $FeCl_3$ and dispersed in 100 mL DI H_2O. The mixture was stirred at 250 rpm at room temperature for 24 h. The water was then removed using a rotary evaporator. The remaining solid was placed in a drying oven at 70 °C overnight to remove any residual water. The sample was then placed in a quartz boat crucible in a tube furnace and first treated at 100 °C for 1 h, and then at 900 °C for 2 h under Ar (4 $Lmin^{-1}$) before being allowed to cool naturally.

i)



1-ethyl, 3 methyl imidazolium dicyanamide

ii)



1-ethyl, 3 methyl imidazolium acetate

Figure 2: Structure of i) 1-ethyl, 3 methyl imidazolium dicyanamide and ii) 1-ethyl, 3-methyl imidazolium acetate

5.2.3 Fenton Oxidation Reactions

0.3 g LDPE powder, 0.06 – 0.12 g solid catalyst, and 10 mL 3-9 % (w/w) H_2O_2 solution was added to a Milestone Flexiwave high pressure SK-15 Teflon vessel along with a stir bar. The pH of the solution was adjusted to 1 using conc. HNO_3. Optimal reaction conditions were a 10 min ramp time, 3 h hold at 180 °C, stir speed 900 rpm and 800 W upper power limit although the power output stabilised ~ 300 W for each reaction. Once the reaction was complete and had cooled, it was Buchner filtered to separate the catalyst and any unreacted LDPE from the product mixture. The mass loss of LDPE was calculated by the equation below.

$$Mass\ Loss\ LDPE = \frac{W_0 - W_1}{W_0}\ x\ 100\ \%$$ **Eqn. 1**

Where W_0 is the initial weight of LDPE added to the reaction and W_1 is the weight of unreacted LDPE after the reaction. The product mixture was characterised by HPLC.

5.2.4 Product Analysis by High Performance Liquid Chromatography (HPLC)

See Experimental Chapter 2 for details on column specifications and sample preparation. The concentration of each product present in the sample was calculated against calibration curves that were made by standards of carboxylic acids: succinic, formic, glutaric, acetic, adipic, propionic, butyric and pimelic acid, shown in Figure 3. The yield was calculated relative to the initial weight of LDPE as shown below.

$$Mass\ of\ end\ product\ (g) = Conc\ of\ end\ product\ (gL^{-1})\ x\ reaction\ volume\ (L)$$ **Eqn. 2**

$$Yield\ of\ Organic\ Products\ (\%) = \frac{Mass\ of\ end\ products\ (g)}{Mass\ of\ starting\ material\ (g)}\ x\ 100\ \%$$ **Eqn. 3**

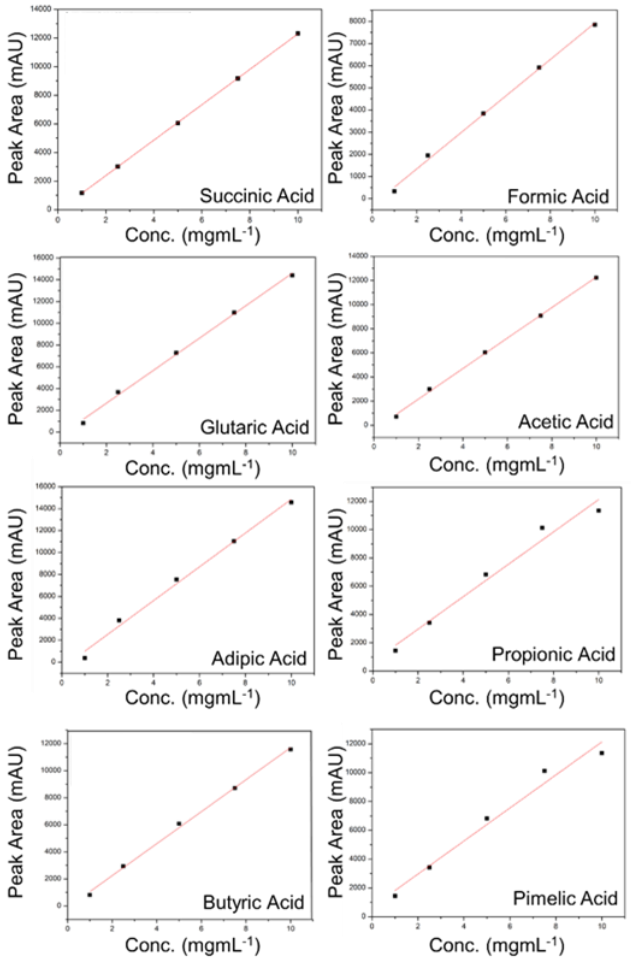


Figure 3: HPLC calibration curve results for the acid standards.

5.3 Results and Discussion

5.3.1 Synthesis and Characterisation of Metal Oxide Composites as Heterogeneous Fenton Catalysts

Three Fe_2O_3-based oxides were synthesised using Bi, Cu and Ce as secondary metal oxides. These metal oxides were chosen based on literature reports that have identified them as metals that promote synergistic effects with Fe in Fenton-type reactions.

Fe_2O_3-BiOCl: Selected for its MW absorbing properties and efficiency as a Fenton catalyst. Shen *et al*.[27] reported Fe_3O_4-BiOCl to be a highly efficient microwave-assisted Fenton catalyst for the degradation of toluene nitration wastewater.

Fe_2O_3-CuO: Chosen as it is well reported to exhibit strong synergistic behaviour when paired with Fe_2O_3 for photo-Fenton reactions.[28]

Fe_2O_3-CeO_2: Selected as similar composites have been reported to exhibit synergistic effects and enhance for Fenton oxidation of pollutants.[29]

X-ray photoelectron spectroscopy (XPS) was used to assess surface elemental composition, metal oxidation states, and active oxygen species that directly influence catalytic activity, and shown in Figure 4. The Fe 2p core levels for each catalyst are shown in Figure 4 a). The Fe_2O_3 showed two distinct peaks at 711.5 eV and 729.6 eV, which were assigned to Fe $2p_{3/2}$ and Fe $2p_{1/2}$, respectively. A satellite peak was observed at 720 eV and all peaks were in excellent agreement with those previously reported for Fe_2O_3.[30] For the bimetallic catalysts, a shift in the Fe $2p_{3/2}$ peak was observed indicative of a change in Fe electronic environment on coordination to a secondary metal. This was most pronounced for Fe_2O_3-CuO where disappearance of the satellite peak is noted, suggesting the formation of Fe^{2+}. Stronger metal-metal interaction may be expected for the CuO catalyst, as it was the only catalyst synthesised by precipitation method.

The O 1s XPS core levels for each of the catalysts is shown in Figure 4 b). Three O environments were identified for each bimetallic composite which were attributed to a metal-oxygen bond (M-O), surface OH groups and adsorbed surface H_2O.[31] In metal-oxide systems, the M–O peak is typically observed in the binding energy range of 529 - 531 eV. For the Fe_2O_3, Fe_2O_3–BiOCl, Fe_2O_3–CuO, and Fe_2O_3–CeO_2 catalysts, the peak appears at 529.5, 530.1, 529.6, and 529.1 eV, respectively, reflecting variations in the electronic environment caused by the different metals. The presence of a peak at 530.1 eV for Fe_2O_3-BiOCl has been reported to indicate the existence of O^{2-} from the Bi-O bond.[32] Lower binding energies for the Fe_2O_3-CeO_2 catalyst have been previously reported for lattice O environments for CeO_2.[33] The shifts in binding energies for the OH and OH_2 environments in the samples can be influenced by the presence of defect sites and the electronegativity of the metals.

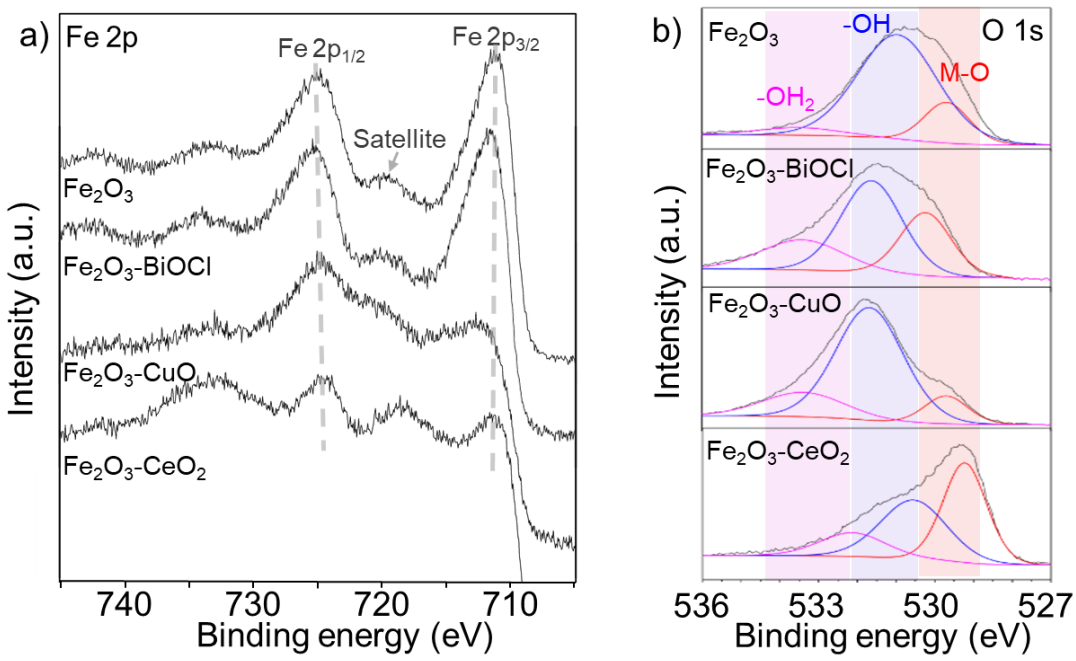


Figure 4: a) Fe 2p core level XPS analysis of metal oxide catalysts, b) O 1s core level XPS analysis of metal oxide catalysts.

The valence states of Bi, Cu and Ce in each of the catalysts were determined using the Bi 4f, Cu 2p and Ce 3d XPS core levels, respectively and the results are shown **in** Figure 5 a)-c). The Bi 4f shows two main peaks at 159.0 eV and 164.3 eV which were attributed to the $4f_{7/2}$ and $4f_{5,2}$ and exhibit a spin orbital doublet splitting of 5.3 eV which confirms the presence of Bi^{3+} in BiOCl.[34] The peaks appearing at 161.2 eV and 166.9 eV were attributed to the Bi $4f_{7/2}$ and Bi $4f_{5/2}$ of Bi_2O_3 indicative of surface oxidation of the BiOCl during synthesis.[35] The Cu 2p spectrum shows two peaks at 934.4 eV and 954.6 eV corresponding Cu $2p_{3/2}$ and Cu $2p_{1/2}$, respectively and are characteristic of Cu^{2+}.[36] Three satellite peaks are also observed at binding energies of 941.2 eV, 943.9 eV and 962.6 eV and confirm the CuO state in Fe_2O_3-CuO.[37] Lastly, the Ce 3d spectrum shows the presence of eight peaks, which can be attributed to $3d_{3/2}$ and $3d_{5/2}$ spin-orbit coupling.[38] The peaks at binding energies of 882.0 eV, 884.2, 888.9 eV and 897.2 eV were assigned to the $3d_{5/2}$ and the peaks at binding energies of 900.9 eV, 902.9 eV, 907.6 eV and 916.9 eV were assigned to the $3d_{3/2}$ ionisation. The peaks at binding energies of 882.0 eV, 888.9 eV, 897.2 eV, 900.9 eV, 907.6 eV and 916.9 eV can all be attributed to Ce^{4+} in the sample and

confirm the dominant species is Ce^{4+}.[39] The presence of peaks at 884 eV and 902.9 eV are indicative of reduction of Ce^{4+} to Ce^{3+} at the catalyst surface.

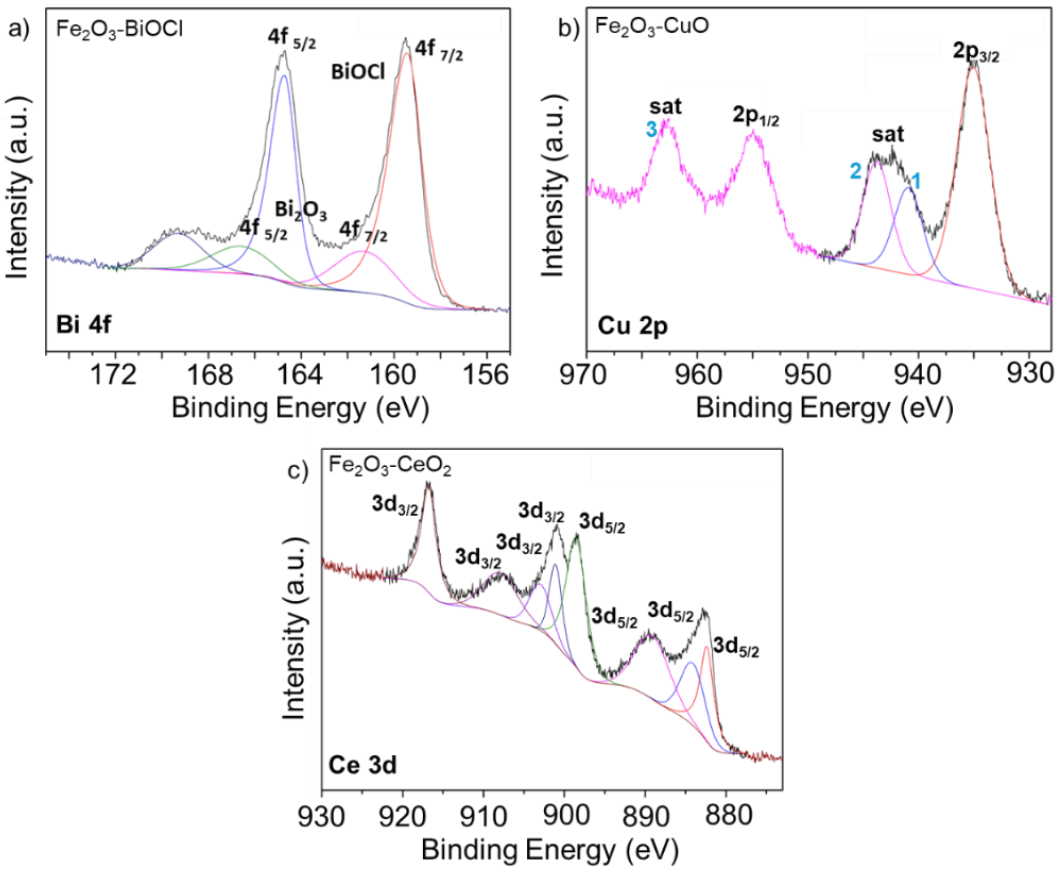


Figure 5: a) Bi 4f XPS core level for Fe_2O_3-BiOCl, b) Cu 2p XPS core level for Fe_2O_3-CuO, Ce 3d XPS core level for Fe_2O_3-CeO_2.

Catalytic evaluation of metal oxide catalysts in Fenton Oxidation of LDPE

The catalytic performance of the metal oxide catalysts in the Fenton oxidative degradation of LDPE was evaluated to assess the synergistic effect relative to Fe_2O_3. For these reactions, pure LDPE powder was used. The results for the screening of the catalysts are shown in Figure 6 a). The Fe-CeO_2 catalyst was the most effective catalyst achieving 100 % mass loss and a 54 % acid yield. The Fe_2O_3-CuO and Fe_2O_3-BiOCl catalysts also gave a 100 % mass loss LDPE, however achieved yields of only 22 % and 26 %, respectively. In terms of mass loss, all metal oxide composites outperformed the Fe_2O_3 catalyst, which

only reached a 74 % mass loss, and all other catalysts resulted in > 90 % mass loss demonstrating a clear synergistic effect across all systems. The Fe_2O_3-MnO_2 catalyst showed relatively poor catalytic activity (90 % mass loss, 19 % yield), so this catalyst was not further characterised.

Another important factor to consider was the metal leaching of the catalyst into the product mixtures. Leaching contaminates the product mixture, deactivates the catalyst and inhibits catalyst recovery and potential recyclability.[40] Figure 6 b) shows images of product mixtures after 3 h of reaction time for each of the catalysts. The Fe_2O_3 (1) and Fe_2O_3-CuO (3) showed clear signs of metal leaching into the product mixture. Red iron sludge was observed for the Fe_2O_3, while some Fe sludge as well as complete blue colouration of the product mixture for Fe_2O_3-CuO, indicative of copper(II) formation. The Fe_2O_3-BiOCl (2) and Fe_2O_3-MnO_2 (5) solutions showed lower levels of leaching, however small red iron sludge particles were visible in the product mixtures. The Fe_2O_3-CeO_2 catalyst showed no visible leaching making it the most advantageous catalyst system. The lower level of leaching for the Fe_2O_3-CeO_2 catalyst may be a reason for the higher acid yield compared to the other catalysts which gave high mass loss but poor acid yield. Metal leaching can promote the formation of homogeneous Fenton species which can further catalyse the conversion of carboxylic acids to CO_2 resulting in over oxidation.[41]

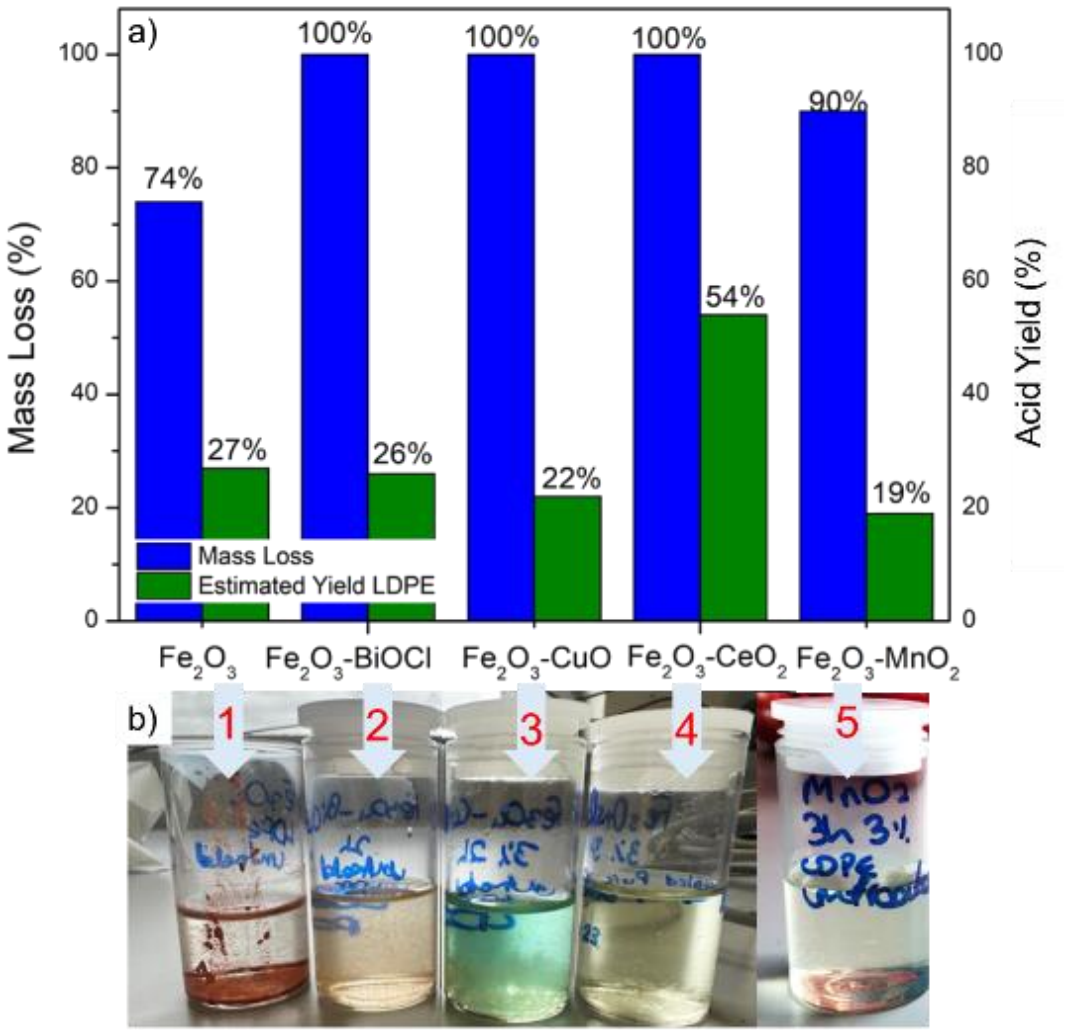


Figure 6: a) acid product mixtures for metal oxide catalysts, b) acid product mixtures after 3h for each of the catalyst systems.

From screening metal oxide composite catalysts, it was evident that the addition of a second metal improved the Fenton catalytic activity in the oxidative degradation of LDPE. The Fe_2O_3-CeO_2 catalyst achieved simultaneous highest mass loss LDPE and acid yield which was attributed to the stability of the catalyst as no metal leaching was observed in the product mixture. These results provided the rationale for the subsequent detailed investigation of Fe-CeO_2 as a heterogeneous Fenton catalyst for the Fenton oxidation of LDPE in Chapter 6.

5.3.2 Synthesis and Characterisation of Carbon-based Heterogeneous Fenton Catalysts

The initial catalysts screened were $FeCl_2$ as a homogeneous catalyst, Fe^{II} immobilised on AC (Fe^{II}/AC) and the bare AC was also tested to confirm whether activity arises from grafted Fe rather than the support. Preliminary results of the catalyst screening in Fenton oxidation of LDPE are shown in Table 1. Under thermal autoclave conditions (150 °C, 24 h), the homogeneous $FeCl_2$ catalyst showed negligible conversion. Using identical reagent quantities under microwave (MW) irradiation (150 °C, 3 h) a mass loss LDPE of 36 % was achieved, highlighting the role of MW irradiation in facilitating depolymerisation reactions, likely due to dielectric absorption by aqueous H_2O_2, which promotes localised heating at the polymer–liquid interface. Under the same MW-assisted conditions, Fe^{II}/AC catalyst achieved 39 % mass loss. Increasing the temperature to 170 °C (MW, 3 h) raised mass loss to 68 % for both catalysts. The bare AC support showed moderate activity (32 %), suggesting that the Fenton activity of the Fe was primarily responsible for the efficacy for the reactions.

Table 1: Initial catalyst screening for Fenton Oxidation LDPE.

Catalyst	Loading	H_2O_2 (%)	Temp (°C)	Time (h)	Mass Loss LDPE (%)
$FeCl_2$ (autoclave)	10 wt. %	5 % (w/w) (6 mL)	150 °C	24 h	< 10 %
$FeCl_2$ (MW)	10 wt. %	5 % (w/w) (6 mL)	150 °C	3 h	36 %
Fe^{II}/AC (MW)	10 wt. %	5 % (w/w) (6 mL)	150 °C	3 h	39 %
$FeCl_2$ (MW)	10 wt. %	3 % (w/w) (10 mL)	160 °C	3 h	68 %
Fe^{II}/AC (MW)	10 wt. %	3 % (w/w) (10 mL)	160 °C	3 h	68 %
AC (MW)	10 wt. %	3 % (w/w) (10 mL)	160 °C	3 h	32 %

*All reactions carried out at pH1.

Catalyst design was further refined to create heteroatom-doped carbon supports with immobilised iron (Fe), targeting well-dispersed Fe sites and improved stability against leaching. The IL/Fe-doped carbon nanomaterials were prepared using ionic liquid precursors with the same cation (1-ethyl, 3-

methyl imidazolium) but different anions as shown in Figure 7. The first anion was dicyanamide (IL-CN), a nitrogen-rich structure containing two azide groups. The second was the acetate anion (IL-OAc). The aim of the study was to assess how the different anions affect the material properties through various characterisation techniques and subsequently, their activity as Fenton catalysts for the oxidative degradation of LDPE. A schematic representation of the catalyst synthesis is shown in Figure 7.

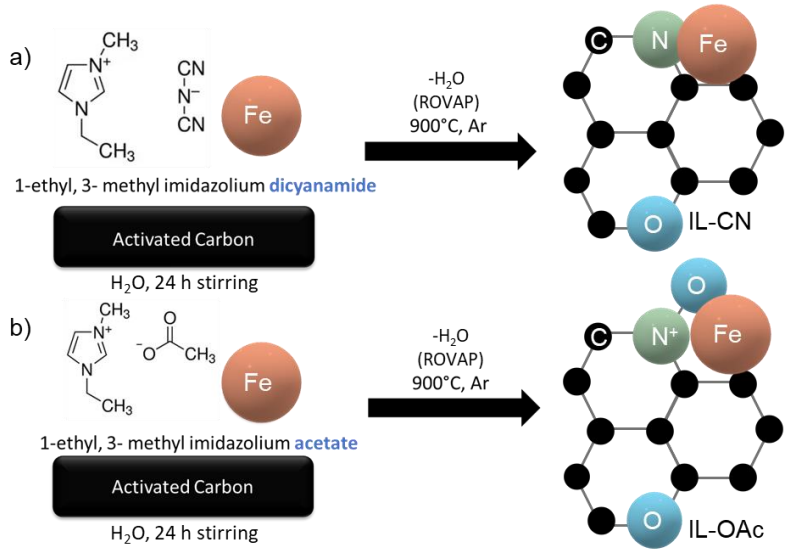


Figure 7: Synthesis of a) IL-CN catalyst and b) IL-OAc catalyst by impregnation method and thermal treatment.

Powder XRD (Figure 8) shows a broad reflection at ≈25.5° 2θ in both IL-CN and IL-OAc was assigned to the (002) crystal plane of carbon and is characteristic for graphitic carbon structures[42]. The peak appears slightly sharper in the IL-CN sample suggesting a higher degree of carbon ordering/crystallisation. Interestingly, a significant difference was noted in the dominant Fe phases. IL-CN showed reflections attributed to magnetite Fe_3O_4: 30.0, 37.5, 44.4 and 62.6 °2θ and were assigned to the (220), (311), (400) and (440) crystal planes, respectively.[43] In contrast, IL-OAc shows predominantly metallic Fe^0 phases with peaks at 45.0, 65.0 and 82.5 °2θ, assigned to the (110), (200) and (220) crystal planes of body centred cubic (BCC) α-Fe, respectively. The predominance of Fe^0 in

the IL–OAc catalyst is attributed to the decomposition of the OAc anion to CO at high temperatures, which promotes carbothermal reduction of iron oxides to Fe^0 during pyrolysis.[44]

$$Fe_2O_3 + 3CO \rightarrow 2Fe^0 + 3CO_2$$ **Eqn. 4**

$$Fe_3O_4 + 4CO \rightarrow 3Fe^0 + 4CO_2$$ **Eqn. 5**

In contrast, the nitrogen-rich IL–CN surface likely introduces N-dopant sites that anchor Fe species, stabilising iron oxide phases and suppressing complete reduction to Fe^0 under identical conditions. Minor amounts of hematite (Fe_2O_3) were also identified in XRD analysis in both samples with reflections at 2θ 33.0 and 36.1 ° indexed to the (104) and (110) planes , respectively.

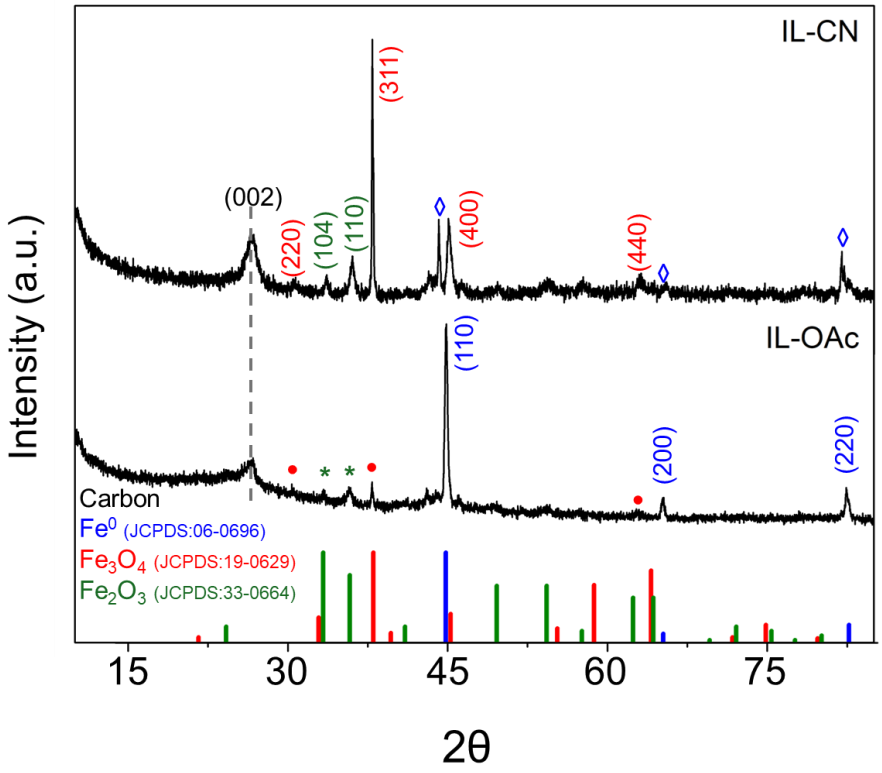


Figure 8: XRD patterns of IL-CN and IL-OAc.

Figure 9 shows SEM and TEM analysis the IL-CN and IL-OAc catalysts revealing that the IL precursor significantly influenced the resulting catalyst morphology. SEM images of the IL-CN sample (Figure 9 a) and b)), display spherical and cubic iron oxide particles (~80 – 150 nm) immobilised on the carbon

surface which was further supported by TEM analysis shown in Figure 9 c) and d). HAADF-STEM with EDS confirmed the co-localisation of Fe and O consistent with iron oxide, in agreement with XRD identification shown in Figure 9 e).

In contrast, SEM (Figure 9 f) and g)) of the IL–OAc–derived catalyst reveals multi-walled carbon nanotubes (MWCNT) with large diameter (~ 100 nm). TEM (Figure 9 h) and i)) confirms concentric graphitic walls typical of MWCNTs and EDS mapping (Figure 9 j)) shows good Fe distributed along and within the nanotube structures. The acetate anions likely decompose to CO during annealing, promoting carbothermal reduction to metallic Fe^0 which is widely reported as an active catalyst for CNT growth via transient Fe carbide formation.[45] This mechanistic pathway correlates with the XRD analysis showing predominant Fe^o in the IL–OAc sample.

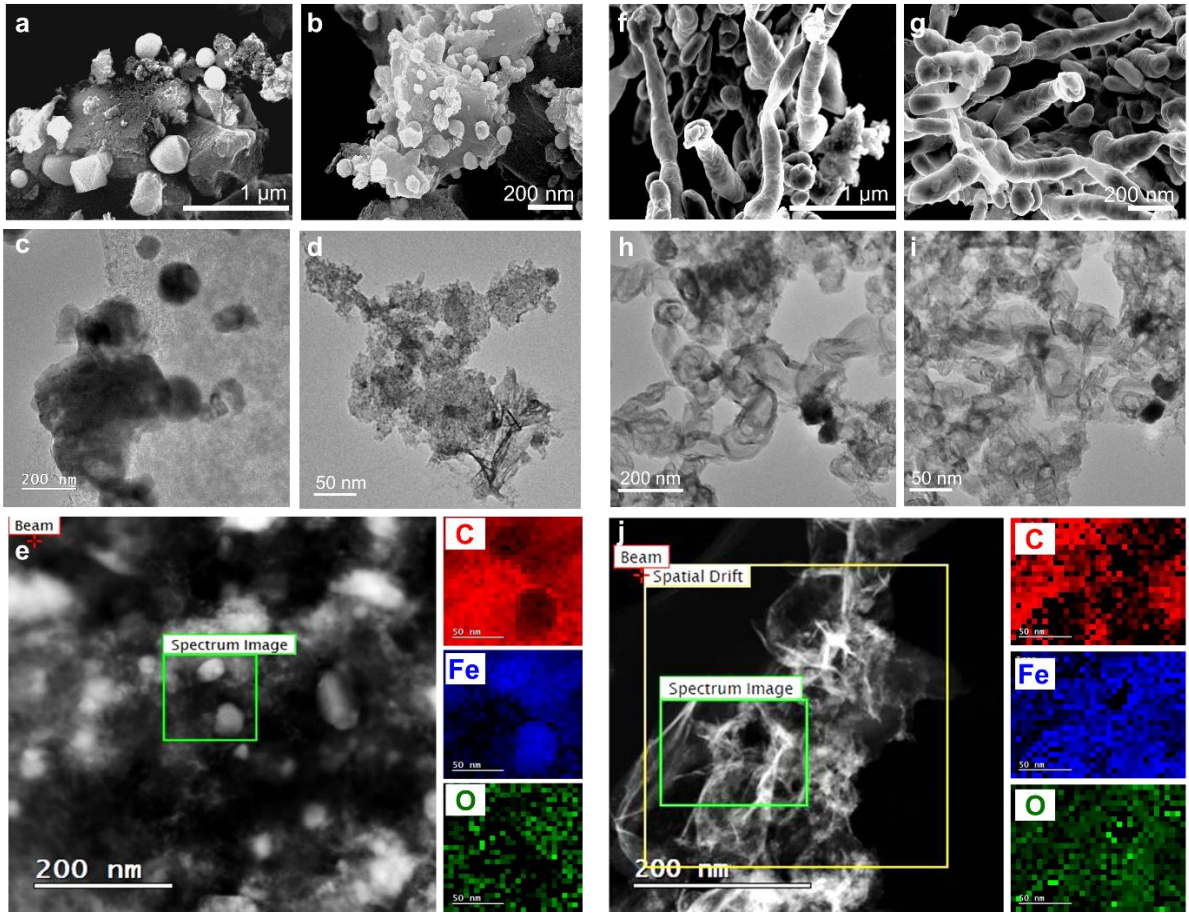


Figure 9: a) & b) SEM of IL-CN catalyst, c) & d) TEM of IL-CN catalyst, e) EDS analysis of IL-CN catalyst, f) & g) SEM of IL-OAc catalyst, h) & i) TEM of IL-OAc catalyst, j) EDS analysis of IL-OAc catalyst.

XPS (Figure 10) was employed to assess the surface chemistry of the samples. Figure 10 a) shows the Fe 2p core level of the IL-CN and IL-OAc catalysts which display two distinct peaks at BEs of 711.5 and 725.5 eV, assigned to the Fe $2p_{3/2}$ and Fe $2p_{1/2}$ doublet. A satellite peak was also present at 719.5 eV, characteristic of Fe_2O_3 indicating surface oxidation of Fe_3O_4 as identified by XRD analysis to Fe_2O_3.[30] No apparent peak was apparent in the 706 - 707 eV region of IL-OAc corresponding to Fe^0, as suggested by XRD analysis likely attributed to ambient surface oxidation.[46] Additionally, the lower Fe 2p signal in IL-OAc compared to IL-CN is attributed to reduced surface accessibility of the Fe embedded within MWCNTs, whereas IL-CN has larger iron oxide nanostructures dispersed on the surface, as supported by SEM and TEM. The C1s core level spectra are shown in Figure 10 b) were deconvoluted into 6 components at 284.8, 285.4, 286.8, ~287.7, 288.9 and 291.5, assigned to the C-C, C=C, C-O, C=O, O-C=O and the π-π* shake up environments, respectively.[47] Minor BE shifts between the samples likely reflect differences in the N/O chemical environments arising from the anion precursors.

The N 1s spectra for both samples are shown in Figure 10 c). The IL-CN sample showed two environments at BE of 399.4 eV and 401.2 eV, attributed to amine and amide functionalities[48] or if incorporated in a ring structure, aromatic pyridinic and pyrrolic N functionalities[49]. The IL-OAc sample also has peaks appearing at slightly lower BE (398.6 and 400.9 eV, respectively) possibly indicating a higher fraction of ring incorporated N functionalities such as pyridinic N, which appear at a lower BE than aliphatic amine N groups due to a shift in electron density.[49] Similarly, the pyrrolic N will appear at slightly lower BE than aliphatic amide N. A minor component at 403.3 eV is seen for IL-OAc, attributed to oxidised N species, possibly formed from oxygen-rich acetate–derived environments.[50]

The O 1s spectra for IL-CN and IL-OAc is shown in Figure 10 d) and 3 distinct peaks were identified for both catalysts at 530.2 eV, 530.8/9 eV and 532.7 eV, assigned to lattice Fe-O, interfacial and carbonyl type oxygen Fe-O-C and C-O, respectively.[51]. The lower intensity Fe-O peak seen for IL-OAc compared to IL-CN is attributed to attenuation of Fe signal due to being embedded within the MWCNTs, consistent with previous analysis.

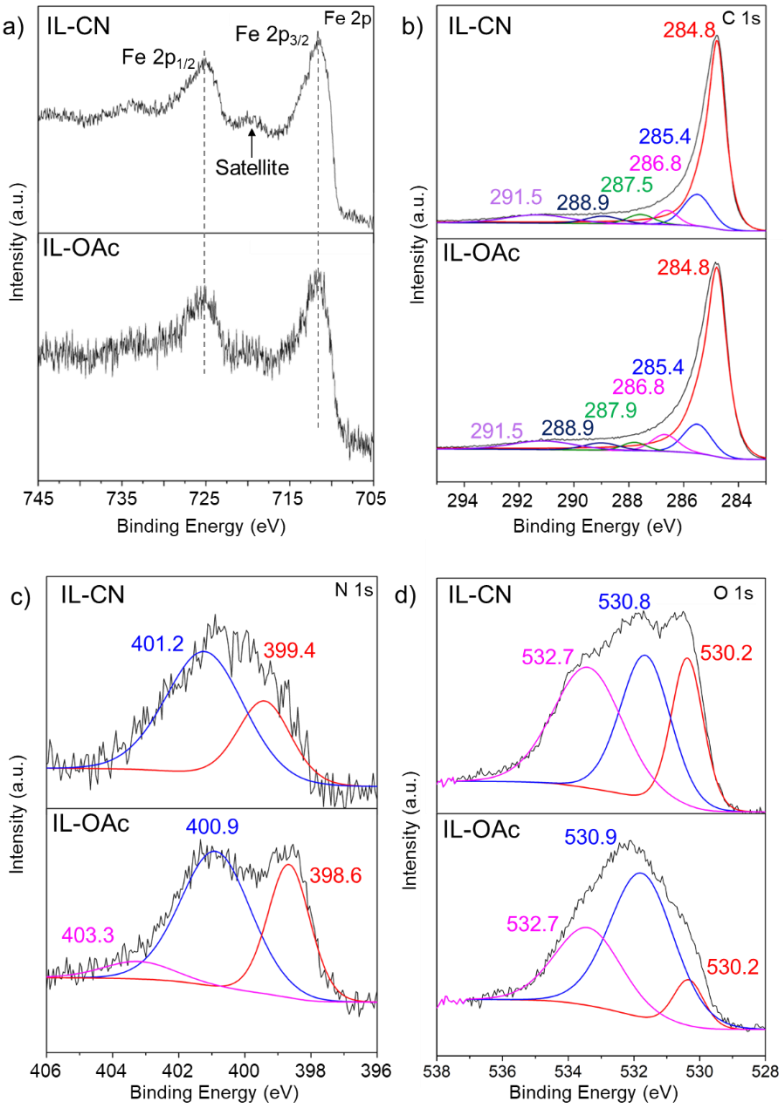


Figure 10: XPS analysis of the IL-CN and IL-OAc samples a) Fe 2p, b) C1s and c) N1s core level scans.

Catalytic evaluation of carbon-based catalysts in Fenton Oxidation of LDPE

LDPE pretreatment and surface characterisation: Fenton reactions were evaluated on post-consumer LDPE which was cut into 1x1 mm squares. A chemical surface pre-treatment was performed by stirring the LDPE in 10 % HNO_3 overnight to introduce surface O and N functionalities, making the LDPE surface more susceptible to oxidative degradation. Images of the LDPE before and after HNO_3 treatment (Figure 11 a) show yellow colouration, indicative of surface nitrate species. FTIR analysis (Figure 11 b), confirmed the presence of surface N and O functional groups after treatment. Untreated LDPE showed absorption bands at 2968, 2874, 1462 cm^{-1}, attributed to C-H stretching (methyl and methylene), C=C stretching, and C-H bending of polyethylene, respectively.[52] After HNO_3 treatment, new bands appeared at 3262, 1693, 1541, 1250 and 1203 cm^{-1} and were attributed to N-H stretching, C=O stretching, N-H / N-O bend, C-N / C-O stretching and C-O stretching environments, respectively and confirmed successful surface functionalisation of the LDPE surface.

Fenton oxidation screening: The preliminary results for the Fenton oxidation of surface treated LDPE are shown in Figure 11 c) and d). The reaction screening conditions were: 0.3 g LDPE, 10 mL 3 % H_2O_2, 0.12 g catalyst, 160 °C, pH 1 for 3 h. The superior performance of the IL-OAc catalyst as seen in Figure 11 was attributed to the higher dispersion of Fe throughout the catalyst as well as the presence of Fe^0 which has been reported to be an excellent Fenton catalyst. Fe^0 has attracted attention as a Fenton catalyst due to its superior reaction efficiency over other phases of Fe owing to its highly reductive properties. From equations 1 and 2 below, Fe^0 can readily be converted to Fe^{2+} via the loss of two electrons, which can reduce the formation of ferric hydroxides by recycling Fe^{3+}, enhancing Fenton reaction kinetics.[24, 25]

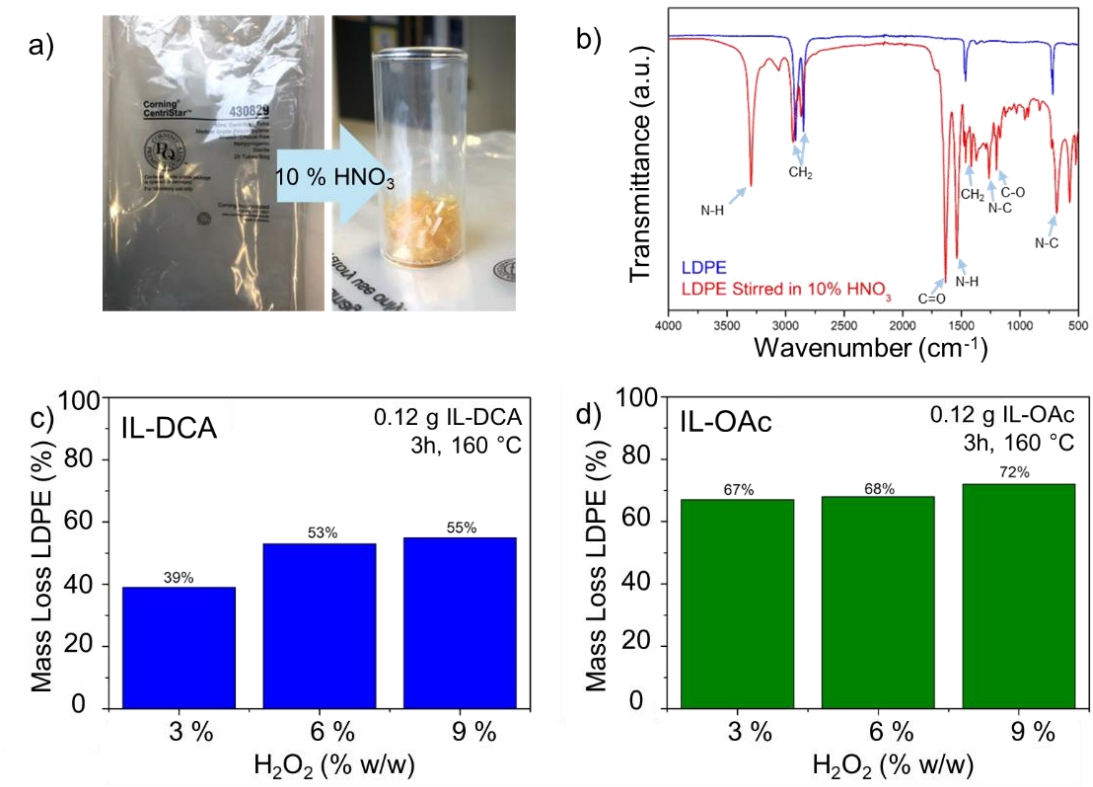


Figure 11: a) Post-consumer LDPE pre and most surface pre-treatment, b) FTIR of surface-treated LDPE, effect of catalyst loading for c) IL-CN and d) IL-OAc, effect of H_2O_2 concentration for e) IL-CN and f) IL-OAc.

When other reaction parameters such as catalyst loading were probed, poor reproducibility was sometimes observed with post-consumer LDPE packaging, attributed to additives and plasticisers.[53] Consequently, pure LDPE powder obtained from Sigma Aldrich was used to allow for more accurate correlations to the catalyst design and optimisation. Initially, the pure LDPE powder was dispersed in 10 % HNO_3 to perform the same pretreatment as the post-consumer plastic, however its hydrophobicity prevented adequate wetting as shown in Figure 12 a), therefore the surface pretreatment step was removed for all further experiments.

A representative HPLC chromatogram of the oxidation products is shown in Figure 12 b). Eight principal carboxylic acids were identified: succinic acid, formic acid, glutaric acid, acetic acid, formic acid, butyric acid, adipic acid, propionic acid and pimelic acid. Concentrations of these acids increased with reaction

time. Time-resolved reactions using both catalysts are summarised in Figure 12. Both catalysts showed a steady increase in mass loss LDPE and acid yield over time. While the acid yield for IL-OAc increases 5 % to 37 % (2 → 3 h), the acid yield for the IL-CN catalysts plateaued (10 % to 13 % from 2 → 3 h).

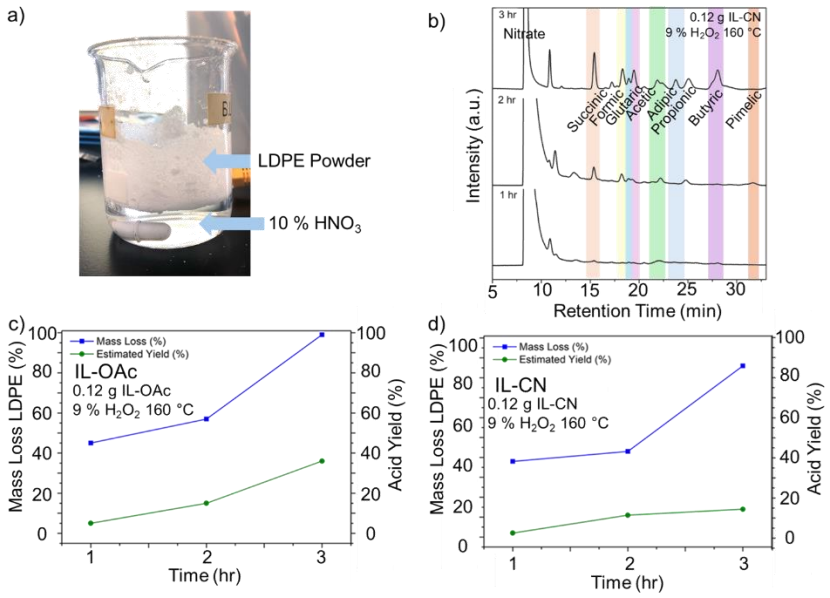


Figure 12: a) hydrophobicity of LDPE powder, b) HPLC analysis of time series products for IL-CN, c) time series mass loss and acid yield results for c) IL-OAc, d) IL-CN.

The superior performance of IL–OAc is consistent with its higher Fe dispersion and presence of Fe^{0} which can sustain Fe^{2+} regeneration and accelerate the Fenton reaction. The acid-yield plateaued for IL–CN alongside continued mass loss suggests over-oxidation or mineralisation likely due to leaching of surface iron oxide aggregates in acidic environments. Overall, the initial screening identified that carbon-supported catalysts were effective supports for the Fenton oxidative degradation of LDPE.

5.4 Conclusion & outlook

In this work, we established a microwave-assisted, heterogeneous Fenton route to depolymerise LDPE into carboxylic acids using two catalyst families: Fe oxide composites and carbon-supported Fe catalysts. This method development also established and validated an HPLC protocol for acid

characterisation for the mono-and dicarboxylic acids, enabling quantitative tracking of product distributions.

Fe-oxide composites: Bimetallic systems (Fe_2O_3 coupled with BiOCl, CeO_2, CuO and MnO_2) outperformed bare Fe_2O_3. The Fe_2O_3-CeO_2 catalyst was the best performing, achieving a mass loss LDPE of 100 % and an acid yield of 54 % with no metal leaching. This system is further developed in Chapter 6.

Carbon based catalysts: Ionic-liquid precursors controlled surface chemistry and nanostructure morphology. The N-rich dicyanamide anion (IL–CN) gave N,O-doped graphitic carbon with Fe-oxide aggregates (mainly Fe_3O_4 with surface Fe_2O_3). The O-rich acetate route (IL–OAc) yielded N,O-doped MWCNTs with well-dispersed Fe^o, from acetate-to-CO carbothermal reduction. The IL-OAc catalyst achieved 99 % mass loss and 39 % acid yield in initial screening. Despite showing promising Fenton activity, it was not possible to conduct a full catalytic study within the thesis timeframe because biochar as a low-energy, renewable Fenton-type platform was prioritised as the carbon support (Chapter 7). Nonetheless, the work developed on IL-directed iron catalyst will be carried forward in a separate study.

5.5 References:

(1) Shojaei, B.; Abtahi, M.; Najafi, M. Chemical recycling of <scp>PET</scp> : A stepping-stone toward sustainability. *Polymers for Advanced Technologies* **2020**, *31* (12), 2912-2938. DOI: 10.1002/pat.5023.
(2) Analytics, C. *Web of Science: Search Results for "Chemical Recycling PET"*. Clarivate Analytics, 2025. https://www.webofscience.com/wos/woscc/summary/cfa45566-8cea-4caa-b107-4234d5d6ec0b-01712bf818/relevance/1 (accessed 29/07/2025).
(3) Analytics, C. *Web of Science: Search Results for "Chemical Recycling LDPE"*. Clarivate Analytics, 2025. https://www.webofscience.com/wos/woscc/summary/2f43f459-39b5-45b5-acd8-dbcdb149379c-01712c19eb/relevance/1 (accessed 29/07/2025).
(4) *Market volume of polyethylene worldwide from 2015 to 2022, with a forecast for 2023 to 2030 (in million metric tons)*. July 5, 2023. https://www.statista.com/statistics/1245162/polyethylene-market-volume-worldwide/ (accessed April 09, 2025).
(5) *Market volume of polyethylene terephthalate worldwide from 2015 to 2022, with a forecast for 2023 to 2030 (in million metric tons)* July 5, 2023. https://www.statista.com/statistics/1245264/polyethylene-terephthalate-market-volume-worldwide/?utm_source=chatgpt.com (accessed April 09, 2025).
(6) Sun, J.; Dong, J.; Gao, L.; Zhao, Y.-Q.; Moon, H.; Scott, S. L. Catalytic Upcycling of Polyolefins. *Chemical Reviews* **2024**, *124* (16), 9457-9579. DOI: 10.1021/acs.chemrev.3c00943.
(7) Qie, Z.; Xiang, H.; Xiang, H.; Zou, R.; Alhelali, A.; Alhassawi, H.; Ding, S.; Jiao, Y.; Holmes, S. M.; Garforth, A. A.; et al. Catalytic pyrolysis of high-density polyethylene (HDPE) over hierarchical ZSM-5 zeolites produced by microwave-assisted chelation-alkaline treatment. *Fuel* **2024**, *368*, 131532. DOI: https://doi.org/10.1016/j.fuel.2024.131532.
(8) Shen, X.; Zhao, Z.; Li, H.; Gao, X.; Fan, X. Microwave-assisted pyrolysis of plastics with iron-based catalysts for hydrogen and carbon nanotubes production. *Materials Today Chemistry* **2022**, *26*, 101166. DOI: https://doi.org/10.1016/j.mtchem.2022.101166.
(9) Ding, K.; Liu, S.; Huang, Y.; Liu, S.; Zhou, N.; Peng, P.; Wang, Y.; Chen, P.; Ruan, R. Catalytic microwave-assisted pyrolysis of plastic waste over NiO and HY for gasoline-range hydrocarbons production. *Energy Conversion and Management* **2019**, *196*, 1316-1325. DOI: https://doi.org/10.1016/j.enconman.2019.07.001.
(10) Bäckström, E.; Odelius, K.; Hakkarainen, M. Trash to Treasure: Microwave-Assisted Conversion of Polyethylene to Functional Chemicals. *Industrial & Engineering Chemistry Research* **2017**, *56* (50), 14814-14821. DOI: 10.1021/acs.iecr.7b04091.
(11) Hu, K.; Zhou, P.; Yang, Y.; Hall, T.; Nie, G.; Yao, Y.; Duan, X.; Wang, S. Degradation of Microplastics by a Thermal Fenton Reaction. *ACS ES&T Engineering* **2022**, *2* (1), 110-120. DOI: 10.1021/acsestengg.1c00323.
(12) Ortiz, D.; Munoz, M.; Nieto-Sandoval, J.; Romera-Castillo, C.; de Pedro, Z. M.; Casas, J. A. Insights into the degradation of microplastics by Fenton oxidation: From surface modification to mineralization. *Chemosphere* **2022**, *309*, 136809. DOI: https://doi.org/10.1016/j.chemosphere.2022.136809.
(13) Chow, C.-F.; Wong, W.-L.; Ho, K. Y.-F.; Chan, C.-S.; Gong, C.-B. Combined Chemical Activation and Fenton Degradation to Convert Waste Polyethylene into High-Value Fine Chemicals. *Chemistry – A European Journal* **2016**, *22* (28), 9513-9518. DOI: https://doi.org/10.1002/chem.201600856 (accessed 2024/01/23).
(14) Nguyen, V. S.; Chang, Y.; Phillips, E. V.; DeWitt, J. A.; Sievers, C. Mechanocatalytic Oxidative Cracking of Poly(ethylene) Via a Heterogeneous Fenton Process. *ACS Sustainable Chemistry & Engineering* **2023**, *11* (20), 7617-7623. DOI: 10.1021/acssuschemeng.3c01054.
(15) Thomas, N.; Dionysiou, D. D.; Pillai, S. C. Heterogeneous Fenton catalysts: A review of recent advances. *J Hazard Mater* **2021**, *404* (Pt B), 124082. DOI: 10.1016/j.jhazmat.2020.124082 From NLM.
(16) Gokulakrishnan, B.; Satishkumar, G. Facilely prepared heterogeneous Fenton catalyst Fe(Fe0.69Al0.31)2O4@C for catalytic wet peroxide oxidation of ciprofloxacin in batch and continuous reactor: Reaction intermediates and toxicity evaluation. *Separation and Purification Technology* **2024**, *333*, 125690. DOI: https://doi.org/10.1016/j.seppur.2023.125690.

(17) Wang, J.; Tang, J. Fe-based Fenton-like catalysts for water treatment: Catalytic mechanisms and applications. *Journal of Molecular Liquids* **2021**, *332*, 115755. DOI: https://doi.org/10.1016/j.molliq.2021.115755.
(18) Kaur, G.; Kumar, H.; Singla, M. Diverse applications of ionic liquids: A comprehensive review. *Journal of Molecular Liquids* **2022**, *351*, 118556. DOI: https://doi.org/10.1016/j.molliq.2022.118556.
(19) Ranjbar Sahraie, N.; Paraknowitsch, J. P.; Göbel, C.; Thomas, A.; Strasser, P. Noble-Metal-Free Electrocatalysts with Enhanced ORR Performance by Task-Specific Functionalization of Carbon using Ionic Liquid Precursor Systems. *Journal of the American Chemical Society* **2014**, *136* (41), 14486-14497. DOI: 10.1021/ja506553r.
(20) Rodrigues, C. S. D.; Soares, O. S. G. P.; Pereira, M. F. R.; Madeira, L. M. Fenton's oxidation using iron-containing activated carbon as catalyst for degradation of p-nitrophenol in a continuous stirred tank reactor. *Journal of Water Process Engineering* **2021**, *44*, 102386. DOI: https://doi.org/10.1016/j.jwpe.2021.102386.
(21) Adachi, A.; El Ouadrhiri, F.; Saleh, E. A. M.; Althomali, R. H.; Kassem, A. F.; Ibtissam, E. M.; Moharam, M. M.; Husain, K.; Eloutassi, N.; Lahkimi, A. Iron-doped catalyst synthesis in heterogeneous Fenton like process for dye degradation and removal: optimization using response surface methodology. *SN Applied Sciences* **2023**, *5* (12), 342. DOI: 10.1007/s42452-023-05543-0.
(22) John, J.; Ajit, K.; Krishnan, H.; Kizhakkethil Youseph, A. S. Performance of iron – doped activated carbon synthesised from cocoa husk as a cathode catalyst in microbial fuel cell powered Fenton process. *Journal of Chemical Technology & Biotechnology* **2024**, *99* (9), 1964-1975. DOI: https://doi.org/10.1002/jctb.7697 (accessed 2025/04/09).
(23) Rubeena, K. K.; Hari Prasad Reddy, P.; Laiju, A. R.; Nidheesh, P. V. Iron impregnated biochars as heterogeneous Fenton catalyst for the degradation of acid red 1 dye. *Journal of Environmental Management* **2018**, *226*, 320-328. DOI: https://doi.org/10.1016/j.jenvman.2018.08.055.
(24) Tian, Y.; Zhou, M.; Pan, Y.; Cai, J.; Ren, G. Pre-magnetized Fe0 as heterogeneous electro-Fenton catalyst for the degradation of p-nitrophenol at neutral pH. *Chemosphere* **2020**, *240*, 124962. DOI: https://doi.org/10.1016/j.chemosphere.2019.124962.
(25) Messele, S. A.; Soares, O. S. G. P.; Órfão, J. J. M.; Bengoa, C.; Stüber, F.; Fortuny, A.; Fabregat, A.; Font, J. Effect of activated carbon surface chemistry on the activity of ZVI/AC catalysts for Fenton-like oxidation of phenol. *Catalysis Today* **2015**, *240*, 73-79. DOI: https://doi.org/10.1016/j.cattod.2014.03.063.
(26) Adeleye, A. S.; Keller, A. A.; Miller, R. J.; Lenihan, H. S. Persistence of commercial nanoscaled zero-valent iron (nZVI) and by-products. *Journal of Nanoparticle Research* **2013**, *15* (1), 1418. DOI: 10.1007/s11051-013-1418-7.
(27) Shen, X.; Cai, Z.; Hu, J.; Sun, B. Highly Efficient Microwave-Assisted Fenton Degradation of Toluene Nitration Wastewater over Microwave-Responsive Catalyst of Fe3O4−BiOCl. *ChemistrySelect* **2022**, *7* (33), e202200804. DOI: https://doi.org/10.1002/slct.202200804 (accessed 2025/04/04).
(28) Asenath-Smith, E.; Ambrogi, E. K.; Barnes, E.; Brame, J. A. CuO enhances the photocatalytic activity of Fe2O3 through synergistic reactive oxygen species interactions. *Colloids and Surfaces A: Physicochemical and Engineering Aspects* **2020**, *603*, 125179. DOI: https://doi.org/10.1016/j.colsurfa.2020.125179.
(29) Xu, L.; Wang, J. Magnetic Nanoscaled Fe3O4/CeO2 Composite as an Efficient Fenton-Like Heterogeneous Catalyst for Degradation of 4-Chlorophenol. *Environmental Science & Technology* **2012**, *46* (18), 10145-10153. DOI: 10.1021/es300303f.
(30) Yamashita, T.; Hayes, P. Analysis of XPS spectra of Fe2+ and Fe3+ ions in oxide materials. *Applied Surface Science* **2008**, *254* (8), 2441-2449. DOI: https://doi.org/10.1016/j.apsusc.2007.09.063.
(31) Dupin, J.-C.; Gonbeau, D.; Vinatier, P.; Levasseur, A. Systematic XPS studies of metal oxides, hydroxides and peroxides. *Physical Chemistry Chemical Physics* **2000**, *2* (6), 1319-1324, 10.1039/A908800H. DOI: 10.1039/A908800H.

(32) Dong, W.; Xie, T.; Wu, Z.; Peng, H.; Ren, H.; Meng, F.; Lin, H. Oxygen-vacancy-rich BiOCl materials with ultrahigh photocatalytic efficiency by etching bismuth glass. *RSC Advances* **2021**, *11* (61), 38894-38906, 10.1039/D1RA06961F. DOI: 10.1039/D1RA06961F.
(33) Ahmad, K.; Raza, W.; Khan, R. A. Fabrication of picric acid sensor using cerium oxide-modified glassy carbon electrode. *Journal of Materials Science: Materials in Electronics* **2024**, *35* (12), 846. DOI: 10.1007/s10854-024-12621-5.
(34) Lokhande, V.; Youn, D.; Malavekar, D.; Ji, T. Synergistic effect of Fe and BiOCl in enhancing electrocatalytic performance for oxygen evolution reaction. *Heliyon* **2023**, *9* (10), e20811. DOI: 10.1016/j.heliyon.2023.e20811 From NLM.
(35) Wu, K.; Qin, Z.; Zhang, X.; Guo, R.; Ren, X.; Pu, X. Z-scheme BiOCl/Bi–Bi2O3 heterojunction with oxygen vacancy for excellent degradation performance of antibiotics and dyes. *Journal of Materials Science* **2020**, *55* (9), 4017-4029. DOI: 10.1007/s10853-019-04300-2.
(36) Lv, W.; Li, L.; Meng, Q.; Zhang, X. Molybdenum-doped CuO nanosheets on Ni foams with extraordinary specific capacitance for advanced hybrid supercapacitors. *Journal of Materials Science* **2020**, *55* (6), 2492-2502. DOI: 10.1007/s10853-019-04129-9.
(37) Liu, Y.; Cao, X.; Jiang, D.; Jia, D.; Liu, J. Hierarchical CuO nanorod arrays in situ generated on three-dimensional copper foam via cyclic voltammetry oxidation for high-performance supercapacitors. *Journal of Materials Chemistry A* **2018**, *6* (22), 10474-10483, 10.1039/C8TA00945G. DOI: 10.1039/C8TA00945G.
(38) Wang, L.; Meng, F.; Li, K.; Lu, F. Characterization and optical properties of pole-like nano-CeO2 synthesized by a facile hydrothermal method. *Applied Surface Science* **2013**, *286*, 269-274. DOI: https://doi.org/10.1016/j.apsusc.2013.09.067.
(39) Bortamuly, R.; Konwar, G.; Boruah, P. K.; Das, M. R.; Mahanta, D.; Saikia, P. CeO2-PANI-HCl and CeO2-PANI-PTSA composites: synthesis, characterization, and utilization as supercapacitor electrode materials. *Ionics* **2020**, *26* (11), 5747-5756. DOI: 10.1007/s11581-020-03690-7.
(40) Yang, M.; Liu, W.; Liu, Q.; Chen, Z.; Cao, J.; Luo, J.; Xing, M. Constrained Heterogeneous CoFe2O4/ZnO/PMS Fenton-Like System for Industrial Wastewater Remediation with Recyclability and Zero Metal Loss. *Angewandte Chemie International Edition* **2025**, *64* (11), e202421797. DOI: https://doi.org/10.1002/anie.202421797 (accessed 2025/07/30).
(41) Kuan, C.-C.; Chang, S.-Y.; Schroeder, S. L. M. Fenton-Like Oxidation of 4-Chlorophenol: Homogeneous or Heterogeneous? *Industrial & Engineering Chemistry Research* **2015**, *54* (33), 8122-8129. DOI: 10.1021/acs.iecr.5b02378.
(42) Awadallah-F, A.; Al-Muhtaseb, S. Carbon Nanoparticles-Decorated Carbon Nanotubes. *Scientific Reports* **2020**, *10* (1), 4878. DOI: 10.1038/s41598-020-61726-4.
(43) Zhuang, L.; Zhang, W.; Zhao, Y.; Shen, H.; Lin, H.; Liang, J. Preparation and Characterization of Fe3O4 Particles with Novel Nanosheets Morphology and Magnetochromatic Property by a Modified Solvothermal Method. *Scientific Reports* **2015**, *5* (1), 9320. DOI: 10.1038/srep09320.
(44) Du, Y.; Dai, M.; Naz, I.; Hao, X.; Wei, X.; Rong, R.; Peng, C.; Ali, I. Carbothermal reduction synthesis of zero-valent iron and its application as a persulfate activator for ciprofloxacin degradation. *Separation and Purification Technology* **2021**, *275*, 119201. DOI: https://doi.org/10.1016/j.seppur.2021.119201.
(45) Wirth, C. T.; Bayer, B. C.; Gamalski, A. D.; Esconjauregui, S.; Weatherup, R. S.; Ducati, C.; Baehtz, C.; Robertson, J.; Hofmann, S. The Phase of Iron Catalyst Nanoparticles during Carbon Nanotube Growth. *Chemistry of Materials* **2012**, *24* (24), 4633-4640. DOI: 10.1021/cm301402g.
(46) Zhang, B.; Zhu, B.-H.; Wang, X.; You, S.-B. Nanoscale Zero Valent Iron Supported by Biomass-Activated Carbon for Highly Efficient Total Chromium Removal from Electroplating Wastewater. In *Water*, 2020; Vol. 12.
(47) Chen, X.; Xiaohui, W.; and Fang, D. A review on C1s XPS-spectra for some kinds of carbon materials. *Fullerenes, Nanotubes and Carbon Nanostructures* **2020**, *28* (12), 1048-1058. DOI: 10.1080/1536383X.2020.1794851.
(48) Dementjev, A. P.; de Graaf, A.; van de Sanden, M. C. M.; Maslakov, K. I.; Naumkin, A. V.; Serov, A. A. X-Ray photoelectron spectroscopy reference data for identification of the C3N4 phase in carbon–

nitrogen films. *Diamond and Related Materials* **2000**, *9* (11), 1904-1907. DOI: https://doi.org/10.1016/S0925-9635(00)00345-9.
(49) dos Reis, G. S.; Bergna, D.; Grimm, A.; Lima, E. C.; Hu, T.; Naushad, M.; Lassi, U. Preparation of highly porous nitrogen-doped biochar derived from birch tree wastes with superior dye removal performance. *Colloids and Surfaces A: Physicochemical and Engineering Aspects* **2023**, *669*, 131493. DOI: https://doi.org/10.1016/j.colsurfa.2023.131493.
(50) Azuara-Tuexi, G.; Muñoz-Sandoval, E.; Guirado-López, R. A. N 1s core-level binding energies in nitrogen-doped carbon nanotubes: a combined experimental and theoretical study. *Physical Chemistry Chemical Physics* **2023**, *25* (5), 3718-3736, 10.1039/D2CP04701B. DOI: 10.1039/D2CP04701B.
(51) Ghosh, A.; Ghosh, S.; Seshadhri, G. M.; Ramaprabhu, S. Green synthesis of nitrogen-doped self-assembled porous carbon-metal oxide composite towards energy and environmental applications. *Scientific Reports* **2019**, *9* (1), 5187. DOI: 10.1038/s41598-019-41700-5.
(52) Rodríguez Lamar, Y.; Noboa, J.; Torres Miranda, A. S.; Almeida Streitwieser, D. Conversion of PP, HDPE and LDPE Plastics into Liquid Fuels and Chemical Precursors by Thermal Cracking. *Journal of Polymers and the Environment* **2021**, *29* (12), 3842-3853. DOI: 10.1007/s10924-021-02150-1.
(53) Hahladakis, J. N.; Velis, C. A.; Weber, R.; Iacovidou, E.; Purnell, P. An overview of chemical additives present in plastics: Migration, release, fate and environmental impact during their use, disposal and recycling. *Journal of Hazardous Materials* **2018**, *344*, 179-199. DOI: https://doi.org/10.1016/j.jhazmat.2017.10.014.

Chapter 6

Heterogeneous Fenton-type Oxidative Degradation of LDPE to Valuable Acid Products Using a Nanostructured Fe-CeO_2 Solid Solution Catalyst

Rachel Breen[1,2], Justin Holmes[1,2], Gillian Collins[1,2]*

[1] School of Chemistry, University College Cork, Cork, T12 YN60, Ireland.

[2] AMBER Centre, Sustainability Institute, University College Cork, Cork, T23 XE10, Ireland.

Publication: ***Breen, R**.; Holmes, J. D.; Collins, G. Heterogeneous Fenton-type oxidative degradation of low-density polyethylene to valuable acid products using a nanostructured Fe–CeO_2 solid solution catalyst. Catalysis Science & Technology **2025**, 10.1039/D4CY01384K. DOI: 10.1039/D4CY01384K.*

Abstract

The chemical conversion of waste plastic polymers to useful commodity chemicals has become crucial to helping tackle the issue of global plastic waste today. Polyolefins maintain the highest production rate and lowest recycling rate worldwide due to their inert chemical structures. This work shows the synthesis of solid-solution Fe-CeO_2 catalyst as an excellent heterogeneous catalyst for Fenton-type oxidative degradation of low-density polyethylene to achieve high yields of organic acids. The catalyst was synthesised in 3 molar ratios of Fe:Ce and it was found that the molar ratio of iron and cerium was crucial for catalytic performance with the Fe-CeO_2 1:1 catalyst giving the highest yields of acid products. The catalyst achieved 91 % mass loss and 71 % organic acid at pH 7, with 1 wt. % catalyst loading. The use of a multi-metal Fenton system resulted in a synergistic effect, displaying superior activity to systems with only one Fenton active metal. The heterogeneous nature of the catalyst this allowed for easy recovery and demonstrated excellent recyclability in multiple cycles. The high recyclability performance was attributed to the stability of the solid solution structure.

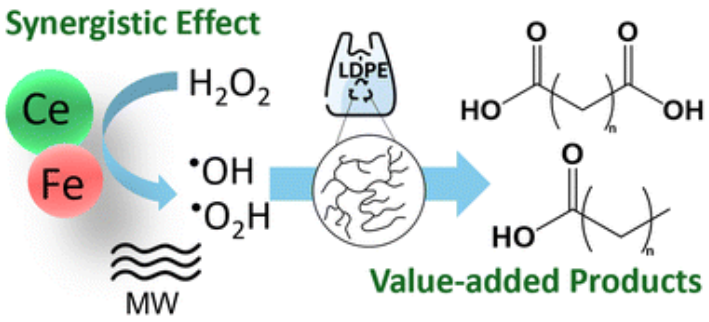


Table of Contents Graphic

6.1 Introduction

Our over reliance on single-use plastics has become apparent by the ever-increasing production rates worldwide and uncontrollable accumulation of plastics in our environment. Today, we produce about 400 million tonnes of plastic waste annually with this figure projected to reach 1.1 billion tonnes in 2050.[1-3] A report in 2022 stated that only 9 % of plastic is recycled globally, while the rest is mismanaged (22 %), sent to landfill (49 %) or incinerated (19 %).[2] As a result of this, the use of chemical recycling to convert waste plastic into useful chemicals has gained huge traction in the world of research today. Many literature reports have shown methods of depolymerising polymer plastics into useful monomers or commodity chemicals for use as feedstock in pharmaceutical, cosmetic or industrial fields.[4-7]

Chemical recycling of condensation polymers such as polyesters, polyamides and polycarbonates[8-10] to produce monomers and commodity chemicals has been widely researched. In contrast, chemical recycling of polyolefins such as low-density polyethylene (LDPE), linear low-density polyethylene (LLDPE) and high density polyethylene (HDPE) remain highly challenging due to the inert nature of their structures and the lack of polar functional groups along linear alkane chains.[11] LDPE has the highest primary waste generation out of all synthetic polymer plastics owing to its high production rate as a versatile polyolefin.[12] This high production rate is not met with equal recycling efforts, however, as only 3 % of recycled plastic worldwide is LDPE shown in Supplementary Information Figure S1. This is the lowest recycling rate of all other plastic polymers.[13] Alternative recycling efforts currently in place

for polyolefins mainly involve high energy processes such as pyrolysis, gasification and hydrocracking.[14-16]

In more recent years, oxidative degradation processes have attracted growing interest as degradation pathways for polyolefins. The photocatalytic oxidation of polystyrene has been shown to produce aromatic oxygenates using graphitic carbon nitride[17] and $FeCl_3$[18]. In contrast, the more stable polyolefins such as PE require reactive or activated oxygen species to convert C-C polymers into small oxygenated molecules.[19] Controlled thermolysis can produce longer chain fatty acids that can then be oxidised over manganese catalysts to produce valuable surfactants.[20] Microwave-assisted oxidative degradation of PE in nitric acid solutions yields dicarboxylic acid products, which are valuable for the production of polyesters and amides.[21, 22,] The use of nitric acid as a reaction media introduces undesirable side products such as NO_x gases and amine/amide degradation products.[21]

Fenton and Fenton-like advanced oxidation processes are well studied for environmental applications such as the destruction of a wide variety of organic pollutants, and contaminants[23, 24] Traditionally, Fenton's reagent involves the activation of H_2O_2 in the presence of Fe^{2+} and Fe^{3+} ions to produce hydroxyl ($HO^{\bullet}$) and hydroperoxyl ($HO_2^{\bullet}$) radicals, which act as non-selective oxidants.[25] As the Fenton reaction takes place in aqueous medium without the need for hazardous or environmentally damaging organic solvents, it is a green and favourable oxidation process. Fenton oxidation can be a homogeneous (typically metal salts) or a heterogeneous process. Heterogeneous Fenton catalysts reported in the literature include iron oxides[26] and mixed metal oxides[27] as well as iron-based catalysts loaded on materials such as zeolites[28] and graphene oxide[29]. Heterogeneous Fenton-type catalysts have many benefits over homogeneous Fenton catalysts as they often can be used at a wider pH range, prevent iron sludge formation and can be more easily recovered which means they have the potential to be recycled.[30]

Fenton degradation has been reported in the literature for the oxidative degradation of microplastics (MP), where the aim is total destruction of the plastics to gaseous products rather than conversion to

commodity chemicals.[31] Hu *et al.*[32] reported 96 % weight loss MPs in 16 h at a pH of ~1 using a homogeneous Fe^{2+} salt (4 mM) with 1 gL^{-1} MPs. Another group[33] reported reaction times of 7.5 h for MP degradation at a pH of 3 also using a homogeneous Fe^{3+} salt added at continual doses (5 doses of 750 mgL^{-1} 1 every 1.5 h) with 20 mgL^{-1} of MPs. Morĉar *et al.*[34] also reported the degradation of MPs using homogeneous Fe^{2+} at loadings of 10-12 wt. % with an optimal reaction pH of 3 but the reaction did not proceed in the absence of UV light for LDPE due to its structural stability, a common challenge encountered for LDPE.

Commonly, the efficiency of chemical plastic recycling is expressed in terms of the mass retention or diameter reduction, a measure that focuses only on whether the plastic waste is sufficiently degraded, rather than the products formed.[32, 34] The oxidation products are primarily short chain dicarboxylic acids which can be used as precursors to produce polymers and biopolymers and therefore depolymerisation protocols to maximise the yield of organic acids are hugely beneficial.

To overcome the inert nature of PE, a chemical pre-treatment with H_2SO_4 prior to Fenton degradation has been used to improve its hydrophilicity, followed by grafting of Fe^{3+} ions to the polymer. [35, 36] The chemical pre-treatment enables milder reaction conditions and short reaction time but also results in the formation of undesirable sulfonated by-products. One interesting approach to overcome the chemical inertness of PE is mechano-catalytic oxidative cracking of PE to yield shorter alkane fragments as well as CO, CO_2, O_2, and H_2O as by-products, illustrating the diversity of the Fenton-type of chemistry for plastic degradation.[37] There is a gap in the literature for heterogeneous Fenton catalysts for LDPE degradation that require a low loading, no pretreatment, can be used at neutral pH, and can be tailored to produce useful acid products without over-oxidation to gaseous products.

While Fe is the traditional Fenton metal, the literature has been expanding to report many other redox active metals as excellent Fenton catalysts.[38] The incorporation of a second Fenton-active metal with Fe in mixed metal oxide systems has been widely reported to exhibit a strong synergistic effect.[39-42] CeO_2 is widely accepted as an excellent catalyst for many applications owing to its' ability to redox

cycle between 3^+ and 4^+ states, resulting in high capacity for oxygen storage.[43, 44] These properties also make it an excellent Fenton catalyst, and it has been reported for use in organic pollutant degradation.[26] Commonly, CeO_2 is coupled with another metal typically by doping which results in the formation of oxygen vacancies, further improving catalytic activity.[45] Fe doped CeO_2 is a commonly reported catalyst for Fenton organic pollutant degradation[46, 47] owing to its stability, high surface area, reactivity, reusability and oxygen mobility.[48, 49] The dissolution of Fe in a larger crystal structure such as CeO_2 can create a superior Fenton-type catalyst as it can prevent precipitation and accumulation of soluble Fe sludge. Additionally, a synergistic effect is reported for iron/cerium complexes as Fenton catalysts.[47]

Microwave-assisted heating has proven to be beneficial for Fenton-type reactions by stimulating the redox cycle of metal ions. [50, 51] Microwaves can penetrate directly through a sample, forming hot spots on more polar or conductive species in a mixture.[52] In this case, Fe-doped ceria is an excellent microwave absorbing catalyst, meaning hot spots will be present on the catalyst surface improving reaction efficiency. Microwave assisted depolymerisation has also become popular for plastic degradation due to increased energy efficiency compared to conventional thermal heating.[53]

This work reports the synthesis of an Fe-CeO_2 solid solution as a catalyst for the microwave-assisted Fenton oxidative degradation of LDPE. The catalyst was characterised by XRD, Raman, XPS, FTIR, TXRF, SEM, TEM and EDX. The aim of this work is to maximise the yield of mono and dicarboxylic acids formed from LDPE oxidative degradation. Additionally, the catalyst was effective at low loadings (1 wt. %), at neutral pH and showed excellent recyclability over 6 cycles. To our knowledge, this is the first use of an Fe-CeO_2 solid solution recyclable heterogeneous catalyst for the Fenton oxidation of polyethylene under neutral pH.

Experimental Section

Experimental details including catalyst synthesis and characterisation, Fenton oxidation procedure and product analysis can be found in the Supplementary Information.

6.2 Results and Discussion

6.2.1 Synthesis and Characterisation of Fe-CeO_2 Catalyst

The Fe-CeO_2 solid solution catalysts were synthesised by co-precipitation method (see experimental section for details). Figure 1 a) shows the Raman spectra collected for CeO_2, Fe_2O_3 and the Fe-CeO_2 composites made in 3 different molar ratios: 1:2, 1:1 and 2:1. The strong band arising at 468 cm^{-1} for the bare CeO_2 was assigned to the F_{2g} Raman mode of fluorite cubic ceria.[48, 54] Broadening of this band and a decrease in intensity was observed with increasing Fe content, indicative of Fe-Ce interaction in the doped systems. A notable shift of the fluorite peak to lower wavenumbers along with this decrease in intensity shows a decrease in the CeO_2 crystallite size likely due to the dissolution of Fe^{3+} ions throughout the CeO_2 lattice and formation of a solid solution. Broadening of the F_{2g} mode was also attributed to the presence of lattice defects.[55, 56] The modes at 227, 298, 404, 497 and 611 cm^{-1} were assigned to the A_{1g} or E_g modes of α-Fe_2O_3 and were only observed in the Fe_2O_3 and the Fe-CeO_2 2:1 catalyst due to saturation of the ceria lattice and formation of Fe_2O_3 on the catalyst surface. The absence of these peaks in the Fe-CeO_2 catalysts with a molar ratio of 1:2 and 1:1, is indicative of solid solution formation. The weaker intensity of the Fe_2O_3 Raman bands compared to those of CeO_2 were attributed to differences in crystallinity or particle size of the phases present[56], but have also been reported due to the strong absorbance of Fe2O3 in this region of the Raman spectrum.[55, 57]

The XRD patterns of the catalysts shown in Figure 1 b) supports Raman analysis on formation of a solid solution. The diffraction peaks at 28.4, 32.9, 47.3, 56.2, 59.1, 69.3, 76.7 and 79.0° in 2θ were assigned to the (111), (200), (220), (311), (222) and (400) lattice planes of CeO2 with a cubic fluorite ($Fm\bar{3}m$) crystal structure, respectively (JCPDS 65-5923). The presence of these peaks in the XRD pattern of each of the three solid solutions shows the preservation of the cubic fluorite CeO_2 structure on addition of the Fe^{3+}. Furthermore, the broadening and decreased intensity of the CeO_2 peaks in the solid solutions is commonly attributed to the shrinking of the overall lattice size on replacement of the larger Ce^{4+} ions with smaller Fe^{3+} ions. The iron oxide showed peaks at 21.1, 33.1, 36.5, 41.1, 50.3, 53.0, 58.9 and

61.2 ° in 2θ, are assigned to the (012), (104), (110), (113), (024), (116), and (018) lattice planes of α-Fe_2O_3 (JCPDS 33-0664) in agreement with the literature.[58] These peaks are not observed in the Fe-CeO_2 catalysts with molar ratios of 1:1 and 1:2, consistent with the formation of a solid solution.[59] The CeO_2 crystallite size was also estimated using the Scherrer equation[60] in Figure S2 (see Supplementary Information) showing a decrease in size from 18 nm in the bare CeO_2 to 4.8 nm for the 1:2 catalyst, 2.9 nm for the 1:1 catalyst and 2.7 for the 2:1 catalyst. The decrease in crystallite size on addition of Fe to the CeO_2 lattice structure is to be expected as inclusion of smaller Fe ions into the CeO_2 lattice will shrink the overall lattice size. A small decrease in crystallite size was seen between the Fe-CeO_2 1:1 and Fe-CeO_2 2:1 catalysts due to the CeO_2 lattice becoming saturated with Fe ions and the crystallite size only slightly decreases as the excess iron is forming as Fe_2O_3 rather than being further incorporated into the CeO_2 lattice, as also observed in the Raman spectra and XRD patterns. FTIR analysis was also carried out on each of the catalysts shown in Supplementary Information Figure S3. The broad bands at 440 cm^{-1} and 525 cm^{-1} attributed to Fe-O stretching becomes less intense as the Fe content decreases in each of the solid solutions in excellent agreement with the Raman and XRD analysis. The broad band at ~3450 cm^{-1} was assigned to -OH stretching vibrations and is characteristic of adsorbed surface water molecules.[61]

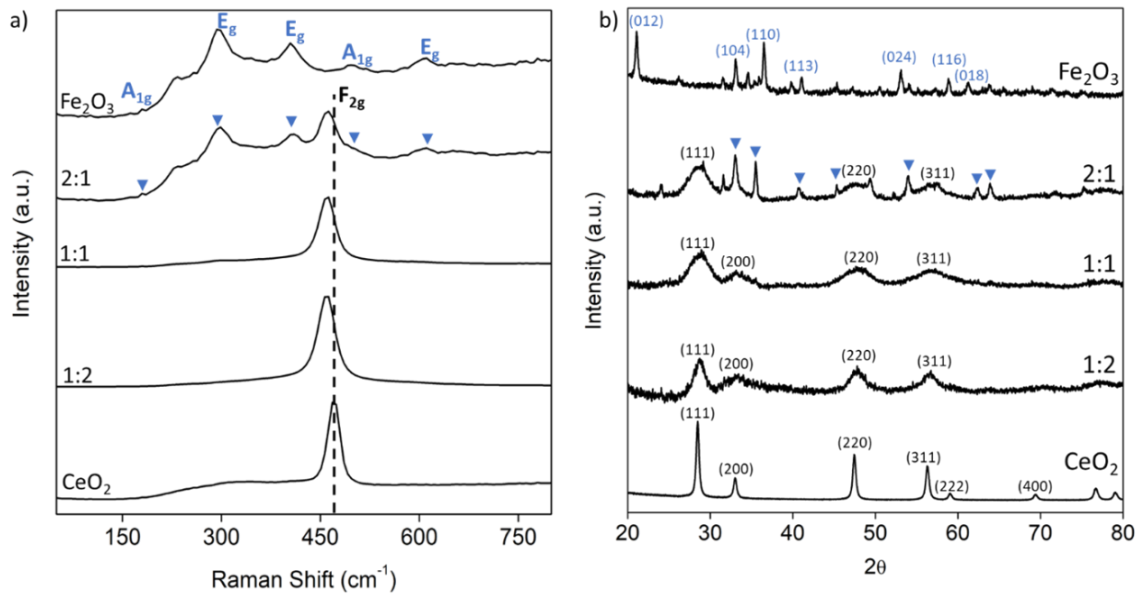


Figure 1: a) Raman analysis of Fe_2O_3, CeO_2, and Fe-CeO_2 solid solutions and b) XRD patterns of Fe_2O_3, CeO_2, and Fe-CeO_2 solid solutions.

XPS analysis was used to assess the surface chemistry of the solid solutions, specifically the valence state of the cerium and iron species in the solid solution as well as the oxygen vacancies that were present. XPS confirmed that Fe and Ce were present in ratios of 2:1, 1:1 and 1:2 for each respective catalyst and correlated well with other quantitative analysis on Fe and Ce carried out in this study. The survey scan for each catalyst is shown in Supplementary Information Figure S4 and confirmed the presence of Fe and Ce within the samples. The Ce 3d region was used to establish the dominant oxidation state of Ce in each of the samples. The Ce 3d XPS spectra for bare CeO_2 and each of the solid solutions, shown in Figure 2 a), were in excellent agreement with Ce 3d XPS spectra for CeO_2 in the literature[62, 63] and showed eight distinct peaks all corresponding to either Ce^{3+} or Ce^{4+} core levels. The peak labels *v* and *u* correspond to the spin-orbit doublets of Ce $3d_{5/2}$ and Ce $3d_{3/2}$, respectively. The quantitative data of Ce^{4+} and Ce^{3+} in CeO_2 and each of the solid solutions was calculated and is shown in Figure 2 b). (see Experimental section for further details).

The peak denoted u''' is the reported fingerprint peak for Ce^{4+} Ce $3d_{3/2}$ state and was present in all samples.[64, 65] Additionally, the peaks denoted u, u'' and u''', and v, v'' and v''' are the final states of the Ce^{4+} Ce $3d_{3/2}$ and Ce $3d_{5/2}$, respectively. The final states for Ce^{3+} are expressed as u_0 and u', and v_0 and v', corresponding to the Ce $3d_{3/2}$ and Ce $3d_{5/2}$, respectively.[66] The percentage of Ce^{4+} sites dropped from 80 % in the CeO_2 sample to 48 %, 56 % and 42 % in the 1:2, 1:1 and 2:1 samples, respectively, and was attributed to the substitution of the Ce^{4+} sites with Fe^{3+} sites in the CeO_2 lattice on formation of a solid solution. An increase in Ce^{3+} sites from 20 % in CeO_2 to 52 %, 44 % and 58 % in the 1:2, 1:1 and 2:1 samples, respectively, and was associated with an increase in oxygen vacancies within the solid solution which have been shown to increase catalytic activity in CeO_2 systems.[61] Furthermore, the presence of Ce^{3+} and Ce^{4+} in an almost equal ratio in the catalyst will help to promote Fenton reactivity as discussed in the catalytic evaluation section.

Figure **2** c) shows the Fe 2p spectra for Fe_2O_3 and each of the Fe-CeO_2 composites. Two distinct peaks at binding energies of 711.5 eV and 725.3 eV corresponded to Fe $2p_{3/2}$ and Fe $2p_{1/2}$, respectively and an additional satellite peak is present at 719.5 eV further confirming the presence of Fe^{3+} and were all in good agreement with values reported for Fe_2O_3[67] and confirmed that surface iron present in the samples is in the +3 valence state.[68] A shift of the Fe $2p_{3/2}$ peak to lower binding energies was observed with decreasing Fe content in the solid solution catalysts and was attributed to Fe-Ce interactions in the solid solution catalysts, specifically an increase of electron density occurring with a smaller concentration of Fe^{3+} within the lattice from the 2:1 to 1:2 samples. The Fe 3p spectra, shown in Figure S5 a) was in agreement with the literature for Fe_2O_3[67] and similar to the Fe2p core level, a slight shift to lower binding energies was observed for the solid solutions which was also attributed to Fe-Ce electronic interactions.

The O1s spectra for the Fe_2O_3, CeO_2, and Fe-CeO_2 solid solutions are shown in Figure S5 b). The peak at a BE of ~529 eV for each of the samples was assigned to the metal-oxygen (M-O) or O^{2-} species within the structure. The peak at a higher binding energy of ~531 eV is assigned to oxygen defects,

commonly reported for transition metal oxide species and are indicative of regions where the coordination number of O is smaller than in regular sites.[69] The formation of oxygen defects within the lattice structure as well as an increase in Ce^{3+} sites is attributed to the reduction of particle size on incorporation of Fe into the CeO_2 lattice and can contribute to enhanced oxygen mobility or improved redox properties of the catalyst.[46] A third peak arising at ~533 eV was assigned to surface hydroxyls which may arise from water adsorption and is in agreement with the literature.[70]

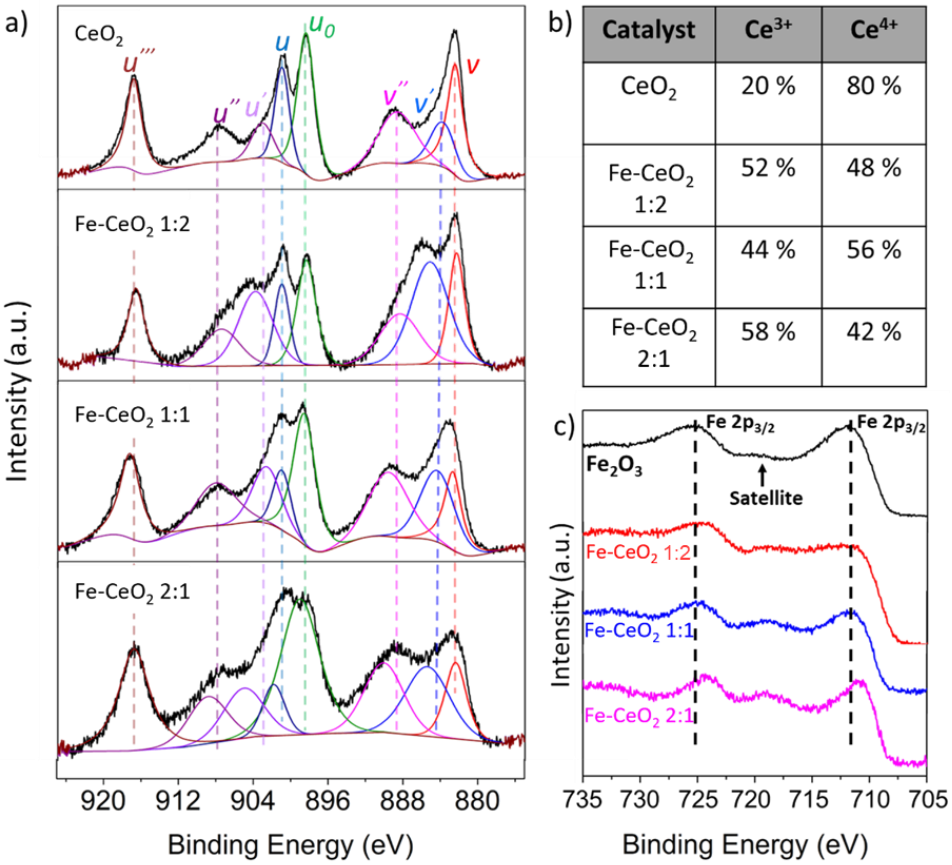


Figure 2: a) Ce 3d core level XPS spectrum for CeO_2 and the Fe-CeO_2 solid solutions b) quantitative data from the Ce3d core level scans and c) Fe 2p core level XPS spectrum for Fe_2O_3 and the Fe-CeO_2 solid solutions.

SEM was used to assess the morphology of the Fe-CeO_2 solid solution catalysts as shown in Figure 3 a)-c) showing needle-like nanostructures. Ceria nanorods have been reported to have superior

catalytic properties for water-gas shift reaction over other ceria morphologies owing to a higher lattice strain resulting in increased oxygen vacancies.[71] Another study reported ceria nanorods to have increased oxygen vacancies leading to higher Ce^{3+} content and therefore enhanced activity for the hydrogenation of cinnemaldehyde.[72] EDX analysis of the Fe-CeO_2 1:1 catalyst is shown in Figure 3 d) and illustrates an even dispersion of Fe and Ce throughout the sample. Further EDX mapping was carried out using HAADF-STEM for the Fe-CeO_2 2:1, 1:1 and 1:2 catalysts which is shown in the Supplementary Information Figure S6. The EDX maps show the Fe is uniformly dispersed in catalysts with a Fe-CeO_2 molar ratio of 1:1 and 1:2, while the catalyst with molar ratio 2:1 shows some segregated Fe regions, attributed to the presence of Fe_2O_3, in good agreement with the XRD and Raman analysis. This observation is also confirmed by high resolution TEM analysis, as shown in Figure 3 e)-j). TEM images of each of the catalysts (e)-g)) shows the formation of aggregates of small diameter nanoparticles. The mean particle diameter and standard deviations were approximated from the images to be 5.3 ±1.2 nm (Fe-CeO_2 1:2), 4.9 ± 1.7 nm (Fe-CeO_2 1:1) and 3.8 ± 0.8 nm (Fe-CeO_2 2:1) and the size distribution histograms are shown in SI Figure S7. Figure 3 h)-j) shows the HRTEM of each of the catalyst with the FFT of each in the inset of the images. The Fe-CeO_2 1:2 solid solution confirms the presence of cubic fluorite ceria from the presence of the (200), (111) and (220) lattice fringes with *d*-spacing of 0.298 nm, 0.340 nm and 0.170 nm, respectively.[73] The inset shows four strong rings assigned to the (111), (200), (220) and (311) crystal planes of crystalline cubic fluorite ceria ($Fm\bar{3}m$). The Fe-CeO_2 1:1 catalyst showed lattice fringes with *d*-spacings of 0.336 nm, 0.211 nm and 0.168 nm which were assigned to the (111), (200) and (220) CeO_2 planes. A decrease in the *d*-spacing for the Fe-CeO_2 1:1 catalyst compared to the Fe-CeO_2 1:2 samples can be attributed to the shrinkage of the CeO_2 lattice on an increase of Fe content.[74] The *d*-spacing for the Fe-CeO_2 2:1 catalyst, illustrated in in Figure 3 j), shows the CeO_2 (111) *d*-spacing further decreases to 0.327 nm, evidencing shrinkage of the ceria lattice due to Fe incorporation. The Fe-CeO_2 2:1 sample is the only sample that showed the presence of an Fe_2O_3 crystal plane with a *d*-spacing of 0.376 nm, which was assigned to the (012) plane of hexagonal

Fe_2O_3 and further supports the Raman and XRD analysis. The FFT pattern shows the formation of Fe_2O_3 with a hexagonal lattice showing the (104), (012) and (110) planes.[75, 76]

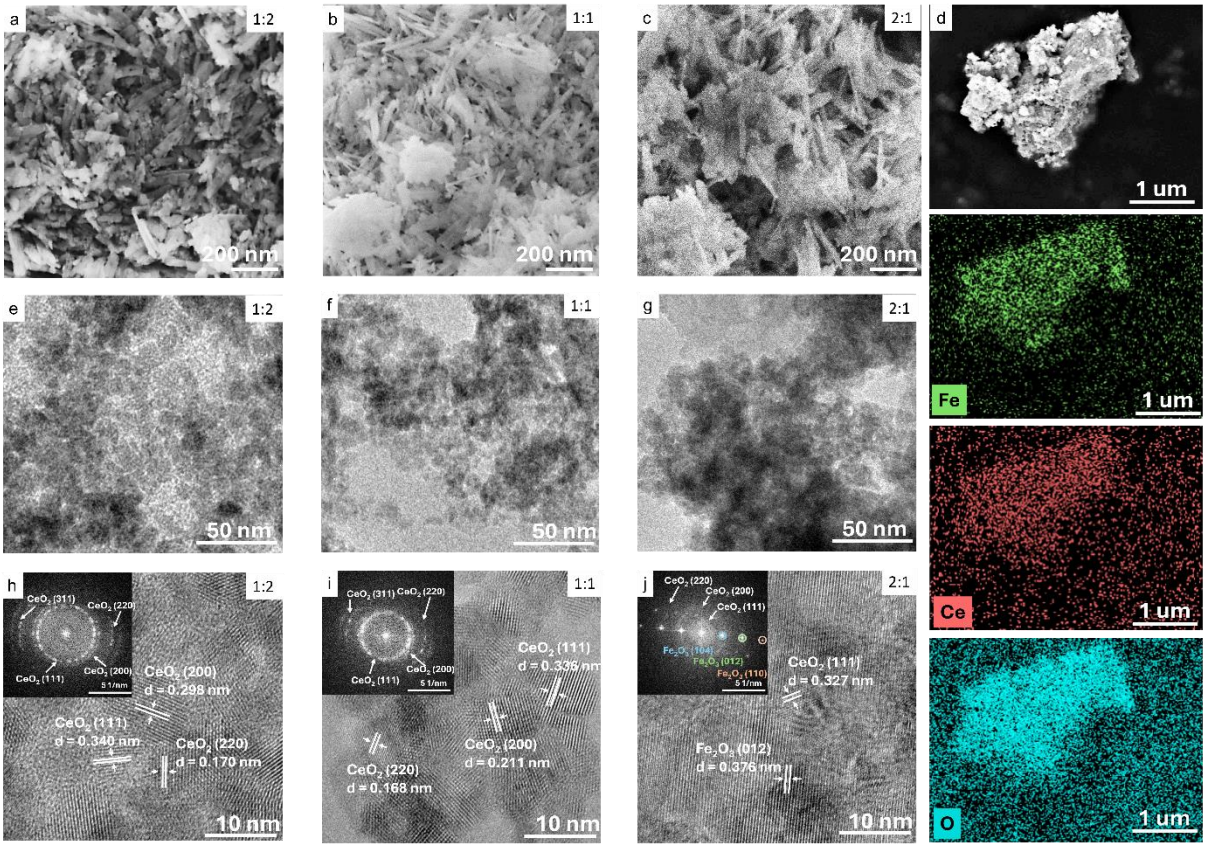


Figure 3: a)-c) SEM images of Fe-CeO_2 catalyst with Fe:Ce molar ratios of 1:2, 1:1 and 2:1, d) SEM and corresponding EDX of Fe-CeO_2 1:1, e)-g) TEM images of Fe-CeO_2 1:2, 1:1 and 2:1, h)-j) HRTEM with FFT of Fe-CeO_2 1:2, 1:1 and 2:1.

Figure S8 a) shows the total reflection X-ray fluorescence (TXRF) spectra for each solid solution catalyst, which was used to further quantify Fe and Ce in the catalysts. The spectrum shows peaks assigned to the emission lines of $L_{\alpha1}$, $L_{\beta1}$, $L_{\gamma1}$ and $L_{\gamma2}$ for Ce and of $K_{\alpha1}$ and $K_{\beta1}$ for Fe. The quantitative data is shown in Table S1 and confirmed that molar ratios of Fe and Ce in each Fe-CeO_2 catalyst was in excellent agreement with the precursor ratio used in the synthesis.

6.2.2 Catalytic evaluation of Fe-CeO_2 solid solution catalyst for oxidative degradation of polyethylene

The Fe-CeO_2 solid solutions were tested as heterogeneous Fenton-type catalysts in the microwave-assisted oxidative degradation of LDPE with the aim of maximising the yield of organic acids. The use of microwave assisted heating has many benefits over conventional thermal heating due to the uniform heat transfer and rapid volumetric heating which has been shown to increase reaction rates and higher product yields in reactions involving chemical plastic degradation.[77, 78] While a specific microwave-assisted Fenton mechanism has not yet been proposed, the reactivity under MW-assisted heating is likely due to the use of catalytic metals with high microwave absorbing properties as well as a polar solvent with a high dielectric constant contributing to specific "hot spots" being created at catalyst-solvent interfaces.[52, 79, 80] The degradation products were identified and quantified using HPLC by establishing calibration curves for eight acid standards: succinic acid, formic acid, glutaric acid, acetic acid, adipic acid, propionic acid, butyric acid and pimelic acid, shown in Figure S9 a). The retention times of each standard are shown in Figure S9 b) and a typical chromatogram of the degradation products is shown in Figure S9 c).

Initially, the reactions were carried out using typical Fenton conditions such as acidic solution (pH 1) and an catalyst mass loading of 10 wt. %.[32, 34] A mass of 0.3 g LDPE was used along with 10 mL of a H_2O_2 solution 9 % (w/w). The reproducibility of the reactions over three reactions was approximated to be within an error of ±10 %. Figure 4 a) shows the effect of temperature and stir speed on the reaction efficiency. The mass loss for LDPE shows an almost linear response to temperature increasing from 20% at 150 °C to 90 % at 180 °C. The reaction also favoured high stir speeds, attributed to the hydrophobic surface of the LDPE and the heterogeneous nature of the reactions. Optimal microwave reaction conditions were 180 °C for 3 h with 1900 rpm stir speed. Figure 4 b), shows the performance of the Fe-CeO_2 solid solution catalysts as well as Fe_2O_3 and CeO_2. While both Fe_2O_3 and CeO_2 both act as catalysts under these conditions, the combined use of Fe-CeO_2 as the catalyst gave higher mass loss

and yields, indicating a synergistic effect between the Fe and CeO_2. Synergistic effects in multi-metal Fenton catalysts have been reported to be attributed to the presence of multivalent ions which play distinct roles in the catalytic mechanism.[81] In the reaction, the lower valent metal (Ce^{3+}, Fe^{2+}) nucleophilically attacks the O-O bond of the H_2O_2 to generate a hydroxyl radical ($^{\bullet}OH$) and, the higher valent metal (Ce^{4+}, Fe^{3+}) electrophilically abstracts the H from the H_2O_2 generating hydroperoxyl radicals ($HO_2^{\bullet}$)[81] . The Fe-CeO_2 2:1 and Fe-CeO_2 1:2 catalysts had similar activity with mass losses of 81 % and 74 % and yields of 63 % and 60 %, respectively. They were both outperformed by the Fe-CeO_2 1:1 catalyst with a 94% mass loss and 78 % yield. The Fe-CeO_2 2:1 catalyst may be less effective due to aggregates of iron oxides disrupting the synergistic effect of the solid solution structure. The Fe-CeO_2 1:2 catalyst may be less effective due to the lower Fe content.[46]

As it was the best performing catalyst, Fe-CeO_2 1:1 was used to study the effect of the H_2O_2 concentration and catalyst loading on both the mass loss and acid yield. Figure 4 c) illustrates the interplay between H_2O_2 concentration and catalyst loading. When using 10 wt. % catalyst loading, the mass loss and yield increased linearly with the H_2O_2 concentration and excellent performance was observed using 9 % (w/w) H_2O_2 with a mass loss LDPE of 94 % and an acid yield of 78 %. At very high catalyst loading of 30 wt. % full mass loss is observed but the organic acid yield decreases with increasing H_2O_2 concentration due to over-oxidation of the acid products to gaseous reagent such as CO_2. This indicates that catalyst system could be tuned to gaseous products which has been a strategy used for the destruction of microplastics. [22]

One key advantage of heterogeneous Fenton systems over homogeneous Fenton systems is their operation over a wide pH range.[26] The effect of solution pH was evaluated for the Fe-CeO_2 1:1 catalyst at a pH of 1, 4 and 7 and the results are shown in Figure 4 d). While a trend of decreased yield with increasing pH was noted, good catalytic activity at neutral pH was still observed, with a mass loss of 77% and acid yield of 55 %. The main product found for the reaction at pH 1 was butyric acid, while formic acid was the main product for the reaction at pH 4 and pH 7 indicative of mechanistic

differences in the degradation process. The different reaction products under acidic conditions may be attributed to the presence of nitric acid contributing to LDPE degradation and oxidation through the formation radicals from HNO_3 under MW irradiation.[22] Implementing the oxidative degradation reaction at a neutral pH is more favourable as a safer and greener reaction protocol. Additionally, removing the use of nitric acid limits the formation of unwanted nitrate contaminants in the product mixture.[21] HPLC analysis of the product shown in Supplementary Information Figure S10 show a significant decrease in the nitrate peak intensity when nitric acid was not added to the reaction mixture. A minor nitrate peak is still present due to the use of nitrate stabilisers in both H_2SO_4 and H_2O_2.

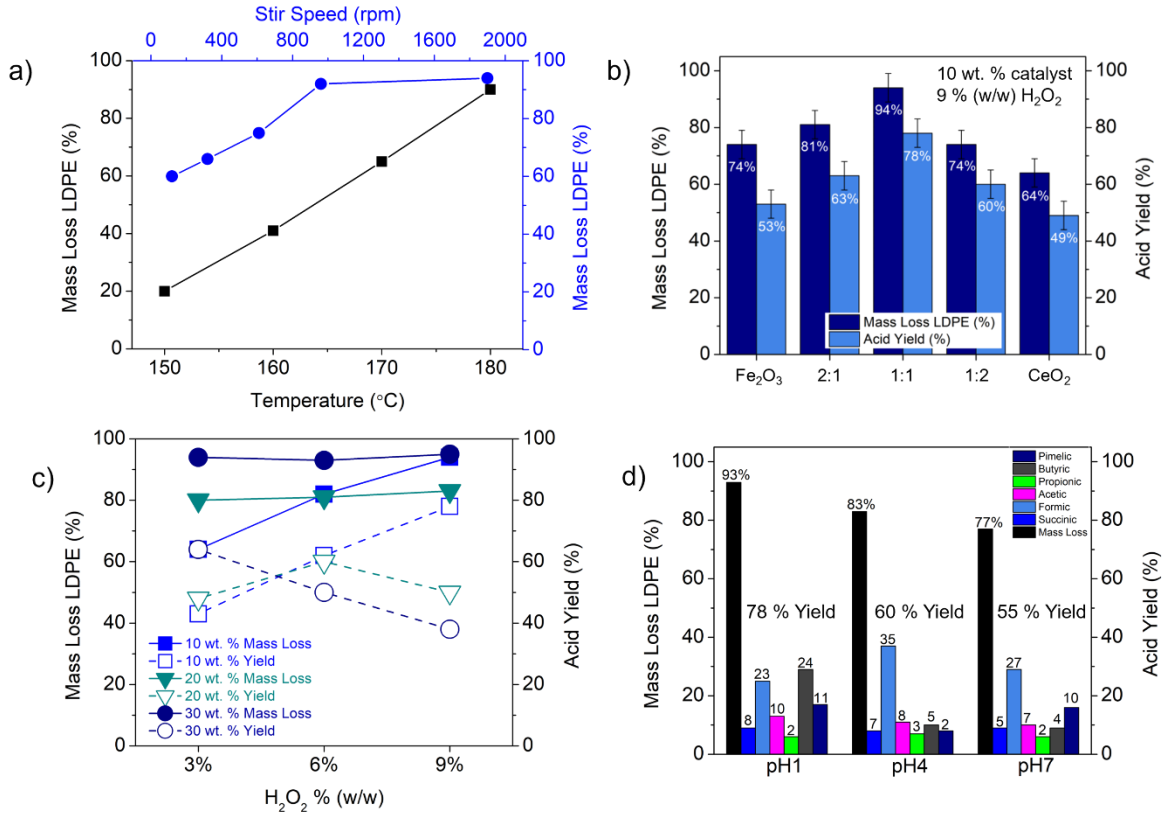


Figure 4: a) effect of stir speed and temperature on mass loss LDPE (0.3 g LDPE, pH 1, 10 wt. % catalyst loading (0.03 g), 10 mL 9 % H_2O_2), b) catalyst screening at pH1 (0.3 g LDPE, 10 wt. % catalyst loading (0.03 g), 10 mL 9 % H_2O_2 (w/w), c) effect of H_2O_2 concentration and catalyst loading on acid yield (0.3 g LDPE, pH 1), d) catalytic results at pH 1, 4 and 7 with product distribution (0.3 g LDPE, 10 wt. % catalyst loading (0.03 g), 10 mL 9 % H_2O_2).

6.2.3 Catalytic Optimisation of Polyethylene Degradation under Neutral pH

The Fenton catalytic degradation of LDPE at neutral pH is highly advantageous, so these conditions were further optimised to maximise the organic acid yield at pH 7 and evaluate the product composition. For the screening study, 0.5 g of LDPE, Fe-CeO_2 1:1 catalyst with loadings ranging from 1 – 15 wt. % were used with 10 mL solutions of H_2O_2 ranging from 5 – 15 % (w/w). Figure 5 a) shows the LDPE mass loss and total organic acid yield as a function of H_2O_2 concentration when using different catalyst loadings (1, 5 and 10 wt. %) under neutral pH and illustrate that both catalyst loading an H_2O_2 concentration play a crucial role in determining the mass loss and organic acid yield. From Figure 5 it can be seen that at lower H_2O_2 concentration (5 w/w %) the mass loss increases with the increasing catalyst loading, yet the yield of the organic acid remained similar. As the H_2O_2 concentration is increased to 10 w/w % all catalysts showed higher mass losses and yields. The effect of further increases in H_2O_2 concentration was dependent on catalyst loading. When using 10 wt% catalyst loading under neutral pH, the mass loss and yield both decreased suggesting catalyst deactivation under these reaction conditions. A well reported deactivation mechanism with increased catalyst loading in heterogeneous systems is catalyst deactivation due to agglomeration.[82] Decreased mass loss and yield were not observed for the reactions carried out acidic conditions even under high loading conditions likely owing to the presence of nitric acid contributing to degradation of the LDPE.

Figure 5 illustrates that under neutral reaction conditions lower catalyst loadings with higher H_2O_2 concentrations are optimal to the achieve simultaneous high mass loss and high organic yields. For example, at 1 wt% catalyst loading and 5 % w/w H_2O_2, the mass loss of LDPE was only 41% (19 % yield), but this increased to a mass of 91% and yield of 71 % using 15% w/w H_2O_2. Figure 5 b) illustrates the organic acid yields and product distributions as a function of the catalyst loading and H_2O_2 concentration. The dominant products present at low H_2O_2 concentrations are succinic, formic, acetic and propionic acid. As H_2O_2 concentrations increase, the formation of longer chain acids, pimelic,

glutaric, and butyric acid is observed in the mixtures. While butyric acid was the dominant acid formed under pH 1, at pH 7 butyric acid was absent or only a minor component of the acid mixture.

Shown in Supplementary Information Figure S11, the reaction carried out in the absence of a catalyst (0.5 g LDPE and 10 mL H_2O_2 15 % (w/w)) gave a 15 % mass LDPE loss and 8 % acid yield. The reaction carried out in the absence of H_2O_2 (0.5 g LDPE, 1 wt. % catalyst 10 mL H_2O) gave a mass loss of 10 % and an acid yield of 8 %. These results show the importance of the presence of both catalyst and H_2O_2 in the reaction.

The Fe-CeO_2 solid solution catalysts of different molar ratios as well as Fe_2O_3 and CeO_2 catalysts were then screened again at the optimised pH 7 conditions (1 wt. % catalyst loading 10 mL 15 % H_2O_2 (w/w) shown in Figure 5 c). A similar synergistic effect was observed at pH 7 as was observed with reaction carried out at pH 1. All the solid solution catalysts display good activity, as shown in Figure 5 c) but the Fe-CeO_2 1:1 catalyst was again found to be the best performing. The catalyst performance of CeO_2 was relatively poor under neutral conditions (mass loss 41 %, yield 15 %). The redox cycle of Ce^{4+} to Ce^{3+} has been reported to form cerium-peroxide complexes ($\equiv Ce^{3+}$-OOH) which are stable at pH 7 and therefore do not degrade to radicals.[83] The good performance of the solid solution catalysts relative to CeO_2 at neutral pH suggests that when Ce is in the form of Fe-CeO_2 solid solution structure, the cerium-peroxide complexes are not as stable or may not form at all, another benefit of the solid solution catalyst structure.

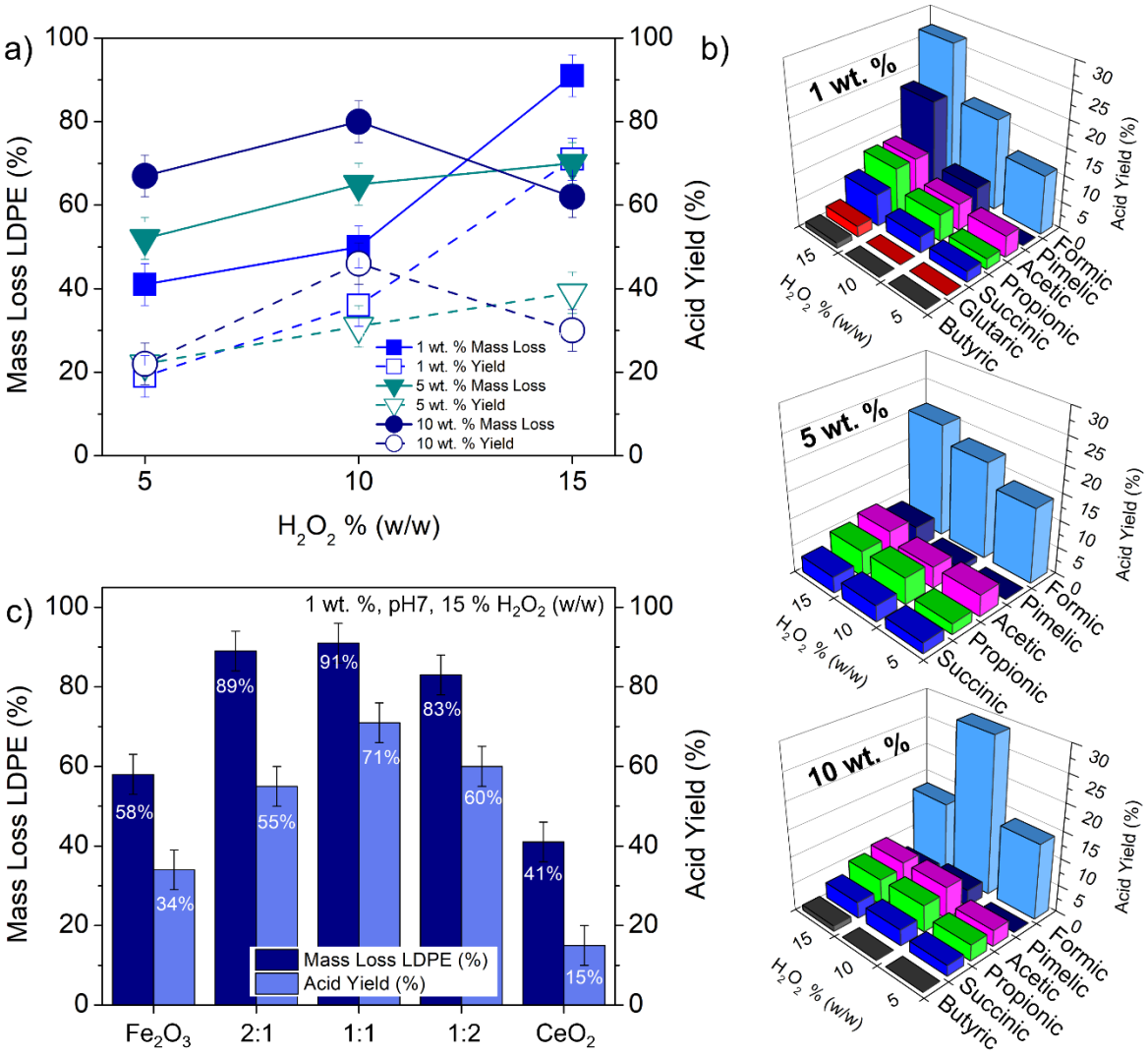


Figure 5: a) effect of H_2O_2 concentration and catalyst loading on mass loss and acid yield at pH 7 (0.5 g LDPE), b) effect of catalyst loading and H_2O_2 concentration on product distribution at 1 wt. %, 5 wt. % and 10 wt. % catalyst loading, and 5, 10 and 15 % (w/w) H_2O_2, respectively, c) catalyst screening at optimised conditions (0.5 g LDPE, 1 wt. % catalyst loading, 10 mL 15 % H_2O_2 (w/w), pH 7).

6.2.4 Reaction Time Series

A time series was carried out to evaluate the products formed in the oxidative degradation process of LDPE after 1 h, 2 h and 3 h of reaction time. Figure 6 a) shows the mass loss and yield for the Fe-CeO_2 catalyst with different molar ratios which all increase linearly with time. The Fe:Ce molar ratio clearly

plays a role in catalytic efficiency in terms of mass loss and organic acid yield. The Fe-CeO_2 catalyst with molar ratio of 1:1 resulted in the highest mass loss and acid yields. Figure 6 b) shows the reaction product distributions obtained from each catalyst over the reaction. The initial degradation products were succinic acid, formic acid and acetic acid and similar for all catalysts. The formation of longer chain acids, propionic acid, and pimelic acid and small amounts of glutaric and butyric acid was observed in each product mixture as the reaction proceeded. After 3 h of reaction time, the highest yields were obtained with the Fe-CeO_2 1:1 catalyst. Interestingly, a larger amount of pimelic acid (18 %) was observed in the Fe-CeO_2 1:1 product mixture relative to the Fe-CeO_2 2:1 (6 %) and the Fe-CeO_2 1:2 (9 %) catalysts. While the origin of the pimelic acid is not clear, it is likely due to the optimised tuning of the ratio of Fe and Ce in the catalyst. While the mechanisms are not comparable, high yields of pimelic acid have also previously been reported for thermal aerobic oxidation with molecular oxygen[84], and NO_x/O_2 systems.[85] FTIR analysis of the LDPE after 1 h, 2 h and 3 h reaction times is shown in Figure 6 c) and identified the formation of C=O and C-O groups due to surface oxidation of the polymer from attack of $HO^{\bullet}$ and $HO_2^{\bullet}$ radicals in solution. The carbonyl index was measured to be 0.85, 1.78 and 4.40 for the 1 h, 2 h and 3 h residual LDPE respectively (see Supplementary Information for details). SEM images in Figure 6 d) show the physical change in surface texture of the LDPE with an increase in surface roughness during the reaction. Small pore-like structures of approximately 5 µm diameter were observed after 1 h of reaction time and an increase in surface roughness of the over time is clearly observed. Additionally, an increase in surface oxygen can be observed from the EDX elemental mapping as the reaction proceeds, correlating with the FTIR analysis. XPS analysis of the residual LDPE surface after 3 h of reaction time shown in Supplementary information Figure S12 and showed four peaks at 284.7 eV, 285.4 eV, 286.9 eV and 288.8 eV which were attributed to C-C, C-O, C=O and O-C=O species on the LDPE surface, respectively.[86]

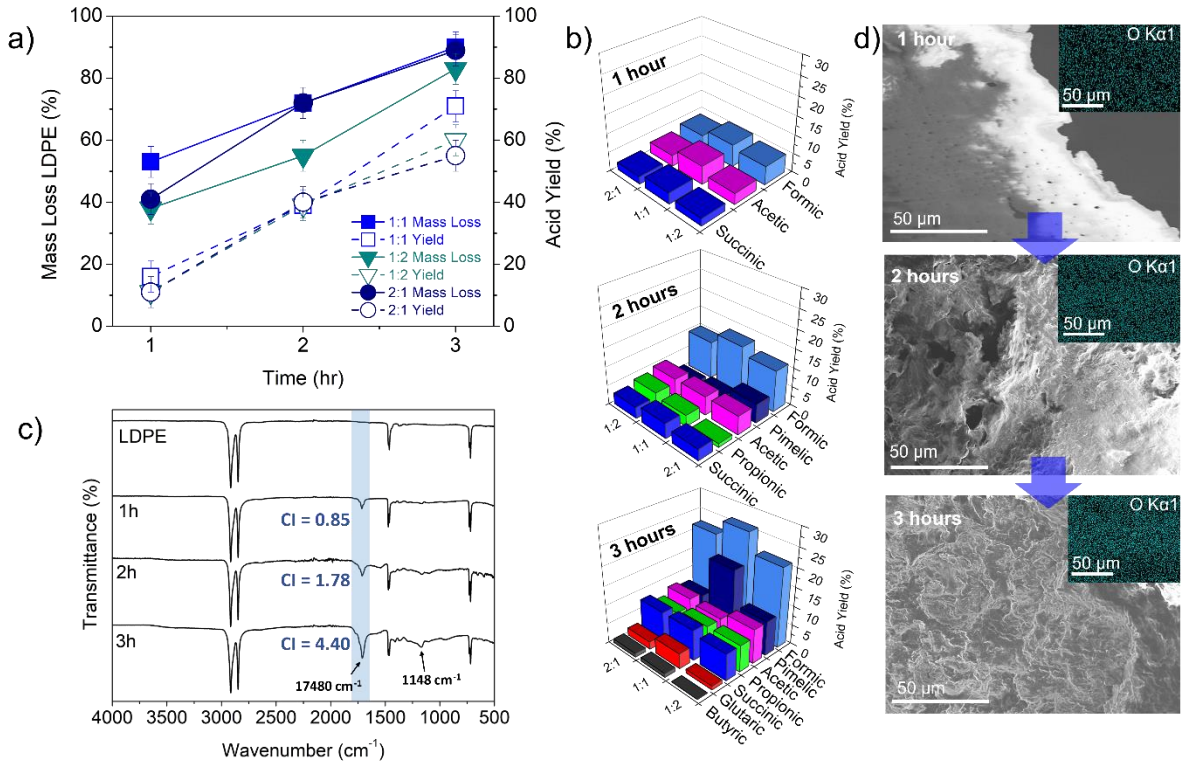


Figure 6: a) Time series results for Fe-CeO_2 1:2, 1:1 and 2:1 catalysts (0.5 g LDPE 1 wt. % catalyst, 15 % (w/w) H_2O_2), b) product distribution, c) FTIR analysis of LDPE residue surface after 1h, 2h and 3h reaction times with carbonyl index (CI), d) SEM of LDPE residue surface with oxygen EDX maps after 1h, 2h and 3h of reaction time.

6.2.5 Catalytic Recyclability

The results of the recyclability performance test of the Fe-CeO_2 1:1 catalyst are shown in Figure 7 a). The catalyst was found to be effective over 6 cycles with no loss in acid yield over each cycle. The superior recyclability performance can be accredited to the conservation of Ce^{4+} and Ce^{3+} ratio as determined by XPS shown in Figure 7 b) and no significant leaching of the Fe. TXRF (shown in Supplementary Information Figure S13 analysis confirmed the preservation of the 1:1 Fe:Ce molar ratio of the catalyst after 6 cycles. The high recyclability performance was attributed to the ability of the

solid solution structure to retain the 1:1 Fe:Ce molar ratio as no Fe sludge leaching was evident as it was after reactions using Fe_2O_3.

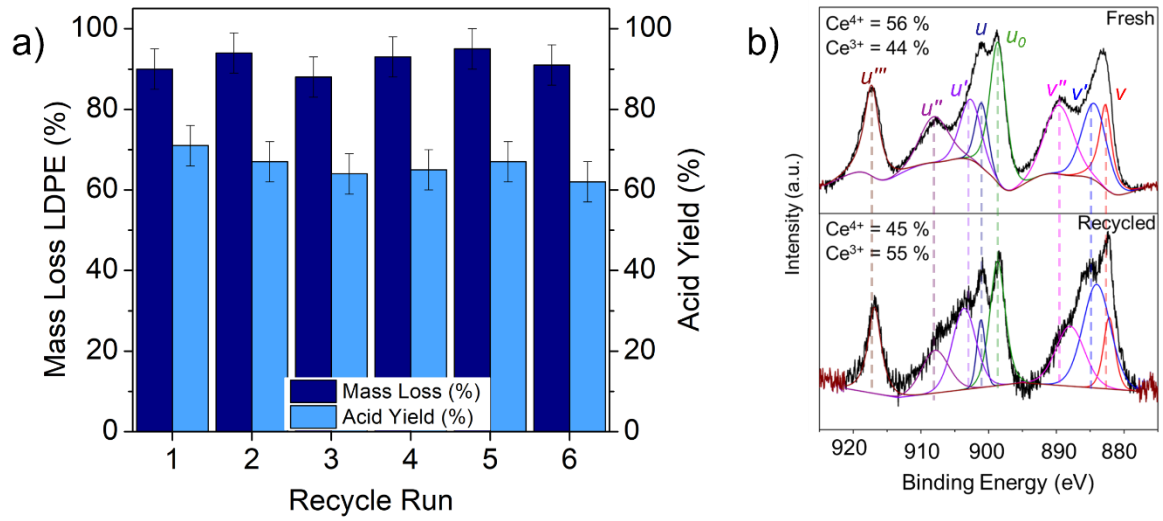


Figure 7: a) Recyclability performance of catalyst (0.5 g LDPE, 1 wt. % catalyst, 15 % (w/w) H_2O_2, 3 h, 180 °C, b) Ce 3d XPS of fresh and recycled catalyst.

Due to the complex nature of the oxidation process, Fenton oxidation mechanisms are still being proposed for heterogeneous systems. However, the catalytic efficiency and recyclability of the Fe-CeO_2 catalyst at neutral pH can almost certainly be attributed to its solid solution structure. Metal leaching from various heterogeneous iron oxide Fenton catalysts under these reaction conditions is well known which is highly unfavourable due to metal contamination of the product mixture.[26, 87]

The heterogeneous Fenton mechanism is not fully understood owing to multiple reaction pathways, different coordination chemistries between H_2O_2 and metal catalysts and difficulty tracking the short-lived radical complexes that form in the reaction. However, a compilation of the accepted general mechanisms for heterogeneous Fe and Ce at acidic and neutral pH are summarised in Table 1. The decomposition rate of H_2O_2 in heterogeneous Fenton chemistry is said to be proportional to the concentration of H_2O_2 and the surface area of the catalyst.[88] The heterogeneous Fe mechanism at

acidic pH is shown in table entry 1 and involves the adsorption of H_2O_2 on to the Fe^{3+} surface. This is subsequently followed by the formation of surface Fe^{2+} and a superoxide species owing to electron transfer from peroxide ligand to metal species. This leads to the formation of $HO^{\bullet}$ radicals which can interact with H_2O_2 and undergo chain reactions resembling homogeneous Fenton processes. Similarly, at acidic pH, cerium is proposed to form Ce/H_2O_2 complexes shown in entry 2 which subsequently degrade to $HO^{\bullet}$ and $HO_2^{\bullet}$ by an electron transfer pathway.

The widely accepted heterogeneous Fenton mechanism for Fe^{3+} (goethite) at neutral pH is shown in entry 3. The interaction of the Fe^{3+}-OH catalyst surface with H_2O_2 forms a stabilised H_2O_2 complex referred to as $(H_2O_2)_s$. A ligand-to-metal charge transfer then results in the formation of and Fe^{2+} transition state complex which then dissociates to form a $HO_2^{\bullet}$ radical. The regeneration of Fe^{3+} in the system then leads to the subsequent formation of $HO^{\bullet}$ radicals. In comparison, CeO_2 is not as effective Fenton heterogeneous catalysts at neutral pH due to the formation of stable Ce/H_2O_2 complexes which do not degrade to radicals at pH7 shown in entry 4, but the beneficial effect between Fe and Ce, plays an important role in the activity of Fe-CeO_2 solid solution catalyst.

Electron spin resonance (ESR) is a useful tool often used to monitor radical formation in Fenton systems. As the microwave vessels used in this study are sealed, it is not possible to possible to obtain in-situ aliquots of the reaction mixture for accurate ESR analysis. Other groups who have studied in-situ radical formation from Fe/Ce systems by ESR have reported the predominant active species to be $^{\bullet}OH$[89, 90]. Although the heterogeneous Fenton mechanism is exceptionally complex, literature has broadly defined the radical cycle in a series of 3 simple equations. The initiation step (Eqn. 1) of the Fenton reaction can generally be defined as the generation of $^{\bullet}OH$ from the redox decomposition of H_2O_2 over a Fenton catalyst (Fe, Ce). In the propagation step (Eqn. 2), the generated $^{\bullet}OH$ subsequently oxidises the LDPE chain which occurs through its own series of initiation, propagation and termination reactions. Termination (Eqn. 3) of the $^{\bullet}OH$ radical occurs when it comes into contact with the Fenton catalyst again, oxidising it and forming ^{-}OH as a result.[91, 92]

$$H_2O_2 + Fe^{2+} \rightarrow Fe^{3+} + HO^{\bullet} + HO^{-}$$ **Eqn. 1**

$$RHR' + HO^{\bullet} + HO^{-} \rightarrow ROHR' + H_2O$$ **Eqn. 2**

$$HO^{\bullet} + Fe^{2+} \rightarrow Fe^{3+} + HO^{-}$$ **Eqn. 3**

Nguyen *et al.*[37] proposed a multi-step Fenton oxidation mechanism of polyethylene by mechano-catalytic cracking, followed by C-C cleavage in the PE chain. The reaction equations are described in Table 1 entry 5. Radicals produced from the heterogeneous Fenton mechanism form a secondary alcohol species. Further oxidation by radical attack leads to formation of a ketone susceptible to further oxidation via Baeyer-Villiger oxidation to an ester group. This is followed by hydrolysis of the ester group to a carboxylic acid. Terminal alcohol groups can also be oxidised to a carboxylic acid. Formic and acetic acid have been reported as the main oxidation products from polyethylene.[93]

Table 1: Redox Cycles of Fe and Ce acidic and neutral pH and Mechanism of Oxidation of PE

Mechanism	Equation	Ref
1. Heterogeneous Fe (acidic pH)	$H_2O_2 + \equiv Fe^{3+} \leftrightarrow \equiv Fe^{3+}(O_2H) + H^+$ $\equiv Fe^{3+}(O_2H) \rightarrow \equiv Fe^{2+} + HO_2\cdot/(O_2^{\bullet-} + H^+)$ $\equiv Fe^{2+} + H_2O_2 \rightarrow \equiv Fe^{3+} + HO^{\bullet} + OH^-$ $H_2O_2 + HO^{\bullet} \rightarrow HO_2\cdot/(O_2^{\bullet-} + H^+) + H_2O$	88
2. Heterogeneous Ce (acidic pH)	$\equiv Ce^{4+} + H_2O_2 \rightarrow \equiv Ce^{4+}(O_2H) + H^+$ $\equiv Ce^{4+}(O_2H) \rightarrow \equiv Ce^{3+} + HO_2\cdot$ $\equiv Ce^{3+} + H_2O_2 \rightarrow \equiv Ce^{4+} + HO^{\bullet} + OH^-$	94
3. Heterogeneous Fe (neutral pH)	$\equiv Fe^{3+} - OH + H_2O_2 \leftrightarrow (H_2O_2)_s$ $(H_2O_2)_s \leftrightarrow (\equiv Fe^{2+\bullet}O_2H) + H_2O$ $(\equiv Fe^{2+\bullet}O_2H) \rightarrow \equiv Fe^{2+} + HO_2\cdot$ $\equiv Fe^{2+} + H_2O_2 \rightarrow \equiv Fe^{3+} - OH + {}^{\bullet}OH$	95
4. Heterogeneous Ce (neutral pH)	$\equiv Ce^{4+} + H_2O_2 \rightarrow \equiv Ce^{4+}(O_2H) + H^+$	94, 96

	$\equiv Ce^{4+}(O_2H) \nrightarrow$	
5. Oxidation of PE	**1. Heterogeneous Fenton** $RHR' + H_2O_2 \rightarrow ROHR' + H_2O$ **2. Oxidation** $ROHR' + H_2O + H_2O_2 \rightarrow RCOR' + 2H_2O$ **3. Baeyer-Villiger Oxidation** $RCOR' + H_2O_2 \rightarrow RCOOR' + H_2O$ **4. Hydrolysis** $RCOOR' + H_2O \rightarrow \boldsymbol{RCOOH}$ **5a. Oxidation** $ROH + H_2O_2 \rightarrow RCOH + 2H_2O$ **5b. Oxidation** $RCOH + H_2O_2 \rightarrow \boldsymbol{RCOOH} + H_2O$ **Over-oxidation to gaseous products:** $RCOH \rightarrow CO \uparrow + RH$ $RCOOH \rightarrow CO_2 \uparrow + RH$ **Decarbonylation / Radical Transfer**	[37, 96]

6.3 Conclusions

This work demonstrates that the microwave-assisted oxidative degradation of LDPE can be effectively tuned to obtain a mixture of carboxylic acid products limiting over-oxidation to gaseous products. The heterogeneous Fenton process was proven successful at neutral pH which is favourable as no acid addition is required minimising undesirable side products. No pre-treatment was required for the LDPE, allowing for a one-step degradation process. The synergistic effect, specifically the redox cycle of iron and cerium and the importance of tuning their molar ratios in the system has been demonstrated with the Fe-CeO_2 1:1 achieving the highest LDPE mass loss of 91% and organic acid yields

of 71% at neutral pH. The excellent recyclability of the catalyst was attributed to the solid solution structure which allowed for the preservation of Fe and Ce in a 1:1 ratio as well as the preservation of optimal ratios of Ce^{3+} and Ce^{4+} after 6 cycles. The main products obtained were formic acid as well as acetic acid, succinic acid and pimelic acid which are all valuable polymer precursors. Overall, the work shows that the Fe-CeO_2 solid solution catalyst performs exceptionally as a Fenton-type heterogeneous catalyst, providing a valuable pathway for the oxidative degradation of LDPE to valuable products.

Conflicts of interest

There are no conflicts to declare.

Acknowledgements

We acknowledge Science Foundation Ireland grant number (AMBER Grant No: 12/RC2278_P2). We thank the Advanced Microscopy Laboratory at Trinity College Dublin for TEM analysis, Bernal Institute University of Limerick for access to XPS facilities and Tyndall National Institute for access to SEM and XRD facilities.

6.4 References:

(1) Hopewell, J.; Dvorak, R.; Kosior, E. Plastics recycling: challenges and opportunities. *Philosophical Transactions of the Royal Society B: Biological Sciences* **2009**, *364* (1526), 2115-2126. DOI: 10.1098/rstb.2008.0311 (acccessed 2024/01/30).
(2) He, P.; Chen, L.; Shao, L.; Zhang, H.; Lü, F. Municipal solid waste (MSW) landfill: A source of microplastics? -Evidence of microplastics in landfill leachate. *Water Research* **2019**, *159*, 38-45. DOI: https://doi.org/10.1016/j.watres.2019.04.060.
(3) Barnes, D. K. A.; Galgani, F.; Thompson, R. C.; Barlaz, M. Accumulation and fragmentation of plastic debris in global environments. *Philosophical Transactions of the Royal Society B: Biological Sciences* **2009**, *364* (1526), 1985-1998. DOI: 10.1098/rstb.2008.0205 (acccessed 2024/01/30).
(4) Meys, R.; Frick, F.; Westhues, S.; Sternberg, A.; Klankermayer, J.; Bardow, A. Towards a circular economy for plastic packaging wastes – the environmental potential of chemical recycling. *Resources, Conservation and Recycling* **2020**, *162*, 105010. DOI: https://doi.org/10.1016/j.resconrec.2020.105010.
(5) Jiang, J.; Shi, K.; Zhang, X.; Yu, K.; Zhang, H.; He, J.; Ju, Y.; Liu, J. From plastic waste to wealth using chemical recycling: A review. *Journal of Environmental Chemical Engineering* **2022**, *10* (1), 106867. DOI: https://doi.org/10.1016/j.jece.2021.106867.
(6) Huang, J.; Veksha, A.; Chan, W. P.; Giannis, A.; Lisak, G. Chemical recycling of plastic waste for sustainable material management: A prospective review on catalysts and processes. *Renewable and Sustainable Energy Reviews* **2022**, *154*, 111866. DOI: https://doi.org/10.1016/j.rser.2021.111866.
(7) Liu, Y.; Shi, J.; Jin, H.; Guo, L. Chemical recycling methods for managing waste plastics: a review. *Environmental Chemistry Letters* **2024**, *22* (1), 149-169. DOI: 10.1007/s10311-023-01664-5.
(8) Watanabe, M.; Matsuo, Y.; Matsushita, T.; Inomata, H.; Miyake, T.; Hironaka, K. Chemical recycling of polycarbonate in high pressure high temperature steam at 573 K. *Polymer Degradation and Stability* **2009**, *94* (12), 2157-2162. DOI: https://doi.org/10.1016/j.polymdegradstab.2009.09.010.
(9) Stuyck, W.; Janssens, K.; Denayer, M.; De Schouwer, F.; Coeck, R.; Bernaerts, K. V.; Vekeman, J.; De Proft, F.; De Vos, D. E. A sustainable way of recycling polyamides: dissolution and ammonolysis of polyamides to diamines and diamides using ammonia and biosourced glycerol. *Green Chemistry* **2022**, *24* (18), 6923-6930, 10.1039/D2GC02233H. DOI: 10.1039/D2GC02233H.
(10) Casey, É.; Breen, R.; Gómez, J. S.; Kentgens, A. P. M.; Pareras, G.; Rimola, A.; Holmes, J. D.; Collins, G. Ligand-Aided Glycolysis of PET Using Functionalized Silica-Supported Fe2O3 Nanoparticles. *ACS Sustainable Chemistry & Engineering* **2023**, *11* (43), 15544-15555. DOI: 10.1021/acssuschemeng.3c03585.
(11) Thiounn, T.; Smith, R. C. Advances and approaches for chemical recycling of plastic waste. *Journal of Polymer Science* **2020**, *58* (10), 1347-1364. DOI: https://doi.org/10.1002/pol.20190261 (acccessed 2024/01/30).
(12) Geyer, R.; Jambeck, J. R.; Law, K. L. Production, use, and fate of all plastics ever made. *Sci Adv* **2017**, *3* (7), e1700782.
(13) *The Round Up Plastic Waste Statistics*. 2023. https://theroundup.org/plastic-waste-statistics/ (accessed.

(14) Anuar Sharuddin, S. D.; Abnisa, F.; Wan Daud, W. M. A.; Aroua, M. K. A review on pyrolysis of plastic wastes. *Energy Conversion and Management* **2016**, *115*, 308-326. DOI: https://doi.org/10.1016/j.enconman.2016.02.037.
(15) Solis, M.; Silveira, S. Technologies for chemical recycling of household plastics – A technical review and TRL assessment. *Waste Management* **2020**, *105*, 128-138. DOI: https://doi.org/10.1016/j.wasman.2020.01.038.
(16) Piovano, A.; Paone, E. The reductive catalytic upcycling of polyolefin plastic waste. *Current Research in Green and Sustainable Chemistry* **2022**, *5*, 100334. DOI: https://doi.org/10.1016/j.crgsc.2022.100334.
(17) Cao, R.; Zhang, M.-Q.; Hu, C.; Xiao, D.; Wang, M.; Ma, D. Catalytic oxidation of polystyrene to aromatic oxygenates over a graphitic carbon nitride catalyst. *Nature Communications* **2022**, *13* (1), 4809. DOI: 10.1038/s41467-022-32510-x.
(18) Oh, S.; Stache, E. E. Chemical Upcycling of Commercial Polystyrene via Catalyst-Controlled Photooxidation. *Journal of the American Chemical Society* **2022**, *144* (13), 5745-5749. DOI: 10.1021/jacs.2c01411.
(19) Sullivan, K. P.; Werner, A. Z.; Ramirez, K. J.; Ellis, L. D.; Bussard, J. R.; Black, B. A.; Brandner, D. G.; Bratti, F.; Buss, B. L.; Dong, X.; et al. Mixed plastics waste valorization through tandem chemical oxidation and biological funneling. *Science* **2022**, *378* (6616), 207-211. DOI: 10.1126/science.abo4626 (acccessed 2024/06/25).
(20) Xu, Z.; Munyaneza, N. E.; Zhang, Q.; Sun, M.; Posada, C.; Venturo, P.; Rorrer, N. A.; Miscall, J.; Sumpter, B. G.; Liu, G. Chemical upcycling of polyethylene, polypropylene, and mixtures to high-value surfactants. *Science* **2023**, *381* (6658), 666-671. DOI: 10.1126/science.adh0993 (acccessed 2024/06/25).
(21) Pinsuwan, K.; Opaprakasit, P.; Petchsuk, A.; Dubas, L.; Opaprakasit, M. Chemical recycling of high-density polyethylene (HDPE) wastes by oxidative degradation to dicarboxylic acids and their use as value-added curing agents for acrylate-based materials. *Polymer Degradation and Stability* **2023**, *210*, 110306. DOI: https://doi.org/10.1016/j.polymdegradstab.2023.110306.
(22) Bäckström, E.; Odelius, K.; Hakkarainen, M. Trash to Treasure: Microwave-Assisted Conversion of Polyethylene to Functional Chemicals. *Industrial & Engineering Chemistry Research* **2017**, *56* (50), 14814-14821. DOI: 10.1021/acs.iecr.7b04091.
(23) Wang, Y.; Gao, P.; Wei, Y.; Jin, Y.; Sun, S.; Wang, Z.; Jiang, Y. Silver nanoparticles decorated magnetic polymer composites (Fe3O4@PS@Ag) as highly efficient reusable catalyst for the degradation of 4-nitrophenol and organic dyes. *Journal of Environmental Management* **2021**, *278*, 111473. DOI: https://doi.org/10.1016/j.jenvman.2020.111473.
(24) Ziembowicz, S.; Kida, M. Limitations and future directions of application of the Fenton-like process in micropollutants degradation in water and wastewater treatment: A critical review. *Chemosphere* **2022**, *296*, 134041. DOI: https://doi.org/10.1016/j.chemosphere.2022.134041.
(25) Meyerstein, D. Re-examining Fenton and Fenton-like reactions. *Nature Reviews Chemistry* **2021**, *5* (9), 595-597. DOI: 10.1038/s41570-021-00310-4.
(26) Thomas, N.; Dionysiou, D. D.; Pillai, S. C. Heterogeneous Fenton catalysts: A review of recent advances. *J Hazard Mater* **2021**, *404* (Pt B), 124082. DOI: 10.1016/j.jhazmat.2020.124082 From NLM.
(27) Fontecha-Cámara, M. A.; Moreno-Castilla, C.; López-Ramón, M. V.; Álvarez, M. A. Mixed iron oxides as Fenton catalysts for gallic acid removal from aqueous solutions. *Applied Catalysis B: Environmental* **2016**, *196*, 207-215. DOI: https://doi.org/10.1016/j.apcatb.2016.05.032.

(28) Nidheesh, P. V. Heterogeneous Fenton catalysts for the abatement of organic pollutants from aqueous solution: a review. *RSC Advances* **2015**, *5* (51), 40552-40577, 10.1039/C5RA02023A. DOI: 10.1039/C5RA02023A.
(29) Wang, X.; Yin, R.; Zeng, L.; Zhu, M. A review of graphene-based nanomaterials for removal of antibiotics from aqueous environments. *Environmental Pollution* **2019**, *253*, 100-110. DOI: https://doi.org/10.1016/j.envpol.2019.06.067.
(30) Lai, C.; Shi, X.; Li, L.; Cheng, M.; Liu, X.; Liu, S.; Li, B.; Yi, H.; Qin, L.; Zhang, M.; et al. Enhancing iron redox cycling for promoting heterogeneous Fenton performance: A review. *Science of The Total Environment* **2021**, *775*, 145850. DOI: https://doi.org/10.1016/j.scitotenv.2021.145850.
(31) Dos Santos, N. d. O.; Busquets, R.; Campos, L. C. Insights into the removal of microplastics and microfibres by Advanced Oxidation Processes. *Science of The Total Environment* **2023**, *861*, 160665. DOI: https://doi.org/10.1016/j.scitotenv.2022.160665.
(32) Hu, K.; Zhou, P.; Yang, Y.; Hall, T.; Nie, G.; Yao, Y.; Duan, X.; Wang, S. Degradation of Microplastics by a Thermal Fenton Reaction. *ACS ES&T Engineering* **2022**, *2* (1), 110-120. DOI: 10.1021/acsestengg.1c00323.
(33) Ortiz, D.; Munoz, M.; Nieto-Sandoval, J.; Romera-Castillo, C.; de Pedro, Z. M.; Casas, J. A. Insights into the degradation of microplastics by Fenton oxidation: From surface modification to mineralization. *Chemosphere* **2022**, *309*, 136809. DOI: https://doi.org/10.1016/j.chemosphere.2022.136809.
(34) Bule Možar, K.; Miloloža, M.; Martinjak, V.; Radovanović-Perić, F.; Bafti, A.; Ujević Bošnjak, M.; Markić, M.; Bolanča, T.; Cvetnić, M.; Kučić Grgić, D.; et al. Evaluation of Fenton, Photo-Fenton and Fenton-like Processes in Degradation of PE, PP, and PVC Microplastics. In *Water*, 2024; Vol. 16.
(35) Ghatge, S.; Yang, Y.; Ko, Y.; Yoon, Y.; Ahn, J.-H.; Kim, J. J.; Hur, H.-G. Degradation of sulfonated polyethylene by a bio-photo-fenton approach using glucose oxidase immobilized on titanium dioxide. *Journal of Hazardous Materials* **2022**, *423*, 127067. DOI: https://doi.org/10.1016/j.jhazmat.2021.127067.
(36) Chow, C.-F.; Wong, W.-L.; Ho, K. Y.-F.; Chan, C.-S.; Gong, C.-B. Combined Chemical Activation and Fenton Degradation to Convert Waste Polyethylene into High-Value Fine Chemicals. *Chemistry – A European Journal* **2016**, *22* (28), 9513-9518. DOI: https://doi.org/10.1002/chem.201600856 (acccessed 2024/01/23).
(37) Nguyen, V. S.; Chang, Y.; Phillips, E. V.; DeWitt, J. A.; Sievers, C. Mechanocatalytic Oxidative Cracking of Poly(ethylene) Via a Heterogeneous Fenton Process. *ACS Sustainable Chemistry & Engineering* **2023**, *11* (20), 7617-7623. DOI: 10.1021/acssuschemeng.3c01054.
(38) Liu, Y.; Wang, J. Multivalent metal catalysts in Fenton/Fenton-like oxidation system: A critical review. *Chemical Engineering Journal* **2023**, *466*, 143147. DOI: https://doi.org/10.1016/j.cej.2023.143147.
(39) Ribeiro, J. P.; Gomes, H. G. M. F.; Sarinho, L.; Marques, C. C.; Nunes, M. I. Synergies of metallic catalysts in the Fenton and photo-Fenton processes applied to the treatment of pulp bleaching wastewater. *Chemical Engineering and Processing - Process Intensification* **2022**, *181*, 109159. DOI: https://doi.org/10.1016/j.cep.2022.109159.
(40) Li, X.; Tian, Z.; Liang, K.; Wang, Y. Enhanced photo-Fenton degradation performance over multi-metal co-supported SAPO-18 zeolites by promoted active species yield. *Journal of Photochemistry and Photobiology A: Chemistry* **2019**, *379*, 79-87. DOI: https://doi.org/10.1016/j.jphotochem.2019.04.032.

(41) Lu, H.; Zhu, Z.; Zhang, H.; Zhu, J.; Qiu, Y.; Zhu, L.; Küppers, S. Fenton-Like Catalysis and Oxidation/Adsorption Performances of Acetaminophen and Arsenic Pollutants in Water on a Multimetal Cu–Zn–Fe-LDH. *ACS Applied Materials & Interfaces* **2016**, *8* (38), 25343-25352. DOI: 10.1021/acsami.6b08933.
(42) Diao, Y.; Yan, Z.; Guo, M.; Wang, X. Magnetic multi-metal co-doped magnesium ferrite nanoparticles: An efficient visible light-assisted heterogeneous Fenton-like catalyst synthesized from saprolite laterite ore. *Journal of Hazardous Materials* **2018**, *344*, 829-838. DOI: https://doi.org/10.1016/j.jhazmat.2017.11.029.
(43) Heckert, E. G.; Seal, S.; Self, W. T. Fenton-Like Reaction Catalyzed by the Rare Earth Inner Transition Metal Cerium. *Environmental Science & Technology* **2008**, *42* (13), 5014-5019. DOI: 10.1021/es8001508.
(44) Montini, T.; Melchionna, M.; Monai, M.; Fornasiero, P. Fundamentals and Catalytic Applications of CeO2-Based Materials. *Chemical Reviews* **2016**, *116* (10), 5987-6041. DOI: 10.1021/acs.chemrev.5b00603.
(45) Laguna, O. H.; Centeno, M. A.; Arzamendi, G.; Gandía, L. M.; Romero-Sarria, F.; Odriozola, J. A. Iron-modified ceria and Au/ceria catalysts for Total and Preferential Oxidation of CO (TOX and PROX). *Catalysis Today* **2010**, *157* (1), 155-159. DOI: https://doi.org/10.1016/j.cattod.2010.04.011.
(46) Gogoi, A.; Navgire, M.; Sarma, K. C.; Gogoi, P. Fe3O4-CeO2 metal oxide nanocomposite as a Fenton-like heterogeneous catalyst for degradation of catechol. *Chemical Engineering Journal* **2017**, *311*, 153-162. DOI: https://doi.org/10.1016/j.cej.2016.11.086.
(47) Xu, L.; Wang, J. Magnetic Nanoscaled Fe3O4/CeO2 Composite as an Efficient Fenton-Like Heterogeneous Catalyst for Degradation of 4-Chlorophenol. *Environmental Science & Technology* **2012**, *46* (18), 10145-10153. DOI: 10.1021/es300303f.
(48) Laguna, O. H.; Centeno, M. A.; Boutonnet, M.; Odriozola, J. A. Fe-doped ceria solids synthesized by the microemulsion method for CO oxidation reactions. *Applied Catalysis B: Environmental* **2011**, *106* (3), 621-629. DOI: https://doi.org/10.1016/j.apcatb.2011.06.025.
(49) Wang, H.; Tsilomelekis, G. Catalytic performance and stability of Fe-doped CeO2 in propane oxidative dehydrogenation using carbon dioxide as an oxidant. *Catalysis Science & Technology* **2020**, *10* (13), 4362-4372, 10.1039/D0CY00586J. DOI: 10.1039/D0CY00586J.
(50) Qi, Y.; Zuo, Q.; Mei, Y.; Yao, T.; Wu, J. Porous NiCo2O4 Sheet Catalysts for the Microwave-Assisted Fenton Reaction. *ACS Applied Nano Materials* **2020**, *3* (7), 7152-7160. DOI: 10.1021/acsanm.0c01474.
(51) Shen, X.; Cai, Z.; Hu, J.; Sun, B. Highly Efficient Microwave-Assisted Fenton Degradation of Toluene Nitration Wastewater over Microwave-Responsive Catalyst of Fe3O4−BiOCl. *ChemistrySelect* **2022**, *7* (33), e202200804. DOI: https://doi.org/10.1002/slct.202200804 (acccessed 2024/06/04).
(52) Muley, P. D.; Wang, Y.; Hu, J.; Shekhawat, D. Microwave-assisted heterogeneous catalysis. In *Catalysis: Volume 33*, Spivey, J., Han, Y.-F., Shekhawat, D. Eds.; Vol. 33; The Royal Society of Chemistry, 2021; p 0.
(53) Faust, K.; Denifl, P.; Hapke, M. Recent Advances in Catalytic Chemical Recycling of Polyolefins. *ChemCatChem* **2023**, *15* (13), e202300310. DOI: https://doi.org/10.1002/cctc.202300310 (acccessed 2024/07/04).
(54) Mukherjee, D.; Rao, B. G.; Reddy, B. M. CO and soot oxidation activity of doped ceria: Influence of dopants. *Applied Catalysis B: Environmental* **2016**, *197*, 105-115. DOI: https://doi.org/10.1016/j.apcatb.2016.03.042.

(55) Bao, H.; Chen, X.; Fang, J.; Jiang, Z.; Huang, W. Structure-activity Relation of Fe2O3–CeO2 Composite Catalysts in CO Oxidation. *Catalysis Letters* **2008**, *125* (1), 160-167. DOI: 10.1007/s10562-008-9540-3.
(56) Loridant, S. Raman spectroscopy as a powerful tool to characterize ceria-based catalysts. *Catalysis Today* **2021**, *373*, 98-111. DOI: https://doi.org/10.1016/j.cattod.2020.03.044.
(57) Book Reviews. Announcements. **1997**, *15* (3-4), 533-559. DOI: doi:10.1515/CORRREV.1997.15.3-4.533 (acccessed 2023-12-08).
(58) Qayoom, M.; Shah, K. A.; Pandit, A. H.; Firdous, A.; Dar, G. N. Dielectric and electrical studies on iron oxide (α-Fe2O3) nanoparticles synthesized by modified solution combustion reaction for microwave applications. *Journal of Electroceramics* **2020**, *45* (1), 7-14. DOI: 10.1007/s10832-020-00219-2.
(59) Liu, H.; Wu, Y.; Liu, L.; Chu, B.; Qin, Z.; Jin, G.; Tong, Z.; Dong, L.; Li, B. Three-dimensionally ordered macroporous Fe-doped ceria catalyst with enhanced activity at a wide operating temperature window for selective catalytic reduction of NOx. *Applied Surface Science* **2019**, *498*, 143780. DOI: https://doi.org/10.1016/j.apsusc.2019.143780.
(60) Rahdar, A.; Aliahmad, M.; Samani, M.; HeidariMajd, M.; Susan, M. A. B. H. Synthesis and characterization of highly efficacious Fe-doped ceria nanoparticles for cytotoxic and antifungal activity. *Ceramics International* **2019**, *45* (6), 7950-7955. DOI: https://doi.org/10.1016/j.ceramint.2019.01.108.
(61) Tsoncheva, T.; Rosmini, C.; Dimitrov, M.; Issa, G.; Henych, J.; Němečková, Z.; Kovacheva, D.; Velinov, N.; Atanasova, G.; Spassova, I. Formation of Catalytic Active Sites in Hydrothermally Obtained Binary Ceria–Iron Oxides: Composition and Preparation Effects. *ACS Applied Materials & Interfaces* **2021**, *13* (1), 1838-1852. DOI: 10.1021/acsami.0c16326.
(62) Maslakov, K. I.; Teterin, Y. A.; Popel, A. J.; Teterin, A. Y.; Ivanov, K. E.; Kalmykov, S. N.; Petrov, V. G.; Petrov, P. K.; Farnan, I. XPS study of ion irradiated and unirradiated CeO2 bulk and thin film samples. *Applied Surface Science* **2018**, *448*, 154-162. DOI: https://doi.org/10.1016/j.apsusc.2018.04.077.
(63) Maslakov, K. I.; Teterin, Y. A.; Ryzhkov, M. V.; Popel, A. J.; Teterin, A. Y.; Ivanov, K. E.; Kalmykov, S. N.; Petrov, V. G.; Petrov, P. K.; Farnan, I. The electronic structure and the nature of the chemical bond in CeO2. *Physical Chemistry Chemical Physics* **2018**, *20* (23), 16167-16175, 10.1039/C8CP01442F. DOI: 10.1039/C8CP01442F.
(64) Bêche, E.; Charvin, P.; Perarnau, D.; Abanades, S.; Flamant, G. Ce 3d XPS investigation of cerium oxides and mixed cerium oxide (CexTiyOz). *Surface and Interface Analysis* **2008**, *40* (3-4), 264-267. DOI: https://doi.org/10.1002/sia.2686 (acccessed 2024/01/23).
(65) Soni, S.; Srivats, V.; Kumar, S.; Dalela, B.; Mishra, M.; Singh, R.; Gupta, G.; Alvi, D. P.; Dalela, S. Structural, optical and magnetic properties of Fe-doped CeO2 samples probed using X-ray photoelectron spectroscopy. *Journal of Materials Science: Materials in Electronics* **2018**, *29*. DOI: 10.1007/s10854-018-9060-x.
(66) Hasegawa, T.; Shahed, S. M. F.; Sainoo, Y.; Beniya, A.; Isomura, N.; Watanabe, Y.; Komeda, T. Epitaxial growth of CeO2(111) film on Ru(0001): Scanning tunneling microscopy (STM) and x-ray photoemission spectroscopy (XPS) study. *The Journal of Chemical Physics* **2014**, *140* (4), 044711. DOI: 10.1063/1.4849595 (acccessed 1/24/2024).
(67) Yamashita, T.; Hayes, P. Analysis of XPS spectra of Fe2+ and Fe3+ ions in oxide materials. *Applied Surface Science* **2008**, *254* (8), 2441-2449. DOI: https://doi.org/10.1016/j.apsusc.2007.09.063.

(68) Bagus, P. S.; Nelin, C. J.; Brundle, C. R.; Crist, B. V.; Lahiri, N.; Rosso, K. M. Origin of the complex main and satellite features in Fe 2p XPS of Fe2O3. *Physical Chemistry Chemical Physics* **2022**, *24* (7), 4562-4575, 10.1039/D1CP04886D. DOI: 10.1039/D1CP04886D.
(69) Dupin, J.-C.; Gonbeau, D.; Vinatier, P.; Levasseur, A. Systematic XPS studies of metal oxides, hydroxides and peroxides. *Physical Chemistry Chemical Physics* **2000**, *2* (6), 1319-1324, 10.1039/A908800H. DOI: 10.1039/A908800H.
(70) Xu, Y.; Zhang, H.; Gong, D.; Chen, Y.; Xu, S.; Qiu, P. Solar water splitting with nanostructured hematite: the role of oxygen vacancy. *Journal of Materials Science* **2022**, *57* (42), 19716-19729. DOI: 10.1007/s10853-022-07885-3.
(71) Si, R.; Flytzani-Stephanopoulos, M. Shape and Crystal-Plane Effects of Nanoscale Ceria on the Activity of Au-CeO2 Catalysts for the Water–Gas Shift Reaction. *Angewandte Chemie International Edition* **2008**, *47* (15), 2884-2887. DOI: https://doi.org/10.1002/anie.200705828 (acccessed 2024/09/09).
(72) Wei, X.; Rang, X.; Zhu, W.; Xiang, M.; Deng, Y.; Jiang, F.; Mao, R.; Zhang, Z.; Kong, X.; Wang, F. Morphology effect of CeO2 on Ni/CeO2 catalysts for selective hydrogenation of cinnamaldehyde. *Chemical Physics* **2021**, *542*, 111079. DOI: https://doi.org/10.1016/j.chemphys.2020.111079.
(73) Liu, S.; Liao, X.; Zhang, Q.; Zhang, Y.; Wang, H.; Zhao, Y. Crystal-Plane and Shape Influences of Nanoscale CeO2 on the Activity of Ni/CeO2 Catalysts for Maleic Anhydride Hydrogenation. In *Nanomaterials*, 2022; Vol. 12.
(74) Matussin, S. N.; Khan, F.; Harunsani, M. H.; Kim, Y.-M.; Khan, M. M. Visible-Light-Induced Photocatalytic and Photoantibacterial Activities of Co-Doped CeO2. *ACS Omega* **2023**, *8* (13), 11868-11879. DOI: 10.1021/acsomega.2c07058.
(75) Ali, I.; Neskoromnaya, E. A.; Melezhik, A. V.; Babkin, A. V.; Kulnitskiy, B. A.; Burakov, A. E.; Burakova, I. V.; Tkachev, A. G.; Almalki, A. S. A.; Alsubaie, A. Magnetically active nanocomposite aerogels: preparation, characterization and application for water treatment. *Journal of Porous Materials* **2022**, *29* (2), 545-557. DOI: 10.1007/s10934-021-01175-0.
(76) Thomas, P.; Sreekanth, P.; Abraham, K. E. Nanosecond and ultrafast optical power limiting in luminescent Fe2O3 hexagonal nanomorphotype. *Journal of Applied Physics* **2015**, *117* (5), 053103. DOI: 10.1063/1.4906852 (acccessed 6/5/2024).
(77) Scé, F.; Cano, I.; Martin, C.; Beobide, G.; Castillo, Ó.; de Pedro, I. Comparing conventional and microwave-assisted heating in PET degradation mediated by imidazolium-based halometallate complexes. *New Journal of Chemistry* **2019**, *43* (8), 3476-3485, 10.1039/C8NJ06090H. DOI: 10.1039/C8NJ06090H.
(78) Casey, É.; Breen, R.; Pareras, G.; Rimola, A.; Holmes, J. D.; Collins, G. Guanidine functionalized porous SiO2 as heterogeneous catalysts for microwave depolymerization of PET and PLA. *RSC Sustainability* **2024**, *2* (4), 1040-1051, 10.1039/D3SU00425B. DOI: 10.1039/D3SU00425B.
(79) Li, H.; Zhang, C.; Pang, C.; Li, X.; Gao, X. The Advances in the Special Microwave Effects of the Heterogeneous Catalytic Reactions. *Frontiers in Chemistry* **2020**, *8*, Review.
(80) Selvam, E.; Luo, Y.; Ierapetritou, M.; Lobo, R. F.; Vlachos, D. G. Microwave-assisted depolymerization of PET over heterogeneous catalysts. *Catalysis Today* **2023**, *418*, 114124. DOI: https://doi.org/10.1016/j.cattod.2023.114124.
(81) Lefort, D.; Fossey, J.; Gruselle, M.; Nedelec, J.-Y.; Sorba, J. Reactivity and selectivity of homolytic substitution reactions on the peroxyacid group. *Tetrahedron* **1985**, *41* (19), 4237-4252. DOI: https://doi.org/10.1016/S0040-4020(01)97196-0.

(82) Argyle, M. D.; Bartholomew, C. H. Heterogeneous Catalyst Deactivation and Regeneration: A Review. In *Catalysts*, 2015; Vol. 5, pp 145-269.
(83) Wang, Y.; Shen, X.; Chen, F. Improving the catalytic activity of CeO2/H2O2 system by sulfation pretreatment of CeO2. *Journal of Molecular Catalysis A: Chemical* **2014**, *381*, 38-45. DOI: https://doi.org/10.1016/j.molcata.2013.10.003.
(84) Smak, T. J.; de Peinder, P.; Van der Waal, J. C.; Altink, R.; Vollmer, I.; Weckhuysen, B. M. Oxidative Conversion of Polyethylene Towards Di-Carboxylic Acids: A Multi-Analytical Approach. *ChemSusChem* **2024**, *17* (7), e202301198. DOI: https://doi.org/10.1002/cssc.202301198 (acccessed 2024/08/30).
(85) Pifer, A.; Sen, A. Chemical Recycling of Plastics to Useful Organic Compounds by Oxidative Degradation. *Angewandte Chemie International Edition* **1998**, *37* (23), 3306-3308. DOI: https://doi.org/10.1002/(SICI)1521-3773(19981217)37:23<3306::AID-ANIE3306>3.0.CO;2-B (acccessed 2024/09/10).
(86) Zafar, R.; Park, S. Y.; Kim, C. G. Comparison of surficial modification of micro-sized polyethylene in between by UV/O3 and UVO submerged system. *Environmental Engineering Research* **2022**, *27* (3), 210028-210020. DOI: 10.4491/eer.2021.028.
(87) Kuan, C.-C.; Chang, S.-Y.; Schroeder, S. L. M. Fenton-Like Oxidation of 4-Chlorophenol: Homogeneous or Heterogeneous? *Industrial & Engineering Chemistry Research* **2015**, *54* (33), 8122-8129. DOI: 10.1021/acs.iecr.5b02378.
(88) Chen, Y.; Miller, C. J.; Waite, T. D. Heterogeneous Fenton Chemistry Revisited: Mechanistic Insights from Ferrihydrite-Mediated Oxidation of Formate and Oxalate. *Environmental Science & Technology* **2021**, *55* (21), 14414-14425. DOI: 10.1021/acs.est.1c00284.
(89) Zhang, N.; Chen, J.; Fang, Z.; Tsang, E. P. Ceria accelerated nanoscale zerovalent iron assisted heterogenous Fenton oxidation of tetracycline. *Chemical Engineering Journal* **2019**, *369*, 588-599. DOI: https://doi.org/10.1016/j.cej.2019.03.112.
(90) Zhang, N.; Tsang, E. P.; Chen, J.; Fang, Z.; Zhao, D. Critical role of oxygen vacancies in heterogeneous Fenton oxidation over ceria-based catalysts. *Journal of Colloid and Interface Science* **2020**, *558*, 163-172. DOI: https://doi.org/10.1016/j.jcis.2019.09.079.
(91) Bello, M. M.; Abdul Raman, A. A.; Asghar, A. A review on approaches for addressing the limitations of Fenton oxidation for recalcitrant wastewater treatment. *Process Safety and Environmental Protection* **2019**, *126*, 119-140. DOI: https://doi.org/10.1016/j.psep.2019.03.028.
(92) Munoz, M.; de Pedro, Z. M.; Casas, J. A.; Rodriguez, J. J. Preparation of magnetite-based catalysts and their application in heterogeneous Fenton oxidation – A review. *Applied Catalysis B: Environmental* **2015**, *176-177*, 249-265. DOI: https://doi.org/10.1016/j.apcatb.2015.04.003.
(93) Bevilacqua, E. M.; English, E. S.; Gall, J. S. Mechanism of polyethylene oxidation. *Journal of Applied Polymer Science* **1964**, *8* (4), 1691-1698. DOI: https://doi.org/10.1002/app.1964.070080419 (acccessed 2024/11/07).
(94) Bokare, A. D.; Choi, W. Review of iron-free Fenton-like systems for activating H2O2 in advanced oxidation processes. *Journal of Hazardous Materials* **2014**, *275*, 121-135. DOI: https://doi.org/10.1016/j.jhazmat.2014.04.054.
(95) Lin, S.-S.; Gurol, M. D. Catalytic Decomposition of Hydrogen Peroxide on Iron Oxide: Kinetics, Mechanism, and Implications. *Environmental Science & Technology* **1998**, *32* (10), 1417-1423. DOI: 10.1021/es970648k.
(96) Ji, P.; Wang, L.; Chen, F.; Zhang, J. Ce3+-centric organic pollutant elimination by CeO2 in the presence of H2O2. *ChemCatChem* **2010**, *2* (12), 1552-1554.

6.5 Appendix I: Supporting Information

Heterogeneous Fenton-type Oxidative Degradation of LDPE to Valuable Acid Products Using a Nanostructured Fe-CeO_2 Solid Solution Catalyst

***Breen, R**.; Holmes, J. D.; Collins, G. Heterogeneous Fenton-type oxidative degradation of low-density polyethylene to valuable acid products using a nanostructured Fe–CeO_2 solid solution catalyst. Catalysis Science & Technology **2025**, 10.1039/D4CY01384K. DOI: 10.1039/D4CY01384K.*

Experimental

Chemicals and Materials

Hydrogen peroxide (30%), nitric acid (65%), iron (III) chloride ($FeCl_3.4H_2O$), cerium (IV) sulfate ($Ce(SO_4)_2$), cerium oxide nano powder, and sodium hydroxide pellets (NaOH) were all purchased from Sigma Aldrich. LDPE powder (500 um), with a density of 0.91-0.96 gml^{-1} was purchased from Thermo Fischer.

CeO_2 reference: CeO_2 nano powder was calcinated at 450 °C for 4h and used without any further treatment.

Fe_2O_3 reference: 2 g $FeCl_3.4H_2O$ was added to a round bottom flask along with 50 mL deionised H_2O. The mixture was stirred at room temperature for 10 minutes before the pH was adjusted to 12 using 1 M NaOH solution. When the desired pH was achieved and a rusty brown precipitate had crashed out, mixture was refluxed for 2 h at 100 °C under N_2 with stirring. The solid Fe_2O_3 particles were then collected by suction filtration and dried in an oven at 75 °C overnight. The resulting solid was then calcinated at 450 °C for 4 h.[1]

Fe-CeO_2 1:1 solid solution: A solution of 0.755 g $FeCl_3$ in 25 mL DI H_2O and 1.933 g $Ce(SO_4)_2.4H_2O$ in 25 mL DI H_2O were combined to form a 1:1 molar ratio of Fe:Ce and stirred at room temperature for 10 minutes before the pH was adjusted to 12 using 1 M NaOH solution and a red/brown precipitate

appeared. The mixture was refluxed for 2 h at 100 °C under N_2 with stirring. The resulting particles were collected by suction filtration and dried in an oven at 75 °C overnight. The solid was then calcinated at 450 °C under air for 4h. For different Fe:Ce ratios, the masses of salt precursors were adjusted accordingly.

Fe-Ce 1:2: A solution of 0. 0.378 g $FeCl_3$ in 25 mL DI H_2O and 0.2M 1.933 g $Ce(SO_4)_2.4H_2O$ in 25 mL DI H_2O were combined to form a 1:2 molar ratio of Fe:Ce and synthesis method was continued as above.
Fe-Ce 2:1: A solution of 0.755 g $FeCl_3$ in 25 mL DI H_2O and 0.967 g $Ce(SO_4)_2.4H_2O$ in 25 mL DI H_2O were combined to form a 2:1 molar ratio of Fe:Ce and synthesis method was continued as above.



Figure S1: $FeCl_3$ and $CeSO_4$ solutions before coprecipitation synthesis step.

Oxidative Degradation of LDPE to Carboxylic Acids:

0.3 - 0.5 g LDPE, catalyst loadings of 1 – 30 wt. % and 10 mL of H_2O_2 solutions from 3 – 15 % (w/w) were added to a Milestone Flexiwave high pressure SK-15 Teflon vessel along with a stir bar. For a 15 % H_2O_2 solution, 5 mL of Millipore H_2O and 5 mL 30 % (w/w) H_2O_2 were added to the vessel. The H_2O_2 was added last to minimise peroxide degradation prior to the reaction. Typical reaction conditions were a 10 min ramp time, 3 h hold at 180 °C, stir speed 1800 rpm using a crosshair stir bar, and 1200

W upper power limit (reactions only typically required ~300 W). Once the reaction was complete and had cooled, it was Buchner filtered to separate the catalyst and any unreacted LDPE from the product mixture. The mass loss of LDPE was calculated by the equation below.

$$Mass\ Loss\ LDPE = \frac{W_0 - W_1}{W_0}\ x\ 100\ \%$$

Where W_0 is the initial weight of LDPE added to the reaction and W_1 is the weight of unreacted LDPE after the reaction. The product mixture was characterised by HPLC.

HPLC Analysis of Products

The product mixture was analysed using an Agilent 1200 HPLC coupled to a UV detector (210 nm). 500 uL of product mixture was added to 500 uL of mobile phase to give a dilution factor of 2. The column used was an Agilent Hi-Plex H (300 x 7.7 mm) size exclusion column. The mobile phase was 2.5 mM sulfuric acid at a flow rate of 0.5 $mLmin^{-1}$ and the temperature was set to 50 °C, following Bäckström et al.'s method and the column specifications. The concentration of each product present in the sample was then calculated against calibration curves that were made by standards of carboxylic acids: succinic, formic, glutaric, acetic, adipic, propionic, butyric and pimelic acid. The yield was calculated relative to the initial weight of LDPE as shown below.

$$Mass\ of\ end\ product\ (g) = Conc\ of\ end\ product\ (gL^{-1})\ x\ reaction\ volume\ (L)$$

$$Yield\ of\ Organic\ Products\ (\%) = \frac{Mass\ of\ end\ products\ (g)}{Mass\ of\ starting\ material\ (g)}\ x\ 100\ \%$$

Materials Characterisation

Raman spectroscopy was performed using an Oceanview InVia Raman Spectrometer using a 25 mW Ar-ion laser under 532 nm excitation. The beam was focused onto the samples using a 50x objective lens and spectra were collected using a RenCam CCD camera.

X-ray Diffraction (XRD) was carried out on a PANalytical X'Pert PRO with Cu Kα radiation and a constant step of 0.0098° 2θ and a counting time of 149.97 seconds per step. Crystallite size was calculated by the Scherrer equation shown below.

$$D_{hkl} = \frac{k_\lambda}{B_{hkl} cos\theta_{hkl}}$$

Where D_{hkl} is the crystallite size perpendicular to the hkl plane, k is a constant (0.9) for spherical samples with cubic symmetry, λ is the wavelength of x-ray radiation, B_{hkl} is the full width at half maximum (FWHM) of the hkl diffraction peak and θ_{hkl} is the Bragg angle of the (hkl) peak. It is worth commenting that there is limited accuracy with the Scherrer equation for smaller crystallite sizes due to factors such as strain, instrument broadening and shape effects, however for the purpose of this study, it can be used to support other analysis methods.

X-ray Photoelectron Spectroscopy (XPS) was carried out using a KRATOS ACIS 165 monochromatised X-ray photoelectron spectrometer equipped with an Al Kα (hv = 1486.6 eV) X-ray source. Spectra were collected at a take-off angle of 90 ° and all spectra were referenced to the C 1s peak at 284.8 eV. The quantitative data of Ce^{4+} and Ce^{3+} in CeO_2 and each of the solid solutions were calculated using the expressions as reported by Suresh et al.[2]

$$\%\, Ce^{3+} = \frac{A_{Ce^{3+}}}{A_{Ce^{3+}} + A_{Ce^{4+}}} \times 100\%$$

$$\%\, Ce^{4+} = \frac{A_{Ce^{4+}}}{A_{Ce^{3+}} + A_{Ce^{4+}}} \times 100\%$$

Where $A_{Ce^{3+}} = v_0 + v' + u_0 + u'$ and $A_{Ce^{4+}} = v + v'' + v''' + u + u'' + u'''$ are the sum of the areas of the fitted peaks corresponding to Ce^{3+} and Ce^{4+}.

Fourier Transform Infrared Spectroscopy (FT-IR) spectra were recorded on a Perkin Elmer Spectrum Two FT-IR Spectrometer operating in the range of 4000-450 cm^{-1} with a resolution of 4 cm^{-1} and spectra were averaged from 20 scans. The carbonyl index was estimated using the SAUB method as outlined by Almond et al[3]

$$Carbonyl\ Index\ (CI) = \frac{Area\ under\ band \sim 1748\ cm^{-1}}{Area\ under\ band \sim 1465\ cm^{-1}}$$

It is important to note that the carbonyl index may be less representative when the CH reference peak shifts during degradation, as changes in the reference band affect the carbonyl-to-CH ratio.

Total reflection X-ray fluorescence spectroscopy was (TXRF) was carried out using an S2 Picofox TXRF Spectrometer with a scan time of 250 s. Quantification using an internal standard and correlating concentration of analyte with relative sensitivities to the net intensities of the analyte and the Ni internal standard was calculated by the following equation[4].

$$C_A = \frac{\frac{N_A}{S_A}}{\frac{N_{IS}}{S_{IS}}} \times C_{IS}$$

Where C_A and C_{IS} are the concentrations of the analyte and the IS, respectively. N_A and N_{IS} refer to the net intensities of the analyte and the internal standard, and S_A and S_{IS} are the relative sensitivities of the analyte and internal standard, respectively.

Scanning electron microscopy (SEM) and EDS mapping was performed on a Zeiss Supra 40 high resolution SEM at an accelerating voltage of 5 kV. Transmission electron microscopy (TEM) analysis was performed using a FEI Titan TEM, at an operating voltage of 300 kV.

Supporting Figures:

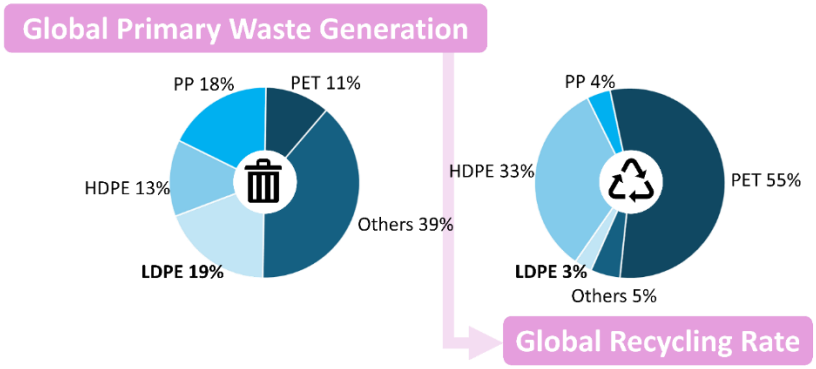


Figure S2: a) Global primary waste generation[11], b) Global recycling rate by polymer type.[5]

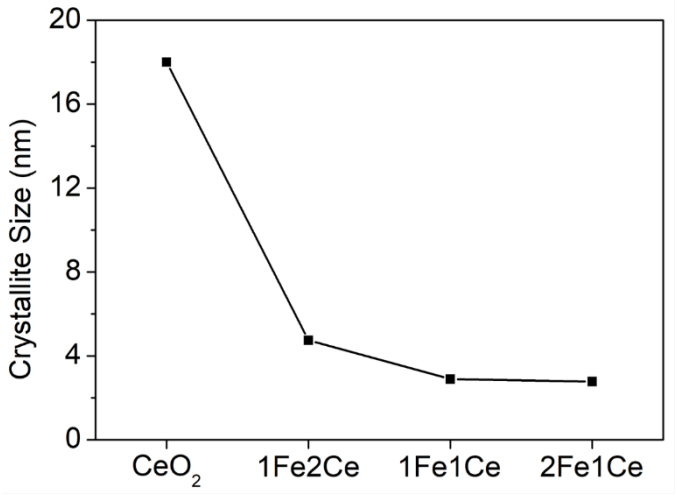


Figure S3: Decreasing crystallite size with increasing Fe content as calculated by Scherrer equation.

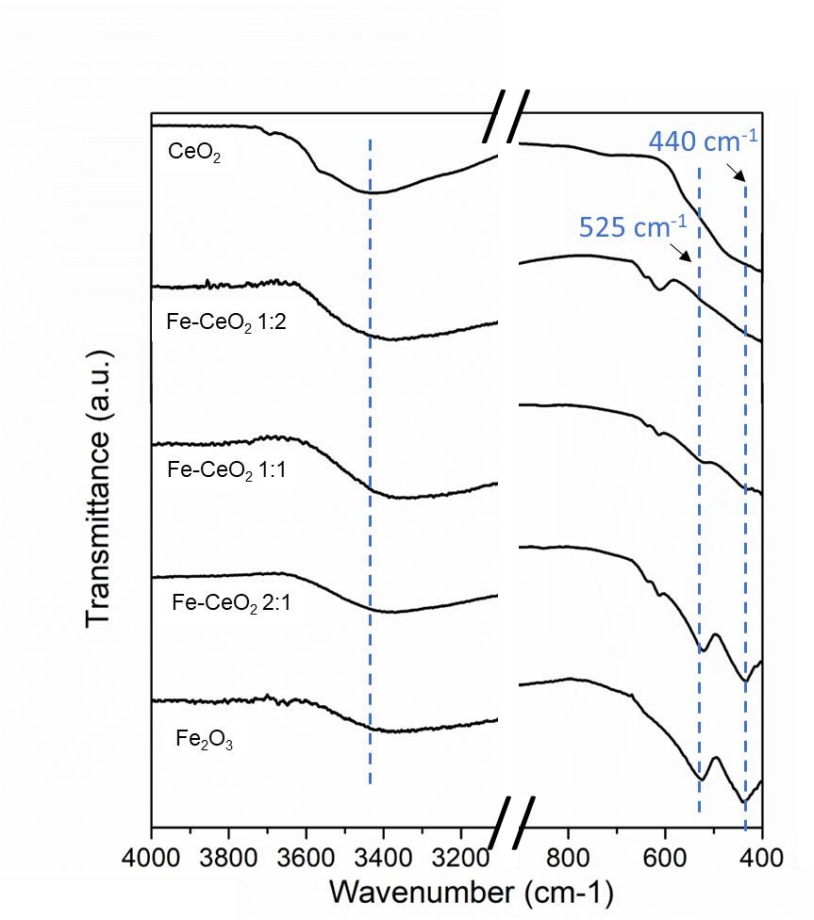


Figure S4: FTIR of CeO_2, Fe_2O_3 and each of the Fe-CeO_2 solid solution catalysts.

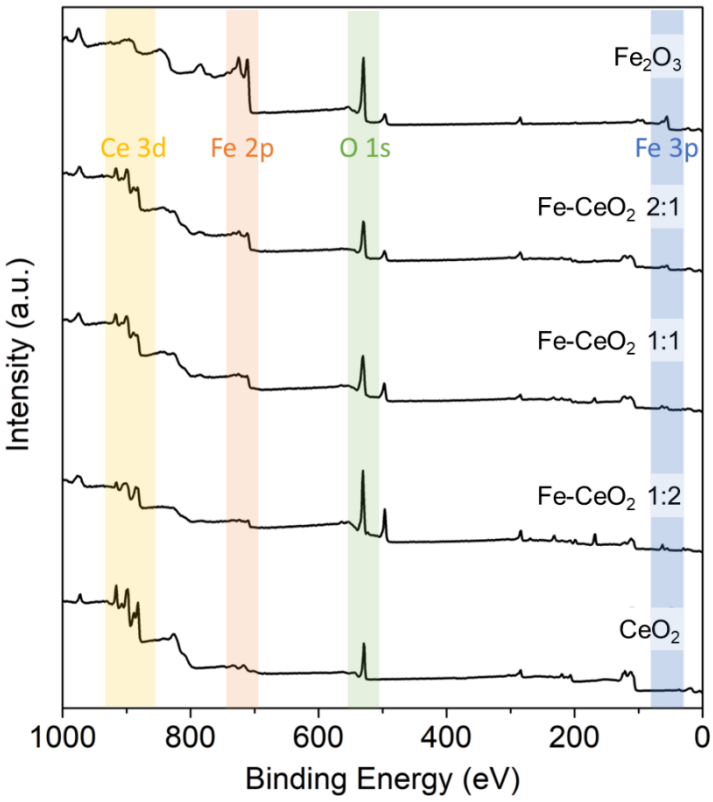


Figure S5: XPS Survey scans for Fe_2O_3, CeO_2, and each of the Fe-CeO_2 solid solution catalysts.

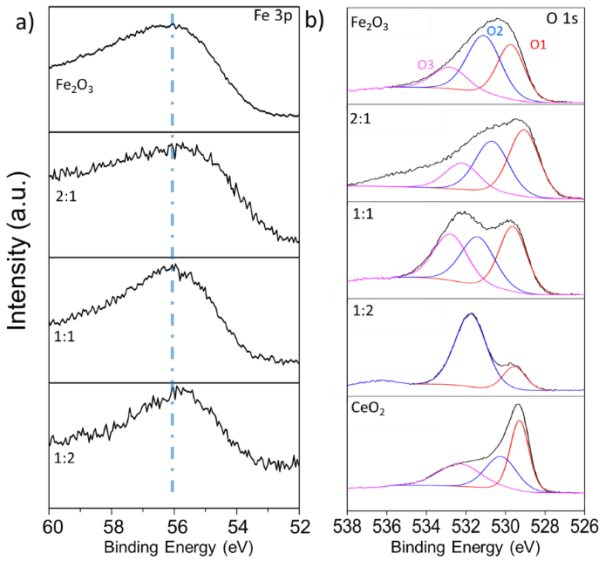


Figure S6: a) Fe 3p XPS for Fe_2O_3 and the Fe-CeO_2 solid solutions and b) O 1s XPS for Fe_2O_3, CeO_2 and the Fe-CeO_2 solid solutions.

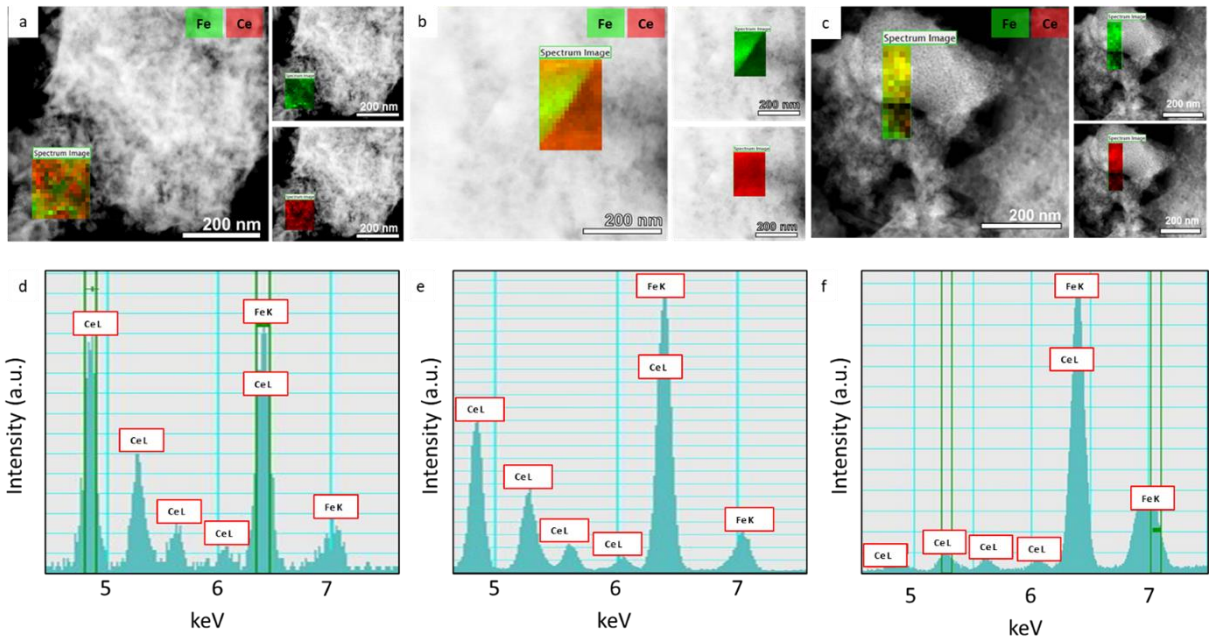


Figure S7: HAADF and EDX of a) Fe-CeO_2 1:2, b) Fe-CeO_2 1:1 and c) Fe-CeO_2 2:1 and d)-f) corresponding EDX spectra.

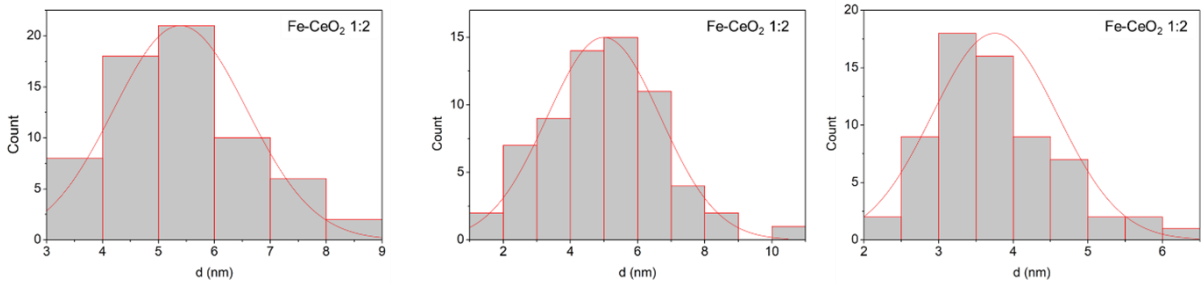


Figure S8: Size distribution histograms of the Fe-CeO_2 1:2, 1:1 and 2:1 catalysts.

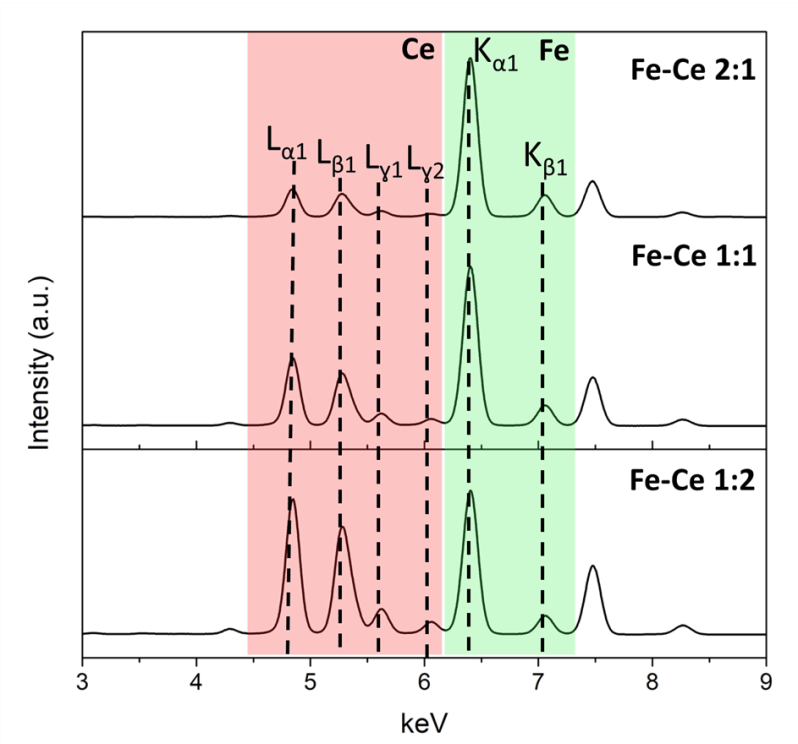


Figure S9: TXRF Spectra of the Fe-CeO_2 catalysts. (Ni IS peaks at 7.4 keV and 8.3 keV)

Table S1: Quantification from TXRF.

Catalyst	Element	(gL^{-1})	($molL^{-1}$)	Molar Ratio
Fe-CeO_2 2:1	Fe	3.0703	0.055	2:1
	Ce	3.4933	0.025	
Fe-CeO_2 1:1	Fe	2.2296	0.040	1:1
	Ce	5.9871	0.042	
Fe-CeO_2 1:2	Fe	1.3937	0.025	1:2
	Ce	8.536	0.060	

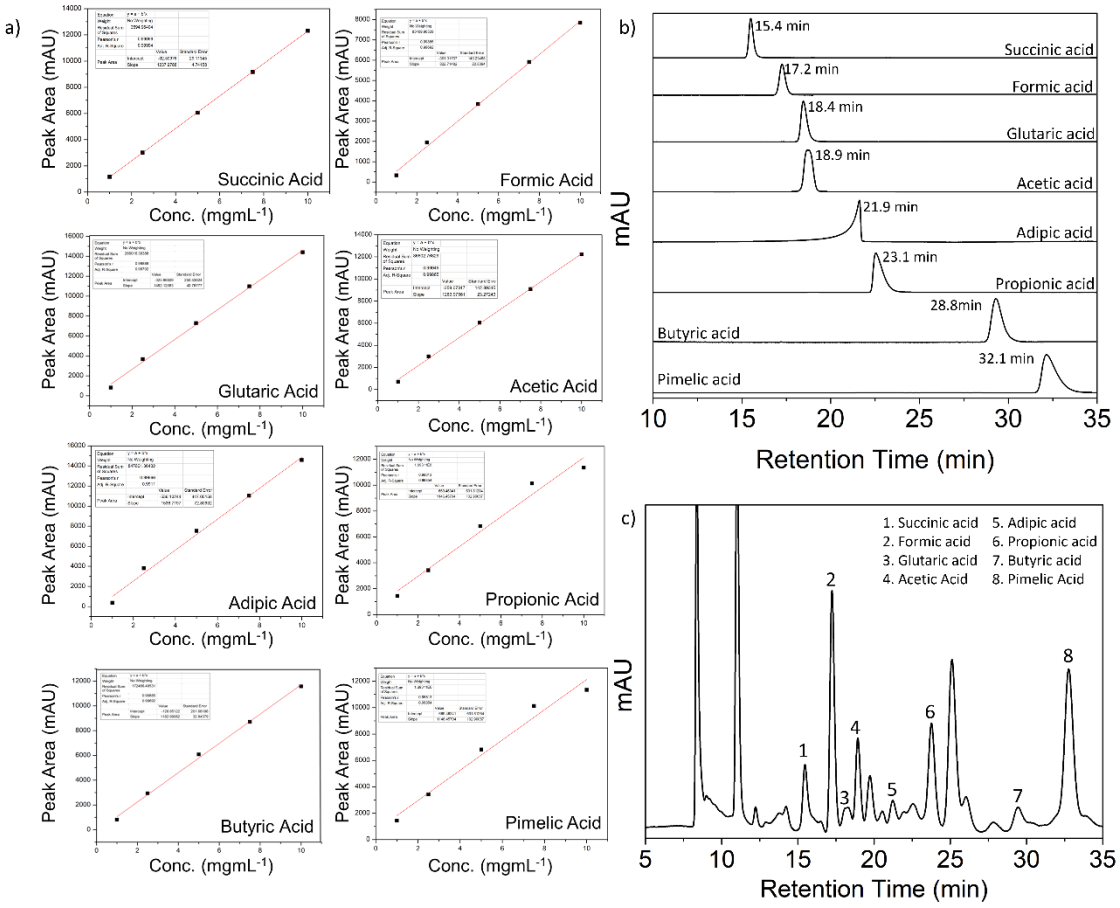


Figure S10: a) Calibration curves for each of the acid standards, b) retention times of the acid standards, c) typical chromatogram of LDPE degradation products.

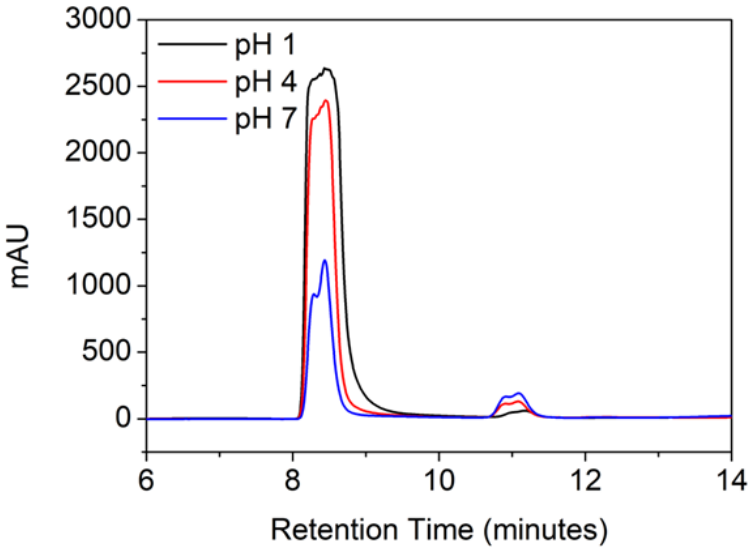


Figure S11: HPLC chromatograms at pH1, 4 and 7 showing nitrate peak.

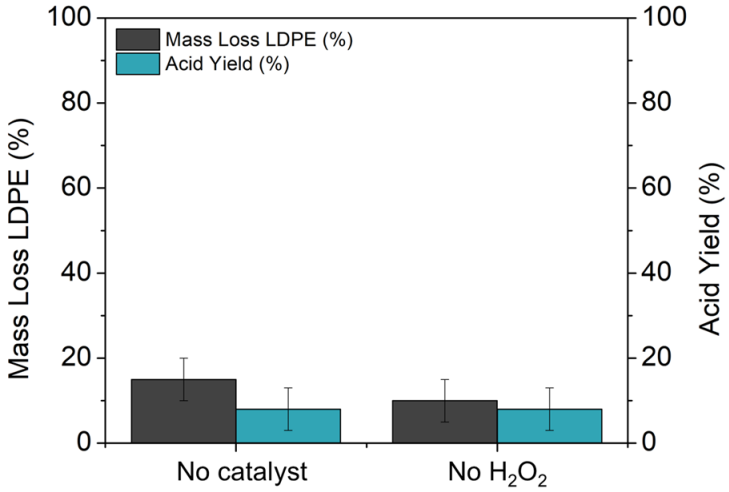


Figure S12: Reaction results with no catalyst (0.5 g LDPE, 10 mL 15 % (w/w) H_2O_2) and no peroxide (0.5 g LDPE, 1 wt. % catalyst, 10 mL H_2O).

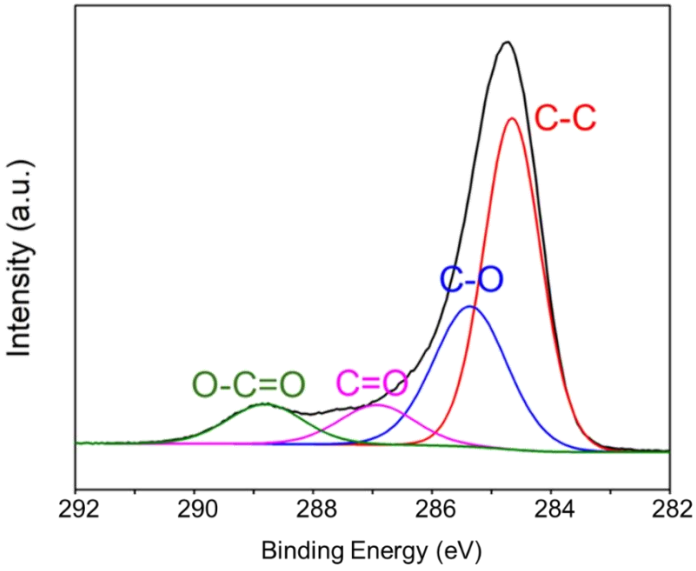


Figure S13: C1s XPS core level of residual LDPE after 3 h of reaction time.

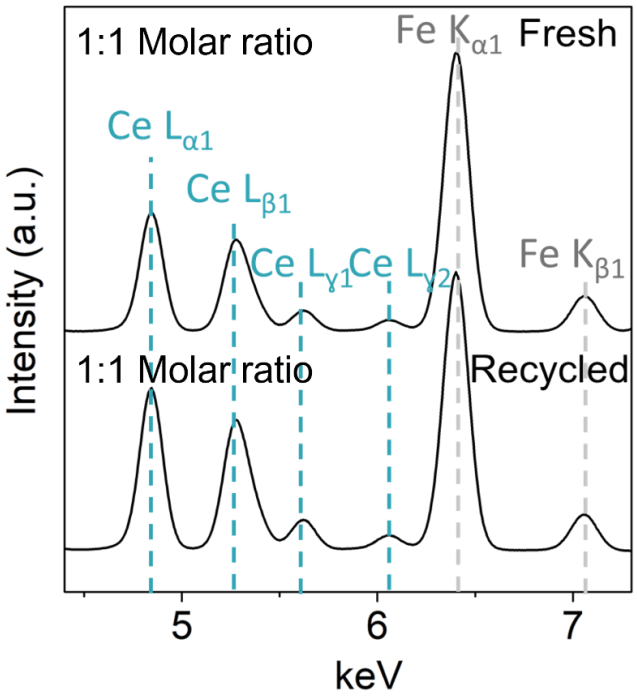


Figure S14: TXRF analysis of Fresh and Recycled Fe-CeO_2 catalyst.

References:

(1) Farahmandjou, M.; Soflaee, F. Synthesis and Characterization of α-Fe2O3 Nanoparticles by Simple Co-Precipitation Method. *Physical Chemistry Research* **2015**, *3* (3), 191-196. DOI: 10.22036/pcr.2015.9193.
(2) Suresh, R.; Ponnuswamy, V.; Mariappan, R. Effect of annealing temperature on the microstructural, optical and electrical properties of CeO2 nanoparticles by chemical precipitation method. *Applied Surface Science* **2013**, *273*, 457-464. DOI: https://doi.org/10.1016/j.apsusc.2013.02.062.
(3) Almond, J.; Sugumaar, P.; Wenzel, M. N.; Hill, G.; Wallis, C. Determination of the carbonyl index of polyethylene and polypropylene using specified area under band methodology with ATR-FTIR spectroscopy. **2020**, *20* (1), 369-381. DOI: doi:10.1515/epoly-2020-0041 (accessed 2024-02-05).
(4) Schmeling, M. Total reflection X-ray fluorescence. **2019**, *4* (7). DOI: doi:10.1515/psr-2017-0161 (accessed 2024-02-29).
(5) Wimberger, L.; Ng, G.; Boyer, C. Light-driven polymer recycling to monomers and small molecules. *Nature Communications* **2024**, *15* (1), 2510. DOI: 10.1038/s41467-024-46656-3.

6.6 Appendix II:

Characterisation of Fe-CeO_2 Nanoflakes Synthesised by Cryogenic Exfoliation Method

Preface

This appendix presents work funded by the AMBER Centre under a collaborative proposal that I co-wrote with Dr Jack Maughan (School of Physics, TCD). The purpose of the award (valued €2500) was to promote interdisciplinary collaboration between AMBER postgraduate researchers. I led the synthesis of the Fe-CeO_2 solid-solution nanomaterials the characterisation of the exfoliated products, while Dr Maughan led the cryogenic exfoliation process.

Abstract

Cryogenic exfoliation was used to transform a nanocrystalline Fe-CeO_2 solid solution powders into amorphous 2D nanoflakes with high defect densities. Post-exfoliation, structural surface and electronic characterisation revealed significantly altered physicochemical properties, resulting in a greater density of oxygen vacancies, an increased Ce^{3+}/Ce^{4+} ratio, higher porosity and enhanced thermal stability, while maintaining a uniform distribution of Fe and Ce. These defect-rich nanoflakes exhibit properties suited to oxidation catalysis, oxygen evolution reaction (OER) and reverse water-gas shift reaction. Given its scalability and benign process conditions, cryogenic exfoliation offers a versatile route for producing functional 2D metal oxide catalysts.

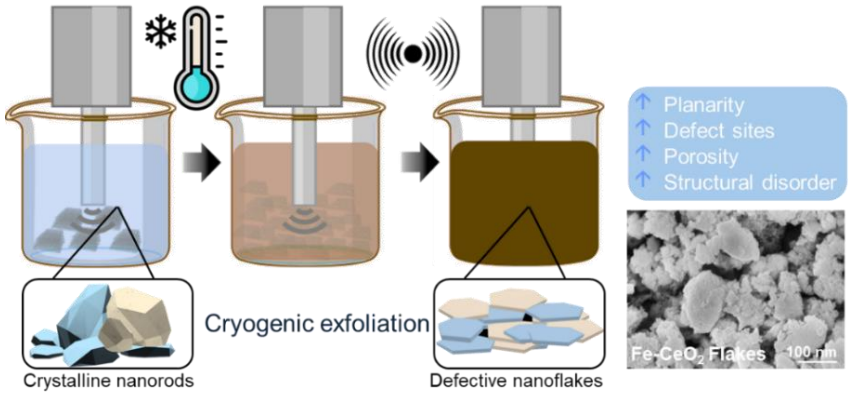


Table of Contents Graphic

Introduction

Cerium and doped cerium-based oxide nanostructures have gained significant attention in recent years due to their desirable properties such as their robust fluorite crystal structure, stress resistance, high chemical and thermal stability and electronic conductivity making them ideal versatile materials for research and industrial applications.[1] In particular, CeO_2 shows promise in semiconductors, photocatalysis, water splitting/OER, redox catalysis and other applications.[2, 3] Cerium is also one of the most abundant rare earth metals.

Despite these advantages, pristine CeO_2 can be catalytically limited e.g. in oxidation[4] and OER[5] due to a low density of reactive surface sites sites on stable cubic CeO_2. Doping is a powerful strategy to tailor surface reactivity by introducing defects such as oxygen vacancies. Substitutional dopants displace Ce^{4+} in the fluorite lattice altering crystal symmetry and facilitating Ce^{4+}/Ce^{3+} redox. Oxygen vacancies can form via incorporation of aliovalent cations which is described in equation 1 and the Kröger-Vink notation is described in equation 2.[6]

$$O^{2-} + 2Ce^{4+} \leftrightarrow 2Ce^{3+} + \frac{1}{2}O_2 \quad \textbf{Eqn. 1}$$

$$O_o^x \leftrightarrow V_o^{\bullet\bullet} + 2e' + \frac{1}{2}O_2 \quad \textbf{Eqn. 2}$$

Where O_o^x, denotes a lattice oxygen, $V_o^{\bullet\bullet}$, denotes oxygen vacancies which are doubly charged and e' electrons in the Ce 4f band, respectively.[7]

Among dopants, Fe-doped CeO_2 has gained attention in numerous applications in catalysis[8] including photocatalysis[9], electrocatalysis[5], energy storage[10], medical applications[11] and gas sensing[12]. Fe is favourable for doping CeO_2 when compared with other metals such as Ni and Co, due to its enhanced redox properties, oxygen storage capacity, redox cycling and oxygen vacancy sites. Fe-CeO_2 solid solution catalysts have been found to exhibit enhanced selectivity over bare CeO_2 for the oxidative dehydrogenation of propane[13], NO reduction[14], water oxidation[5] and oxidative degradation of

polyethylene[4]. Incorporation of Fe into a CeO_2 lattice can also lower the band gap energy due to the formation of intrinsic defects.[15]

There is growing evidence that defect-rich and/or amorphous mixed oxides can enhance redox performance. Kim et al.[16] reported chemically induced amorphisation of CeO_2-TiO_2 using H_2O_2 to increase redox activity by weakening the Ce-O-Ce bonds making them more susceptible to reduction. Amorphous Fe oxyhydroxide on CeO_2, synthesised via hydrothermal method followed by a galvanic displacement where Fe^{2+} displaced Ce^{4+} to form Ce^{3+} and Fe-OOH, showed excellent OER catalytic performance attributed to improved electron transfer.[17] Amorphous 2D CeO_2 nanosheets prepared via a top-down method using supercritical CO_2 showed enhanced photoluminescence properties due to increased vacancy defects from the cleavage of Ce-O bonds.[18] Defect-rich Fe-doped CeO_2 nanosheets were also reported to be excellent OER catalysts by Zhang and co-workers and displayed tuneable OER performance with calcination.[19] The Fe/CeO_2 catalyst architecture was also active for the reverse water-gas shift reaction, showing higher stability over 12 h than commercial Cu-Zn catalyst which underwent significant deactivation after the same time.[20] Brackmann and co-workers synthesised Fe-CeO_2 solid solution catalysts for the NO reduction by CO[14] which altered the crystallite, size, density, band gap, lattice parameter and porosity of the CeO_2 and led to improved performance and selectivity for the reaction. Other synthesis methods reported for 2D CeO_2 include ultrasonic spray pyrolysis[21] and solvothermal method[22, 23].

Liquid phase exfoliation (LPE) is a widely used top-down route to 2D materials, first popularised for graphene.[24] Where materials are non-layered in the bulk, cryogenic exfoliation can be used to induce microcracks along weaker planes in the bulk structure using liquid nitrogen (N_2), enabling subsequent sonication to form of nanosheet structures.[25] Two synthesis routes are common: (i) the bulk material is pre-treated with liquid N_2, then sonicate in a solvent, or (ii) freeze the dispersion in liquid N_2 first, then sonicate. In both cases, the extremely low temperatures induce cracks in the bulk material and when combined with sonication lead to the formation of nanosheets. Cryogenic exfoliation has

produced 2D morphologies from layered[25, 26] and non-layered materials[27] ranging from metals, non-metals and metal oxides. Hematene (2D α-Fe_2O_3)[28] was prepared by LPE from highly oriented large crystals in the bulk material. Other energy intensive methods for the preparation of 2D materials include rapid "gel-blowing" exfoliation process involving forming a gel with metal salt precursors followed by flash pyrolysis which was reported for the synthesis of nonlayered 2D metal and mixed-metal oxide nanosheets by Wang and co-workers.[29]

When compared to crystalline analogues, 2D amorphous nanomaterials can exhibit enhanced surface area, abundant defect sites, strong in-plane covalency and grain boundary-free transport, enabling faster diffusion and electron transfer.[31] Amorphous 2D metal oxides such as cobalt-vanadium hydr(oxy)oxide[32] and nickel phosphate-decorated nickel cobalt hydroxide[33], outperform their crystalline counterparts in energy storage and transformation processes. LPE can also produce amorphous 2D materials e.g. red phosphorous which exhibited high stability as electrode materials.[30]

Physical exfoliation offers good scalability and supports greener manufacturing. Cryogenic exfoliation increases exfoliation efficiency with lower energy input than many chemical routes because materials become brittle at lower temperatures making it easier to fracture and separate layers and it also avoids toxic solvents/ reagents, enhancing environmental compatibility.

Here, we report the cryogenic exfoliation of a nanocrystalline Fe-CeO_2 solid solution to yield highly defective, amorphous 2D Fe-CeO_2 nanoflakes. The materials are characterised by XRD, Raman, DSC, BET, UV-Vis, SEM, EDX, TEM and XPS. Post-exfoliation, the dispersion of Fe and Ce throughout the material is conserved while O vacancy concentration, Ce^{3+}/Ce^{4+} ratio, porosity and thermal stability increase relative to the crystalline precursor. These features are desirable properties for applications such as catalytic oxidation.

Materials and Methods:

Material Synthesis

B_Fe-CeO_2 (Bulk material): Fe-CeO_2 solid solution were synthesised by coprecipitation method. A solution of 0.755 g $FeCl_3$ in 25 mL DI H_2O and 1.933 g $Ce(SO_4)_2.4H_2O$ in 25 mL DI H_2O were combined to form a 1:1 molar ratio of Fe:Ce and stirred at room temperature for 10 minutes before the pH was adjusted to 12 using 1 M NaOH solution and a red/brown precipitate appeared. The mixture was refluxed for 2 h at 100 °C under N_2 with stirring. The resulting particles were collected by suction filtration and dried in an oven at 75 °C overnight. The solid was then calcinated at 450 °C under air for 4h.

Ex_Fe-CeO2 (Exfoliated material): Cryogenic exfoliation was carried out by submerging a glass vial of Fe-CeO_2 and 1 mg/mL PVP in 20 mL IPA in liquid N_2 for 3 minutes. The material was then immediately placed in a sonic bath and sonicated at 37 kHz for 5 minutes. This cycle of cryogenic fracturing and sonication was then repeated a total of 5 times, followed by bath sonication for 2 h. Size selection was carried out on the resultant dispersion by liquid cascade centrifugation, between 1000 and 6000 RPM.

Materials Characterisation

X-ray Diffraction (XRD) was carried out on a PANalytical X'Pert PRO with Cu Kα radiation and a constant step of 0.0098° 2θ and a counting time of 149.97 seconds per step.

Raman spectroscopy was performed using an Oceanview InVia Raman Spectrometer using a 25 mW Ar-ion laser under 532 nm excitation. The beam was focused onto the samples using a 50x objective lens and spectra were collected using a RenCam CCD camera.

DSC was carried out on Netzsch DSC300 Classic from a temperature range of 20 °C to 600 °C under N_2 with a flow rate of 250 ml/min.

The sorption analyses were performed on a Micromeritics Tristar II surface area and porosity analyser. Prior to analysis, each sample was de-gassed for three hours at 150 °C and measurements were

performed at -169.15°C (77 K). The surface area was determined using the BET (Brunauer-Emmett Teller) method. The pore volume, pore diameter and pore size distribution were determined using the BJH (Barrett-Joyner-Halenda) method.[34]

Scanning electron microscopy (SEM) and Energy Dispersive X-ray Spectroscopy (EDS) mapping was performed on a Zeiss Supra 40 high resolution SEM at an accelerating voltage of 5 kV.

TEM was performed using a JEOL 2100 electron microscope at an operating voltage of 200 kV and FEI Titan TEM at an operating voltage of 300 kV. Image J software was used to determine the *d*-spacing for crystal structures.

X-ray Photoelectron Spectroscopy (XPS) was carried out using a KRATOS ACIS 165 monochromatised X-ray photoelectron spectrometer equipped with an Al Kα (hv = 1486.6 eV) X-ray source. Spectra were collected at a take-off angle of 90 ° and all spectra were referenced to the C 1s peak at 284.8 eV.

Synthesis and Characterisation:

The Fe-CeO_2 solid solution was obtained through co-precipitation method and the resulting solid underwent cryogenic exfoliation as illustrated in Figure 1. The cryogenic exfoliation process yielded 2D Fe-CeO_2 nanoflakes which were extensively characterised to evaluate the chemical and physical properties arising from cryogenic exfoliation.

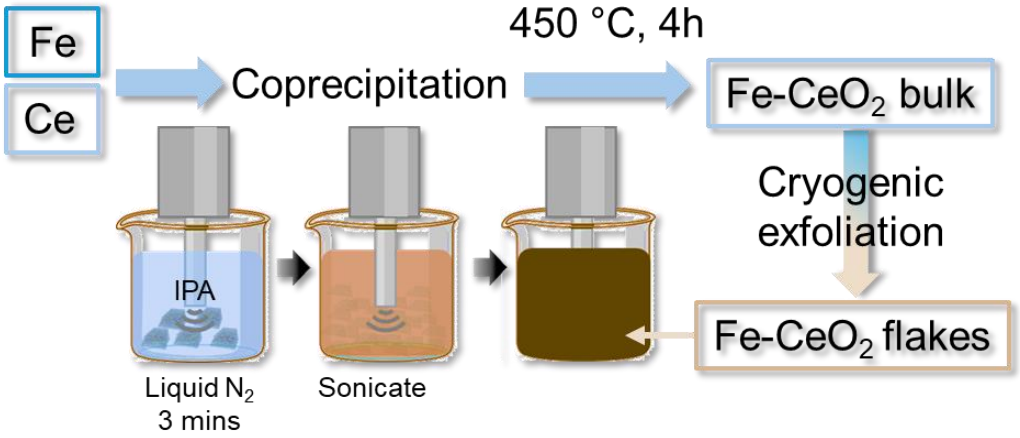


Figure 1: Schematic for the synthesis of Fe-CeO_2 nanoflakes by cryogenic exfoliation.

The SEM analysis of the as synthesised B_Fe-CeO_2 (Figure 2 a) and b)) shows densely packed needle-like nanostructures. After cryogenic exfoliation a clear morphological transition is observed. The Ex_Fe–CeO_2 exhibits randomly oriented nanoflakes with irregular edge (Figure 2 c)-e), evidencing successful fragmentation of the bulk metal oxide to a quasi 2D morphology. The flake size distribution was estimated by measuring flake length from SEM images, shown in Figure 2 f). A mean flake size of ~ 0.18 µm was estimated with most flakes < 0.3 µm, indicating efficient fragmentation and size control during exfoliation. EDX mapping shown in Figure 2 g) confirms the homogeneous dispersion of Fe, Ce and O across the nanoflakes, suggesting the cryogenic exfoliation process does not result in phase separation.

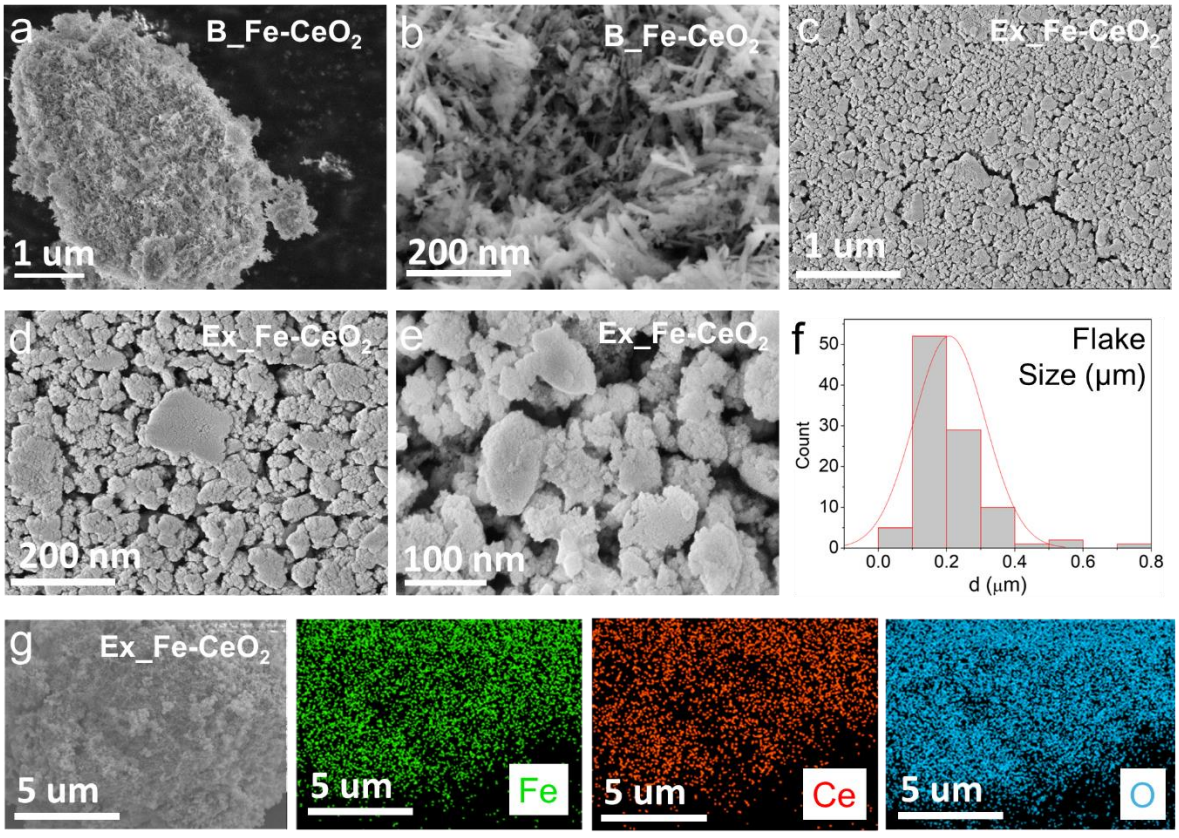


Figure 2: a) & b) SEM images of B_Fe-CeO_2, c), d) and e) SEM images of Ex_Fe-CeO_2, f) size distribution data for nanoflake diameter, g) EDX analysis of Ex_Fe-CeO_2.

TEM analysis was used to further characterise the structure and crystallinity of the B_Fe-CeO_2 and Ex_Fe-CeO_2 and the results are shown in Figure 3. Prior to exfoliation, B_Fe-CeO_2 appears as aggregates

of polycrystalline nanoparticles as shown in Figure 3 a). High-resolution TEM reveals lattice fringes and *d*-spacing of *d* = 0.329 nm indexed to CeO_2 (111) plane, shown in Figure 3 b). The corresponding FFT (Figure 3 c), shows rings with discrete spots, characteristic of a polycrystalline material. After exfoliation, the Ex_Fe-CeO_2 displays flake-like regions shown in Figure 3 d)-e) and is in excellent agreement with SEM analysis. The exposed lattice fringes gave *d*-spacings of 0.330 nm, again consistent with CeO_2 (111) crystal phase which is a well reported phase orientation for CeO_2 nanoflake growth of owing to its high stability.[35, 46] The presence of darker regions were observed in the HRTEM of the defective CeO_2 which has previously been reported for defective CeO_2[37] and can be attributed to a rough defective surface and the formation of oxygen vacancy clusters. The FFT of Ex_Fe-CeO_2 (Figure 3 f) shows faint and diffuse rings, indicative of reduced long-range order and characteristic of amorphous CeO_2.[16] The presence of one faint ring assigned to the CeO_2 (111) aligns well with the XRD analysis presented later.

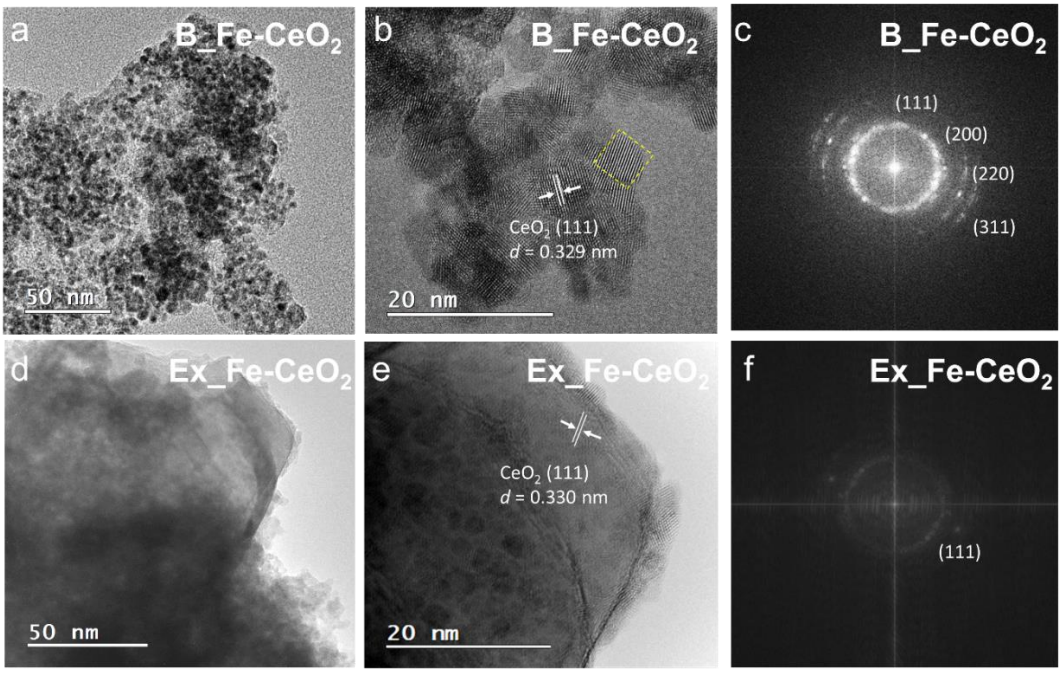


Figure 3: a)-c) TEM, HRTEM and FFT of B_Fe-CeO_2, d)-f) TEM, HRTEM and FFT of Ex_Fe-CeO_2 flakes, respectively.

Figure 4 a) shows the XRD analysis of the bulk Fe-CeO_2 solid solution (B_Fe-CeO_2) and the resulting nanoflakes after cryo-exfoliation (Ex_Fe-CeO_2). XRD of the B_Fe-CeO_2 shows diffractions peaks at 2θ ~

28.4, 32.9, 47.3, 56.2, 59.1, 69.3, 76.7 and 79.0 2θ indexed to the (111), (200), (220), (311), (222), and (400) lattice planes of cubic fluorite CeO_2 respectively, with $Fm\bar{3}m$ space group (JCPDS 65-5923).[15] After cryogenic exfoliation, the Ex_Fe-CeO_2 nanoflakes exhibited very broad and low-intensity peaks, indicative of a predominantly amorphous structure with minimal long range order. Cryogenic exfoliation of a structurally defective bulk material facilitates cleavage along pre-existing defect planes, which can lead to the formation of an amorphous two-dimensional material.[30] A very broad peak was observed at 28.4 2θ suggests residual short-range ordering related to the (111) crystal plane in agreement with TEM analysis and orientations of previously reported CeO_2 nanoflakes.[23, 35] Raman analysis of both samples, shown in Figure 4 b) was used to identify defects induced from the cryogenic exfoliation. Both samples display the F_2g mode of cubic fluorite ceria at 467 cm^{-1}. In Ex_Fe-CeO_2, this band broadens and decreases in relative intensity, consistent with higher defect density and local disorder in highly defective CeO_2[36, 37]. Additional peaks at approximately 300 cm^{-1}, 600 cm^{-1}, 790 cm^{-1}, 1310 cm^{-1} and 2250 cm^{-1} were present for Ex_Fe-CeO_2 and are commonly associated with oxygen defect-related features, suggesting significant lattice disorder and the presence of non-stoichiometric cubic ceria.[38,39]

Differential scanning calorimetry (DSC) was used to assess the thermal stability of each material and shown in Figure 4 c). Both materials show a broad endothermic event near 100 °C attributed to the desorption of physisorbed H_2O or loosely bound hydroxyl groups. This peak is much stronger in B_Fe-CeO_2 suggesting greater water uptake, most likely attributed to the aqueous synthesis. A second exothermic event ~300 °C appears for B_Fe-CeO_2, attributed to structural relaxation of lattice strain arising from Fe doping, previously reported for crystalline metal oxides and metal-organic framenworks.[40, 41] A final weak exotherm ~500 °C is observed for the B_Fe-CeO_2 attributed to crystallisation of defect regions within the solid solution structure such as oxygen vacancy ordering or Fe migration.[40] The peak is very weak in the Ex_Fe-CeO_2. The lack of these events in the Ex_Fe-CeO_2 flakes suggests greater thermal stability of the defect network formed during the cryoexfoliation process.

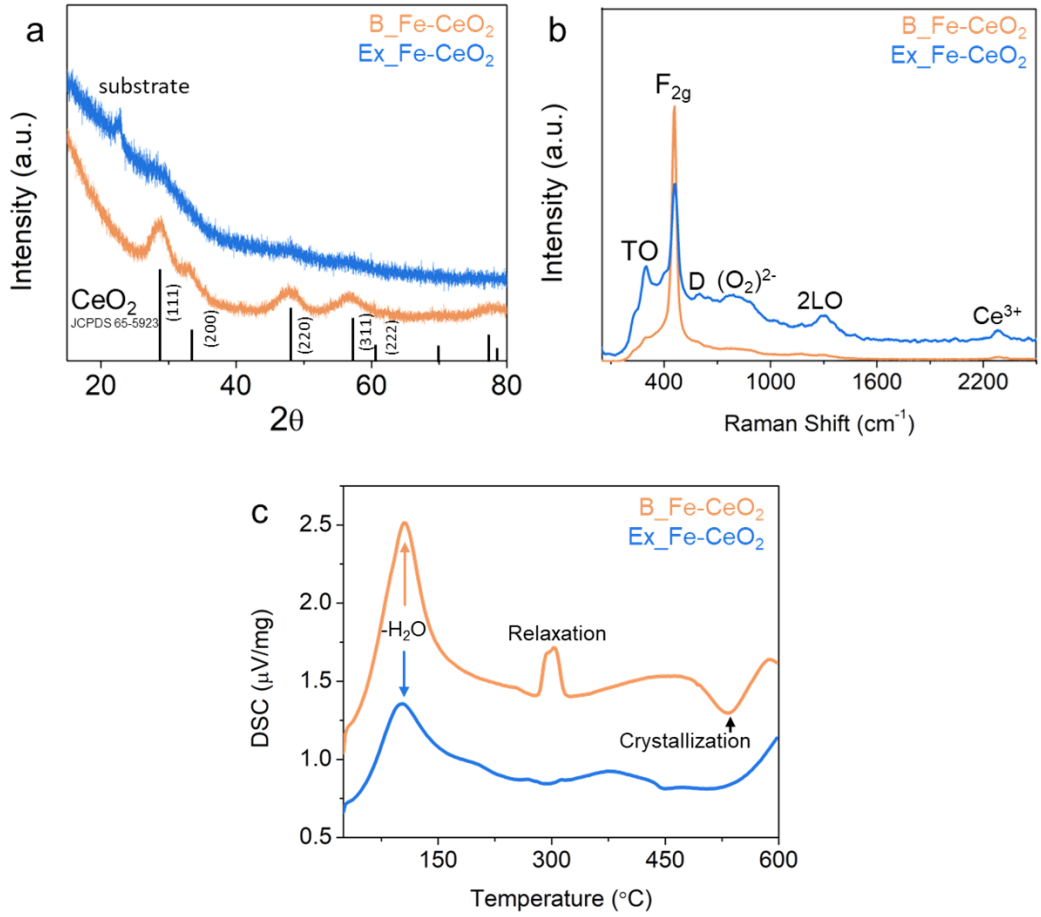


Figure 4: a) XRD of B_Fe-CeO_2 and Ex_Fe-CeO_2, b) Raman spectra of B_Fe-CeO_2 and Ex_Fe-CeO_2 and c) DSC curves for B_Fe-CeO_2 and Ex_Fe-CeO_2.

The N_2 adsorption-desorption isotherms for both samples are shown in Figure 5 a) and both materials show type IV isotherms with a H3-type hysteresis loop, associated with capillary condensation in mesoporous materials.[42] The pore distribution curves and properties for both samples are shown in Figure 3 b) and Table 1, respectively. The B_Fe-CeO_2 has a higher surface area (101.7 m^2/g) than the Ex_Fe-CeO_2 (71.9 m^2/g), but the Ex_Fe-CeO_2 displays a higher pore volume and pore width than the B_Fe-CeO_2, consistent with crack formation along grain boundaries during exfoliation resulting in large pores and intrinsic defects.

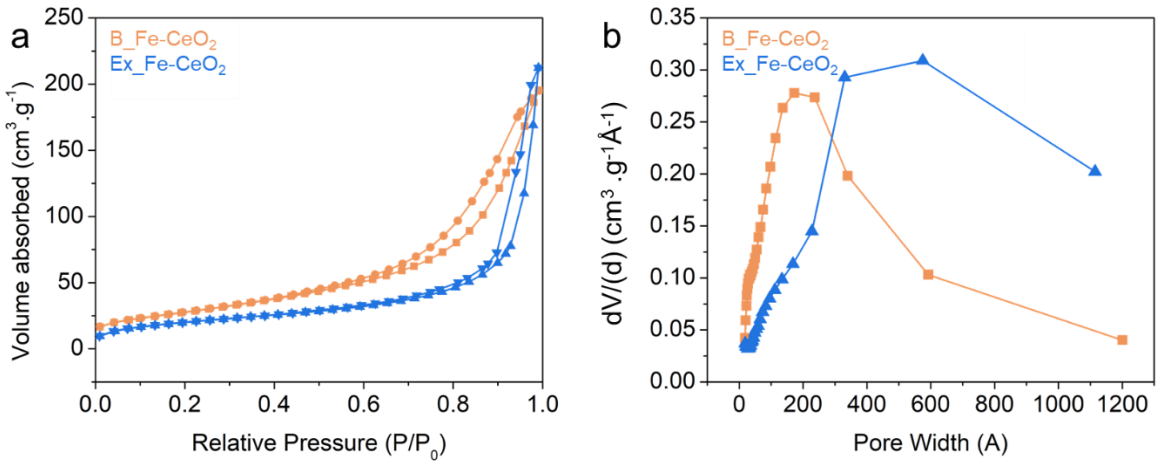


Figure 5: BET analysis of B_Fe-CeO_2 and Ex_Fe-CeO_2 a) N_2 sorption isotherms and b) pore diameter curves.

Table 1: BET Surface area, pore volume and average pore width for B_Fe-CeO_2 and Ex_Fe-CeO_2.

Material	Specific surface area (m^2/g)	Pore volume (m^3/g)	Average Pore Width (nm)
B_Fe-CeO_2	101.7	0.30	10.2
Ex_Fe-CeO_2	71.9	0.32	20.1

Figure 6 a) shows the UV-vis analysis of B_Fe-CeO_2 and Ex_Fe-CeO_2. The Ex_Fe-CeO_2 sample exhibits higher overall absorbance with a maximum at ~ 305 nm. The B_Fe-CeO_2 bulk material shows a broader, lower intensity band with a maximum absorption occurring ~ 309.5 nm. Such band broadening has previously been linked to a reduced crystallite size[43] while a red-shift has been attributed to charge transfer between Fe^{3+} electrons with the O 2p conduction band and Ce 4f valence band as the Fe^{3+} energy level is situated within the band gap of Fe-CeO_2.[14] The corresponding Tauc plots (Figure 6 b) using a direct transition model was used to estimate the direct band gap of B_Fe-CeO_2 and Ex_Fe-CeO_2 which were 2.76 eV and 2.97 eV, respectively. These values are both lower than the obtained literature values of CeO_2 which has been reported to be 3.05 eV[44], 3.16 eV[14] and 3.07 eV[45]. Although the

exfoliated material shows a slightly wider band gap than the bulk, it remains narrowed relative to undoped CeO_2, suggesting a more stable electronic configuration, consistent with the DSC results. The enhanced UV absorption intensity of Ex_Fe-CeO_2 can be ascribed to defect-induced mid-gap states (from oxygen vacancies and Ce^{3+} sites), which provide additional optical transitions and strengthen light-matter interaction despite the increased band gap.

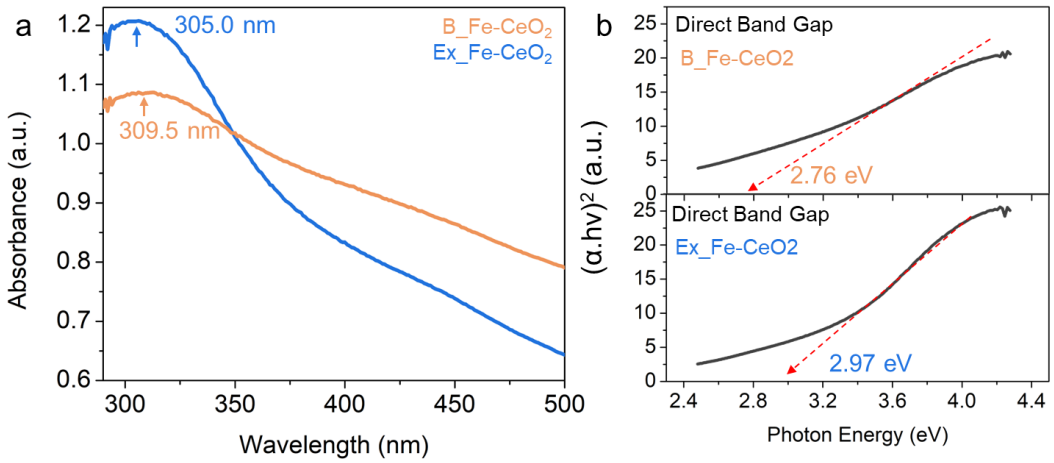


Figure 6: a) UV-Vis and b) Tauc plot of Fe-CeO_2 B_Fe-CeO_2 and Ex_Fe-CeO_2.

XPS was used to identify changes in the surface chemistry and valence states of iron or cerium in the material during the exfoliation process. Figure 7 a) shows the Ce 3d core level XPS spectra used to determine the dominant oxidation state of Ce in each sample. Both samples exhibit the characteristic multiplet structure of ceria labelled $v_o/v'/v''/v'''$ ($Ce3d_{5/2}$) and $u_0/u'/u''/u'''$ ($Ce3d_{3/2}$). The peak at a BE of 917 eV labelled u''' is the fingerprint peak for Ce^{4+} and was present in both samples.[47] The pre-exfoliated sample had 8 peaks all corresponding to either Ce^{3+} or Ce^{4+}. The peaks labelled *u* correspond to the spin-orbit doublets of $Ce3d_{3/2}$ while the peaks labelled *v* correspond to the spin-orbit doublets of $Ce3d_{5/2}$.[48]

After exfoliation, the *u* and *u'* peaks are not present in the sample, and a new peak denoted v''' which corresponds to Ce^{4+} appeared, From peak-area analysis the ratio of Ce^{3+}/Ce^{4+} was calculated and was

found to be 0.79 for B_Fe-CeO_2, but increased to 1.44 after exfoliation, likely due to the formation of a highly defective structure.

The Fe 3p spectra are shown in Figure 7 b) and show two peaks at binding energies of 711.5 eV and 725.3 eV which correspond to Fe $2p_{3/2}$ and Fe $2p_{1/2}$, respectively. An additional satellite peak is present at 719.5 eV further confirming the presence of Fe^{3+} and were all in good agreement with values reported for surface iron present in the +3 valence state.[49] A shift of the Fe $2p_{3/2}$ peak to higher binding energies was observed after the cryogenic exfoliation process suggesting modified Fe–O / Fe–Ce interactions arising from the more defective surface environment. The O 1s core level spectra for the B_Fe-CeO_2 and Ex_Fe-CeO_2 are shown in Figure 7 c). The B_Fe-CeO_2 show three O components resolved at BE of 529.4 eV, 531.4 eV and 532.8 eV, assigned to electron-rich lattice O^{2-}, surface hydroxyl (OH) groups or adsorbed O_2 and adsorbed H_2O, respectively.[37] In Ex_Fe–CeO_2, an additional feature appears at 530 eV which was assigned to surface superoxide/peroxide-like species (O_2^{2-}/O^-) species, which is consistent with literature reports of defective CeO_2 compared with non-defective CeO_2.[37] The appearance of this component also agrees with Raman analysis.

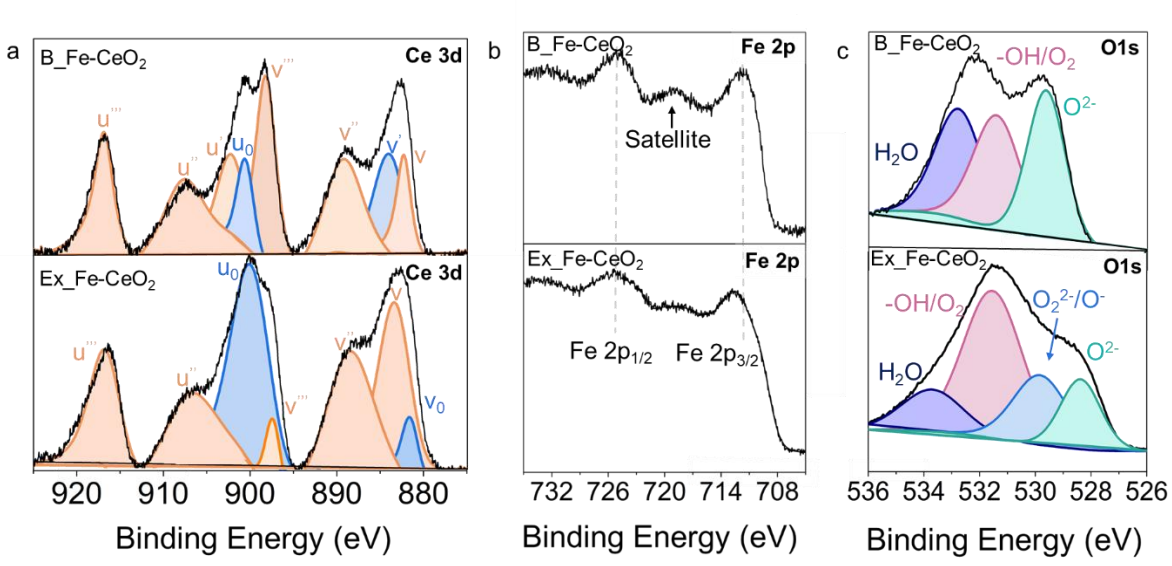


Figure 7: XPS analysis of a) Ce 3d, b) Fe 3p and c) O1s core levels for B_Fe-CeO_2 and Ex_Fe-CeO_2.

Conclusions

Cryogenic exfoliation was successfully applied to a crystalline Fe-CeO_2 solid solution, producing highly defective, amorphous 2D Fe-CeO_2 nanoflakes. Detailed characterisation revealed substantial modifications in physicochemical properties, including increased oxygen vacancy concentration, a higher Ce^{3+}/Ce^{4+} ratio, enhanced porosity and improved thermal stability. Importantly, the uniform Fe–Ce distribution was preserved within the nanoflakes. These properties highlight cryogenic exfoliation as a viable strategy for synthesising defect-rich, amorphous 2D Fe–CeO_2, with potential applications in oxidation catalysis, the oxygen evolution reaction, and the reverse water–gas shift reaction. Given its scalability and environmentally benign conditions, offers cryogenic exfoliation offers a promising route for the sustainable production of functional 2D metal oxide nanomaterials.

References

(1) Abdulwahab, K. O.; Khan, M. M.; Jennings, J. R. Doped Ceria Nanomaterials: Preparation, Properties, and Uses. *ACS Omega* **2023**, *8* (34), 30802-30823. DOI: 10.1021/acsomega.3c01199.
(2) Vinitha, P.; Arularasu, M. V.; Vignesh, R. A review on green synthesis and applications of CeO2 nanomaterials – An eco-friendly approach. *Chemistry of Inorganic Materials* **2025**, *5*, 100084. DOI: https://doi.org/10.1016/j.cinorg.2024.100084.
(3) Koyale, P. A.; Delekar, S. D. A review on practical aspects of CeO2 and its composites for photoelectrochemical water splitting. *International Journal of Hydrogen Energy* **2024**, *51*, 515-530. DOI: https://doi.org/10.1016/j.ijhydene.2023.06.251.
(4) Breen, R.; Holmes, J. D.; Collins, G. Heterogeneous Fenton-type oxidative degradation of low-density polyethylene to valuable acid products using a nanostructured Fe–CeO2 solid solution catalyst. *Catalysis Science & Technology* **2025**, 10.1039/D4CY01384K. DOI: 10.1039/D4CY01384K.
(5) Sun, Q.; Liu, Y.; Li, X.; Guo, X.; Huang, W.-H.; Zhu, Y.; Wang, Z.; Chueh, C.-C.; Chen, C.-L.; Peng, Y.-K.; et al. Highly Disordered Fe-Doped CeO2 with Oxygen Vacancies Facilitates Electrocatalytic Water Oxidation. *Energy & Fuels* **2023**, *37* (13), 9434-9443. DOI: 10.1021/acs.energyfuels.3c00621.
(6) Cam, T. S.; Omarov, S. O.; Chebanenko, M. I.; Izotova, S. G.; Popkov, V. I. Recent progress in the synthesis of CeO2-based nanocatalysts towards efficient oxidation of CO. *Journal of Science: Advanced Materials and Devices* **2022**, *7* (1), 100399. DOI: https://doi.org/10.1016/j.jsamd.2021.11.001.
(7) Sun, C.; Li, H.; Chen, L. Nanostructured ceria-based materials: synthesis, properties, and applications. *Energy & Environmental Science* **2012**, *5* (9), 8475-8505, 10.1039/C2EE22310D. DOI: 10.1039/C2EE22310D.
(8) Bao, H.; Chen, X.; Fang, J.; Jiang, Z.; Huang, W. Structure-activity Relation of Fe2O3–CeO2 Composite Catalysts in CO Oxidation. *Catalysis Letters* **2008**, *125* (1), 160-167. DOI: 10.1007/s10562-008-9540-3.
(9) Channei, D.; Inceesungvorn, B.; Wetchakun, N.; Ukritnukun, S.; Nattestad, A.; Chen, J.; Phanichphant, S. Photocatalytic Degradation of Methyl Orange by CeO2 and Fe–doped CeO2 Films under Visible Light Irradiation. *Scientific Reports* **2014**, *4* (1), 5757. DOI: 10.1038/srep05757.
(10) Ma, Y.; Ma, Y.; Giuli, G.; Euchner, H.; Groß, A.; Lepore, G. O.; d'Acapito, F.; Geiger, D.; Biskupek, J.; Kaiser, U.; et al. Introducing Highly Redox-Active Atomic Centers into Insertion-Type Electrodes for Lithium-Ion Batteries. *Advanced Energy Materials* **2020**, *10* (25), 2000783. DOI: https://doi.org/10.1002/aenm.202000783 (accessed 2025/04/17).
(11) Jampaiah, D.; Srinivasa Reddy, T.; Kandjani, A. E.; Selvakannan, P. R.; Sabri, Y. M.; Coyle, V. E.; Shukla, R.; Bhargava, S. K. Fe-doped CeO2 nanorods for enhanced peroxidase-like activity and their application towards glucose detection. *Journal of Materials Chemistry B* **2016**, *4* (22), 3874-3885, 10.1039/C6TB00422A. DOI: 10.1039/C6TB00422A.
(12) Esmaeili, C.; Ashtiani, S.; Regmi, C.; Laposa, A.; Voves, J.; Kroutil, J.; Friess, K.; Povolny, V.; Lotfian, S. Preparation and characterisation of NH3 gas sensor based on PANI/Fe-doped CeO2 nanocomposite. *Heliyon* **2024**, *10* (15), e34801. DOI: https://doi.org/10.1016/j.heliyon.2024.e34801.

(13) Wang, H.; Tsilomelekis, G. Catalytic performance and stability of Fe-doped CeO2 in propane oxidative dehydrogenation using carbon dioxide as an oxidant. *Catalysis Science & Technology* **2020**, *10* (13), 4362-4372, 10.1039/D0CY00586J. DOI: 10.1039/D0CY00586J.
(14) Brackmann, R.; Toniolo, F. S.; Schmal, M. Synthesis and Characterization of Fe-Doped CeO2 for Application in the NO Selective Catalytic Reduction by CO. *Topics in Catalysis* **2016**, *59* (19), 1772-1786. DOI: 10.1007/s11244-016-0698-4.
(15) Brito, P. C. A.; Santos, D. A. A.; Duque, J. G. S.; Macêdo, M. A. Structural and magnetic study of Fe-doped CeO2. *Physica B: Condensed Matter* **2010**, *405* (7), 1821-1825. DOI: https://doi.org/10.1016/j.physb.2010.01.054.
(16) Kim, M.; Park, G.; Lee, H. Local Structure and Redox Properties of Amorphous CeO2-TiO2 Prepared Using the H2O2-Modified Sol-Gel Method. In *Nanomaterials*, 2021; Vol. 11.
(17) Sun, X.; Guan, X.; Feng, H.; Zheng, D.; Tian, W.; Li, C.; Li, C.; Yan, M.; Yao, Y. Enhanced activity promoted by amorphous metal oxyhydroxides on CeO2 for alkaline oxygen evolution reaction. *Journal of Colloid and Interface Science* **2021**, *604*, 719-726. DOI: https://doi.org/10.1016/j.jcis.2021.06.149.
(18) Guo, Z.; Yang, H.; Tian, Q.; Ma, W.; Xu, Q.; Han, B. CO2-Assisted Fabrication of 2D Amorphous CeO2 and Its Application in Photoluminescence Enhancement. *ChemNanoMat* **2022**, *8* (10), e202200269. DOI: https://doi.org/10.1002/cnma.202200269 (accessed 2025/05/22).
(19) Zhang, H.; Xia, L.; Li, Y.; Tang, J.; Wang, L.; Zhong, S. Defect-rich Fe-doped CeO2 nanosheets as effective oxygen evolution electrocatalysts. *Inorganic Chemistry Communications* **2022**, *141*, 109531. DOI: https://doi.org/10.1016/j.inoche.2022.109531.
(20) Watanabe, R.; Karasawa, F.; Yokoyama, C.; Oshima, K.; Kishida, M.; Hori, M.; Ono, Y.; Satokawa, S.; Verma, P.; Fukuhara, C. Highly stable Fe/CeO2 catalyst for the reverse water gas shift reaction in the presence of H2S. *RSC Advances* **2023**, *13* (17), 11525-11529, 10.1039/D3RA01323E. DOI: 10.1039/D3RA01323E.
(21) Xue, S.-F.; Li, Y.-J.; Zheng, F.-H.; Bian, X.; Wu, W.-Y.; Yang, C.-H. Characterization of CeO2 microspheres fabricated by an ultrasonic spray pyrolysis method. *Rare Metals* **2021**, *40* (1), 31-39. DOI: 10.1007/s12598-020-01594-z.
(22) Li, C.; Li, R.; Fu, C.; Song, X.; Gu, M. Solvothermal synthesis of titania/ceria. *Rare Metals* **2011**, *30* (1), 544-547. DOI: 10.1007/s12598-011-0343-0.
(23) Joseph, A.; Perikkathra, S.; Thomas, T. Novel 2D CeO2 nanoflakes as a high-performance asymmetric supercapacitor electrode material. *Journal of Energy Storage* **2023**, *68*, 107757. DOI: https://doi.org/10.1016/j.est.2023.107757.
(24) Kaur, H.; Coleman, J. N. Liquid-Phase Exfoliation of Nonlayered Non-Van-Der-Waals Crystals into Nanoplatelets. *Advanced Materials* **2022**, *34* (35), 2202164. DOI: https://doi.org/10.1002/adma.202202164 (accessed 2025/05/30).
(25) Wang, H.; Lv, W.; Shi, J.; Wang, H.; Wang, D.; Jin, L.; Chao, J.; van Aken, P. A.; Chen, R.; Huang, W. Efficient Liquid Nitrogen Exfoliation of MoS2 Ultrathin Nanosheets in the Pure 2H Phase. *ACS Sustainable Chemistry & Engineering* **2020**, *8* (1), 84-90. DOI: 10.1021/acssuschemeng.9b04057.
(26) Wang, Y.; Liu, Y.; Zhang, J.; Wu, J.; Xu, H.; Wen, X.; Zhang, X.; Tiwary, C. S.; Yang, W.; Vajtai, R.; et al. Cryo-mediated exfoliation and fracturing of layered materials into 2D quantum dots. *Science Advances 3* (12), e1701500. DOI: 10.1126/sciadv.1701500 (accessed 2025/05/30).
(27) Zhang, C.; Xu, Y.; Lu, P.; Wei, C.; Zhu, C.; Yao, H.; Xu, F.; Shi, J. Cryogenic Exfoliation of Non-layered Magnesium into Two-Dimensional Crystals. *Angewandte Chemie International Edition*

2019, *58* (26), 8814-8818. DOI: https://doi.org/10.1002/anie.201903485 (accessed 2025/05/30).
(28) Puthirath Balan, A.; Radhakrishnan, S.; Woellner, C. F.; Sinha, S. K.; Deng, L.; Reyes, C. d. l.; Rao, B. M.; Paulose, M.; Neupane, R.; Apte, A.; et al. Exfoliation of a non-van der Waals material from iron ore hematite. *Nature Nanotechnology* **2018**, *13* (7), 602-609. DOI: 10.1038/s41565-018-0134-y.
(29) Wang, D.; Zhou, W.; Zhang, R.; Zeng, J.; Du, Y.; Qi, S.; Cong, C.; Ding, C.; Huang, X.; Wen, G.; et al. Mass Production of Large-Sized, Nonlayered 2D Nanosheets: Their Directed Synthesis by a Rapid "Gel-Blowing" Strategy, and Applications in Li/Na Storage and Catalysis. *Advanced Materials* **2018**, *30* (43), 1803569. DOI: https://doi.org/10.1002/adma.201803569 (accessed 2025/05/30).
(30) Kaur, H.; Konkena, B.; Gabbett, C.; Smith, R.; McCrystall, M.; Tian, R.; Roy, A.; Carey, T.; Vega-Mayoral, V.; Nicolosi, V.; et al. Amorphous 2D-Nanoplatelets of Red Phosphorus Obtained by Liquid-Phase Exfoliation Yield High Areal Capacity Na-Ion Battery Anodes. *Advanced Energy Materials* **2023**, *13* (6), 2203013. DOI: https://doi.org/10.1002/aenm.202203013 (accessed 2025/06/03).
(31) Liu, J.; Hao, R.; Jia, B.; Zhao, H.; Guo, L. Manipulation on Two-Dimensional Amorphous Nanomaterials for Enhanced Electrochemical Energy Storage and Conversion. In *Nanomaterials*, 2021; Vol. 11.
(32) Liu, J.; Ji, Y.; Nai, J.; Niu, X.; Luo, Y.; Guo, L.; Yang, S. Ultrathin amorphous cobalt–vanadium hydr(oxy)oxide catalysts for the oxygen evolution reaction. *Energy & Environmental Science* **2018**, *11* (7), 1736-1741, 10.1039/C8EE00611C. DOI: 10.1039/C8EE00611C.
(33) Chodankar, N. R.; Dubal, D. P.; Ji, S.-H.; Kim, D.-H. Self-Assembled Nickel Pyrophosphate-Decorated Amorphous Bimetal Hydroxides 2D-on-2D Nanostructure for High-Energy Solid-State Asymmetric Supercapacitor. *Small* **2019**, *15* (19), 1901145. DOI: https://doi.org/10.1002/smll.201901145 (accessed 2025/06/03).
(34) Brunauer, S.; Emmett, P. H.; Teller, E. Adsorption of Gases in Multimolecular Layers. *Journal of the American Chemical Society* **1938**, *60* (2), 309-319. DOI: 10.1021/ja01269a023.
(35) Ding, H.; Yang, J.; Ma, S.; Yigit, N.; Xu, J.; Rupprechter, G.; Wang, J. Large Dimensional CeO2 Nanoflakes by Microwave-Assisted Synthesis: Lamellar Nano-Channels and Surface Oxygen Vacancies Promote Catalytic Activity. *ChemCatChem* **2018**, *10* (18), 4100-4108. DOI: https://doi.org/10.1002/cctc.201800784 (accessed 2025/02/27).
(36) Loridant, S. Raman spectroscopy as a powerful tool to characterize ceria-based catalysts. *Catalysis Today* **2021**, *373*, 98-111. DOI: https://doi.org/10.1016/j.cattod.2020.03.044.
(37) Liang, F.; Yu, Y.; Zhou, W.; Xu, X.; Zhu, Z. Highly defective CeO2 as a promoter for efficient and stable water oxidation. *Journal of Materials Chemistry A* **2015**, *3* (2), 634-640, 10.1039/C4TA05770H. DOI: 10.1039/C4TA05770H.
(38) Schmitt, R.; Nenning, A.; Kraynis, O.; Korobko, R.; Frenkel, A. I.; Lubomirsky, I.; Haile, S. M.; Rupp, J. L. M. A review of defect structure and chemistry in ceria and its solid solutions. *Chemical Society Reviews* **2020**, *49* (2), 554-592, 10.1039/C9CS00588A. DOI: 10.1039/C9CS00588A.
(39) Acharya, S. A.; Gaikwad, V.; Sathe, V.; Kulkarni, S. Influence of gadolinium doping on the structure and defects of ceria under fuel cell operating temperature. *Applied Physics Letters* **2014**, *104*, 113508-113508. DOI: 10.1063/1.4869116.
(40) Darabian, L. M.; Gonçalves, G. R.; Schettino, M. A.; Passamani, E. C.; Freitas, J. C. C. Synthesis of nanostructured iron oxides and study of the thermal crystallization process using

DSC and in situ XRD experiments. *Materials Chemistry and Physics* **2022**, *285*, 126065. DOI: https://doi.org/10.1016/j.matchemphys.2022.126065.
(41) Pires, J. Simultaneous Thermogravimetry-Differential Scanning Calorimetry (TG-DSC) in Nanoporous Materials: Examples of Data for Zeolites, Metal–Organic Frameworks (MOFs), Clay Based and Mesostructured Solids. *Journal of Inorganic and Organometallic Polymers and Materials* **2024**, *34* (8), 3346-3359. DOI: 10.1007/s10904-024-03048-w.
(42) Thommes, M.; Kaneko, K.; Neimark, A. V.; Olivier, J. P.; Rodriguez-Reinoso, F.; Rouquerol, J.; Sing, K. S. W. Physisorption of gases, with special reference to the evaluation of surface area and pore size distribution (IUPAC Technical Report). **2015**, *87* (9-10), 1051-1069. DOI: doi:10.1515/pac-2014-1117 (accessed 2025-07-22).
(43) Yao, X.; Tang, C.; Ji, Z.; Dai, Y.; Cao, Y.; Gao, F.; Dong, L.; Chen, Y. Investigation of the physicochemical properties and catalytic activities of Ce0.67M0.33O2 (M = Zr4+, Ti4+, Sn4+) solid solutions for NO removal by CO. *Catalysis Science & Technology* **2013**, *3* (3), 688-698, 10.1039/C2CY20610B. DOI: 10.1039/C2CY20610B.
(44) Silambarasan, R.; Perisetti, U. S. S. S.; Ramesh, A.; Anbalagan, K. UV Light-Driven Photocatalytic Performance of CeO2 and Co Ion-Doped CeO2 Nanoparticles: High-Efficiency Electrochemical and Chromaticity Blue LED Application. *ChemistrySelect* **2024**, *9* (40), e202402609. DOI: https://doi.org/10.1002/slct.202402609 (accessed 2025/07/22).
(45) Yue, L.; Zhang, X.-M. Structural characterization and photocatalytic behaviors of doped CeO2 nanoparticles. *Journal of Alloys and Compounds* **2009**, *475* (1), 702-705. DOI: https://doi.org/10.1016/j.jallcom.2008.07.096.
(46) Cui, R.; Lu, W.; Zhang, L.; Yue, B.; Shen, S. Template-Free Synthesis and Self-Assembly of CeO2 Nanospheres Fabricated with Foursquare Nanoflakes. *The Journal of Physical Chemistry C* **2009**, *113* (52), 21520-21525. DOI: 10.1021/jp9065168.
(47) Maslakov, K. I.; Teterin, Y. A.; Ryzhkov, M. V.; Popel, A. J.; Teterin, A. Y.; Ivanov, K. E.; Kalmykov, S. N.; Petrov, V. G.; Petrov, P. K.; Farnan, I. The electronic structure and the nature of the chemical bond in CeO2. *Physical Chemistry Chemical Physics* **2018**, *20* (23), 16167-16175, 10.1039/C8CP01442F. DOI: 10.1039/C8CP01442F.
(48) Hasegawa, T.; Shahed, S. M. F.; Sainoo, Y.; Beniya, A.; Isomura, N.; Watanabe, Y.; Komeda, T. Epitaxial growth of CeO2(111) film on Ru(0001): Scanning tunneling microscopy (STM) and x-ray photoemission spectroscopy (XPS) study. *The Journal of Chemical Physics* **2014**, *140* (4), 044711. DOI: 10.1063/1.4849595 (accessed 1/24/2024).
(49) Bagus, P. S.; Nelin, C. J.; Brundle, C. R.; Crist, B. V.; Lahiri, N.; Rosso, K. M. Origin of the complex main and satellite features in Fe 2p XPS of Fe2O3. *Physical Chemistry Chemical Physics* **2022**, *24* (7), 4562-4575, 10.1039/D1CP04886D. DOI: 10.1039/D1CP04886D.

Chapter 7

Combined Fenton-type Oxidation and Anaerobic Digestion of Polyethylene to Methane Using Biochar-Derived Catalysts

Rachel Breen [a b], Anga Hackula [c d], Justin D. Holmes [a b], David M. Wall [c d], Gillian Collins [a b *]

[a]AMBER Centre, Sustainability Institute, University College Cork, Cork, T23 XE10, Ireland.

[b] School of Chemistry, University College Cork, Cork, T12 YN60, Ireland.

[c] SFI MaREI Centre for Energy, Climate and Marine, Sustainability Institute, University College Cork, Cork, Ireland.

[d] Civil, Structural and Environmental Engineering, School of Engineering and Architecture, University College Cork, Cork, Ireland

Publication: ***Breen, R****.; Hackula, A.; Holmes, J. D.; Wall, D. M.; Collins, G. Combined Fenton-type Oxidation and Anaerobic Digestion of Polyethylene to Methane Using Biochar Catalysts. ACS Sustainable Chemistry and Engineering (in review).*

Abstract

Chemical recycling of plastic polymers offers an attractive alternative to current waste management methods which are failing to meet large global production volumes. Polyethylene is particularly challenging due to its chemical inertness and mechanical recycling limitations. Fenton and Fenton-type oxidation is emerging as a more environmentally friendly chemical recycling route for polyethylene when compared with high temperature pyrolysis. Typically, metal catalysts are reported for Fenton oxidation, however, carbon materials have also been reported to exhibit Fenton-type activity. Biochar is a product of biomass pyrolysis and is gaining traction as a sustainable and renewable source of carbon. Depending on the source and pyrolysis temperature, different biochar samples can possess a wide variation of material properties making them useful for catalytic applications. This work discusses the characterisation of biochar from wood and grain, pyrolysed at 300 °C and 700 °C and assesses their

performance as heterogeneous Fenton-type catalysts for the oxidative degradation of low-density polyethylene (LDPE) to a mixture of carboxylic acid products. Low-cost separation routes such as chromatography can pose challenges for mixtures of low molecular weight acids; therefore, we propose anaerobic digestion as a route of bioconversion of the carboxylic acid mixture to produce methane.

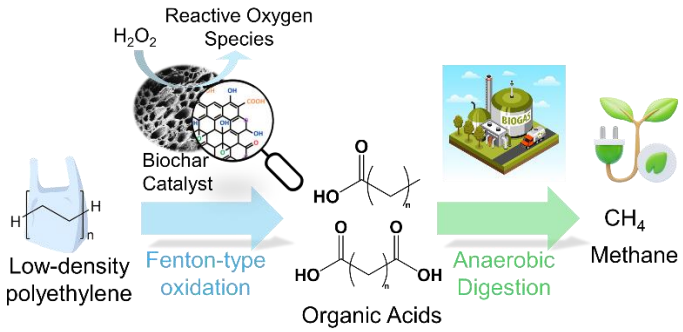


Table of Contents Graphic

7.1 Introduction

Plastics, particularly those resistant to degradation such low-density polyethylene (LDPE), have become integral to modern society due to attractive characteristics such as versatility, durability, and cost-effectiveness. However, their widespread use has contributed significantly to a growing global waste crisis. It is estimated that from an annual production yield of 413 million tons (2023) of plastic only 20 % are effectively recycled, resulting in an accumulation in landfills and natural ecosystems.[1] The persistence of non-biodegradable plastics, coupled with poor recycling methods, highlights the urgent need for innovative waste management solutions aligned with circular economy principles. A fundamental component of these principles is waste valorisation, transforming discarded materials into valuable resources.

In recent decades, significant progress has been made on the chemical recycling of polyolefins such as polyethylene and polypropylene. However, some challenges remain due to their composition of chemically inert, hydrophobic hydrocarbon chains.[2] Chemical recycling efforts for polyolefins currently

involve energy intensive processes such as gasification and high temperature pyrolysis.[3] Catalytic depolymerisation strategies, including catalytic pyrolysis, tandem metathesis and oxidation, enable the transformation of polyolefins under milder conditions.[4, 5]

Oxidative degradation methods have been developed to yield short-chain oxygenated products such as acids, alcohols and ketones.[6-8] These methods often require chemical pretreatment to chemically activate the polyethylene[9] and the use of hazardous reagents such as nitric acid.[10] Typically, the oxidative degradation of polyethylene produces a mixture of carboxylic acids. The downstream separation of the individual acids, while highly desirable, presents significant challenges when using low-cost techniques such as extraction.[11] Therefore, a process that can convert the acid mixtures to a single chemical product would be a useful strategy and forms the motivation of the work presented here. Aqueous oxidative degradation techniques such as Fenton oxidation, are attractive as they yield water-soluble products that are amenable to biological conversion via processes such as anaerobic digestion (AD), thereby mitigating the need for costly separation steps.

The enzymatic conversion of biomass and biodegradable plastics into biofuels such as biomethane is well demonstrated.[12, 13] In this process, biomass is transformed into short chain carboxylic acids, such as propionic and butyric acid, commonly referred to as volatile fatty acids (VFAs), which are then converted to biomethane via AD. The process is facilitated through the actions and syntrophic interactions of various bacteria, including hydrolytic, acidogenic, acetogenic (acetate- and hydrogen-forming) microbes, as well as acetoclastic (converting acetic acid to methane (CH_4)) and hydrogenotrophic (converting hydrogen to CH_4) methanogens. During these steps, side products such as H_2S, H_2, CO_2 are formed, providing H sources that contribute to CH_4 formation.[14]

Interestingly, the VFAs produced in acidogenesis share structural similarities to the carboxylic acid products produced via oxidative degradation of polyethylene. In our recent work[7], we demonstrated that LDPE can be catalytically degraded via advanced oxidative processes with moderate to high yields of short chain carboxylic acids such as formic acid, acetic acid and propionic acid. Plastics like LDPE are

resistant to biological degradation and therefore unsuitable for direct AD, with studies showing negligible breakdown of LDPE under typical conditions.[15] Here, we demonstrate the combination of oxidation degradation of LDPE using a biochar Fenton-type catalyst followed by further upgrading to methane through AD, illustrated in Figure 1.

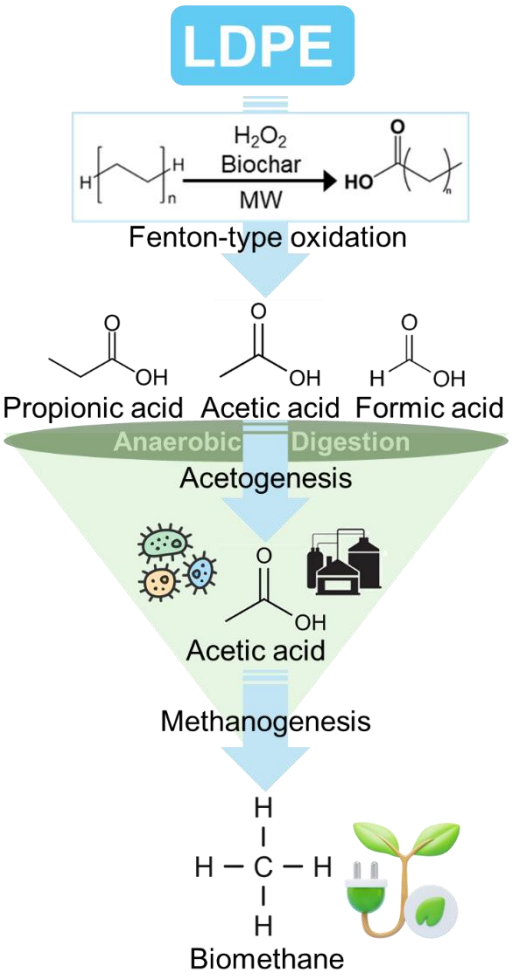


Figure 1: Schematic representation of LDPE bioconversion to methane through combined Fenton-type oxidation and anaerobic digestion. *MW = microwave-assisted heating.

Fenton-type oxidation involves the generation of reactive oxygen species such as oxygen radicals from H_2O_2, using a peroxide-activating catalyst. Traditional metal-based Fenton catalysts are highly effective and have been widely implemented in applications such as pollutant degradation,[16, 17] wastewater

treatment[18, 19], and plastic oxidation.[20] Challenges such as metal leaching and iron sludge formation limit their broader applicability.[21] To address these issues, metal-free Fenton catalysts have emerged as a more environmentally friendly, potentially cost-effective, and sustainable alternative to metal-based catalysts. Gong et al.[22] used density functional theory (DFT) to model H_2O_2 activation on metal-free, modified graphene Fenton-type catalysts. B, N, P, or S doping led to H_2O_2 cleavage into surface-bound O and H_2O, while oxygen-containing graphene with edge-located −OH, C=O, or −COOH groups promoted formation of surface-bound −OH. These pathways differed from classical Fenton systems, yielding chemisorbed species rather than free $^{\bullet}OH$. Lyu et al.[23] developed a 4-phenoxyphenol (POP)-functionalised reduced graphene oxide (rGO) catalyst with C−O−C bridges forming dual reaction centres: electron-rich O sites reduce H_2O_2 to $^{\bullet}OH$, while electron-poor C sites accept electrons from pollutants, enhancing H_2O_2 activation without metals and overcoming limitations such as sludge formation and pH constraints. Similarly, quinone-like surface groups on rGO were found to be efficient metal-free Fenton catalysts, activating H_2O_2 to form $^{\bullet}OH$ achieving radical turn over frequencies comparable to metal-based catalysts.[24] One drawback of graphene oxides (GO) is the hazards associated with its synthesis, commonly known as Hummer's method,[25] which involves the use of concentrated sulfuric acid (H_2SO_4), potassium permanganate ($KMnO_4$) and H_2O_2 and a cost-benefit analysis is often required to justify the use of GO in catalytic applications.

Biomass-derived Fenton-type catalysts present a potentially greener alternative. Biochar is an emerging sustainable carbon-based material with a wide range of applications including carbon sequestration, soil quality improvement, pesticide detoxification and catalysis.[26] Biochar is produced by pyrolysis of biomass under a limited oxygen environment, typically conducted at temperatures ranging from 300 to 900 ^{o}C.[27] Higher pyrolysis temperatures tend to increase surface area and porosity, although usually at the cost of reducing the abundance of surface functional groups through volatilisation.[28] Biochar-based catalysts have been reported as Fenton catalysts for a variety of applications such as degradation of tetracycline[29], electrocatalysis[30], Cu(II) removal[31] and sulfamethoxazole oxidation.[32] Investigation of biochar as a metal-free Fenton catalyst found that COOH

groups are key active sites for electron transfer pathways for H_2O_2 activation due to electron-donating properties.[33] Aiming to replace current catalyst technologies with biomass-derived catalysts will result in less hazardous chemical synthesis and utilisation of renewable feedstocks in excellent alignment with the 12 Principles of Green Chemistry.

Here, we evaluate biochar derived from two different feedstocks – grain-derived digestate (DG) and wood biomass (WB), both pyrolysed at 300 °C (DG300, WB300) and 700 °C (DG700, WB700), as Fenton-type catalysts for the oxidative degradation of LDPE to yield short chain carboxylic acid products. These acids are subsequently utilized as substrates in an AD process to produce methane as a single, more easily processed product for which established technologies are already available. Finally, a mass and energy balance analysis of the system was carried out to assess the material and energy flows of the system.

Experimental Section

All materials and methods including biochar preparation, Fenton oxidation procedure, HPLC analysis, materials characterisation, details on AD and mass and energy balance calculations can be found in the **Supporting Information**.

7.2 Results

7.2.1 Biochar Characterisation

The structural properties of the biochars were characterised using XRD and Raman spectroscopy. These techniques allow for assessment of the degree of structural disorder in biochar. The XRD patterns are shown in Figure 2 a) and confirm the presence of predominantly amorphous carbon structures across all samples. A broad peak in the 18 – 25° 2θ range is characteristic of the (002) plane of amorphous carbon. A small sharper peak at approximately 22.5° 2θ suggests the presence of partially crystalline cellulose polymorphs[34], and is more pronounced in the WB300 and WB700 biochar. A slight peak shift to lower 2θ values and an increase in peak intensity for the WB700 sample is

observed, indicative of lattice strain due to increased carbonisation. Another broad peak at 43° 2θ was assigned to the (100) plane of turbostatic carbon.[35] Two additional diffraction peaks at 26.5 2θ and 28.3 2θ in the DG300 and to a lesser extent DG700 were assigned to crystalline SiO_2[36] and KCl[37] arising from mineral content in grain-derived samples.

The Raman analysis for the biochar samples is shown in Figure 2 b). All samples exhibited three characteristic bands at 1350 cm^{-1},1590 cm^{-1} and 2793 cm^{-1}, corresponding to the disordered (D) carbon mode, graphitic (G) carbon mode, and the 2D or G'-band, respectively. The D-band is associated with structural defects and disordered sp^3-hybridised carbon, while the G-band arises from in-plane vibrations of sp^2-bonded carbon atoms in graphitic domains.[35] The ratio of the D to G band intensities (I_D/I_G) gives a measure of structural disorder, with higher values indicating a lower degree of graphitisation. The results are shown in Figure 2 b). An increase in I_D/I_G from 0.93 to 1 was observed for the DG300 to DG700 sample, indicative of a lower degree of graphitisation at higher pyrolysis temperatures for the grain-derived biochar. In contrast, a decrease in I_D/I_G from 0.9 to 0.84 was observed for the WB300 to the WB700 sample, suggesting greater graphitisation at higher pyrolysis temperatures. These observations are consistent with those of lignin structures at higher temperatures, while DG300 and DG700 lacking in lignin with presence of inorganic components tend to form more defective carbon with a lower degree of graphitisation. The 2D-band is an overtone of the D-band and can give an indication of the number of graphene layers in a carbon material. The 2D-band in all biochar samples is very broad with low intensity, which confirms the presence of a highly disordered, amorphous carbon with weak stacking of graphene layers in agreement with the XRD analysis.

Brunauer–Emmett–Teller (BET) analysis was performed to evaluate the surface area and porosity of the biochar samples. It is well reported that N_2 adsorption can pose challenges for the characterisation of biochars due surface micropores and pore blockage due to ash and mineral content.[38, 39] In this case, it was found that the DG300 and WB300 biochars were unsuitable for N_2 sorption studies likely due

the presence of macropores – the N_2 adsorption isotherms and pore distribution curves for DG300 and WB300 are shown in the Supporting Information Figure S2 a)-d). Figure S2 e) and f) shows the N_2 adsorption–desorption isotherms for the DG700 and WB700 biochar. The DG700 biochar exhibited a type IV isotherm with clear hysteresis loop characteristic of mesoporous materials, showing the effect of a higher carbonisation temperature on pore size. The isotherm for WB700 also displayed type IV characteristics, although with a pronounced open-loop hysteresis. The origin of this behaviour remains unclear, however similar observations in wood-derived biochars have been attributed to irreversible pore swelling during the adsorption process.[40, 41] The BET surface areas were determined as 4 m^2/g and 402 m^2/g for the DG700 and WB700, respectively. The high surface area for the WB700 biochar can be attributed to the high lignin content leading to better graphitisation during pyrolysis. The pore distribution curves for DG700 and WB700 are shown in Figure S3 g) and h) and WB700 exhibits a significantly higher and narrower mesopore population than DG700, indicative of greater pore volume and more uniform porosity. The cumulative pore volumes for the DG700 and WB700 were found to be 0.005 cm^2/g and 0.23 cm^2/g, respectively, indicative that the presence of mineral content can lead to pore blockage in DG700, while the lignin-rich nature of the WB700 resulted in a more porous, higher surface area carbon structure.

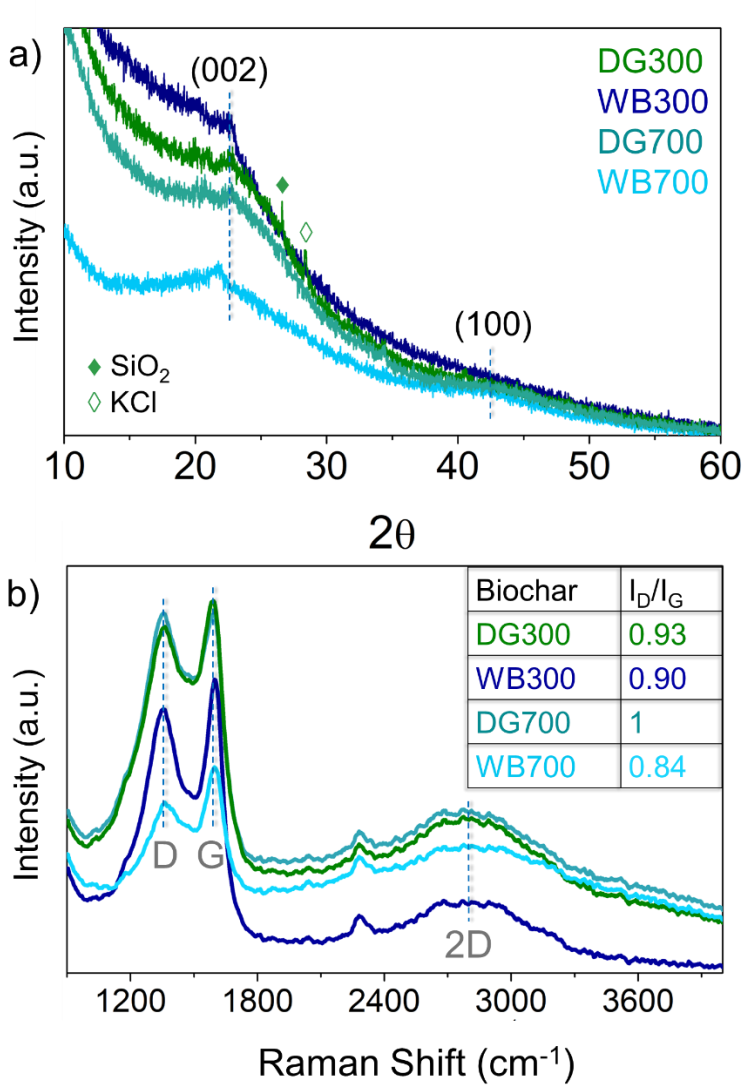


Figure 2: a) XRD patterns of DG300, WB300, DG700 and WB700, b) Raman spectra of DG300, WB300, DG700 and WB700.

SEM coupled with EDX was used to evaluate the morphology and chemical composition of the biochar and is shown in Figure 3. Distinct morphological and elemental differences were observed from the grain (DG) and wood (WB) sources pyrolysed at 300 and 700 °C. SEM images of the biochars at lower magnifications (Figure 3 a)-d)) reveal irregularly shaped particles approximately 100 µm in size. Notably, DG700 and WB700 exhibit a greater abundance of smaller, flake-like particles, likely resulting from pyrolysis at elevated temperatures. At closer magnifications shown in Figure 3 e), DG300 exhibits a highly porous, irregular structure with a rough surface, while WB300 (Figure 3 c)) shows a more

organised, honeycomb-like porous structure typical of lignocellulosic biomass.[42] In contrast, pyrolysis at 700 °C results in more compact structures in both DG700 and WB700, shown in Figure 3 b) and d), respectively, with more narrow or collapsed pores and smoother surfaces due to increased carbonisation.[43] All biochar samples contain channel-like structures which have been linked to the vigorous volatilisation of material during the pyrolysis process. The EDX spectra confirms that all biochars are predominantly composed of C and O, but grain derived biochars, especially DG300, also show notable traces of Na, Si, P, and K, reflecting the higher mineral content of grain biomass.[44] Wood-derived biochars display a simpler elemental profile, dominated by C and O with no detectable minerals. A significant decrease in O content is observed at a pyrolysis temperature of 700 °C (DG700 and WB700), suggesting volatilisation of O-containing functional groups. In the DG samples, O content drops from 15.97 % at 300 °C to 8.6 % at 700 °C, while in the WB samples, it decreases from 22.22% to 6.12% over the same temperature range. Overall, the results demonstrate that the type of biomass feedstock and the pyrolysis temperature significantly influence physiochemical properties of biochar.

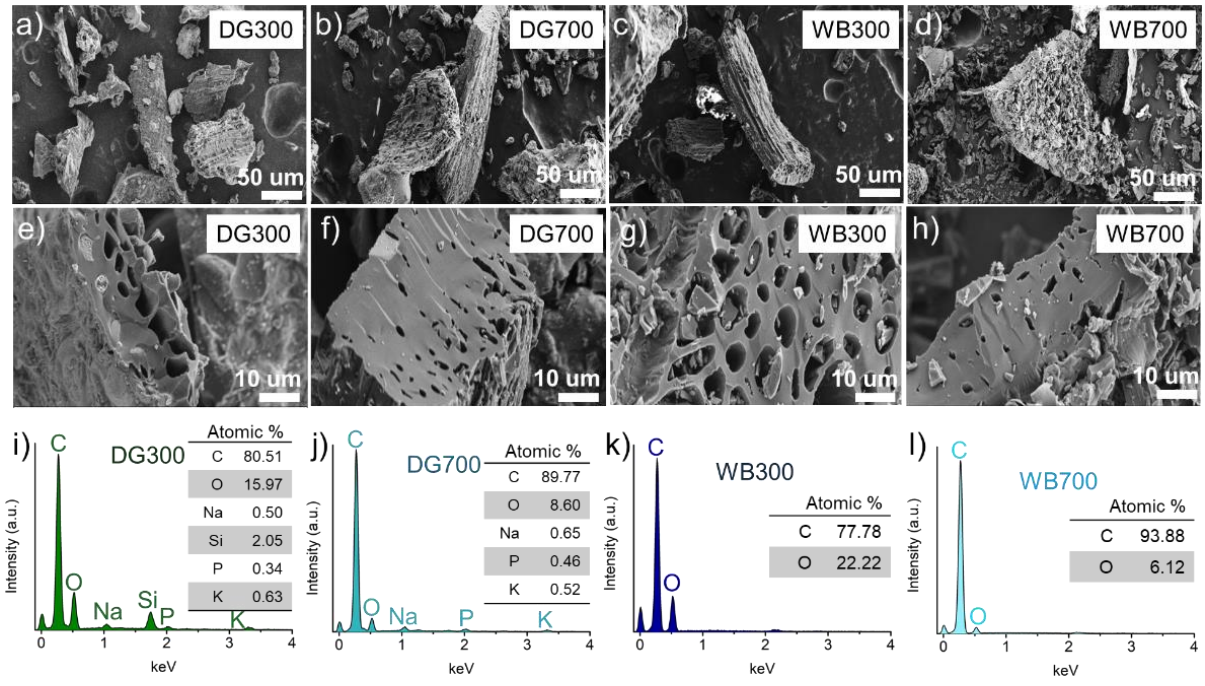


Figure 3: SEM images at low magnification of a) DG300, b) DG700, c) WB300 and d) WB700, and high magnification of e) DG300, f) DG700, g) WB300 and h) WB700, EDX data of i) DG300, j) DG700, k) WB300 and l) WB700.

Surface analysis of the biochar samples was carried out using XPS to evaluate the states of C, O and N in the biochars. The high-resolution O 1s core level spectra for the DG300, DG700, WB300 and WB700 biochars is shown in Figure 4 a). The DG300, DG700 and WB300 exhibited three separate component peaks at binding energies (BE) of 531.2, 533.1 and 535.2 eV which were assigned to C=O, C-O and C-OH, respectively.[45, 46] Interestingly, the WB300 sample is predominantly C-O which may arise from the lignin/cellulose-rich wood feedstock. A slight upshift in the BE of the O functionalities was observed for the WB700 sample which was attributed to greater graphitisation as O bound in aromatic systems will appear at higher BE.[47] The high-resolution C 1s spectra for the DG300, DG700, WB300 and WB700 are shown in Figure 4 b). Five separate component peaks were identified at binding energies of approximately 284.7 eV, 285.5 eV, 286.5 eV, 288.7 eV and 290.1 eV which were assigned to C=C, C-C, C-O, C=O and O-C=O, respectively.[35, 46] The presence of inorganic contaminants is evident for the DG300 and DG700 samples as two extra peaks at 293.3 eV and 296 eV were assigned to the K 2p region which is consistent with EDX analysis and has been previously reported for mineral-rich biochars.[48] For the WB300 and WB700 samples, an extra peak at approximately 292 eV was assigned to the π-π* satellite peak of aromatic carbon.[49] The relative contribution of each functionality calculated from the areas of the peaks in the C1s spectra for each biochar are tabulated in **Table S2**. The relative contribution of sp^2 C=C is higher in the WB300 (57.16 %) and the WB700 (65.98 %) catalysts than the DG300 (46.25 %) and DG700 (39.90 %) catalysts, which suggests a higher level of aromaticity arising for biochars derived from wood feedstock and is in agreement with XRD and Raman analysis. The C:O ratio was calculated from the C1s spectrum based on the peak assignments is also shown in **Table S2**. The C:O for the DG300 and DG700 samples was 2.81 and 2.79, respectively. Negligible change in the C:O from DG300 to DG700 may suggest that the surface O present in the grain-derived biochars is predominantly inorganic complexes with Na, K or Si which will not undergo volatisation at 700 °C. In contrast, the C:O for the WB300 and WB700 was 1.70 and 2.63, respectively, which is indicative of the loss of volatile O functional groups at 700 °C.[50] The WB300 catalyst had the highest relative O content of all the biochars.

The N 1s spectra (Figure 4 c) offers an interesting insight into the differences in chemical composition of biochar from different sources. Both DG300 and DG700 exhibit peaks at BE of ~398 eV and 400 eV, attributed to amine and amide functionalities in the biochar structure[51] or aromatic pyridinic and pyrrolic N functionalities,[52] which may arise due to the presence of fertilizers or proteins from the grain source.[53] Only trace amounts of N were identified in the WB300 and WB700 biochar samples (SI Figure S3), which is consistent with a wood feedstock.

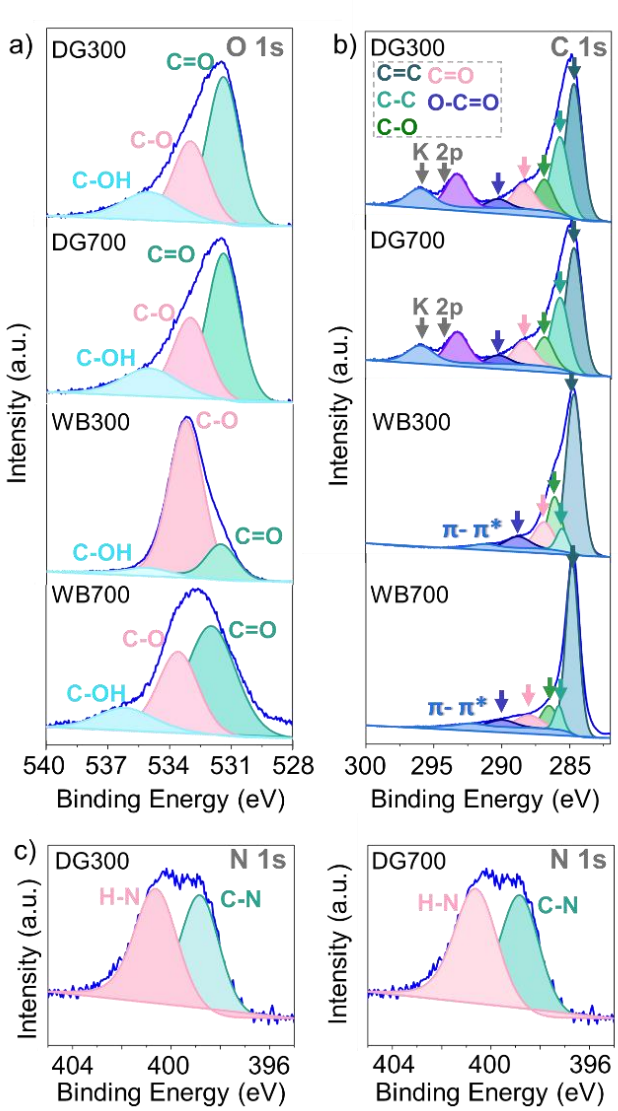


Figure 4: a) O1s XPS spectra for DG300, DG700, WB300, WB700, b) C1s XPS spectra for DG300, DG700, WB300, WB700, c) N1s XPS spectra for DG300 and DG700 (see SI for WB300 and WB700 N1s).

7.2.2 Catalytic Evaluation of Biochar for Fenton-type Oxidative Degradation of LDPE

Following characterisation of the physiochemical properties of the prepared biochars, their performance was evaluated as Fenton-type catalysts for the oxidative degradation of LDPE. Here, we aimed to determine which biochar exhibited the highest catalytic activity based solely on its surface functionality without reliance on added transition metals. The catalytic activity is measured based on mass loss LDPE relative to its initial mass, and acid yield as determined by HPLC (see Experimental Section for details). The aim of this study is to maximise the yield of short chain carboxylic acid products while minimising over-oxidation to gaseous products such as CO_2. The main acid products screened for via HPLC were formic acid (CH_2O_2), acetic acid ($C_2H_4O_2$), propionic acid ($C_3H_6O_2$), butyric acid ($C_4H_8O_2$), succinic acid ($C_4H_6O_4$), glutaric acid ($C_5H_8O_4$) adipic acid ($C_6H_{10}O_4$) and pimelic acid ($C_7H_{12}O_4$). The Fenton oxidative degradation experiments were conducted under conditions described in the Experimental Section. While Fenton reactions are typically carried out at acidic pH to stabilise iron-based catalysts, the biochar catalysts in this study demonstrated effective activity at neutral pH (pH 7). This is a significant advantage, eliminating the need for hazardous acids to adjust solution pH prior to the reaction.

The mass loss LDPE and acid yield results for DG300, DG700, WB300, and WB700 are shown in Figure 5 a). The WB300 catalyst showed the highest performance, achieving 86 % mass loss LDPE and a 56 % acid yield. The overall catalyst performance is determined by an interplay of factors, such as O-containing functionalities, porosity, surface area, and degree of aromaticity.[23, 24] The overall trend in terms of acid yield was WB300 > DG300 > WB700 > DG700. The superior performance of the wood-derived biochars compared to the grain-derived samples suggests that lignocellulosic feedstocks are more favourable for Fenton oxidation applications. This difference may be linked to the higher inorganic content in digestate-derived biochar, which can hinder catalytic activity. For example, phosphate ion adsorption has been shown to block active sites for zero valent iron Fenton catalyst inhibiting the regeneration of Fe^{2+}(aq).[54] There have also been several reports on the inhibitory effects of sulfates (SO_2^{4-}) and chlorides (Cl^-) due to $^{\bullet}OH$ scavenging in the Fenton oxidation reactions.[55-57] For

this reason, the DG300 and DG700 biochars may have resulted in radical scavenging, hindering the Fenton-type oxidation of LDPE.

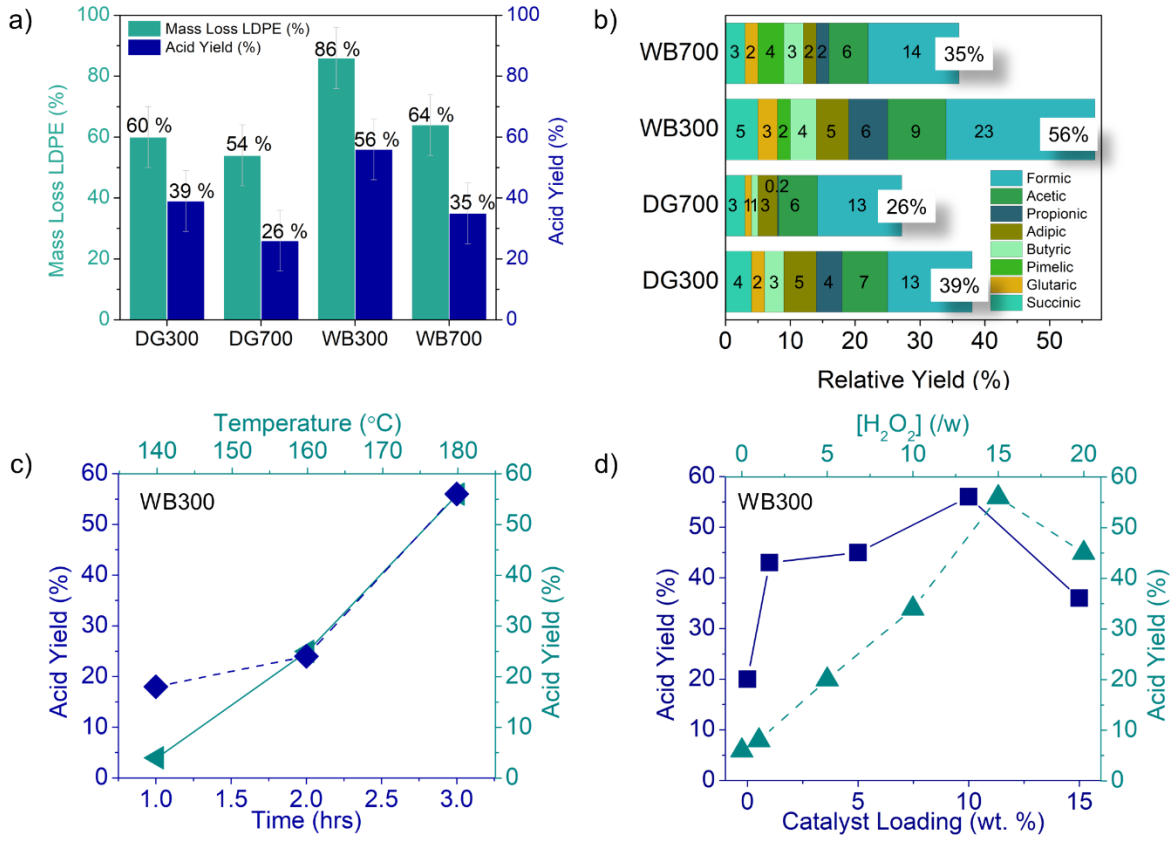


Figure 5: Catalytic evaluation of biochar a) mass loss LDPE and acid yield results of all biochar samples (0.5 g LDPE, 10 wt. % catalyst, 15 % H_2O_2 (w/w), 3 h, 180 °C) b) product distributions for the biochar samples, c) total acid yield as a function of temperature and time using WB300 biochar catalyst, d) total acid yield as a function of catalyst loading and H_2O_2 concentration using WB300 catalyst.

The distribution of acid products from the Fenton-type oxidation of LDPE using each biochar catalyst (10 wt. % loading, 15 % (w/w) H_2O_2, 3 h, 180 °C) are shown in Figure 5 b). The primary products were short chain carboxylic acids. Formic and acetic acid made up 23 % and 9 % of the WB300 product mixture, respectively. Propionic acid, butyric acid and succinic acid contributed 4 %, 6 % and 5 %, respectively. Succinic acid has been reported to be the main degradation product in LDPE oxidative

degradation pathways due to a kinetically favourable transition state.[10] Other longer chain acids such as glutaric acid and pimelic acid were present in quantities of 3 % and 2 %, respectively. This product profile suggests that the formation of shorter chain acids (< C4) is more favourable than longer chain acids. No significant differences in product distribution were observed between the different biochar catalysts, indicating that while catalyst type affects overall yield, it has limited influence on product selectivity under these conditions.

The influence of time and temperature on the acid yield for the WB300 is shown in Figure 5 c). It was observed that acid yield increases linearly with temperature. A time series (**Fig 5 c**)) shows a sharp increase in acid yield from 24 % to 56 % between 2 and 3 h. Extended reaction times or temperatures above 180 °C were avoided, as they could compromise the integrity of the PTFE vessels used. Figure S4 shows the pseudo first-order fit for the WB300 and DG300 catalysts to approximate a rate constant in terms of LDPE mass loss over time. A good linear fit was established for the DG300 and WB300 catalyst systems giving R^2 values of 0.94 and 0.99 respectively. The pseudo-first order rate coefficients for the catalyst systems were calculated from the slope of the linear fit to be $k = 5.25x10^{-5}s^{-1}$ for DG300 and $k = 8.31x10^{-5}s^{-1}$ for WB300. While these values provide a useful basis for comparison of degradation behavior, it is important to note that LDPE oxidative degradation is a multi-step process influenced by complex physical and chemical mechanisms such as radical production, random chain scission and morphological changes which are simplified using this method.

The effect of H_2O_2 concentration and catalyst loading for the system is illustrated in Figure 5 d). Interestingly, a 5 % acid yield was obtained with no H_2O_2 in the system (H_2O only). This may be attributed to the formation of $HO^{\bullet}$ from H_2O under MW irradiation in the presence of carbon.[58] A slight increase in acid yield to 8 % was observed on the addition of 1 % (w/w) H_2O_2. This increased to 21 % and 34 % for concentrations of 5 and 10 % (w/w), respectively. The optimal H_2O_2 concentration was 15 % (w/w) with an acid yield of 56 %. A further increase of H_2O_2 to the system results in a decrease of acid yield which may be attributed to the over-oxidation of acid products to gaseous products such as

CO_2 and H_2O.[59] The effect of catalyst loading is illustrated in Figure 5 d). In the absence of a catalyst in 15 % H_2O_2 (w/w), an acid yield of 20 % was achieved due to the generation of radicals from H_2O_2 under microwave (MW) irradiation.[60] Introducing 1 wt. % catalyst increased the acid yield to 44 %, further increasing to 47 % and 56 % for 5 and 10 wt. % catalyst, respectively. However, a decrease in acid yield (36%) is observed with higher catalyst loadings of 15 wt. %. A decrease in mass loss LDPE is also observed, indicating catalyst deactivation under higher catalyst loading.[61]

7.2.3 Conversion of Carboxylic Acid Products to Methane via Anaerobic Digestion

Implementing advanced oxidation processes such as Fenton oxidation is effective for converting a low-value waste stream such as LDPE into a mixture of high-value carboxylic acids. However, the low molecular weight, high water solubility, polarity and amphoteric nature of short-chain acids make separation of complex mixtures through low-cost methods challenging. The costs of advanced separation technologies could potentially outweigh the market value of the individually recovered acids. It is well reported that these short chain carboxylic acids, also referred to as volatile fatty acids (VFAs), such as propionic acid, acetic acid and butyric acid play a crucial role in AD process to yield biogas.[62, 63] In that regard, AD can be used as a way of bioconversion of the complex acid mixture into biogas - primarily composed of methane. This strategy simplifies the product stream and may mitigate potential separation costs. The resulting methane can then be further upgraded via well-established thermochemical routes.[64]

The product mixtures obtained from the WB300 and DG300 catalysts were evaluated for methane production via AD in parallel with the product mixture from a metal-based (Fe-CeO_2) Fenton catalyst reported in a previous study.[7] This comparison aimed to assess the conversion efficiency of the carboxylic acid products to be obtained from metal free biomass-derived catalysts relative to a metal-based catalyst. Details of the batch methane production experiments can be found in the **Supporting Information.** The AD process was conducted over 25 days and ceased when methane production

plateaued. To monitor the consumption of carboxylic acids during AD, periodic aliquots of the mixtures were analysed by HPLC (Figure 6). The acids quantified throughout the process were formic, propionic, acetic, and succinic acid, as these were present in quantifiable concentrations throughout the process.

Across all three systems, two clear metabolic phases were identified. A significant decrease in concentration of succinic, formic and propionic acid and a simultaneous increase in acetic acid concentrations was observed from day 0 to day 5, indicating acetogenesis. During this phase, carboxylic acids are converted to acetic acid via β-oxidation producing acetyl-CoA - a key precursor for acetic acid formation. The steady decline of acetic acid concentration from day 5 to day 25 across all systems is indicative of active acetoclastic methanogenesis as the acetic acid is converted to methane. Samples derived from the WB300 and DG300 catalysts show a sharper increase in acetic acid by day 4 compared to the metal Fe-CeO_2 catalyst. The acid concentration increased by 0.31 g/L (WB300) and 0.39 g/L (DG300), respectively, compared with 0.24 g/L for the Fe-CeO_2 system. This may arise due to metal contamination in the acid mixture, as CeO_2 nanoparticles have previously been reported to inhibit methane production in AD.[65]

While formic acid does not undergo acetogenesis, it plays a crucial role in AD via alternative pathways. Formic acid can be oxidised to CO_2 and H_2, which are then used in hydrogenotrophic methanogenesis to yield biomethane. Some methanogens can also directly convert formate to methane by reduction with H_2 and it can assist electron transfer between microorganisms.[66] From the HPLC results, formic acid is completely consumed in the WB300 and DG300 systems by day 4, while 0.15 g/L formic acid was still detected in the Fe-CeO_2 mixture, further suggesting potential process inhibition in the metal catalysed reaction. The reappearance of formic acid on day 10 in all systems, which is typically associated with acidogenesis, may also suggest a metabolic imbalance or potential process inhibition.[67] Additionally, the acetic-to-propionic acid ratio can be used as an indicator of AD health with values below 1 suggesting inhibited or suboptimal AD process. [60] Interestingly on day 10, the

acetic-to-propionic acid ratio was 0 in the Fe-CeO_2 system, while it was 0.91 in both WB300 and DG300 systems, suggesting that the biochar-catalysed systems showed less process inhibition than the metal-catalysed system.

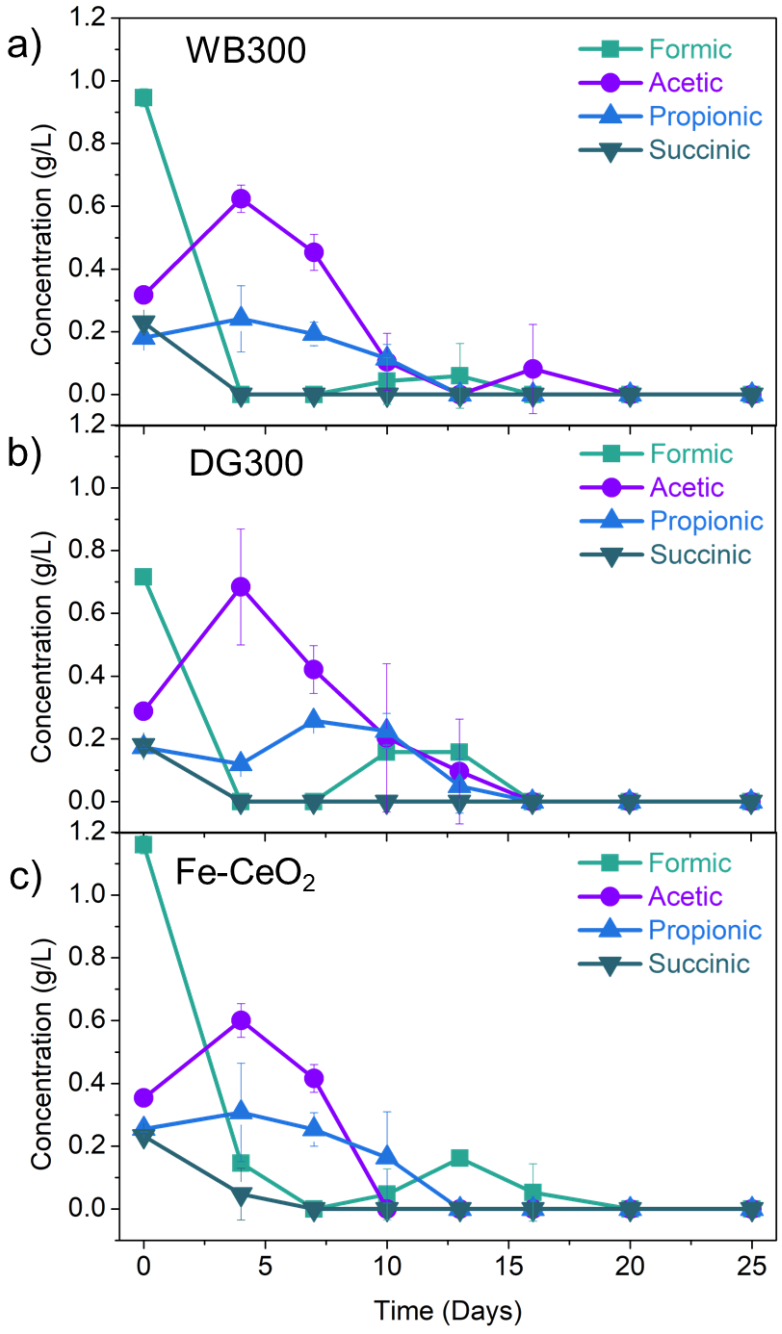


Figure 6: Concentrations of acids in AD systems over 25 days determined by HPLC for a) WB300, b) DG300 and c) Fe-CeO_2.

The corresponding methane production over 25 days is shown in Figure 7. Unreacted LDPE powder was implemented as a control in the AD system, which was inactive for methane production over 25 days. Acid mixtures obtained from WB300, DG300, and Fe-CeO_2 catalysts, all supported progressive methane production, with a gradual increase observed from day 0 to day 16. A clear correlation was observed between the acid yield of LDPE degradation mixtures and the biomethane yield from AD process. The Fe-CeO_2 catalyst, which produced the highest acid yield from LDPE oxidative degradation (71 %), also gave the highest methane yield of 174.7 mL CH_4 / g COD. This was followed by the WB300 catalyst, which yielded 164.2 mL CH_4/g COD from a 56 % acid yield, and the DG300 biochar gave the lowest methane yield of 151.5 mL CH_4/g COD, with a 39 % acid yield. However, these differences are not considered statistically significant ($p < 0.05$), indicating that within experimental variability, all systems produced comparable levels of methane regardless of catalyst type. The biodegradability index (BI), which describes the ratio between the achieved methane yields and the theoretical methane yield (350 mL CH_4/gCOD), was calculated to be 0.6, 0.56, and 0.52 for the Fe-CeO_2, WB300, and DG300 systems, respectively, and reflects moderate biodegradability across all systems. Collectively, the results confirm successful conversion of the acid product mixtures obtained from LDPE degradation to methane using a combined chemical-biochemical approach.

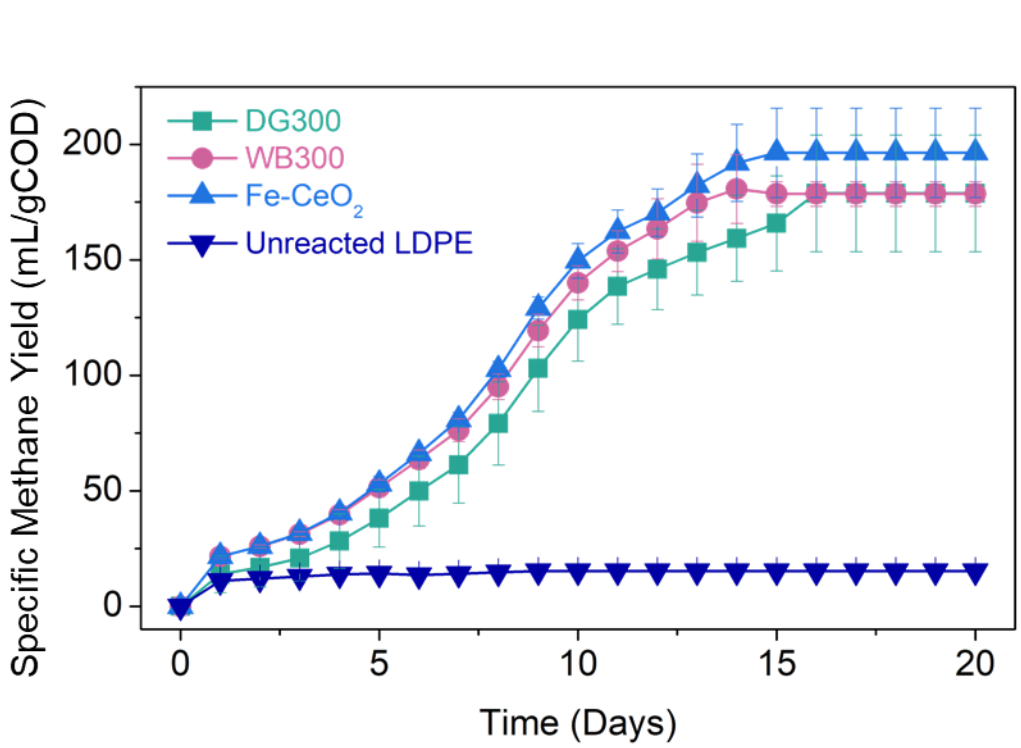


Figure 7: Specific methane production assay curves (mL/g COD) for unreacted LDPE powder control, Fe-CeO_2, WB300, and DG300 during AD of corresponding acid mixtures.

7.2.4 Mass and Energy balance: System Mass and Energy Balances of Integrated LDPE oxidation and Anaerobic Digestion

Mass and energy balances are critical tools for evaluating the real-world viability of catalytic processes within the circular economy. While identifying an effective catalyst is an essential first step, it does not guarantee successful translation to industrial scale. Mass and energy balances help pinpoint inefficiencies and resource bottlenecks across the process chain such as high water or energy demands, thereby guiding where process improvements are needed. In this context, they serve as a bridge between lab-scale catalytic performance and scalable, sustainable system design, ensuring that promising catalysts can be integrated into circular systems both efficiently and economically.

Theoretical analysis of mass and energy balance for the three catalyst systems were calculated based on process flows outlined in Supporting Information Figure S1. The system efficiencies were calculated based on the energy inputs of the system vs. energy generated by the system (see supporting

information for full details). The results for the WB300 system are shown in Figure 8 a) and b), and the mass and energy balance of the DG300 and Fe-CeO_2 systems are shown in the Supporting Information Figure S5. The WB300 system represents an integrated biorefinery system, which incorporates pyrolysis of wood biochar (obtained from whiskey barrels), Fenton-type oxidation of LDPE, and AD of the carboxylic acid mixture to methane. The process efficiencies were calculated relative to the input energy and energy produced from AD and pyrolysis products (where applicable). Among the three systems the WB300 biochar process demonstrated the highest process efficiency of 9 %, which was attributed to moderate methane production and a renewable catalyst source. Nearly all inputs were converted into digestate (21.92 t) with small yields of methane (0.07 t). While LDPE contributes a high energy input in the WB300 system (43,380 MJ), only a small fraction is recovered in usable forms such as biogas (3,622 MJ) and syngas/bio-oil (1,049 MJ), with nearly 46,000 MJ lost through process inefficiencies. The energy balance analysis of all three systems suggests that the majority of energy losses occur during Fenton oxidation, contributing significantly to the overall process inefficiency. To overcome this, the exothermic nature of the Fenton oxidation reaction could be utilised and capturing 50 % of this heat through a heat exchanger could substantially improve energy efficiency raising it to 49 % for the WB300 system. Based on the mass and energy balances, this system could benefit from waste heat recovery, catalyst reuse, and water recirculation to enhance process efficiency.

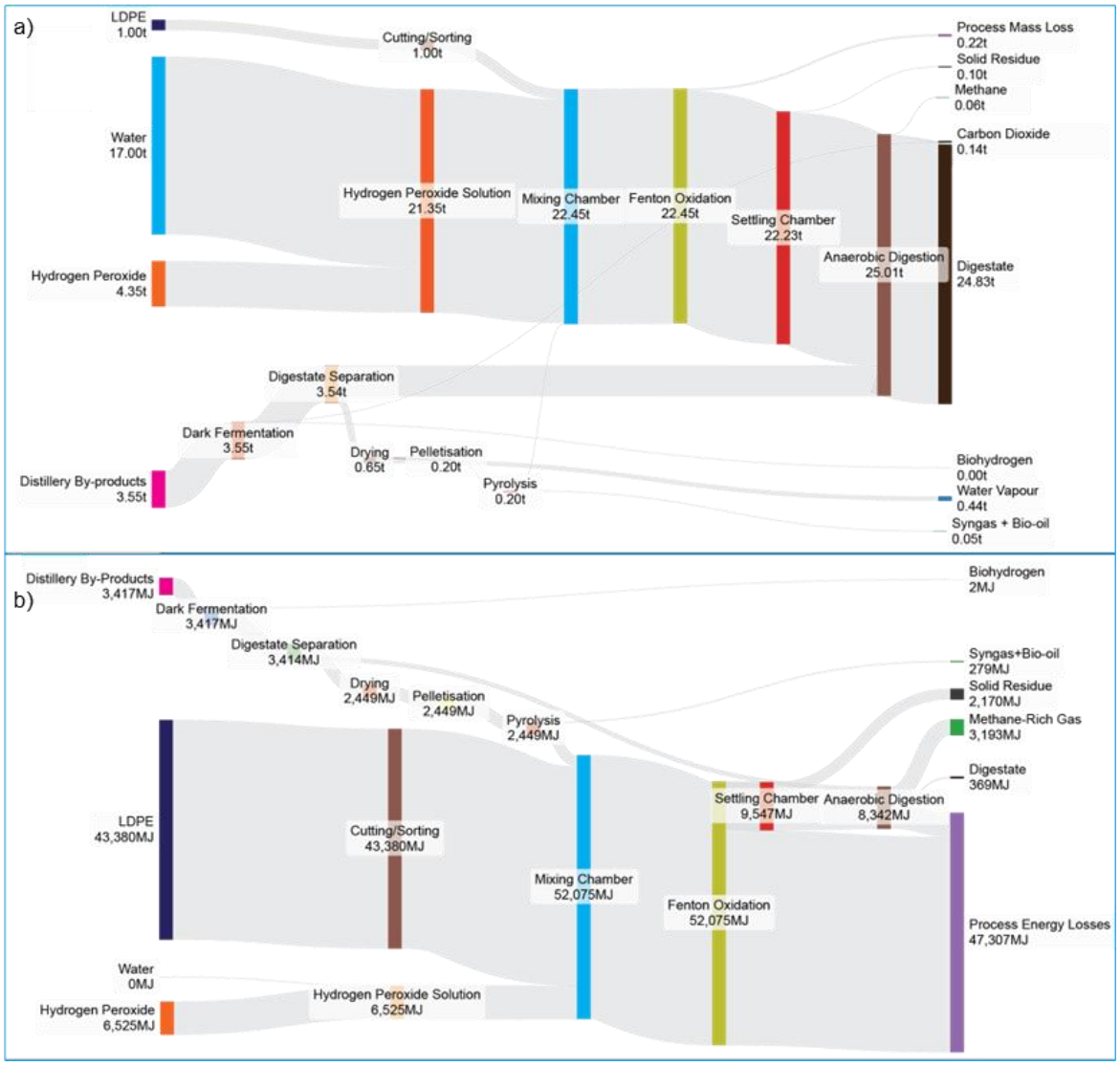


Figure 8: a) Mass balance for the WB300 system, b) energy balance for the WB300 system.

7.3 Conclusions and Future Work

This study demonstrates the successful application of biomass-derived Fenton-type catalysts for metal free oxidative degradation of LDPE and subsequent conversion to methane. The biomass source and pyrolysis temperature significantly influenced the surface chemistry and physical properties of the biochars. The wood-derived biochar catalyst pyrolysed at 300 °C (WB300) exhibited the highest performance attributed to its high oxygen content, sp^2 C and moderate degree of graphitisation, factors that support the formation of dual reaction centres crucial for H_2O_2 activation in metal-free systems. Optimal reaction conditions identified were 10 wt. % catalyst loading and a H_2O_2

concentration of 15 % (w/w), under which the WB300 catalyst achieved an acid yield of 56 %. It is important to note here the variability in the physicochemical properties of biochar arising from its complex and heterogeneous structure. This can pose challenges to reproducibility and limit the robustness of its catalytic performance across studies. AD was effectively employed for conversion of carboxylic acid mixtures to methane. It was found that, irrespective of the catalyst used, methane yields were statistically similar, indicating that biochar-based metal-free catalysts can match the performance of metal-based catalyst in downstream conversion. A mass and energy balance revealed the WB300 catalyst achieved the highest energy efficiency (9 %), with most energy losses attributed to heat generated during the Fenton oxidation step. Theoretical analysis suggests that integrating heat recovery through industrial heat exchangers could elevate the system efficiency to approximately 49%, presenting a promising route for energy integration and renewable energy.

Mass and energy balances also serve a broader role beyond evaluating efficiency as they provide a vital framework for identifying key areas where process improvements would be needed. While a catalyst may show impressive performance at the lab scale, real-world deployment requires understanding resource inputs, waste outputs, and energy dynamics across the entire system. These balances help bridge the gap between catalyst discovery and scalable application, offering practical guidance for aligning catalytic innovation with the goals of the circular economy. This concept in this work is particularly well-suited for integration into industries with high thermal energy demands or residual biomass availability, such as distilleries, breweries, or agri-food processing facilities, where heat recovery systems and circular resource use are already common. While further optimisation is needed, this study highlights a promising circular strategy for converting end-of-life plastics into valuable products using biomass-derived catalysts and integrated bioconversion pathways aligned with established upcycling technologies.

Supporting Information

Materials and chemicals, experimental details including biochar preparation, Fe-CeO_2 preparation, Fenton-type oxidation procedure, HPLC analysis, materials characterisation techniques, AD information including inoculum details and batch biomethane experiments, biodegradability index and energy yield calculations, mass and energy balance calculations, statistical significance, BET analysis, C 1s XPS area contributions table, N1s XPS for WB300 and WB700, LDPE degradation kinetics, mass and energy balance diagrams for DG300 and Fe-CeO_2.

Acknowledgements

We acknowledge Science Foundation Ireland grant number (AMBER Grant No: 12/RC2278_P2) and Irish Research Council under award number GOIPG/2021/932. The authors also wish to acknowledge funding from Taighde Ēireann (Research Ireland) through the MaREI Centre for Energy, Climate and Marine under Grant 12/RC/2302_P2. We thank Bernal Institute University of Limerick for access to XPS facilities, Glantreo for access to BET facilities and Tyndall National Institute for access to SEM and XRD facilities.

7.4 References:

(1) Zhao, X.; Korey, M.; Li, K.; Copenhaver, K.; Tekinalp, H.; Celik, S.; Kalaitzidou, K.; Ruan, R.; Ragauskas, A. J.; Ozcan, S. Plastic waste upcycling toward a circular economy. *Chemical Engineering Journal* **2022**, *428*, 131928. DOI: https://doi.org/10.1016/j.cej.2021.131928.
(2) Thiounn, T.; Smith, R. C. Advances and approaches for chemical recycling of plastic waste. *Journal of Polymer Science* **2020**, *58* (10), 1347-1364. DOI: https://doi.org/10.1002/pol.20190261 (accessed 2024/01/30).
(3) Piovano, A.; Paone, E. The reductive catalytic upcycling of polyolefin plastic waste. *Current Research in Green and Sustainable Chemistry* **2022**, *5*, 100334. DOI: https://doi.org/10.1016/j.crgsc.2022.100334.
(4) Anuar Sharuddin, S. D.; Abnisa, F.; Wan Daud, W. M. A.; Aroua, M. K. A review on pyrolysis of plastic wastes. *Energy Conversion and Management* **2016**, *115*, 308-326. DOI: https://doi.org/10.1016/j.enconman.2016.02.037.
(5) Huang, J.; Veksha, A.; Chan, W. P.; Giannis, A.; Lisak, G. Chemical recycling of plastic waste for sustainable material management: A prospective review on catalysts and processes. *Renewable and Sustainable Energy Reviews* **2022**, *154*, 111866. DOI: https://doi.org/10.1016/j.rser.2021.111866.
(6) Sun, J.; Dong, J.; Gao, L.; Zhao, Y.-Q.; Moon, H.; Scott, S. L. Catalytic Upcycling of Polyolefins. *Chemical Reviews* **2024**, *124* (16), 9457-9579. DOI: 10.1021/acs.chemrev.3c00943.
(7) Breen, R.; Holmes, J. D.; Collins, G. Heterogeneous Fenton-type oxidative degradation of low-density polyethylene to valuable acid products using a nanostructured Fe–CeO2 solid solution catalyst. *Catalysis Science & Technology* **2025**, 10.1039/D4CY01384K. DOI: 10.1039/D4CY01384K.
(8) Chow, C.-F.; Wong, W.-L.; Ho, K. Y.-F.; Chan, C.-S.; Gong, C.-B. Combined Chemical Activation and Fenton Degradation to Convert Waste Polyethylene into High-Value Fine Chemicals. *Chemistry – A European Journal* **2016**, *22* (28), 9513-9518. DOI: https://doi.org/10.1002/chem.201600856 (accessed 2024/01/23).
(9) Ghatge, S.; Yang, Y.; Ko, Y.; Yoon, Y.; Ahn, J.-H.; Kim, J. J.; Hur, H.-G. Degradation of sulfonated polyethylene by a bio-photo-fenton approach using glucose oxidase immobilized on titanium dioxide. *Journal of Hazardous Materials* **2022**, *423*, 127067. DOI: https://doi.org/10.1016/j.jhazmat.2021.127067.
(10) Bäckström, E.; Odelius, K.; Hakkarainen, M. Trash to Treasure: Microwave-Assisted Conversion of Polyethylene to Functional Chemicals. *Industrial & Engineering Chemistry Research* **2017**, *56* (50), 14814-14821. DOI: 10.1021/acs.iecr.7b04091.
(11) Inyang, V. M.; Lokhat, D. Separation of Carboxylic Acids: Conventional and Intensified Processes and Effects of Process Engineering Parameters. In *Valorization of Biomass to Value-Added Commodities: Current Trends, Challenges, and Future Prospects*, Daramola, M. O., Ayeni, A. O. Eds.; Springer International Publishing, 2020; pp 469-505.
(12) Hosseini Koupaie, E.; Dahadha, S.; Bazyar Lakeh, A. A.; Azizi, A.; Elbeshbishy, E. Enzymatic pretreatment of lignocellulosic biomass for enhanced biomethane production-A review. *Journal of Environmental Management* **2019**, *233*, 774-784. DOI: https://doi.org/10.1016/j.jenvman.2018.09.106.
(13) Osman, A. I.; Mehta, N.; Elgarahy, A. M.; Al-Hinai, A.; Al-Muhtaseb, A. a. H.; Rooney, D. W. Conversion of biomass to biofuels and life cycle assessment: a review. *Environmental Chemistry Letters* **2021**, *19* (6), 4075-4118. DOI: 10.1007/s10311-021-01273-0.
(14) Singh, A. K.; Pal, P.; Rathore, S. S.; Sahoo, U. K.; Sarangi, P. K.; Prus, P.; Dziekański, P. Sustainable Utilization of Biowaste Resources for Biogas Production to Meet Rural Bioenergy Requirements. In *Energies*, 2023; Vol. 16.
(15) Alassali, A.; Moon, H.; Picuno, C.; Meyer, R. S. A.; Kuchta, K. Assessment of polyethylene degradation after aging through anaerobic digestion and composting. *Polymer Degradation and Stability* **2018**, *158*, 14-25. DOI: https://doi.org/10.1016/j.polymdegradstab.2018.10.014.
(16) Adachi, A.; El Ouadrhiri, F.; Saleh, E. A. M.; Althomali, R. H.; Kassem, A. F.; Ibtissam, E. M.; Moharam, M. M.; Husain, K.; Eloutassi, N.; Lahkimi, A. Iron-doped catalyst synthesis in heterogeneous

Fenton like process for dye degradation and removal: optimization using response surface methodology. *SN Applied Sciences* **2023**, *5* (12), 342. DOI: 10.1007/s42452-023-05543-0.
(17) Cheng, Y.; Zhang, S.; Wang, Z.; Wang, B.; You, J.; Guo, R.; Zhang, H. Review on spinel ferrites-based materials (MFe2O4) as photo-Fenton catalysts for degradation of organic pollutants. *Separation and Purification Technology* **2023**, *318*, 123971. DOI: https://doi.org/10.1016/j.seppur.2023.123971.
(18) Omar, B. M.; Zyadah, M. A.; Ali, M. Y.; El-Sonbati, M. A. Pre-treatment of composite industrial wastewater by Fenton and electro-Fenton oxidation processes. *Scientific Reports* **2024**, *14* (1), 27906. DOI: 10.1038/s41598-024-78846-w.
(19) Min, X.; Changyong, W.; Yuexi, Z. Advancements in the Fenton Process for Wastewater Treatment. In *Advanced Oxidation Processes*, Ciro, B.-L. Ed.; IntechOpen, 2020; p Ch. 4.
(20) Bule Možar, K.; Miloloža, M.; Martinjak, V.; Radovanović-Perić, F.; Bafti, A.; Ujević Bošnjak, M.; Markić, M.; Bolanča, T.; Cvetnić, M.; Kučić Grgić, D.; et al. Evaluation of Fenton, Photo-Fenton and Fenton-like Processes in Degradation of PE, PP, and PVC Microplastics. In *Water*, 2024; Vol. 16.
(21) Thomas, N.; Dionysiou, D. D.; Pillai, S. C. Heterogeneous Fenton catalysts: A review of recent advances. *J Hazard Mater* **2021**, *404* (Pt B), 124082. DOI: 10.1016/j.jhazmat.2020.124082 From NLM.
(22) Gong, B.; Ku, C.; Yu, H.-Q.; Sit, P. H. L. Predicting the Mechanisms for H2O2 Activation and Phenol Oxidation Catalyzed by Modified Graphene-Based Systems Using Density Functional Theory. *ACS Applied Materials & Interfaces* **2022**, *14* (31), 35682-35693. DOI: 10.1021/acsami.2c08129.
(23) Lyu, L.; Yu, G.; Zhang, L.; Hu, C.; Sun, Y. 4-Phenoxyphenol-Functionalized Reduced Graphene Oxide Nanosheets: A Metal-Free Fenton-Like Catalyst for Pollutant Destruction. *Environmental Science & Technology* **2018**, *52* (2), 747-756. DOI: 10.1021/acs.est.7b04865.
(24) Espinosa, J. C.; Navalón, S.; Primo, A.; Moral, M.; Sanz, J. F.; Álvaro, M.; García, H. Graphenes as Efficient Metal-Free Fenton Catalysts. *Chemistry – A European Journal* **2015**, *21* (34), 11966-11971. DOI: https://doi.org/10.1002/chem.201501533 (accessed 2024/12/09).
(25) Xu, Y.; Bai, H.; Lu, G.; Li, C.; Shi, G. Flexible Graphene Films via the Filtration of Water-Soluble Noncovalent Functionalized Graphene Sheets. *Journal of the American Chemical Society* **2008**, *130* (18), 5856-5857. DOI: 10.1021/ja800745y.
(26) Amalina, F.; Krishnan, S.; Zularisam, A. W.; Nasrullah, M. Recent advancement and applications of biochar technology as a multifunctional component towards sustainable environment. *Environmental Development* **2023**, *46*, 100819. DOI: https://doi.org/10.1016/j.envdev.2023.100819.
(27) Deng, B.; Yuan, X.; Siemann, E.; Wang, S.; Fang, H.; Wang, B.; Gao, Y.; Shad, N.; Liu, X.; Zhang, W.; et al. Feedstock particle size and pyrolysis temperature regulate effects of biochar on soil nitrous oxide and carbon dioxide emissions. *Waste Management* **2021**, *120*, 33-40. DOI: https://doi.org/10.1016/j.wasman.2020.11.015.
(28) Hackula, A.; Ning, X.; Collins, G.; Jackson, S. A.; O'Leary, N. D.; Deng, C.; O'Shea, R.; Murphy, J. D.; Wall, D. M. Investigating the effects of whiskey-barrel derived biochar addition to anaerobic digestion at a distillery: A study on energy yield and system efficiency. *Energy Conversion and Management: X* **2024**, *23*, 100654. DOI: https://doi.org/10.1016/j.ecmx.2024.100654.
(29) Wang, J.; Zhang, Z.; Wu, F.; Sun, W.; Wang, F.; Han, J.; Pan, Y.; Wu, G. Facile fabrication of Fe3O4-Biochar hybrid nanomaterials as catalysts for Photo-Fenton degradation of tetracycline. *Optical Materials* **2023**, *143*, 114156. DOI: https://doi.org/10.1016/j.optmat.2023.114156.
(30) Li, H.-C.; Ji, X.-Y.; Pan, X.-Q.; Liu, C.; Liu, W.-J. Ionothermal Carbonization of Biomass to Construct Fe, N-Doped Biochar with Prominent Activity and Recyclability as Cathodic Catalysts in Heterogeneous Electro-Fenton. *ACS ES&T Engineering* **2021**, *1* (1), 21-31. DOI: 10.1021/acsestengg.0c00001.
(31) Zhu, Y.; Fan, W.; Feng, W.; Wang, Y.; Liu, S.; Dong, Z.; Li, X. Removal of EDTA-Cu(II) from Water Using Synergistic Fenton Reaction-Assisted Adsorption by Nanomanganese Oxide-Modified Biochar: Performance and Mechanistic Analysis. *ACS ES&T Water* **2021**, *1* (5), 1302-1312. DOI: 10.1021/acsestwater.1c00031.
(32) Tu, Y.; Peng, Z.; Huang, J.; Wu, X.; Kong, L.; Liang, Z.; Yang, L.; Lin, Z. Preparation and Characterization of Magnetic Biochar Nanocomposites via a Modified Solvothermal Method and Their

Use as Efficient Heterogeneous Fenton-like Catalysts. *Industrial & Engineering Chemistry Research* **2020**, *59* (5), 1809-1821. DOI: 10.1021/acs.iecr.9b04590.
(33) Tian, W.; Lin, J.; Tian, Z.; Ncube, S.; Zhang, H.; Cortés, E.; Sun, H.; Wang, S. Biomass Native Structure Into Functional Carbon-Based Catalysts for Fenton-Like Reactions. *Advanced Functional Materials* **2025**, *n/a* (n/a), 2508759. DOI: https://doi.org/10.1002/adfm.202508759 (accessed 2025/06/24).
(34) Zhu, C.-h.; Fang, Z.; Su, T.-c.; Li, X.-k.; Liu, Q.-y. Cellulase immobilized on mesoporous biochar synthesized by ionothermal carbonization of cellulose. *Cellulose* **2018**, *25* (4), 2473-2485. DOI: 10.1007/s10570-018-1704-8.
(35) Bin Mobarak, M.; Pinky, N. S.; Mustafi, S.; Chowdhury, F.; Nahar, A.; Akhtar, U. S.; Quddus, M. S.; Yasmin, S.; Alam, M. A. Unveiling the reactor effect: a comprehensive characterization of biochar derived from rubber seed shell via pyrolysis and in-house reactor. *RSC Advances* **2024**, *14* (41), 29848-29859, 10.1039/D4RA05562D. DOI: 10.1039/D4RA05562D.
(36) Liu, Y.; Zhao, X.; Li, J.; Ma, D.; Han, R. Characterization of bio-char from pyrolysis of wheat straw and its evaluation on methylene blue adsorption. *Desalination and Water Treatment* **2012**, *46* (1), 115-123. DOI: https://doi.org/10.1080/19443994.2012.677408.
(37) Sahoo, S. S.; Vijay, V. K.; Chandra, R.; Kumar, H. Production and characterization of biochar produced from slow pyrolysis of pigeon pea stalk and bamboo. *Cleaner Engineering and Technology* **2021**, *3*, 100101. DOI: https://doi.org/10.1016/j.clet.2021.100101.
(38) Maziarka, P.; Wurzer, C.; Arauzo, P. J.; Dieguez-Alonso, A.; Mašek, O.; Ronsse, F. Do you BET on routine? The reliability of N2 physisorption for the quantitative assessment of biochar's surface area. *Chemical Engineering Journal* **2021**, *418*, 129234. DOI: https://doi.org/10.1016/j.cej.2021.129234.
(39) Skic, K.; Adamczuk, A.; Gryta, A.; Boguta, P.; Tóth, T.; Jozefaciuk, G. Surface areas and adsorption energies of biochars estimated from nitrogen and water vapour adsorption isotherms. *Scientific Reports* **2024**, *14* (1), 30362. DOI: 10.1038/s41598-024-81030-9.
(40) Maziarka, P.; Sommersacher, P.; Wang, X.; Kienzl, N.; Retschitzegger, S.; Prins, W.; Hedin, N.; Ronsse, F. Tailoring of the pore structures of wood pyrolysis chars for potential use in energy storage applications. *Applied Energy* **2021**, *286*, 116431. DOI: https://doi.org/10.1016/j.apenergy.2020.116431.
(41) Braida, W. J.; Pignatello, J. J.; Lu, Y.; Ravikovitch, P. I.; Neimark, A. V.; Xing, B. Sorption Hysteresis of Benzene in Charcoal Particles. *Environmental Science & Technology* **2003**, *37* (2), 409-417. DOI: 10.1021/es020660z.
(42) Dong, H.; Zhang, L.; Shao, L.; Wu, Z.; Zhan, P.; Zhou, X.; Chen, J. Versatile Strategy for the Preparation of Woody Biochar with Oxygen-Rich Groups and Enhanced Porosity for Highly Efficient Cr(VI) Removal. *ACS Omega* **2022**, *7* (1), 863-874. DOI: 10.1021/acsomega.1c05506.
(43) Liang, D.; Xie, Q.; Liu, J.; Xie, F.; Liu, D.; Wan, C. Mechanism of the evolution of pore structure during the preparation of activated carbon from Zhundong high-alkali coal based on gas–solid diffusion and activation reactions. *RSC Advances* **2020**, *10* (55), 33566-33575, 10.1039/D0RA06105K. DOI: 10.1039/D0RA06105K.
(44) Kataya, G.; Charif, Z. E.; Badran, A.; Cornu, D.; Bechelany, M.; Hijazi, A.; Sukkariyah, B.; Issa, M. Evaluating the impact of different biochar types on wheat germination. *Scientific Reports* **2024**, *14* (1), 28663. DOI: 10.1038/s41598-024-76765-4.
(45) Chen, Z.; Wang, X.; Xue, B.; Li, W.; Ding, Z.; Yang, X.; Qiu, J.; Wang, Z. Rice husk-based hierarchical porous carbon for high performance supercapacitors: The structure-performance relationship. *Carbon* **2020**, *161*, 432-444. DOI: https://doi.org/10.1016/j.carbon.2020.01.088.
(46) Simões dos Reis, G.; Mayandi Subramaniyam, C.; Cárdenas, A. D.; Larsson, S. H.; Thyrel, M.; Lassi, U.; García-Alvarado, F. Facile Synthesis of Sustainable Activated Biochars with Different Pore Structures as Efficient Additive-Carbon-Free Anodes for Lithium- and Sodium-Ion Batteries. *ACS Omega* **2022**, *7* (46), 42570-42581. DOI: 10.1021/acsomega.2c06054.
(47) Wang, X.; Chen, Z.; Wang, C.; Zhang, L. Ultrahigh and kinetic-favorable adsorption for recycling urea using corncob-derived porous biochar. *Scientific Reports* **2024**, *14* (1), 8131. DOI: 10.1038/s41598-024-58538-1.

(48) Danhassan, U. A.; Zhang, X.; Qi, R.; Ali, M. M.; Sheng, K.; Lin, H. Insight into synthesis and catalytic performance of mesoporous electroactive biochar for aqueous sulfide adsorptive oxidation. *Journal of Environmental Chemical Engineering* **2023**, *11* (5), 110619. DOI: https://doi.org/10.1016/j.jece.2023.110619.
(49) Ilić, M.; Haegel, F.-H.; Lolić, A.; Nedić, Z.; Tosti, T.; Ignjatović, I. S.; Linden, A.; Jablonowski, N. D.; Hartmann, H. Surface functional groups and degree of carbonization of selected chars from different processes and feedstock. *PLOS ONE* **2022**, *17* (11), e0277365. DOI: 10.1371/journal.pone.0277365 (accessed 2025/01/09).
(50) Tomczyk, A.; Sokołowska, Z.; Boguta, P. Biochar physicochemical properties: pyrolysis temperature and feedstock kind effects. *Reviews in Environmental Science and Bio/Technology* **2020**, *19* (1), 191-215. DOI: 10.1007/s11157-020-09523-3.
(51) Dementjev, A. P.; de Graaf, A.; van de Sanden, M. C. M.; Maslakov, K. I.; Naumkin, A. V.; Serov, A. A. X-Ray photoelectron spectroscopy reference data for identification of the C3N4 phase in carbon–nitrogen films. *Diamond and Related Materials* **2000**, *9* (11), 1904-1907. DOI: https://doi.org/10.1016/S0925-9635(00)00345-9.
(52) dos Reis, G. S.; Bergna, D.; Grimm, A.; Lima, E. C.; Hu, T.; Naushad, M.; Lassi, U. Preparation of highly porous nitrogen-doped biochar derived from birch tree wastes with superior dye removal performance. *Colloids and Surfaces A: Physicochemical and Engineering Aspects* **2023**, *669*, 131493. DOI: https://doi.org/10.1016/j.colsurfa.2023.131493.
(53) de Oliveira Paiva, I.; de Morais, E. G.; Jindo, K.; Silva, C. A. Biochar N Content, Pools and Aromaticity as Affected by Feedstock and Pyrolysis Temperature. *Waste and Biomass Valorization* **2024**, *15* (6), 3599-3619. DOI: 10.1007/s12649-023-02415-x.
(54) Ling, R.; Chen, J. P.; Shao, J.; Reinhard, M. Degradation of organic compounds during the corrosion of ZVI by hydrogen peroxide at neutral pH: Kinetics, mechanisms and effect of corrosion promoting and inhibiting ions. *Water Research* **2018**, *134*, 44-53. DOI: https://doi.org/10.1016/j.watres.2018.01.065.
(55) Deng, Y.; Rosario-Muniz, E.; Ma, X. Effects of inorganic anions on Fenton oxidation of organic species in landfill leachate. *Waste Management & Research* **2012**, *30* (1), 12-19. DOI: 10.1177/0734242X10378185 (accessed 2025/07/22).
(56) Ratanatamskul, C.; Chintitanun, S.; Masomboon, N.; Lu, M.-C. Inhibitory effect of inorganic ions on nitrobenzene oxidation by fluidized-bed Fenton process. *Journal of Molecular Catalysis A: Chemical* **2010**, *331* (1), 101-105. DOI: https://doi.org/10.1016/j.molcata.2010.08.007.
(57) Siedlecka, E. M.; Więckowska, A.; Stepnowski, P. Influence of inorganic ions on MTBE degradation by Fenton's reagent. *Journal of Hazardous Materials* **2007**, *147* (1), 497-502. DOI: https://doi.org/10.1016/j.jhazmat.2007.01.044.
(58) Quan, X.; Zhang, Y.; Chen, S.; Zhao, Y.; Yang, F. Generation of hydroxyl radical in aqueous solution by microwave energy using activated carbon as catalyst and its potential in removal of persistent organic substances. *Journal of Molecular Catalysis A: Chemical* **2007**, *263* (1), 216-222. DOI: https://doi.org/10.1016/j.molcata.2006.08.079.
(59) Nguyen, V. S.; Chang, Y.; Phillips, E. V.; DeWitt, J. A.; Sievers, C. Mechanocatalytic Oxidative Cracking of Poly(ethylene) Via a Heterogeneous Fenton Process. *ACS Sustainable Chemistry & Engineering* **2023**, *11* (20), 7617-7623. DOI: 10.1021/acssuschemeng.3c01054.
(60) Zhao, D.; Cheng, J.; Hoffmann, M. R. Kinetics of microwave-enhanced oxidation of phenol by hydrogen peroxide. *Frontiers of Environmental Science & Engineering in China* **2011**, *5* (1), 57-64. DOI: 10.1007/s11783-010-0251-9.
(61) Argyle, M. D.; Bartholomew, C. H. Heterogeneous Catalyst Deactivation and Regeneration: A Review. In *Catalysts*, 2015; Vol. 5, pp 145-269.
(62) Magdalena, J. A.; Greses, S.; González-Fernández, C. Impact of Organic Loading Rate in Volatile Fatty Acids Production and Population Dynamics Using Microalgae Biomass as Substrate. *Scientific Reports* **2019**, *9* (1), 18374. DOI: 10.1038/s41598-019-54914-4.

(63) Hackula, A.; O'Shea, R.; Murphy, J. D.; Wall, D. M. Developing distillery biorefineries through dark fermentation of whiskey production by-products: the effect of organic loading rate on decarbonisation pathways. *Energy Conversion and Management* **2024**, *301*, 118064. DOI: https://doi.org/10.1016/j.enconman.2024.118064.
(64) Tsapekos, P.; Khoshnevisan, B.; Alvarado-Morales, M.; Zhu, X.; Pan, J.; Tian, H.; Angelidaki, I. Upcycling the anaerobic digestion streams in a bioeconomy approach: A review. *Renewable and Sustainable Energy Reviews* **2021**, *151*, 111635. DOI: https://doi.org/10.1016/j.rser.2021.111635.
(65) García, A.; Delgado, L.; Torà, J. A.; Casals, E.; González, E.; Puntes, V.; Font, X.; Carrera, J.; Sánchez, A. Effect of cerium dioxide, titanium dioxide, silver, and gold nanoparticles on the activity of microbial communities intended in wastewater treatment. *Journal of Hazardous Materials* **2012**, *199-200*, 64-72. DOI: https://doi.org/10.1016/j.jhazmat.2011.10.057.
(66) Thiele Jurgen, H.; Zeikus, J. G. Control of Interspecies Electron Flow during Anaerobic Digestion: Significance of Formate Transfer versus Hydrogen Transfer during Syntrophic Methanogenesis in Flocs. *Applied and Environmental Microbiology* **1988**, *54* (1), 20-29. DOI: 10.1128/aem.54.1.20-29.1988 (accessed 2025/07/23).
(67) Drosg, B. *Process monitoring in biogas plants*; IEA bioenergy Paris, France, 2013.

7.5 Appendix I: Supporting Information

Combined Fenton-type Oxidation and Anaerobic Digestion of Polyethylene to Methane Using Biochar-Derived Catalysts

***Breen, R**.; Hackula, A.; Holmes, J. D.; Wall, D. M.; Collins, G. Combined Fenton-type Oxidation and Anaerobic Digestion of Polyethylene to Methane Using Biochar Catalysts. ACS Sustainable Chemistry and Engineering (in review).*

Materials and Chemicals

Hydrogen peroxide (30%), iron (III) chloride ($FeCl_3.4H_2O$) and cerium (IV) sulphate ($Ce(SO_4)_2$) were purchased from Sigma Aldrich. LDPE powder (500 um), with a density of 0.91-0.96 gml^{-1} was purchased from Fischer Ireland.

Methods

Whiskey Barrel Biochar

Recycled whiskey barrels were processed into sawdust, dried at 105 °C for 24 hours and filtered with a 2 mm sieve. A Nabertherm R50/250/12 tube furnace was used to pyrolyse the material for 1 hour at 300 °C and 700 °C in a nitrogen atmosphere (>99.998% Nitrogen) at a heating ramp up rate of 10 °C/min. After pyrolysis, the biochar was allowed to cool to room temperature, ground with a mortar and pestle, and sieved through a 0.5mm mesh. The biochar was placed in zip-lock bags and stored in a desiccator prior to use. The biochar produced was termed WB300 and WB700.[1]

Digestate Biochar

The digestate biochar was produced from a laboratory scale dark fermenter processing distillery by-products[2]. The digestate solid fraction was isolated using a cotton muslin cloth sourced from a local supplier. The solid fraction was subsequently dried for 24 hours at 105 °C. After drying, the digestate was blended with a kitchen blender and filtered with a 2 mm sieve. The dried digestate was stored in a desiccator prior to pyrolysis. The methodology used to produce the digestate biochar was identical

to the production of the whiskey barrel biochar[1]. Briefly, the Nabertherm R50/250/12 tube furnace was used to pyrolyse the digestate for 1 hour at 300 °C and 700 °C in a nitrogen atmosphere (>99.998% Nitrogen) at a heating ramp up rate of 10 °C/min. After pyrolysis, the biochar was allowed to cool to room temperature, ground with a mortar and pestle, and sieved through a 0.5mm mesh. The biochar was placed in zip-lock bags and stored in a desiccator prior to use. The biochar produced was termed DG300 and DG700.

Fe-CeO_2 Reference Synthesis

A solution of 0.755 g $FeCl_3$ in 25 mL DI H_2O and 1.933 g $Ce(SO_4)_2.4H_2O$ in 25 mL DI H_2O were combined to form a 1:1 molar ratio of Fe:Ce and stirred at room temperature for 10 minutes before the pH was adjusted to 12 using 1 M NaOH solution and a red/brown precipitate appeared. The mixture was refluxed for 2 h at 100 °C under N_2 with stirring. The resulting particles were collected by suction filtration and dried in an oven at 75 °C overnight. The solid was then calcinated at 450 °C under air for 4h.[3]

Oxidative Degradation of LDPE to Carboxylic Acids:

0.5 g LDPE, catalyst with loadings ranging from 1 – 15 wt. % and 10 mL of H_2O_2 solution with concentration ranging from 5 - 15 % (w/w) were added to a Milestone Flexiwave high pressure SK-15 Teflon vessel along with a stir bar. For a 15 % H_2O_2 solution, 5 mL of Millipore H_2O and 5 mL 30 % (w/w) H_2O_2 were added to the vessel. The H_2O_2 was added last to minimise peroxide degradation prior to the reaction. Typical reaction conditions were a 10 min ramp time, 3 h hold at 180 °C, stir speed 1800 rpm using a crosshair stir bar, and 1200 W upper power limit (reactions only typically reached ~300 W). Once the reaction was complete and had cooled, it was Buchner filtered to separate the catalyst and any unreacted LDPE from the product mixture. The mass loss of LDPE was calculated by Equation 1.

$$Mass\ Loss\ LDPE = \frac{W_0 - W_1}{W_0}\ x\ 100\ \%$$ **Eqn.1**

Where W_0 is the initial weight of LDPE added to the reaction and W_1 is the weight of unreacted LDPE after the reaction. The product mixture was characterised by HPLC.

The kinetics of the LDPE degradation reaction were approximated using a simplified pseudo-first order fit and was derived according to the Equation 2.

$$\frac{d[X]}{dt} = -k[X] \quad \textbf{Eqn.2}$$

Where X is the mass of LDPE at time t and k is the pseudo first-order rate constant. Integrating the equation between time $t = 0$ and corresponding masses $[X]_0$ and $[X]_t$, yields equation 3:

$$\ln\left(\frac{[X]}{[X]_0}\right) = -kt \quad \textbf{Eqn.3}$$

This linear form allows for an approximation of the rate constant k to be obtained from the slope of the plot of $\ln\left([X]/[X]_0\right)$ versus time.

HPLC Analysis of Products

The products were analysed as per our previous work.[3] The product mixture was analysed using an Agilent 1200 HPLC coupled to a UV detector (210 nm). 500 uL of product mixture was added to 500 uL of mobile phase to give a dilution factor of 2. The column used was an Agilent Hi-Plex H (300 x 7.7 mm) size exclusion column. The mobile phase was 2.5 mM sulfuric acid at a flow rate of 0.5 mL/min and the temperature was set to 50 °C, following Bäckström et al.'s method and the column specifications.[4] The concentration of each product present in the sample was then calculated against calibration curves that were made by standards of carboxylic acids: succinic, formic, glutaric, acetic, adipic, propionic, butyric and pimelic acid. The yield was calculated relative to the initial weight of LDPE as shown below.

$$Mass\ of\ end\ product\ (g) = Conc\ of\ end\ product\ (g/L)\ x\ reaction\ volume\ (L)$$ **Eqn. 4**

$$Yield\ of\ Organic\ Products\ (\%) = \frac{Mass\ of\ end\ products\ (g)}{Mass\ of\ starting\ material\ (g)}\ x\ 100\ \%$$ **Eqn. 5**

Materials Characterisation:

Standard APHA 2540G protocols were used to attain the total solids and volatiles solids content of the materials[5]. The COD concentrations were measured using Reagecon COD cuvette vials (420721) and a spectrometer (Hach Lange DR 3900). The pH was attained using the Mettler Toledo™ F20 pH meter.

Scanning electron microscopy (SEM) and Energy Dispersive X-ray Spectroscopy (EDS) mapping was performed on a Zeiss Supra 40 high resolution SEM at an accelerating voltage of 5 kV.

The sorption analyses were performed on a Micromeritics Tristar II surface area and porosity analyser. Prior to analysis, each sample was de-gassed for three hours at 400°C and measurements were performed at -169.15°C (77 K). The surface area was determined using the BET (Brunauer-Emmett Teller) method. The pore volume, pore diameter and pore size distribution were determined using the BJH (Barrett-Joyner-Halenda) method.[6]

X-ray Diffraction (XRD) was carried out on a PANalytical X'Pert PRO with Cu Kα radiation and a constant step of 0.0098° 2θ and a counting time of 149.97 seconds per step.

Raman spectroscopy was performed using an Oceanview InVia Raman Spectrometer using a 25 mW Ar-ion laser under 532 nm excitation. The beam was focused onto the samples using a 50x objective lens and spectra were collected using a RenCam CCD camera.

X-ray Photoelectron Spectroscopy (XPS) was carried out using a KRATOS ACIS 165 monochromatised X-ray photoelectron spectrometer equipped with an Al Kα (hv = 1486.6 eV) X-ray source. Spectra were collected at a take-off angle of 90 ° and all spectra were referenced to the C 1s peak at 284.8 eV.

Anaerobic Digestion Information and Techniques:

Table S1: Compositional characteristics of materials (APHA 2540G)

	LDPE	**DG300**	**WB300**
Ash (%TS)	~0	10.8	<1
Volatile Solids (%TS)	99.9	88.5	
C (%TS)	86.0	67.1	60
H (%TS)	14.0	3.5	4
N (%TS)	~0	~0	~0
O (%TS)	~0	29.4	36
Specific surface area (m^2/ g)		0.01	0.481
Pore volume (cm^3/ g)		~0	~0
Higher heating value (MJ/ kgTS)		22.4	19.5
Lower heating value (MJ/ kgTS)		20.9	18.4

Where: [a] Biochar yield = total mass of biochar per total solid mass of whiskey barrel added

Inoculum for Anaerobic Digestion Experiments

Cattle slurry sourced from a local farm was used as inoculum for the batch experiments. The inoculum was sieved with a 5 mm mesh to remove any material from incomplete digestion and other solid particles. The inoculum was allowed to degas for 35 days in a laboratory scale stirred reactor at mesophilic temperatures. To acclimatise the feedstock to the new substrate, 1 g COD / $L_{reactor}$ was fed in batch mode with the feedstock (processed plastic liquid fraction) for 15 days. The dry and volatile solids of the inoculum were 1.85% and 1.14% on a wet weight basis.

Batch Biomethane Experiments

The biochemical methane potential batch experiment of the processed plastic was utilised to evaluate the biomethane production of the liquid fraction of the processed LDPE. The batch assays were operated with an inoculum-to-substate ratio of 2:1 on a volatile solid (VS) to chemical oxygen demand (COD) basis[7].

6 groups were established: Group 1-3 correspond to the Fenton oxidation of the LDPE using digestate biochar, whiskey barrel biochar, and Fe-CeO_2 as catalysts, respectively. Group 4 corresponds with unprocessed LDPE. Group 5 used Cellulose (1.66 g) as a substrate, which served as a positive control to evaluate the activity of the inoculum. A blank group (Group 6), consisting of inoculum only, was used to remove any residual gasses from the inoculum. Each group was run in triplicate. For each assay, 200 ml of inoculum was added, along with the required sample volume. To accommodate for the different COD, the volume of the BMPs was adjusted to 300ml with deionised water[8]. The pH of the BMP assays was adjusted to 7.5 with 6M sodium hydroxide and purged with nitrogen sourced from BOC (Nitrogen (Oxygen Free), Part Number: 44-W; concentration: >99.998% nitrogen) before experiments[9]. Anaerobic conditions were achieved by purging the assays with nitrogen. The experiments were conducted on the Bioprocess Automatic Bioprocess Control ™ AMPRS II system under mesophilic conditions (37±1 °C). The experiments took 25 days to complete.

Biodegradability Index and Substrate Energy Yield Calculation

The biodegradability index (BI) describes the ratio between the achieved experimental specific biomethane yield (BMP) and the theoretical methane yield. The biodegradability index also encompasses the activity factor of the inoculum.

$$BI = \frac{SMY_{actual}}{SMY_{theoretical} \times AF}$$

Where: SMY_{actual} is the experimental specific methane yield (mL CH_4/ g COD); $SMY_{theoretical}$ is the theoretical methane yield, which is 350 mL CH_4/ g COD; AF is the activity factor of the inoculum taken from the result of the cellulose group (%).

The energy yields were calculated by multiplying the biomethane yield with the respective lower heating value (LHV) of methane. The LHV of methane (CH_4) was assumed to be 50 MJ/ kg CH_4 at standard temperature and pressure (STP). The theoretical energy content (MJ / kg TS) of LDPE, which is a hydrocarbon, was estimated using the following formula[10]:

$$\mathrm{HHV_{LDPE}} = 0.303(\mathrm{C}) + 1.423\ (H)$$

Where: HHV_{LDPE} is the higher heating value (MJ/ kgTS). C and H are the total solid (TS) percentage of carbon and hydrogen, respectively.

Mass and Energy Balance: Preliminary System Mass and Energy Balances of Integrated Fenton Oxidation and Anaerobic Digestion

A black box model approach was adopted using the known input-output relationships and assumptions from the literature. To maintain a clearer focus on material flows and intrinsic process yields, the energy analysis neglects energy inputs for thermal energy (heat), and electricity. To account for the different catalyst sub-processes, three integrated systems were evaluated.

System 1 – Digestate Biochar Catalyst (DG300) System (Figure S1 A) represents an integrated biorefinery system, which incorporates dark fermentation for digestate and hydrolysate production, pyrolysis, Fenton oxidation, and anaerobic digestion. The energy inputs considered for this system were the distillery by-products, LDPE, and the hydrogen peroxide solution.

System 2 – Whiskey Barrel Biochar Catalyst (WB300) System (Figure S1 B) represents an integrated biorefinery system, which incorporates pyrolysis of whiskey barrels, Fenton oxidation, and anaerobic digestion. The energy inputs for this system were the whiskey barrels, LDPE, and the hydrogen peroxide solution.

System 3 – Metal Catalyst System (Fe-CeO_2) (Figure S1 C) represents a system which incorporates Fenton oxidation and anaerobic digestion. The energy inputs for this system were the LDPE, and the hydrogen peroxide solution. The metal catalyst serves as a catalyst and does not combust like biochar or traditional fuels, as such the energy contribution was neglected for System 3.

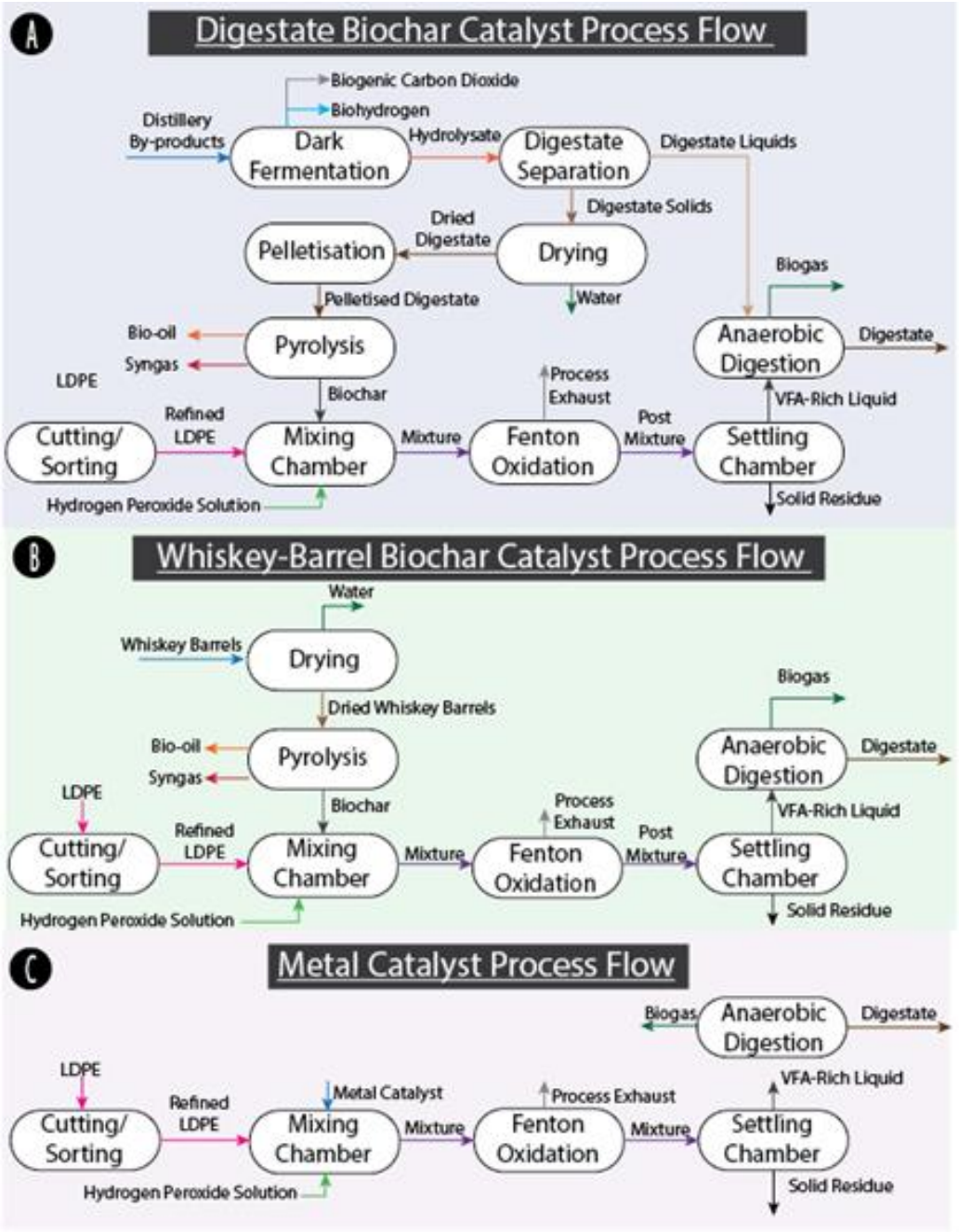


Figure S1: Process flow of an integrated anaerobic digestion and Fenton oxidation process using digestate biochar (A), whiskey barrels biochar (B) and Fe-CeO_2 (C) as a catalyst (System 1).

The assumptions for the mass and energy balance were made for all the systems and adapted from a prior study.[1] The system efficiency of the systems were measure using the following equation:

$$h_{eff} = \frac{Q_{out}}{Q_{in}} = \frac{Q_{biogas} + Q_{syngas\&bio-oil}}{Q_{in_{LDPE}} + Q_{in_{H_2O_2}} + Q_{whiskey\ barrels} + Q_{DF_{feedstock}}} \quad \textbf{Eqn. 6}$$

Where: h_{eff}= the system energy efficiency of the system; Q_{out} = the energy generated by the system; Q_{in} = the energy inputs of the system; Q_{biogas} = the energy produced from biogas generated in anaerobic digestion and dark fermentation (for System 1); $Q_{syngas\&bio-oil}$ = the energy of the syngas and bio-oil generated from pyrolysis; $Q_{in_{LDPE}}$ = energy of LDPE; $Q_{whiskey\ barrels}$= energy of the whiskey barrel (for System 2); $Q_{in_{H_2O_2}}$= energy of the hydrogen peroxide.

Statistical Significance

The built-in Microsoft Excel data analysis Tool-Pak feature was used to evaluate the statistical significance (one-way analysis of variance) of the data. Results less than 0.05 ($p<0.05$) were deemed to be statistically significant.

Supporting Figures

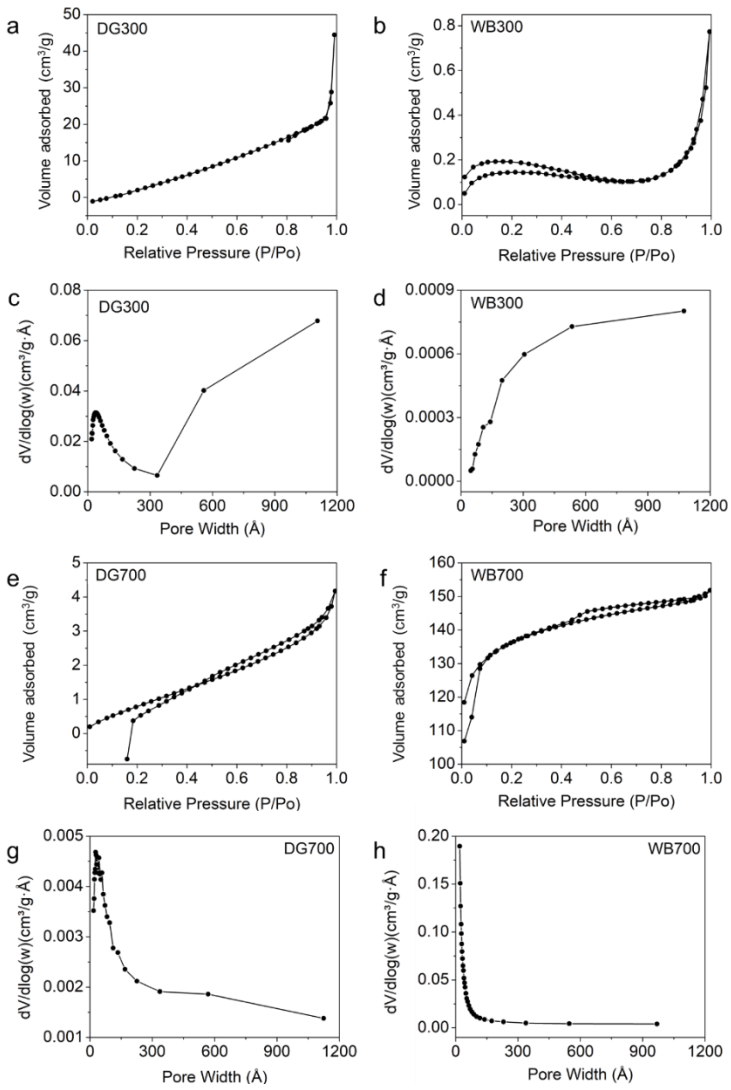


Figure S2: a) and b) Pore distribution curves for Dg700 and WB700 samples, respectively, N_2 sorption isotherm with pore distribution curve inset for c) DG300 and d) WB300.

Table S2: Relative contributions of surface functionalities calculated from peak area from C 1s spectra using *CASA XPS* software.

	DG300	**DG700**	**WB300**	**WB700**
Component	***% (Peak Area)***	***% (Peak Area)***	***% (Peak Area)***	***% (Peak Area)***
C=C	46.25	39.90	57.16	65.98
C-C	27.54	33.74	5.82	6.43
C-O	11.16	12.80	17.44	10.45
C=O	11.13	9.25	11.59	9.41
O-C=O	3.91	4.31	6.04	5.35

π-π*	-	-	1.94	2.37
C/O*	2.81	2.79	1.70	2.63

**Sum of C-C and C=C divided by sum of C-O, C=O, O-C=O and π-π*.*

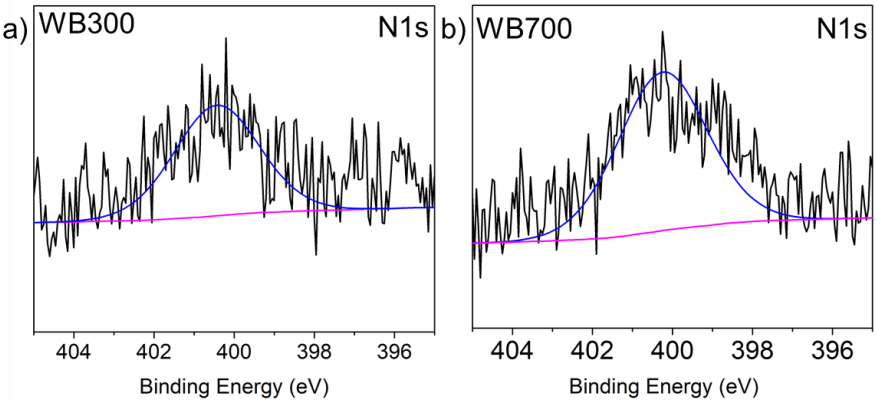


Figure S3: N1s for WB300 and WB700 samples.

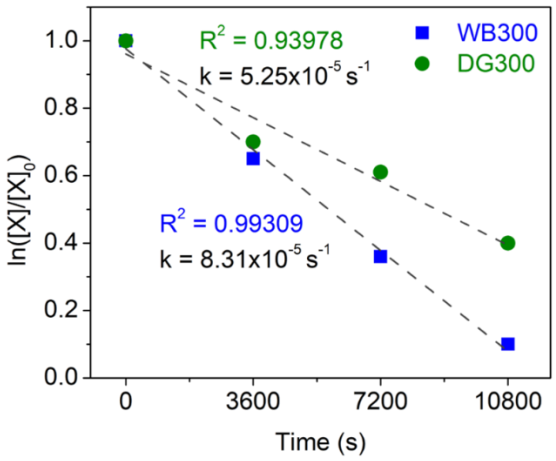


Figure S4: Pseudo first-order fit for WB300 and DG300 catalysts, where X = mass at time *t* and X_0 = initial mass LDPE (0.5 g).

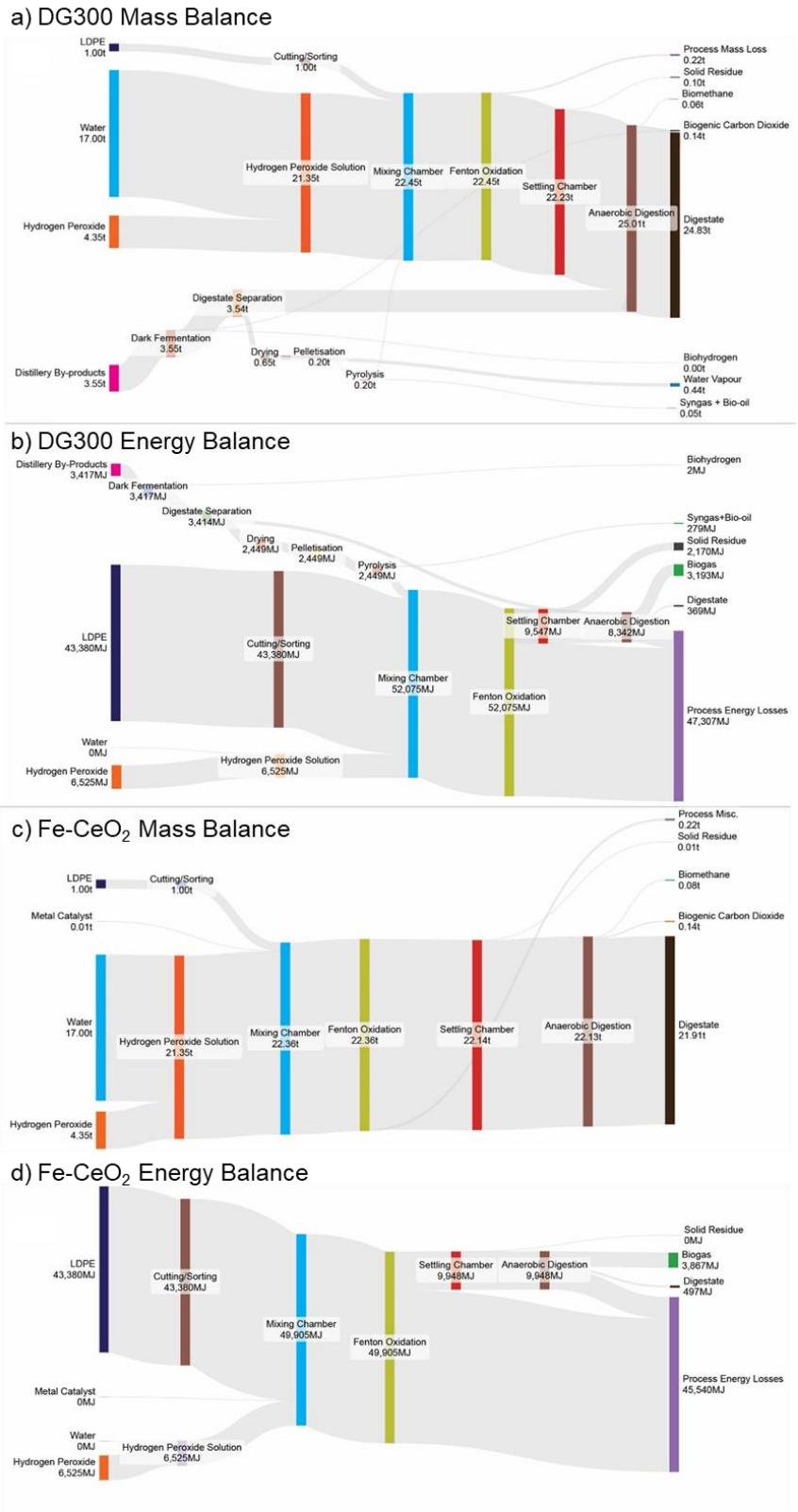


Figure S5: a) Mass and b) energy balance diagrams for the DG300 system, c) mass and d) energy balance diagrams for the Fe-CeO_2 system.

References:

(1) Hackula, A.; Ning, X.; Collins, G.; Jackson, S. A.; O'Leary, N. D.; Deng, C.; O'Shea, R.; Murphy, J. D.; Wall, D. M. Investigating the effects of whiskey-barrel derived biochar addition to anaerobic digestion at a distillery: A study on energy yield and system efficiency. *Energy Conversion and Management: X* **2024**, *23*, 100654. DOI: https://doi.org/10.1016/j.ecmx.2024.100654.
(2) Hackula, A.; O'Shea, R.; Murphy, J. D.; Wall, D. M. Developing distillery biorefineries through dark fermentation of whiskey production by-products: the effect of organic loading rate on decarbonisation pathways. *Energy Conversion and Management* **2024**, *301*, 118064. DOI: https://doi.org/10.1016/j.enconman.2024.118064.
(3) Breen, R.; Holmes, J. D.; Collins, G. Heterogeneous Fenton-type oxidative degradation of low-density polyethylene to valuable acid products using a nanostructured Fe–CeO2 solid solution catalyst. *Catalysis Science & Technology* **2025**, 10.1039/D4CY01384K. DOI: 10.1039/D4CY01384K.
(4) Bäckström, E.; Odelius, K.; Hakkarainen, M. Trash to Treasure: Microwave-Assisted Conversion of Polyethylene to Functional Chemicals. *Industrial & Engineering Chemistry Research* **2017**, *56* (50), 14814-14821. DOI: 10.1021/acs.iecr.7b04091.
(5) William. C. Lipps, E. B. B.-H., & T. E. Baxter,. *Standard Methods for the Examination of Water and WastewaterTM*. American Public Health Association, American Water Works Association, and Water Environment Federation. , 2022. https://connect.wef.org/s/store#/store/browse/detail/a2n1S000000wznrQAA (accessed.
(6) Brunauer, S.; Emmett, P. H.; Teller, E. Adsorption of Gases in Multimolecular Layers. *Journal of the American Chemical Society* **1938**, *60* (2), 309-319. DOI: 10.1021/ja01269a023.
(7) Johannesson, G. H.; Crolla, A.; Lauzon, J. D.; Gilroyed, B. H. Estimation of biogas co-production potential from liquid dairy manure, dissolved air flotation waste (DAF) and dry poultry manure using biochemical methane potential (BMP) assay. *Biocatalysis and Agricultural Biotechnology* **2020**, *25*, 101605. DOI: https://doi.org/10.1016/j.bcab.2020.101605.
(8) Deng, C.; Lin, R.; Kang, X.; Wu, B.; Wall, D.; Murphy, J. D. Improvement in biohydrogen and volatile fatty acid production from seaweed through addition of conductive carbon materials depends on the properties of the conductive materials. *Energy* **2022**, *239*, 122188. DOI: https://doi.org/10.1016/j.energy.2021.122188.
(9) Kang, X.; Lin, R.; Wu, B.; Li, L.; Deng, C.; Rajendran, K.; Sun, Y.; O'Shea, R.; Murphy, J. D. Towards green whiskey production: Anaerobic digestion of distillery by-products and the effects of pretreatment. *Journal of Cleaner Production* **2022**, *357*, 131844. DOI: https://doi.org/10.1016/j.jclepro.2022.131844.
(10) Demirbas, A.; Ak, N.; Aslan, A.; Sen, N. Calculation of higher heating values of hydrocarbon compounds and fatty acids. *Petroleum Science and Technology* **2018**, *36* (11), 712-717. DOI: 10.1080/10916466.2018.1443126.

7.6 Appendix II:

A Collaborative Co-Curricular Undergraduate Research Experience on Sustainable Materials: Analysis of Biochar using the Boehm Titration and Spectroscopic Techniques

Rachel Breen[1,2], Conor Goggin[1], Justin Holmes[1,2], Gillian Collins[1,2*]

[1] School of Chemistry, University College Cork, Cork, T12 YN60, Ireland.

[2] AMBER Centre, Environmental Research Institute, University College Cork, Cork, T23 XE10, Ireland.

Publication: ***Breen, R**.; Goggin, C.; J.; Holmes, J. D.; Collins, G. A Collaborative Cocurricular Undergraduate Research Experience on Sustainable Materials: Analysis of Biochar Using the Boehm Titration and Spectroscopic Techniques. ACS J. Chem. Educ. 2025, 102, 3, 1323–1332 DOI: 10.1021/acs.jchemed.4c01110*

Abstract

The use of renewable feedstocks such as biomass aligns with global priorities such as sustainability and climate change. Integrating these materials into experiments helps students understand the real-world relevance of chemistry in addressing environmental challenges. Here, we show the use of biochar as a renewable feedstock provides an inquiry-based laboratory activity that gives students the opportunity to engage in an authentic investigative process. This activity describes a co-curricular summer workshop carried out with undergraduate students who had no prior research experience. The activity combined the Boehm titration as a chemical method for the analysis of biochar coupled with spectroscopic techniques. The workshop was designed to be collaborative in nature where students collectively contributed to the overall experimental results and discussion. The motivation for the activity stems from a student undertaking a longer Undergraduate Research Experience (URE) in the form of summer research placement and based on this work designing a research experience workshop that could be rolled out to benefit a larger number of students. We believe this approach of

using longer or individual UREs to develop research-focused initiatives could be readily adopted to other UREs to promote and develop research skills.



TOC

7.6.1 Introduction

Chemistry laboratory experiments remain at the core of many undergraduate chemistry programs, but typical teaching practices can result in students learning disconnected pieces of knowledge, lacking context to the relevance of chemistry to everyday life.[1, 2] The acquisition of knowledge through discrete facts makes it difficult for students to understand and interpret complex chemical systems and their properties. For example, analytical techniques are often taught as individual topics and while this is important for gaining specific knowledge, students often lack training in how to correlate and analyse multiple data sets collated from different analytical techniques.[3, 4]

Standard practical laboratories can represent an expository learning environment with predetermined and specified outcomes where students simply follow a procedure in a lab manual, favouring hands-on rather than minds-on learning.[5] Laboratory practicals tend to follow traditional branches of inorganic, organic, physical and analytical chemistry which can lead to compartmentalising knowledge and techniques to specific subdisciplines of chemistry.[6, 7] In contrast, nearly all aspects of chemistry research involve the incorporation of multiple techniques and methodologies. Confinement to traditional sub-disciplines is a fading concept, especially through the lens of sustainable and green chemistry where a deeper, systems-thinking approach is required.[8-10]

The benefit of Undergraduate Research Experiences (UREs) as active- and inquiry-based pedagogies are well recognised in providing enhanced student learning experiences and increased student success, through gaining technical skills, critical thinking and personal skills such as communication.[11, 12] It can further impact on student retentions, career decisions and promote the uptake of students pursuing a PhD.[13-15] While students at the latter stage of their degree programme usually engage in a course-based undergraduate research experience (CURE),[16-18] such as a research-based project as part of the curriculum, students earlier in their degree typically have a limited understanding and little to no experience of the research process.[19] Internship-style immersive UREs where undergraduate students spend several weeks working within a research group, such as summer research placements, provide a formative experience at undergraduate level.[20] Students typically benefit from one-to-one interaction with a PhD or postdoctoral researcher and exposure to an interdisciplinary, collaborative learning experience that is very different from traditional undergraduate practical laboratory teaching. However, these schemes usually involve a small number of undergraduate students working with individual faculty members within their laboratories. Therefore, the development of initiatives such as summer co-curricular activities to expose a greater number of undergraduate students to the research process earlier in their undergraduate career has several benefits to student learning and builds student research skills.[21, 22, 23, 24]

7.6.2 Motivation and Objectives of Activity

The motivation for this activity was underpinned by an undergraduate student conducting an eight-week URE in the form of a summer research internship. The question to be addressed was: How can an individual URE be redesigned to benefit a larger undergraduate audience? To address this, the objective was to design a research-focused activity in the form of a research-focused workshop, involving a collaborative research experiment, where results were gathered collectively. The activity was carried out over the summer (three weeks prior to the semester starting) and involved second- and third-year undergraduates of a four-year undergraduate program who had no prior experience of

research-based laboratory activities. The workshop was an optional, non-graded co-curricular activity. The workshop was advertised by email to undergraduate students as an optional research experience workshop on sustainable chemistry and materials. The following description was provided to the students: 'Participants will engage in experimental activities and analysis, discussions, and collaborative tasks related to sustainable materials. It offers a great opportunity to engage in scientific research and get an insight into what chemistry research is really like'. There were ten undergraduate participants, and the instructors of the activity were the undergraduate student undertaking the summer URE and a doctoral student. The activity was overseen by a faculty member. The activity duration was 2.5 hours however, 3 hours was allowed overall for the workshop.

7.6.3 Experimental Focus and Design

Surface chemistry is a complex and nuanced field that often presents several misconceptions for students, such as assuming surfaces are ideally flat and homogenous. Obtaining an accurate and comprehensive picture of the chemical functionality at surfaces and interfaces is challenging and often relies on analysis compiled from multiple techniques. Understanding the surface chemistry of bio-derived materials further adds to this complexity due to the variability of biobased materials. However, the use of renewable feedstocks are central concepts to green and sustainable chemistry and processing biomass feedstocks in a laboratory environment[25-28] is an excellent opportunity to connect these principles, promote critical thinking and engage students in systems thinking, which is typically not extensively taught in the undergraduate chemistry curriculum.[29-32] Figure 1 depicts the preparation process from biomass to biochar, emphasising key applications and the significance of surface chemistry in these contexts.

In this context, biochar represents an excellent material as a platform to integrate systems thinking and inquiry-based learning to enhance students' understanding of the interconnectedness and complexity of scientific, environmental problems and societal challenges in the development of sustainable materials.[33, 34] Biochar is a renewable feedstock, produced through pyrolysis of biomass.

The surface chemistry of biochar is rich in oxygen-containing functional groups such as carboxyl, hydroxyl and phenolic groups. These groups play a key role in determining the performance and functionality of biochar, which can vary widely depending on the feedstock and pyrolysis conditions.[35] While publications on biochar research are extensive, its use in undergraduate laboratory experiments is limited. Several laboratory experiments use biochar as an adsorbent and UV-Vis adsorption to study adsorption of species such as methylene blue[36, 37] salicylic acid and nitroaniline,[38] and phosphates.[39] This work differs from these experiments as the focus of this activity is on surface characterisation of biochar rather than demonstrating a specific application of biochar. More significantly, this work describes a research experience workshop aiming to offer undergraduate students a more informative and realistic experience of research through working alongside a peer who had gained research experience during their URE. While other publications in this area typically emphasise student performance in laboratory reports, this initiative is aimed to inspire undergraduates to pursue research opportunities and promote the development of research skills.

This activity uses the Boehm titration method as an analytical tool for the quantification of oxygen-containing surface groups that can be used for a wide variety of carbon materials. It is an attractive undergraduate experiment for practicing and reinforcing a variety of basic laboratory skills, e.g. potentiometric titrations, filtration, pipetting, pH paper and reflux set-up. The activity was designed as a collaborative experiment, where students used different biochars, and the results were used collectively. In addition to this chemical method of surface characterisation, several spectroscopy techniques are utilised in the activity for surface and chemical compositional analysis.

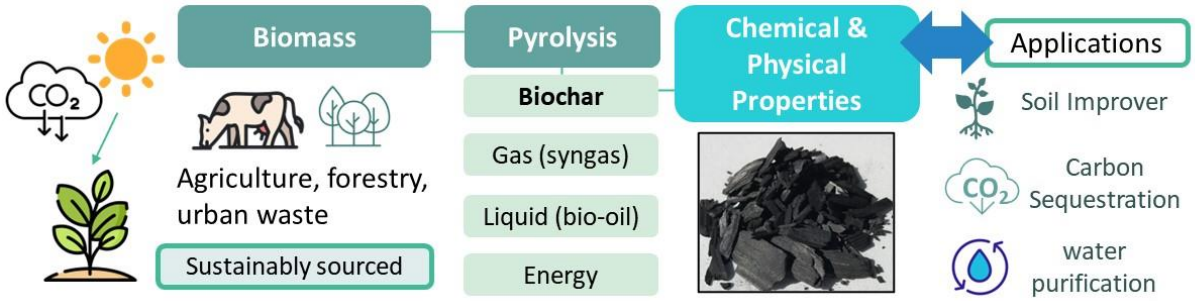


Figure 1: Schematic illustrating the preparation and applications of biochar from biomass. Shown to students as part of the introductory presentation.

Student Learning Objectives:

- To acquire a more unified and integrated view of chemical knowledge to be able to build connections between central ideas in surface chemistry and sustainable materials.
- To gain an understanding of and engage in a collaborative experiment, be involved in peer-to-peer teaching and group learning.
- Develop skills in interpreting spectroscopic data using various spectroscopic techniques and how to draw meaningful conclusions about material properties.
- Enhance problem-solving abilities by formulating hypotheses to address challenges encountered during research, such as unexpected results.
- Engage in critical thinking to address challenges and opportunities in the field of surface chemistry and sustainable materials.
- Gain experience in a research environment to consider pursuing postgraduate research after their undergraduate studies.

Experimental Design and Activity

The activity reported here describes the research workshop that was carried out. Figure 2 illustrates the activities of the workshop and the connection between the URE and a breakdown of the workshop

activities. We believe the concept of using UREs to design research-focused workshops could be adopted to other UREs such as course-based research projects.

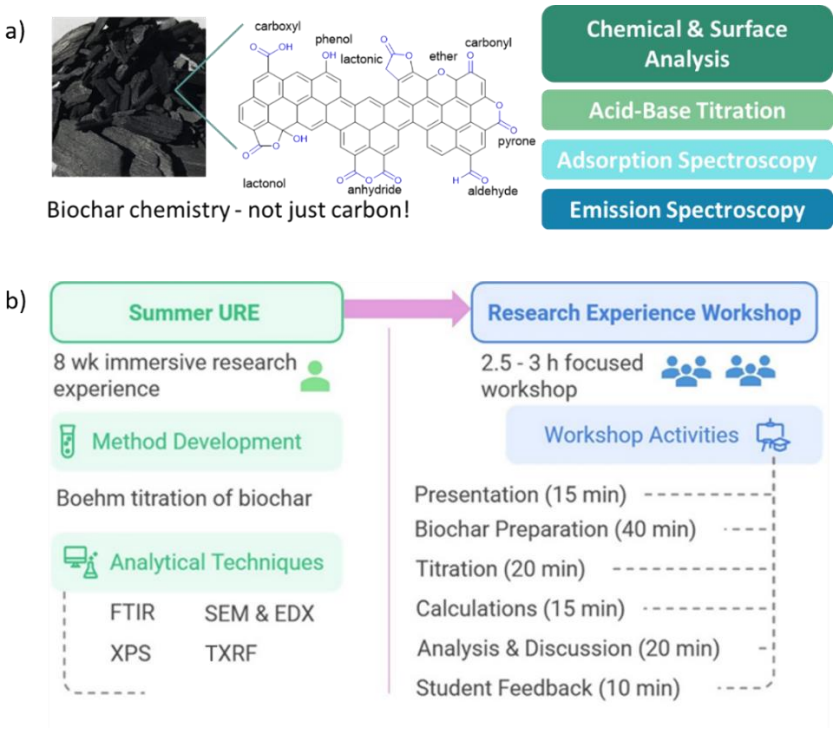


Figure 2: Schematic highlighting the complex surface chemistry of biochar and activities that will be done in the workshop and the connection between the activities of the URE and how they were redesigned as a shorter research experience workshop.

See Supporting Information for hazards associated with the experiment, detailed experimental descriptions, structure and flow schematic for the activity (Figure S1), instructor notes, practical considerations and experimental modifications that can be used depending on time allocated and the skill level of the students. The activity was designed as a collaborative experiment, where students used different biochars, and the results were used collectively. Different student groups were assigned different biochar samples and bases meaning that everyone's data would collaboratively be used for the Boehm calculations.

The Boehm titration is a method used for quantitative analysis of oxygen functional groups on a wide range of carbon materials.[40] Specific oxygen-containing functional groups have varying acidities which can be selectively neutralised by different bases. However, using the Boehm titration for the analysis of biochars requires some caution as biochar may also be composed of inorganic basic components such as oxides, hydroxides and carbonates, as well as inorganic acidic species e.g. humic-like structures, silica and organic acids, that can be divergently solubilised in the Boehm bases, introducing inaccuracies into the titration, which is well discussed by Graber *et al.*[41] To avoid this biochars can be pretreated with acid and/or base washing prior to the titration. Four biochar samples were used in this activity; biochar derived from wood (WD) and biochar derived from digestate (DG) each prepared at temperatures of 300 °C (WD300, DG300) and 700 °C (DG700 and DG700). Activated carbon was used as a reference carbon and as an example where the results were already complete to show the students. The biochars were not pretreated prior to the Boehm titration and the purpose of this was to intentionally return an unexpected result (a negative value) in the Boehm calculation, to promote problem solving in a research setting and also to promote discussion of the results.

Activity 1: Presentation

A short presentation was given to the students overviewing the aims of the workshop, describing what biochar is and detailing the specific activities and analysis techniques that would be carried out in the workshop. One aspect highlighted in the presentation was that the biochar, while dominantly carbon, may contain other elements. We encouraged the students to think about the life cycle of the material through the course of the activity.

Activity 2: Preparation of Biochar for assessment by the Boehm Method

The Boehm titration works based on different oxygen-containing functionalities possessing different acidities and therefore can undergo selective neutralisation with different bases, specifically sodium bicarbonate ($NaHCO_3$) sodium carbonate (Na_2CO_3) and sodium hydroxide (NaOH). Carboxylic groups

(pK_a = 3–6), lactonic groups (pK_a = 7–9) and phenolic groups (pK_a = 8–11) are the three main oxygen-containing surface functionalities of carbon materials, as illustrated in Figure 3.[31,34]

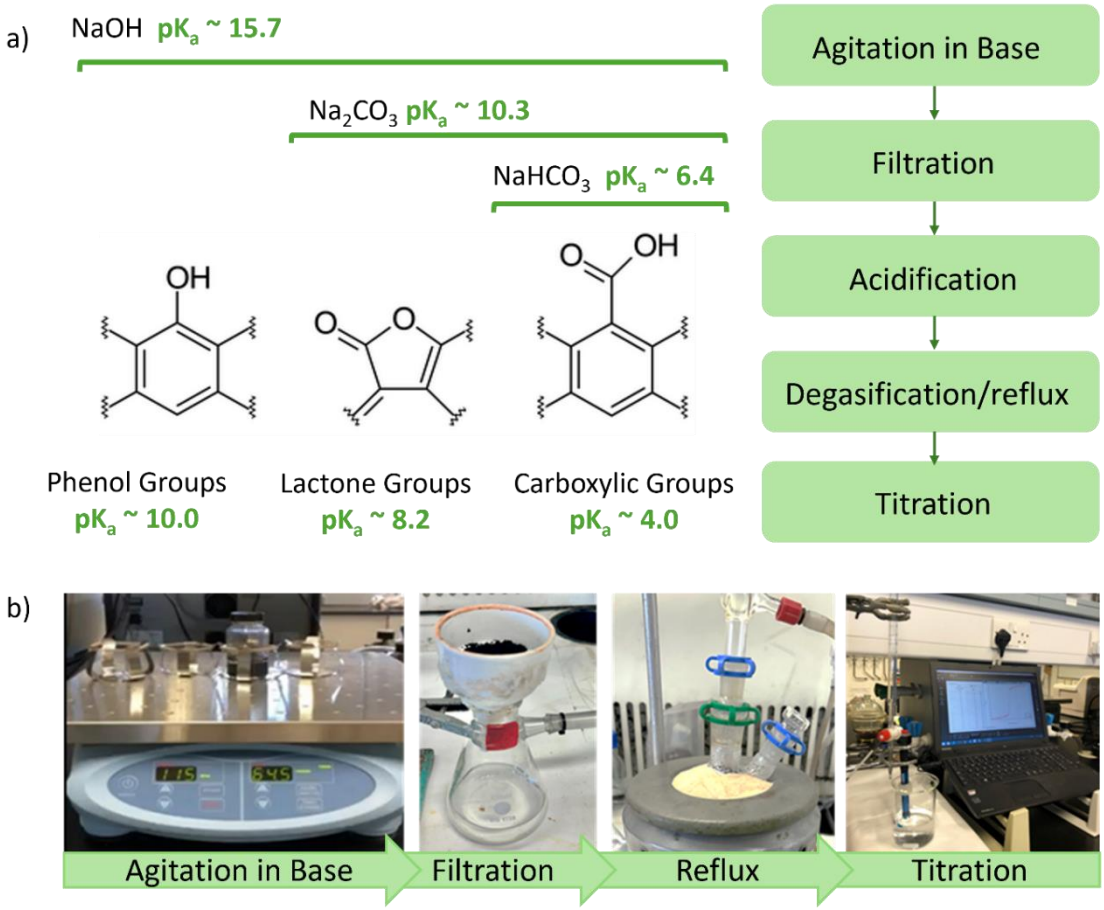


Figure 3: a) Schematic illustrating the Boehm titration principle of selective neutralisation of oxygen functional groups according to their acidity, using multiple bases and b) flow process and pictures of the specific steps for the titration.

The first step of the Boehm titration is dispersion and agitation of the biochar in a base overnight (NaOH, $NaHCO_3$ or Na_2CO_3), see Supporting Information for more detailed description. This is the only step of the Boehm titration that needs to be prepared beforehand. In the activity the students still completed this step *i.e.* they added the base to the dry biochar and placed in on the agitator (picture 1 in Figure 3) or stirrer but used a prepared biochar that had been left stirring overnight. The biochar was then filtered and the liquid collected (picture 2 in Figure 3).

The next step is acidification of the liquid fraction (see Supporting Information for detailed description). Briefly, 5 mL aliquots of the filtrate were transferred to 50 mL round bottom flasks and acidified with 0.05 M HCl. The aim of this step is to add acid until a pH of 2 or 3 is achieved indicating the HCl is in excess. This was achieved by adding different HCl volumes depending on the specific nature of the biochar. For the purposes of time, the students were told the volume of acid to add to the filtrate by providing them with a table. As shown in Table 1, 15 mL of 0.05 M HCl was initially added followed by addition of HCl in 5 mL increments and the pH was tested with pH paper after each addition. Tabulating the data can help students to identify which biochar samples have more basic or acidic properties, initiating thought and discussion about the surface chemistry of the biochar during the experiment.

While the exact volume of acid added will depend on the biochar, one point worth highlighting is that biochar samples dispersed in monoprotic bases (NaOH and $NaHCO_3$) will require less acid compared to samples dispersed in diprotic base (Na_2CO_3). Based on the students' knowledge of equilibrium constants for acids and base (typically covered in first year chemistry), students should be able to rationalise that as a diprotic base, in water the carbonate ion (CO_3^{2-}) can undergo two sequential protonation steps.

Table 1 illustrates representative student data for acidification using different biochar samples. The final preparation step in the Boehm titration is degassing to remove dissolved CO_2. This was carried out by doing a standard reflux set up as shown in Figure 3. Bubbling inert gas through the solution can be done as an alternative to reflux for removing dissolved CO_2.

Table 1: Representative student results showing pH measurement using pH paper, after acidification of samples dispersed in NaOH, $NaHCO_3$ and Na_2CO_3 using 0.05 M HCl.

	Base: NaOH				
Biochar	**AC**	**DG300***	**DG700**	**WD300**	**WD700**

Total HCl (mL)	pH	pH	pH	pH	pH
15	3	8	7	3	5
20	2	3	4	3	4
25	2	3	3	3	3
30	2	2	2	3	3
	Base: $NaHCO_3$				
Biochar	AC	DG300	DG700	WD300	WD700
Total HCl (mL)	pH	pH	pH	pH	pH
15	3	7	8	4	5
20	3	4	6	3	4
25	3	3	4	3	3
30	3	2	3	3	3
	Base: Na_2CO_3				
Biochar	AC	DG300	DG700	WD300	WD700
Total HCl (mL)	pH	pH	pH	pH	pH
15	8	8	8	8	8
20	7	8	7	7	8
25	5	8	7	6	7
30	3	7	6	4	6
35	3	5	5	3	5
40	3	3	4	3	4
45	3	3	3	3	3

50	3	3	3	3	3

Sample Codes: AC = acidified activated carbon, DG300 = digestate biochar prepared at 300 °C, DG700 = digestate biochar prepared at 700 °C, WD300 = wood biochar prepared at 300 °C, WD700 = wood biochar prepared at 700 °C.* Full sample calculation is given in Supporting Information for WD300 biochar.

Activity 3: Boehm Titration:

The acidified, degassed solutions were than titrated against standardised 0.05 M NaOH solution using a pH probe and Capstone PASCO software. Representative titration curves are shown in Figure 4, and the end point of each titration is tabulated as shown in Table 2.

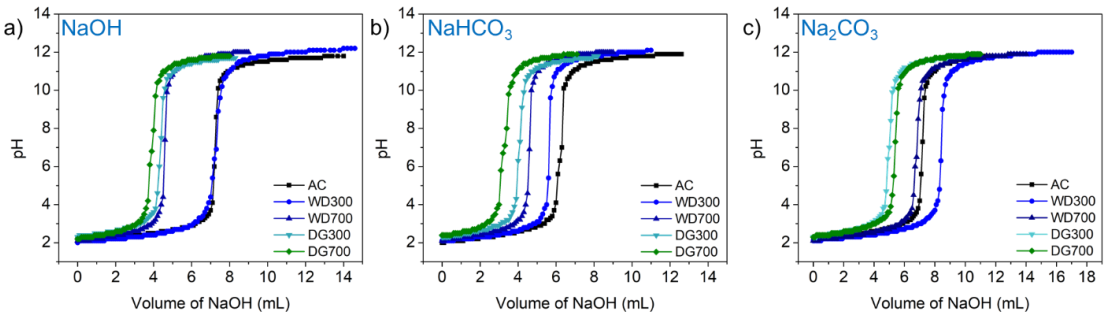


Figure 4: Titration curves for AC, WD300, WD700, DG300 and DG700 from agitation bases a) NaOH, b) $NaHCO_3$ and c) Na_2CO_3.

Table 2: Titration end points data obtained from different biochar samples.

Biochar Sample	V_{NaOH} **(mL)**	V_{NaHCO_3} **(mL)**	$V_{Na_2CO_3}$ **(mL)**
AC	7.2	6.3	7.2
WD300*	7.3	5.6	8.4
WD700	4.6	4.6	6.8

DG300	4.4	4.0	4.9
DG700	3.9	3.3	5.4

* Sample calculation using these values is illustrated in the Supporting Information.

Activity 4: Calculating Surface Functionalities

The students used the end point values determined from the titrations to calculate the amount of phenolic (Ar-OH), lactonic (-COOR) and carboxylic (-COOH) groups present on the biochar surface according to the equations adapted from Wu *et al.*[40] The calculation can be divided into three parts which include calculating (i) the volume of HCl that was added in the acidification step (data from Table 1), ΔV_{HCl} (ii) the number of moles of each base that reacted during the agitation step, n and (iii) concentration of oxygen functional groups, C. The equations are illustrated below, and the Supporting Information illustrates a completed sample calculation using data from Boehm titrations carried out with the WD300 biochar (data illustrated with * in Table 1 and Table 2).

i) Volume of Reacted HCl, (ΔV_{HCl}):

$$\Delta V_{HCl} = V_{HCl} - \frac{\Delta V_{NaOH} \cdot C_{NaOH}}{C_{HCl}} \qquad \textbf{Eqn. 1}$$

Where V_{HCl} is the volume of 0.05 M HCl used in the acidification step that is recorded in Table 2. ΔV_{NaOH} is the endpoint for the titration. C_{NaOH} is the concentration of NaOH in the titration (0.05 M). C_{HCl} is the concentration of HCl in the acidification step (0.05 M).

ii) Number of moles of each base, (*n*)

$$n_{NaOH} = C_{NaOH} \cdot V_{NaOH} - C_{HCl} \cdot \Delta V_{HCl} \qquad \textbf{Eqn. 2 a}$$

$$n_{Na_2CO_3} = 2C_{Na_2CO_3} \cdot V_{Na_2CO_3} - C_{HCl} \cdot \Delta V_{HCl} \qquad \textbf{Eqn. 2 b}$$

$$n_{NaHCO_3} = C_{NaHCO_3} \cdot V_{NaHCO_3} - C_{HCl} \cdot \Delta V_{HCl} \qquad \textbf{Eqn. 2 c}$$

Where n is the number of moles of base that reacted during the agitation step, $C_{NaOH}, C_{Na_2CO_3}$ and C_{NaHCO_3} is the concentration of the base solution used in the agitation step (0.05 M). $V_{NaOH}, V_{Na_2CO_3}$ and V_{NaHCO_3} is the volume of base used in the agitation step (0.025 L). C_{HCl} is the concentration of HCl used in the acidification step (0.05 M).

iii) Concentration of Functional Groups, C:

$$C_{-COOH} = n_{NaHCO_3}/m \qquad \textbf{Eqn. 3 a}$$

$$C_{-COOR} = (n_{Na_2CO_3} - n_{NaHCO_3})/m \qquad \textbf{Eqn. 3 b}$$

$$C_{Ar-OH} = (n_{NaOH} - n_{Na_2CO_3})/m \qquad \textbf{Eqn. 3 c}$$

Where C is the concentration of functional group, m is the mass of carbon used in the dispersion and agitation step, and n is the number of moles of base that reacted during the agitation step.

Table 3: Concentration of different oxygen containing functional groups determined using the Boehm method for each sample. See Supporting Information for worked sample calculation.

Biochar Sample	C_{-COOH} *µmol g^{-1}*	C_{-COOR} *µmol g^{-1}*	C_{Ar-OH} *µmol g^{-1}*
AC	87	387	0
WD300*	430	530	-420
WD700	-27	480	-480
DG300	-53	386	-286
DG700	-70	476	-430

* Worked sample calculation using these values is illustrated in the Supporting Information.

Activity 5: Spectroscopic Analysis using FTIR

Figure 5 illustrates representative FTIR spectra of the wood derived biochars collected by the students during the workshop. All the students had previous experience of collecting FTIR data as well as theoretical knowledge of FTIR. The presence of the oxygen containing functional groups can be readily observed in the WD300 biochar and not very well resolved for the other biochars. The specific surface chemistry is highly dependent on the feedstock and preparation conditions, but in general biochar prepared at higher annealing temperatures has a higher degree of aromatisation and lower amount of oxygen containing functionalities, which can be clearly observed in comparing the WD300 biochar to the WD700 in Figure 5.[42] The FTIR analysis of the digestate samples is shown in supporting information Figure S2.

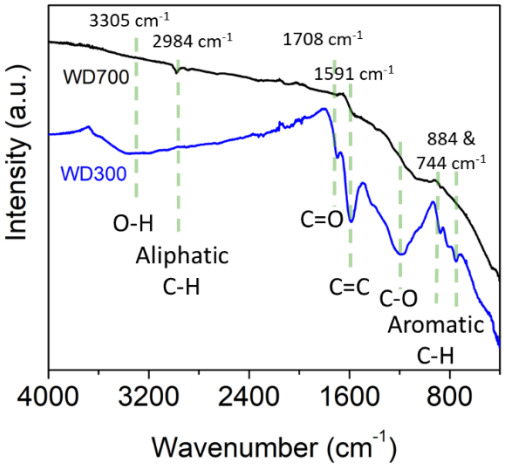


Figure 5: FTIR analysis of wood derived biochar prepared at 300 °C and 700 °C.

Activity 6: Group Discussion

The group discussion was carried out in parallel with additional chemical analysis of the biochar. Further details of how this was managed are outlined in the Supporting Information. The Boehm titration quantifies carboxylic, lactonic and phenolic groups in carbon samples and sample results obtained from collaborative analysis of different biochars are shown in Table 3. It was found that all biochar samples contained a large amount of lactonic groups with the WD300 biochar containing the highest concentration. The WD300 sample was the most similar to the acidified activated carbon

sample as it also contained carboxylic groups. This result correlated well with the FTIR analysis and reflects the oxygen rich chemistry expected for a wood-sourced biochar sample and low annealing temperature. The effect of the preparation temperature is illustrated in the wood derived biochar as the WD700 biochar showed a significant reduction in the carboxylic acid groups, which further correlates the Boehm results with the FTIR analysis.

An apparently anomalous result obtained from the Boehm method is the negative values obtained from the phenolic groups and to a lesser extent the carboxylic acid groups, except for the WD300, which showed a positive value. These negative values are not observed with the commercial activated carbon. Students were asked if they had any theories on what this could mean, thinking about the calculations used in the experiment and the acid-base nature of the titration used for the Boehm method.

As part of the discussion students were reminded of the schematic in Figure 3 illustrating the Boehm titration principle of selective neutralisation of oxygen functional groups according to their acidity: (i) the NaOH will accept protons from all Brønsted acid species (carboxylic acids and phenols), (ii) the Na_2CO_3 will accept protons from functionalities with pKa values < 10.3 (iii) $NaHCO_3$ will accept protons from functionalities with pKa values < 6.4. The application of the Boehm method to biochar can introduce biases to the method through the following mechanisms (i) dissolution of the inorganic or ash fraction with the Boehm reactants, would contradict the premise that the reactants will only have interactions with organic surface functional groups, and (ii) reactive biochar components containing acidic or basic groups may dissolve when reacted with the Boehm reagents, especially during the base dispersion step, forming dissolved organic carbon (DOC).[43] The generation of negative values using the Boehm titration is well reported in biochar due to various mechanisms such as the inorganic components in the biochar leading to unexpected results.[40]

In the initial presentation, it was suggested that non-carbon elements may be present in biochar samples from different sources. Students were not told specifically what non-carbon species the

biochars contained but rather that they should consider the biomass used of the preparation of the biochar material and the life cycle of the material. Students were asked to reflect on this and think about what species might be present in the biochar sample. Most students were able to make the connection between the presence of chemical species that could give rise to the unexpected titration results. The elements most identified by students were potassium, phosphorus and nitrogen, as these are present in fertiliser. To further rationalise the results obtained from the Boehm method, chemical compositional analysis of the biochar was carried out to support the Boehm results.

Activity 7: Chemical Analysis of Biochar

Chemical compositional analysis of the biochar was carried out using total reflection x-ray fluorescence (TXRF). TXRF is a fast (typical scan <60 seconds) and easy non-destructive method for the students to measure the elemental composition of a material. Figure 6a displays representative spectra of the digestate biochars and confirms the presence of trace minerals within the sample and the absolute values generated from the S2 Picofox software (µg) are shown in Table 4 (see Supporting Information for details). The DG300 had the highest and most diverse mineral content and showed the presence Na, Mg, P, Cl, K and Ca, which is to be expected as digestate is nutrient rich. It is interesting to note the P to K ratio is about 1:3, indicating that the digestate biochar has potential as an agricultural soil improver. The DG700 biochar, only showed the presence of K, suggesting other minerals were volatised at the higher preparation temperature. In contrast to the digestate derived biochar, the wood derived biochar showed much lower total mineral content and were more similar at different synthesis temperatures, as shown in Table 4. Shown in Figure S3, the AC reference material showed no signals in the TXRF scan as expected.

While TXRF is a fast and convenient analytical method to identify chemical composition, it is unsuitable for light elements and spectroscopic techniques such as XPS and EDX, are commonly employed in surface and chemical analysis.[44] This analysis was gathered by the undergraduate student doing the

Summer URE, and while the students of the workshop could not obtain hands-on experience in gathering the XPS and EDX analysis, it nonetheless is an excellent opportunity to demonstrate (i) the use of correlative analysis in research to draw more meaningful conclusions,[45, 46] (ii) illustrate the fundamental operating principles of different spectroscopic techniques and (iii) that specific methodologies have advantages and disadvantages which need to be considered when selecting an analysis method.

Figure 6b shows the XPS survey spectra of the digestate biochar that was shown to the students. In addition to the surface sensitivity of XPS, it is also suitable for the analysis of C, O and N. It can be readily seen that the XPS analysis correlated with the TXRF analysis, also showing inorganic species, Na, K, Cl and P. EDX mapping (Figure 6c) provides spatial information about the location of the specific elements and again correlates well with TXRF and XPS analysis.

The chemical analysis data provided a good basis for group discussion. The detection of nitrogen groups in the biochar is significant as they will contribute to the basicity of the surface (ammonia, ammonium ions, amine and amide functional groups) of the biochar, resulting in the overconsumption of HCl in the acidification step prior to titration, which further supports the results obtained through the Boehm titration. Students were asked to theorise on the origin of these elements thinking about the material originating from biomass and anaerobic digestion. One interesting element detected in the digestate biochar was tin. While the origin of the Sn is unclear, it served as a useful result for students to think more holistically, beyond the analysis and consider the life cycle of the material, from its starting point as biomass to production into biochar, taking into account it may be a contaminant in the biomass or was introduced at storage, preparation stage or even a cross-contamination in the lab.

Overall, the additional characterisation of the biochar reveals the complex chemistry of the biochar structure and supports an explanation for the Boehm titration results. This led to a discussion on the need to critically assess the Boehm method, a methodology originally designed for pure carbons, when applying it to biochar. Finally, we discussed how the biochar could be pretreated to remove the non-

carbon components. Pre-treating the biochar with NaOH can remove any solubilisable acidic functionalities, and then treating with HCl can remove solubilisable basic functionalities.

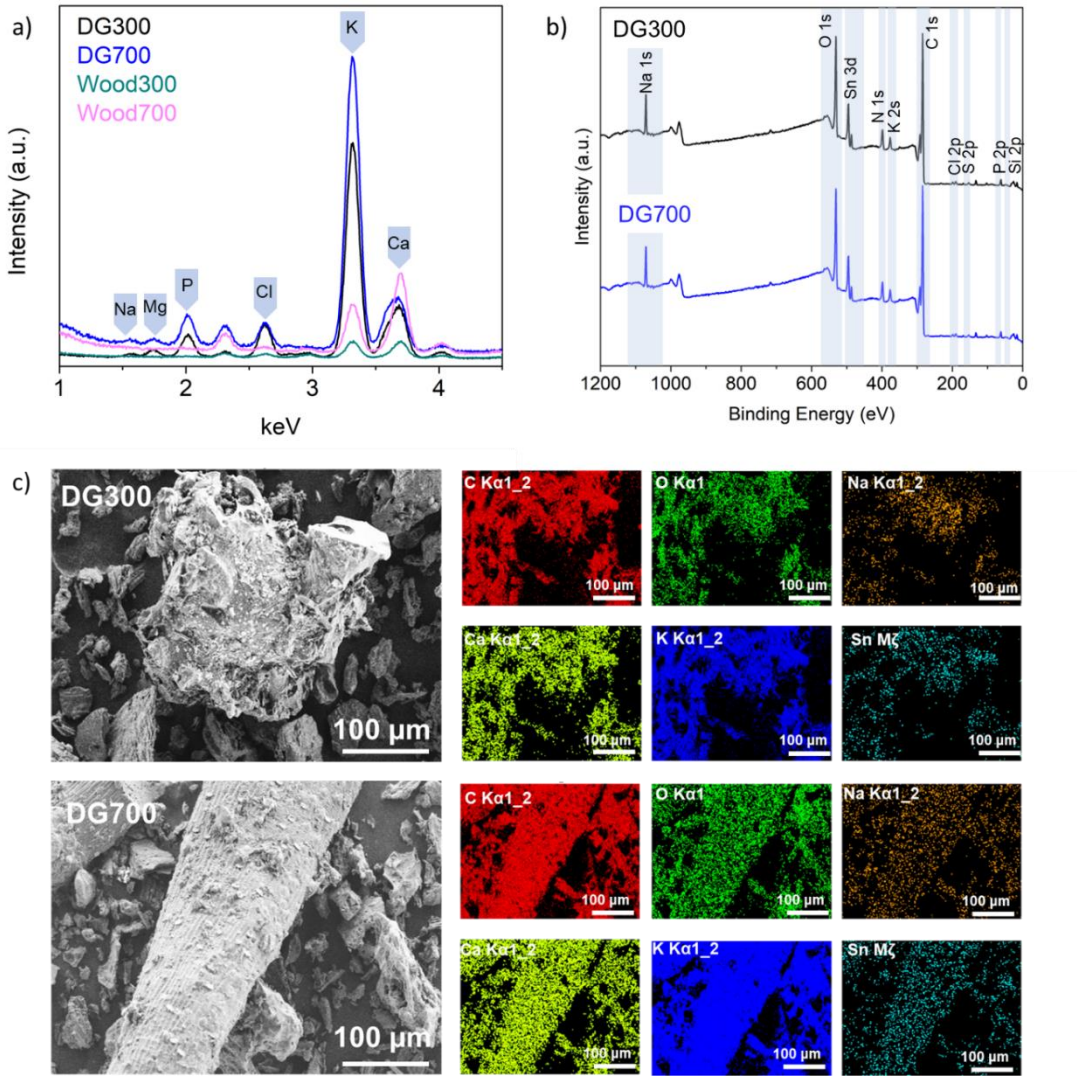


Figure 6: a) TXRF scan of biochars DG300, DG700, WD300 and WD700 sample, b) XPS survey of DG300 and DG700 sample and c) SEM with EDX mapping of the DG300 and DG700 samples.

Table 4: TXRF data measured as an absolute value generated from the S2 Picofox software.

Sample	Na (µg)	Mg (µg)	P (µg)	Cl (µg)	K (µg)	Ca (µg)	Total (µg)
DG300	2.06	0.07	0.12	0.07	0.18	0.03	2.53

DG700	-	-	-	-	0.28	-	0.28
WD300	-	-	0.002	-	0.01	0.01	0.022
WD700	-	-	-	0.003	0.02	0.03	0.053

7.6.4 Student Feedback

A student survey was carried out pre and post activity and the results are displayed in Figure 7. Students were not familiar with biochar as a material and had a poor understanding on the concept of sustainable materials. Student feedback showed improvement in understanding and comments from student survey evidenced that students enjoyed the interaction with the doctoral students and obtained a better understanding of the research process. Specific student comments demonstrated increased motivation in pursuing further research.

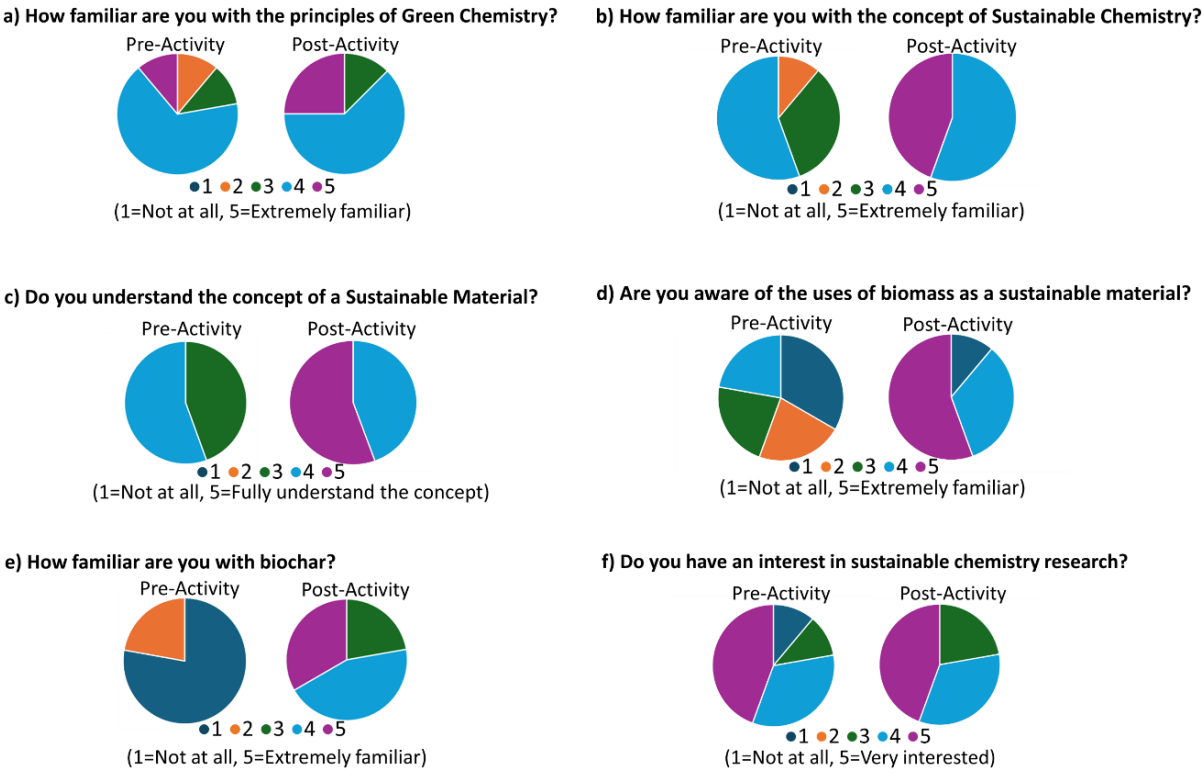


Figure 7: Summary of the pre and post activity survey. (10 respondents)

The survey also had an open comment box for student input. Below are quotes taken from the student survey. The positive feedback comments received from the students indicate a better understanding and appreciation into the research process. While the survey was largely qualitative, it nonetheless provides supporting evidence that the key objectives of this activity were achieved.

'*Going in I was sure I wanted an industry placement but now I'm also considering research thanks to the workshop, which piqued my interest in research.'*

'Enjoyable lab, learned a lot and gave insight into what research is like.'

'Great workshop. Real life application of undergraduate experiments.'

'Really enjoyed seeing the research side of chemistry.'

7.6.5 Pedagogical Reflection

The use of biochar as a renewable feedstock provides a genuine inquiry-based laboratory activity that gave students the opportunity to engage in an investigative research process. It highlights that investigative methodologies are not a 'one size fits all' and that methodologies can have bias depending on the nature of the substance being analysed. For example, the Boehm titration returned a typical result for activated carbon, but the biochar samples give rise to unexpected results that required further investigation. Rationalising these results by using different chemical analysis techniques enabled students to build a wider picture of the chemical complexity of biochar and how the use of multiple analytical techniques contributed to a better understanding of material properties and promote research skills. Students also benefited from the collaborative nature of the workshop where they collectively contributed to the experimental results and discussion. While the activity was designed as a research experience the activity could be easily adapted to a conventional laboratory

experiment. The Supporting Information outlines Practical Considerations and Modifications to the Experiment offers several suggestions to modify the experiment.

7.6.6 Conclusions

Co-curricular research experiences provide a valuable opportunity for students to develop their scientific research skills and gain insight in the research process. This activity developed a succinct research-based workshop from a longer URE, in this case an undergraduate doing a summer internship. This approach has many advantages, including enabling a greater number of students to experience research, promotes peer-led teaching and group learning. This activity was conducted outside of the semester, but we believe this approach could also be applied to curriculum based UREs where research-orientated workshops could be designed from individual UREs with a focus on developing UG research skills.

Supporting Information

- Notes for instructor
    - Experimental Description
    - Sample Calculation
    - Blank Data Table Templates
    - FTIR Analysis
    - TXRF Analysis
    - Practical Considerations and Modifications to Experiment
    - Extension to the Experiment
- Supplementary Data

Acknowledgements

We acknowledge Science Foundation Ireland grant number (AMBER Grant No: 12/RC/2278_P2). We acknowledge and thank the Royal Society of Chemistry for supporting CG in the work. We thank the Circular Economy, Energy and Environment Systems Group at University College Cork for providing biochar samples for this experiment.

7.6.7 References:

(1) Gilbert, J. K. On the Nature of "Context" in Chemical Education. *International Journal of Science Education* **2006**, *28* (9), 957-976. DOI: 10.1080/09500690600702470.
(2) Carroll, M. K. Moving from Recommendations to Innovations: Increasing the Relevancy and Effectiveness of Chemistry Education. *Journal of Chemical Education* **2013**, *90* (7), 816-819. DOI: 10.1021/ed3008796.
(3) Boyce, M. C.; Singh, K. Student Learning and Evaluation in Analytical Chemistry Using a Problem-Oriented Approach and Portfolio Assessment. *Journal of Chemical Education* **2008**, *85* (12), 1633. DOI: 10.1021/ed085p1633.
(4) Jeffery, A. J.; Rogers, S. L.; Pringle, J. K.; Zholobenko, V. L.; Jeffery, K. L. A.; Wisniewski, K. D.; Haxton, K. J.; Emley, D. W. Thinglink and the Laboratory: Interactive Simulations of Analytical Instrumentation for HE Science Curricula. *Journal of Chemical Education* **2022**, *99* (6), 2277-2290. DOI: 10.1021/acs.jchemed.1c01067.
(5) Salta, K.; Ntalakou, E.; Tsiortos, Z. Review of Hands-On Laboratory Experiments Employing Household Supplies. *Journal of Chemical Education* **2022**, *99* (7), 2563-2571. DOI: 10.1021/acs.jchemed.2c00037.
(6) Chi, M.; Zheng, C.; He, P. Reframing Chemical Thinking Through the Lens of Disciplinary Essential Questions and Perspectives for Teaching and Learning Chemistry. *Science & Education* **2023**. DOI: 10.1007/s11191-023-00438-3.
(7) Campbell, C. D.; Midson, M. O.; Bergstrom Mann, P. E.; Cahill, S. T.; Green, N. J. B.; Harris, M. T.; Hibble, S. J.; O'Sullivan, S. K. E.; To, T.; Rowlands, L. J.; et al. Developing a skills-based practical chemistry programme: an integrated, spiral curriculum approach. **2022**, *4* (3), 243-257. DOI: doi:10.1515/cti-2022-0003 (acccessed 2024-08-29).
(8) Andrade, R. S.; Zuin, V. G. Formative Dimensions for Green and Sustainable Chemical Education: A Qualitative Evaluation Tool of the Formative Level of Experimental Processes. *Journal of Chemical Education* **2023**, *100* (6), 2281-2291. DOI: 10.1021/acs.jchemed.3c00053.
(9) Blatti, J. L.; Garcia, J.; Cave, D.; Monge, F.; Cuccinello, A.; Portillo, J.; Juarez, B.; Chan, E.; Schwebel, F. Systems Thinking in Science Education and Outreach toward a Sustainable Future. *Journal of Chemical Education* **2019**, *96* (12), 2852-2862. DOI: 10.1021/acs.jchemed.9b00318.
(10) Talanquer, V.; Szozda, A. R. An Educational Framework for Teaching Chemistry Using a Systems Thinking Approach. *Journal of Chemical Education* **2024**, *101* (5), 1785-1792. DOI: 10.1021/acs.jchemed.4c00216.
(11) Seymour, E.; Hunter, A.-B.; Laursen, S. L.; DeAntoni, T. Establishing the benefits of research experiences for undergraduates in the sciences: First findings from a three-year study. *Science Education* **2004**, *88* (4), 493-534. DOI: https://doi.org/10.1002/sce.10131 (acccessed 2024/08/29).
(12) Clark, T. M.; Ricciardo, R.; Weaver, T. Transitioning from Expository Laboratory Experiments to Course-Based Undergraduate Research in General Chemistry. *Journal of Chemical Education* **2016**, *93* (1), 56-63. DOI: 10.1021/acs.jchemed.5b00371.
(13) Russell, S. H.; Hancock, M. P.; McCullough, J. Benefits of Undergraduate Research Experiences. *Science* **2007**, *316* (5824), 548-549. DOI: 10.1126/science.1140384 (acccessed 2024/08/29).
(14) Lopatto, D. Undergraduate research experiences support science career decisions and active learning. *CBE Life Sci Educ* **2007**, *6* (4), 297-306. From NLM.
(15) Wierzchowski, A.; Wink, D. Students' Experiences with the Science and Engineering Practices in a Workshop-Based Undergraduate Research Experience. *Journal of Chemical Education* **2024**, *101* (6), 2266-2278. DOI: 10.1021/acs.jchemed.4c00035.
(16) Watts, F. M.; Rodriguez, J.-M. G. A Review of Course-Based Undergraduate Research Experiences in Chemistry. *Journal of Chemical Education* **2023**, *100* (9), 3261-3275. DOI: 10.1021/acs.jchemed.3c00570.
(17) Auchincloss, L. C.; Laursen, S. L.; Branchaw, J. L.; Eagan, K.; Graham, M.; Hanauer, D. I.; Lawrie, G.; McLinn, C. M.; Pelaez, N.; Rowland, S.; et al. Assessment of Course-Based Undergraduate Research

Experiences: A Meeting Report. *CBE—Life Sciences Education* **2014**, *13* (1), 29-40. DOI: 10.1187/cbe.14-01-0004 (acccessed 2024/08/29).
(18) Linn, M. C.; Palmer, E.; Baranger, A.; Gerard, E.; Stone, E. Undergraduate research experiences: Impacts and opportunities. *Science* **2015**, *347* (6222), 1261757. DOI: 10.1126/science.1261757 (acccessed 2024/08/29).
(19) Karukstis, K. K. Broadening Participation in Undergraduate Research. *Journal of Chemical Education* **2008**, *85* (11), 1474. DOI: 10.1021/ed085p1474.
(20) Nguyen, H. A.; Miura-Stempel, E.; Morrison, C. M.; Dixon, G. J.; Homer, M. K.; Dou, F. Y.; Snow, A.; Golder, M. R.; Cossairt, B. M. A Summer Research Program for Community College Students Led by Graduate Students at the University of Washington. *Journal of Chemical Education* **2024**, *101* (7), 2693-2702. DOI: 10.1021/acs.jchemed.3c01277.
(21) Calvin, J. J.; Ondry, J. C.; Dahl, J. C.; Sedlak, A. B.; McKeown-Green, A.; Wang, X.; Crook, M. F.; Gleason, S. P.; Hauwiller, M. R.; Baranger, A. M.; et al. Research Group-Led Undergraduate Research Program: Analyzing and Improving a Versatile Springboard for First-Year Undergraduates. *Journal of Chemical Education* **2022**, *99* (2), 799-809. DOI: 10.1021/acs.jchemed.1c01065.
(22) Love, O.; Heying, M.; Steed, P. R.; Wasileski, S. A. Development and Implementation of a Research-Preparative General Chemistry Laboratory Course: Chemistry of Beverages. *Journal of Chemical Education* **2024**, *101* (7), 2757-2764. DOI: 10.1021/acs.jchemed.4c00335.
(23) Nixon, K. L.; Crabb, E. M.; Seery, M. K. A Cocurricular Context-Based Enrichment Program to Enhance Scientific Skills Development. *Journal of Chemical Education* **2024**, *101* (7), 2656-2664. DOI: 10.1021/acs.jchemed.3c00965.
(24) Cruz, D. J. L.; Guidote, A. M., Jr.; Lee Yu, H. L.; Adarlo, G. M. Assessing the Lasting Impact of Co-Curricular Service Learning in Undergraduate Chemistry. *Journal of Chemical Education* **2024**, *101* (5), 1932-1940. DOI: 10.1021/acs.jchemed.3c01333.
(25) Mackenzie, L. S.; Tyrrell, H.; Thomas, R.; Matharu, A. S.; Clark, J. H.; Hurst, G. A. Valorization of Waste Orange Peel to Produce Shear-Thinning Gels. *Journal of Chemical Education* **2019**, *96* (12), 3025-3029. DOI: 10.1021/acs.jchemed.8b01009.
(26) Austen, L. I.; Dugmore, T. I. J.; Matharu, A. S.; Hurst, G. A. Byproduct Valorization: From Spent Coffee Grounds to Fatty Acid Ethyl Esters. *Journal of Chemical Education* **2023**, *100* (1), 327-335. DOI: 10.1021/acs.jchemed.2c00728.
(27) Ribeiro, L. S.; Órfão, J. J. M.; Pereira, M. F. R. Direct Catalytic Conversion of Lignocellulosic Biomass Wastes to Ethylene Glycol: Practical Learning for Chemical Engineering Students. *Journal of Chemical Education* **2024**, *101* (8), 3493-3499. DOI: 10.1021/acs.jchemed.4c00527.
(28) Hwang, H. L.; Jadhav, S. R.; Silverman, J. R.; John, G. Sweet and Sustainable: Teaching the Biorefinery Concept through Biobased Gelator Synthesis. *Journal of Chemical Education* **2014**, *91* (10), 1563-1568. DOI: 10.1021/ed3007764.
(29) Orgill, M.; York, S.; MacKellar, J. Introduction to Systems Thinking for the Chemistry Education Community. *Journal of Chemical Education* **2019**, *96* (12), 2720-2729. DOI: 10.1021/acs.jchemed.9b00169.
(30) Dicks, A. P.; D'eon, J. C.; Morra, B.; Kutas Chisu, C.; Quinlan, K. B.; Cannon, A. S. A Systems Thinking Department: Fostering a Culture of Green Chemistry Practice among Students. *Journal of Chemical Education* **2019**, *96* (12), 2836-2844. DOI: 10.1021/acs.jchemed.9b00287.
(31) Mahaffy, P. G.; Matlin, S. A.; Whalen, J. M.; Holme, T. A. Integrating the Molecular Basis of Sustainability into General Chemistry through Systems Thinking. *Journal of Chemical Education* **2019**, *96* (12), 2730-2741. DOI: 10.1021/acs.jchemed.9b00390.
(32) Hurst, G. A.; Slootweg, J. C.; Balu, A. M.; Climent-Bellido, M. S.; Gomera, A.; Gomez, P.; Luque, R.; Mammino, L.; Spanevello, R. A.; Saito, K.; et al. International Perspectives on Green and Sustainable Chemistry Education via Systems Thinking. *Journal of Chemical Education* **2019**, *96* (12), 2794-2804. DOI: 10.1021/acs.jchemed.9b00341.

(33) Igboanugo, B. I.; Naiho, O. I. Effectiveness of Inquiry-Based Chemistry Learning on Students' Attitudes and Knowledge of Climate Change Mitigation Behaviors. *Journal of Chemical Education* **2024**, *101* (8), 3318-3325. DOI: 10.1021/acs.jchemed.4c00367.
(34) Reyes, K. M. D.; Bruce, K.; Shetranjiwalla, S. Green Chemistry, Life Cycle Assessment, and Systems Thinking: An Integrated Comparative-Complementary Chemical Decision-Making Approach. *Journal of Chemical Education* **2023**, *100* (1), 209-220. DOI: 10.1021/acs.jchemed.2c00647.
(35) Janu, R.; Mrlik, V.; Ribitsch, D.; Hofman, J.; Sedláček, P.; Bielská, L.; Soja, G. Biochar surface functional groups as affected by biomass feedstock, biochar composition and pyrolysis temperature. *Carbon Resources Conversion* **2021**, *4*, 36-46. DOI: https://doi.org/10.1016/j.crcon.2021.01.003.
(36) Doble, J.; Wilson, G.; Wainman, J. W. Kinetic and Thermodynamic Analysis of the Adsorption of Methylene Blue onto Biochar. *Journal of Chemical Education* **2023**, *100* (10), 4040-4046. DOI: 10.1021/acs.jchemed.3c00518.
(37) Arrebola, J. C.; Rodríguez-Fernández, N.; Caballero, Á. Decontamination of Wastewater Using Activated Biochar from Agricultural Waste: A Practical Experiment for Environmental Sciences Students. *Journal of Chemical Education* **2020**, *97* (11), 4137-4144. DOI: 10.1021/acs.jchemed.0c00202.
(38) Karunanayake, A. G.; Bombuwala Dewage, N.; Todd, O. A.; Essandoh, M.; Anderson, R.; Mlsna, T.; Mlsna, D. Salicylic Acid and 4-Nitroaniline Removal from Water Using Magnetic Biochar: An Environmental and Analytical Experiment for the Undergraduate Laboratory. *Journal of Chemical Education* **2016**, *93* (11), 1935-1938. DOI: 10.1021/acs.jchemed.6b00154.
(39) Crisler, G. B., II; Perera, V.; Hernandez, C. G.; Orr, A.; Davis, R.; Moore, J.; Smith, J.; Varco, J.; Schauwecker, T.; Brown, A.; et al. Phosphate in Soils: An Undergraduate Exploration of Soil Texture, Chemistry, and Amendment. *Journal of Chemical Education* **2020**, *97* (4), 1077-1082. DOI: 10.1021/acs.jchemed.9b00529.
(40) Wu, H.; Lu, W.; Chen, Y.; Zhang, P.; Cheng, X. Application of Boehm Titration for the Quantitative Measurement of Soot Oxygen Functional Groups. *Energy & Fuels* **2020**, *34* (6), 7363-7372. DOI: 10.1021/acs.energyfuels.0c00904.
(41) Tsechansky, L.; Graber, E. R. Methodological limitations to determining acidic groups at biochar surfaces via the Boehm titration. *Carbon* **2014**, *66*, 730-733. DOI: https://doi.org/10.1016/j.carbon.2013.09.044.
(42) Chen, J.; Zhou, J.; Zheng, W.; Leng, S.; Ai, Z.; Zhang, W.; Yang, Z.; Yang, J.; Xu, Z.; Cao, J.; et al. A complete review on the oxygen-containing functional groups of biochar: Formation mechanisms, detection methods, engineering, and applications. *Science of The Total Environment* **2024**, *946*, 174081. DOI: https://doi.org/10.1016/j.scitotenv.2024.174081.
(43) Fidel, R. B.; Laird, D. A.; Thompson, M. L. Evaluation of Modified Boehm Titration Methods for Use with Biochars. *Journal of Environmental Quality* **2013**, *42* (6), 1771-1778. DOI: https://doi.org/10.2134/jeq2013.07.0285 (acccessed 2024/12/16).
(44) Hercules, D. M. Electron Spectroscopy: Applications for Chemical Analysis. *Journal of Chemical Education* **2004**, *81* (12), 1751. DOI: 10.1021/ed081p1751.
(45) Wiskam, V.; Fichtner, W.; Kramb, V.; Nintschew, A.; Schneider, J. S. Infrared Spectroscopy: A Versatile Tool in Practical Chemistry Courses. *Journal of Chemical Education* **1995**, *72* (10), 952. DOI: 10.1021/ed072p952.
(46) Simpson, J. M.; Rivera, O. Gas Chromatography and Molecular Modeling: A Correlation Experiment for the Undergraduate Laboratory. *Journal of Chemical Education* **2001**, *78* (7), 942. DOI: 10.1021/ed078p942.

7.6.8 Supporting Information

A Collaborative Co-Curricular Undergraduate Research Experience on Sustainable Materials: Analysis of Biochar using the Boehm Titration and Spectroscopic Techniques

***Breen, R**.; Goggin, C.; J.; Holmes, J. D.; Collins, G. A Collaborative Cocurricular Undergraduate Research Experience on Sustainable Materials: Analysis of Biochar Using the Boehm Titration and Spectroscopic Techniques. ACS J. Chem. Educ. 2025, 102, 3, 1323–1332 DOI: 10.1021/acs.jchemed.4c01110*

Notes for Instructor

1. Experimental Description:
2. Sample Calculation
3. Blank Data Table Templates
4. FTIR Analysis
5. TXRF Analysis
6. Practical Considerations and Modification
7. Extension to the Experiment

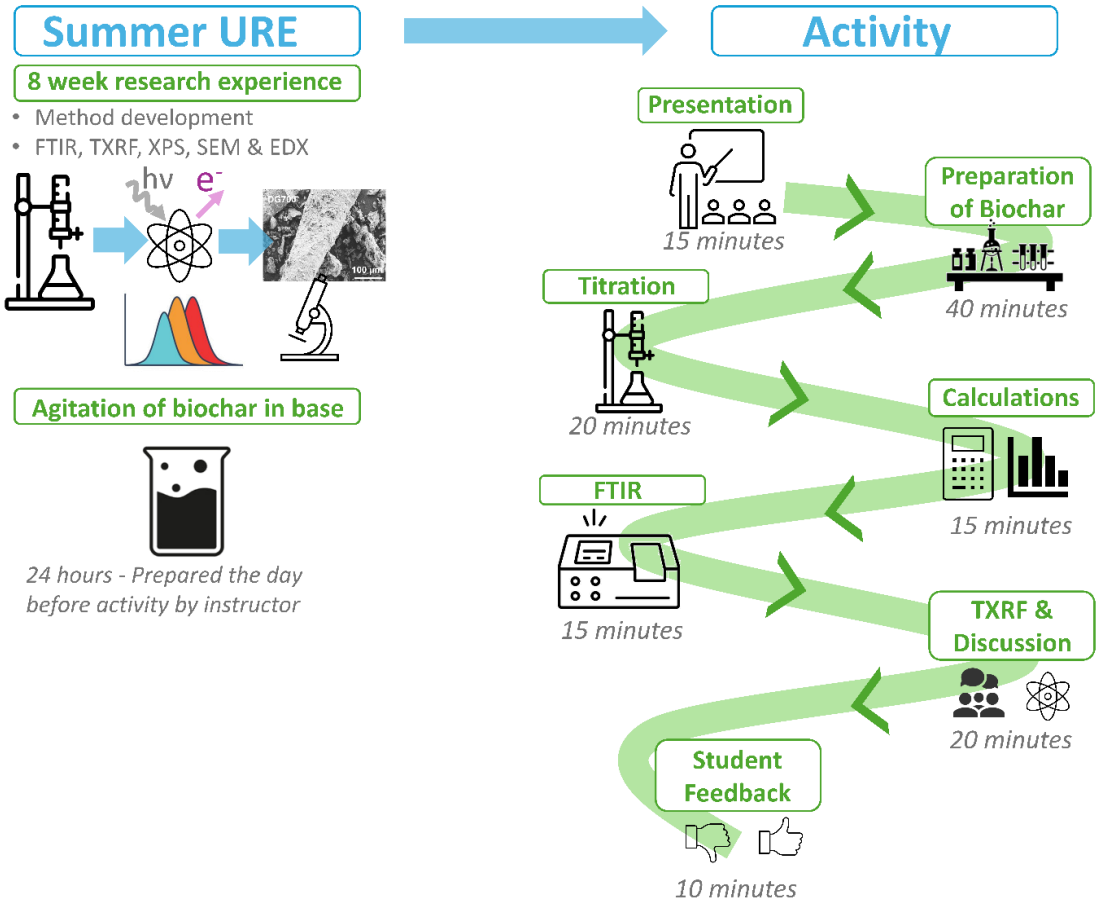


Figure S1: Class structure and flow schematic for the activity.

Experience

1. Experimental description

Hazards

This experiment presents low degree of the hazard including mild irritants and corrosives (dilute NaOH & HCl solutions). Standard safety precautions and proper PPE, lab coat, glasses and gloves should be used when performing this activity.

Boehm Preparation and Titration

1.1 Dispersion and Agitation of Biochar in Base.

This process is conducted prior to students' arrival**.** 0.75 g of biochar was added to a 100 mL jar containing 25 mL 0.05 M of NaOH, $NaHCO_3$ or Na_2CO_3. Sample dispersion was achieved through 24 h of shaking at 115 rpm. In the workshop students still completed this step of the process *i.e.* they pipetted the base and added it to dry biochar and put it on the agitator but used one of the overnight samples for their experiments.

Shaking was used as the form of agitation as high-speed magnetic stirring has been shown to disrupt the structure of the carbon surface, however a standard stirrer on a low rpm setting could also be used.[1] The screw-top jar lids were left on to avoid contamination, but loose to account for any possible gas production leading to pressure build-up. This long-period of agitation allowed for the bases to react with any surface acidic functional groups. The resulting mixture consisted of H_2O from neutralised functional groups, dissolved CO_2, and an unknown amount of unreacted base. This mixture was filtered by Buchner filtration to remove any solid carbon from the liquid fraction.

1.2 Acidification of Liquid Fraction

In this step the excess HCl reacted with any residual base in solution forming an acidic mixture. 5 mL aliquots of the filtrates from part 1 were transferred to 50 mL round bottom flasks and acidified with 0.05 M HCl to achieve a pH of 2-3 which is tested using pH paper. The amount of acid that will be required will depend on the specific biochar. It is not necessary to provide students with the volume of acid to, but for this activity the students were provided with a table specifying the volume, shown in the Table 1 in the main paper. As shown in Table 1, main paper, 15 mL of HCl was first added, followed by 5 mL aliquots of HCl. The pH of the solution was tested after each addition with pH paper and recorded in the Table 1. [2] Acidified activated carbon was used as a reference material. The resulting pH of all mixtures was between 2 and 3 which was indicative that HCl was present in excess.

1.3 Degasification of Acidified Sample

The round bottom flasks were placed in a heating mantle and refluxed for 30 minutes at 100 °C with stirring at 300 rpm.[3] This step allows for the removal of any dissolved CO_2 from the samples which

would have further acidified the samples affecting titration results. After the reflux period the flasks were sealed and left to cool to room temperature.

1.4 Titration of Degassed Sample against NaOH

Once cool, the samples were titrated against 0.05 M NaOH solution using a pH probe and capstone PASCO software. For complete accuracy, the NaOH solution can be standardised by titration with potassium hydrogen phthalate prior to titration. Sample titration curves obtained are shown in the main text. Our activity used potentiometric titrations but a standard pH procedure with an indicator such as phenolphthalein can be used as an alternative.

2. Blank Data Tables

The students were provided with the tables below to complete during the activity. AC was used as a reference and to show the students an example of the data that was complete.

Acidification tables:

	Base: NaOH				
Biochar	**AC**	**DG300**	**DG700**	**WD300**	**WD700**
Total HCl (mL)	**pH**	**pH**	**pH**	**pH**	**pH**
15	3				
20	2				
25	2				
30	2				
	Base: $NaHCO_3$				
Biochar	**AC**	**DG300**	**DG700**	**WD300**	**WD700**

Total HCl (mL)	pH	pH	pH	pH	pH
15	**3**				
20	3				
25	3				
30	3				
	Base: Na_2CO_3				
Biochar	**AC**	**DG300**	**DG700**	**WD300**	**WD700**
Total HCl (mL)	**pH**	**pH**	**pH**	**pH**	**pH**
15	8				
20	7				
25	5				
30	3				
35	3				
40	3				
45	3				
50	3				

Titration table:

Biochar Sample code	V_{NaOH} *(mL)*	V_{NaHCO_3} *(mL)*	$V_{Na_2CO_3}$ *(mL)*

3. Worked Sample Calculation for Oxygen Surface Functionalities

The students used the end point values from the titrations to calculate the content of phenolic (Ar-OH), lactonic (-COOR) and carboxylic (-COOH) groups present on the biochar surface. These were calculated according to the equations adapted from Wu *et al.*[4]

A sample calculation using the Boehm titrations conducted with results from WD300 sample is outlined below:

Results for WD300 for acidification step:

Base (25 mL of 0.05 M base added to biochar)	**Volume of 0.05 HCl (V_{HCl}) added to reach pH 2/3 (mL)**
NaOH	30
$NaHCO_3$	30
Na_2CO_3	50

Results for WD300 for titration step:

Biochar Sample	V_{NaOH} (mL)	V_{NaHCO_3} (mL)	$V_{Na_2CO_3}$ (mL)
WD300	7.3	5.6	8.4

Base: NaOH

(i) Volume of Reacted HCl, ΔV_{HCl}:

$$\Delta V_{HCl} = V_{HCl} - \frac{\Delta V_{NaOH} \cdot C_{NaOH}}{C_{HCl}}$$

$$\Delta V_{HCl} = 0.03\ L - \frac{0.0073\ L \cdot 0.05\ \text{M}}{0.05\ \text{M}}$$

$$\Delta V_{HCl} = 0.0227\ \text{L}$$

(ii) Moles NaOH, n_{NaOH}:

$$n_{NaOH} = C_{NaOH} \cdot V_{NaOH} - C_{HCl} \cdot \Delta V_{HCl}$$

$$n_{NaOH} = 0.05\ M \cdot 0.025\ \text{L} - 0.05\ M \cdot 0.0227\ \text{L}$$

$$n_{NaOH} = 1.15 \times 10^{-4}\ \text{mol}$$

Base $NaHCO_3$:

(i) Volume of Reacted HCl, ΔV_{HCl}:

$$\Delta V_{HCl} = V_{HCl} - \frac{\Delta V_{NaOH} \cdot C_{NaOH}}{C_{HCl}}$$

$$\Delta V_{HCl} = 0.03\ L - \frac{0.0056\ \text{L} \cdot 0.05\ \text{M}}{0.05\ \text{M}}$$

$$\Delta V_{HCl} = 0.0243\ \text{L}$$

(ii) Moles $NaHCO_3$, n_{NaHCO_3} :

$$n_{NaHCO_3} = C_{NaHCO_3} \cdot V_{NaHCO_3} - C_{HCl} \cdot \Delta V_{HCl}$$

$$n_{NaHCO_3} = 0.05\ \text{M} \cdot 0.025\ \text{L} - 0.05\ M \cdot 0.0243\ \text{L}$$

$$n_{NaHCO_3} = 3.25 \times 10^{-5}\ \text{mol}$$

Base Na_2CO_3:

(i) Volume of Reacted HCl, ΔV_{HCl}:

$$\Delta V_{HCl} = V_{HCl} - \frac{\Delta V_{NaOH} \cdot C_{NaOH}}{C_{HCl}}$$

$$\Delta V_{HCl} = 0.05\ \text{L} - \frac{0.0085\ \text{L} \cdot 0.05\ \text{M}}{0.05\ \text{M}}$$

$$\Delta V_{HCl} = 0.0415\ \text{L}$$

(ii) Moles Na_2CO_3, $\boldsymbol{n_{Na_2CO_3}}$:

$$n_{Na_2CO_3} = 2C_{Na_2CO_3} \cdot V_{Na_2CO_3} - C_{HCl} \cdot \Delta V_{HCl}$$

$$n_{Na_2CO_3} = 2 \cdot 0.05\ \text{M} \cdot 0.025\ \text{L} - 0.05\ M \cdot 0.0415\ \text{L}$$

$$n_{Na_2CO_3} = 4.3 \times 10^{-4}\ \text{mol}$$

Concentration of Functional Group, $\boldsymbol{C}$:

Carboxylic groups, -COOH:

$$C_{-COOH} = n_{NaHCO_3}/m$$

$$C_{-COOH} = 1.15 \times 10^{-4}\ \text{mol} / 0.75\ \text{g}$$

$$\boldsymbol{C_{-COOH} = 4.3 \times 10^{-5}\ \text{mol g}^{-1}}$$

Lactonic groups, -COOR:

$$C_{-COOR} = (n_{Na_2CO_3} - n_{NaHCO_3})/m$$

$$C_{-COOR} = (4.3 \times 10^{-4}\ \text{mol} - 3.25 \times 10^{-5}\ \text{mol})/ 0.75\ \text{g}$$

$$\boldsymbol{C_{-COOR} = 5.3 \times 10^{-4}\ \text{mol g}^{-1}}$$

Phenolic, Ar-OH

$C_{Ar-OH} = (n_{NaOH} - n_{Na_2CO_3})/m$

$C_{Ar-OH} = (1.15 \times 10^{-4}\ \text{mol} - 4.3 \times 10^{-4}\ \text{mol})/0.75\ \text{g}$

$\boldsymbol{C_{Ar-OH} = -4.2 \times 10^{-4}\ \text{mol g}^{-1}}$

4. FTIR Analysis

FTIR analysis was carried out using a Perkin Elmer Spectrum Two FT-IR Spectrometer in the range of 4000-450 cm^{-1} with a resolution of 4 and an average of 20 scans.

5. TXRF Analysis

Total reflection X-ray fluorescence spectroscopy was (TXRF) was carried out using an S2 Picofox TXRF Spectrometer with a scan time of 250 s. Absolute quantification was used to approximately quantify the inorganic components in the biochar. This quantification type is based on the measured absolute sensitivity for Ni for the instrument and is approximated by the software according to the following equation:

$$m_i = \frac{N_i \cdot S_{Ni}}{S_i \cdot s_{Ni} \cdot T \cdot I}$$

Where m_i is the absolute amount of an analysed element within the sample, N_i is the net pulse number within the measurement spectrum of the analyte, S_{Ni} is the relative sensitivity of Ni, S_i is the relative sensitivity of the analyte, s_{Ni} is the absolute sensitivity of Ni in counts ($s^{-1}ng^{-1}mA^{-1}$), T is the measurement time and I is the tube current in mA. (adapted from the Bruker S2 Picofox TXRF manual)

6. Practical Considerations and Modification to the Experiment

- A key objective in this activity was to demonstrate that the nature of the biomass feedstock has an impact on the biochar that is produced and therefore four biochar samples were used. Feedstock specific biomass can be purchased from chemical suppliers. Biochar can also be purchased in gardening and horticulture stores. If it is not possible to obtain different types of biochar the activity could be run with a single sample and pretreated with acids or bases to change the surface chemistry.
- Commercial acidified activated carbon was used a reference, and results were shown as an example. This was a helpful guide to students, however activated carbon could be used as a specimen sample and then compared with biochar sample. Another alternative if it is not possible to obtain biochar is comparing commercial activated carbon and acidified activated carbon by stirring in nitric acid overnight.
- The degassing of the biochar sample takes 30 minutes. During this period FTIR analysis and standardisation of the NaOH to be used in the titration could be carried out however this period could also be used for discussion.
- It is not possible to distinguish between the biochar samples so sample labelling at each step e.g. the Buchner funnels after filtration and beaker used for the acidification step is very important.
- The most effective method of degasification reported is direct bubbling nitrogen through the solution[3], however, for the purpose of undergraduate activity and accessibility, reflux is sufficient in this case.
- Prior to the Boehm titration, biochar can be pretreated to remove the inorganic components if desired. Pre-treating the biochar with NaOH can remove solubilisable acidic species, and then with HCl to remove solubilisable basic components. This was not carried out in the

activity as the intention was to illustrate the impact of the inorganic species on the Boehm method and engage student thinking and promote discussion on chemical analysis.

- Where a pH probe and appropriate software are not available, a standard titration method using a chemical indicator such as phenolphthalein could be used to determine the end point. An agitator was used to stir the biochar overnight, but a stirrer plate could also be used.
- TXRF was used in this experiment as it is a user friendly, benchtop instrument with fast scan speeds. It is a commonly used instrument in wastewater and soil analysis and there may be scope for borrowing the instrument from other research groups. Other chemical analysis methods of biochar sample could be used inductively coupled plasma-mass spectrometry (ICP-MS).

The final discussion and TXRF analysis were carried out in parallel. In the initial presentation, the students were shown slides about biochar from different sources, highlighting non-carbon elements that may be present in such samples. During the discussion, the students were asked to reflect on this and propose some elements they may think come from wood and digestate-derived biochars. In this time the concept of TXRF analysis was introduced to screen for inorganic components in the samples. While the TXRF scan was running, the URE and doctoral student presented XPS and EDX findings they had collected over the summer, showing the UG students the elemental composition of the digestate biochars, and demonstrating a variety of techniques that can be used to characterise a biomass-derived material.

A schematic of the class structure and flow with time approximations is shown below in **Figure S1**.

Extension to the Experiment

One extension to this activity that is particularly valuable would be to include error analysis. Error analysis is not always considered in undergraduate practical laboratory. In a research setting, these

titrations should be carried out in at least duplicates or triplicates for accuracy and to allow for error. This was highlighted to the students during the workshop but not done, however if the activity was reduced to one biochar sample, this could be done. An error analysis was carried out by the undergraduate undertaking the URE and is described below. The average values and standard deviations for the titrations can be calculated as follows:

Average value, $\bar{n}$:

$$\bar{n} = \frac{n_1 + n_2}{2}$$

Where n_1 and n_2 are the moles of base calculated from the end point from titrations 1 and 2, respectively.

Standard Deviation, σ_n:

$$\sigma_n = \sqrt{\frac{(n_1 - \bar{n})^2 - (n_2 - \bar{n})^2}{2 - 1}}$$

Concentration of Functional Groups, *C*:

$$C_{-COOH} = \bar{n}_{NaHCO_3} /m$$

$$C_{-COOR} = (\bar{n}_{Na_2CO_3} - \bar{n}_{NaHCO_3}) /m$$

$$C_{Ar-OH} = (\bar{n}_{NaOH} - \bar{n}_{Na_2CO_3}) /m$$

Where *m* is the mass of carbon used in the dispersion step.

Standard Deviation of Functional Groups, *σ*:

$$\sigma_{-COOH} = \frac{\sigma_{n_{NaHCO_3}}}{m}$$

$$\sigma_{-COOR} = \frac{\sqrt{\sigma^2_{n_{NaHCO_3}} + \sigma^2_{n_{Na_2CO_3}}}}{m}$$

$$\sigma_{Ar-OH} = \frac{\sqrt{\sigma^2_{n_{NaOH}} + \sigma^2_{n_{Na_2CO_3}}}}{m}$$

Supplementary Data:

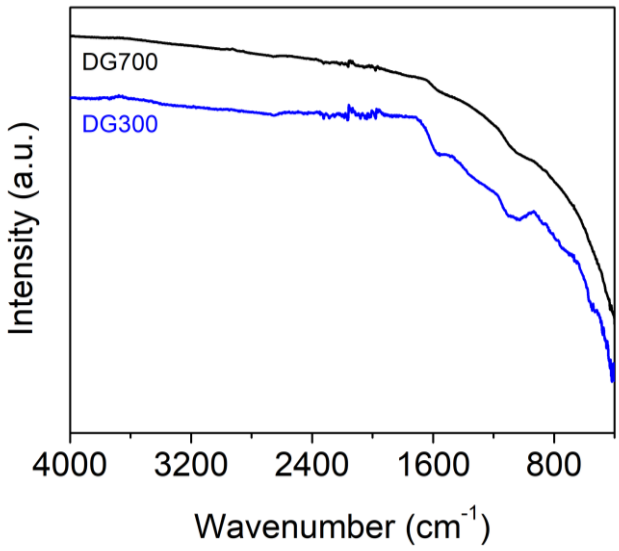


Figure S2: FTIR analysis of the digestate biochar prepared at 300 °C and 700 °C.

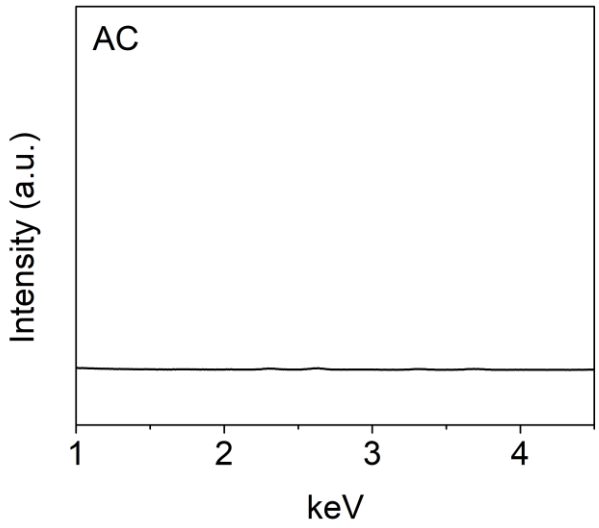


Figure S3: Reference TXRF of AC.

References:

(1) Oickle, A. M.; Goertzen, S. L.; Hopper, K. R.; Abdalla, Y. O.; Andreas, H. A. Standardization of the Boehm titration: Part II. Method of agitation, effect of filtering and dilute titrant. *Carbon* **2010**, *48* (12), 3313-3322. DOI: https://doi.org/10.1016/j.carbon.2010.05.004.
(2) Ren, H.; Cunha, E.; Sun, Q.; Li, Z.; Kinloch, I. A.; Young, R. J.; Fan, Z. Surface functionality analysis by Boehm titration of graphene nanoplatelets functionalized via a solvent-free cycloaddition reaction. *Nanoscale Advances* **2019**, *1* (4), 1432-1441, 10.1039/C8NA00280K. DOI: 10.1039/C8NA00280K.
(3) Goertzen, S. L.; Thériault, K. D.; Oickle, A. M.; Tarasuk, A. C.; Andreas, H. A. Standardization of the Boehm titration. Part I. CO2 expulsion and endpoint determination. *Carbon* **2010**, *48* (4), 1252-1261. DOI: https://doi.org/10.1016/j.carbon.2009.11.050.
(4) Wu, H.; Lu, W.; Chen, Y.; Zhang, P.; Cheng, X. Application of Boehm Titration for the Quantitative Measurement of Soot Oxygen Functional Groups. *Energy & Fuels* **2020**, *34* (6), 7363-7372. DOI: 10.1021/acs.energyfuels.0c00904.

Chapter 8

Conclusions and Outlook

8.1 Conclusions and Outlook

The aim of this work was to design and optimise heterogeneous catalysts for the chemical recycling of plastic waste. Emphasis was placed on the optimisation of each catalyst system including rationale for catalyst design and extensive catalyst characterisation to form a holistic understanding of each reaction system. This work focused on the conversion of low-quality plastic waste to higher value commodity chemicals. The main motivation for the doctoral work presented in this thesis is that current plastic waste management strategies such as incineration and landfill are zero-yield disposal methods, while mechanical recycling leads to a lower quality product. Chemical recycling promotes a circular economy by recovering useful chemicals and materials from low quality waste streams.

Two main plastics were focused on in this thesis: polyethylene terephthalate (PET) and low-density polyethylene (LDPE). Chapter 3 and Chapter 4 discuss PET depolymerisation, while Chapters 5, 6 and 7 focus on LDPE depolymerisation. Chapter 3 and 4 were motivated by extensive literature on efficient homogeneous catalysts for PET depolymerisation, contrasted with the limited reports available on heterogeneous catalyst design for PET glycolysis. Chapter 3 discusses the design of ligand-aided Fe_2O_3 nanoparticles as heterogeneous catalysts for the glycolysis of PET, which is published in ACS Sustainable Chemistry and Engineering.[1] In this work, five ligands were evaluated; NH_2, $NHNH_2$, NH_2SB, $NHNH_2SB$ and a pincer ligand (where SB is Schiff base). These ligands were grafted on mesoporous cellular foam SiO_2 as a high-surface area support (ligand-only catalysts), and Fe^{3+} was immobilised via precipitation (NH_4OH) (metal ion immobilised catalysts). From here, nanoparticles were prepared two ways; calcination at 450 °C and chemical reduction using $NaBH_4$. Calcination resulted in volatisation of the organic ligands, while chemical reduction preserved the organic ligands. The nanoparticle catalysts prepared by chemical reduction resulted in the highest conversion of PET to the monomer bis(2 hydroxyethyl terephthalate) (BHET) which was attributed to a dual catalytic mechanism from the Lewis

base properties of the N-rich ligands and the Lewis acid properties of the Fe_2O_3 nanoparticles which simultaneously activate the PET and EG to enhance reaction efficiency. One unexpected result from this work is that the ligand-modified SiO_2 exhibited moderate catalytic activity. This motivated the catalyst design for Chapter 4: guanidine functionalised porous SiO_2 as heterogeneous catalysts for microwave depolymerisation of PET and PLA, published in RSC Sustainability.[2] In this chapter, three guanidine ligands were immobilised on porous SiO_2 to form heterogeneous analogues which were evaluated for the glycolysis of PET to BHET and the methanolysis of PLA to methyl lactate (MeLa). Implementation of microwave heating was demonstrated in this chapter for the first time in this thesis, and it was found that reaction times were dramatically shortened, from 3 h to 30 min for PET glycolysis and 72 h to 30 min for the methanolysis of PLA to MeLa. The dicyanadiamide (DCD) ligand achieved the highest PET conversion and BHET yield which was attributed to the N-rich sites on this ligand increasing its Lewis basicity and therefore its ability to nucleophilically activate ethylene glycol. The experimental results were supported with density functional theory (DFT) which was carried out as part of a collaboration with Dr Pareras and Prof. Rimola of the University of Barcelona. An alternative PET glycolysis pathway was also carried out by swapping out ethylene glycol with 1,4 butanediol to yield bis (4-hydroxybutyl) terephthalate (BHBT), a valuable precursor for biodegradable plastic. The success of this reaction was particularly notable, as it was first attempted with an Fe-based catalyst. The Fe, acting as a Lewis acid, catalysed an unfavourable ring-closing side reaction to produce tetrahydrofuran (THF), underscoring the importance of rational catalyst design. The effect of catalyst support using MW-assisted heating was also evaluated in this chapter, exchanging the SiO_2 for activated carbon (AC), and it was found to improve the activity of the DCG ligand from a mass loss PET of 50 % on SiO_2 to 100 % on AC under MW irradiation. This was attributed to the superior MW-absorbing abilities of AC over SiO_2, creating hot spots and accelerating the reaction. Overall, this chapter demonstrated the design and synthesis of heterogeneous metal-free multifunctional catalysts for the conversion of PET to two different valuable monomers, and PLA to a useful green solvent. Continuing this work, it is imperative that the optimisation of scaled-up reactions is further developed

to shift chemical recycling from lab-scale to industry scale. The implementation of microwave heating and heterogeneous catalysts has the potential to create energy efficient processes with recoverable and recyclable catalysts and systems with no catalyst contamination in the product. Polyester glycolysis is particularly important given the fast fashion industry's heavy reliance on synthetic polyester. As this sector continues to expand, global polyester waste increases, making the scale-up of this process crucial. Polyester depolymerisation is currently stuck in pilot scale due to affordability and accessibility issues. A report by Systemiq[3] identifies 10 levers that have been proposed to achieve polyester recycling scale-up across industry, which focus on designing for recyclability, improving sorting and collection, advancing recycling technologies, scaling infrastructure, fostering collaboration, ensuring quality, making recycling economically viable, engaging consumers, and supporting with policies. The goal in the EU is to increase polyester depolymerisation capacity 10-fold by 2035 which would lower greenhouse gas emissions by 55 % when compared with virgin polyester production.

The motivation for the subsequent chapters of this thesis resulted from the observation that PET was being widely researched, while the literature lacked research outputs on the chemical recycling of polyolefins. Additionally, figures stated that the relative production rates of polyolefins such as LDPE (19 %) were significantly higher than PET (11 %), while global recycling rates of LDPE (3 %) were much lower than PET (55 %). The chemical inertness of polyolefins makes them a particularly challenging group of plastics to chemically depolymerise in closed-loop systems such as polyester glycolysis. Many literature reports on the chemical recycling of polyolefins include energy intensive processes such as high temperature pyrolysis (> 300 °C) or the use of hazardous reagents such as HNO_3 or pressurised O_2.[4, 5] The aim for this work was to develop a milder upcycling route for polyolefins. The development of a chemical recycling route for polyolefins is reported in Chapter 5: "Method Development**:** Heterogeneous Catalysts for Fenton Oxidation of LDPE". In this chapter, two catalyst groups were established: metal oxide composite catalysts and carbon-based catalysts. Each group was evaluated as heterogeneous Fenton-type catalysts for LDPE oxidation to yield carboxylic acid products. Carbon-based catalysts were synthesised via two ionic liquid (IL) precursors, $FeCl_3$ and activated carbon to yield

a heterogeneous Fe on nitrogen/oxygen doped carbon support. Surprisingly, the different IL precursors gave way to significant physiochemical differences in the catalysts. The dicyanamide-containing precursor (IL-CN), rich in N sites, led to a high surface area carbon material with regions of immobilised iron oxide structures attributed to N anchor sites. The acetate-containing precursor (IL-OAc) led to the formation of multiwalled carbon nanotube (MWCNT) structures containing well dispersed Fe^0 throughout. The mechanism for this was thought to proceed via a carbothermal reduction mechanism upon thermal decomposition of OAc to CO, with the formation of Fe^0 acting as a nucleation site for the growth of MWCNT. The IL-CN catalyst outperformed the IL-CN catalyst, which was attributed to well-dispersed Fe^0 as well as O-containing sites. Metal-oxide composites were also selected as a group due to the well-reported synergistic effect of bimetallic Fenton systems. Coupling Fe with another metal can stabilise the Fe and aid with ion regeneration in the Fenton reaction. This effect was observed across all three composite catalysts: Fe_2O_3-CuO, Fe_2O_3-CeO_2 and Fe_2O_3-BiOCl which all outperformed Fe_2O_3 in conversion of LDPE to acid products. This result was attributed to a synergistic and stabilisation effect arising from the bimetallic system. Another important aspect evaluated for these catalysts was catalyst stability, specifically metal leaching into the product mixture after the reaction. Visible Cu and Fe leaching was observed for the CuO catalyst, while some Fe leaching was observed in the Fe_2O_3-BiOCl catalyst. No visible leaching was observed for the Fe_2O_3-CeO_2 which also achieved the highest mass loss LDPE and acid yield. This catalyst system was subsequently expanded upon which led to the development of Chapter 6. The carbon-based catalysts were not pursued further due to energy-intensive synthesis; however, it motivated the use of biochar as a Fenton-type catalyst in Chapter 7. While the literature was limited on Fenton catalysts for polyethylene oxidation, the purpose of this chapter was to provide an overview of different Fenton-type catalyst systems and their efficacy for oxidative conversion of polyethylene to carboxylic acid products.

In Chapter 6, the Fe_2O_3-CeO_2 catalyst was synthesised via coprecipitation to yield a Fe-CeO_2 solid solution to further enhance catalyst stability. This work is published in RSC Catalysis Science and Technology.[6] The catalyst was synthesised in 3 ratios of Fe/Ce: 2:1, 1:1 and 1:2. A synergistic effect was

observed in all the solid solution catalysts compared with Fe_2O_3 and CeO_2 which was attributed to enhanced stability as well as the presence of defect sites, O vacancies, and increased Ce^{3+} sites. The best performing catalyst was the Fe-CeO_2 1:1 achieving a 90 % mass loss LDPE and 71 % acid yield at pH 7 and 1 wt. % catalyst loading. The efficacy of the catalyst at pH7 was significant, as it removes the need for the addition of acid to adjust the pH. The catalyst also showed excellent recyclability which was attributed to its heterogeneous nature and structural stability. This chapter demonstrated the successful conversion of LDPE to carboxylic acids at relatively mild conditions, and focused on optimising yield of valuable acids, contrasting with other literature reports on Fenton oxidation of plastic where the aim is complete oxidation to gaseous products. The LDPE mass was also scaled up from 0.3 g to 0.5 g in this work, and future work would involve optimising scale-up of this process as well as carrying out technoeconomic assessments. Additionally, the industrial microwave reactor system used in this work did not allow for reaction probing in situ. To fully understand the complex reaction mechanism of heterogeneous Fenton-type catalysts with H_2O_2 when subject to an energy source such as MW-irradiation, UV light or heat, in-situ probing such as Raman or XPS would be beneficial as well as radical probe experiments such as the use of electron spin resonance (ESR) spectroscopy to identify the dominant reactive oxygen species.

Association with AMBER led to a collaboration with the school of physics in Trinity College Dublin investigating the synthesis of 2D Fe-CeO_2, from the Fe-CeO_2 solid solution synthesised in Chapter 5, via cryogenic exfoliation method and is presented in Appendix 6. The final product was a highly defective, porous, and amorphous Fe-CeO_2 featuring quasi-2D nanoflake structures. Cryogenic exfoliation can successfully yield 2D structures from a non-layered material without using harsh chemicals for etching, making the process more environmentally friendly. The resulting material has potential applications in catalytic oxidation processes including OER or water-gas shift reactions. Evaluating their performance in such areas will be a part of the future work for this project. They may be particularly advantageous as an electrode material for the electrochemical upcycling of plastic waste into value-added products due to enhanced defect sites and amorphous nature.[7]

The progression from metal-based to metal-free catalysts for PET glycolysis at the beginning of the thesis is what motivated the development of Chapter 7. The aim for Chapter 7 was to develop a metal-free catalyst for the Fenton-type oxidation of LDPE. Metal-free Fenton catalysts reported in the literature are typically graphene oxide (GO) analogues.[8] The hazardous synthesis associated with GO made the use of this catalyst unfavourable, however, evaluation of the literature showed increasing interest in biochar as a sustainable carbon material. This led to the evaluation of four different biochar types for their activity as Fenton-type catalysts for the chemical upcycling of LDPE, outlined in Chapter 7. Biochar from a grain source (DG) and a wood source (WB) were used synthesised at 300 °C and 700 °C resulting in four catalysts (DG300, DG700, WB300, WB700). EDX and XRD analysis identified inorganic contaminants such as N, P Na and K in the grain-sourced biochar arising from soil mineral content. Raman and XRD identified the wood-sourced biochar pyrolysed at 700 °C to have achieved the highest level of graphitisation owing to a lignin-rich structure. The wood-sourced biochar pyrolysed at 300 °C had the highest O content which was observed to decrease at 700 °C due to volatisation. The WB300 catalyst achieved the highest mass loss of LDPE and acid yield, which was attributed to the higher O content and some degree of graphitisation, which can form dual reaction centres that can result in a Fenton-type activation of H_2O_2. While mixtures of carboxylic acid products are valuable, the question remained about challenges associated with separation of complex mixtures of low molecular weight, water soluble carboxylic acids. This led to the motivation for a collaboration with the School of Engineering in UCC to explore the use of anaerobic digestion as a means of bioconversion of the carboxylic acid mixtures to biomethane. The use of anaerobic digestion was suggested due to similarities in the carboxylic acid mixtures to volatile fatty acids (VFAs) that are often reported as intermediate products in the bioconversion of biomass to biomethane via anaerobic digestion. Furthermore, yielding methane as the product allows for a simplified product stream for which there are already well-established technologies. For the anaerobic digestion tests, the WB300 and DG300 acid product mixtures were tested in parallel with the Fe-CeO_2 product mixture from Chapter 6. Biomethane yields were statistically similar for all catalysts tested, showing that biochar-based metal-

free catalysts can match the performance of metal-based ones in downstream bioconversion. Mass and energy balances identified the WB300 catalyst as the most energy-efficient (9 %), with major losses arising from heat in the Fenton oxidation step. Integrating industrial heat recovery could raise efficiency to ~49 %, a well-established practice in industry. Beyond quantifying efficiency, these balances provide a framework for process optimisation and play a crucial role in translating lab-scale catalyst performance into scalable, circular economy applications - particularly in industries with high thermal energy demand or biomass availability, such as distilleries, breweries, and agri-food processing. Going forward, the wider application of mass and energy balances will be essential to enhance the viability of small-scale catalytic plastic depolymerisation processes as they are scaled up for real-world use. Achieving this transition will depend on close collaboration with engineers, whose expertise in process design, heat integration, and scale-up can bridge the gap between experimental feasibility and industrial implementation.

Appendix 7 presents a publication arising from work related to Chapter 7, centred on the characterisation of biochar. This project was conducted in collaboration with a student undertaking an Undergraduate Research Experience during a summer placement. The work led to a sustainable materials workshop for undergraduate students and was subsequently published as an activity in ACS Journal of Chemical Education. This work uses multiple approaches to characterise the surface chemistry of biochar. Additional characterisation such as TXRF and EDX highlighted the complex chemistry of the biochar structure and provides context for interpreting unusual Boehm titration results. This raised the need to critically evaluate the Boehm method, which was originally developed for pure carbons, when applying it to biochar. The purpose of this work was to promote peer-led learning and to develop a cocurricular experience for students, building laboratory and research skills. Working with undergraduate students through summer placements and workshops is a highly valuable part of the PhD program, as it helps develop stronger scientific communication skills and transfer laboratory skills.

In conclusion, this work has demonstrated how advances in catalytic depolymerisation can contribute to the development of more sustainable strategies for managing plastic waste. Importantly, these findings reinforce the role of chemical recycling in diverting plastics from landfill and incineration and enabling their integration into a circular economy through the upcycling of waste into higher-value products. Continued interdisciplinary collaboration will be essential to bridge the gap between optimisation and implementation, ultimately making chemical recycling a viable component of the global response to plastic pollution. Translating these findings from laboratory to real-world applications will require careful scale-up, process optimisation, and collaboration with industry to ensure technical feasibility and economic viability.

8.2 References:

(1) Casey, É.; Breen, R.; Gómez, J. S.; Kentgens, A. P. M.; Pareras, G.; Rimola, A.; Holmes, J. D.; Collins, G. Ligand-Aided Glycolysis of PET Using Functionalized Silica-Supported Fe2O3 Nanoparticles. *ACS Sustainable Chemistry & Engineering* **2023**, *11* (43), 15544-15555. DOI: 10.1021/acssuschemeng.3c03585.
(2) Casey, É.; Breen, R.; Pareras, G.; Rimola, A.; Holmes, J. D.; Collins, G. Guanidine functionalized porous SiO2 as heterogeneous catalysts for microwave depolymerization of PET and PLA. *RSC Sustainability* **2024**, *2* (4), 1040-1051, 10.1039/D3SU00425B. DOI: 10.1039/D3SU00425B.
(3) Systemiq. *The Textile Recycling Breakthrough: Why policy must lead the scale-up of polyester recycling in Europe.*; 2025. https://www.systemiq.earth/downloads/Systemiq-The_Textile_Recycling_Breakthrough-Why_policy_must_lead_the_scale-up_of_polyester_recycling_in_Europe-EN.pdf (accessed 11/08/2025).
(4) Smak, T. J.; de Peinder, P.; Van der Waal, J. C.; Altink, R.; Vollmer, I.; Weckhuysen, B. M. Oxidative Conversion of Polyethylene Towards Di-Carboxylic Acids: A Multi-Analytical Approach. *ChemSusChem* **2024**, *17* (7), e202301198. DOI: https://doi.org/10.1002/cssc.202301198 (acccessed 2024/08/30).
(5) Bäckström, E.; Odelius, K.; Hakkarainen, M. Trash to Treasure: Microwave-Assisted Conversion of Polyethylene to Functional Chemicals. *Industrial & Engineering Chemistry Research* **2017**, *56* (50), 14814-14821. DOI: 10.1021/acs.iecr.7b04091.
(6) Breen, R.; Holmes, J. D.; Collins, G. Heterogeneous Fenton-type oxidative degradation of low-density polyethylene to valuable acid products using a nanostructured Fe–CeO2 solid solution catalyst. *Catalysis Science & Technology* **2025**, 10.1039/D4CY01384K. DOI: 10.1039/D4CY01384K.
(7) Kim, J.; Masoumilari, S.; Park, Y.; Lee, S.; Kyung, D.; Masoumi, Z. Advancements in the Electrochemical Upcycling of Waste Plastics into High-Value Products. In *Crystals*, 2025; Vol. 15.
(8) Espinosa, J. C.; Navalón, S.; Primo, A.; Moral, M.; Sanz, J. F.; Álvaro, M.; García, H. Graphenes as Efficient Metal-Free Fenton Catalysts. *Chemistry – A European Journal* **2015**, *21* (34), 11966-11971. DOI: https://doi.org/10.1002/chem.201501533 (acccessed 2024/12/09). Liao, Q.; Wang, D.; Ke, C.; Zhang, Y.; Han, Q.; Zhang, Y.; Xi, K. Metal-free Fenton-like photocatalysts based on covalent organic frameworks. *Applied Catalysis B: Environmental* **2021**, *298*, 120548. DOI: https://doi.org/10.1016/j.apcatb.2021.120548. Oliveira, W. L.; de Oliveira, E. F.; do Carmo Batista, W. V. F.; Mourão, H. A. J. L.; Mendes Pires, M. J.; Coelho, R. M.; Atta Diab, G. A.; Teixeira, I. F.; Marques, G.; Mastelaro, V. R.; et al. A metal-free catalyst based on g-C3N4 functionalized with cyamelurate-like groups: Catalytic properties and mechanism of a new heterogeneous Fenton-like catalyst. *Carbon* **2023**, *214*, 118366. DOI: https://doi.org/10.1016/j.carbon.2023.118366.